Mathematical Engineering

Hassan Gomaa

Modeling with Knowledge and Data

Concepts and Applications for Engineers

Springer

Mathematical Engineering

Series Editors
Bernhard Weigand
Institute of Aerospace Thermodynamics, University of Stuttgart, Stuttgart, Germany

Jan-Philip Schmidt
Universität of Heidelberg, Heidelberg, Germany

Advisory Editors
Günter Brenn
Institut für Strömungslehre und Wärmeübertragung, TU Graz, Graz, Austria

David Katoshevski
Ben-Gurion University of the Negev, Beer-Sheva, Israel

Jean Levine
CAS-Mathematiques et Systemes, MINES-ParsTech, Fontainebleau, France

Jörg Schröder
Institute of Mechanics, University of Duisburg-Essen, Essen, Germany

Gabriel Wittum
Goethe-University Frankfurt am Main, Frankfurt am Main, Germany

Bassam Younis

Civil and Environmental Engineering, University of California, Davis, Davis, USA

Today, the development of high-tech systems is unthinkable without mathematical modeling and analysis of system behavior. As such, many fields in the modern engineering sciences (e.g. control engineering, communications engineering, mechanical engineering, and robotics) call for sophisticated mathematical methods in order to solve the tasks at hand.

The series Mathematical Engineering presents new or heretofore little-known methods to support engineers in finding suitable answers to their questions, presenting those methods in such manner as to make them ideally comprehensible and applicable in practice.

Therefore, the primary focus is—without neglecting mathematical accuracy—on comprehensibility and real-world applicability.

To submit a proposal or request further information, please use the PDF Proposal Form or contact directly: Dr. Thomas Ditzinger (thomas.ditzinger@springer.com)

Indexed by SCOPUS, zbMATH, SCImago.

Hassan Gomaa

Modeling with Knowledge and Data
Concepts and Applications for Engineers

Springer

Hassan Gomaa
Strategic Projects Co-Innovation, Cognite, Oslo, Norway

ISSN 2192-4732 e-ISSN 2192-4740
Mathematical Engineering
ISBN 978-3-658-50678-0 e-ISBN 978-3-658-50679-7
https://doi.org/10.1007/978-3-658-50679-7

© The Editor(s) (if applicable) and The Author(s), under exclusive license to Springer Nature Switzerland AG 2026

This work is subject to copyright. All rights are solely and exclusively licensed by the Publisher, whether the whole or part of the material is concerned, specifically the rights of translation, reprinting, reuse of illustrations, recitation, broadcasting, reproduction on microfilms or in any other physical way, and transmission or information storage and retrieval, electronic adaptation, computer software, or by similar or dissimilar methodology now known or hereafter developed. Unless otherwise expressly agreed by the Publisher in writing, the Publisher does not authorise use or reproduction of all or any part of this work in any manner for the purpose of training, fine-tuning, evaluating, or developing artificial intelligence models, technologies, or systems. In accordance with Article 4(3) of the EU Directive 2019/790 on copyright and related rights in the Digital Single Market, the Publisher expressly reserves all rights with respect to this work under the text and data mining exception of the directive.

The use of general descriptive names, registered names, trademarks, service marks, etc. in this publication does not imply, even in the absence of a specific statement, that such names are exempt from the

relevant protective laws and regulations and therefore free for general use.

The publisher, the authors and the editors are safe to assume that the advice and information in this book are believed to be true and accurate at the date of publication. Neither the publisher nor the authors or the editors give a warranty, expressed or implied, with respect to the material contained herein or for any errors or omissions that may have been made. The publisher remains neutral with regard to jurisdictional claims in published maps and institutional affiliations.

This Springer imprint is published by the registered company Springer Fachmedien Wiesbaden GmbH, part of Springer Nature.
The registered company address is: Abraham-Lincoln-Str. 46, 65189 Wiesbaden, Germany

To my wife Amanda, with all my love,
and in loving memory of my father,
Prof. Dr. Saad Gomaa

Preface

The material in this book evolved from lectures on *Data Driven Modeling and Machine Learning* and *Dimensional Analysis and Similitude Theory*, which I taught over the past decade to aerospace engineering students in the final stages of their master's studies. Both courses touch on the broader theme of mathematical modeling and emphasize the value of combining physical reasoning with data driven methods to build models that are both practical and meaningful. The interplay between first principles and data gradually emerged as the central thread, and this balance forms the backbone of the present work.

Engineering disciplines are traditionally grounded in analytical methods. Curricula emphasize first principles, conservation laws, and mathematical models as the basis for design and analysis. At the same time, engineering practice relies heavily on data from experiments, operational measurements, and numerical simulations. While resources on physical modeling and machine learning are widely available, guidance on integrating these perspectives into coherent models for engineering applications remains rather limited.

In my own research and industrial work, particularly in turbomachinery engineering and with industrial data, I have often faced the challenge of developing or applying models that bridge these two worlds, combining first-principle knowledge with data. A system can rarely be described entirely from first principles, and data alone is seldom sufficient to capture the behavior of industrial systems in a meaningful and interpretable way. In practice, hybrid models that combine physics and data often become essential. At the same time, they raise important questions: how much physics should be retained, how should data be integrated, and how can we ensure that the resulting models remain useful, reliable, and generalizable? These questions provided the motivation for this book.

The book is intended for graduate students, early stage researchers, and practitioners engaged in the modeling of physical systems,

particularly in applied and industrial contexts. The focus lies at the intersection of mathematical modeling in thermo-fluid systems, including fluid mechanics, multiphase flows, heat transfer, and turbomachinery, and classical machine learning. Rather than serving as a comprehensive reference in any single area, the book offers a practical entry point into combining physical insight with data driven reasoning. The goal is to show how models can be both interpretable and predictive, firmly grounded in physics yet responsive to the realities of imperfect data. At the same time, they should benefit from the generalisability that physics based reasoning makes possible.

The book is organized into three parts. After an introduction to the foundations of modeling, Part I develops the physical background with a focus on thermo-fluid systems, starting from dimensional analysis, progressing through governing equations, simplifications, and canonical cases that often serve as reference solutions. Part II shifts the perspective to uncertainty and data. Here, probability theory, applied statistics, and classical machine learning are presented with an emphasis on the needs of engineers, who often have strong calculus backgrounds but less exposure to statistical reasoning. Part III brings knowledge and data together in practice. It first considers self-contained processes, where variables and boundary conditions can be well defined, and then addresses complex industrial systems, where operational factors, uneven data, and changing environments introduce additional challenges.

Many people have supported me in bringing this book to completion. I am especially grateful to Prof. Dr.-Ing. habil. Bernhard Weigand, who provided me with the opportunity to continue teaching at the University of Stuttgart and to remain engaged with curious and motivated students. His mentorship during my research years and beyond has had a profound impact on my life, and his encouragement greatly supported me in completing this book. I also thank Hannes Mandler, my discussion partner throughout our joint lecture, whose research work provided the basis for the example on eddy viscosity turbulence modeling in the section, and who contributed many

valuable comments on the manuscript. My thanks also go to Markus Lempke and Norbert Roth, who have been thoughtful discussion partners over many years, and to Aleksandra Knödelseder, whose careful notes on the chapter were greatly appreciated. I am very grateful for the excellent cooperation with Springer during the preparation of this manuscript. Finally, I owe heartfelt thanks to my family for their patience, understanding, and constant support, which made the completion of this book possible.

I hope that readers will find the concepts presented in this book useful, informative, and applicable in their own work. If you wish to share your thoughts, comments, or critiques, I would be glad to hear from you at *kdml.gomaa@gmail.com*.

Hassan Gomaa
Oslo, Norway
September 2025

Competing Interests The author has no competing interests to declare that are relevant to the content of this manuscript.

Symbols

Physical Symbols

Symbol	Description	Unit
A	area/cross-sectional area	m^2
A^*	critical (throat) area	m^2
$\mathbf{A}$	feature/design matrix	–
a	speed of sound	m/s
a_s	specific surface area	$\mathrm{m}^2/\mathrm{m}^3$
c	absolute velocity (turbomachinery)	m/s
c_m	meridional velocity (turbomachinery)	m/s
c_θ	tangential component of c (turbomachinery)	m/s
c_p	specific heat at constant pressure	J/(kg K)
c_v	specific heat at constant volume	J/(kg K)
d	pipe diameter	m
d_h	hydraulic diameter ($4A/P$)	m
D	characteristic length/diameter	m
D	sphere diameter ($2R$)	m
E	total internal energy	J
E_{kin}	kinetic energy	J
E_{pot}	potential energy	J
E_{tot}	total mechanical energy	J
$\dot{E}_{\mathrm{diss}}$	total dissipation rate	W
e	specific internal energy	J/kg
$\mathbf{F}$	external force	N
F_D	drag force	N
f	characteristic frequency	1/s
f	Darcy friction factor	–
f_F	Fanning friction factor ($= f/4$)	–

Symbol	Description	Unit
$\mathbf{f}$	body force per unit mass	$\mathrm{m/s^2}$
$\mathbf{f}$	body force per unit volume	$\mathrm{N/m^3}$
g	gravitational acceleration	$\mathrm{m/s^2}$
H	hydraulic head	m
H	enthalpy	J
h	specific enthalpy	J/kg
h_t	total (stagnation) enthalpy	J/kg
h	convective heat transfer coefficient	$\mathrm{W/(m^2\,K)}$
h_v	volumetric heat transfer coefficient	$\mathrm{W/(m^3\,K)}$
I	electric current (SI base)	A
J	luminous intensity (SI base)	cd
J_1, J_2, J_3	strain-rate invariants	–
k	thermal conductivity	W/(m K)
k_t	turbulent kinetic energy	$\mathrm{m^2/s^2}$
K	bulk modulus ($= 1/\kappa_T$)	Pa
L	length (SI base)	m
L^+	dimensionless entrance length l_e/d_h	–
$\mathscr{L}$	characteristic length scale	m
ℓ	length/pipe length/pendulum length	m
$\ell_1, \ell_2, \cdots$	geometry length scales	m
ℓ_m	mixing length	m
m	mass	kg
m	number of observations	–
$\dot{m}$	mass flow rate	kg/s
M	mass (SI base)	kg
M	molar mass	kg/kmol
n	rotational speed (rev/time)	rev/min
n	number of samples/trials	–
p	pressure	Pa

Symbol	Description	Unit
p_a	ambient (back) pressure	Pa
p_e	nozzle exit static pressure	Pa
p_{in}	inlet static pressure	Pa
p_{out}	outlet static pressure	Pa
p_t	total (stagnation) pressure	Pa
p^*	critical pressure	Pa
p_∞	free-stream/ambient pressure	Pa
P	power/shaft power	W
P	probability measure	–
P_k	turbulence production rate	m^2/s^3
q	specific heat (heat per unit mass)	J/kg
Q	volumetric flow rate	m^3/s
Q	heat	J
$\dot{q}_v$	volumetric heat transfer rate	W/m^3
$\dot{q}_w$	wall heat flux	W/m^2
$\dot{Q}$	heat transfer into control volume	W
r	pipe radius	m
r	radial coordinate	m
$\mathscr{R}$	universal gas constant	J/(mol K)
R	specific gas constant	J/(kg K)
R	sphere radius	m
R_1, R_2	principal curvature radii	m
s	streamline coordinate/arc length	m
s	specific entropy	J/(kg K)
S	entropy	J/K
$\mathbf{S}$	strain-rate tensor	1/s
T	temperature	K
T	oscillation period	s
T	time (SI base)	s

Symbol	Description	Unit
T^*	critical static temperature	K
T_t	total (stagnation) temperature	K
T_∞	free-stream/bulk temperature	K
T_w	wall temperature	K
$\mathbf{T}$	total stress tensor	Pa
$\mathbf{t}$	tangent unit vector	–
$\boldsymbol{\tau}$	viscous stress tensor	Pa
τ	torque (turbomachinery)	N m
τ	time/characteristic timescale	s
τ_η	Kolmogorov time scale	s
τ_w	wall shear stress	Pa
u	velocity	m/s
$\mathbf{u}$	velocity vector	m/s
$\dot{\mathbf{u}}$	acceleration	$\mathrm{m/s^2}$
u^*	critical velocity (throat)	m/s
u_η	Kolmogorov velocity scale	m/s
u_∞	free-stream velocity	m/s
u_τ	friction velocity	m/s
u_x, u_r, u_φ	cylindrical velocity components	m/s
u_r, u_θ	radial/polar velocities (sphere)	m/s
U	blade speed ($U = \Omega r$)	m/s
$\mathscr{U}$	characteristic velocity scale	m/s
v	specific volume ($= 1/\rho$)	$\mathrm{m^3/kg}$
v	wall-normal velocity component	m/s
V	volume	$\mathrm{m^3}$
w	relative velocity (turbomachinery)	m/s
w_θ	tangential component of w	m/s
W_{shaft}	shaft power	W
$\dot{W}$	work rate	W

Symbol	Description	Unit
x	streamwise position/displacement	m
$x_1, \cdots, x_n$	input variables/coords	–
X	random variable	–
$\mathbf{X}$	reference position	m
y	dependent variable	–
y	wall-normal coordinate	m
y^+	nondimensional wall distance	–
z	vertical coordinate	m

Greek Letters and Parameters

Symbol	Description	Unit
α	absolute flow angle (turbomachinery)	rad
α	exponential decay parameter (pendulum)	s^{-1}
α_p	isobaric thermal expansivity	1/K
α	significance level (Type I error probability, statistics)	–
α	thermal diffusivity $k/(\rho c_p)$	m^2/s
β	relative flow angle (turbomachinery)	rad
β	probability of Type II error (statistics)	–
β_v	isochoric pressure coefficient	1/K
δ	damping ratio	–
ϵ	random error (regression)	–
η	Kolmogorov length scale	m
η	similarity variable (boundary layer theory)	–
γ	heat capacity ratio/isentropic exponent c_p/c_v	–
κ	interface mean curvature	1/m
κ	von Kármán constant	–
κ_s	isentropic compressibility	1/Pa
κ_T	isothermal compressibility	1/Pa
λ_b	bulk viscosity coefficient	Pa s

Symbol	Description	Unit
λ	eigenvalue (general)	–
λ	Poisson rate parameter (probability)	–
λ	Weibull scale parameter	–
μ	dynamic viscosity	Pa s
μ	mean of a distribution (statistics)	–
μ_X	mean of random variable X	–
ν	kinematic viscosity	m^2/s
ν_t	turbulent eddy viscosity	m^2/s
ν_G	kinematic viscosity of gas	m^2/s
Ω	sample space (probability)	–
Ω	angular velocity	rad/s
ω	elementary outcome (probability)	–
ω	angular frequency (general/damped)	rad/s
ω_0	natural angular frequency (undamped)	rad/s
ψ	specific dissipated energy	J/kg
ψ	stream function	–
ϕ	velocity potential (flow)	–
ϕ	phase shift in oscillatory motion	rad
φ	elliptic blending parameter (turbulence model)	–
Φ	viscous dissipation function	W/m^3
Ψ	stream function (Stokes flow)	–
ρ	density	kg/m^3
σ	standard deviation (regression/statistics)	–
σ^2	variance (regression/statistics)	–
σ	surface tension	N/m
σ_i	singular value of $\mathbf{A}$	–
θ	nondimensional temperature	–
$\boldsymbol{\theta}$	model coefficients	–
Θ	thermodynamic temperature (SI base)	K

Abbreviations

Abbrevation	Description
AOR	Acceptable Operating Range
BEP	Best Efficiency Point
CDF	Cumulative Distribution Function
CLT	Central Limit Theorem
DE	Drive End
DEXPI	Data Exchange for the Process Industry
DNS	Direct Numerical Simulation
FS3D	Free Surface 3D simulation code
HPC	High Pressure Compressor
HPT	High Pressure Turbine
IQR	Interquartile Range
ISO	International Organization for Standardization
LLN	Law of Large Numbers
LPC	Low Pressure Compressor
LPT	Low Pressure Turbine
MAD	Median Absolute Deviation
MTBF	Mean Time Between Failures
NDE	Non-Drive End
NOR	Not Allowed Operating Range
ODE	Ordinary Differential Equation
OREDA	Offshore Reliability Data
PDE	Partial Differential Equation
PDF	Probability Density Function
PCA	Principal Component Analysis
POR	Preferred Operating Range
QUDT	Quantities, Units, Dimensions, and Data Types
RANS	Reynolds-Averaged Navier–Stokes
RUL	Remaining Useful Life
SI	International System of Units

Abbrevation	Description
SST	Shear Stress Transport model
SVD	Singular Value Decomposition

Characteristic Dimensionless Numbers

Symbol	Description	Definition
Bo	Bond number	$Bo = \rho g \mathscr{L}^2 / \sigma$
c_f	skin friction coefficient	$c_f = \tau_w / (\frac{1}{2}\rho u^2)$
C_D	drag coefficient	$C_D = F_D / (\frac{1}{2}\rho U_\infty^2 A)$
Ec	Eckert number	$Ec = \mathscr{U}^2 / (c_p \Delta T)$
η	generic efficiency	–
η_D	diffuser efficiency	–
η_P	pump efficiency	–
η_T	turbine efficiency	–
Fr	Froude number	$Fr = \mathscr{U} / \sqrt{g\mathscr{L}}$
f	Darcy friction factor	$f = \Delta p / (\rho u^2/2) d_h/\ell$
f_F	Fanning friction factor	$f_F = f/4 = c_f$
Gr	Grashof number	$Gr = \alpha_p \Delta T g \mathscr{L}^3 / \nu^2$
δ	dimensionless film thickness	$\delta = h/d$
Ma	Mach number	$Ma = u/c$
Nu	Nusselt number	$Nu = h\mathscr{L}/k$
Nu_x	local Nusselt number	$Nu_x = hx/k$
Oh	Ohnesorge number	$Oh = \mu / \sqrt{\rho\sigma\mathscr{L}}$
Pe	Péclet number	$Pe = RePr$
Pr	Prandtl number	$Pr = \nu/\alpha$
Pr_t	turbulent Prandtl number	$Pr_t = \nu_t / a_t$
ψ	stage loading coefficient	$\psi = \Delta h_t / U^2$
φ	local flow coefficient	$\varphi = c_m / U$
Φ	flow coefficient (turbomachinery)	$\Phi = Q/(\Omega D^3)$
Ψ	pressure/head coefficient (turbomachinery)	$\Psi = (\Delta p/\rho)/(\Omega^2 D^2)$

Symbol	Description	Definition
Re	Reynolds number	$Re = \mathscr{U}\mathscr{L}/\nu$
Re_x	Reynolds number based on x	$Re_x = u_\infty x/\nu$
Re_L	Reynolds number (plate length L)	$Re_L = u_\infty L/\nu$
Re_D	Reynolds number (sphere diameter D)	$Re_D = \rho u_\infty D/\mu$
Re_τ	friction Reynolds number	–
Re_{crit}	critical Reynolds number (transition)	–
Sr	Strouhal number	$Sr = f\mathscr{L}/\mathscr{U}$
St	Stanton number	$St = h/(\rho c_p \mathscr{U})$
Tu	turbulence intensity	$Tu = u'/u$
$\tilde{D}$	specific diameter (turbomachinery)	$\tilde{D} = D(gH)^{1/4}/Q^{1/2}$
$\tilde{n}$	specific speed (turbomachinery)	$\tilde{n} = nQ^{1/2}/(gH)^{3/4}$
$\tilde{P}$	power coefficient (turbomachinery)	$\tilde{P} = (P/\rho)/(\Omega^3 D^5)$
We	Weber number	$We = \rho\mathscr{U}^2\mathscr{L}/\sigma$
ζ	loss coefficient	–

Mathematical Operators and Notation

Symbol	Description
$A \cap B$	intersection of events A, B
$A \cup B$	union of events A, B
A^c	complement of event A
$A - B = A \backslash B$	set difference
$\approx$	approximately (numerical value)
χ^2	chi-squared variable/distribution
δ	Dirac delta function
$\det(\mathbf{A})$	determinant of a matrix/tensor $\mathbf{A}$
$\emptyset$	empty set
F	F-statistic (variance ratio)
D/Dt	material (substantial) derivative
$\Gamma(x)$	Gamma function

Symbol	Description
$\int$	integral operator (line, surface, or volume integral)
$\oint$	closed-path (contour) integral operator
$\langle X \rangle$	expectation operator, alternative to $E[X]$
$\mathscr{B}(n, p)$	binomial distribution
$\mathscr{L}(\mu, \sigma)$	lognormal distribution
$\mathscr{N}(\mu, \sigma)$	normal distribution
$\mathscr{P}(\lambda)$	Poisson distribution
$\mathscr{U}(a, b)$	continuous uniform distribution
$\mathscr{U}\{a, b\}$	discrete uniform distribution
∇	gradient operator
$\nabla \cdot \mathbf{u}$	divergence of velocity $\mathbf{u}$
$\nabla \times \mathbf{u}$	curl of velocity $\mathbf{u}$
∇^2	Laplacian operator
∇^4	biharmonic operator
$\mathscr{O}(q)$	order of magnitude estimate
$Cov(X, Y)$	covariance between X and Y
$dim(x)$	dimension operator of x
$E[X]$	expected value of random variable X
$K(X)$	kurtosis
$S(X)$	skewness
$tr(\mathbf{A})$	trace of a matrix/tensor $\mathbf{A}$
$P(A)$	probability of event A
$P(A \mid B)$	conditional probability of A given B
$P(A \cap B)$	joint probability of A and B
$P(A \cup B)$	probability of union of A and B
$P(A^c)$	probability of complement of A
$\sim$	proportional to (functional relation)
t	t-score (statistics)
$Var(X)$	variance of X
z	z-score (statistics)

Symbol	Description
u	mean/bulk velocity (Reynolds decomposition)
u'	velocity fluctuation (Reynolds decomposition)
X_n	sample mean of n observations
$\mathbf{S}$	mean strain rate tensor

Contents

1 Hybrid Modeling in Engineering

1.1 Mathematical Modeling

1.1.1 Engineering Context

1.1.2 Hybrid Models

1.1.3 Causation in Hybrid Models

1.1.4 The Iterative Learning Process

1.1.5 Scope and Structure of the Book

1.2 Fundamental Concepts in Modeling

1.2.1 System and Variables

1.2.2 Scale, Dimensionality, and Coupling

1.2.3 Model Characteristics

1.3 Modeling Purpose, Objective, and Strategy

1.3.1 Modeling Purpose

1.3.2 Modeling Objective

1.3.3 Modeling Strategy

1.4 Prior Knowledge

1.4.1 Knowledge

1.4.2 Knowledge Representation

1.5 Data for Modeling

1.5.1 Data Types

1.5.2 Data Sources

1.5.3 Data Quality

References

Part I Physical Systems Knowledge and Behavior

2 Dimensional Analysis

2.1 Physical Variables and Equations

2.2 The Π—Theorem

2.2.1 Application in Model Development

2.2.2 Solitary Base Quantity

2.2.3 Single Dimensionless Product

References

3 Governing Equations

3.1 Fluid and Flow Properties

3.1.1 Thermodynamic Variables

3.1.2 Kinematic Variables

3.1.3 Transport and Interfacial Properties

3.1.4 Variable Material Property

3.2 Conservation Laws

3.2.1 Fundamental Conservation Principles

3.2.2 Material Derivatives

3.2.3 Continuity Equation

3.2.4 Momentum Equation

3.2.5 Energy Equation

3.2.6 Entropy Transport Equation

3.3 Boundary Conditions

References

4 Simplifications and Scales

4.1 Fluid Models
4.1.1 Incompressible Fluid Models
4.1.2 Compressible Fluid Models
4.2 Flow Regimes and Scales
4.2.1 Compressible Flows
4.2.2 Viscous Flow
4.2.3 Boundary Layer Flow
4.2.4 Dissipation and Convective Heat Transfer
4.2.5 Turbulent Flow
4.2.6 Free-Surface Flows
4.3 Simplified Equations
4.3.1 Boundary Layer Flow Equations
4.3.2 Euler Equations
4.3.3 Potential Flow
4.3.4 Creeping Flow
4.4 Similarity in Fluid Systems
4.4.1 Incompressible Flow Machines
4.4.2 Compressible Flow Machines
4.4.3 Flow Machine Classification
4.4.4 Local Flow Parameters
References
5 Basic Flow Cases
5.1 Quasi-One-Dimensional Flow
5.1.1 Stagnation State

5.1.2 Flow with Variable Cross-Section
5.1.3 Compressible Flow Phenomena
5.1.4 Turbomachinery
5.1.5 Subscale Modeling
5.2 External Flow
5.2.1 Laminar Boundary Layer Equations
5.2.2 Flow Past a Sphere
5.3 Internal Flow
5.3.1 Circular Pipe Flow
5.3.2 Turbulent Flow
5.3.3 Incompressible Pipe Flow
References

Part II Uncertainty, Data, and Learning

6 Probability Theory
6.1 Fundamentals of Probability
6.1.1 Random Experiments
6.1.2 Events and Event Spaces
6.2 Probability Distributions
6.2.1 Random Variable
6.2.2 Probability Map
6.2.3 Probability Distribution and Density Function
6.2.4 Distribution Parameters
6.2.5 Independence, Uncorrelatedness, and Covariance
6.3 Special Distributions

6.3.1 Uniform Distribution
6.3.2 Binomial Distribution
6.3.3 Poisson Distribution
6.3.4 Normal Distribution
6.3.5 Lognormal Distribution
6.3.6 Weibull Distribution
6.4 Limit Theorems
6.4.1 Law of Large Numbers
6.4.2 Central Limit Theorem
References
7 Statistical Methods for Data Analysis
7.1 Descriptive Statistics and Data Visualization
7.1.1 Location Statistics
7.1.2 Dispersion and Shape Statistics
7.1.3 Normalization
7.1.4 Graphical Summarization of Data
7.2 Distributions for Inference
7.2.1 t-Distribution
7.2.2 χ^2-Distribution
7.2.3 F-Distribution
7.3 Confidence Intervals
7.4 Hypothesis Testing
7.4.1 Hypothesis Testing Terminology
7.4.2 Distribution Tests

7.4.3 Location Tests
7.4.4 Dispersion Tests
References
8 Machine Learning and Prediction
8.1 Regression
8.1.1 Linear Regression for Linear Hypothesis
8.1.2 Solution Approach
8.1.3 Nonlinear Hypothesis
8.1.4 Overfitting and Regularization
8.2 Classification
8.2.1 Logistic Regression
8.2.2 Performance Measures
8.2.3 Multiclass Classification
8.3 Clustering
8.4 Dimensionality Reduction
8.5 Anomaly Detection
References

Part III Engineering Applications Modeling

9 Modeling Isolated Physical Processes
9.1 Damped Pendulum Motion
9.1.1 Governing Equation and Motion
9.1.2 Oscillatory Behavior
9.1.3 Energy Balance and Dissipation
9.2 Relaxation Behavior of a Spherical Particle

9.2.1 Governing Equation and Motion
9.2.2 Creeping Flow Relaxation
9.2.3 Moderate Reynolds Flow Relaxation
9.3 Heat Transfer in External Boundary Layer Flow
9.3.1 Numerical Solution and Classical Correlation
9.3.2 Asymptotic Behavior of Wall Temperature Gradient
9.3.3 Extending Asymptotic Limits Into a Unified Correlation
9.4 Impact of a Drop on a Wetted Surface
9.4.1 Physics and Dimensional Analysis of Splashing
9.4.2 DNS-Based Data Generation
9.4.3 Hybrid Correlation Development for Splashing Onset
9.5 Eddy Viscosity Turbulence Model
9.5.1 Optimal Eddy Viscosity from DNS
9.5.2 DNS Data for Channel Flow
9.5.3 Model Development and Evaluation
References
10 Industrial System Modeling
10.1 Industrial Domain
10.1.1 Industrial Context
10.1.2 Industrial Domain Knowledge
10.1.3 Industrial System Hierarchy
10.1.4 Sensor Contextualization
10.1.5 System Coupling in Industrial Equipment
10.2 Component Level Modeling of a Centrifugal Pump

10.2.1 Centrifugal Pump Characteristics

10.2.2 Reliability Estimation Based on Operating Range

10.2.3 Dataset for Pump Operation

10.3 System-Level Modeling of a Two-Stage Centrifugal Compressor

10.3.1 Two-Stage Centrifugal Compressor Dataset

10.3.2 Operating Profile

10.3.3 Performance Profile

10.3.4 Condition Profile

10.4 Data Centric Analysis of Turbofan Engine Degradation

10.4.1 Turbofan Dataset Description

10.4.2 Operational Settings

10.4.3 Degradation Trends and Fault Modes

References

11 Conclusion

Appendix A: A Curvilinear Coordinates

Appendix B: Selected Analytical Solutions

Appendix C: Mathematical Background

References

Index

© The Author(s), under exclusive license to Springer Fachmedien Wiesbaden GmbH, part of Springer Nature 2026
H. Gomaa, *Modeling with Knowledge and Data*, Mathematical Engineering
https://doi.org/10.1007/978-3-658-50679-7_1

1. Hybrid Modeling in Engineering

Hassan Gomaa[1] ✉
(1) Strategic Projects Co-Innovation, Cognite, Oslo, Norway

Mathematical modeling in engineering lies at the intersection of theory, data, and application. In this chapter, we introduce the foundational concepts and motivations for hybrid modeling, which combines physics-based understanding with data-driven methods to describe, predict, and analyze real-world systems. We begin by outlining the principles of mathematical modeling and the structure of hybrid models, including their treatment of causality and their role in iterative learning processes. We then introduce a framework for understanding the modeling process through its essential components, that is, the system under study, the modeling objective and strategy, the role of prior knowledge, and the treatment of data. These elements are introduced in turn, providing a conceptual foundation for the remainder of the book.

1.1 Mathematical Modeling

In mathematical modeling, we aim to address real physical problems using mathematical tools and methods. For a given problem, we seek to create structured representations, that is, a model of real-world systems. In the late nineteenth century, the physicist Heinrich Hertz reflected on the nature of scientific models and the representation of physical phenomena (Hertz 1894, 2003) and wrote

The most direct, and in a sense the most important, problem which our conscious knowledge of nature should enable us to solve is the anticipation of future events, so that we may arrange our present affairs in accordance with such anticipation. As a basis for the solution of this problem we always make use of our knowledge of events which have already occurred, obtained by chance observation or by prearranged experiment. In endeavoring thus to draw inferences as to the future from the past, we always adopt the following process. We form for ourselves images or symbols of external objects; and the form which we give them is such that the necessary consequents of the images in thought are always the images of the necessary consequents in nature of the things pictured. In order that this requirement may be satisfied, there must be a certain conformity between nature and our thought. [...] Various images of the same objects are possible, and these images may differ in various respects. We should at once denote as inadmissible all images which implicitly contradict the laws of our thought. Hence we postulate in the first place that all our images shall be **logically permissible** or, briefly, that they shall be permissible. We shall denote as incorrect any permissible images, if their essential relations contradict the relations of external things, i.e., if they do not satisfy our first fundamental requirement. Hence we postulate in the second place that our images shall be **correct**. But two permissible and correct images of the same external objects may yet differ in respect of **appropriateness**. Of two images of the same object that is the more appropriate which pictures more of the essential relations of the object, the one which we may call the more distinct. Of two images of equal distinctness the more appropriate is the one which contains, in addition to the essential characteristics, the smaller number of superfluous or empty relations, the simpler of the two. Empty relations cannot be altogether avoided: they enter into the images because they are simply images, images produced by our

mind and necessarily affected by the characteristics of its mode of portrayal.

In his beautifully written reflection, Hertz presents ideas that can be interpreted as three essential criteria a proper model should satisfy

- **Logical Permissibility** The model must be internally consistent and follow the rules of logic and mathematics. Models that contain contradictions or violate first-principle understanding are inadmissible.
- **Correctness** The model should accurately reflect the essential relationships of the real-world system it represents. That is, it should agree with known laws and empirical observations.
- **Appropriateness** Among various correct and admissible models, the most useful one is the clearest and simplest. It should capture the key aspects of the system while minimizing unnecessary complexity.

These three criteria continue to offer a foundational perspective for evaluating and constructing mathematical models in science and engineering. The engineering domains considered in this book are characterized by a particularly strong interplay between theoretical foundations and empirical data. We concentrate on thermo-fluid systems, including fluid mechanics, multiphase flows, heat transfer, and turbomachinery, where physical understanding is well established and often supplemented with data in the modeling process.

1.1.1 Engineering Context

Classical engineering sciences draw from a well-established body of knowledge rooted in physics and mathematics, developed over the past two centuries. This knowledge supports the design and operation of complex systems across industries such as power generation, oil and gas, refining and chemicals, maritime operations, and transportation. Our attention centers on engineering research and development in thermo-fluid systems, where the core knowledge is constituted by the **first-principle equations** comprising

- Conservation of mass, momentum, torque, and energy
- The second law of thermodynamics
- Material properties, including thermophysical properties

The physical phenomena involved in these first principles, such as convection or diffusion, as well as their mathematical descriptions, are well understood. In the various disciplines, thermodynamics, fluid mechanics, and their subfields such as viscous fluid flow, convective heat and mass transfer in turbine components, axial compressor design, and others, there exists an enormously rich body of research, applications, and special first-principle solutions, that form the foundation of domain-specific knowledge.

In Sect. 1.4, we explore what constitutes knowledge and how it can be represented in abstracted form. Part I of this book is dedicated to representative physical knowledge of engineering systems, with a focus on fluid and thermo-fluid systems and processes.

1.1.2 Hybrid Models

Beyond first principles, data have always played a critical role in developing, validating, and refining engineering models. In real-world systems, many effects are not fully captured by purely first-principle-based models. Thus, we often combine physics-based models with data-driven components, an approach referred to as **hybrid modeling**. Hybrid modeling integrates the strengths of both physics-based and data-driven approaches. Physical models provide interpretability and generalizability, while data enable the capture of complex behaviors not easily described analytically. Statistical or machine learning methods can extract patterns directly from experimental, operational, or simulated data without explicitly modeling the physical processes involved. The synergy of combining these approaches ideally results in models that are both interpretable and accurate.

The resulting **model** is an abstract mathematical representation of a process or system of interest, and serves as a projection of real-world behavior. A model typically includes the following key components

1. **Physical variables** $(x_1, x_2, \ldots, x_n) \in \mathbb{R}^n$ represent the key quantities that describe the behavior of the physical system. They may include thermodynamic, kinematic, or geometric properties, and form the input space over which the model operates. Further classification and discussion are provided in Sect. 1.2.1.
2. **Model structure** defines the mathematical form of the model, describing how variables are related. This typically includes
   - Dimensionless groups $(\Pi_1, \Pi_2, \ldots, \Pi_d) \in \mathbb{R}^d$ that capture scale-invariant relationships between variables, as introduced in Chap. 2.
   - A functional relationship $y = f(x_1, x_2, \cdots, x_n)$, which maps input variables to outputs. This function may follow a specific ansatz and should preserve dimensional consistency wherever applicable.
3. **Model parameters** define the numerical values or coefficients that specify the behavior of the model. These may include constants derived from physical laws, empirical fits to data, or tunable terms in parametric functions.
4. **Model scope** defines the domain in which the model is valid and expected to produce accurate results. Mathematically, this includes the admissible input space $\mathscr{X} \subseteq \mathbb{R}^n$ over which the model can be applied. The model is assumed to yield reliable outputs $y = f(x)$ for all $x \in \mathscr{X}$ within this domain, ideally with quantified accuracy. Outside the defined scope, extrapolation may lead to significant errors due to unmodeled effects or violated assumptions. The model scope is typically constrained by the physical assumptions, simplifications, and the data used during model development or calibration.

Hybrid models lie on a spectrum between purely knowledge-based and purely data-driven approaches, as illustrated in Fig. 1.1. In the

figure, model components informed by theoretical knowledge are shown in green, while those inferred from data are shown in blue.

In pure **knowledge-driven modeling**, the underlying mechanics of the process are sufficiently understood to allow for a complete formulation based solely on first principles. These models are typically derived from differential equations grounded in physical laws and require substantial mathematical formulation. To make these equations analytically or computationally accessible, strong simplifications of real-world conditions are often necessary. While such models, commonly referred to as **white-box models**, offer high levels of interpretability and insight into causality, their precision in representing reality can be limited by the very assumptions and simplifications that make them solvable. As described in Fig. 1.1, in white-box models both the structure of the model and its parameters are derived directly from physical understanding. A classic example is the calculation of the wall shear stress for a flat plate subjected to laminar flow without a pressure gradient. This is captured by the well-known Blasius boundary layer solution, discussed in Sect. 5.2.1. Here, the Navier-Stokes equations are simplified through the introduction of a similarity variable, which reduces the system to an ordinary differential equation. Solving this equation and evaluating the velocity gradient at the wall yields the exact wall shear stress.

At the opposite end of the spectrum lies pure **data-driven modeling**, where the underlying physical principles are fully disregarded, and only the input-output relationships observed in the data are modeled. These so-called **black-box models** solely rely on statistical correlations or machine learning algorithms to approximate behavior directly from data. However, they offer little to no interpretability, lack transparency, and may violate basic physical constraints or causality. Because they are not grounded in physical reasoning, black-box models tend to generalize poorly beyond the range of the training data and typically have limited or no extrapolation capabilities.

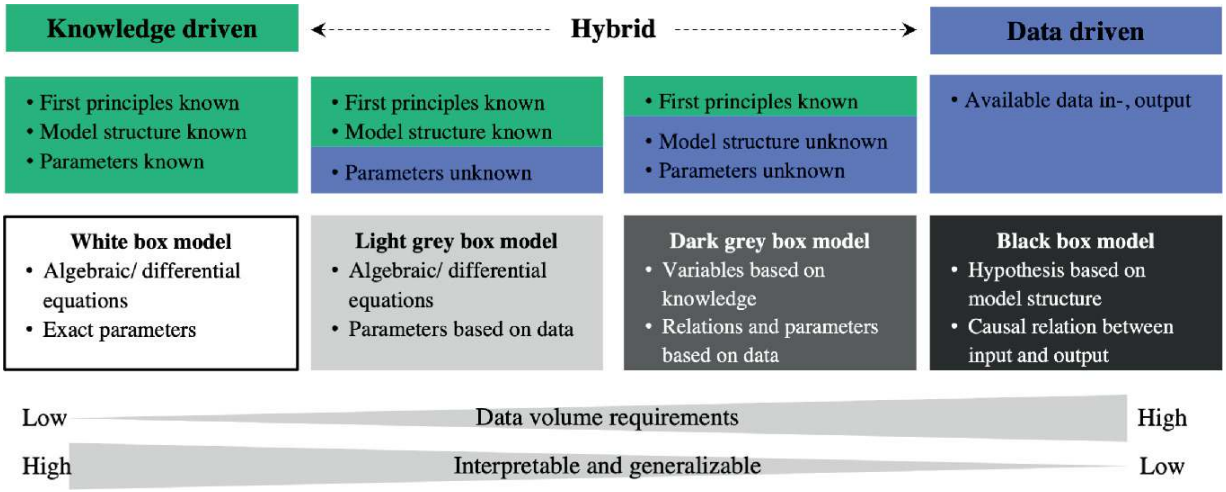


Fig. 1.1 Overview of mathematical modeling approaches categorized by the extent of incorporated physical knowledge. Figure adapted from Isermann (2016)

Gray-box models, as illustrated in Fig. 1.1, represent a middle ground with a combination of knowledge-based and data-driven modeling approaches. These models are partially formulated using first principles, while certain components, such as unknown parameters or functional relationships, are inferred from data. Wherever feasible, the model structure adheres to established physical laws and domain knowledge, while data is used to augment the model where detailed understanding is limited or unavailable.

Light-gray-box models preserve a structure derived from governing equations and physical reasoning. However, parameters within this structure, such as closure terms or empirical coefficients, are calibrated using data. For example, consider the estimation of the heat transfer coefficient along a flat plate at arbitrary Prandtl numbers. As discussed in Sect. 9.3, the functional structure may be adapted from the analytical solution valid for $\mathrm{Pr} = 1$, but to account for variable Prandtl numbers, coefficients must be inferred from data. Typical data-driven tools applied in this context include regression methods, which allow for systematic parameter estimation while maintaining interpretability.

In contrast, **dark-gray-box models** rely on data to infer both the model structure and its parameters. The functional form is not derived analytically, but domain knowledge remains important. It can support

the construction of meaningful dimensionless groups or inform the selection of plausible ansatz functions. However, the governing relationships themselves must be identified from the data. This process often involves dimensional analysis, exploratory data analysis and unsupervised learning techniques to reveal underlying patterns, trends, and latent structures that guide the development of the model.

Generally, as we move from pure knowledge to pure data, the volume of data required increases to maintain model quality. Inferring full functional relationships (dark gray box) demands significantly more data than fitting parameters to known relations (light gray box). Thus, augmenting data with physical knowledge improves both interpretability and generalization. The discussed classification is intended to be illustrative rather than rigid, as real modeling approaches often blur the boundaries between the listed categories.

The problems considered in this book involve n input variables, typically ranging from tens to hundreds depending on the complexity of the system. In data-driven settings, the number of observations m is generally much larger than the number of variables, thus $m \gg n$. This leads to well overdetermined systems, which are common in practical data-driven modeling scenarios. Given our focus on small to mid-sized data sets, we restrict ourselves to classical machine learning techniques and exclude deep learning and neural networks in this book. Nevertheless, we acknowledge the rapidly evolving field of *Physics-Informed Neural Networks*, which aim to incorporate physical laws into deep learning architectures. While promising, they are beyond the scope of this book. Readers interested in deep learning approaches are encouraged to consult specialized literature on the subject.

1.1.3 Causation in Hybrid Models

Across the spectrum of hybrid models, the understanding and treatment of causality differs. While physical models typically embed causality through governing equations and known mechanisms, data-driven models rely on observed associations without enforcing causal direction. Hybrid models are in between these views and must

reconcile the mechanistic structure of physics with the flexibility of statistical learning.

To illustrate the distinction, we draw on the concepts of causation, correlation, and association (Altman and Krzywinski 2015). **Causation** implies a directional relationship in which one quantity directly influences another; it expresses a cause-and-effect mechanism, indicating that one event is the result of another. For example, increasing the rotational speed of a pump causes an increase in pressure head. **Correlation**, in contrast, is a statistical measure that quantifies how strongly two variables co-vary, that is, how they change together. For instance, outlet temperature and pressure drop in a heat exchanger may show a strong correlation in operational data. However, this does not necessarily mean that one causes the other, as both may be influenced by a common factor such as the inlet mass flow rate. Methods for quantifying correlation are discussed in Chap. 6. While this distinction is clear in theory, establishing causality in practice is far more challenging than measuring correlation. The term **association** is not always formally defined in statistical literature, and broadly refers to any statistical relationship between variables. In practical terms, it means that knowing something about one variable provides some information about another, without necessarily implying a specific form or direction of dependence.[1]

In engineering, causality is typically assumed to be embedded in the physics of the system. Governing equations, derived from conservation laws for mass, momentum, and energy, describe how system variables evolve over time and space. Inputs such as boundary conditions, actuator settings, or control signals initiate system changes, while outputs such as pressure, flow rate, or temperature emerge from solving these equations. This structure imposes a natural directionality, that is causes precede effects, and physical influence propagates along known and constrained pathways. While these models impose deterministic relationships, the interpretation of causality still relies on assumptions about model completeness, inputs, and boundary conditions.

In contrast, data-driven models capture associations by estimating conditional distributions[2] of the form $P(Y \mid X)$, that is, the probability of observing *Y* given input *X*. However, these models do not determine whether *X* causes *Y* or merely correlates with it. Unless explicitly designed for causal inference, they cannot distinguish true cause-and-effect mechanisms. This becomes especially important when using black-box models in engineering applications, where changes to system inputs or conditions may break the learned patterns, leading to unreliable predictions.

Beyond these practical limitations of generalization, this issue also reflects a deeper theoretical boundary. As Pearl (2009) emphasizes, statistical associations such as $P(Y \mid X)$, no matter how accurate, are not sufficient to justify causal conclusions. Pearl (2009) states

> These considerations imply that the slogan "correlation does not imply causation" can be translated into a useful principle: one cannot substantiate causal claims from associations alone, even at the population level - behind every causal conclusion there must lie some causal assumption that is not testable in observational studies.

Causal claims therefore require assumptions beyond the data itself, introduced through structural knowledge or deliberate model design. The challenge in hybrid modeling is not only to combine knowledge and data, but also to preserve or reconstruct meaningful causal relationships when integrating empirical components, recognizing that full recovery may not be possible without additional data or structural assumptions.

1.1.4 The Iterative Learning Process

Modeling is the act of constructing a mathematical representation that captures the essential behavior of a real-world system. As illustrated in Fig. 1.2, and often discussed in literature on mathematical modeling (Peters et al. 2013; Box et al. 2005), this process mirrors the scientific

method and follows an iterative cycle of hypothesis, prediction, and validation.

The cycle begins with the **real-world problem** of interest. To analyze it mathematically, it must first be abstracted into a simplified and idealized form that defines a **mathematical problem**. This transformation is necessary because real-world systems are messy, uncertain, and influenced by many unobserved or varying factors. Nature itself does not follow equations but simply unfolds. Theoretical models, such as Newton's laws, do not dictate reality but approximate recurring patterns. They capture essential behavior while remaining idealized representations. Solving the mathematical problem yields a **mathematical solution**, which must then be interpreted in the context of the original physical system. This interpretation is validated empirically through experiments, measurements, or simulations. The iterative process continues until satisfactory agreement between the model and the real-world system is achieved. In this way, modeling becomes a dialogue between theory and reality and serves as a means to refine understanding.

This cycle naturally aligns with the classical scientific method, reflecting the roles of **deduction** and **induction**. Deduction uses theoretical models to predict outcomes, which are then tested against data. Induction uses discrepancies or patterns in the data to revise or improve the model. A model, like a scientific hypothesis, embodies assumptions about how a system behaves. When predictions and observations disagree, this feedback prompts a revision of the model or even of the underlying assumptions. In practice, this may involve collecting new data, refining the experimental setup, or reconsidering the relevant variables. Through this ongoing interaction between theory and evidence, both understanding and model fidelity improve progressively (Box et al. 2005).

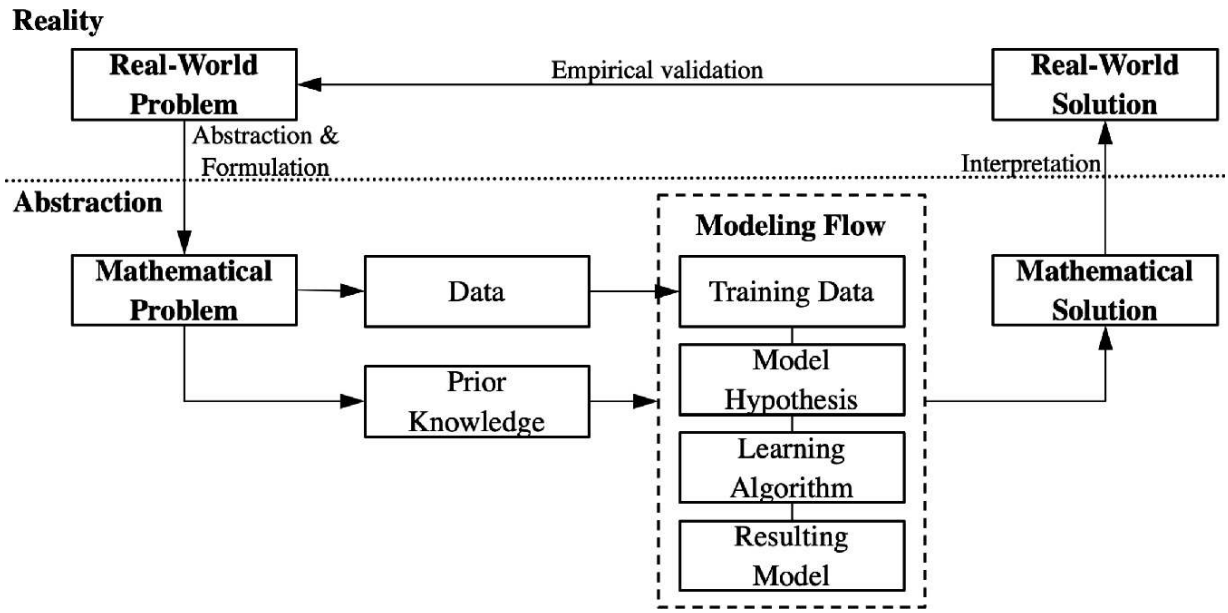


Fig. 1.2 Schematic of the modeling process as an iterative learning cycle, connecting scientific reasoning with data-driven model development

We now turn our attention to the practical steps of this modeling cycle, focusing on how physical knowledge and data are integrated to construct useful models, as outlined in the lower loop of Fig. 1.2. The **modeling flow** concerns the path from the mathematical problem to the resulting solution. It involves integrating prior knowledge and data through a sequence of steps: selecting training data, defining a model hypothesis, applying a learning algorithm, and evaluating the resulting model. The modeling flow, adapted from von Rueden et al. (2023), can be divided into four main components, each offering a point of entry for incorporating physical knowledge

1. **Training data** represents empirical observations of the system, often originating from experiments, simulations, or real-world operation. This data forms the foundation for learning patterns or estimating unknown quantities. The selection and preprocessing of data, such as filtering, normalization, or feature extraction, should respect physical constraints and known relationships. For example, ensuring unit consistency or applying nondimensionalization can significantly improve model generalizability. Where domain knowledge is available, it can guide which measurements are

relevant and which derived quantities, such as a calculated reference power or Reynolds number, may enhance the learning process.

2. **Model hypothesis** refers to the structural form of the model, that is the mapping from inputs to outputs. In a pure data-driven context, this may be a flexible functional approximation with minimal prior assumptions. In hybrid modeling, however, the hypothesis can be constructed to reflect known physics. This might involve choosing an ansatz function based on theoretical analysis, enforcing known symmetries or conservation laws, or embedding analytical submodels as part of a broader data-driven framework. Every model regards an isolated system. It necessarily abstracts from the full complexity of the real world by selecting a subset of variables and interactions to include. This simplification makes modeling tractable but also affects the limits of the model's applicability. Dimensional analysis, described in Chap. 2, plays a particularly important role in guiding model structure, especially when the governing equations are not fully known.
3. **Learning algorithm** determines how model parameters are adjusted based on training data. In traditional machine learning, this typically involves optimization procedures that minimize a loss function. In hybrid modeling, the learning algorithm can incorporate prior knowledge in several ways, for example by including physics-based constraints as penalty terms or by regularizing parameters toward physically plausible values. Thus, the learning process itself becomes informed by physical insight.
4. **Resulting model** refers to the final outcome of the modeling process, which is a mathematical object that can be used for prediction, control, or interpretation. The quality of this model is evaluated based on both its agreement with data and its consistency with physical principles. Interpretability, the ability to generalize beyond the training data, and adherence to physical laws are especially important in engineering applications. For instance, a

model may reproduce known limiting behavior exactly, such as the asymptotics of high or low Reynolds number flows, while adapting intermediate regimes using empirical data. In the end, the model must be judged not only by statistical performance but also by how well it represents the known behavior of the physical system.

Many challenges in data-driven engineering models mirror those identified by Box et al. (2005) in experimental science. These include measurement uncertainty, spurious correlations, and difficulties in capturing complex interactions. Such issues arise across all data sources, including experiments, simulations, and operational measurements, each with its own limitations. In engineering applications, models built purely on correlations can be misleading and often fail to generalize beyond observed conditions.

Techniques like regularization can help to control complexity but do not replace the need for physical structure. Hybrid modeling addresses this by embedding domain knowledge into the modeling process through constraints, informed variable selection, and structured model design. By integrating theory with data, hybrid models improve interpretability, robustness, and generalization in complex engineering systems.

1.1.5 Scope and Structure of the Book

This book is intended for graduate students, early-stage researchers, and practitioners working on modeling physical systems, particularly in industrial and applied domains. It lies at the intersection of mathematical modeling, classical machine learning, and engineering knowledge. Rather than serving as an exhaustive reference in any single area, the book provides an entry point into combining physical insight with data-driven methods to build interpretable, generalizable, and practical models.

The aim is to introduce essential concepts across these domains and help readers understand how to navigate between them. Examples and applications throughout the book focus primarily on thermo-fluid

systems, including flows, heat transfer, and turbomachinery. However, the modeling strategies and ideas are applicable across a broad range of physical systems. A working knowledge of calculus, linear algebra, and basic engineering subjects such as thermodynamics, fluid mechanics, and turbomachinery is assumed. No prior background in probability, statistics, or machine learning is required.

An inherent challenge in discussing hybrid modeling is that it spans multiple domains. The structure of the book reflects this interdisciplinarity. The remainder of this **introductory chapter** outlines key modeling concepts, moving from physical systems to concepts related to knowledge and data. We discuss modeling purpose, objective, and strategy to support deliberate and well defined modeling efforts. This includes being explicit about what the model is meant to achieve, the perspective from which it is built, and the gap it is intended to fill. Our goal is to support the development of higher quality models that are guided by the three attributes discussed earlier, namely logical permissibility, correctness, and appropriateness.

Part I introduces physical knowledge and governing principles. We begin with general structures that arise from the use of physical variables and dimensional reasoning. From there, we move to the governing equations that define physical systems, then to how these can be simplified with respect to specific flow regimes and dominant physical effects. Part I concludes with selected examples of canonical cases in fluid mechanics, heat transfer, and turbomachinery.

Part II focuses on uncertainty, data, and statistical learning. We start by establishing the basics of probability theory. This is followed by applied statistics, including both descriptive and inferential tools, before transitioning into selected methods from classical machine learning. The goal is to build an understanding of how uncertainty is handled, how data can be interpreted and used, and how patterns can be extracted in a structured way to support modeling tasks.

Part III brings these threads together through application-driven modeling of physical processes and engineered systems. In Chap. 9, we focus on processes that are relatively well isolated from their

environment, such as laboratory experiments or high-fidelity simulations, and therefore allow us to control the influencing variables and isolate the process to observe. In contrast, Chap. 10 addresses complex industrial systems, with a particular focus on turbomachinery. Here, we work with operational data from systems that are running in the field. These are inherently difficult to isolate and analyze, as the influencing factors cannot be controlled and are often affected by environmental and system-level interactions.

Throughout the book, the focus is on integrating physical understanding with empirical evidence to develop models that are both interpretable and reliable. Purely theoretical models may overlook real-world complexity, while purely data-driven models may lack transparency and generalizability. By combining physical principles with data, we aim to support the development of models that remain accurate under uncertainty, respect known system behavior, and are applicable to real engineering problems.

1.2 Fundamental Concepts in Modeling

Effective modeling begins with a clear definition of the system and the variables that describe its behavior. This section introduces these foundational concepts and examines structural features such as scale, dimensionality, and coupling, which shape model complexity and formulation. These considerations provide the groundwork for selecting a suitable modeling strategy aligned with the problem at hand.

1.2.1 System and Variables

Meaningful models require a clear understanding of the system and the key variables that govern its behavior over time.

System To define the object of interest, we introduce the concept of a **system**. This abstraction, common across engineering disciplines, is here understood from a thermodynamic perspective. It serves as the

primary subject of modeling and describes a specified quantity of matter, bounded in space and time.

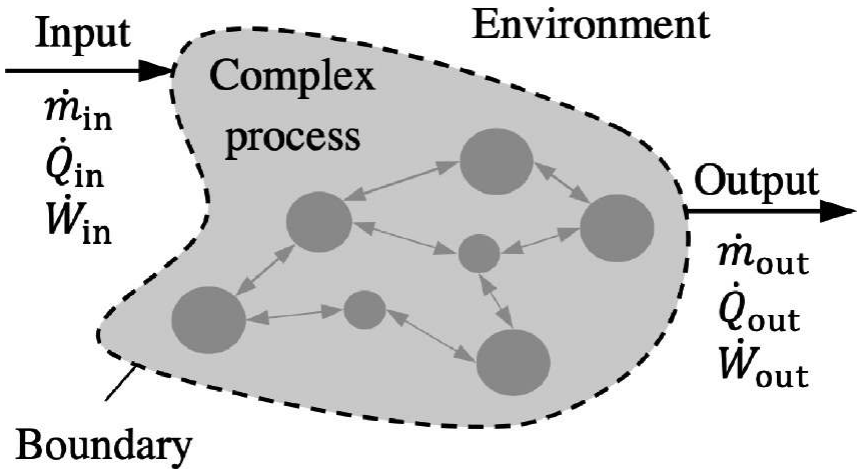


Fig. 1.3 The system to be modeled represents an abstraction of inner sub-entities and their interaction

The **system boundary** separates the system from its environment, and it may be fixed or variable. Boundaries are characterized by their ability to exchange matter, energy, or information with the surroundings, and these exchanges are referred to as **flows**. Depending on their direction, flows are considered system inputs or outputs, as illustrated in Fig. 1.3. For the systems considered here, we assume that information can always cross the system boundary. Typical information flows include incoming control signals (inputs) and the observability of internal system states through measurements (outputs).

Most systems in engineering are **open systems**, meaning they allow for the exchange of both mass and energy with the environment. In contrast, **closed systems** exchange only energy but not mass. An **isolated system** is sealed off from its surroundings entirely, with no exchange of mass or energy. A system insulated from heat flow is called **adiabatic**.

Within the system, **processes** take place. These processes represent interactions among the internal entities and mechanisms. They determine how the system transforms inputs into outputs, and how the internal state evolves over time. A **system model** captures this

transformation behavior. It describes how inputs influence outputs, how internal variables change, and how the system responds under different conditions. In practice, a system model abstracts away the detailed internal interactions and simplifies the overall dynamics to their essential characteristics. The model does not replicate each sub-entity and their behavior individually. Instead, it serves as a surrogate that captures the overall behavior of the system as a whole.[3]

Systems contain matter and in this book, we restrict our analysis to continua. As discussed further in Sect. 3.1.1, in the simplest case, a system can consist of a single substance with uniform properties, referred to as a **homogeneous system**. A container filled with water at $30\,^{\circ}\mathrm{C}$ is a typical example. More complex systems composed of different substances or phases are called **heterogeneous systems**. A container partially filled with air and partially with water is a typical example.

Systems can differ widely in both size and complexity. A system may represent a single, isolated physical process, a part, a component, a complete machine, or a larger assembly of multiple machines. For instance, the flow around a sphere, the boundary layer over a flat plate, or the impact of a drop on a liquid surface are examples of systems involving a **single isolated process**. A **part** might be the impeller of a centrifugal pump, which induces radial fluid flow and increases pressure. A more intricate example is a turbine blade in a gas turbine, which extracts work from high-temperature, high-pressure gas flows. Due to the extreme thermal loads, turbine blades require complex internal and external cooling, often involving elaborate flow passages and heat transfer enhancement features. A **component** consists of multiple interacting parts. A compressor, for example, includes both rotor and stator blade rows. The rotor imparts work to the gas, raising its pressure while reducing its volume. **Equipment** refers to assemblies of several components, such as a gas turbine, which integrates a compressor, a combustion chamber, and a turbine into a single interacting system. On an even larger scale, entire power plants,

chemical processing facilities, or marine vessels can be treated as systems of multiple interacting machines.

The purpose of defining the system is to provide a clear understanding of the object to be modeled and how it interacts with its environment. In practice, isolating a system from its environment is a necessary abstraction that enables targeted analysis. By defining a system boundary and selectively including only the relevant interactions, we reduce the complexity of the physical world to a manageable scope. This simplification allows for the development of models that focus on key mechanisms and dominant effects, while postponing or excluding less significant external influences. The degree of isolation is guided by the modeling objective, and careful consideration is required to ensure that essential interactions are not neglected.

The extent to which a process can be isolated also shapes the modeling approach. In well-controlled systems, such as laboratory-scale experiments or controlled simulations, the process of interest can be effectively isolated, allowing boundary conditions to be specified precisely and the relevant variables to be directly influenced. In these cases discussed in Chap. 9, the system definition typically includes a geometric domain along with prescribed values for quantities such as temperature, pressure, or velocity, as discussed in Sect. 3.3. In contrast, larger industrial systems, such as for instance found in turbomachinery, discussed in Chap. 10, often involve multiple interacting subsystems and are significantly influenced by neighboring systems. Here, the system includes mass, work, and heat flows between components or stages, and the boundary conditions may be uncertain, time-varying, or only partially observable. These more complex systems are less amenable to idealized isolation and often require hybrid approaches that combine physical insight with data-driven inference. A well-prepared system definition, tailored to the degree of separation from the environment, provides a natural starting point for identifying the relevant model variables and understanding how they relate to inputs, outputs, and internal states.

Physical Variables To describe a system mathematically, we begin by identifying the physical variables that characterize it. These are measurable properties of the system or quantities that can be derived from them. In engineering, such variables represent most system features and may take the form of scalars, vectors, or tensors. The terms variable and physical variable are used interchangeably in this text. While some variables may remain constant in time or space, they are still considered variables in a modeling context, as they can vary between different system instances or conditions. In some cases, categorical variables may also be used, as will be discussed in Sect. 1.5. The essential requirement is that the quantity be quantifiable, either through direct measurement or through derivation from other measured values.

The use of physical variables has structural consequences for model formulation, expressed in the form of nondimensional groups, which are explored through dimensional reasoning in Sect. 2.1. Further distinctions based on data value type and measurement scale are covered in Sect. 1.5.1. As will be discussed in Sect. 3.1, from a domain perspective, variables can be categorized according to the type of physical quantity they represent within the system. **Thermodynamic variables**, such as pressure or temperature, describe the energetic state of the system. **Kinematic variables**, such as velocity or acceleration, characterize the system's motion. **Transport properties**, including viscosity or thermal conductivity, quantify how momentum, energy, or mass is transferred within the system or across its boundaries. In addition, **geometric variables**, such as length or diameter, define the system's spatial configuration.

From a modeling perspective, physical variables can be grouped and classified in different, complementary ways. From a system perspective, we distinguish between **input variables**, which originate from the environment and act upon the system, and **output variables**, which are observable responses of the system. Input variables include both control signals and environmental influences. Output variables describe measurable effects, such as pressure, force, or flow rate. In between

these two categories lie the **system state variables**, which describe the internal condition of the system. These state variables may not be directly observable but are essential for capturing the system's dynamic behavior. **Parameters** represent a fourth category. They are quantities that remain constant for a specific system instance but can vary across systems or conditions. Parameters include material properties, geometric dimensions, and empirical constants used in modeling.

While outputs are typically modeled as functions of inputs, state variables describe the evolution of the system over time. Parameters play a key role in shaping system behavior and often need to be identified or estimated during the model development process.

Another common distinction is between independent and dependent variables, reflecting how quantities relate within a model. Independent variables are specified externally or assumed known in advance, such as time, spatial coordinates, or operating conditions. Dependent variables are outcomes determined by the model based on the independent variables. In regression and machine learning, these are often called **features** or **predictors** (independent), and **targets** or **responses** (dependent). Continuous predictors may be referred to as **covariates**, categorical ones as **factors**.

Mathematically, independence means that the value of each independent variable can be specified without directly determining the others. While this abstraction is convenient for model formulation but may not reflect the actual physical relationships among input variables. In engineering systems, physical dependencies or correlations between inputs often exist. For example, pressure and temperature in a thermodynamic system may be linked through an equation of state. In such cases, treating inputs as independent is a modeling simplification rather than a literal description of the underlying physics.

Another important distinction is between observable and latent variables. **Observable variables** are those that can be directly measured or observed, such as temperature, velocity, or force. In contrast, **latent variables**, also referred to as internal variables, are not directly accessible through measurement, but are necessary to fully

describe the system's internal behavior. These quantities must be inferred indirectly, typically through a mathematical model that relates them to observable data. Examples include internal energy states, turbulence quantities, or sub-resolution phenomena that cannot be captured by available instrumentation.

Whether a variable is considered observable or latent often depends on the resolution of the measurement system or the fidelity of the simulation. In hybrid modeling, latent variables may be inferred using data-driven techniques, especially in situations where direct observation is not possible but domain knowledge suggests their presence is essential for accurately describing the system behavior.

These distinctions offer different lenses through which physical variables can be understood and organized. Each reflects a particular aspect of how information is represented, used, or inferred in the modeling process.

1.2.2 Scale, Dimensionality, and Coupling

Understanding a system's characteristic scales, dimensionality, and degree of coupling is essential for selecting an appropriate modeling strategy, as will be discussed in Sect. 1.3.3. These structural features define model complexity and influence data requirements, model formulation, and the suitability of physics-based, data-driven, or hybrid approaches. Early characterization helps determine whether available data can resolve the key physical effects, which simplifications are justified, and how much modeling effort is needed to meet the desired fidelity.

Scale Physical processes unfold across a range of spatial and temporal scales. Examples include boundary layer thickness and turbulent dissipation length as spatial scales, or diffusion time in heat conduction as a temporal scale. These characteristic scales are set by the underlying physical mechanisms, as will be discussed in Sect. 4.2. Modeling requires identifying the relevant variables and the scales at which they operate. It must also be assessed whether these variables can be directly measured or need to be derived. The data resolution

must be fine enough to capture the dynamics of interest. If available spatial or temporal resolution is too coarse, key behaviors may be missed and model performance will suffer.

Dimensionality Dimensionality refers to both the number of independent variables needed to describe a system and its physical extent in space and time. Mathematically, it is useful to establish an initial hypothesis about how many and which independent variables the model must resolve. Physically, systems may be described in zero, one, two, or three spatial dimensions, with time adding complexity depending on whether the process is steady, periodic, or unsteady. The chosen dimensional setting should match the behavior of interest and the modeling objective. Some problems can be adequately captured by zero-dimensional models. Others may require temporal resolution or spatial variation across one or more dimensions.

Spatial representations are typically expressed in Cartesian, cylindrical, or spherical coordinates, chosen to align with symmetry or dominant directions and enable dimensional reduction. Lower-dimensional models often result from averaging and are useful for capturing bulk behavior. They are generally easier to compute, more robust to uncertainty, and less sensitive to modeling assumptions. Still, higher dimensionality does not necessarily guarantee greater accuracy, especially when data is limited or uncertain.

Degree of Coupling Alongside scale and dimensionality, the degree of coupling is a key aspect of problem characterization. Coupling describes the interdependence between variables, physical phenomena, governing equations, or subsystems. It may arise from interactions such as fluid-structure dynamics, multiphase flows, or conjugate heat transfer. It can also result from material properties that depend on internal states, for example, temperature-dependent viscosity or compressibility. Coupling within the governing equations is discussed in Sect. 4.1, and coupling via boundary conditions in Sect. 3.3.

Strongly coupled phenomena are tightly interdependent and typically occur on similar spatial and temporal scales. Capturing their interaction accurately often requires solving the governing equations

simultaneously. In other cases, the coupling is weak and can be handled through staggered or iterative approaches. The degree of coupling affects not only the numerical treatment and computational cost, but also the applicability of simplifications. Higher-fidelity models often require stronger coupling to capture key interactions.

In large-scale industrial systems, coupling may occur at the system level. Subsystems can be tightly integrated, requiring concurrent solution of interacting components, or loosely coupled, exchanging information only at interfaces. These aspects are discussed further in Chap. 10. Multidisciplinary coupling, such as between fluid flow, heat transfer, and structural mechanics, is another common challenge in engineering applications. Whether a system is treated as decoupled, weakly coupled, or fully coupled depends on the dominant physics, modeling goals, and available data.

In addition to physical and disciplinary coupling, model-level coupling plays an increasingly important role in modern engineering workflows. This involves integrating models with different levels of detail, scale, or abstraction into a unified simulation or decision-making framework. A typical example is the embedding of a surrogate model for a small-scale process, such as turbulence or heat transfer enhancement, into a larger-scale system simulation. Such integration places specific demands on the surrogate model. It must be compatible with the interface of the host model, remain valid under varying conditions, and be efficient enough for repeated use. Successful coupling of models also requires careful attention to the consistency of variables, the treatment of uncertainty, and the way assumptions are carried across the system.

Framing the problem in terms of scale, dimensionality, and coupling enables early assessment of data needs, modeling strategy, and simplification potential. It provides a practical foundation for building reliable, efficient, and physically meaningful models.

1.2.3 Model Characteristics

Mathematical models can be categorized based on their structural and functional attributes. These characteristics help to determine the suitability of a model for a given system or process and inform decisions about model formulation, implementation, and evaluation. Several classification schemes are common in the literature, including those based on transparency of internal mechanisms, mathematical structure, and computational properties (Peters et al. 2013; DuChateau and Zachmann 2002). Ultimately, the choice reflects both the nature of the problem and the model's intended purpose, in line with Hertz's reflection at the beginning of this chapter.

As introduced in Sect. 1.1.2, the **model structure** refers to the mathematical form that maps inputs to outputs, along with the assumptions that define the model's domain of validity. A central distinction in modeling is how strongly the structure reflects the internal mechanisms of the physical system. This is often described by the previously introduced white-box to black-box spectrum, which closely aligns with the classification of mechanistic versus empirical models. White-box models are fully mechanistic, meaning they are based entirely on known physical laws and offer full transparency regarding causality and internal structure. Black-box models are fully empirical and rely solely on observed input-output data, without explicitly representing the underlying physics. Gray-box models represent the broad range in between. They incorporate physical knowledge where available and use data to describe parts of the system that are not fully understood. This classification reflects both how much prior knowledge informs the model and how transparent its internal behavior remains.

Interpretability Interpretability refers to how easily a model's internal structure and outputs can be understood and related to physical or system behavior. Models grounded in physical principles tend to be more interpretable, as their components align with known mechanisms. However, highly interpretable models are often limited in flexibility and rely on simplifying assumptions. Data-driven models may be less transparent, especially when complex functional forms or high-

dimensional representations are used. Purely data-driven models may achieve high accuracy within observed conditions but provide little insight and may not generalize reliably. Interpretability plays a central role in model validation, communication, and deployment, particularly when models inform decision-making or require trust under uncertainty. Hybrid models seek to balance these aspects by combining physical structure with data-driven components.

Several important classifications relate to the **mathematical formulation** of a model and how it represents time, uncertainty, and system dynamics.

Static and Dynamic Models can be distinguished by their treatment of time. Static models describe systems in which variables are not explicitly dependent on time. These models often represent steady-state behavior or equilibrium conditions. Dynamic models, in contrast, account for the evolution of system variables over time and are typically expressed using differential or difference equations. In physical systems, dynamic models are required whenever transient behavior or time-dependent processes are essential to capturing the system's response.

Deterministic and Stochastic Models differ on incorporating the treatment of uncertainty. Deterministic models assume that system behavior is fully governed by known relationships and parameters. For a given set of initial and boundary conditions, the outcome is uniquely defined. Stochastic models[4] incorporate randomness or uncertainty, either in the system inputs, parameters, or internal dynamics. These models are useful when the system is affected by variability that cannot be captured deterministically, for example due to noise, unknown mechanisms, or measurement uncertainty. An example is the propagation of uncertain boundary conditions through a flow field, such as modeling sprays with variable drop-size distributions entering a gas stream.

Linear and Nonlinear Models Linearity refers to the mathematical properties of the governing equations or operators. A model is considered linear if it satisfies the principles of additivity and

homogeneity, expressed mathematically as $L[\alpha\, x + \beta\, y] = \alpha\, L[x] + \beta\, L[y]$. Here, L denotes a linear operator, such as a matrix in a system of linear equations or a differential operator in a differential equation. The symbols x and y represent system variables or functions, in our context typically dependent variables, such as system states or outputs, and α and β are arbitrary scalars. This definition applies across algebraic, ordinary differential, and partial differential equations. Linearity enables the use of superposition, supports decomposition of complex problems, and often allows closed-form analytical solutions. However, many physical systems are fundamentally nonlinear due to effects such as convective transport, phase transitions, chemical reactions, or feedback loops. Nonlinear models are typically more difficult to solve and to analyze, but they are often necessary to capture the essential system behavior. It is also worth noting that a model may be linear in its parameters while still containing nonlinear relationships between the input variables. Such structures are common in regression models and are especially relevant in hybrid modeling, where interpretable parameter estimation is often desirable, as will be discussed in Sect. 8.1.

Beyond mathematical structure, models can also be characterized by their **computational properties** and their integration into engineering workflows.

Fidelity and Computational Complexity Model fidelity refers to how accurately a model represents the physical behavior and dynamics of a system, including its spatial and temporal resolution, dimensionality, and coupling. As discussed in Sect. 1.2.2, these aspects determine the structural complexity the model must reflect. High-fidelity models resolve fine scales, include multiple dimensions, and capture strong interactions between physical phenomena. They preserve more of the governing mechanisms but are more demanding in terms of data, computation, and numerical stability. Lower-fidelity models simplify or omit such features, making them easier to calibrate and more practical for tasks like control, optimization, or system integration. The appropriate level of fidelity depends on the modeling

objective, system complexity, and available resources. For instance, a mean-line model of a turbine stage captures overall performance using averaged quantities and reduced dimensionality, while a full CFD simulation resolves detailed flow, heat transfer, and multiphysics effects. Both may describe the same system but serve different purposes depending on accuracy, cost, and application context.

Modularity and Reusability In engineering practice, models are often integrated into broader simulation environments or control systems. A modular model is designed with clear interfaces and separation of components, which facilitates validation, reuse, and integration with other models. Reusability is especially important in an industrial context, where subsystems may be developed independently but must operate consistently within a broader framework. Modular models also support lifecycle applications, enabling updates or replacements of components without requiring changes to the overall system architecture.

Scope and Generalizability The scope of a model defines the range of conditions and system configurations for which it can be reliably used. Generalizability refers to the model's ability to remain accurate when applied beyond its original training or calibration data. This is particularly important in operational settings, where exact conditions may not be known in advance. Physically informed models tend to generalize better because they are constrained by known laws and limiting behaviors. In contrast, purely data-driven models may perform well within the training domain but often lack reliability when extrapolated.

Model characteristics such as linearity, fidelity, or physical abstraction span a multidimensional space shaped by the needs of the task. These choices are often guided less by the physics itself than by the model's intended use. As emphasized by Hertz, a model should not only be logically consistent and correct but also purposeful in the context of its application. Different formulations may be equally valid from a theoretical perspective, yet differ in how effectively they support

the modeling objective. The next section outlines how to define that objective and its role in shaping the modeling strategy.

1.3 Modeling Purpose, Objective, and Strategy

Before turning to equations or data, it is essential to define why a model is being developed, what it should achieve, and how it will be constructed. Taking this step early brings intentionality and clarity to the modeling effort, helping to ensure that resources are used effectively and results are aligned with practical needs. This section introduces three central elements of any modeling process, that is purpose, objective, and strategy.

The modeling **purpose** clarifies the motivation for building the model. The modeling **objective** translates this purpose into a concrete technical task. The modeling **strategy** outlines how the model will be constructed given the available knowledge and data.

As emphasized in Sect. 1.1.4, modeling is an iterative process. Assumptions may be revised, data gaps identified, and strategies refined as the work evolves. Purpose, objective, and strategy are typically revisited and adjusted over multiple development cycles in response to new insights and as requirements become clearer.

1.3.1 Modeling Purpose

It is often tempting to jump straight into simulations, data analysis, or model tuning. However, best practice begins with clearly defining the purpose of the modeling effort. This reflection sets the foundation for everything that follows and ensures the model is developed with intention and direction. The modeling purpose answers the question

Why is this model being developed?

The more specific and well defined the purpose, the more aligned and efficient the modeling process becomes. A clearly stated purpose ensures the model serves a meaningful role, whether to explain physical behavior, guide experiments, support prediction, or inform design and decisions. It also helps to identify success criteria, to

determine appropriate assumptions, and to clarify the model's role within the broader engineering or research context.

Typical questions that help guiding the modeling purpose include

- What is the motivation for developing this model? What problem does it aim to solve, and why is a new model necessary?
- What existing models or approaches are available, and how does this one differ? What specific gap or limitation does it address?
- What is the intended use of the model? What decisions, insights, or actions will it support, and in what context (e.g., simulation, analysis, design)?
- What is the specific subject of the model, and what key behavior or physical mechanism must it capture?
- What are the critical requirements, such as accuracy, speed, robustness, interpretability, or integration to evaluate success of the model?

Depending on the context, modeling purposes often fall into one or more of the following common categories

- **Understanding a process** Reveal and analyze internal physical mechanisms of a system to support explanation, hypothesis development, and deeper insight into internal dynamics that may not be directly observable through experiments alone.
- **Developing subscale models** Represent small-scale processes, such as turbulence or heat transfer, that cannot be resolved at the system level. Subscale models provide closures, empirical correlations, or effective properties.
- **Creating surrogate models** Approximate high-fidelity simulations or experiments to enable fast evaluations. Surrogates are used in design exploration, optimization, and uncertainty analysis.
- **Quantifying uncertainty** Characterize variability in system behavior due to uncertain inputs or model assumptions. This includes sensitivity analysis, uncertainty propagation, and support for risk-informed decisions.

- **Extending model validity** Generalize existing models beyond their original assumptions or model scope. This may involve refining simplifications or incorporating additional physical effects.
- **Supporting experimental design** Guide experiments by identifying critical variables, relevant regimes, expected sensitivities, and designing effective measurement methodologies.
- **Embedding models in toolchains or workflows** Integrate models into simulation environments or automated pipelines. These models must be usable, fast, and robust under operational constraints.

Ultimately, the modeling purpose provides essential context and acts as a compass for the development process. It helps manage trade-offs, guide decisions, and define success in practical terms. As discussed at the beginning of this chapter, Heinrich Hertz emphasized that a model must not only be logically sound and correct, but also appropriate. That appropriateness is directly tied to the model's purpose. A model that does not serve its intended role, no matter how accurate or mathematically rigorous, falls short. Being deliberate about purpose ensures that modeling efforts are grounded in relevant and actionable criteria for success.

1.3.2 Modeling Objective

Once the modeling purpose is clear, the next step is to define the modeling objective. While the purpose captures the motivation, the objective translates it into a concrete and actionable modeling task. It specifies what is to be modeled and what the model is expected to produce or explain. At its core, the objective answers the question

What is the model intended to represent, predict, or explain?
This marks the shift from motivation to technical formulation. The objective focuses on the physical system, component, or process under study, and begins to define the model's structure and scope. This includes identifying key phenomena, relevant inputs and outputs, and the domain within which the model is expected to perform.

- The **specific subject** of the model: What system, component, or process is to be represented?
- The **essential behavior** to be captured: What physical mechanism or interaction is central?
- The **input space**: What are the relevant independent variables, and over what range should the model operate?
- The **output behavior**: What quantities should the model predict or describe?

This step may also introduce simplifications, such as modeling dimensionality, for example steady versus transient behavior or 0D to 3D representations, as well as physical assumptions like compressibility, flow regime distinctions such as laminar or turbulent, and the nature of boundary conditions. While these aspects are further developed in the modeling strategy, early recognition of such constraints helps define the model's scope and limitations from the start.

1.3.2.1 Critical Model Requirements

Beyond defining what the model should do, the modeling objective also introduces the concept of **critical model requirements**. These are performance attributes or constraints that determine whether the model is suitable for its intended use. They ensure the model is not only technically correct but also practically effective. Wherever possible, critical requirements should be **quantified**. This enables objective assessment, supports validation, and makes trade-offs explicit. The examples below illustrate common functional and non-functional requirements, though specific needs will depend on context.

Functional requirements describe what the model must achieve in terms of behavior, accuracy, and performance.

- **Accuracy of predictions** The model must reproduce physical quantities within a defined error margin. *For example:* Mean absolute error below $5\,\%$ across the operating range for a continuous variable.

For a categorical output, correctly classify flow regime in at least $90\,\%$ of test cases.

- **Computational efficiency** The model must be fast enough to support repeated evaluations or integration into larger simulation frameworks. *For example:* Complete one evaluation within $5\,\mathrm{ms}$ to enable time-stepped simulations or parametric studies.
- **Robustness and numerical stability** The model must remain stable and has to yield physically plausible results over a broad range of inputs, including edge cases. *For example:* No unbounded outputs outside the training domain, and predictions remain within physically valid limits.
- **Generalizability** The model must maintain acceptable performance across different operating conditions, input ranges, or system geometries. *For example:* Accuracy drops by less than $10\,\%$ when applied to unseen configurations.
- **Compliance with physical laws** The model must respect core physical principles such as conservation of mass, momentum, and energy, and remain consistent across spatial and temporal scales. This includes dimensional homogeneity, correct asymptotic behavior, and validity in both reduced-order and full formulations. *For example:* Mass and momentum balance errors remain below $1\,\%$ in all test cases, and model behavior scales consistently when moving from two-dimensional to one-dimensional representations.
- **Analytical integrability** In some applications, the model must be analytically integrable to enable symbolic manipulation or further processing. *For example:* The model's functional form supports closed-form integration for control design or analysis.

Non-functional requirements describe how the model should be used, maintained, and integrated into broader systems and workflows.

- **Integration capability** The model must work seamlessly within existing simulation or design environments. *For example:* Implemented in Python with standardized input and output interfaces to enable use in automated toolchains.

- **Interpretability and maintainability** The model should be understandable and modifiable by engineers or researchers. *For example:* Built using clear functional forms rather than opaque black-box structures.
- **Extendability and modularity** The model should allow future adaptation or reuse in related configurations. *For example:* New sensor inputs can be added without retraining the full model.
- **Support for uncertainty quantification** The model should enable the analysis of output uncertainty due to input variability or model assumptions. *For example:* Ability to propagate input distributions and produce confidence intervals for outputs.
- **Documentability** The model should be easy to describe, explain, and share in written form, including its assumptions and limitations. *For example:* Concisely expressible in a form suitable for reports or technical documentation.
- **Portability and parallelizability** The model should execute efficiently across platforms and support high-performance computing. *For example:* Implementation supports multi-core or distributed execution.

These are illustrative examples of requirements intended to highlight the kinds of trade-offs that often arise in practice. Their relevance and priority depend on the model's intended role. For instance, a subscale model embedded in a simulation toolchain may emphasize computational efficiency, numerical stability, and interface compatibility. In contrast, a model for design optimization may prioritize generalizability and predictive accuracy. Conflicts between requirements are common. Improving accuracy can increase computational cost, while enforcing physical consistency may limit flexibility. Navigating these trade-offs requires contextual judgment and, again, a clear understanding of the model's purpose.

In summary, the modeling objective defines the system to be modeled and the expectations the model must meet. It provides the technical foundation on which modeling strategies are built and

evaluated. The strategy follows directly from the objective and is shaped by available data, domain knowledge, and modeling constraints.

1.3.3 Modeling Strategy

Once the modeling purpose and objective are defined, the next step is to formulate a modeling strategy, that is a plan for how the model will be built given the problem context, available domain knowledge, and accessible data. This strategy guides the integration of these elements into a coherent modeling flow, as illustrated in Fig. 1.2. It addresses the central question

How will the model be developed to achieve its objective?

Modeling Approach A key decision is where the model lies on the spectrum between first-principles and data-driven approaches, as introduced in Sect. 1.1.2. This choice shapes the modeling workflow, tools, and validation steps. It is typically informed by

- The availability of theoretical understanding or governing equations, and the nature of the unknowns, from individual parameters to full model structure.
- The amount, quality, and relevance of data.
- Whether parameters are physically interpretable or must be inferred purely from data.
- The critical model requirements, such as interpretability, generalizability, accuracy, and computational efficiency, discussed in Sect. 1.3.2.
- Existing models or approaches in the domain that offer starting points or reference baselines.

As noted in Sect. 1.1.2, this choice is not binary but rather a placement along a continuous scale, with conceptual reference points illustrated in Fig. 1.1.

Prior Knowledge Assessing prior knowledge and including it meaningfully in the model are central elements of the overall modeling strategy. This includes both theoretical understanding and empirical insight relevant to the system. Section 1.4 discusses types of knowledge

and their representation, while Part I provides concrete examples from thermo-fluid systems. Relevant considerations for using prior knowledge to define the model backbone include

- Choosing the appropriate level of abstraction and modeling granularity, including spatial and temporal resolution.
- Identifying relevant dimensionless groups and scaling laws, as discussed in Chap. 2 and Sect. 4.4.
- Applying fundamental physical principles such as conservation of mass, momentum, and energy, along with simplifications based on symmetry, dominant mechanisms, or asymptotic behavior, as detailed in Chaps. 3 and 4.
- Enforcing dimensional consistency and known limiting behaviors in model formulations.
- Reusing or adapting existing models and empirical correlations from the literature.

Data A structured treatment of data is essential for successful modeling. Section 1.5 discusses data sources and quality considerations, while Chap. 7 introduces descriptive statistical tools. Understanding both the strengths and limitations of the data is critical, particularly for the data-driven components used. Relevant considerations include

- Planning data acquisition and determining what kind of data is needed and where it can be sourced.
- Structuring raw or semi-structured data into a consistent and usable format.
- Assessing data quality by identifying noise, bias, sparsity, or systematic errors, and reflecting on how uncertainty may propagate through the modeling process.
- Exploring the data through summary statistics, distributional analysis, and visualization to identify patterns, anomalies, or trends that can inform feature selection or model formulation.

1.3.3.1 Modeling Flow

As introduced in Sect. 1.1.4, the modeling flow can be structured into four interconnected components, namely training data, model hypothesis, learning algorithm, and resulting model. Each element of the modeling flow can incorporate prior knowledge to varying degrees. Approaches to data-driven modeling under uncertainty are presented in Part II. The following outlines relevant considerations for each component.

Training Data The training dataset is the empirical foundation of the model and must be prepared carefully. Key considerations include

- Data preparation steps, including cleaning, preprocessing, and outlier treatment.
- Feature engineering based on physical insight, such as nondimensionalization or extending with meaningful derived variables.
- Feature selection to reduce dimensionality and focus the model on the most informative variables.
- Construction of training and test splits, ensuring that the data distribution is representative of the modeling domain and sufficiently covers the relevant scope.
- Addressing uncertainty or noise in the data by identifying potential sources of measurement error and applying filtering, smoothing, or estimating noise levels statistically.

Model Hypothesis The model hypothesis defines the mathematical relationship between inputs and outputs. Depending on the modeling strategy, this relationship can be based on

- Simplified governing equations, derived through nondimensionalization, physical insight, or identifying balances between dominant physical mechanisms.
- Functional expressions such as power laws, polynomial fits, or log-linear relations, guided by physical intuition.
- Fully flexible structures such as Gaussian processes or support vector machines, if interpretability is not a core requirement.

The dimensionality of the dataset should guide model complexity to ensure the structure is supported by available data and avoids overfitting or underdetermination. The strategy should also specify how model parameters will be determined, whether through theoretical derivation, calibration using experiments or simulations, or statistical inference. Enforcing known boundary behavior and asymptotic limits improves both extrapolation and interpretability.

Learning Algorithm The learning algorithm defines how the model is trained from available data. The choice of algorithm depends on

- The mathematical form of the model, in particular whether it is linear or nonlinear with respect to its parameters.
- The dimensionality of the feature space and the amount of available training data.
- The applied cost function, whether focused on prediction error, regularization, or adherence to physical constraints.

As will be discussed in Chap. 8, regularization helps prevent overfitting, promotes model simplicity, and supports the integration of known physical constraints. In hybrid models, it can be specifically designed to penalize unphysical behavior and guide the model toward physically consistent solutions.

Resulting Model The final model must be evaluated and refined as needed. Key steps in this phase include

- Validating model performance using independent test data, benchmark problems, or analytical solutions.
- Defining quantitative metrics aligned with critical requirements, such as accuracy, runtime, robustness, or consistency with physical laws.
- Performing sensitivity analysis to identify fragile parameters, evaluate model behavior near domain boundaries, and assess risks of extrapolation beyond trained domain.
- Refining the model iteratively by revisiting its structure, assumptions, or training process where performance is insufficient.

- Preparing for deployment by defining how the model will be used in practice, such as embedding it in simulations, and specifying interface requirements like source terms or boundary conditions based on model outputs.
- Testing and calibrating the model within the full system or workflow to ensure stability, consistency, and reliable performance under operational conditions.

In summary, the modeling strategy translates abstract intent into a structured and executable plan. It defines how knowledge and data are combined, how the model is formulated and validated, and how success is measured.

1.4 Prior Knowledge

This section discusses what constitutes knowledge in our context and how it can be represented. We follow the framework proposed by von Rueden et al. (2023), who systematically classify types of knowledge, their representations, and methods of integration with machine learning. They introduce the term **informed machine learning** to describe approaches that combine data with explicitly represented prior knowledge. Unlike conventional machine learning, where prior knowledge is often embedded implicitly through labeling or feature engineering, informed machine learning emphasizes formal incorporation of knowledge into the pipeline as a separate, formally represented source. The authors propose a taxonomy based on the origin of the knowledge, its representation, and the stage at which it enters the machine learning workflow. While their work spans a wide range of domains, including vision, language, and semantics, we adapt their classification to the present engineering context.

1.4.1 Knowledge

The term **knowledge** is difficult to define universally, as it quickly enters philosophical territory. Here, we adopt a pragmatic and operational view, guided by the iterative learning cycle introduced in

Sect. 1.1.4, where hypotheses and data interact in a cycle of refinement and validation to develop formal understanding.

In this context, knowledge refers to the collective body of formalized understanding, empirical insight, and contextual awareness that enables structured interpretation, representation, and prediction of physical systems. This includes several dimensions, which are neither exhaustive nor mutually exclusive

Theoretical knowledge includes fundamental laws such as thermodynamic principles and conservation equations (see Chap. 3). It also covers simplifications derived from first principles, such as one-dimensional turbomachinery flow models (Sect. 5.1.4).

Empirical knowledge encompasses relationships obtained from experimental or simulation data, such as correlations for friction factors or Nusselt numbers. These often embed prior understanding and are used in practical modeling of fluid behavior (see Chap. 5).

Structural knowledge relates to the organization and interaction of physical systems. It includes the inherent structure of physical quantities, as reflected in the use of dimensionless numbers (see Chap. 2), and principles that preserve system behavior under scaling (Chap. 4). It also covers system topology, dominant mechanisms, and component interactions (Sect. 10.1).

Domain knowledge captures context-specific insights often embedded in engineering practices, standards, and operational constraints. This includes knowledge of failure mechanisms, performance regimes, and industry-specific priorities, which vary across fields such as power generation, chemical processing, or aerospace. Domain knowledge is often documented in standards (e.g., ISO 14224 International Organization for Standardization (2016)), curated datasets (e.g., OREDA Technology et al. (2015)), and standard procedures (see Sect. 10.1).

Heuristic expert knowledge refers to informal, experience-based practices such as rules of thumb or operator intuition. It may appear in

shift logs, root cause analyses, or engineering reports, and is often transmitted verbally. This knowledge arises from hands-on familiarity and can bridge gaps where formal models or sensors fall short.

The first three categories are typically formalized and validated through scientific processes. They are often sufficient when modeling isolated physical processes. In contrast, for complex systems such as machinery or industrial operations, understanding the interdependencies between components becomes critical. In such cases, structural, domain, and heuristic knowledge play a key role, as further elaborated in Sect. 10.1.

A central aspect of knowledge is its **formalization**. This refers to the extent to which knowledge is explicitly structured and expressed in a standardized form. The level of formalization depends on how the knowledge is captured, documented, and expressed, from informal text to precise mathematical form. In general, the more formal and structured the representation, the easier it becomes to incorporate that knowledge into machine learning workflows (von Rueden et al. 2023), as touched upon in Sect. 1.3.3.

1.4.2 Knowledge Representation

Knowledge representation refers to the formal structuring of knowledge in a way that allows it to be interpreted, processed, or embedded into modeling workflows. In this section, we adapt the classification of von Rueden et al. (2023) to the context of thermo-fluid systems, highlighting the diverse forms of engineering knowledge

Algebraic equations express relationships using equalities or inequalities involving physical constants, parameters, and variables. These may represent either fundamental laws or empirically derived approximations. Examples include thermodynamic identities and material property equations (Sect. 3.1.1), as well as friction factor or heat transfer correlations (Chap. 5). Algebraic forms are especially common in discrete models, where physical systems are treated as

collections of finite elements. In such settings, physical principles are expressed through algebraic rather than differential relations. This contrasts with continuous models, where the same principles appear as differential equations (DuChateau and Zachmann 2002). In machine learning, algebraic knowledge is often embedded in the loss function, where it imposes physical constraints during model training (von Rueden et al. 2023).

Differential equations describe how quantities evolve in time and space by relating functions to their derivatives. These include ordinary and partial differential equations and require initial and boundary conditions. They are central to physical modeling and govern transport phenomena such as momentum, heat, and mass transfer, as discussed in Sect. 3.2. They also appear in simplified forms for specific regimes (see Chap. 4) or for particular problems such as the Blasius boundary layer flow in Sect. 4.3.1.

Invariances refer to properties or relationships that remain unchanged under specific transformations, such as translation, rotation, reflection, scaling, or shifts. Recognizing such invariances is essential for simplifying models and enabling generalization across a wide range of physical configurations and scales. For instance, spatial symmetries, such as those exhibited by the stress tensor, are often directly reflected in the structure of the governing equations, as discussed in Chap. 3. A particularly important type of invariance in the context of physical variables is invariance under a change of units. This principle motivates the use of nondimensional numbers, which express physical relationships independently of specific measurement systems, as introduced in Sect. 2. It also forms the basis for the similitude and scaling laws in turbomachinery, detailed in Sect. 4.4. These invariances are not merely mathematical conveniences, but reflect the physical structure of the system and help ensure models remain valid and interpretable across regimes.

Logic rules encode conditional, qualitative, or discrete knowledge using formal logical expressions, grounded in Boolean logic, e.g., if *A*

then *B*. These rules are particularly useful for capturing decision boundaries, switching behavior, or system changes related to specific conditions. In physical modeling, logic rules may guide model selection based on regime changes, such as distinguishing between laminar and turbulent flow using Reynolds number thresholds (see Chap. 4). At the system level, logic rules define discrete behaviors such as control logic, state transitions in response to operational conditions, or failure modes. Such constructs are widely used in rule-based control, diagnostics, and supervisory systems where decisions must be made based on qualitative inputs or thresholds. While simple in form, logic rules are a powerful means of embedding expert knowledge or engineering heuristics, particularly when physical models alone are insufficient to describe system behavior across operational modes.

Knowledge graphs represent structured relationships among entities such as objects, variables, concepts, or events. In these graphs, entities are modeled as nodes, while edges encode the nature of their interrelation. This representation facilitates the integration of information across heterogeneous sources and enables reasoning over complex system configurations. Within engineering contexts, knowledge graphs can be used to represent hierarchical structures, functional dependencies, or component relationships for a given system configuration, as illustrated in Sect. 10.3. They also provide a flexible framework for codifying domain-specific ontologies. For instance, the QUDT ontology (Hodgson et al. 2025) defines standardized concepts for quantities, units, and dimensions, thereby supporting semantic consistency and data interoperability. More broadly, knowledge graphs serve as an effective tool for organizing domain knowledge in a machine-interpretable format, which is especially valuable in applications involving diagnostics, system integration, or hybrid modeling strategies where both structured knowledge and data must coexist.

Stochastic relations capture uncertainty and variability in systems through probabilistic constructs. These representations are grounded in probability theory and involve random variables, distributions,

dependencies, and inferential principles, as discussed in Chaps. 6 and 7. In engineering modeling, statistical relations are essential for quantifying the effects of noise, incomplete knowledge, or variability in system parameters. Examples include part-to-part variability due to manufacturing tolerances, stochastic part-load distributions, and uncertain boundary conditions. In their basic form, statistical relationships manifest as confidence intervals associated with physical quantities, expressing the expected range of variation due to underlying uncertainty, as detailed in Sect. 7.3. A typical example arises in reliability analysis, where statistical data are curated in tabular form, such as the OREDA failure databases (Technology et al. 2015), which provide statistics on failure event frequency and criticality in industrial machinery. When incorporated into modeling frameworks, statistical relations enable robust prediction, uncertainty quantification, and learning under incomplete or noisy data, including Bayesian approaches and probabilistic machine learning methods.

Human feedback encompasses implicit, experiential knowledge conveyed through interaction, observation, or intervention. Unlike structured knowledge forms, human feedback is often unformalized and context-dependent. It may be conveyed through operator actions, annotations, gestures, or verbal instructions. In engineering systems, such feedback is especially valuable in situations where automated models fall short, either due to incomplete sensing, evolving system conditions, or unmodeled effects. For example, an operator might override a control system based on subtle acoustic or vibrational cues indicative of an incipient fault, which are not captured by existing sensor data or models.

1.5 Data for Modeling

Data is the second foundational component of the modeling process, complementing the structural and theoretical insight provided by prior

knowledge. While knowledge encodes physical laws, assumptions, and constraints, data offers empirical evidence from which patterns can be extracted, models can be trained, and predictions can be validated. This section introduces essential concepts related to data in engineering modeling, including its types, sources, and quality attributes.

We adopt the terminology and definitions of ISO 8000-8 (International Organization for Standardization 2015) on information and data quality, which defines **data** as a reinterpretable representation of information in a formalized manner suitable for communication, interpretation, or processing. Here, **information** refers to meaningful observations about facts, events, processes, or concepts within a defined context, and **metadata** is data that describes other data.

In our context, it is important to distinguish between data and knowledge. Data, such as simulation results, sensor readings, or experimental measurements, are not considered knowledge on their own. Rather, it consists of raw informational artifacts generated by observation, computation, or physical processes. These artifacts gain meaning when analyzed, interpreted, or synthesized to reveal structure, identify relationships, or support predictions. In that sense, data serves as empirical evidence for building, calibrating, and validating models. Through processes such as empirical correlation development, model calibration, surrogate modeling, and uncertainty quantification, data becomes structured and generalized, moving beyond its raw form to directly contribute to the formation of knowledge.

The following sections examine how data are classified, where it originates from, and how its quality can be assessed. These considerations define the data layer that complements the prior knowledge layer described in Sect. 1.4. As illustrated in Fig. 1.2, together they form the foundation for hybrid modeling strategies.

1.5.1 Data Types

Most data can be broadly categorized as either **categorical** or **numerical**, as illustrated in Fig. 1.4. Categorical data is non-numerical and classifies observations based on qualitative attributes. It is typically textual or descriptive in nature. Examples include fluid types (e.g., water, oil, air), material classes (e.g., polymer, metal, ceramic), or flow regimes (e.g., laminar, turbulent). The values within a categorical variable are often referred to as **labels**. Well-defined categorical variables consist of mutually exclusive labels, meaning that assigning one label excludes the possibility of assigning another within the same variable. While each observation can typically be assigned to exactly one label, some observations may not fall into any defined category.

Numerical data, by contrast, represent quantitative attributes and are expressed using numbers. It is further divided into **discrete** and **continuous** types. Discrete data consist of countable, indivisible units, such as the number of stages in a compressor, the number of blades on a rotor, or the number of droplets formed in a splash event. Continuous data can take any value within a specified range and include measurements such as specimen width, experiment duration, or sensor outputs like pressure, velocity, and temperature.

There is often a trade-off between precision and interpretability. While numerical data carries higher resolution, categorical descriptions are often more intuitive to comprehend. For example, describing water as *hot* or *cold* may be more immediately meaningful than specifying its exact temperature. Depending on context or audience, the same information is frequently converted between numerical and categorical forms.

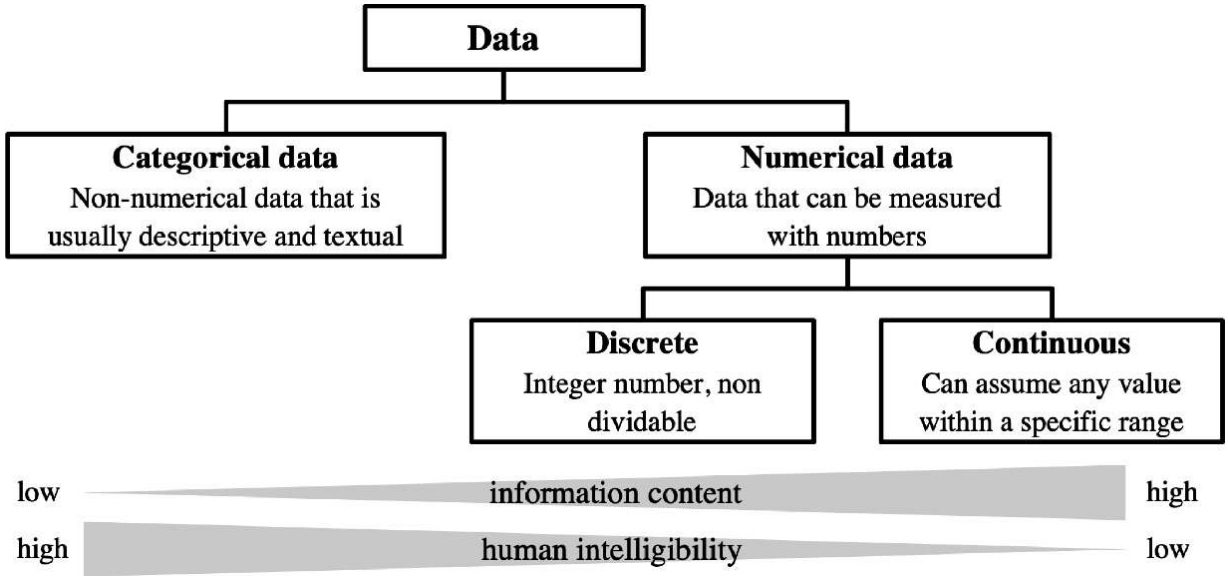


Fig. 1.4 Classification of data types

Data types are fundamental not only to the meaning a variable can convey but also to the mathematical operations that can be applied. They determine the appropriate measurement scale, influence the choice of probability distributions (see Chap. 6), descriptive statistics (see Sect. 7.1) and guide the selection of analysis methods used throughout this text.

Measurement Scales Measurement scales classify variables according to the type of information they encode and the mathematical operations that can be meaningfully applied. As shown in Fig. 1.5, each scale is associated with specific data types and determines how values can be compared, ordered, or combined.

The **nominal scale** applies to categorical data where the values serve purely as labels without any inherent order. The only valid comparisons are equality and inequality. Examples include fluid types (e.g., water, oil, air), or sensor types (e.g., thermocouple, strain gauge, accelerometer), where no ranking among categories is implied.

The **ordinal scale** also applies to categorical data but introduces a meaningful order among labels. An example is surface roughness levels classified as smooth, medium, or rough. While comparisons such as < or > are meaningful, the intervals between categories are not. This means that addition or subtraction is not valid for ordinal data.

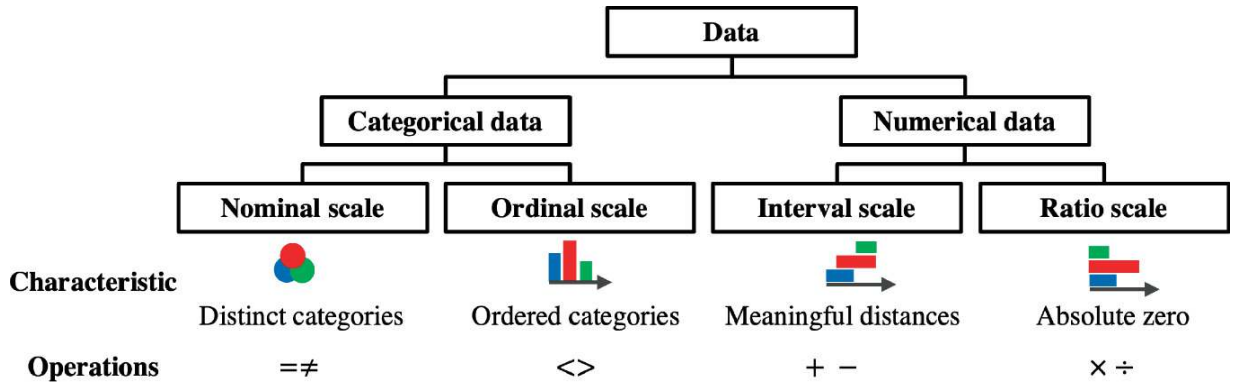


Fig. 1.5 Overview of measurement scales and their associated operations

The **interval scale** and **ratio scale** apply to numerical data, including both discrete and continuous variables. Interval scales support ordered values with meaningful differences, but they lack a **true zero**. As a result, additive operations are valid, but multiplicative ones are not. A classic example is temperature in degrees Celsius. A value of $20\,^{\circ}\mathrm{C}$ is not twice as hot as $10\,^{\circ}\mathrm{C}$, since the zero point is arbitrary.

Ratio scales extend interval scales by including an absolute zero, enabling both addition and multiplication. Examples include temperature in Kelvin, pressure, mass, and length. Variables measured on a ratio scale can be meaningfully multiplied or divided, which makes them suitable for constructing dimensionless products, as discussed in Chap. 2.

It is also common to transform interval-scale variables into ratio-scale ones by focusing on differences. For instance, while a temperature of $20\,^{\circ}\mathrm{C}$ is not twice as hot as $10\,^{\circ}\mathrm{C}$, a temperature difference of $\Delta T = 20\,^{\circ}\mathrm{C}$ is indeed twice that of $\Delta T = 10\,^{\circ}\mathrm{C}$. Similarly, while time itself is typically measured on an interval scale, time **duration** behaves as a ratio variable.

1.5.2 Data Sources

Once the types and characteristics of data are understood, it is essential to consider the sources from which the data originates. In engineering, data area typically obtained from four main sources. These are theoretical analysis, numerical simulation, experimental investigations,

and operational measurements. Each of these sources provides data with distinct characteristics and plays a different role in the modeling process. Often, they are used in combination, with each complementing the strengths and limitations of the others. Despite their differences, all data sources are grounded in prior understanding of the system. This includes identifying relevant physical variables, distinguishing between input and output quantities, and defining the context in which the data will be used. In every case, the act of generating or selecting data is informed by assumptions, whether theoretical, physical, or operational, that shape the way systems are observed and represented.

This section introduces the four main sources of data and outlines the investigative approaches by which they are typically obtained. Operational measurements are introduced in general terms here and discussed in more detail in Chap. 10.

1.5.2.1 Theoretical Analysis

Theoretical analysis generates data through analytical or semi-analytical solutions of governing equations. These solutions are typically derived from first principles, such as conservation laws, constitutive relations, and physical constraints. By applying simplifying assumptions, the equations are reduced to a form that captures the dominant effects in a particular regime. This process often involves assuming specific flow characteristics, estimating the relative importance of terms through dimensional analysis, and neglecting contributions considered negligible. The aim is to obtain a simplified mathematical formulation that preserves the essential physics of the problem.

The resulting expressions may take the form of closed-form solutions, implicit relationships, or parametric equations that can be evaluated numerically. These solutions often serve as reference cases and are particularly useful for capturing asymptotic behavior or validating other models. Classical examples include steady viscous flow over a flat plate at high Reynolds number or the drag on a sphere in the low-velocity regime. Further examples are provided in Chap. 5.

The primary strength of analytical solutions lies in their clarity. They reveal the structure of the underlying physical relationships and offer functional dependencies between key variables and parameters. Compared to purely numerical or experimental results, they are often more interpretable and broadly applicable. They expose core physical mechanisms and can inform both model design and validation. However, deriving such solutions is rarely straightforward. It requires theoretical insight, mathematical skill, and often iterative refinement of assumptions. Although limited to idealized scenarios, analytical methods remain a foundational tool in physical modeling and are central to many hybrid approaches.

Several challenges can limit the applicability of exact solutions

Higher dimensionality As the number of spatial dimensions increases, solving the equations becomes significantly more complex, especially for systems governed by partial differential equations.

Nonlinear terms Nonlinearities complicate the analysis, and exact solutions are rare. Techniques such as linearization, similarity methods, or variable transformations can be used to manage this complexity.

Variable boundary conditions Time- or space-dependent boundaries can prevent exact solutions and may require approximations or numerical methods.

Complex geometries Realistic configurations often defy analytical solutions and must be simplified or approximated.

As a result, analytical results are typically limited to idealized cases with simple geometries, well-defined boundary conditions, and narrow operating ranges. Nevertheless, many classic solutions in the literature, including those by Lamb (1932), continue to provide value both as benchmarks and sources of insight.

Analytical solutions also play a key role in hybrid modeling. In some cases, they provide exact representations of simple systems. More

commonly, they help shape the structure of surrogate models, particularly when the original solution is valid only within a limited regime. For instance, known asymptotic behavior or limiting cases can guide the choice of base functions or help anchor extrapolations.

When closed-form expressions are unavailable or difficult to evaluate, analytical results can be sampled across a parameter space to generate datasets. These datasets can then be used for surrogate modeling, as will be discussed in the context of the thermal boundary layer in Sect. 5.2.1. This approach helps bridge the gap between theory and data by converting analytical insight into structured, accessible information for modern modeling pipelines.

1.5.2.2 Numerical Simulation

Numerical simulations provide approximate solutions to physical problems by solving the governing equations under specified boundary and initial conditions. As with theoretical analysis, the starting point is a mathematical description of the system, typically in the form of partial differential equations that express conservation laws, constitutive relations, and relevant physical assumptions such as compressibility or turbulence.

To enable computation, the continuous domain is discretized using methods such as finite differences, finite volumes, or finite elements. This transforms the governing equations into algebraic systems that can be solved numerically. Time integration schemes, iterative solvers, and matrix-based methods are then used to obtain an approximate solution that satisfies convergence criteria. Numerical solvers are often general-purpose, designed to handle classes of problems rather than single cases. For standard applications such as structural mechanics, fluid flow, or heat transfer, commercial and open-source solvers are widely available. For more specialized systems, custom or in-house solvers are commonly used, particularly in research and industrial settings where greater control or domain-specific modeling is required.

Setting up a simulation for a specific problem involves a sequence of decisions and parameter definitions

Definition of physical and computational setup This includes assigning material properties, defining model parameters (e.g., turbulence model parameters), configuring subscale models where applicable, and setting solver controls such as convergence thresholds or time step settings.

Domain discretization The geometry is converted into a mesh or grid that approximates the continuous domain using discrete elements. The mesh must capture important geometric features as well as local solution behavior, including boundary layers and near-wall gradients. It must also satisfy quality criteria to ensure accuracy, numerical stability, and convergence.

Boundary and initial conditions These specify the behavior of the system at the domain edges and at the beginning of the simulation and determine the results.

After execution, simulation results must be processed and interpreted. Post-processing involves exploring the computed outputs to gain physical insight and to extract specific quantities of interest.

Simulations are a powerful means of analyzing complex systems across a wide range of scales and geometries. They provide spatially and temporally resolved data that is often difficult or impossible to obtain through physical experiments. Because the simulation environment is fully defined, parameters can be varied systematically while others are held constant. This allows isolation of specific effects and helps link changes in inputs to their physical consequences.

However, simulations must be set up carefully to produce meaningful results. The most common sources of error stem from incomplete or inaccurate parameterization, such as poor discretization, unrealistic or ill-defined boundary conditions, or inappropriate solver settings. Modern solvers are robust and will often produce results even for questionable setups. As a consequence, it may be difficult to recognize when simulation outputs are physically incorrect or misleading. While simulation tools are now widely accessible, achieving

high-quality results still demands deep domain knowledge and practical experience. This is especially true for complex problems such as heat transfer. A critical mindset is essential. Practitioners should approach simulation outputs with caution and validate them against theoretical expectations or experimental observations wherever possible.

Simulations typically generate large volumes of data. Processing this data often requires significant computational resources, including parallel machines or high-performance clusters. Each simulation run corresponds to a specific configuration defined by a set of input parameters. To investigate the influence of individual variables or trends across a range of conditions, simulations must be repeated systematically. This increases the volume of data and computational cost, often motivating the use of surrogate models to approximate simulation outputs more efficiently.

1.5.2.3 Experimental Investigations

To avoid terminological confusion, we begin by distinguishing between a scientific experiment and experimental investigations. A **scientific experiment** refers to the structured methodology of acquiring empirical data to wither support or refute a hypothesis, as described in Sect. 1.1.4. In this subsection, we use the term **experiment** to refer to **experimental investigations**, meaning the acquisition of data that reflect how outcomes change in response to varying conditions, based on sensing and measuring physical quantities.

Experimental investigations are typically carried out in purpose-built laboratory setups. They are not merely data collection exercises, but play a central role in the iterative learning process introduced in Sect. 1.1.4. Like modeling, they involve forming expectations about system behavior, designing controlled setups to test those expectations, and using the resulting data to refine understanding. When observations deviate from expectations, this may prompt revisions in the test configuration, measurement approach, or underlying assumptions, following the same hypothesis-prediction-verification

loop that underpins scientific reasoning and hybrid modeling. Designing and maturing an experimental setup to a stage that supports valid, reproducible, and reliable measurements is therefore a demanding task. It typically involves the following stages.

Phenomenological subject of investigation The first step is to define the target phenomenon and how it will be measured. This is grounded in prior knowledge of the system. The physical variables involved are identified and a hypothesis about their relationships is formulated. These variables are classified by role, distinguishing inputs from outputs, and noting whether inputs are controllable or uncontrollable and whether they are directly measurable. In some cases, the process outcome can be observed directly, such as droplet deposition or splashing during impact. In other cases, it must be inferred from other measurements, such as estimating heat transfer coefficients from surface temperature data. In such cases, the method for deriving the target quantity from raw measurements must be clearly defined.

Scale and dimensionality The physical scale and dimensionality of the process strongly influence experimental design and instrumentation. Scale analysis provides expected value ranges for key variables and helps assess measurement feasibility. Some regimes are difficult or impractical to access, such as measuring drag on a full-scale aircraft or capturing the impact of a micrometer-sized droplet at high velocity. In these cases, dimensional analysis provides a structured framework for designing scaled experiments that preserve physical similarity, as will be discussed in Chap. 2 and Sect. 4.4.

Test rig design Once the phenomenology and scaling considerations are established, the experimental setup is developed. This includes selecting instrumentation, designing the data acquisition pipeline, and defining how measurement data will be stored. Sensor selection depends on the quantity of interest, the measurement location, and whether the data is to be collected at a point, along a line, over a plane, or in a full 3D field. Instrumentation should ideally have a minimal

influence on the process. For instance, Pitot tubes and hot-wire anemometers are intrusive but provide pointwise data. Non-intrusive techniques like particle image velocimetry (PIV) can capture flow fields across a plane. Each sensing method requires corresponding data acquisition hardware and software. Data processing is integral to experimental planning. This includes data storage and real-time acquisition infrastructure, along with analysis tools. Some quantities are measured directly, while others are computed from raw data. For example, image processing might be used for pattern recognition, and heat conduction models may be applied to derive heat transfer coefficients. High-speed imaging often generates large volumes of data, making data infrastructure critical. Error estimation and propagation analysis are essential to assess the reliability of results.

Assembly and calibration Once the setup is built, it is assembled and calibrated. Calibration ensures each sensor performs within its specified tolerance and helps quantify and reduce measurement uncertainty.

Measurement series execution Measurement campaigns should follow principles of statistical test design, often guided by Design of Experiments (DoE). Structured test planning improves the informativeness, reproducibility, and efficiency of the results.

Experimental setups are typically tailored to investigate specific physical processes. The level of instrumentation and the resolution of data acquisition vary depending on the required precision and scope of the investigation. Well-designed experiments are powerful because they are grounded in physical reality. Unlike theoretical or numerical analyses, which operate within idealized or abstract models, experiments reflect the complexity of real-world systems.

However, this realism also introduces unavoidable uncertainty. Sources include material property variation, manufacturing variability, and measurement noise. Real materials are not perfectly homogeneous and may vary spatially or change over time due to aging. Manufacturing

introduces tolerances, and surfaces intended to be smooth will exhibit some degree of roughness in practice.

These sources of variability make it challenging to achieve both high reproducibility and high reliability in experimental results. Even under tightly controlled laboratory conditions, it is difficult to hold all input variables constant and eliminate external influences such as ambient temperature or humidity. In practice, the ability to isolate the effect of a single variable often depends on the required precision and demands significant experimental effort.

1.5.2.4 Operational Measurements

Operational measurements refer to data collected from real-world industrial systems. These systems include equipment such as compressors on offshore platforms, pumps in processing plants, or heat exchangers in chemical facilities. Unlike experimental investigations, which are carefully designed to explore specific behaviors under controlled conditions, operational measurements are collected passively during routine system operation. The primary goal is not to gain physical insight or validate hypotheses, but to monitor performance, detect faults, and ensure safe, efficient, and reliable operation.

In industrial environments, sensors are integrated into systems to support process control and condition monitoring. These sensors are connected to control systems that regulate variables such as flow rate, temperature, or pressure to keep them within prescribed limits. Instrumentation in these settings is selected for robustness, maintainability, and responsiveness rather than scientific precision. For example, a pressure sensor on a pipeline may be used to trigger a control action or shutdown protocol, not to resolve fine-scale turbulence.

The operational context imposes clear constraints. The system operates under business-driven objectives such as maximizing throughput, minimizing downtime, or ensuring safety. Variations in input conditions arise incidentally as part of normal operation and are

not introduced intentionally. Changes in temperature, flow, or load result from process demands or environmental influences, not from a structured plan designed to explore system behavior. The system is not reconfigured to isolate variables, but instead runs to fulfill its intended industrial purpose.

Consequently, operational data reflects the system's actual behavior in practice, including its variability, disturbances, and noise. While measurements may be continuous and high-frequency, they are often incomplete or affected by external influences such as ambient temperature shifts, equipment fouling, or material wear. Sensor placement is typically dictated by accessibility or integration standards, rather than optimal observability, which means critical internal states may remain unmeasured or only indirectly observable.

As will be discussed in Chap. 10, operational data remain a valuable resource. It provides insight into long-term trends, supports maintenance strategies, and forms the foundation of industrial monitoring platforms. However, because it is not the result of a controlled experimental process, using it for model development requires caution. Inferring causality or detailed physical behavior from such data is difficult and often depends on strong prior knowledge or the availability of complementary information.

1.5.3 Data Quality

Understanding the types and sources of data lays the foundation for evaluating its quality. Data quality is a critical concern in any modeling effort, as the reliability and feasibility of data-driven components, such as empirical analysis and model development, depend directly on the quality of the input data.

To assess data quality systematically, we follow the framework defined in ISO 8000-8 (International Organization for Standardization 2015), which distinguishes three core categories, that is syntactic, semantic, and pragmatic. **Syntactic quality** concerns whether data conform to defined structural rules, including schemas, metadata, value ranges, and data types. **Semantic quality** refers to how accurately data

reflect the real-world entities or phenomena they represent. **Pragmatic quality** addresses whether the data are relevant and usable for a specific purpose, as judged by the user within a given context.

The standard further distinguishes between verification and validation. **Verification** confirms, through objective evidence, that data meet specified requirements. This typically applies to syntactic and semantic quality. **Validation**, by contrast, evaluates whether data is appropriate for a particular use case, and is central to assessing pragmatic quality (International Organization for Standardization and International Electrotechnical Commission 2008; Det Norske Veritas Germanischer Lloyd (DNV GL) 2017). In practice, data quality is assessed through the following commonly observed attributes.

Completeness The degree to which all required data elements are present. This is primarily a syntactic concern. Typical issues include

- Missing values due to sensor failure or sampling gaps
- Absent metadata or documentation
- Incomplete indexing, such as missing timestamps
- Partially recorded variables or incomplete records

Validity The extent to which data conform to defined structural or domain-specific constraints. Also a syntactic concern, common issues include

- Violations of format, type, or value constraints
- Values outside physically meaningful or permissible ranges
- Use of deprecated or undefined codes or categories
- Structural errors in time series, such as irregular intervals

Uniqueness The extent to which each record or data point is unambiguous and non-redundant. While related to validity, this dimension emphasizes data identity. Issues may include

- Duplicate rows or repeated timestamps
- Overlapping or redundant identifiers or entity references
- Repetition of spatial or temporal coordinates
- Collisions in composite keys or index structures

Accuracy The degree to which data truthfully represent the physical quantity or system behavior it is intended to measure. This reflects semantic quality. Typical concerns include

- **Noise** arising from random fluctuations not reflective of true system dynamics.
- **Outliers** due to measurement error or rare but valid phenomena, distinguishing between the two often requires expert judgment.
- **Non-repeatability or non-reproducibility**, where repeated measurements yield inconsistent results under seemingly identical conditions.
- **Bias** representing systematic deviation due to sensor placement, environmental interference, numerical approximation, or experimental design. Unlike noise, bias affects all measurements consistently and can propagate undetected through modeling pipelines, distort parameter estimation, and mislead interpretation.

Consistency The degree to which data remain coherent and non-contradictory across time, systems, and sources. Typically associated with semantic quality, common issues include

- Inconsistent units, variable naming, or metadata standards
- Conflicting values across different sources or within logs
- Irregular sampling rates or misaligned time grids
- Contradictory annotations or incomplete synchronization across data channels

While ISO 8000-8 does not prescribe specific quality dimensions, it offers a useful framework for organizing quality assessment. For example, syntactic quality requires a fully specified data structure and rule set. These enable verification procedures that are objective and repeatable (International Organization for Standardization and International Electrotechnical Commission 2008; Det Norske Veritas Germanischer Lloyd (DNV GL) 2017).

Pragmatic assessment of data quality goes beyond verification and must be considered holistically in relation to the modeling objective

and strategy. Even data that are complete, valid, and accurate may be unfit for use if sampled at the wrong scale, missing critical variables, or misaligned with modeling assumptions. Evaluating this aspect requires the modeler's judgment, domain knowledge, and exploratory analysis. It involves understanding the intended use of the data and ensuring it supports the specific goals of the modeling task.

References

Altman N, Krzywinski M (2015) Association, correlation and causation. Nat Methods 12(10):899–900
[https://doi.org/10.1038/nmeth.3587]

Box GEP, Hunter JS, Hunter WG (2005) Statistics for experimenters: design, innovation, and discovery. Wiley series in probability and statistics. Wiley

Det Norske Veritas Germanischer Lloyd (DNV GL). DNVGL-RP-0497:2017 – data quality assessment framework, 2017. Recommended Practice published by DNV GL

DuChateau P, Zachmann DW (2002) Applied partial differential equations. Dover books on mathematics. Dover Publications

Hertz H (1894) Die Prinzipien der Mechanik in neuem Zusammenhange dargestellt. Barth, Leipzig, 1894. Translated as The Principles of Mechanics Presented in a New Form

Hertz H (2003) The principles of mechanics presented in a new form. Dover Publications

Hodgson R et al (2025) Quantities, units, dimensions and types (QUDT) schema. www.qudt.org. Version 3.1.0

International Organization for Standardization (2015) ISO 8000-8:2015 – data quality – part 8: information and data quality: concepts and measuring. Standard published by the International Organization for Standardization

International Organization for Standardization (2016) ISO 14224:2016 – petroleum, petrochemical and natural gas industries – collection and exchange of reliability and maintenance data for equipment, 2016. ISO Standard

International Organization for Standardization and International Electrotechnical Commission. ISO/IEC 25012:2008 – software engineering – software product quality requirements and evaluation (SQuaRE) – data quality model, 2008. International Standard published by ISO and IEC

Isermann R (2016) Engine modeling and control: modeling and electronic management of internal combustion engines. Springer, Berlin

Lamb H (1932) Hydrodynamics. The University Press

Pearl J (2009) Causal inference in statistics: an overview. Stat Surv 3:96–146 [MathSciNet][https://doi.org/10.1214/09-SS057]

Peters G, Ortlieb CP, Dresky C, Gasser I, Günzel S (2013) Mathematische Modellierung: Eine Einführung in zwölf Fallstudien. Springer Fachmedien Wiesbaden

SINTEF Technology, Society, Norges teknisk-naturvitenskapelige universitet, and DNV GL (2015) OREDA: Offshore and Onshore Reliability Data Handbook. Topside Equipment. Number v. 1 in OREDA: Offshore and Onshore Reliability Data Handbook. OREDA Participants

von Rueden L, Mayer S, Beckh K, Georgiev B, Giesselbach S, Heese R, Kirsch B, Pfrommer J, Pick A, Ramamurthy R, Walczak M, Garcke J, Bauckhage C, Schuecker J (2023) Informed machine learning - a taxonomy and survey of integrating prior knowledge into learning systems. IEEE Trans Knowl Data Eng 35(1):614–633

Footnotes

1 Correlation always implies association, but not causation. Causation implies association, but not necessarily correlation, especially in the presence of nonlinear or complex relationships (Altman and Krzywinski 2015).

2 As discussed in Chap. 8, classical parametric models such as **linear regression** assume $Y = \beta X + \epsilon$ with $\epsilon \sim \mathcal{N}(0, \sigma)$, implying $P(Y \mid X) \sim \mathcal{N}(\beta X, \sigma)$. **Logistic regression** is used to model the conditional probability $P(Y = 1 \mid X) = 1/(1 + e^{-\beta X})$.

3 In this book, we use the term system model in a broader sense. In the context of industrial systems, the term **process model** may be used to emphasize the modeling of a specific physical transformation within a system. Unless otherwise stated, both terms are used interchangeably, as they serve the same purpose of describing how inputs lead to outputs through internal mechanisms governed by physical laws.

4 Stochastics is a collective term for the two fields of probability theory and statistics.

Part I
Physical Systems Knowledge and Behavior

© The Author(s), under exclusive license to Springer Fachmedien Wiesbaden GmbH, part of Springer Nature 2026
H. Gomaa, *Modeling with Knowledge and Data*, Mathematical Engineering
https://doi.org/10.1007/978-3-658-50679-7_2

2. Dimensional Analysis

Hassan Gomaa[1] ✉
(1) Strategic Projects Co-Innovation, Cognite, Oslo, Norway

In this part, we examine the role of physical knowledge in the modeling of engineering systems, with a particular emphasis on fluid and thermo-fluid processes. The chapters are organized to follow a logical progression from general, domain-independent modeling principles to increasingly specific representations of physical phenomena. This mirrors the typical approach in engineering modeling, which often starts with broadly applicable concepts, such as dimensional analysis or conservation laws, and gradually incorporates system-specific assumptions, physical approximations, and targeted simplifications to address specific practical problems.

We begin with this present chapter, which introduces the abstract structure of physical variables and equations, and presents the Π-theorem as a foundational tool for uncovering intrinsic relationships within physical models. By reformulating these relationships in terms of dimensionless numbers, we expose invariance properties that support generalization across units, scales, and geometries. This abstraction is a critical step in reducing complexity and developing physically grounded models. At this stage, the discussion remains largely agnostic to any specific application domain.

Chapter 3 introduces the primary variables and governing equations central to modeling fluid and thermal systems. We review key thermodynamic and mechanical quantities for describing the state and evolution of fluids, and derive the conservation laws for mass, momentum, energy, and entropy that serve as the foundation of continuum models.

These equations are accompanied by typical boundary conditions that arise in common physical applications.

In Chap. 4, we explore how the general governing equations can be simplified to extract dominant behavior in specific physical regimes. This includes identifying relevant terms in the equations, selecting appropriate fluid models, and analyzing characteristic regimes. We also introduce similarity principles that reduce model complexity and enable generalizable results based on scaled experiments or reduced-order representations. Particular attention is given to scaling laws in the context of turbomachinery, where dimensional analysis supports the interpretation and transferability of experimental results across different configurations and operating conditions.

Chapter 5 concludes this part by presenting a set of basic, canonical flow cases that capture essential physical phenomena, and illustrates the application of the governing equations and their simplifications to representative engineering problems. These include quasi-one-dimensional flows such as isentropic nozzle flow and shock waves, external flows described by boundary layer theory, and internal flows through pipes and ducts under laminar and turbulent conditions. These cases serve not only as didactic examples and benchmarks for model validation, but also as foundational elements for more complex system-level models discussed in later chapters.

2.1 Physical Variables and Equations

In engineering problems, we mostly work with physical variables, that is, quantities that carry both a numerical value and a physical dimension. These variables are linked through equations that reflect physical behavior. A fundamental requirement is that any valid physical equation must be dimensionally homogeneous, meaning that it must hold true regardless of the units used. The outcome of a physical calculation cannot depend on arbitrary choices of unit systems. To ensure this, physical relationships are expressed using dimensionless products, which are combinations of variables that remain unchanged when the unit system is altered. These products not only ensure consistency but also expose deeper structure of the system. By expressing relationships in terms of dimensionless numbers, we reveal invariance properties that support generalization across unit

systems, scales, and geometries. This is a crucial step toward simplifying complex systems and constructing models that are both robust and physically meaningful.

The foundation for this approach is provided by the Π-theorem, which will be introduced in Sect. 2.2. Before that, we establish the necessary groundwork by examining the structure of physical quantities, their dimensional representations, and the criteria for physically valid equations. For more extensive treatments of dimensional analysis, we refer to Simon et al. (2017) for illustrative examples, and to Görtler (1975), Sonin (2001) and Hunt (2009) for deeper theoretical discussions.

For the precise description of properties of objects and events in the physical world, the fundamental term of a **physical quantity** is introduced. A physical quantity represents a **measurable property** of an object and allows for its quantitative description and analysis. Physical quantities are organized into a constitutive system of **base quantities**, which are selected by convention. Each base quantity is regarded as independent and possesses its own **dimension** that cannot be expressed in terms of another base quantity. Following the common SI convention BIPM (2019), seven base quantities are defined. These are length (L), mass (M), time (T), thermodynamic temperature (Θ), electric current (I), amount of substance (N), and luminous intensity (J). The collection of all base quantities $[L\ M\ T\ \Theta\ I\ N\ J]$ is referred to as the **base quantity system**.

A physical quantity x is expressed as the product of a numeric value and a **unit**. The unit scales for base quantities must be ratio scales, i.e., they assume absolute zeros. The value range of such quantities thus corresponds to the domain of non-negative real numbers, hence $x \in \mathbb{R}^+$, where unity defines the referencing standard for the **base units**. The seven base units defined by the SI system BIPM (2019) are the meter (m), kilogram (kg), second (s), kelvin (K), ampere (A), mole (mol), and candela (cd).[1]

Following Sonin (2001), mathematical operations are formalized for base quantities by specifying the operations of comparison and addition. These operations are only defined between quantities of the same kind. For quantities of different kinds, no such operations exist. Suppose a, b, and c are base quantity samples of the same kind, then

1. the comparison operation determines equality ($a = b$) or inequality ($a \neq b$), and

2. the addition operation defines the sum of two samples a and b as $c = a + b$.

Based on these, further mathematical operations can be defined by analogy with operations on pure numbers

3. for $a + b = c$ the comparison (using $\geq$ and $\leq$) of like quantities yields $c \geq a$ and $c \geq b$,
4. for $a + b = c$ is equivalent to the subtraction $a = c - b$,
5. for $a + a = b$ is equivalent to multiplication $b = 2\ a$,
6. for $a + a = b$, this is equivalent to division $a = b/2$.

As a consequence, the value of a quantity can be expressed as a multiple of its defined base unit. Constructed from the base quantity system, all other physical quantities can be expressed, known as **derived quantities**. Derived quantities may be defined by expressions, such as area $A = \int\ dx\ dy$, velocity $u = dx/dt$, or motivated by a physical law, such as force, heat, or work. In all cases, the dimension of any derived quantity[2] can be expressed in power-law form using the base quantity dimensions

$$\begin{aligned} \dim\,(x) &= L^{a_1} M^{a_2} T^{a_3} \Theta^{a_4} I^{a_5} N^{a_6} J^{a_7} \\ &= \textstyle\prod_{i=1}^{m} X_i^{a_i}\ , \end{aligned} \tag{2.1}$$

where X_i denotes the *i*-th base quantity and the exponent $a_i \in \mathbb{Q}$. Equation (2.1), also known as the Bridgman formula, allows the unit of any quantity to be expressed as a product of powers of the base units. It also provides the transformation rule for the numerical value of a quantity when base units are changed. A variable *x* is called **dimensionless** when all exponents vanish

$$\dim\,(x) = 1 \qquad \Longleftrightarrow \qquad a_i = 0 \quad \forall \quad i = 1, \ldots, m\ . \tag{2.2}$$

The numerical value of dimensionless variables remains **invariant** under changes in the base unit system.

Physical equations describe functional relationships between physical variables, independent of the choice of unit system. For a relation to constitute a valid and meaningful physical equation, it must be dimensionally homogeneous. This means that both sides of an equality or inequality must have the same dimension. Likewise, all terms in a sum must share the same physical dimension, and any function argument must be dimensionless. To illustrate this, let a, b, c, d, e, f, g be physical quantities. Then the expression $a = b + (c + d^2)/e + f \sin(-g)$ is physically meaningful only if g is dimensionless, c and d^2 have the same dimension, and a, b, c/e, d^2/e, and f all share the same dimension. A crucial consequence of dimensional homogeneity is that physical equations remain valid regardless of the chosen unit system.

In the context of physical equations, one often encounters **physical constants** with fixed numerical values and associated dimensions. These constants may arise when certain variables in a formula are assigned specific values to simplify calculations. For instance, when converting pump pressure difference to the equivalent water column height, one may use the relation $\Delta p = \rho g \Delta h$. Assigning standard values $\rho = 997\ \mathrm{kg/m^3}$ and $g = 9.81\,\mathrm{m/s^2}$ yields $\Delta h = \Delta p / 9.8\ \mathrm{kN/m^3}$. In empirical relationships, one sometimes encounters dimensionally inhomogeneous expressions. Such formulas can be homogenized by introducing a dimensional constant. From a dimensional analysis perspective, these dimensional constants are treated as independent variables.

2.2 The Π—Theorem

The Π-theorem forms the foundation of dimensional analysis and is applied in mathematically equivalent formulations across model theory and similitude theory. It states that physical quantities can appear only in the form of dimensionless products in general functional dependencies, regardless of the specific form of the underlying equation.

Let $x_1, \ldots, x_n$ denote the n relevant physical variables for the problem under consideration. The Π-theorem asserts that any physical equation involving these variables can be transformed into an equivalent equation involving d dimensionless products $\Pi_1, \Pi_2, \ldots, \Pi_d$, thus

(2.3)

$$y = f(x_1, x_2, \ldots, x_n) \qquad \Longleftrightarrow \qquad \frac{y}{x_1^{k_1} x_2^{k_2} \cdots x_n^{k_n}} = g(\Pi_1, \Pi_2, \ldots, \Pi_d) \ .$$

The number of independent dimensionless products is given by $d = n - r$, where r is the rank of the dimension matrix, introduced later, and corresponds to the number of linearly independent base quantity dimensions involved. As will be shown, the theorem is constructive in the sense that it provides a formalism to determine the dimensionless products from the original physical variables. The explicit formulation in Eq. (2.3) is equivalent to the implicit form[3]

$$f(x_1, x_2, \ldots, x_n) = 0 \qquad \Longleftrightarrow \qquad f(\Pi_1, \Pi_2, \ldots, \Pi_d) = 0 \ . \tag{2.4}$$

We now convert the equation involving dimensional quantities into its dimensionless counterpart, demonstrating the equivalence in Eq. (2.4). To construct the dimensionless products $\Pi_1, \Pi_2, \ldots, \Pi_d$, we seek the exponents that each variable x_j, for $j = 1, \ldots, n$, takes in each product. In total, we determine $d \times n$ exponents, which we arrange into the matrix $\mathbf{K} \in \mathbb{Q}^{d \times n}$. To begin, we consider a single dimensionless product before generalizing. Any such product takes the form

$$\Pi = \textstyle\prod_{j=1}^{n} x_j^{k_j} \quad \text{, with} \quad k_j \in \mathbb{Q} \ . \tag{2.5}$$

Each physical variable x_j has a known dimension, expressible as a product of base quantities

$$\dim\,(x_j) = \textstyle\prod_{i=1}^{m} X_i^{a_{ij}} \quad \forall \quad j = 1, \ldots, n \ , \tag{2.6}$$

The exponents a_{ij} denote the dimension of x_j with respect to the i-th base quantity. We collect these into the **dimension matrix** $\mathbf{A} = (a_{ij}) \in \mathbb{Q}^{m \times n}$. Each row represents one base quantity, and each column represents a physical variable. For Π to be dimensionless, the combined dimension must be unity, thus

$$\dim\,(\Pi) = \textstyle\prod_{j=1}^{n} \dim\,(x_j)^{k_j} = 1 \ . \tag{2.7}$$

Substituting Eq. (2.6) into Eq. (2.7) gives

(2.8)

$$\prod_{j=1}^{n} \prod_{i=1}^{m} X_i^{a_{ij}k_j} = 1 \ .$$

Because the base quantities X_i are independent, dimensional unity must hold for each of the base quantities individually, thus

$$\prod_{j=1}^{n} X_i^{a_{ij}k_j} = 1 \quad \forall \quad i = 1, \ldots, m \ . \tag{2.9}$$

Taking logarithms reduces this to a linear system

$$\sum_{j=1}^{n} a_{ij}k_j = 0 \qquad \forall \quad i = 1 \ldots m \ . \tag{2.10}$$

Or in matrix form

$$\mathbf{A}\ \mathbf{k} = \mathbf{0} \text{ ,with } \quad \mathbf{A} \in \mathbb{Q}^{m \times n}, \ \ \mathbf{k} \in \mathbb{Q}^{n} \ . \tag{2.11}$$

Since typically $n > m$, the system is underdetermined and homogeneous. A meaningful physical relation requires $m < n$, since otherwise all variables could be independently dimensional, and no nontrivial relation can exist between them. With at most $m \leq 7$ (reflecting the number of SI base quantities), the dimension matrix $\mathbf{A}$ has rank $r \leq m$. We now restrict $\mathbf{A}$ to its r linearly independent rows, giving $\mathbf{A} \in \mathbb{Q}^{r \times n}$.

The solution space of the homogeneous system is $d = n - r$ dimensional, yielding d linearly independent solutions. To solve the system, we decompose the matrix

$$\mathbf{A} = [\mathbf{B} \mid \mathbf{C}] \quad \text{with} \quad \mathbf{B} \in \mathbb{Q}^{r \times d}, \ \mathbf{C} \in \mathbb{Q}^{r \times r} \ . \tag{2.12}$$

Here, $\mathbf{C}$ is a nonsingular submatrix and is invertible, thus $\det(\mathbf{C}) \neq 0$. The exponent vector is partitioned accordingly to

$$\mathbf{k} = \begin{bmatrix} \mathbf{k_B} \\ \mathbf{k_C} \end{bmatrix} \quad \text{with} \quad \mathbf{k_B} \in \mathbb{Q}^{d}, \ \mathbf{k_C} \in \mathbb{Q}^{r} \ , \tag{2.13}$$

so that the linear system from Eq. (2.11) becomes

$$\mathbf{B}\mathbf{k_B} + \mathbf{C}\mathbf{k_C} = \mathbf{0} \ . \tag{2.14}$$

In the matrix equation, the first term represents the d free parameters, while the second term imposes the r linear constraints. Since $\mathbf{C}$ is invertible, the system can be solved explicitly as

$$\mathbf{k_C} = -\mathbf{C}^{-1}\mathbf{B}\ \mathbf{k_B}\ . \tag{2.15}$$

For each dimensionless product, the free parameters $\mathbf{k_B}$ are assigned, and the corresponding values for $\mathbf{k_C}$ are determined via Eq. (2.15) to satisfy the r constraints. To span the full d-dimensional solution space, corresponding to the exponents of all independent dimensionless products, Eq. (2.15) is evaluated d times using linearly independent vectors for $\mathbf{k_B}$. For simplicity, the identity matrix $\mathbf{I}_d$ is chosen as a basis to supply these d linearly independent vectors. These vectors are not only linearly independent but also orthonormal. Transposing the resulting vectors $\mathbf{k}$ gives the exponent matrix $\mathbf{K} \in \mathbb{Q}^{d\times n}$ as

$$\mathbf{K} = \left[\ \mathbf{I}_d\ \middle|{-}\mathbf{C}^{-1}\mathbf{B}\mathbf{I}_d\ \right]^\top\ . \tag{2.16}$$

Substituting into Eq. (2.5) expands the dimensionless products as

$$\begin{aligned}
\Pi_1 &= x_1^1\ x_2^0\ x_3^0\ \cdots\ x_d^0\ x_{d+1}^{k_{1,d+1}} \cdots\ x_n^{k_{1,n}}\ , \\
\Pi_2 &= x_1^0\ x_2^1\ x_3^0\ \cdots\ x_d^0\ x_{d+1}^{k_{2,d+1}} \cdots\ x_n^{k_{2,n}}\ , \\
&\vdots \\
\Pi_d &= x_1^0\ x_2^0\ x_3^0\ \cdots\ x_d^1\ x_{d+1}^{k_{d,d+1}} \cdots\ x_n^{k_{d,n}}\ .
\end{aligned} \tag{2.17}$$

In each product, the first d exponents stem from the chosen free parameters, here $\mathbf{I}_d$, and the last r are solutions of the constraint equations. Substituting into Eq. (2.4) gives

$$f(\Pi_1, \Pi_2, \ldots, \Pi_d, x_{d+1}, \ldots, x_n) = 0\ . \tag{2.18}$$

To show that the dependency on $x_{d+1}, \ldots, x_n$ is artificial, consider a unit change of base quantities with scaling factors α_i, such that $X_i = \alpha_i X_i'$ for all $i = 1, \ldots, m$. This induces

$$x_j = x_j' \textstyle\prod_{i=1}^{r} \alpha_i^{a_{ij}} \quad \forall\ j = 1, \ldots, n\ . \tag{2.19}$$

Substituting into Eq. (2.21), the dimensionless products remain unchanged, since they are invariant under unit system changes. The last *r* variables however are affected, with

$$f(\Pi_1, \Pi_2, \ldots, \Pi_d, x'_{d+1} \prod_{i=1}^{r} \alpha_i^{a_{i,d+1}}, \ldots, x'_n \prod_{i=1}^{r} \alpha_i^{a_{i,n}}) = 0 \ . \tag{2.20}$$

Taking logarithms yields the system of equations

$$\sum_{i=1}^{r} a_{ij} \ln(\alpha_i) = \ln(x'_j) - \ln(x_j) \qquad \forall \quad j = d+1, \ldots, n \ . \tag{2.21}$$

The unknowns are the scaling factors $\ln(\alpha_i)$. The coefficient matrix corresponds to the transposed nonsingular submatrix $\mathbf{C}^\top$, which has full rank. Therefore, the system admits a unique solution for the *r* scaling factors. It follows that we can assign arbitrary values to x'_j and uniquely determine the corresponding scaling factors such that the transformation $x_j \mapsto x'_j$ holds for all $j = d+1, \ldots, n$. For example, we may choose the transformed values $x'_j = 1$, in which case Eq. (2.21) simplifies to $f(\Pi_1, \ldots, \Pi_d, 1, \ldots, 1) = 0$. The fact that we can arbitrarily assign values to these variables implies that a meaningful physical relation cannot depend on them. The functional dependency therefore reduces to

$$f(\Pi_1, \Pi_2, \ldots, \Pi_d) = 0 \ . \tag{2.22}$$

It is important to note that the specific form of the dimensionless products in Eq. (2.22) is not unique. The solution spans a *d*-dimensional vector space, meaning that there exist infinitely many valid representations of the dimensionless groups. Each corresponds to a different choice of *d* linearly independent exponent vectors. The construction shown here is based on selecting the identity matrix $\mathbf{I}_d$ as a basis for the free parameters, which results in the first *d* variables appearing linearly, with unit exponent, in each Π_i, as seen in Eq. (2.17). This choice is purely conventional and carries no physical meaning.

The Π-groups themselves are mathematically defined constructs and are not physically unique. For example, Π_1^2, $1/\Pi_1$, or Π_1/Π_2 are all equally valid representations of dimensionless combinations. These alternative forms result from different, but still linearly independent,[4] choices of the free

parameters. As long as the exponent vectors span the same *d*-dimensional space, the corresponding products are valid and equivalent from the standpoint of dimensional analysis.

Example 2.1 To illustrate the calculation procedure, consider the flow around a sphere. The drag force F_D on a sphere of diameter D depends on the flow velocity u, the fluid density ρ, and the dynamic viscosity μ Simon et al. (2017). The functional relationship is assumed to be of the form

$$F_D = f(u, \mu, \rho, D) \ .$$

All physical quantities are described using the base quantities length, mass, and time, so their dimensions are given in terms of *LMT*. The corresponding dimension matrix is

---

Table

The problem involves $n = 5$ physical variables. The last three variables form a lower triangular submatrix, indicating that the dimension matrix has full rank $r = 3$. Hence, we expect to find $d = n - r = 2$ independent dimensionless products. These take the general form

$$\Pi_i = F_D^{k_{1i}} \ u^{k_{2i}} \ \mu^{k_{3i}} \ \rho^{k_{4i}} \ D^{k_{5i}} \quad i = 1, \ldots, d \ . \tag{2.23}$$

The task is to determine the exponent matrix $\mathbf{K} \in \mathbb{Q}^{d \times n}$. Since the last three columns are linearly independent, they form a suitable choice for the nonsingular submatrix $\mathbf{C} \in \mathbb{Q}^{r \times r}$, which can be inverted. The system of equations for the constrained exponents becomes

$$\begin{bmatrix} -1 & -3 & 1 \\ 1 & 1 & 0 \\ -1 & 0 & 0 \end{bmatrix} \begin{bmatrix} k_3 \\ k_4 \\ k_5 \end{bmatrix} = - \begin{bmatrix} 1 & 1 \\ 1 & 0 \\ -2 & -1 \end{bmatrix} \begin{bmatrix} k_1 \\ k_2 \end{bmatrix}$$

$$\begin{bmatrix} k_3 \\ k_4 \\ k_5 \end{bmatrix} = - \begin{bmatrix} 0 & 0 & -1 \\ 0 & 1 & 1 \\ 1 & 3 & 2 \end{bmatrix} \begin{bmatrix} 1 & 1 \\ 1 & 0 \\ -2 & -1 \end{bmatrix} \begin{bmatrix} k_1 \\ k_2 \end{bmatrix}$$

$$\begin{bmatrix} k_3 \\ k_4 \\ k_5 \end{bmatrix} = \begin{bmatrix} -2 & -1 \\ 1 & 1 \\ 0 & 1 \end{bmatrix} \begin{bmatrix} k_1 \\ k_2 \end{bmatrix}$$

This system provides *r* constraints with *d* free parameters. Choosing the identity matrix $\mathbf{I}_d$ as basis for the free parameters $\begin{bmatrix} k_1 & k_2 \end{bmatrix}^\top$ yields the exponent matrix $\mathbf{K}$ and the corresponding dimensionless products

$$\mathbf{K} = \begin{bmatrix} 1 & 0 & -2 & 1 & 1 \\ 0 & 1 & -1 & 1 & 1 \end{bmatrix} \quad \Rightarrow \quad \Pi_1 = \frac{F_D \rho}{\eta^2} \ , \quad \Pi_2 = \frac{u \rho D}{\eta} \ . \tag{2.24}$$

Choosing the identity matrix effectively results in the drag force F_D and the velocity *u* appearing linearly in Π_1 and Π_2, respectively. For practical applications, the more commonly used nondimensional group is the drag coefficient

$$C_D = \frac{F_D}{\rho u^2 D^2} = \frac{\Pi_1}{\Pi_2^2} \ , \tag{2.25}$$

which combines the basic Π-groups into a physically interpretable form.

2.2.1 Application in Model Development

The dimensional argument is a powerful approach for tackling engineering modeling problems. With mere algebra, the dimensional structure of the original variables can be condensed into meaningful dimensionless groups.

The use of dimensionless products in model development is beneficial, as the resulting equations inherently satisfy the fundamental requirements of meaningful physical relations. In particular, the developed models are dimensionally homogeneous by construction and invariant under unit transformations. This confers a higher degree of generality and applicability to the resulting model formulations.

In its application,dimensional analysis is mathematically exact. It produces dimensionless groups for any given set of physical variables with known dimensions. However, the dimensional argument does not offer a *free lunch*, as it may sometimes seem. It requires prior knowledge of the relevant independent variables and their physical dimensions. If the chosen set of variables is incomplete, important effects may be omitted and the analysis becomes misleading. Conversely, including superfluous variables can obscure the result and lead to unnecessarily complex expressions.

A sound starting point for identifying the essential variables is the analysis of the governing physical laws, ideally supported by a deliberate selection of simplifying assumptions. In general, dimensional analysis alone does not assess the physical relevance of the preselected variables, nor does it judge the interpretability or utility of the resulting dimensionless groups. Rather, dimensional analysis is best understood as a powerful tool in the iterative modeling process, supporting hypothesis formation, model refinement, and comparison against data, until satisfactory agreement is achieved, as discussed in Sect. 1.1.4.

From a purely algebraic perspective, dimensional analysis provides valuable **structural insights** for problem-solving, particularly in the special cases discussed in the following.

2.2.2 Solitary Base Quantity

When a base quantity appears in only one of the selected variables, we refer to it here as a **solitary base quantity**, and to the associated variable as a solitary variable. In the dimension matrix, this becomes evident as a row with only one nonzero entry. Since no other variable contains this base quantity, its dimension cannot be canceled. As a result, the solitary variable cannot meaningfully relate to the other variables in the set through a physical equation. Such cases indicate a poorly posed composition of the preselected variables. If the solitary variable is a dependent variable, it is

formally considered obsolete and can be disregarded in the dimensional analysis.

To illustrate, consider the case of an oscillating pendulum Simon et al. (2017), where a mass *m* is attached to the end of a pendulum of length ℓ. We are interested in the characteristic oscillation period τ. A first attempt at selecting relevant variables yields $\tau = f(\ell, m, g)$ with the corresponding dimension matrix

---

Table

Here, only *m* contains the mass dimension *M*. Since no other variable shares this dimension, *m* cannot participate in a dimensionless product. This suggests either that a relevant variable containing mass is missing, or that *m* is physically irrelevant in this context. Assuming the latter, the remaining variables yield a single dimensionless product $\Pi = \tau\sqrt{g/\ell}$.

If instead the solitary variable is the dependent variable, this indicates that a relevant independent variable is missing. To illustrate, revisit the example of flow around a sphere discussed previously in Sect. 2.2. We again seek the drag force F_D on a sphere as a function of its diameter *D*, the flow velocity *u*, and fluid properties. In an attempt to reduce the number of variables, the dynamic viscosity μ and density ρ are replaced by the kinematic viscosity $\nu = \mu/\rho$, yielding the proposed relation $F_D = f(u, \nu, D)$, with the corresponding dimension matrix

---

Table

Here, F_D is the only variable containing the mass dimension *M*. Since none of the independent variables share this dimension, a dimensionless product involving F_D cannot be formed. This signals that a relevant independent variable, such as μ or ρ, has been incorrectly omitted. The variable composition must thus be incomplete.

2.2.3 Single Dimensionless Product

In general, dimensional analysis does not provide information about the functional form the dimensionless products take. However, in the special case where there is only a single dimensionless product, that is, $d = 1$, the

situation is more constrained. In this case, the dimensionless product must be constant $\Pi = \text{const.}$. This implies that the dimensional structure alone fully determines the functional form of the relation between the variables. The result is not merely a scaling relation, but a fixed proportionality that holds across systems with the same dimensional structure.

To illustrate, consider the speed of sound a in a gas, where the gas state is characterized by pressure p and density ρ Simon et al. (2017). The dimension matrix is given by

---

Table

Here, $n = 3$ and the rank of the dimension matrix is $r = 2$, leaving $d = n - r = 1$ independent dimensionless product. The resulting product is $\Pi = a\sqrt{\rho/p}$. Since this is the only dimensionless group, dimensional analysis implies that $\Pi = \text{const.}$, and thus $a \sim \sqrt{p/\rho}$.

For an ideal gas, this constant can be determined from thermodynamic principles as $\text{const.} = \sqrt{\gamma}$, where γ is the isentropic exponent of the gas. This case highlights how dimensional analysis, in combination with minimal physical insight, can directly yield both the structure and proportional form of a model.

References

BIPM (2019) Le Système international d'unit s/The International System of Units (The SI Brochure). Bureau international des poids et mesures, 9th edition, 2019. www.bipm.org

Görtler H (1975) Dimensionsanalyse: Theorie der physikalischen Dimensionen mit Anwendungen. Springer

Hunt JK (2009) Lecture notes on applied mathematics, methods and models. University of California, Davis, Department of Mathematics

Simon V, Weigand B, Gomaa H (2017) Dimensional analysis for engineers. Springer, Mathematical engineering
[https://doi.org/10.1007/978-3-319-52028-5]

Sonin AA (2001) The physical basis of dimensional analysis, 2nd edn. Department of mechanical engineering, MIT

Footnotes

1 Within the SI system, the base units are defined by declaring fixed numerical values for seven defining constants: the hyperfine transition frequency of the caesium-133 atom $\Delta\nu_{Cs}$, speed of light in vacuum *c*, Planck constant *h*, elementary charge *e*, Boltzmann constant *k*, Avogadro constant N_A, and the luminous efficacy K_{cd} of 540 THz monochromatic radiation. These constants cover both fundamental natural constants and selected technical constants. They are chosen to provide a stable and universal reference, enabling practical realization with minimal uncertainties BIPM (2019).

2 With the exception of counts, plane angles, and solid angles, which are considered to have unit dimension.

3 In the implicit formulation, *y* is not treated as an independent variable but rather as one of the dependent variables. While this changes the count of variables by one, it does not affect the rank of the dimension matrix or the further derivation.

4 When referring to independent dimensionless products, this denotes that the corresponding vectors of exponents are linearly independent. The independence refers to the mathematical structure of the exponent space, not the physical quantities themselves.

© The Author(s), under exclusive license to Springer Fachmedien Wiesbaden GmbH, part of Springer Nature 2026
H. Gomaa, *Modeling with Knowledge and Data*, Mathematical Engineering
https://doi.org/10.1007/978-3-658-50679-7_3

3. Governing Equations

Hassan Gomaa[1] ✉
(1) Strategic Projects Co-Innovation, Cognite, Oslo, Norway

This chapter presents the constitutive foundation for describing thermo-fluid systems, grounded in the fundamental laws of mechanics and thermodynamics. We begin by introducing the key physical variables that characterize the thermodynamic state, kinematic motion, and transport behavior of fluids. These variables form the basis for expressing conservation laws and enable a consistent description of the mechanisms governing fluid motion and heat transfer. At the core of this chapter are four universally valid conservation laws

- Conservation of mass
- Conservation of momentum
- Conservation of energy (First Law of Thermodynamics)
- Irreversibility of natural processes (Second Law of Thermodynamics).

Each law is introduced in its integral form, followed by its reformulation into a differential representation to describe the local evolution of the respective quantities. Special attention is given to identifying the role and physical meaning of individual terms within the governing equations. This aims to provide a basis for understanding the dominant mechanisms in a given flow situation and for selecting appropriate modeling assumptions or boundary conditions. Unless otherwise noted, the analysis is limited to Newtonian fluids and pure substances, under conditions where the continuum hypothesis holds and local thermodynamic equilibrium is assumed.

3.1 Fluid and Flow Properties

This section introduces the fundamental physical properties that characterize fluid behavior and govern flow dynamics. These properties, expressed as field variables in continuum formulations, describe how fluids store internal energy, undergo deformation, and enable the transport of mass, momentum, and heat. They form the material basis for the conservation laws developed in the subsequent sections and provide the necessary closure relations for physically consistent modeling. Following the classification proposed by White (1991), we distinguish three main categories of properties

- **Thermodynamic properties**, such as pressure, density, temperature, enthalpy, and entropy, which describe the energetic state of the fluid.

- **Kinematic properties**, such as velocity, acceleration, vorticity, and strain rates, which characterize the motion and deformation of fluid elements.
- **Transport and interfacial properties**, such as viscosity, thermal conductivity, and surface tension, which quantify diffusive processes and surface effects.

3.1.1 Thermodynamic Variables

Thermodynamic variables describe the macroscopic state of a substance and form the foundation for modeling physical behavior in thermo-fluid systems. As introduced in Sect. 1.2.1, we adopt the concept of a system as a macroscopic control volume or material element, within which we analyze physical processes. The system contains a substance that undergoes transformations driven by energy and mass exchange.

In the following, we develop a consistent thermodynamic description of such systems. We begin by characterizing pure substances and their phase behavior, then introduce key state variables such as pressure, temperature, and internal energy. We then relate these variables through the First and Second Laws of Thermodynamics, introduce derived quantities such as heat capacities and the speed of sound, and conclude with their interdependence via state equations. Generally, we focus on the macroscopic behavior of pure substances in thermodynamic equilibrium, where continuum assumptions hold and local equilibrium can be assumed.

State of a Pure Substance A **pure substance** refers to a homogeneous material of uniform chemical composition. A substance may exist in any of the three classical states, that is solid, liquid, or gas, each representing a distinct **phase**. A **phase** denotes a subregion of the system that is chemically uniform and exhibits homogeneous physical properties. For example, an ice-water mixture qualifies as a pure substance with coexisting solid and liquid phases, while an air-steam mixture is not a pure substance due to its differing chemical components. During a phase change, the molecular configuration of the substance undergoes significant rearrangement, resulting in substantial changes to its thermodynamic properties. A phase need not be spatially continuous, but it may be dispersed throughout another phase, as in the case of mist droplets in air or vapor bubbles in liquid. The state that a substance assumes under particular temperature and pressure conditions depends on the specific material.

Under certain pressure and temperature conditions, two or even all three phases may coexist in equilibrium. All phase states of a substance can be represented on a surface defined by the variables p, v, and T, commonly visualized in a phase diagram. The diagram shown in Fig. 3.1 is qualitatively representative for most substances. However, water exhibits a notable deviation due to its density anomaly (reaching its maximum density at 4 $^\circ$C). As a result, the solid phase (ice) is less dense than the liquid, leading to a **negative** slope of the solid-liquid boundary in the p–T diagram, which explains why ice floats on the water surface. In contrast to the positive temperature gradient typically observed, the melting temperature of ice **decreases** with increasing pressure. For instance, that is why ice melts under pressure, such as beneath ice skates.

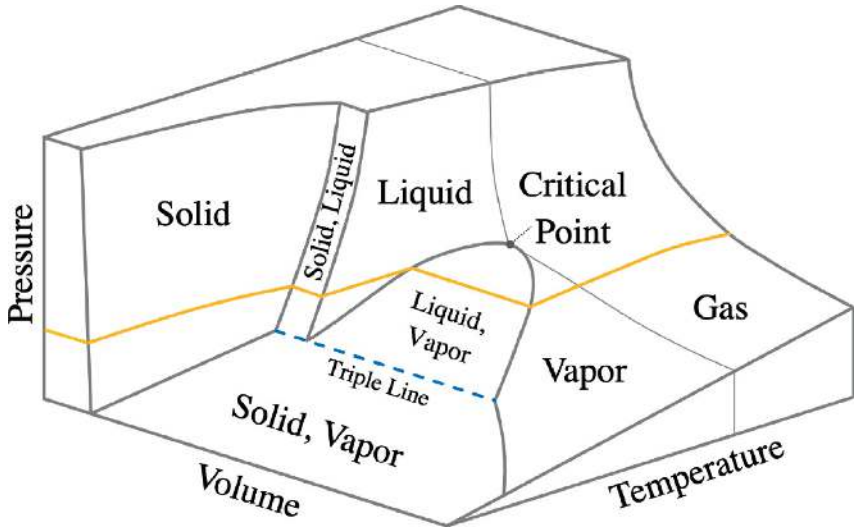


Fig. 3.1 Schematic *p*, *v*, *T* phase diagram for a pure substance

To explore the characteristics of the phase diagram, we follow an isobaric path in Fig. 3.1. At low volumes and low temperatures, the substance resides in the solid phase. Solids consist of tightly packed molecules restricted to vibrational motion and heat addition primarily raises their temperature. Upon reaching the melting point, the substance begins to transition into the liquid phase. During this transformation, known as fusion, the temperature remains constant (for $p = \text{const.}$), and both phases coexist. The heat input required to complete this transition is the **fusion enthalpy**. Like solids, liquids exhibit strong intermolecular forces and nearly constant volume, but they lack a fixed shape, rendering them effectively incompressible. When the substance reaches the boiling line, it enters the liquid-vapor two-phase region. This region is bounded by the **liquid saturation curve** and **vapor saturation curve**. Within this region, pressure and temperature are again coupled, and the required heat input, known as the **vaporization enthalpy**, leads to a change in phase at constant pressure and temperature. Both the boiling temperature and the vaporization enthalpy vary with the prevailing pressure.

At the **triple line**, the solid, liquid, and vapor phases coexist in thermodynamic equilibrium. It is characterized by a unique pressure-temperature pair specific to each substance. Below the triple line pressure, the liquid phase ceases to exist, and only solid-gas coexistence is possible. The **critical point** marks the end of the liquid-vapor saturation curve. It represents the highest pressure and temperature at which the liquid and gas phases can coexist. Beyond this point, the fluid is said to be in a **supercritical state**, in which the distinction between liquid and gas phases vanishes.

In the two-phase region, we quantify the state using the **vapor quality**, defined as the mass fraction of vapor $x = m_{\text{vap}}/(m_{\text{vap}} + m_{\text{liq}}),\ \ x \in [0, 1]$. Here, $x = 0$ corresponds to a saturated liquid, and $x = 1$ to a saturated vapor. Within the two-phase region any specific extensive property, such as *v*, *h*, *u*, *s*, is quantified by the mass weight average between the saturation line. For example, the specific enthalpy is expressed as $h = h_{\text{liq}} + x(h_{\text{vap}} - h_{\text{liq}})$. Table 3.1 summarizes some thermophysical properties for selected substances, including caloric and critical data.

Table 3.1 Caloric and critical data of selected substances according to Verein Deutscher Ingenieure (2013). The boiling point and vaporization enthalpy are provided at 1.013 bar

Beyond the vapor saturation curve, the substance is in the gaseous phase. Near this curve, molecular interactions such as attraction forces and finite molecular size become significant, and real gas models, such as the van der Waals equation, are required Weigand et al. (2016). However, far from the saturation region, where densities are sufficiently low, these interactions become negligible, and the gas can be modeled as **ideal**.

Strictly speaking, thermodynamic state variables are only well-defined under conditions of thermodynamic equilibrium, implying mechanical, thermal, and chemical equilibrium. In this text, we restrict our attention to the continuum regime, where the number of molecules per unit volume is extremely large. The associated molecular interactions occur on temporal and spatial scales far smaller than those of interest to macroscopic modeling. Consequently, deviations from local equilibrium are typically negligible.

Example 3.1 Consider a cube of air with a volume of $1\,\mu\mathrm{m}^3$ at standard conditions. This volume contains approximately 10^8 molecules. Each molecule undergoes about 10^{10} collisions per second. Local thermodynamic equilibrium is typically reached after around $\mathcal{O}(10)$ molecular collisions.

This implies that equilibrium is reached within an extremely short time scale of about $10^{-9}\,\mathrm{s}$ and over a spatial distance on the order of $10^{-9}\,\mathrm{m}$. These characteristic microscopic scales are many orders of magnitude smaller than those encountered in engineering flows regarded here. Therefore, even though the fluid consists of discrete molecules, the averaging over vast numbers of particles justifies the continuum assumption used in macroscopic modeling.

State Variables The thermodynamic state of a substance is defined by its **state variables**, like the pressure p, density ρ, temperature T, internal energy E, enthalpy H and entropy S. The specific volume $v = 1/\rho$ is often used interchangeably with density.[1] Thermodynamic properties can be classified based on how they scale with the size of the system. **Extensive variables**, such as mass, volume, and energy, scale proportionally with the amount of substance. Doubling the mass of the system, for example, doubles its energy and volume. In contrast, **intensive variables**, such as temperature and pressure, are independent of the system size. They describe the local physical state of the material. Dividing extensive properties by a reference quantity such as mass or volume yields specific quantities, for example, specific volume $v = V/m$, specific internal energy $e = E/m$, specific enthalpy $h = H/m$, and specific entropy $s = S/m$. In thermodynamics, we often prefer specific quantities to isolate material behavior from system size. As detailed in the following, to fully define the thermodynamic state of a system, typically two independent intensive variables as well as the system mass m are required.

All state variables depend only on the current state of the system, not on the process by which the state was reached. For example, in a thermodynamic cycle, the system returns to its original state, and each state variable z returns to its initial value, that is $\oint dz = 0$. For a

pure substance, any two independent intensive variables (excluding the two-phase regions mentioned above) uniquely define the thermodynamic state. The remaining variables follow from **state equations**, which can be derived from theory or obtained experimentally. In regions of phase change, such as the liquid–vapor domain, pressure and temperature are not independent. An additional parameter, such as vapor quality, is needed to fully describe the system state. The functional relation between pressure, density, and temperature is called the **thermal state equation**, typically written as $f(p, \rho, T) = 0$. The dependencies of specific internal energy $e(T, v)$, specific enthalpy $h(T, p)$, and specific entropy $s(p, T)$ are referred to as **caloric state equations**.

The **density** ρ represents mass per unit volume. From a molecular perspective, it reflects the number of particles contained in a given space. **Pressure** p and **temperature** T are macroscopic quantities that emerge from the collective motion of molecules. Temperature corresponds to the average kinetic energy of the molecules, while pressure results from the average force exerted by molecular collisions onto a surface. Although these quantities originate from discrete molecular interactions, they are perceived as smooth and continuous properties at the macroscopic level. As illustrated in the previous example, this is due to the extremely large number of molecules involved. Individual molecular events are not resolved. Instead, their aggregate behavior forms the basis of measurable thermodynamic variables.

The specific **internal energy** e represents the amount of energy stored on an atomic and molecular level, such as the molecular kinetic energy, with translational, rotational, and vibrational contributions, as well as intermolecular forces that contribute as potential energy. The internal energy is part of the system's total specific energy $e_{\mathrm{tot}} = e + e_{\mathrm{kin}} + e_{\mathrm{pot}}$. The total energy of a closed system is conserved, as governed by the first law of thermodynamics. As discussed in detail in Sect. 3.2, energy changes occur through interactions with the surroundings in the form of **heat** δq and **work** δw

$$de_{\mathrm{tot}} = \delta q + \delta w \ . \tag{3.1}$$

Energy itself is a property of the system and depends only on its current state. In contrast, heat and work are not state variables, and they represent forms of energy transfer at the system boundaries. The amount of heat or work exchanged during a process depends on the specific path the system follows between two states. Therefore, heat and work are path-dependent **process variables**, and their differentials are not total derivatives. To distinguish them from exact differentials like dE, we write inexact differentials as δq and δw .[2] We adopt a system-centric sign convention, where heat transferred **to** the system and work done **on** the system are considered positive. Conversely, heat lost by the system and work done **by** the system are negative.

Work is a form of energy transfer. Mechanical work involves force applied over a distance, such as $\delta w = \mathbf{f} \cdot d\mathbf{x}$. In thermodynamics, the most common form is pressure-volume work, expressed as $\delta w = -p\, dv$. Other forms include work against gravity, shear stress, surface tension, or electrical work (from charge transport in electric fields). **Heat** transfer occurs due to a temperature difference between a system and its surroundings. The temperature gradient acts as the driving force for this transfer. It can

proceed by conduction (diffusion), thermal radiation (electromagnetic waves), or convection. Convective heat transfer combines conduction with fluid motion, and the diffusive transport is enhanced by the bulk movement of the fluid, making it a distinct and important mechanism, particularly in fluid systems.

In many thermodynamic applications, it is useful to identify which form of energy responds directly to heat transfer. This depends on the type of process considered, specifically whether volume or pressure is held constant. If changes in kinetic and potential energy are negligible, then heat and work transfer affect only the internal energy, and the first law simplifies to $de = \delta q + \delta w$. If the only work involved is pressure-volume work, then $\delta w = -p\,dv$, so for a process at constant volume, no work is performed and the energy change equals the heat added, thus $de = \delta q$. Under constant volume conditions, any heat exchange changes the internal energy directly.

Many technical applications, however, operate under constant pressure conditions ($dp = 0$). In such cases, it is more convenient to use **enthalpy** as the energy measure. The specific enthalpy is defined as

$$h = e + p\,v \ . \tag{3.2}$$

To see how enthalpy responds to heat transfer at constant pressure, consider its total differential, $dh = de + p\,dv + v\,dp$. For systems with constant kinetic and potential energy, and assuming volume work as the only work form, the first law simplifies to $de = \delta q - p\,dv$. Substituting into the enthalpy differential gives $dh = \delta q + v\,dp$. For constant pressure processes, $dp = 0$, and the relation reduces to $dh = \delta q$. Therefore, under isobaric conditions, all supplied heat directly increases the system's enthalpy.

While internal energy and enthalpy are governed by the First Law of Thermodynamics, **entropy** is introduced through the Second Law. Entropy is also a state variable and quantifies the degree of microscopic disorder or randomness in a system. The change in specific entropy can be split into two contributions, an **entropy transfer** term associated with heat exchange across the system boundary, and an **entropy production** term arising from internal irreversible processes Weigand et al. (2016), so that

$$ds = ds_{\text{exch}} + ds_{\text{gen}} \ . \tag{3.3}$$

Entropy transfer is directly linked to the transfer of heat and can be directed into or out of the system. In a closed system where an amount of heat δq is supplied at a boundary temperature T, the transferred specific entropy is given by $ds_{\text{exch}} = \delta q/T$. Note that entropy is transferred only via heat, not via work.

The second term, ds_{gen}, accounts for entropy generated inside the system due to irreversible processes such as viscous dissipation, diffusion, or mixing. As elaborated in Sect. 3.2, and in accordance with the Second Law of Thermodynamics, the generated entropy must be non-negative, thus $ds_{\text{gen}} \geq 0$. The generated entropy is related to the specific energy dissipated within the system $\delta\psi$, with $ds_{\text{gen}} = \delta\psi/T$. Between two equilibrium states 1 and 2, the specific entropy contributions can be integrated as

(3.4)

$$\Delta s_{\text{exch}} = \int_1^2 \frac{\delta q}{T} \ , \qquad \Delta s_{\text{gen}} = \int_1^2 \frac{\delta \psi}{T} \ .$$

Perhaps counterintuitively from an energy conservation perspective, the amount of transferred entropy depends on the temperature at which heat is exchanged. The same amount of heat δq transferred at a higher temperature results in a lower entropy increase. Similarly, entropy production depends on the system's reference temperature. So for a given amount of dissipated energy $\delta \psi$, for instance due to internal friction, a higher reference temperature leads to a smaller amount of produced entropy. Later in Eq. (3.63), both entropy transfer and generation are specified for flow and heat conduction processes.

A central reference case is the **reversible adiabatic** process, also known as an **isentropic** process. In this idealized case, no heat is exchanged ($\delta q = 0$), and no entropy is produced ($ds_{\text{gen}} = 0$). Applying Eq. (3.3), the entropy remains constant throughout the process, thus $ds = 0$.

Heat Capacities In the previous section, we distinguished how heat affects internal energy or enthalpy, depending on whether volume or pressure is held constant. Heat capacities formalize this connection by quantifying how much heat δq is required to raise the temperature of a substance. According to the First Law of Thermodynamics, supplied heat can both increase internal energy and perform work. The amount of heat required to raise the temperature of a substance, that is the **heat capacity**, therefore depends on the nature of the thermodynamic process. In most technical applications, heat is transferred either at constant volume (isochoric process) or constant pressure (isobaric process). The corresponding heat capacities are defined as

$$c_p = \frac{\delta q}{\partial T}\Big|_p = \frac{\partial h}{\partial T}\Big|_p \ , \qquad c_v = \frac{\delta q}{\partial T}\Big|_v = \frac{\partial e}{\partial T}\Big|_v \ . \tag{3.5}$$

These definitions follow directly from the relation between heat and changes in internal energy or enthalpy, depending on the constraints of the process. For all substances, it holds that $c_p \geq c_v$, since at constant pressure, part of the heat is used for expansion work. A general expression relating the two heat capacities can be derived Weigand et al. (2016, p. 54) to

$$c_p = c_v + \left(p + \frac{\partial e}{\partial v}\Big|_T \right) \frac{\partial v}{\partial T}\Big|_p \ . \tag{3.6}$$

The difference $c_p - c_v$ is especially relevant for gases, as detailed in Eq. (3.15). For liquids and solids, thermal expansion is small, thus volume work is normally negligible. In such cases, it is often reasonable to approximate $c_p \approx c_v \approx c$, and to neglect the pressure dependence of c.

A useful dimensionless quantity is the heat capacity ratio, denoted as **adiabatic index** or **isentropic exponent**, defined by

$$\gamma = \frac{c_p}{c_v} \ . \tag{3.7}$$

This ratio plays a key role in the description of reversible thermodynamic processes, particularly in compressible flows, as discussed in Sect. 4.2. For fluids, typical values of γ lie between 1.0 and 1.8, and the ratio is close to unity for liquids. The **speed of sound** is a derived property that characterizes how small pressure or density disturbances propagate through a medium. In fluids, it is defined by the thermodynamic response of pressure to density changes under isentropic conditions, that is, assuming reversible compression and no heat exchange

$$a^2 = \frac{\partial p}{\partial \rho}\Big|_s \ . \tag{3.8}$$

This relation reflects the compressibility of the medium and determines the rate at which acoustic signals travel. Typical orders of magnitude are approximately $100\,\mathrm{m/s}$ in gases, $1000\,\mathrm{m/s}$ in liquids, and $10\,000\,\mathrm{m/s}$ in solids, reflecting increasing stiffness of the medium.

State Equations The fundamental thermodynamic relation, also known as the **Gibbs equation**, connects the primary state variables. It is consistent with the First Law of Thermodynamics and is derived by considering the limit of a lossless process involving reversible pressure-volume work with $\delta w = -p\,dv$ and heat transfer as $\delta q = T\,ds$. For a closed system containing a pure substance,[3] and neglecting changes in kinetic and potential energy, substitution of δw and δq into the First Law of Thermodynamics in Eq. (3.1) yields

$$\begin{aligned} T\,ds &= de + p\,dv \\ &= dh - v\,dp \ . \end{aligned} \tag{3.9}$$

This relation contains only state variables and is therefore independent of the process path. Although derived under the assumption of reversible processes, since it only involves state variables it remains valid for irreversible changes as well Spurk (1996).

As discussed earlier, the thermal equation of state expresses the relationship between pressure, specific volume, and temperature $f(p, v, T) = 0$. Generally, the relation can assume a complicated surface, so we introduce additional thermodynamic coefficients to characterize the surface's local slope

$$\alpha_p = \frac{1}{v}\frac{\partial v}{\partial T}\Big|_p \ , \quad \beta_v = \frac{1}{p}\frac{\partial p}{\partial T}\Big|_v \ , \quad \kappa_T = -\frac{1}{v}\frac{\partial v}{\partial p}\Big|_T \ . \tag{3.10}$$

The derivative α_p is known as the **isobaric thermal expansivity**, and quantifies how the volume of a substance changes with temperature at constant pressure. Gases are highly sensitive to temperature changes, while liquids and solids respond more moderately, though not negligibly, as evidenced by phenomena such as thermometric expansion or natural convection. The coefficient β_v is the **isochoric pressure coefficient**, which describes how the pressure changes with temperature when the volume is held constant. Lastly, κ_T is the **isothermal compressibility**, measuring how the volume of a substance changes under pressure at constant temperature. Its inverse, the **bulk modulus** $K = 1/\kappa_T$, is particularly relevant in the analysis of sound wave propagation White (1991). By

applying the total differential of the thermal state equation, it can be shown that the three coefficients are related by the identity $\alpha_p = p\beta_v\kappa_T$.

Using these, total differentials of specific internal energy, specific enthalpy, and specific entropy can be expressed[4] in terms of *p*, *v*, and *T* as

$$du = c_v\ dT + \left(\frac{T}{p}\frac{\partial p}{\partial T}\Big|_v - 1\right)p\ dv = c_v\ dT - (1-\beta_v T)p\ dv\ , \tag{3.11}$$

$$dh = c_p\ dT + \left(1 - \frac{T}{v}\frac{\partial v}{\partial T}\Big|_p\right)v\ dp = c_p\ dT + (1-\alpha_p T)v\ dp\ , \tag{3.12}$$

$$\begin{aligned} ds &= \frac{\partial p}{\partial T}\Big|_v dv + \frac{c_v}{T}\ dT = \beta_v p\ dv + \frac{c_v}{T}\ dT \\ &= -\frac{\partial v}{\partial T}\Big|_p dp + \frac{c_p}{T}\ dT = -\alpha_p v\ dp + \frac{c_p}{T}\ dT\ . \end{aligned} \tag{3.13}$$

Substituting the rewritten heat capacity $c_v = T\partial s/\partial T|_v$ into the Gibbs relation in Eq. (3.9) allows the specific entropy change to be expressed explicitly as

$$ds = \left(\frac{1}{T}\frac{\partial e}{\partial v}\Big|_T + \frac{p}{T}\right)dv + \frac{c_v}{T}dT\ . \tag{3.14}$$

In addition to entropy, also the functional relationship between the heat capacities c_p and c_v can be derived to Weigand et al. (2016)

$$c_p = c_v - T\frac{\partial p}{\partial T}\Big|_v \frac{\partial v}{\partial T}\Big|_p = c_v + vT\frac{\alpha_p^2}{\kappa_T} = c_v - pvT\alpha_p\beta_v\ . \tag{3.15}$$

This expression demonstrates how the difference in heat capacities is determined by the material's thermal expansivity and compressibility. For an incompressible material or in the limit of negligible thermal expansion, the difference vanishes. Introducing the **isentropic compressibility** $\kappa_s = -(1/v)\partial v/\partial p|_s$ allows to analogously express the adiabatic index as $\gamma = \kappa_T/\kappa_s$ and the speed of sound as $a^2 = v/\kappa_s$.

The above identities form the basis for deriving thermodynamically consistent models for specific materials. In the following, we apply them to derive the two important limiting cases of an ideal gas and an incompressible substance.

Ideal Gas An ideal gas follows the thermal equation of state

$$p\,v = R\,T\ , \tag{3.16}$$

where $R = \mathscr{R}/M$ is the specific gas constant, with the universal gas constant $\mathscr{R} = 8.3145\,\mathrm{J/(mol\ K)}$ and the molar mass *M*. The partial derivatives of this equation yield the thermodynamic coefficients to $\alpha_p = 1/T$, $\kappa_T = 1/p$ and $\beta_v = 1/T$. Evaluating Eqs. (3.11) and (3.12) for an ideal gas shows that internal energy and enthalpy depend solely on temperature, with

(3.17)

$$de = c_v\,dT\ , \qquad dh = c_p\,dT\ .$$

This allows for the integral expressions

$$e(T) = e(T_0) + \int_{T_0}^{\top} c_v(T)\,dT\ , \qquad h(T) = h(T_0) + \int_{T_0}^{\top} c_p(T)\,dT\ , \tag{3.18}$$

where T_0 is an arbitrary reference temperature. Since both *e* and *h* depend only on *T*, they are independent of *v* and *p*. Consequently, also the heat capacities c_p and c_v are functions of temperature only. The relation between the heat capacities is given by $c_p(T) - c_v(T) = R$. Using the adiabatic index $\gamma(T)$, the heat capacities can be alternatively expressed as

$$c_p(T) = \frac{\gamma(T)}{\gamma(T)-1} R\ , \qquad c_v(T) = \frac{1}{\gamma(T)-1} R\ . \tag{3.19}$$

To evaluate the specific entropy change for an ideal gas, we apply Eq. (3.14), resulting in

$$\begin{aligned} ds &= \tfrac{R}{v} dv + \tfrac{c_v}{T} dT \\ &= -\tfrac{R}{p} dp + \tfrac{c_p}{T} dT\ . \end{aligned} \tag{3.20}$$

These expressions show how entropy changes with both volume and temperature, or alternatively with pressure and temperature. For an isentropic process ($ds = 0$), integrating Eq. (3.20) gives the classic isentropic relations

$$p\,v^{\gamma} = \text{const.}\ , \qquad p^{\gamma-1}\,T^{\gamma} = \text{const.} \tag{3.21}$$

The speed of sound in an ideal gas then becomes $a^2 = \gamma\,R\,T$. If the heat capacities c_p and c_v are constant, the gas is termed **calorically perfect**. This is a valid assumption for many monoatomic and noble gases such as He, Ne, and Ar, as well as diatomic gases like O_2, H_2, and N_2 over a considerable temperature range. For more complex molecules, the assumption is often applied within a narrower temperature range to simplify computations, as will be discussed in Sect. 4.1. Under this assumption, the thermodynamic functions simplify to

$$\begin{aligned} e(T) &= e(T_0) + c_v(T - T_0)\ , \\ h(T) &= h(T_0) + c_p(T - T_0)\ , \\ s(p,T) &= s(p_0,T_0) - R\,\ln\left(\tfrac{p}{p_0}\right) + c_p\,\ln\left(\tfrac{T}{T_0}\right)\ . \end{aligned} \tag{3.22}$$

Incompressible Substance A **material of constant density**, such as a liquid or solid, is modeled as incompressible, implying no volume change during thermal or mechanical processes, that is $dv = 0$. This directly implies that $\alpha_p = 0$ and $\kappa_T = 0$. Substituting into Eq. (3.15) shows that the difference between c_p and c_v vanishes, so the heat capacities equalize, thus $c_p = c_v = c$. Evaluating the expressions for internal energy, enthalpy and entropy result to

(3.23)

$$de = c\,dT \ , \qquad dh = c\,dT + v\,dp \ , \qquad ds = \tfrac{c}{T}dT \ .$$

Therefore, for incompressible substances, both internal energy and entropy depend only on temperature, while enthalpy also retains a pressure dependency due to the $p\,v$-work term.

3.1.2 Kinematic Variables

Kinematics describes the motion and deformation of material elements per se, regardless of the forces that cause them. It provides a geometric foundation for analyzing how fluids and solids move, stretch, and rotate. For a rigorous treatment, reference is made to classical continuum mechanics texts such as Chadwick (2013). Notably, many kinematic relations in fluid mechanics have analogs in solid mechanics, replacing the velocity vector $\mathbf{u}$ by displacement components yields corresponding expressions used in elasticity theory Goodier and Timoshenko (1970).

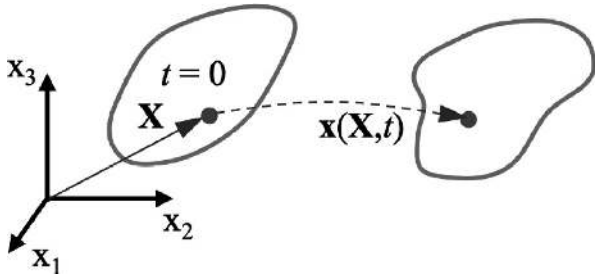


Fig. 3.2 The motion and deformation of a body from its initial reference state

To describe the motion of a material body, we consider it to consist of infinitesimal material elements. At the initial time $t = 0$, these are located at reference positions $\mathbf{X}$, representing the undeformed reference state. Each element may move (translate or rotate) and deform (stretch or shear) as time progresses, changing both its position and internal geometry over time. Its position at time t is described by a mapping $\mathbf{x}(\mathbf{X}, t)$, which tracks the material trajectory. Figure 3.2 illustrates this evolution for a representative point P, using Cartesian coordinates for the sake of clarity.

The **translational velocity** of a material point is defined as the time derivative of its position. The time derivative of velocity yields the **acceleration**

$$\mathbf{u} = \tfrac{d\mathbf{x}}{dt} \ , \qquad \dot{\mathbf{u}} = \tfrac{d\mathbf{u}}{dt} = \tfrac{d^2\mathbf{x}}{dt^2} \ . \tag{3.24}$$

Beyond translation, material elements may also undergo rotation. Local rotation of an infinitesimal fluid element is described by the **vorticity vector** $\boldsymbol{\omega}$, defined as

$$\boldsymbol{\omega} = \nabla \times \mathbf{u} \ . \tag{3.25}$$

A flow field is called **irrotational** if the vorticity vanishes, that is $\boldsymbol{\omega} = \mathbf{0}$.

To quantify deformation, we define the **rate of strain tensor** $\mathbf{S}$. It describes how a material element stretches or shears due to the local velocity gradients. For general orthogonal curvilinear coordinates, the complete form is provided in Eq. (A.15). For illustration, we present here its Cartesian form

$$\mathbf{S} = \begin{pmatrix} S_{11} & S_{12} & S_{13} \\ S_{21} & S_{22} & S_{23} \\ S_{31} & S_{32} & S_{33} \end{pmatrix} = \begin{pmatrix} \frac{\partial u}{\partial x} & \frac{1}{2}\left(\frac{\partial u}{\partial y} + \frac{\partial v}{\partial x}\right) & \frac{1}{2}\left(\frac{\partial u}{\partial z} + \frac{\partial w}{\partial x}\right) \\ \frac{1}{2}\left(\frac{\partial v}{\partial x} + \frac{\partial u}{\partial y}\right) & \frac{\partial v}{\partial y} & \frac{1}{2}\left(\frac{\partial v}{\partial z} + \frac{\partial w}{\partial y}\right) \\ \frac{1}{2}\left(\frac{\partial w}{\partial x} + \frac{\partial u}{\partial z}\right) & \frac{1}{2}\left(\frac{\partial w}{\partial y} + \frac{\partial v}{\partial z}\right) & \frac{\partial w}{\partial z} \end{pmatrix} . \tag{3.26}$$

Here, the components *u*, *v*, and *w* represent the velocity in the *x*, *y*, and *z* directions, respectively. The tensor $\mathbf{S}$ is symmetric by definition. The diagonal terms S_{11}, S_{22}, S_{33} represent normal strain rates that quantify local rates of elongation or compression along each coordinate direction. The off-diagonal terms represent shear strain rates that measure angular deformation and how fluid elements change shape.

The tensor has three transformation **invariants**, which are scalar quantities that remain unchanged under coordinate transformations. These invariants are closely associated with the **principal directions** that represent the coordinate axes along which the tensor becomes diagonal. In this configuration, the off-diagonal components vanish, and the tensor only exhibits normal components. The diagonal entries in this frame are the **principal strain rates**, corresponding to pure extension or compression without shear. Mathematically, the principal strain rates are the eigenvalues of the strain rate tensor $\mathbf{S}$, and the corresponding principal directions are its eigenvectors. They are obtained by solving the eigenvalue problem $\mathbf{S} - \lambda\mathbf{I} = \mathbf{0}$, which yields the characteristic polynomial $|\mathbf{S} - \lambda\mathbf{I}| = -\lambda^3 + J_1\lambda^2 - J_2\lambda + J_3 = 0$. The coefficients J_1, J_2, and J_3 are the tensor invariants, defined as follows

$$\begin{aligned} J_1 &= \text{tr}\,(\mathbf{S}) = S_{11} + S_{22} + S_{33} \ , \\ J_2 &= \begin{vmatrix} S_{22} & S_{23} \\ S_{32} & S_{33} \end{vmatrix} + \begin{vmatrix} S_{11} & S_{13} \\ textsection_{31} & S_{33} \end{vmatrix} + \begin{vmatrix} S_{11} & S_{12} \\ textsection_{21} & S_{22} \end{vmatrix} \\ &= S_{11}S_{22} + S_{22}S_{33} + S_{11}S_{33} - S_{12}^2 - S_{23}^2 - S_{31}^2 \ , \\ J_3 &= \det\,(\mathbf{S}) = S_{11}S_{22}S_{33} + 2S_{12}S_{23}S_{31} - S_{12}^2S_{33} - S_{23}^2S_{11} - S_{31}^2S_{22} \ . \end{aligned}$$

In summary, J_1 is the trace of the tensor, J_2 is the sum of its principal minors (the determinants of the 2×2 submatrices formed by omitting each diagonal element in turn), and J_3 is the determinant of the tensor. Importantly, the trace $\text{tr}\,(\mathbf{S}) = \nabla \cdot \mathbf{u}$ corresponds to the **volumetric strain rate** or dilation rate, meaning the rate at which the fluid element expands or contracts in volume.

In the principal coordinate system, the tensor simplifies to a diagonal matrix with entries S_1, S_2, and S_3. The invariants then reduce to

$$\begin{aligned} J_1 &= S_1 + S_2 + S_3 \ , \\ J_2 &= S_1S_2 + S_2S_3 + S_3S_1 \ , \\ J_3 &= S_1S_2S_3 \ . \end{aligned}$$

These invariants provide coordinate-independent scalar measures of the strain field and are essential in characterizing deformation. They are widely used in both fluid and solid mechanics, particularly in identifying deformation types, such as pure shear, elongation, or rigid-body rotation.

To fully characterize local fluid motion, the velocity gradient tensor $\nabla \mathbf{u}$ can be decomposed into a symmetric and an antisymmetric part. The symmetric part corresponds to the rate of strain tensor $\mathbf{S}$ defined above, which captures stretching and shearing deformation. The antisymmetric part is given by the **rotation rate tensor**

$$\mathbf{\Omega} = \frac{1}{2}\left(\nabla \mathbf{u} - (\nabla \mathbf{u})^{\top}\right) , \tag{3.27}$$

and describes local rigid-body-like rotation. Together, $\mathbf{S}$ and $\mathbf{\Omega}$ span all first-order velocity gradients and provide a complete kinematic description of the fluid motion.

3.1.3 Transport and Interfacial Properties

Transport properties govern how momentum, energy, and mass are diffused within a medium due to molecular motion. These include the **dynamic viscosity** μ, **thermal conductivity** k, and **mass diffusivity** D. In this section, we focus on the first two, as they directly appear in the governing equations of momentum and energy conservation. Each property links a flux, i.e., momentum flux, heat flux, or species flux to a gradient of the associated field variable. Specifically, viscosity relates shear stress to the velocity gradient, while thermal conductivity relates heat flux to the temperature gradient. In addition, we examine the role of **surface tension** σ, which governs the behavior of fluid interfaces and is central to multiphase flows, droplets, and capillary phenomena.

For most fluids, these transport phenomena are isotropic, meaning they are directionally uniform and do not depend on orientation relative to the coordinate axes. This assumption greatly simplifies modeling and is valid for the vast majority of Newtonian fluids encountered in engineering.

Viscosity The fluid viscosity characterizes the internal resistance to tangential or shear motion within the medium. It is associated with the development of frictional forces when adjacent fluid layers slide past one another. It is low for gases and for easily flowing liquids such as water and alcohol, but high for viscous substances like oil and glycerine.

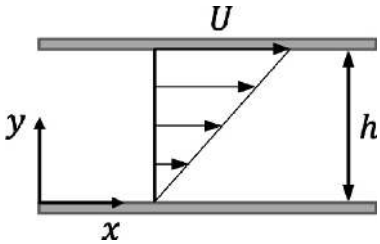


Fig. 3.3 Couette flow between parallel plates with linear velocity profile

The role of viscosity is well illustrated by the classical Couette flow experiment, shown in Fig. 3.3, where a fluid is confined between two parallel plates, one stationary and one

moving at a steady velocity U. For steady flow, the velocity profile is linear, thus $u(y) = Uy/h$, and the shear stress at any point in the fluid is given by

$$\tau_{xy} = \mu \frac{\partial u}{\partial y} \quad . \tag{3.28}$$

The quantity μ is the **dynamic viscosity**, which defines the proportionality between shear stress and velocity gradient. This linear relationship is an empirical observation known as Newton's law of viscosity, and it holds remarkably well for a wide class of fluids called **Newtonian fluids**, to which we limit ourselves in this book. In contrast, **non-Newtonian fluids** exhibit more complex stress-strain behavior that deviates from this linear law White (1991, p. 24).

In flows where both viscous and inertial effects are important, the **kinematic viscosity** $\nu = \mu/\rho$ becomes especially relevant, as it characterizes the ratio of momentum diffusion to inertia. For both gases and liquids, the dynamic viscosity μ is largely independent of pressure, but exhibits strong dependence on temperature. In liquids, viscosity typically decreases with increasing temperature due to weakened intermolecular forces. In gases, by contrast, viscosity increases with temperature, as illustrated in Fig. 3.4.

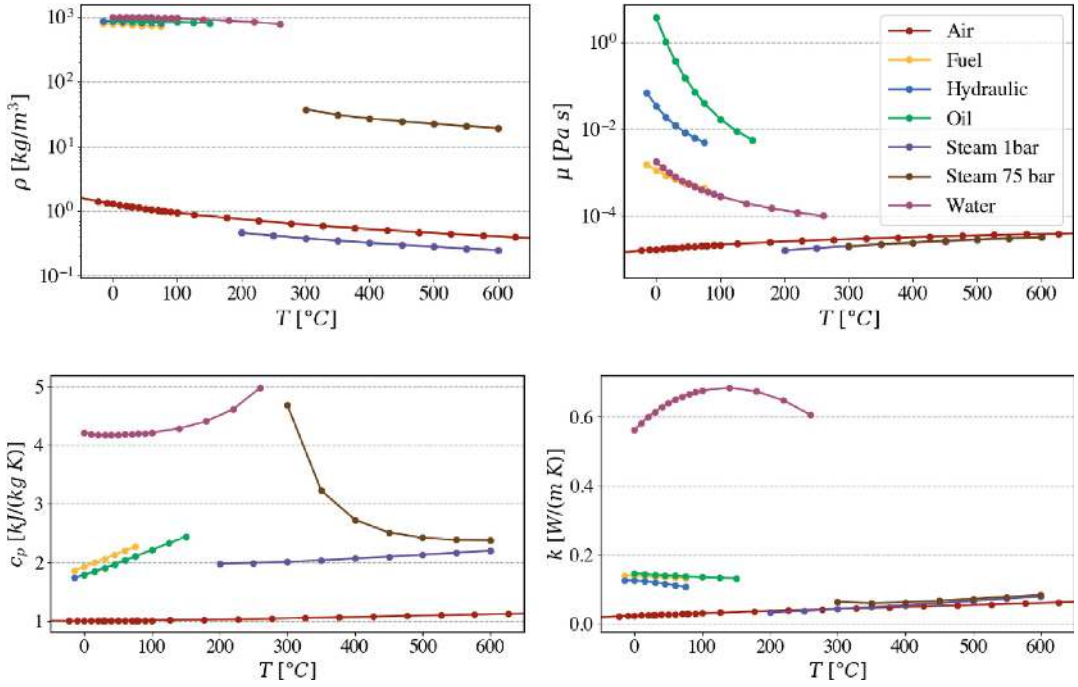


Fig. 3.4 Temperature dependency for density ρ, viscosity μ, heat capacity c_p and thermal conductivity k for selected substances Kays et al. (2005)

Generalizing the previous discussion, shear stresses in a fluid correspond to the off-diagonal components of the rate of strain tensor $\mathbf{S}$. For Newtonian fluids, these stresses are linearly related to the strain rates, with the proportionality factor given by 2μ. While μ governs the response to shear deformation, the additional coefficient λ_b, known as the **bulk viscosity coefficient**, characterizes the fluid's resistance to volume dilatation. Together, these form the **viscous stress tensor**

$$\boldsymbol{\tau} = 2\mu\mathbf{S} + \lambda_b(\nabla \cdot \mathbf{u})\mathbf{I} \ . \tag{3.29}$$

For illustration, the components of $\boldsymbol{\tau}$ in Cartesian coordinates are expanded element-wise to

$$\boldsymbol{\tau} = \begin{pmatrix} \tau_{11} & \tau_{12} & \tau_{13} \\ \tau_{21} & \tau_{22} & \tau_{23} \\ \tau_{31} & \tau_{32} & \tau_{33} \end{pmatrix} = \begin{pmatrix} 2\mu\frac{\partial u}{\partial x} + \lambda_b \nabla \cdot \mathbf{u} & \mu\left(\frac{\partial u}{\partial y} + \frac{\partial v}{\partial x}\right) & \mu\left(\frac{\partial u}{\partial z} + \frac{\partial w}{\partial x}\right) \\ \mu\left(\frac{\partial v}{\partial x} + \frac{\partial u}{\partial y}\right) & 2\mu\frac{\partial v}{\partial y} + \lambda_b \nabla \cdot \mathbf{u} & \mu\left(\frac{\partial v}{\partial z} + \frac{\partial w}{\partial y}\right) \\ \mu\left(\frac{\partial w}{\partial x} + \frac{\partial u}{\partial z}\right) & \mu\left(\frac{\partial w}{\partial y} + \frac{\partial v}{\partial z}\right) & 2\mu\frac{\partial w}{\partial z} + \lambda_b \nabla \cdot \mathbf{u} \end{pmatrix} . \tag{3.30}$$

In this notation, the first index denotes the direction of the surface normal, and the second index the direction of the stress component. The generalized formulation for curvilinear orthogonal coordinates is given in the Appendix Eq. (A.10).

To represent the full state of stress in the fluid, including both pressure forces and viscous effects, we introduce the **total stress tensor** $\mathbf{T}$ as

$$\mathbf{T} = -p\mathbf{I} + \boldsymbol{\tau} = (-p + \lambda_b \nabla \cdot \mathbf{u})\mathbf{I} + 2\mu\mathbf{S} \ . \tag{3.31}$$

As noted by White (1991, p. 67), the interpretation of the bulk viscosity coefficient λ_b is not without ambiguity and has been the subject of debate. The average normal stress is obtained from averaging the diagonal elements of the stress tensor $\mathbf{T}$. Its negative represents the mean normal compression acting on a fluid element and is commonly referred to as the **mechanical pressure** $\bar{p}$. In contrast, the **thermodynamic pressure** p is defined by the fluid's equation of state, typically as a function of density and temperature, $p = p(\rho, T)$. Comparing these two notions of pressure, we find

$$p - \bar{p} = p + \tfrac{1}{3}(T_{11} + T_{22} + T_{33}) = (\lambda_b + \tfrac{2}{3}\mu)\nabla \cdot \mathbf{u} \ , \tag{3.32}$$

which shows that p and $\bar{p}$ are generally not equal in flows with nonzero divergence. The difference arises due to volumetric dilation and is usually small enough to be neglected in most practical applications. However, in strongly compressible flows, such as shock waves, the term can become relevant (Spurk, 1996; White, 1991). In the special case of incompressible flow, where $\nabla \cdot \mathbf{u} = 0$, the two pressures coincide, so $p = \bar{p}$. To simplify the stress formulation and eliminate this ambiguity more generally, we adopt the commonly used **Stokes hypothesis**, which assumes $\lambda_b = -2\mu/3$. With this assumption, the difference $p - \bar{p}$ vanishes identically, regardless of whether the flow is compressible or incompressible. As a result, the thermodynamic pressure p can consistently be interpreted as the mechanical pressure $\bar{p}$, simplifying the momentum equations. This assumption is used throughout this text.

Table 3.2 Material properties covering density ρ, heat capacity c_p, thermal conductivity k, dynamic viscosity μ and kinematic viscosity ν for selected materials at specified temperature and atmospheric pressure. Data from Kays et al. (2005) and Verein Deutscher Ingenieure (2013)

Thermal Conductivity The ability of a material to conduct heat is described by its thermal conductivity k. According to **Fourier's law**, the heat flux vector $\mathbf{q}$, that is the rate of heat transfer per unit area, is proportional to the negative temperature gradient

$$\mathbf{q} = -k\,\nabla T \ . \tag{3.33}$$

The negative sign reflects that heat flows from regions of higher temperature to lower temperature, in agreement with the Second Law of Thermodynamics. The coefficient k is an intensive property that characterizes the intrinsic ability of a material to transfer thermal energy via molecular interactions. Thermal conductivity strongly varies between common substances, spanning over four orders of magnitude. As shown in Table 3.2, gases typically have low thermal conductivity, liquids fall in a moderate range, and solids, particularly metals, exhibit the highest values. This trend reflects the dominant mechanism of heat transfer in each phase, with molecular collisions in gases, intermolecular interactions in liquids, and free electron motion in metals.

While fluids are typically assumed to be isotropic, meaning k is uniform in all directions, some solids, such as crystals or composites, can exhibit anisotropic thermal conductivity. In such materials, heat may conduct more readily along one axis than another, depending on the internal structure. Mathematically, this means that the scalar k must be replaced by a second-order tensor $\mathbf{k}$, and Fourier's law becomes $\mathbf{q} = -\mathbf{k}\nabla T$, with $\mathbf{k}$ varying with material orientation.

Surface Tension As a result of attracting intermolecular forces, surface tension occurs at liquid-gas interfaces. Liquid molecules near the interface are surrounded by a reduced number of neighbors, and therefore experience a net inward force toward the bulk. Molecules at the interface are in an energetically less favorable state compared to those in the bulk. The creation of new surface is therefore energetically costly, so surface tension acts to minimize the interfacial surface area.

Phenomenologically, in a static environment, surface tension acts to smooth out any surface disturbances on a planar interface, and a small contained liquid body tends to evolve toward a spherical shape. Surface tension is an area-specific energy, or equivalently a line-specific force, that acts in all directions within the interface. For an interfacial surface S bounded by a closed contour C, the surface tension force is defined by

$$\mathbf{F} = \oint_C \sigma \, d\mathbf{s} \ , \tag{3.34}$$

where $d\mathbf{s}$ is the incremental arc length along the perimeter C.

Across different liquids, surface tension increases with stronger intermolecular forces and smaller molecular sizes de Gennes et al. (2003). Typical values are around $20\ \mathrm{mN/m}$ for oils, $70\ \mathrm{mN/m}$ for water White (1991), and up to $500\ \mathrm{mN/m}$ for liquid metals, such as mercury, when interfacing with air. Surface tension can vary strongly depending on temperature, chemical composition, or the presence of contaminants. As temperature increases, surface tension decreases and eventually vanishes at the critical point. Finally, it should be mentioned that interfacial tensions at fluid-fluid interfaces between immiscible

substances, such as an oil-water interface, follow the same mechanisms and are modeled analogously.

3.1.4 Variable Material Property

All thermodynamic and transport properties discussed so far are state variables, meaning they depend on the local thermodynamic state of the substance. As introduced in Sect. 3.1.1, the state of a pure substance is defined by two independent variables, commonly temperature and pressure. In general, material properties exhibit a strong dependence on temperature and a weaker, but not always negligible, dependence on pressure Verein Deutscher Ingenieure (2013). An important exception is the gas density, which strongly depends on both pressure and temperature.

Material property values for specific substances are available in standard databases and engineering handbooks, which compile experimentally measured data and equations of state. The body of literature on modeling material properties is extensive and is not intended to be comprehensively reviewed here. Instead, we point to two representative and widely used resources that provide a solid foundation for engineering practice. The VDI Heat Atlas Verein Deutscher Ingenieure (2013) offers a broad compilation of data for heat transfer applications, including pure fluids, mixtures, refrigerants, oils, metals, polymers, and more. Another key reference is the NIST Reference Fluid Thermodynamic and Transport Properties database (REFPROP) Lemmon et al. (2018), which provides high-accuracy data for industrially relevant fluids and mixtures.

For a given engineering application, it is important to estimate the expected range of thermophysical property variation early in the analysis. This assessment helps to determine whether property variability can be neglected or must be included. As detailed in Sect. 4.1, the degree of variation in material properties influences which fluid model assumptions are appropriate, and in turn, dictates the coupling complexity of the governing equations. If the temperature and pressure variations are small, material properties may be treated as constant, leading to considerable simplification of the governing equations. Many technical applications, however, involve wide variations in state conditions. In such cases, the property dependency on state variables must be explicitly accounted for, and suitable functional relationships are required to represent that dependency.

Material properties are typically provided either in the form of tabulated values or as mathematical **correlations**. For pure substances such as water, air, oxygen, nitrogen, and carbon dioxide, curated tabulated datasets are based on experimental measurements Verein Deutscher Ingenieure (2013, D2) and molecular simulation data Lemmon et al. (2018). Figure 3.4 shows representative values of density, viscosity, heat capacity, and thermal conductivity compiled from Kays et al. (2005) for common fluids.

Correlations provide a mathematical expression that describes how a given property changes with temperature or pressure, and are typically used for interpolation within a defined validity range. Developing such correlations involves combining physical insight with data-driven fitting techniques. As discussed in Sect. 1.3.2, correlations may be subject to multiple, often competing requirements. They should be accurate, generalize well over a wide range of conditions, and remain computationally efficient for implementation.

The choice of method depends on the substance and the available data. For substances with well-established property datasets, high precision equations of state are developed using regression techniques. These allow accurate predictions for all thermodynamic and transport properties Verein Deutscher Ingenieure (2013, D3). The applied correlations are typically empirical and tailored to a specific property. For example, Verein Deutscher Ingenieure (2013, D3) provides a 4th-order polynomial correlation for the temperature dependence of dynamic viscosity, with coefficients available for over 200 substances. In cases where no experimental data are available, particularly for mixtures, material properties are often estimated based on the molecular structure. In these methods, the property of the mixture is determined as a combination of the contributions from its components. For more information on these correlation methods and mixture models, the reader is referred to Verein Deutscher Ingenieure (2013).

One often encounters correlations that incorporate some form of a priori physical knowledge to guide the choice of the functional form. For example, to approximate the temperature dependence of gas viscosity or thermal conductivity, a widely used expression is a power-law model derived via dimensional arguments White (1991) to

$$\frac{b}{b_0} = \left(\frac{T}{T_0}\right)^n , \tag{3.35}$$

where b denotes the temperature-dependent property, b_0 is a reference value, and T_0 is the corresponding reference temperature. An extended form of this expression is given by the **Sutherland formula**

$$\frac{b}{b_0} = \left(\frac{T}{T_0}\right)^{3/2} \frac{T_0+S}{T+S} , \tag{3.36}$$

which originates from kinetic gas theory under the assumption of an idealized intermolecular force potential. It was initially developed to describe the viscosity of gases, but is also widely used to approximate thermal conductivity White (1991). The constant S is known as the **Sutherland constant** and characterizes a gas-specific effective interaction temperature. Table 3.3 lists correlation coefficients for both models, along with their respective validity ranges and estimated errors. A compilation of model parameters for many common gases is for example provided in White (1991). In cases where no suitable correlation is available in the open literature, it may be necessary to develop a custom model. This situation may arise, for example, due to mismatched validity ranges, nonstandard fluid mixtures, or specific algorithmic requirements in simulations or control applications.

Table 3.3 Correlation coefficients for power law Eq. (3.35) and Sutherland formula Eq. (3.36) for viscosity and thermal conductivity White (1991)

3.2 Conservation Laws

This section introduces the fundamental conservation laws for mass, momentum, and energy, along with the Second Law of Thermodynamics, which governs irreversibility in thermo-fluid systems. These laws describe how physical quantities evolve within a control volume and form the basis for deriving the governing equations of fluid flow and heat transfer. Each law is stated in its integral form and then reformulated in differential form to capture local field behavior.

3.2.1 Fundamental Conservation Principles

Physical systems are subject to the fundamental conservation of mass m, momentum $m\mathbf{u}$, energy E, and the Second Law of Thermodynamics, which expresses the change of the entropy S. These conservation laws are empirical principles with an axiomatic character, that is, they are not derived but are universally observed. The following relations describe how conserved quantities can change over time under the influence of mechanical and thermodynamic processes.

Mass, momentum, energy, and entropy are all extensive properties. Their values are defined relative to a system of mass m. By default, and for the sake of clarity, we consider in the following conservation laws for **closed systems** that do not permit mass exchange with the surroundings, as illustrated on the left of Fig. 3.5. **Open systems** include inlet and outlet openings for mass transfer across their boundaries, as shown on the right. Any mass flow $\dot{m}$ carries associated momentum, energy, and entropy, and therefore contributes to the respective conservation balances. A system-centric sign convention is adopted in which flows of mass, momentum, energy, and entropy entering the system are considered positive, while flows leaving the system are considered negative. Unlike alternative conventions found in the literature, it is explicitly stated here that both heat and work added to the system are treated as positive contributions.

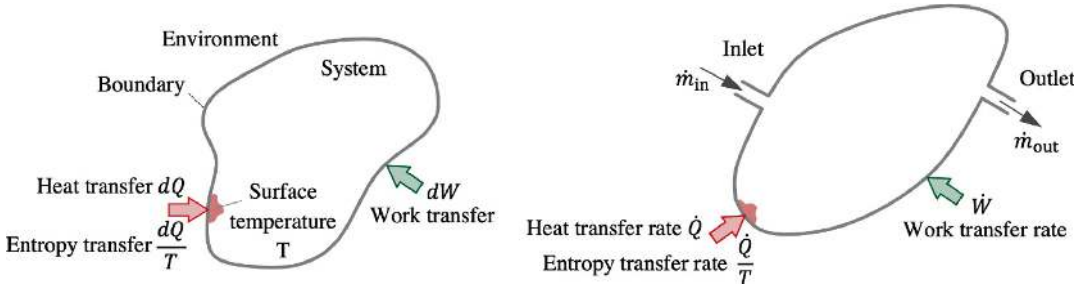


Fig. 3.5 Closed (left) and open (right) systems illustrating heat, work, mass and entropy transfer across the system boundary

The **conservation of mass** states that in a closed system, mass can neither be created nor destroyed, thus

$$\frac{dm}{dt} = 0 \ . \tag{3.37}$$

Hence, system mass can only change in open systems, where mass crosses the system boundary. In such cases, the right-hand side is extended by the net sum of mass flows, $\sum \dot{m}$. The flow is positive when mass enters the system and negative when mass exits.

The **conservation of momentum** is a reformulation of Newton's second law, linking the forces acting on a system to the rate of change of its momentum. A system may experience body forces, such as gravity, and surface forces, such as pressure or shear acting along its boundary. Discrete localized forces also occur in turbomachinery, for instance, the force exerted by a compressor blade due to flow deflection, or stationary obstacles in a flow channel Dixon and Hall (2013). For a closed system of mass *m*, momentum conservation states

$$\frac{d(m\mathbf{u})}{dt} = \sum \mathbf{F} \ . \tag{3.38}$$

As $m\mathbf{u}$ is a vector, the conservation principle applies component-wise in all spatial directions. In the absence of external forces, momentum is conserved. In open systems, the system momentum changes not only due to external forces but also due to momentum carried by mass flows across the boundary. This is expressed by the term $\sum \dot{m}\mathbf{u}$ added to the right-hand side.

The **conservation of energy**, synonymous with the First Law of Thermodynamics, asserts that energy can be transformed but not lost. It allows for conversion among internal, kinetic, and potential energy, as well as between heat and work. Heat and work added to the system increase its total energy. For a process between two equilibrium states $1 \rightarrow 2$, the energy change in a closed system is

$$E_2 - E_1 = \int_1^2 dQ + \int_1^2 dW \ . \tag{3.39}$$

The total energy is defined as $E = m(e + \mathbf{u}^2/2 + \mathbf{g} \cdot \mathbf{z})$, accounting for internal, kinetic, and potential energy. In time-differential form, for a closed system, the First Law of Thermodynamics becomes

$$\frac{dE}{dt} = \sum \dot{Q} + \sum \dot{W} \ . \tag{3.40}$$

Here, $\dot{Q}$ is the rate of heat addition, and $\dot{W}$ is the rate of work done on the system. Positive values denote energy added to the system and negative values indicate energy leaving. For an isolated system, with no heat or work exchange, the total energy remains constant. For open systems, energy is also transferred via mass flow across the system boundary as depicted in Fig. 3.5. The associated contribution is $\sum \dot{m}\left(h + \frac{1}{2}|\mathbf{u}|^2 + gz\right)$, with contributions of specific internal energy *e*, kinetic energy $|\mathbf{u}|^2/2$, and potential energy *gz*. The mass entering or leaving the system also works against the prevailing pressure, displacing a volume. This work corresponds to *pv* and is commonly combined with *e* to the specific enthalpy $h = e + pv$, introduced in Sect. 3.1.1. Note that, for simplicity, we no longer distinguish between exact and inexact differentials in the notation, discussed in Sect. 3.1.1, and uniformly use *dQ* and *dW* for heat and work.

The **Second Law of Thermodynamics** governs the direction of natural processes, indicating a tendency toward increased entropy and disorder. As discussed in Sect. 3.1.1 and visualized in Fig. 3.5, for a closed system receiving heat *dQ* at boundary temperature *T*,

the entropy exchanged is $dS_{\text{exch}} = dQ/T$. The Second Law of Thermodynamics states that the actual entropy change exceeds this exchanged entropy. Between states 1 and 2 it reads

$$S_2 - S_1 \geq \int_1^2 \frac{dQ}{T} \ . \tag{3.41}$$

The directional character of the second law is expressed by the inequality sign, which captures the irreversible nature of real processes. The more dissipation occurs in the process $1 \to 2$, the greater the entropy production. Equation (3.41) quantifies the entropy change due to reversible heat exchange, while the presence of entropy production is only implied by the inequality. To explicitly quantify the degree of irreversibility, we introduce the entropy production term as described in Eq. (3.3), and rewrite the Second Law as

$$S_{\text{gen}} = S_2 - S_1 - \int_1^2 \frac{dQ}{T} \geq 0 \ . \tag{3.42}$$

In differential form, the second law becomes $dS = dQ/T + dS_{\text{gen}}$ with $S_{\text{gen}} \geq 0$. The limiting case of vanishing entropy production corresponds to the equality sign in Eq. (3.42) and represents perfectly reversible processes. A **reversible** process is an idealized and quasistatic lossless transformation that can be run in both forward and backward directions with identical outcomes. The system and its surroundings can be returned to their initial states with no net increase in entropy. In that case, the system's entropy change is solely due to heat transfer dQ/T, and is therefore often coined in the literature as the reversible component.

Real-world processes, however, inherently involve friction, leakage, imperfect heat isolation, and other dissipative constraints, and are therefore **irreversible**. Irreversible processes render a complete restoration of the initial state impossible and are characterized by an increase in the total entropy of the system and its surroundings. All irreversible state changes cause a positive entropy production, thus $S_{\text{gen}} > 0$. Later in the text, the entropy production term is examined in more detail for our relevant cases. It accounts for the dissipation of kinetic energy into internal energy through viscous friction in fluid flow. It also captures the irreversibility associated with heat conduction, highlighting that thermal energy can only diffuse from regions of higher to lower temperature.

Applied to an infinitesimal time interval, the inequality leads to an entropy balance that accounts for temporal changes with

$$\frac{dS}{dt} = \frac{d\dot{Q}}{T} + \dot{S}_{\text{gen}} \ . \tag{3.43}$$

As a consequence of the Second Law, in a closed and fully isolated system, meaning any exchange of mass and energy with the ambient is prohibited, the net entropy can only strictly increase.

For a closed but non-isolated system, entropy changes can result from reversible heat exchange with the ambient, and entropy production can occur as a result of dissipation processes inside the system. Consider a closed and cyclically operating system, such as a

heat engine. It cannot operate continuously unless $\oint dQ/T \leq 0$, meaning entropy must constantly be removed from the system in the form of heat. Likewise, an engine that exclusively transfers heat from a cooler to a hotter reservoir cannot exist. For an open system, the entropy balance is formulated analogously to the conservation equations. Any mass flow across the system boundary involves an exchange of entropy, expressed by the term $\sum \dot{m}s$.

3.2.2 Material Derivatives

The fundamental conservation laws discussed in the previous section apply directly to discrete systems. Often, however, we are interested in the field distribution of a flow, rather than integral system properties. The **field description** resolves variations at specific locations over time and is thus inherently focused on a space-centric notion. As considered in the following, the field equations describe how dependent quantities vary as functions of both space and time. These take the form of partial differential equations or, alternatively, integral equations. We begin with a brief review of the Lagrangian and Eulerian formulations, which represent two frames of reference for describing variations of physical quantities in continua. Subsequently, the conservation laws are reformulated using the Reynolds transport theorem, allowing us to describe the flow field.

In the general context of continua, the Lagrangian and Eulerian formulations differ in the reference frame employed. The **Lagrangian** description adopts a material-centric frame. Here, each material particle is individually followed, and variations in physical quantities are described along its material trajectory. In contrast, the **Eulerian** formulation uses a fixed spatial frame, where different particles pass through the same location over time. Variations in physical quantities are described at fixed locations $\mathbf{x}$ as a functions of time *t*. The Lagrangian viewpoint is convenient when the objective is centered around individual material points, as is common for example in rigid-body dynamics. For flow problems, however, the Eulerian formulation is usually more suitable, with coordinates aligned to the geometry of the problem.

The conservation of mass, momentum, and energy all involve the time rate of change of a property for a specific system. In the differential analysis of some quantity $\phi(\mathbf{x}, t)$, its total differential is expressed as

$$d\phi = \frac{\partial \phi}{\partial t} dt + \frac{\partial \phi}{\partial x} dx + \frac{\partial \phi}{\partial y} dy + \frac{\partial \phi}{\partial z} dz \ . \tag{3.44}$$

Following a material particle along its trajectory, its spatial increment satisfies $d\mathbf{x} = \mathbf{u}dt$. Substituting this into the total differential of ϕ yields the time rate of change along the particle's path

$$\begin{aligned} \frac{D\phi}{Dt} &= \frac{\partial \phi}{\partial t} + u\frac{\partial \phi}{\partial x} + v\frac{\partial \phi}{\partial y} + w\frac{\partial \phi}{\partial z} \\ &= \frac{\partial \phi}{\partial t} + \mathbf{u} \cdot \nabla \phi \ . \end{aligned} \tag{3.45}$$

The temporal change of ϕ must be independent of the chosen frame of reference. The left-hand side represents the material or **substantial derivative**, associated with a particle-

centric frame, and captures the total change of the quantity ϕ in time. The time derivatives appearing in the conservation laws in Eqs. (3.49)–(3.62) correspond to substantial derivatives. The right-hand side corresponds to the fixed spatial frame. It consists of two terms: the **local derivative** $\partial\phi/\partial t$ accounts for temporal changes at a fixed location, while the **convective derivative** $\mathbf{u} \cdot \nabla\phi$ accounts for changes arising from the motion of the material particle through the spatial field.

As material systems are fixed to a specific collection of fluid particles, the conservation laws of mass, momentum, and energy are Lagrangian in nature. They are formulated for a finite integral system where the contained matter always consists of the same moving particles. As this material volume evolves in time, its shape and spatial location change. The time-dependent material volume $\Omega(t) \subseteq \mathbb{R}^3$ shall be enclosed by the piecewise smooth boundary surface $\partial\Omega(t)$, where $\mathbf{n}$ denotes the outward-pointing unit normal vector, as illustrated in Fig. 3.2. To reformulate the conservation laws in a spatially fixed frame, referred to as **control volumes**, we shift to a description consistent with the Eulerian perspective. A control volume is defined spatially and may be either stationary or moving in a prescribed manner. Here we restrict ourselves to fixed domains.

Transformation of the time rate of change for conservation variables is enabled by the Reynolds transport theorem Spurk (1996). For a quantity $\phi(\mathbf{x}, t)$, the theorem states

$$\frac{D}{Dt}\int_{\Omega(t)} \phi \, dV = \int_{\Omega} \frac{\partial \phi}{\partial t} \, dV + \int_{\partial\Omega} \phi \mathbf{u} \cdot \mathbf{n} \, dS \ . \tag{3.46}$$

The left-hand side represents the time rate of change of ϕ for the system, that is, the integral of ϕ over the material volume. It is expressed on the right-hand side as the time change of ϕ over a fixed control volume Ω, coinciding with $\Omega(t)$ at time *t*, plus the net flux of ϕ across the control surface.

Under the condition that $(\phi\mathbf{u})$ is continuously differentiable[5] over Ω, the surface integral, that is the flux term in Eq. (3.46), can be converted into a volume integral.[6] The transport theorem can then be written entirely in terms of volume integrals

$$\begin{aligned} \frac{D}{Dt}\int_{\Omega(t)} \phi \, dV &= \int_{\Omega} \left[\frac{\partial \phi}{\partial t} + \nabla \cdot (\phi \mathbf{u}) \right] dV \\ &= \int_{\Omega} \left[\frac{D\phi}{Dt} + \phi \nabla \cdot \mathbf{u} \right] dV \ , \end{aligned} \tag{3.47}$$

where in the second line we substituted the material derivative from Eq. (3.45). Applying the transport theorem enables derivation of the differential forms of the conservation laws by shifting to an infinitesimally small control volume with side lengths *dx*, *dy*, *dz* in Cartesian coordinates. For a generalization to curvilinear coordinates, refer to Appendix A.

3.2.3 Continuity Equation

Applying the transport theorem to mass conservation as expressed in Eq. (3.37), we apply $Q = \rho$ and assume that the control volume contains no mass sources or sinks. The conservation of mass corresponding to Eq. (3.49) then reads

(3.48)

$$\frac{Dm}{Dt} = \frac{D}{Dt}\int_{\Omega(t)} \rho \, dV = \int_{\Omega} \left[\frac{\partial \rho}{\partial t} + \nabla \cdot (\rho \mathbf{u}) \right] dV = 0 \ .$$

Since the control volume is arbitrary and the integrand is assumed continuous, the integrand must vanish identically. This yields the differential form of the continuity equation

$$\frac{\partial \rho}{\partial t} + \nabla \cdot (\rho \mathbf{u}) = \frac{D\rho}{Dt} + \rho (\nabla \cdot \mathbf{u}) = 0 \ . \tag{3.49}$$

Both formulations, using the local or the material derivative, are equivalent here. For an **incompressible** medium, the density remains constant along the motion of the fluid, implying $D\rho/Dt = 0$. Equation (3.49) then reduces to $\nabla \cdot \mathbf{u} = 0$, so the velocity field is solenoidal. This means that it has no sources or sinks, and equivalently, that the fluid elements maintain constant volume as they move. It is important to note that this does not imply constant density throughout the medium, but rather along the path of each fluid particle.

Closely related to the continuity equation is the **stream function**, which in the context of two-dimensional flows, offers a useful solution strategy. The idea is to define a function of higher differential order that identically satisfies the continuity equation. In Cartesian coordinates, the stream function ψ is defined by

$$\frac{\partial \psi}{\partial x} = -\rho v \quad \text{and} \quad \frac{\partial \psi}{\partial y} = \rho u \ . \tag{3.50}$$

By substituting the stream function in place of the velocity components, the number of dependent variables is reduced by one, while the differential order of the governing equations is increased by one. Besides this mathematical simplification, the stream function also permits a physical interpretation. Its total differential reads

$$d\psi = \frac{\partial \psi}{\partial x} dx + \frac{\partial \psi}{\partial y} \, dy = -\rho v \, dx + \rho u \, dy = \rho \mathbf{u} \cdot d\mathbf{A} = d\dot{m} \ , \tag{3.51}$$

showing that along lines of constant ψ, that is $d\psi = 0$, there is no mass flow across the line, so $d\dot{m} = 0$. The difference in ψ values between two such lines equals the mass flow rate between them. While this relation is shown here for Cartesian coordinates, it holds for any other orthogonal coordinate system. In cylindrical coordinates, for instance, the streamlines form streamtubes, which carry the same physical interpretation.

3.2.4 Momentum Equation

Using the transport theorem in Eq. (3.46), the momentum conservation law from Eq. (3.38) can be transformed into an Eulerian description. That is, balancing the momentum within a control volume yields the integral equation

$$\frac{D}{Dt}\int_{\Omega(t)} \rho \mathbf{u} \, dV = \int_{\Omega} \rho \mathbf{f} \, dV + \int_{\partial\Omega} \mathbf{T} \cdot \mathbf{n} \, dS \ . \tag{3.52}$$

The term on the left represents the rate of change of momentum within the volume. The right-hand side decomposes the total force acting on the control volume into body forces and surface forces. Body forces, such as those due to gravity or apparent forces in a rotating frame of reference, act throughout the entire mass and are expressed in terms of a mass-specific force $\mathbf{f}$. Surface forces act on the boundary of the control volume and depend not only on the position $\mathbf{x}$ and time t but also on the orientation of the local surface element. These surface forces include both the pressure p, which acts normal to the surface in direction $\mathbf{n}$, and the viscous stresses described by Eq. (3.29), causing the element's deformation.

The surface integral representing the action of surface stresses can be converted into a volume integral using the divergence theorem. This allows all terms to be expressed as volume integrals. Since the control volume is arbitrary again and the integrands are assumed to be continuous, the integrand itself must vanish. The integral equation thus yields the differential form of the momentum equation

$$\rho \tfrac{D\mathbf{u}}{Dt} = -\nabla p + \nabla \cdot \boldsymbol{\tau} + \rho \mathbf{f} \ , \tag{3.53}$$

where the viscous stress tensor $\boldsymbol{\tau}$ is given by Eq. (3.29) as $\boldsymbol{\tau} = 2\mu \mathbf{S} + \lambda_b (\nabla \cdot \mathbf{u}) \mathbf{I}$. The acceleration term $D\mathbf{u}/Dt$ contains the convective derivative $(\mathbf{u} \cdot \nabla)\mathbf{u}$, which is nonlinear in nature. This nonlinearity has important implications both physically and mathematically. From a physical perspective, it allows small variations in initial or boundary conditions to grow rapidly, leading to complex and often unpredictable flow behavior. Such phenomena are characteristic of turbulent flows, discussed in detail in Sect. 4.2.5. Mathematically, the nonlinear term poses challenges because the principle of superposition no longer applies, and field solutions become very difficult to approach analytically and increasingly sensitive to initial and boundary conditions.

3.2.5 Energy Equation

Let us consider the First Law of Thermodynamics. As discussed in the context of Eq. (3.40), the change in total system energy E corresponds to the sum of all performed work rates $\dot{W}$ and transferred heat flows $\dot{Q}$, thus

$$\tfrac{DE}{Dt} = \tfrac{D}{Dt} \int_{\Omega(t)} \rho e \, dV = \sum \dot{Q} + \sum \dot{W}. \tag{3.54}$$

The total system energy consists of the mass-specific internal energy e and kinetic energy $\frac{1}{2}\mathbf{u} \cdot \mathbf{u}$. Conservation of energy, therefore, requires

$$\tfrac{D}{Dt} \int_{\Omega(t)} \rho \left[e + \tfrac{1}{2}\mathbf{u} \cdot \mathbf{u} \right] dV = -\int_{p\Omega} \mathbf{q} \cdot \mathbf{n} \, dS + \int_{\partial\Omega} (\mathbf{T} \cdot \mathbf{u}) \cdot \mathbf{n} \, dS + \int_{\Omega} \rho \mathbf{u} \cdot \mathbf{f} \, dV \ . \tag{3.55}$$

The first term on the right-hand side represents the net heat flux across the boundaries of the control volume. The total mechanical power includes the rate of work done by surface forces, expressed through the stress tensor $\mathbf{T} = -p\mathbf{I} + \boldsymbol{\tau}$, and the rate of work done by body forces. Following the same procedure as for the continuity and momentum equations, the integral form is transformed into its differential counterpart:

$$\rho \frac{De}{Dt} + \rho \mathbf{u} \cdot \frac{D\mathbf{u}}{Dt} = -\nabla \cdot \mathbf{q} + \nabla \cdot (\mathbf{T} \cdot \mathbf{u}) + \rho \mathbf{u} \cdot \mathbf{f} \ . \tag{3.56}$$

This equation can be further simplified by eliminating the mechanical power contribution of the momentum equation Eq. (3.53), which cancels identically when applying scalar multiplication by $\mathbf{u}$. The surface force term $\nabla \cdot (\mathbf{T} \cdot \mathbf{u})$ is handled using the product rule, resulting in the two terms $(\nabla \cdot \mathbf{T}^\top) \cdot \mathbf{u} + \mathbf{T}^\top : (\nabla \mathbf{u})$.[7] The second term $\Phi = \boldsymbol{\tau}^\top : (\nabla \mathbf{u})$ corresponds to the rate of viscous **energy dissipation** . Dissipation describes the irreversible transformation of kinetic energy into internal energy due to friction and fluid shear described by $\boldsymbol{\tau}$. To illustrate, the dissipation term Φ is expanded in Cartesian coordinates Kays et al. (2005) reading

$$\begin{aligned} \Phi \ = \mu \Bigg[& 2\left(\tfrac{\partial u}{\partial x}\right)^2 + 2\left(\tfrac{\partial v}{\partial y}\right)^2 + 2\left(\tfrac{\partial w}{\partial z}\right)^2 - \tfrac{2}{3}\left(\tfrac{\partial u}{\partial x} + \tfrac{\partial v}{\partial y} + \tfrac{\partial w}{\partial z}\right)^2 \\ & + \left(\tfrac{\partial u}{\partial y} + \tfrac{\partial v}{\partial x}\right)^2 + \left(\tfrac{\partial v}{\partial z} + \tfrac{\partial w}{\partial y}\right)^2 + \left(\tfrac{\partial w}{\partial x} + \tfrac{\partial u}{\partial z}\right)^2 \Bigg] \ . \end{aligned} \tag{3.57}$$

The first row corresponds to dissipation due to normal viscous stresses, while the second row accounts for shear stresses. Dissipation is always non-negative, thus $\Phi \geq 0$. This is directly evident in the case of incompressible flow, where $\nabla \cdot \mathbf{u} = 0$ for which the negative term in the first row vanishes. All remaining terms are squares and therefore non-negative. The limiting case of zero dissipation corresponds to a reversible process and is only valid for inviscid flows with $\mu = 0$, or in the absence of velocity gradients, thus $\nabla \mathbf{u} = \mathbf{0}$. The general expression of the dissipation term is given for arbitrary curvilinear coordinates in Eq. (A.20) in the appendix.

Substituting simplifies to the time rate of change of the **internal energy** of a material element to

$$\rho \frac{De}{Dt} = -\nabla \cdot \mathbf{q} - p \nabla \cdot \mathbf{u} + \Phi \ . \tag{3.58}$$

In different applications, it is often convenient to reformulate the energy equation in terms of enthalpy or total enthalpy. The **enthalpy** form follows by substituting $h = e + p/\rho$ into Eq. (3.58) and simplifying using the continuity equation. This results in

$$\rho \frac{Dh}{Dt} = \frac{Dp}{Dt} - \nabla \cdot \mathbf{q} + \Phi \ . \tag{3.59}$$

To derive the form for the **total enthalpy**, we return to Eq. (3.56) and substitute $h_t = e + p/\rho + \frac{1}{2}\mathbf{u} \cdot \mathbf{u}$, giving

$$\rho \frac{Dh_t}{Dt} = \frac{\partial p}{\partial t} - \nabla \cdot \mathbf{q} + \nabla \cdot (\boldsymbol{\tau} \cdot \mathbf{u}) + \rho \mathbf{u} \cdot \mathbf{f} \ . \tag{3.60}$$

The concept and interpretation of total enthalpy are discussed in detail in Sect. 5.1.1. The symbolic forms of the terms occurring here are expanded for general orthogonal curvilinear coordinates in Appendix A.

3.2.6 Entropy Transport Equation

To derive the entropy transport equation, the fundamental thermodynamic relation from Eq. (3.9) is applied to a material element as

$$T\frac{Ds}{Dt} = \frac{De}{Dt} - \frac{p}{\rho^2}\frac{D\rho}{Dt} \ . \tag{3.61}$$

Substituting the internal energy equation from Eq. (3.58) and applying the continuity equation, the time rate of change of entropy for a material element becomes

$$\rho\frac{Ds}{Dt} = \frac{\Phi}{T} - \frac{1}{T^2}\mathbf{q}\cdot(\nabla T) - \nabla\cdot\left(\frac{\mathbf{q}}{T}\right) \ , \tag{3.62}$$

so entropy change consists of a transfer term due to heat exchange and a production term due to irreversibilities, the entropy rate for a material element can be expressed as

$$\dot{s}_{\text{exch}} = -\nabla\cdot\left(\frac{\mathbf{q}}{T}\right) \ , \quad \dot{s}_{\text{gen}} = \frac{\Phi}{T} - \frac{1}{T^2}\mathbf{q}\cdot(\nabla T) \ . \tag{3.63}$$

The divergence of the specific entropy flux $\mathbf{q}/T$ represents the reversible contribution and may be positive, negative, or zero depending on the direction of the heat flow. The irreversible contribution $\dot{s}_{\text{gen}}$ corresponds to the specific entropy generation and contains two non-negative terms. The first term involves viscous energy dissipation $\Phi \geq 0$, as expanded in Eq. (3.57), representing the irreversible conversion of kinetic energy into internal energy through friction and shear. The second term arises from temperature diffusion. Since heat flows from regions of higher to lower temperature, that is against the negative gradient of temperature, we have $\mathbf{q}\cdot(\nabla T) \leq 0$, ensuring that the second term is also non-negative. For illustration, the entropy generation term is expanded in Cartesian coordinates as follows

$$\begin{aligned}
\dot{s}_{\text{gen}} \ &= \frac{k}{T^2}\left[\left(\frac{\partial T}{\partial x}\right)^2 + \left(\frac{\partial T}{\partial y}\right)^2 + \left(\frac{\partial T}{\partial z}\right)^2\right] \\
&+ \frac{\mu}{T}\left[2\left(\frac{\partial u}{\partial x}\right)^2 + 2\left(\frac{\partial v}{\partial y}\right)^2 + 2\left(\frac{\partial w}{\partial z}\right)^2 - \frac{2}{3}\left(\frac{\partial u}{\partial x} + \frac{\partial v}{\partial y} + \frac{\partial w}{\partial z}\right)^2\right. \\
&\left. + \left(\frac{\partial u}{\partial y} + \frac{\partial v}{\partial x}\right)^2 + \left(\frac{\partial v}{\partial z} + \frac{\partial w}{\partial y}\right)^2 + \left(\frac{\partial w}{\partial x} + \frac{\partial u}{\partial z}\right)^2\right] \ .
\end{aligned} \tag{3.64}$$

The first line captures entropy production due to heat conduction, while the remaining terms represent contributions from viscous shear and normal stresses. It is important to emphasize that entropy generation is strongly affected by the local reference temperature, which appears in the denominator. At higher temperatures, the same amount of transferred heat or dissipated energy leads to smaller entropy changes Bejan (1995).

The integral representation of the entropy balance becomes

$$\frac{D}{Dt}\int_{\Omega(t)}\rho s \ dV = \int_{\Omega}\left[\frac{\Phi}{T} - \frac{1}{T^2}\mathbf{q}\cdot(\nabla T)\right] \ dV - \int_{\partial\Omega}\frac{1}{T}\mathbf{q}\cdot\mathbf{n} \ dS \ , \tag{3.65}$$

accounting for the entropy production terms that appear as a non-negative volume integral.

3.3 Boundary Conditions

The field equations describe the dependent physical quantities within the considered system. A complete flow description requires specification of boundary and initial conditions. The governing equations and the corresponding boundary conditions must be carefully reconciled to ensure a well-posed problem. Further details on the mathematical formulation of well-posed boundary conditions can be found in the literature on partial differential equations and their classification, such as in the works of DuChateau and Zachmann (2002), Weigand (2015), and Evans (2010). The most common boundary conditions in fluid flow problems involve inlet and outlet conditions, solid surfaces, fluid interfaces, and free surfaces, discussed in the following.

Boundary conditions are typically expressed in terms of velocity $\mathbf{u}$, pressure p, and temperature T, as well as velocity and temperature gradients to represent shear stress and heat flux, requiring their continuity across boundaries.

Inlet and outlet conditions generally require values for $\mathbf{u}$, p, and T along the respective boundaries. The velocity component normal to the boundary, $\mathbf{u} \cdot \mathbf{n}$, determines the effective flux into or out of the control volume. In practice, simplified formulations are often employed. For instance, in numerical simulations, zero-gradient boundary conditions together with sufficiently large computational domains can approximate free-stream conditions.

To consider interface-related conditions, the interface shall be defined implicitly by $\Gamma(\mathbf{x}, t) = 0$, with the unit normal vector $\mathbf{n}$ oriented along the gradient of Γ, that is $\mathbf{n} = \nabla\Gamma/|\nabla\Gamma|$. For 2D and 3D cases, the tangential plane is spanned by one or more principal orthogonal tangent vectors $\mathbf{t}$. Across interfaces, velocity $\mathbf{u}$ and temperature T remain continuous, meaning their values match on both sides at $\Gamma(\mathbf{x}, t) = 0$. Furthermore, the momentum and energy conservation laws must be satisfied across the interface. The stress balance is expressed in terms of the stress vector $\mathbf{n} \cdot \mathbf{T}$, where the stress tensor is $\mathbf{T} = -p\mathbf{I} + \boldsymbol{\tau}$. Its components in normal and tangential directions to the interface are $\mathbf{n} \cdot \mathbf{T} \cdot \mathbf{n}$ and $\mathbf{n} \cdot \mathbf{T} \cdot \mathbf{t}$, respectively. Heat flux across the interface is represented by $\mathbf{q} \cdot \mathbf{n}$.

Solid Interfaces are typically modeled as impenetrable and no-slip surfaces. Denoting fluid-side properties by the subscript f and solid-wall properties by w, the conditions at the wall are

$$\Gamma(\mathbf{x}, t) = 0 : \quad \mathbf{u}_w = \mathbf{u}_f \ , \quad T_w = T_f \ . \tag{3.66}$$

For an arbitrarily shaped, moving wall, the kinematic condition can be derived using the material derivative. In the direction normal to the interface, it implies $D\Gamma/Dt = 0$ on $\Gamma(\mathbf{x}, t) = 0$. Substituting $\mathbf{n}$ yields

$$\tfrac{\partial \Gamma}{\partial t} + \mathbf{u} \cdot \mathbf{n}|\nabla\Gamma| = 0 \ . \tag{3.67}$$

The normal velocity component is therefore

$$u_n = \mathbf{u} \cdot \mathbf{n} = -\frac{1}{|\nabla \Gamma|} \frac{\partial \Gamma}{\partial t} \ . \tag{3.68}$$

In the case of a stationary surface, this simplifies to $u_n = 0$, indicating that there is no flow across the surface in the normal direction. In tangential directions, a no-slip condition is commonly applied, $u_t = \mathbf{u} \cdot \mathbf{t} = 0$. Finite slip velocities appear in limiting flow regimes, such as rarefied gas flows White (1991, Sec. 1.4.2).

The tangential shear stress component relative to the interface is given by $\mathbf{n} \cdot \boldsymbol{\tau} \cdot \mathbf{t}$, which leads to the boundary condition

$$\tau_w = \mu_f \frac{\partial u_t}{\partial n}\Big|_f \ , \tag{3.69}$$

where $u_t = \mathbf{u}_f \cdot \mathbf{t}$ denotes the velocity component tangential to the wall. The heat flux normal to the wall is preserved across the interface, so using Eq. (3.33), the boundary condition reads

$$q_w = k_f \frac{\partial T}{\partial n}\Big|_f \ . \tag{3.70}$$

Fluid Interfaces refer to the surface separating two immiscible fluids, which are labeled here with indices 1 and 2. Across the interface, the velocity, pressure, and temperature remain continuous. This leads to the conditions

$$\Gamma(\mathbf{x}, t) = 0: \quad \mathbf{u}_1 = \mathbf{u}_2 \ , \quad p_1 = p_2 \ , \quad T_1 = T_2 \ . \tag{3.71}$$

In the absence of surface tension, the pressures of both fluids are equal at the interface. The tangential stress balance becomes

$$\tau_1 = \mu_1 \frac{\partial u_t}{\partial n}\Big|_1 = \mu_2 \frac{\partial u_t}{\partial n}\Big|_2 = \tau_2 \ . \tag{3.72}$$

For fluids with different viscosities, $\mu_1 \neq \mu_2$, the velocity gradients in the tangential plane differ proportionally, thus relate by the factor μ_2/μ_1. In limiting cases where the viscosities are vastly different, as in the case of a liquid-gas interface with $\mu_l \gg \mu_g$, the condition may be approximated by $\partial u_t / \partial n|_l \approx 0$, implying that the tangential velocity gradient on the liquid side becomes negligible.

The heat flow condition across the interface is given by

$$q_1 = -k_1 \frac{\partial T}{\partial n}\Big|_1 = -k_2 \frac{\partial T}{\partial n}\Big|_2 = q_2 \ . \tag{3.73}$$

Analogous to the argument concerning viscosity, when the thermal conductivities of the two fluids differ significantly, as in the case of a liquid-gas interface where $k_l \gg k_g$, the boundary condition can be approximated by $\partial T / \partial n|_l \approx 0$, which corresponds to an effectively insulating boundary on the liquid side.

Free Surfaces also describe fluid-fluid interfaces, however with the additional effect of surface tension σ acting at the interface. At the free surface, the stress vector $\mathbf{n} \cdot \mathbf{T}$ must balance the surface tension induced stress jump. This balance[8] can be derived as

$\mathbf{n} \cdot \mathbf{T} = \sigma \mathbf{n}(\nabla \cdot \mathbf{n}) - \nabla \sigma$. Projecting the directional components, the balance in the normal direction becomes

$$\mathbf{n} \cdot \mathbf{T} \cdot \mathbf{n} = \sigma(\nabla \cdot \mathbf{n}) \ . \tag{3.74}$$

The right-hand side represents a jump in normal stress, which occurs for curved surfaces where $\nabla \cdot \mathbf{n} \neq 0$, that is nonzero curvature. As discussed in Sect. 3.1.3, the bulk expansion term $\lambda_b \nabla \cdot \mathbf{u}$ in the stress tensor can typically be neglected. In that case, surface tension manifests purely as a pressure jump across the interface. This pressure jump is often expressed in terms of the surface curvature κ, or alternatively through the principal radii of curvature R_1 and R_2 of the interface

$$\Delta p = \sigma \kappa = \sigma \left(\frac{1}{R_1} + \frac{1}{R_2} \right) \ . \tag{3.75}$$

The pressure is higher on the concave side, where the curvature is tighter and the radius is smaller. For example, in a spherical droplet, the pressure is higher inside the droplet than outside. Surface tension becomes especially relevant at small length scales, where curvature effects dominate, and gives rise to phenomena such as capillary waves, detailed later in Sect. 4.2. In the tangential direction, the stress component balances local gradients in surface tension. Such gradients may arise from variations in temperature or substrate concentration along the interface. The resulting tangential force is known as the Marangoni force, and the stress balance reads

$$\mathbf{n} \cdot \mathbf{T} \cdot \mathbf{t} = \nabla \sigma \cdot \mathbf{t} \ . \tag{3.76}$$

Note that in the tangential direction, the stress balance involves only velocity gradients and not the pressure. Consequently, any nonzero gradient in surface tension will necessarily induce fluid motion along the interface.

Convective Heat Transfer In engineering analyses of flows involving convective heat transfer, the primary interest often lies in the overall heat exchange at the wall, rather than in resolving the detailed flow and temperature fields near the surface. To quantify, the **heat transfer coefficient** is introduced. It characterizes the rate of heat transfer between a fluid and a solid surface and is defined as

$$h = \frac{\dot{q}_w}{T_\infty - T_w} = \frac{-k}{T_\infty - T_w} \frac{\partial T}{\partial n}\Big|_w \ , \tag{3.77}$$

where $T_\infty - T_w$ represents the driving temperature difference between the flow and the wall. For external flows, T_∞ refers to the free-stream temperature, and for internal flows it is typically the bulk reference temperature. The heat transfer coefficient encapsulates the complex interactions occurring within the thermal boundary layer, which are influenced by material properties, the flow regime, and the geometrical configuration of the system. Factors such as whether the flow is laminar or turbulent, the surface roughness, and the shape of the boundary all play a role. Numerous empirical and theoretical correlations are available for *h* in specific cases. These provide effective boundary conditions adapted to

particular geometries and flow conditions, and are frequently related to the friction coefficient, as discussed in Sect. 5.1.5. It is important to note that $\dot{q}_w$ denotes the heat flux per unit surface area. Thus, to enhance the total heat transfer, one may either increase the surface area or optimize the heat transfer coefficient by modifying flow characteristics or material properties.

References

Bejan A (1995) Entropy generation minimization: the method of thermodynamic optimization of finite-size systems and finite-time processes. Taylor & Francis, Mechanical and aerospace engineering series

Chadwick P (2013) Continuum mechanics: concise theory and problems. Dover Books on Physics, Dover Publications

de Gennes PG, Brochard-Wyart F, Quere D (2003) Capillarity and wetting phenomena: drops, bubbles, pearls, waves. Springer

Dixon SL, Hall C (2013) Fluid mechanics and thermodynamics of turbomachinery. Elsevier

DuChateau P, Zachmann DW (2002) Applied partial differential equations. Dover Books on Mathematics, Dover Publications

Evans LC (2010) Partial differential equations. Graduate studies in mathematics. American Mathematical Society

Goodier JN, Timoshenko S (1970) Theory of elasticity. McGraw-Hill

Kays WM, Crawford ME, Weigand B (2005) Convective heat and mass transfer. McGraw-Hill series in mechanical engineering. McGraw-Hill

Lemmon EW, Bell IH, Huber ML, McLinden MO (2018) NIST standard reference database 23: reference fluid thermodynamic and transport properties-REFPROP, version 10.0, National Institute of Standards and Technology. www.nist.gov

Spurk J (1996) Strömungslehre: Einführung in die Theorie der Strömungen. Springer

Verein Deutscher Ingenieure (2013) Springer,VDI-Wärmeatlas. VDI-Buch 11th edn

Weigand B (2015) Analytical methods for heat transfer and fluid flow problems. Springer, Berlin [https://doi.org/10.1007/978-3-662-46593-6]

Weigand B, Köhler J, von Wolfersdorf J (2016) Thermodynamik kompakt, 4th edn. Springer, Berlin

White FM (1991) Viscous fluid flow, 2nd edn. McGraw-Hill

Footnotes

1 Throughout the text, we use ρ and v interchangeably. When using differentials, the relation $dv = -d\rho/\rho^2$ applies.

2 The differential operator for path-dependent process variables is called an inexact or incomplete differential. In notation, δq and δw are used instead of dq or dw to emphasize that their values depend on the path taken, not just the endpoints. They are sometimes denoted using the symbol đ. In contrast to exact differentials like dE, inexact differentials cannot be integrated without knowledge of the path.

3 The formulation for mixtures or chemically reacting systems can be found in Weigand et al. (2016).

4 For derivations, see also Maxwell relations in Weigand et al. (2016).

5 The required continuous differentiability of the transported field can in reality be violated, for example at interfaces between fluids of different densities or across shock waves. Nonetheless, the transport theorem remains valid for such surface discontinuities provided the surface itself is smooth and thus admits a well-defined normal vector at every point Spurk (1996).

6 By applying the divergence theorem Spurk (1996): Let the compact control volume $\Omega \subseteq \mathbb{R}^3$ be enclosed by the piecewise smooth boundary surface $\partial\Omega$ with outward-pointing unit normal $\mathbf{n}$. For any vector field $\mathbf{G}$ that is continuously differentiable on Ω, we have $\int_{\partial\Omega} (\mathbf{G} \cdot \mathbf{n})\, dS = \int_{\Omega} (\nabla \cdot \mathbf{G})\, dV$.

7 For the divergence of the linear map $\mathbf{T} \cdot \mathbf{u}$, the product rule reads $\nabla \cdot (\mathbf{T} \cdot \mathbf{u}) = (\nabla \cdot \mathbf{T}^{\top}) \cdot \mathbf{u} + \mathbf{T}^{\top} : (\nabla \mathbf{u})$, where $:$ denotes the tensorial scalar product. For two second-rank tensors $\mathbf{A}$ and $\mathbf{B}$, the scalar product is defined as $\mathbf{A} : \mathbf{B} = \sum_{ij} A_{ij} B_{ij}$.

8 Formally obtained by applying Stokes' theorem to the surface tension line integral

$$\oint_C \sigma \, d\mathbf{c} = \int_S \sigma \mathbf{n} (\nabla \cdot \mathbf{n}) - \nabla \sigma \, dS \ .$$

© The Author(s), under exclusive license to Springer Fachmedien Wiesbaden GmbH, part of Springer Nature 2026
H. Gomaa, *Modeling with Knowledge and Data*, Mathematical Engineering
https://doi.org/10.1007/978-3-658-50679-7_4

4. Simplifications and Scales

Hassan Gomaa[1] ✉
(1) Strategic Projects Co-Innovation, Cognite, Oslo, Norway

The preceding sections have established the governing equations that describe fluid motion, derived from the fundamental conservation principles of mass, momentum, and energy. These equations constitute the full formulation for Newtonian fluids and remain valid across arbitrary geometries, boundary conditions, and physical regimes. In their general form, they represent a strongly coupled, nonlinear system of partial differential equations that is analytically intractable and typically requires substantial computational effort to solve numerically.

However, in most engineering contexts, exact solutions to the full system are neither required nor practical. Instead, the goal is to simplify the problem to a form that captures the dominant physical mechanisms while remaining tractable for analysis or computation. This is achieved by introducing physically justified assumptions that reduce the number of interacting effects and thereby the mathematical complexity. By focusing on the most relevant terms, one can often neglect secondary phenomena, without significantly affecting the predictive quality of the solution.

For instance, if a flow can be approximated as incompressible and isothermal, the energy equation does not need to be solved, leading to a substantial simplification. In such regimes, classical analytical solutions may be available. These solutions are not only valuable for physical interpretation, but also serve as reduced-order representations that

retain the structure of the underlying physics. As such, they are particularly well suited for integration with data, either as physical priors, interpretable surrogates, or components of hybrid models that combine theory and observation.

This chapter is dedicated to the systematic simplification of the governing equations. We begin by examining different fluid models and how modeling assumptions, such as incompressibility or constant material properties, affect the coupling structure and complexity of the equations. We then identify characteristic physical scales and flow regimes to evaluate the relative importance of competing transport phenomena. This analysis leads to dimensionless groups such as the Reynolds number, Mach number, and Prandtl number, which provide physical insight and offer a quantitative basis for neglecting secondary effects.

Building on this foundation, we derive simplified forms of the governing equations that apply in specific limiting regimes, including inviscid flow, boundary layer flow, creeping flow, and potential flow. Each formulation isolates a dominant balance of physical effects and serves as the basis for canonical models used in engineering analysis and physical understanding. We then introduce the concept of similitude, which formalizes the conditions under which different flow systems can be considered dynamically equivalent. Particular emphasis is placed on scaling relations relevant to turbomachinery performance analysis.

The aim of this chapter is not to catalog all possible flow regimes, but rather to develop a conceptual and practical framework for simplification. By identifying essential mechanisms and eliminating negligible terms, we obtain tractable models that retain physical meaning and are well suited for further analysis or integration with data. In the following Chap. 5, we apply these simplified models to representative flow problems that serve as standard cases in both engineering design and model validation.

4.1 Fluid Models

The governing equations introduced in the previous sections describe the evolution of the primary field variables, velocity $\mathbf{u}$, pressure p, and temperature T, based on the fundamental conservation laws of mass, momentum, and energy. These equations also involve fluid-specific properties such as density ρ, specific internal energy e, specific enthalpy h, dynamic viscosity μ, thermal conductivity k, and specific heat capacity c_p, which must be defined through supplementary thermodynamic and transport relations.

Following the thermodynamic principles introduced in Sect. 3.1.1, the thermodynamic state of a pure substance is defined by two independent variables, typically temperature T and pressure p. The density $\rho(T, p)$ is determined by an algebraic thermal state equation, while the specific enthalpy $h(T, p)$ follows from caloric state relations, commonly involving the specific heat c_p.

Transport properties such as viscosity μ and thermal conductivity k may also vary with the thermodynamic state. Their dependence is usually described via empirical correlations or tabulated data, as discussed in Sect. 3.1.4. In the most general formulation, the conservation laws and the state equations are strongly coupled, meaning that velocity, pressure, temperature, and density interact through nonlinear relations, and the fluid properties μ, k, and c_p appear within differential operators. Consequently, all equations must be solved simultaneously. This fully coupled approach is computationally demanding, even with modern numerical methods.

From Sect. 3.1.1, we recall that the Second Law of Thermodynamics introduces the concept of entropy $s(T, p)$ as an additional state variable. The entropy transport equation is decoupled from the remaining system of equations, so that it does not influence the evolution of $\mathbf{u}$, p, or T. However, it can be evaluated afterward to quantify the irreversibility of processes such as viscous dissipation or heat conduction, and provides a valuable tool for physical interpretation of loss mechanisms.

Among all variables, the density ρ plays a particularly central role in coupling. In compressible flows, ρ is a function of both T and p, typically via a thermal equation of state such as the ideal gas law or more complex formulations like the van der Waals equation. For liquids, the density is often treated as a function of temperature only. If the physical conditions vary only within narrow bounds, it is often justifiable to approximate ρ as constant, with strong impact on the structure and solvability of the governing equations.

This section reviews the most commonly used fluid models and examines how the different assumptions affect the level of equation coupling. The basic distinction is made between incompressible and compressible flow, with an additional consideration for whether material properties such as viscosity or heat capacity are temperature dependent. By selecting an appropriate fluid model, the mathematical complexity of the governing system can be significantly reduced, often enabling decoupling of the energy equation from the momentum equations or simplifying the pressure-density relation. To illustrate this, we present representative forms of the governing equations for two common cases, the incompressible flow with constant material properties, and compressible flow of a perfect gas with temperature-dependent properties. In Sect. 4.3, we will further explore how prevalent flow regimes or scaling arguments may justify further simplifications.

4.1.1 Incompressible Fluid Models

Constant Properties The most basic fluid model assumes constant fluid properties, meaning that ρ, c_p, μ, and k are treated as constant. Under this assumption, the density remains fixed throughout the flow field, implying incompressibility. As detailed further in Sect. 4.2, this is a valid approximation for gas flows with Mach numbers below $\mathrm{Ma} < 0.3$, where compressibility effects are negligible.

For liquids, the assumption of constant properties is often justified when the temperature variations are small, such as in pipe flow. For gases, it is applicable in low-speed flow regimes with limited variation

in pressure and temperature, for example in external aerodynamics around an automobile. Regardless of the application, the validity of the constant property assumption should be checked by estimating the expected ranges of operating conditions and evaluating the sensitivity of fluid properties. With constant properties, the governing equations reduce to the following simplified form

$$\begin{aligned} \nabla \cdot \mathbf{u} &= 0 \ , \\ \rho\left(\tfrac{\partial \mathbf{u}}{\partial t} + \mathbf{u} \cdot \nabla \mathbf{u}\right) &= -\nabla p + \mu \nabla^2 \mathbf{u} + \rho \mathbf{f} \ , \\ \rho c_p\left(\tfrac{\partial T}{\partial t} + \mathbf{u} \cdot \nabla T\right) &= \tfrac{Dp}{Dt} + k \nabla^2 T + \Phi \ . \end{aligned} \tag{4.1}$$

The dissipation term Φ accounts for viscous heating and is defined for general curvilinear coordinates in Eq. (A.20).

Assuming a constant density $\rho = \text{const.}$ reduces the continuity equation to the divergence free condition $\nabla \cdot \mathbf{u} = 0$, indicating a solenoidal velocity field for pure fluids. From a mathematical standpoint, this leads to a decoupling of the pressure and temperature fields. The pressure appears only through its gradient in the momentum equation and is thus only determined up to an additive constant unless specified by boundary conditions. Similarly, the temperature appears only in terms of spatial or temporal derivatives, meaning only relative temperature differences are physically relevant (Panton 1996).

With c_p, μ, and k constant, the energy equation is weakly coupled to the momentum field through the velocity, but not vice versa. The temperature does not influence the velocity nor pressure field. Consequently, the solution procedure can be split, first solving for the velocity and pressure fields using the continuity and momentum equations, and then computing the temperature field from the energy equation. The decoupling also implies that all viscous dissipation, represented by Φ, manifests as internal energy, increasing the fluid temperature (Spurk 1996).

Temperature-Dependent Properties In incompressible flows where material properties vary significantly with temperature, this

dependency must be accounted for. Such temperature-dependent fluid properties become relevant in scenarios like low Mach number gas flows or liquid flows involving a wider temperature range, for instance in oil cooling circuits. Another important case is natural convection, where temperature induced density differences drive fluid motion, such as air rising along a sun-heated vertical wall.

Introducing temperature-dependent material properties introduces additional weak coupling between the momentum and energy equations. The pressure and temperature become indirectly linked through properties such as viscosity $\mu(T)$ or thermal conductivity $k(T)$, which affect momentum diffusion and heat transfer, respectively. Since temperature is a space- and time-dependent field $T(t, \mathbf{x})$, any property dependent on it also becomes a field variable and must remain within the scope of the differential operators. While the temperature itself still appears under derivatives only, the absolute temperature now enters the problem implicitly via its influence on transport properties.

4.1.2 Compressible Fluid Models

Perfect Gas In compressible flows, the perfect gas model, also referred to as a calorically perfect gas, assumes the ideal gas law (3.16) along with constant specific heat capacities c_p and c_v. Under these assumptions, internal energy and enthalpy vary linearly with temperature, such that $h - h_0 = c_p(T - T_0)$ and $e - e_0 = c_v(T - T_0)$. This model applies well to many real gases within moderate temperature and pressure ranges, for example for the external aerodynamic flow around an aircraft. For compression or expansion processes, average values for c_p and $\gamma = c_p/c_v$ are typically used to represent the thermodynamic behavior over the temperature range (Dixon and Hall 2013). The perfect gas assumption forms the basis for many classical results in compressible flow theory, as will be discussed in Sect. 5.1.3. The heat capacity ratio γ, which appears in nearly all compressible flow relations, is constant and plays a central role in wave propagation and isentropic flow analysis.

A defining feature of the perfect gas model is that the density is coupled to pressure and temperature via the thermal state equation $\rho = \rho(p, T)$. This introduces a strong coupling between the continuity, momentum, and energy equations, requiring the full set of governing equations to be solved simultaneously. As mentioned earlier, the entropy $s(T, p)$ is governed by a separate transport equation, and can be evaluated separately. However, for perfect gases, entropy differences between two states can be directly evaluated using the thermodynamic identity derived from the Gibbs relation. Substituting $dh = c_p \ dT$ and the ideal gas law into Eq. (3.9) yields $T \ ds = c_p \ dT + RT \ dp/p$, which can be integrated to the standard form

$$s_2 - s_1 = c_p \ln \tfrac{T_2}{T_1} - R \ln \tfrac{p_2}{p_1} \ . \tag{4.2}$$

Ideal Gas The ideal gas model, also referred to as a thermally perfect gas, extends the perfect gas assumption by allowing temperature-dependent specific heats. The equation of state remains the ideal gas law $p = \rho RT$, but the caloric relations now include temperature-dependent heat capacities, thus

$$c_p = \left(\tfrac{\partial h}{\partial T}\right)_p = \tfrac{dh}{dT} = c_p(T) \ , \qquad c_v = \left(\tfrac{\partial e}{\partial T}\right)_v = \tfrac{de}{dT} = c_v(T) \ . \tag{4.3}$$

As a result, the heat capacity ratio also becomes a function of temperature, that is $\gamma = \gamma(T)$. The fundamental thermodynamic relation between c_p and c_v remains valid in the form of

$$c_p(T) = c_v(T) + R = \tfrac{\gamma(T) R}{\gamma(T) - 1} \ . \tag{4.4}$$

This model becomes necessary when the temperature range is too large for constant heat capacities to remain accurate. Typical applications include high-temperature gas flows, such as turbomachinery stages, where c_p may vary significantly with T. The variation of c_p and γ for dry air is illustrated in Fig. 4.1, based on data from Kays et al. (2005).

The governing equations for a semi-perfect gas read

$$
\begin{aligned}
\frac{\partial \rho}{\partial t} + \nabla \cdot (\rho \mathbf{u}) &= 0 \ , \\
\rho\Big(\frac{\partial \mathbf{u}}{\partial t} + \mathbf{u} \cdot \nabla \mathbf{u}\Big) &= -\nabla p + 2\nabla \cdot (\mu \mathbf{S}) + \rho \mathbf{f} \ , \\
\rho\Big(\frac{\partial (c_p T)}{\partial t} + \mathbf{u} \cdot \nabla (c_p T)\Big) &= \frac{Dp}{Dt} + \nabla \cdot (k \nabla T) + \Phi \ , \\
p &= \rho R T \ , \\
\mu = \mu(T) \ , \quad k &= k(T) \ , \quad c_p = c_p(T) \ .
\end{aligned}
\tag{4.5}
$$

Here, the strain rate tensor $\mathbf{S}$ contains only velocity gradients. It is given in Cartesian form in Eq. (3.26) and generalized for arbitrary coordinates in Eq. (A.15). As in the incompressible case with temperature-dependent properties, the spatial variability of $\mu(T)$, $k(T)$, and $c_p(T)$ requires these coefficients to remain within the differential operators.

Although the state equation remains algebraically simple, the strong coupling among all field variables ρ, p, T, and $\mathbf{u}$ requires the full system to be solved simultaneously. In numerical simulations, this typically involves iterating between updated material properties and evolving solution fields, which increases computational cost and complexity.

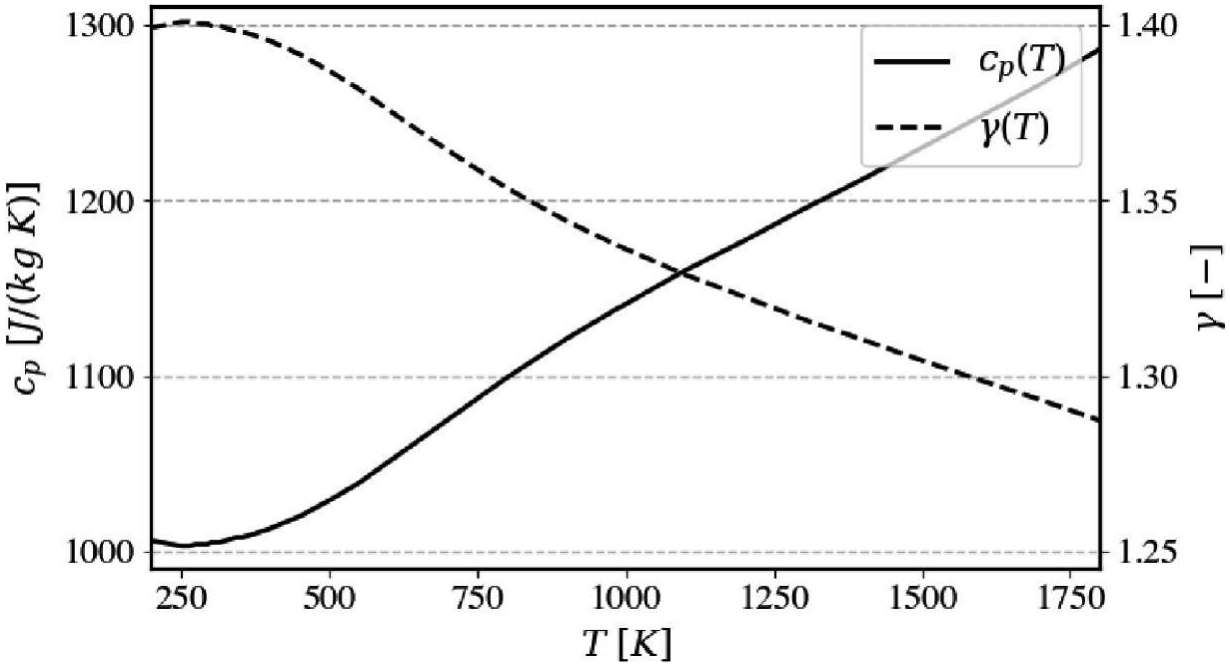


Fig. 4.1 Temperature-dependent heat capacity $c_p(T)$ and heat capacity ratio $\gamma(T)$ for dry air, based on data from Kays et al. (2005)

Steam and Real Fluids When the working fluid departs significantly from ideal gas behavior, real fluid models must be used. A common example is steam, especially in power cycles and steam turbines, where phase change and saturation effects are relevant. In such cases, the ideal gas law no longer applies, and property data must be obtained from accurate tables or real fluid equations of state.

In the wet steam region, where vapor and liquid phases coexist, properties vary sharply with pressure and temperature, and specialized tools such as steam tables (International Association for the Properties of Water and Steam 1997) are used. Thermodynamic quantities such as enthalpy, entropy, and specific volume are interpolated from tabulated data as discussed in Sect. 3.1.1. Although the equations of motion retain a similar structure, the increased complexity of the state relations demands greater computational effort and careful implementation.

4.2 Flow Regimes and Scales

From a dimensional standpoint, we have so far considered only the dimensions of physical quantities. Applying the Π-theorem then allowed us to narrow down the algebraically possible combinations into dimensionless groups. In the following we extend this dimensional argument by incorporating terms from the governing equations, to enhance the reasoning with physical interpretability and contextual insight. This approach not only deepens our understanding of the dimensionless products but also enables us to estimate the order of magnitude of physical scales and identify dominant regimes. Consequently, it facilitates deliberate simplifications of complex problems by focusing on the most relevant effects. Dimensionless groups can be broadly categorized into

- **Geometric variable ratios** that purely provide a nondimensional description of an object's geometrical shape, such as the aspect ratio of a flow channel.

- **Material property ratios** for different materials, such as a density ratio of water to air, or the Pr number, or the isentropic coefficient.
- **Physical terms** comparing the magnitudes of different physical phenomena that comprise mixed geometric, transport and thermodynamic properties. For example, the Re number represents the ratio of inertial to viscous terms.

In the literature, one often finds a methodology where the entire set of governing equations is nondimensionalized to identify the resulting dimensionless groups. For example, White (1991) provides a detailed discussion on the nondimensional form of the Navier-Stokes equations. The methodology applied here is mostly equivalent. Rather than nondimensionalizing entire equations, we deliberately examine specific terms and estimate their respective orders of magnitude.

In this section, we derive and discuss a few key dimensionless products, each representing ratios of **characteristic scales** for the underlying physical phenomena. To illustrate, we construct thought experiments of hypothetical flow problems with characteristic scales, which we use to analyze the respective dimensionless numbers and their associated physical phenomena. This approach also allows us to identify **limiting asymptotic regimes** and the **transition regimes** between them. For instance, as we will discuss, the Reynolds number provides a scale distinguishing the limiting regimes of creeping flow ($\mathrm{Re} \to 0$) and inviscid flow ($\mathrm{Re} \to \infty$). In each regime, different terms dominate, leading to corresponding simplifications in the governing equations and modeling assumptions.

In practical applications, the characteristic scales are intrinsic to the problem under consideration. Estimating the order of magnitude of the relevant dimensionless parameters allows us to quantify the relative importance of the respective physical effects and, consequently, narrow the applicable flow regimes. This further enables us to justify suitable modeling simplifications, such as neglecting minor terms in the full governing equations.

Order-of-magnitude estimates are written as $f = \mathcal{O}(q)$, expressing that the function or derivative f is of the same order of magnitude as the

estimated quantity q. Typically, q is composed of characteristic scales and relevant material properties.

To illustrate, we analyze a problem characterized by a length scale $\mathscr{L}$ and a characteristic velocity $\mathscr{U}$ and focusing on selected terms. For this purpose, we reference the incompressible governing equations presented in Eq. (4.1), repeated here for convenience

$$\begin{aligned} \nabla \cdot \mathbf{u} &= 0 \ , \\ \rho\big(\tfrac{\partial \mathbf{u}}{\partial t} + \mathbf{u} \cdot \nabla \mathbf{u}\big) &= -\nabla p + \mu \nabla^2 \mathbf{u} + \rho \mathbf{f} \ , \\ \rho c_p\big(\tfrac{\partial T}{\partial t} + \mathbf{u} \cdot \nabla T\big) &= \tfrac{Dp}{Dt} + k \nabla^2 T + \Phi \ . \end{aligned} \tag{4.1}$$

For a given problem some of the characteristic scales are directly apparent, while others follow by physical reasoning, such as for instance time scales. The ratio of local derivative to convective derivative results in the **convective time scale** $\tau \sim \mathscr{L}/\mathscr{U}$. This time scale characterizes convectively dominated transport phenomena, such as the time it takes a particle to traverse a flow path following the mean flow, or the wave periods associated with oscillating processes such as vortex shedding behind a cylinder. When expressed as a nondimensional number the ratio is expresses as the so-called **Strouhal number** $\mathrm{Sr} = \mathscr{L}/(\mathscr{U}\tau)$ which is significant in unsteady flow regimes. It is alternatively formulated using the characteristic wave frequency f as $\mathrm{Sr} = f\mathscr{L}/\mathscr{U}$. For steady flows $\mathrm{Sr} \to 0$ effectively tends to zero, reflecting the absence of periodic dynamics. As an unsteady flow example, for the flow past a circular cylinder the Strouhal number takes on a nearly constant dimensionless vortex shedding frequency of $fD/\mathscr{U} \approx 0.2$ over a wide range of Reynolds numbers (White 1991).

The ratio of the local derivative to the diffusive term yields the **diffusive time scale** $\tau \ \mathscr{L}^2/\nu$. This time scale determines the rate of diffusive transport and characterizes the time required for momentum, to diffuse across the characteristic length. It is central to diffusion dominated phenomena, such as the smoothing of velocity gradients in

viscous flows or the expansion time of a solute in a stagnant medium. The time scale is directly transferable to heat and mass transfer processes, where the kinematic viscosity ν is replaced by the thermal diffusivity a for heat transfer and the mass diffusivity D for mass transfer, respectively.

The influence of compressibility and friction has a particularly strong impact on the characterization of the flow field, so we begin with the assessment of their respective relative importance.

4.2.1 Compressible Flows

As discussed in Sect. 3.1.1, liquids can generally be considered incompressible from a thermodynamic perspective, while gases are classified as compressible fluids. For compressible fluids, the effects of compressibility depend on the specific flow regime. Compressibility describes the relative change in a medium's density in response to pressure variations. These effects become significant when pressure changes within the flow field, that is velocity-induced pressure changes, cause noticeable density variations.

Flows in which the density field varies significantly are termed **compressible flows**, whereas those where the change of density ρ can be ignored are referred to as **incompressible flows**. To evaluate compressibility effects, the relative density change with respect to velocity-induced pressure changes, $(p/\rho)(\partial\rho/\partial p)$, is examined. For small variations, the flow can often be approximated as isentropic (Weigand et al. 2016), enabling the differential relationship to be expressed in terms of the speed of sound $\partial p/\partial\rho|_s = a^2$, introduced in Eq. (3.8).

The occurring pressure gradients are closely tied to velocity variations in the flow field. Their magnitude can be estimated in terms of the convective and pressure terms (Schlichting and Truckenbrodt 2001) from the momentum equation in Eq. (4.1) to the Bernoulli-like expression $p/\rho + \mathscr{U}^2/2$. The ratio of the characteristic flow speed $\mathscr{U}$ to the speed of sound a defines the **Mach number**

(4.6)

$$\mathrm{Ma} = \frac{\mathscr{U}}{a} \ ,$$

which serves as a key nondimensional parameter to assess the relevance of compressibility effects. Applying all terms, the relative density change for small Ma numbers can be approximated by

$$\frac{\Delta\rho}{\rho} \approx \frac{1}{2}\left(\frac{\mathscr{U}}{a}\right)^2 = \frac{1}{2}\,\mathrm{Ma}^2 \ . \tag{4.7}$$

For negligible relative density changes $\frac{1}{2}\,\mathrm{Ma}^2 \ll 1$, the flow can be considered incompressible, meaning that the density can be considered constant throughout the flow field. In the literature, the flow is typically assumed **incompressible** for $\mathrm{Ma} \leq 0.3$, which corresponds to relative density changes in the order of $\Delta\rho/\rho \approx 4.5\%$. A more conservative threshold at $\mathrm{Ma} \leq 0.2$ corresponds to $\Delta\rho/\rho \approx 2\%$.

To evaluate the density variations in the flow field for an ideal gas, we might alternatively apply the isentropic flow relations that will be discussed in Sect. 5.1.3. Evaluating these relations for air with $\gamma = 1.4$ at $\mathrm{Ma} = 0.3$ yields a relative density change in the order of $\Delta\rho/\rho_0 \approx 4.4\%$, consistent with the previous estimate. Similarly, evaluating the relative temperature change using Eq. (5.24) results to $\Delta T/T_0 \approx 1.8\%$. For a stagnation temperature of $T_0 = 293\,\mathrm{K}$, this corresponds to a temperature difference of approximately $\Delta T \approx 5\,\mathrm{K}$.

Incompressible flows correspond to the limiting regime where $\mathrm{Ma} \to 0$. In this regime, the flow can often be effectively approximated as incompressible, even if the fluid is inherently compressible, because velocity-induced pressure variations typically result in negligible density changes. However, near the fluid's critical point, the thermodynamic compressibility becomes significant, and small pressure variations can cause large density changes. In this regime, the assumption of incompressibility may break down even at low Mach numbers, as density variations arise primarily from the fluid's thermodynamic state rather than from velocity-induced pressure changes.

For compressible flows, the thermodynamic and flow variables are strongly coupled through the equation of state, as exemplified for an ideal gas in Sect. 4.1. Using the Mach number, compressible flows can be further categorized into distinct regimes, that is, subsonic ($\mathrm{Ma} < 1$), transonic ($\mathrm{Ma} \approx 1$), supersonic ($\mathrm{Ma} > 1$) and hypersonic ($\mathrm{Ma} \gg 1$) flows. In **subsonic flows**, flow properties vary smoothly and continuously, with streamlines remaining smooth throughout. Disturbances in the flow propagate across the entire flow field. In **transonic flows**, regions of the flow exhibit Mach numbers near unity, resulting in a mixed-flow regime. The flow may become locally supersonic, leading to complex interactions between subsonic and supersonic regions. **Supersonic flows** are characterized by the occurrence of shock waves, where flow properties and streamlines change discontinuously. **Shock waves** are abrupt, discontinuous changes in flow properties caused by rapid compression within a very thin region, typically on the order of $\mathcal{O}(10^{-7}\,\mathrm{m})$. Depending on the flow configuration, shock waves can be either normal (perpendicular to the flow direction) or oblique (at an angle to the flow). Over a normal shock wave, the flow decelerates from supersonic to subsonic conditions, whereas behind an oblique shock, the flow can remain supersonic but at a reduced Mach number. The state changes across normal shock waves are discussed in detail in Sect. 5.1.3. In contrast to subsonic flows, disturbances in supersonic flows propagate only downstream and cannot travel upstream. **Hypersonic flows** occur at very high Mach numbers ($\mathrm{Ma} > 5$), where viscous interactions and chemical reactions dominate the flow dynamics (Anderson 2016).

4.2.2 Viscous Flow

To characterize viscous fluid flows, the inertia and viscous terms of the momentum equation in Eq. (4.1) are considered. The local and convective momentum derivatives can be estimated as

$$\rho \frac{\partial u}{\partial t} = \mathcal{O}\left(\frac{\rho \mathscr{U}}{\tau}\right), \quad \rho u \frac{\partial u}{\partial x} = \mathcal{O}\left(\frac{\rho \mathscr{U}^2}{\mathscr{L}}\right) . \tag{4.8}$$

and the viscous term, that is the momentum diffusivity, is of the order

$$\mu \frac{\partial^2 u}{\partial x^2} = \mathscr{O}\left(\frac{\mu \mathscr{U}}{\mathscr{L}^2}\right). \tag{4.9}$$

By comparing the orders of magnitude for the local momentum derivative and momentum diffusivity, a diffusion length scale can be estimated by $L \sim \sqrt{\nu \tau}$.

The **Reynolds number** Re represents the ratio of the inertial, or convective term to the viscous terms

$$\mathrm{Re} = \frac{\mathscr{U}\mathscr{L}}{\nu} \quad . \tag{4.10}$$

For low Reynolds number flows with $\mathrm{Re} \ll 1$, the flow field is dominated by viscous diffusion, while the convective inertia terms are comparatively small. This regime can arise due to low flow velocity, small characteristic lengths, or high fluid viscosity. In the absence of significant body forces, viscous stresses in Eq. (4.1) must be balanced by the pressure gradient. In consequence, the pressure variations scale as $p = \mathscr{O}(\mu U / \mathscr{L})$, or equivalently $p/(\rho \mathscr{U}^2) = \mathscr{O}(1/\ \mathrm{Re})$. The limiting regime in which the convective terms are negligible is commonly referred to as creeping flow or **Stokes flow**. Neglecting the nonlinear convective terms significantly simplifies the mathematical handling of the momentum equation. For Newtonian fluids, the resulting momentum equations become linear, allowing the use of linear differential equation methods. In Sect. 4.3.4 the Stokes equations are derived in full, and in Sect. 5.2.2 they are applied to evaluate the drag force on a sphere.

For high Reynolds number flows with $\mathrm{Re} \gg 1$, the convective inertia terms dominate over the viscous terms. This regime can arise due to low viscosity, high flow velocity, or large characteristic length scales. In this limiting regime, referred to as inviscid flow, the viscous stress terms can be neglected. Assuming that the remaining terms, that is, local acceleration, pressure gradient, and body forces, are still relevant,

neglecting viscosity leads to the so-called **Euler equations**, derived in Sect. 4.3.2.

If, in addition, the Strouhal number St is very small, indicating a small time scale $\tau \ll \mathscr{L}/\mathscr{U}$, the local acceleration becomes negligible, and the flow can be approximated as steady. In a steady inviscid flow, the pressure magnitude scales as $p/(\rho\mathscr{U}^2) = \mathscr{O}(1)$, relating directly to the dynamic pressure. Compared to the previous estimate of pressure variations, this highlights the contrast in pressure variation scales between high and low Reynolds number flows.

However, these simplifications require careful consideration due to the potential emergence of small-scale flow structures, such as boundary layers and turbulence, which can significantly impact the overall flow behavior, as discussed further in the following sections.

4.2.3 Boundary Layer Flow

The flow over a bounding surface is subject to a no-slip condition at the boundary, leading to the formation of a thin transition layer, known as the boundary layer, between the wall and the free flow. Within this layer, the velocity increases gradually from zero at the wall to the bulk flow velocity under the influence of viscosity, as shown in Fig. 4.2. Boundary layers highlight the need for cautious consideration when applying simplifications. Even at high Reynolds numbers, viscous terms govern the flow within the boundary layer, and the flow can be approximated as inviscid only outside this region. The thickness of the boundary layer δ_u for for laminar flow can be estimated by considering that the momentum diffusivity normal to the wall is of the order

$$\mu \frac{\partial^2 u}{\partial y^2} = \mathscr{O}\left(\frac{\mu \mathscr{U}}{\delta_u^2}\right). \tag{4.11}$$

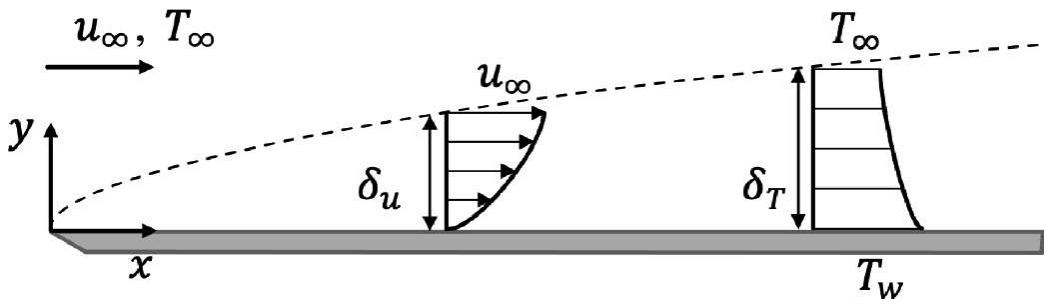


Fig. 4.2 Velocity and thermal boundary layer development over a flat plate, showing thicknesses δ_u and δ_T

Relating this estimate to the convective term estimated in Eq. (4.8) gives $\delta_u/\mathscr{L} \sim \sqrt{\mu/(\rho \mathscr{U} \mathscr{L})}$, and substituting the Reynolds number yields

$$\frac{\delta_u}{\mathscr{L}} \sim \frac{1}{\sqrt{\mathrm{Re}}} \ . \tag{4.12}$$

The induced wall shear stress can be estimated as $\tau_w = \mu(\partial u/\partial y)_w = \mathscr{O}(\mu \mathscr{U}/\delta_u)$. Substituting the estimate for the boundary layer thickness leads to the functional relation $\tau_w \sim \sqrt{\mu \rho U^3/\mathscr{L}}$. From this, the drag coefficient can be estimated as

$$C_D = \frac{2\tau_w}{\rho \mathscr{U}^2} \sim \sqrt{\frac{\mu}{\rho \mathscr{U} \mathscr{L}}} = \frac{1}{\sqrt{\mathrm{Re}}} \ . \tag{4.13}$$

The exact numerical values for the boundary layer thickness and drag coefficient are determined by solving the full boundary layer equations under specific boundary conditions. As derived in detail in Sect. 5.2.1, for a laminar boundary layer flow over a flat plate, the numerical value of the boundary layer thickness in Eq. (4.12) is approximately 5.0, and for the drag coefficient in Eq. (4.13) ≈ 1.328 (Schlichting and Truckenbrodt 2001). These values are valid only for laminar flow conditions.

Similar considerations as for the momentum boundary layer can be applied to derive the **thermal boundary layer**. As depicted in Fig. 4.2, consider a fluid flow with an approaching temperature T_∞ and a wall temperature T_w. A thin transition layer develops between the wall and

the free stream, where the temperature adjusts under the combined effects of thermal advection and diffusion. Analogous to the procedure for the momentum boundary layer, the relevant terms can be estimated from the energy equation in Eq. (4.1) to

$$u\frac{\partial T}{\partial x} = \mathscr{O}\left(\frac{\mathscr{U}\theta}{\mathscr{L}}\right) , \quad \alpha\frac{\partial^2 T}{\partial y^2} = \mathscr{O}\left(\frac{\alpha T}{\delta_T^2}\right) , \tag{4.14}$$

where $\alpha = k/(\rho c_p)$ denotes the thermal diffusivity. Like the kinematic viscosity $\nu = \mu/\rho$, the thermal diffusivity α depends only on fluid properties and has the same dimensions. Their ratio, the **Prandtl number**, is defined as

$$\mathrm{Pr} = \frac{\nu}{\alpha} . \tag{4.15}$$

The Prandtl number measures the relative rates of momentum and thermal diffusion. Rearranging Eq. (4.14), the thermal boundary layer thickness can be estimated as $\delta_T/\mathscr{L} \sim \sqrt{\alpha/(\mathscr{U}\mathscr{L})}$. The corresponding nondimensional argument is the **Peclet number** $\mathrm{Pe} = \mathscr{U}\mathscr{L}/\alpha$, which represents the ratio of advection to thermal diffusion. Substituting $\mathrm{Pe} = \mathrm{Re}\ \mathrm{Pr}$, the thermal boundary layer thickness can be expressed as

$$\frac{\delta_T}{\mathscr{L}} \sim \frac{1}{\sqrt{\mathrm{Pe}}} = \frac{1}{\sqrt{\mathrm{Re}\ \mathrm{Pr}}} . \tag{4.16}$$

Comparing this to the momentum boundary layer thickness from Eq. (4.12), the relationship $\left(\delta_u/\delta_T\right)^2 \sim \mathrm{Pr}$ is obtained for laminar flows. A similar relation applies for low Re -flows, where the convective terms in both momentum and thermal equations are negligible. By comparing the local derivative and diffusivity terms for momentum and thermal processes respectively, the characteristic diffusion lengths are estimated as $\delta_u \sim \sqrt{\nu\tau}$ and $\delta_T \sim \sqrt{\alpha\tau}$. For a given time τ, the ratio of diffusion lengths is $\left(\delta_u/\delta_T\right)^2 \sim \mathrm{Pr}$. This indicates that heat and momentum transfer processes differ significantly depending on the fluid's Pr number. As illustrated in Fig. 4.3 fluids with $\mathrm{Pr} \ll 1$, such as

liquid metals, exhibit high thermal conductivity and low viscosity, resulting in a much thicker thermal boundary layer compared to the momentum boundary layer. Gases have a low viscosity but also low thermal conductivity, and with $\mathrm{Pr} \sim 1$, have boundary layers of similar thickness. Liquids such as water and oils, with $\mathrm{Pr} \gg 1$, have poor thermal conductivity but high viscosity, leading to much thicker momentum boundary layers compared to thermal ones.

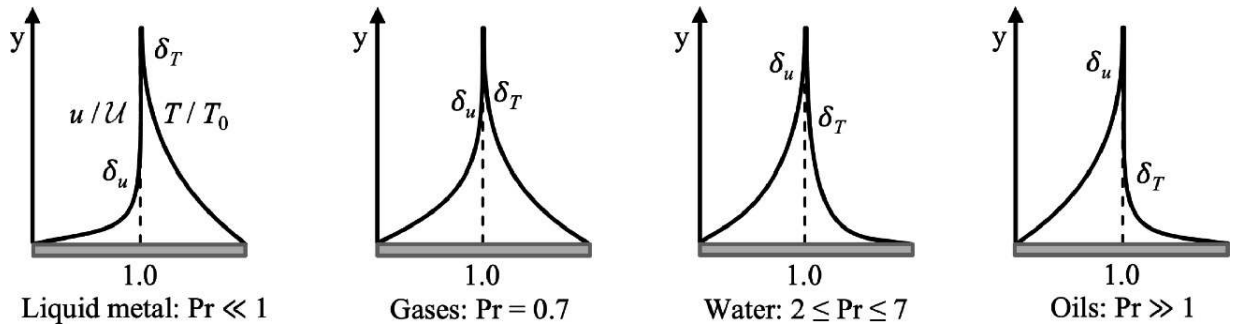


Fig. 4.3 Prandtl number effects on momentum and thermal diffusion (White 1991)

Natural Convection In free or natural convection the motion is driven by gravity acting on small density differences in the fluid (White 1991; Kays et al. 2005). This results in an additional term $-(\rho - \rho_0)\mathbf{g}$ on the right-hand side of the momentum equation of Eq. (4.1). If the density differences arise from temperature variations in the flow field, the relationship between density and temperature can be approximated to $\rho/\rho_0 \approx 1 - \alpha_p \Delta T$, using the thermal expansion coefficient α_p, introduced in Sect. 3.1.1. To evaluate the significance of buoyancy forces, they are compared to convective forces. Convective forces are estimated as $\mathcal{O}(\rho \mathcal{U}^2/\mathcal{L})$, while buoyancy forces are $\mathcal{O}(\alpha_p g \Delta T)$. The resulting ratio $\alpha_p g \Delta T \mathcal{L}/\rho \mathcal{U}^2 = \mathrm{Gr} \,/\, \mathrm{Re}^2$, highlights the relative impact of buoyancy in comparison to inertial effects. Here, Gr denotes the **Grashof number**, defined as

$$\mathrm{Gr} = \frac{\alpha_p \Delta T g \mathcal{L}^3}{\nu^2} \quad . \tag{4.17}$$

The Grashof number represents the ratio of buoyancy forces multiplied by inertial forces to viscous forces squared. It provides a measure of the

importance of natural convection in the flow. For small Gr, viscous forces dominate, and the effect of natural convection is negligible. Moderate Gr, typically in the range of $1 \times 10^3 < \mathrm{Gr} < 1 \times 10^6$, indicate free laminar convection, while very high values $\mathrm{Gr} > 1 \times 10^8$ correspond to turbulent free convection regimes.

4.2.4 Dissipation and Convective Heat Transfer

To characterize the **effect of dissipation** due to viscous heating, we examine the energy equation from Eq. (4.1) focusing on the convective and dissipation terms. The temperature difference is approximated by the driving temperature difference $\Delta T = T_\infty - T_w$ and the terms are estimated as

$$\rho c_p u \frac{\partial T}{\partial x} = \mathscr{O}\left(\frac{\rho c_p \mathscr{U}(T_\infty - T_w)}{\mathscr{L}}\right), \qquad \Phi = \mathscr{O}\left(\frac{\mu \mathscr{U}}{\mathscr{L}^2}\right) . \tag{4.18}$$

Using the **Eckert number**

$$\mathrm{Ec} = \frac{\mathscr{U}^2}{c_p \Delta T} , \tag{4.19}$$

the ratio of viscous dissipation heating to convective heat transfer is expressed as $\mathrm{Ec} \,/\, \mathrm{Re}$. The Eckert number also arises in the pressure term in Eq. (4.1) and is particularly relevant for high-speed boundary layer flows.

For low-speed flows ($\mathrm{Ma} \ll 1$), the Eckert number is typically small, allowing both pressure and dissipation terms to be neglected (White 1991). In such cases, the heat transfer primarily depends on the Peclet number. However, if the driving temperature difference ΔT is small, dissipation effects characterized by Ec may become significant even at low flow speeds. Conversely, at larger ΔT, the Eckert number becomes important only for very high flow velocities.

In practical applications of convective heat transfer, the primary interest often is the total heat transfer between a solid and a surrounding fluid rather than detailed velocity and temperature fields. As introduced in Eq. (3.77), the heat flux is related to the temperature

difference via the heat transfer coefficient h by $\dot{q}_w = h(T_\infty - T_w)$. At the boundary to the solid, the heat flux is $\dot{q}_w = -k\partial T/\partial n|_w$. Equating these expressions gives

$$h = -\frac{k}{T_\infty - T_w} \frac{\partial T}{\partial n}\Big|_w \ . \tag{4.20}$$

Nondimensionalizing with the temperature $\theta = (T - T_w)/(T_\infty - T_w)$, the relation becomes $h\mathscr{L}/k = -\partial\theta/\partial N|_w$. The nondimensional heat transfer coefficient is called the **Nusselt number** with

$$\mathrm{Nu} = \frac{h\mathscr{L}}{k} \ , \tag{4.21}$$

which corresponds to the dimensionless temperature gradient at the wall. For surface heat transfer, a local Nusselt number using the surface coordinate is often employed instead of a global characteristic length. Another alternate dimensionless number used for heat transfer is the **Stanton number**

$$\mathrm{St} = \frac{h}{\rho c_p \mathscr{U}} = \frac{\mathrm{Nu}}{\mathrm{RePr}} \ . \tag{4.22}$$

The Stanton number highlights the geometric similarity between the momentum and thermal boundary layers. It also establishes a relationship between wall shear stress and heat transfer, or in nondimensional terms a similarity between friction coefficient and the Stanton number, as discussed further in Sect. 5.2.1.

To summarize the findings so far, for integral heat transfer problems, that is the total heat transfer across a body, the Nusselt number is expressed as a function of the governing dimensionless parameters

$$\mathrm{Nu} = f(\mathrm{Re}, \mathrm{Pr}, \mathrm{Gr}, \mathrm{Ec}) \ . \tag{4.23}$$

For local heat transfer, surface coordinates are added as dependent variables. However, in many technical applications, the further parameters can be neglected. For moderate to high speeds, the Eckert

number (Ec) and buoyancy effects (Gr) are often negligible. This reduces the average Nusselt number for forced convection to

$$\mathrm{Nu} = f(\mathrm{Re}, \mathrm{Pr}) \ . \tag{4.24}$$

For natural convection, where flow is caused by buoyancy forces and flow speeds are typically low, the Reynolds number becomes negligible, so that typically the functional relationship for the mean Nusselt number reduces to

$$\mathrm{Nu} = f(\mathrm{Gr}, \mathrm{Pr}) \ . \tag{4.25}$$

4.2.5 Turbulent Flow

At low Reynolds numbers, where viscous forces dominate over convective effects, the flow is classified as **laminar**. In this regime, perturbations in the velocity field are damped out, resulting in an orderly, smoothly layered flow with negligible lateral mixing. As the Reynolds number increases, the influence of the nonlinear convection term $\mathbf{u} \cdot \nabla \mathbf{u}$ grows. Viscous effects become less effective at suppressing disturbances, and the flow becomes unstable. Beyond a critical threshold, the flow transitions into the **turbulent** regime.

Turbulent flow is characterized by three-dimensional, irregular, and time-dependent motion that is non-periodic in nature. It exhibits vortex structures over a wide spectrum of spatial and temporal scales, forming a continuous range from large-scale geometry-induced motions to the smallest dissipative eddies. The presence of unsteady eddies enhances lateral momentum and energy transport, substantially increasing both momentum and heat transfer.

The transition to turbulence depends on multiple factors, including the flow configuration, such as internal versus external flows, the critical Reynolds number Re_{crit}, and the level of existing disturbances. For example, pipe flow typically becomes turbulent beyond $\mathrm{Re}_{crit} \approx 2300$ (see Sect. 5.3), while flow over a flat plate transitions at $\mathrm{Re}_{crit} \approx 10^5$.

Turbulence typically originates at solid boundaries, shear interfaces, or from geometric irregularities in the flow path. As a result, turbulent flows are inherently inhomogeneous and anisotropic, particularly near walls (Batchelor 1953; Hunt 2009). The governing equations remain valid, but place high demands on resolution to capture the wide range of scales involved. From a modeling perspective, the nonlinear convective terms in the momentum equation present challenges, and even more so does the pressure gradient term when expressed in terms of velocity, since it is not only nonlinear but also non-local (Pope 2000).

Turbulent flow simulations aim to solve the governing equations for the time-dependent velocity field $\mathbf{u}(\mathbf{x}, t)$. Direct numerical simulation (DNS), for instance, does not employ any turbulence modeling but instead resolves the Navier-Stokes equations at very high spatial and temporal resolution to capture all scales of motion. This approach is computationally expensive and is only feasible for low to moderate Reynolds numbers. Large eddy simulation (LES) resolves only the larger-scale turbulent structures while modeling the influence of the smaller, subgrid-scale motions. LES offers a reduction in computational cost compared to DNS but still remains demanding for complex or high Reynolds number industrial flows.

For most engineering applications, a large class of turbulence models has been developed in which the equations are solved for time-averaged quantities. These include the so-called **Reynolds stress models** and **eddy viscosity models**. Both approaches are based on the Reynolds-averaged Navier-Stokes (RANS) equations, which govern the behavior of the mean flow field. To derive these equations, Reynolds decomposition is applied, separating each flow variable into a time-averaged mean part and a fluctuating part. For velocity, this yields

$$\mathbf{u}(\mathbf{x}, t) = \mathbf{u}(\mathbf{x}) + \mathbf{u}'(\mathbf{x}, t) \ , \tag{4.26}$$

where $\mathbf{u} = (u, v, w)^\top$ denotes the mean velocity vector, and $\mathbf{u}' = (u', v', w')^\top$ represents the velocity fluctuations. In

nondimensional terms, the level of velocity fluctuation is often quantified using the turbulence intensity, defined as $\mathrm{Tu} = \sqrt{(u'^2 + v'^2 + w'^2)/(3u^2)}$. For simple flow configurations, such as flat plates or pipe flows, turbulence intensities typically lie in the range $\mathrm{Tu} \approx 1 - 10\%$. In more complex internal flows and turbomachinery, values up to $\mathrm{Tu} \approx 5 - 20\%$ are common. Conversely, in quiescent environments such as the external flow around vehicles or aircraft, turbulence levels may be as low as $\mathrm{Tu} < 1\%$.

Substituting the Reynolds decomposition into the Navier-Stokes equations and subsequently averaging them yields the governing equations for the mean flow. All linearly appearing fluctuating terms vanish under the averaging operation, leaving only nonlinear terms that involve products of fluctuating quantities. The momentum equation (3.53), for example, becomes

$$\rho\left(\frac{\partial \mathbf{u}}{\partial t} + \mathbf{u} \cdot \nabla \mathbf{u}\right) = -\nabla p + \nabla \cdot (\boldsymbol{\tau} + \boldsymbol{\tau}_t) + \rho \mathbf{f} \ , \tag{4.27}$$

which describes the evolution of the time-averaged flow field. Apart from the time-averaged quantities, this equation retains the same structure as the instantaneous form, but introduces a new term, namely the Reynolds stress tensor $\boldsymbol{\tau}_t$. The **Reynolds stress tensor** contains the averaged products of the fluctuating velocity components. It arises from the nonlinear convective term and embodies the effect of turbulence on the mean flow. For a homogeneous fluid with constant density, the tensor is given by

$$\boldsymbol{\tau}_t = -\rho \begin{pmatrix} u'u' & u'v' & u'w' \\ u'v' & v'v' & v'w' \\ u'w' & v'w' & w'w' \end{pmatrix} . \tag{4.28}$$

The individual components are referred to as the turbulent Reynolds stresses. These fluctuating components are not known **a priori**, and their appearance in the RANS equations introduces additional

unknowns. This is commonly referred to as the **closure problem** of turbulence.

Reynolds averaging simplifies the simulation because only the largest scales of motion need to be resolved, which makes computations more tractable. However, this simplification transfers the challenge to the modeling step. The Reynolds stresses capture the effect of unresolved small-scale turbulence on the mean flow and must be described in terms of known mean flow quantities. This requirement gives rise to the need for turbulence models. These models consist of differential equations or algebraic expressions that provide approximations for the turbulent stresses and associated fluxes, and are formulated to reproduce the overall influence of turbulence on the averaged flow field.

As mentioned earlier, two main classes of RANS models are used. These are Reynolds stress transport models (RSM) and eddy viscosity models. The former directly solves transport equations for the Reynolds stresses and provides a more detailed representation of turbulence but is more complex and requires significantly higher computational effort (White 1991). By contrast, eddy viscosity models estimate the Reynolds stresses by linking them to gradients in the mean flow through the concept of turbulent viscosity. Although these models are less detailed, they are widely used in engineering practice because they offer a feasible balance between accuracy and computational cost. The following sections concentrate on eddy viscosity models, which serve as the basis for many turbulence modeling approaches in industrial applications. The subject of turbulence modeling is extensive and for a comprehensive discussion on turbulence models, readers are referred to specialist literature, such as Pope (2000).

Linear **turbulent viscosity models**, also known as eddy viscosity models, assume that the Reynolds stresses responsible for shear can be modeled as being proportional to the mean rate of strain. Phenomenologically, this reflects the idea that turbulence enhances momentum transfer in a way similar to molecular viscosity. Boussinesq introduced this idea by proposing a turbulent exchange quantity, now

commonly referred to as **turbulent viscosity** or eddy viscosity ν_t, which mimics the relationship found in viscous shear stresses. Mathematically, the Reynolds stress tensor is modeled as

$$\boldsymbol{\tau}_t = 2\rho\nu_t\mathbf{S} - \tfrac{2}{3}\rho k_t\mathbf{I} \ , \tag{4.29}$$

where $\mathbf{S}$ is the mean rate of strain tensor, corresponding to the form introduced in Eq. (3.26) but evaluated using the mean velocities. The quantity k_t denotes the **turbulent kinetic energy**, which corresponds to the trace of the turbulent stress tensor and is given by

$$k_t = \tfrac{1}{2}\left(u'u' + v'v' + w'w'\right) \ . \tag{4.30}$$

In the case of isotropic turbulence, the turbulent kinetic energy simplifies to $k_t = 3/2 \ u'^2$. For a simple shear flow, such as a channel flow or boundary layer, the turbulent shear stress becomes

$$u'v' = \nu_t \tfrac{\partial u}{\partial y} \ . \tag{4.31}$$

The effect of turbulence is thus modeled as an additional viscosity that augments the molecular viscosity appearing in the shear tensor from Eq. (3.31). Importantly, the eddy viscosity ν_t is not a material property of the fluid but a function of the flow field. It is not constant throughout the domain and varies from point to point depending on the local level of turbulence. For example, near solid walls, velocity fluctuations, and hence the turbulent stresses vanish, because both the fluctuating and mean velocities satisfy the no-slip condition. As a result, ν_t tends to zero in wall-adjacent regions. In contrast, in free shear flows such as jets or wakes, where no wall influence is present, the assumption of a constant eddy viscosity often serves as a useful approximation (Spurk 1996, p. 197).

If the turbulent viscosity field $\nu_t(\mathbf{x}, t)$ is known, the Reynolds stresses can be evaluated, and the RANS equations become closed. Dimensional analysis, together with analogy to molecular transport,

offers a useful way to estimate ν_t. The molecular viscosity scales with the product of a characteristic molecular speed and a mean free path. By analogy, turbulent viscosity can be expressed in terms of a characteristic velocity scale and a length scale of the turbulent motion. This leads to the general form $\nu_t = C\mathscr{U}\mathscr{L}$, where $\mathscr{U}$ and $\mathscr{L}$ represent typical velocity and length scales of the flow. While this form often reflects the behavior of large-scale turbulent motion, it does not necessarily hold uniformly throughout the domain. In particular, near solid boundaries, velocity fluctuations vanish due to the no-slip condition, and ν_t must approach zero accordingly. This requires the use of position-dependent scales or damping functions to correctly model the near-wall behavior.

In practice, the choice of how to evaluate ν_t depends on the modeling approach. Different classes of models exist to estimate the turbulent viscosity based on velocity and length scale combinations tailored to the local flow behavior. Zero-equation models prescribe ν_t directly through algebraic relations. A prominent example is the mixing length model, discussed in detail below. One-equation models determine ν_t from the solution of a single modeled transport equation, such as the Spalart-Allmaras model (Pope 2000). Two-equation models solve a transport equation for the turbulent kinetic energy along with an additional equation for either the dissipation rate ε, the vorticity scale ω, or the turbulent length scale $\mathscr{L}$ (White 1991). These include widely used formulations such as the $k-\epsilon$, $k-\omega$, and SST models.

Turbulent fluctuations not only enhance momentum transport, as expressed by the Reynolds stresses, but also increase heat transfer. When the Reynolds decomposition is applied to the energy equation, products of velocity and temperature fluctuations appear in the convective terms, such as $\rho c_p u' T'$. Similar to turbulent stresses, these terms are interpreted as turbulent heat fluxes. They represent the turbulent contribution to the diffusion of the mean temperature field and are expressed as

(4.32)

$$\mathbf{q}_t = -\rho c_p \begin{pmatrix} u'T' \\ v'T' \\ w'T' \end{pmatrix} = -\rho c_p a_t \nabla T \ ,$$

where a_t is the **turbulent diffusivity**.

Similar to turbulent transport represented by ν_t, a_t is also not an intrinsic material property, and instead depends on local flow characteristics and varies throughout the domain.

In analogy to the molecular Prandtl number defined in Eq. (4.15), a **turbulent Prandtl number** can be introduced as the ratio of turbulent momentum diffusivity to turbulent thermal diffusivity defined as

$$\mathrm{Pr}_t = \frac{\nu_t}{a_t} \ . \tag{4.33}$$

It characterizes how the turbulent mixing of momentum compares to that of heat under the same flow conditions. The turbulent Prandtl number is also not a fluid property but depends on the local flow conditions. Assuming steady, unidirectional flow with mean gradients primarily in the wall-normal y-direction, the expression reduces to

$$\mathrm{Pr}_t = \frac{u'v'}{v'T'} \frac{\frac{\partial T}{\partial y}}{\frac{\partial u}{\partial y}} \ . \tag{4.34}$$

This form is commonly applied when turbulent transport in the y-direction dominates, such as in boundary layer or channel flows. However, it does not hold in more complex or strongly three-dimensional flows. Since the turbulent terms $u'v'$ and $v'T'$ describe similar time-averaged convection mechanisms, the turbulent Prandtl number is typically of the order of one. However, Pr_t generally depends on factors such as the Reynolds number, the molecular Prandtl number, and the distance from the wall. For a detailed discussion on modeling the turbulent Prandtl number, readers are referred to Kays et al. (2005).

To further describe turbulent flows and how they are modeled, the following sections provide a more detailed examination of key physical concepts and modeling approaches. First, the nature of energy transfer in turbulence is explored through the concept of vortex breakdown and the energy cascade. This is followed by the introduction of Prandtl's mixing length model, which offers a simple but effective way to approximate turbulent stresses. Lastly, we examine the near-wall behavior of turbulent shear flows and the development of the law of the wall, which plays a crucial role in engineering applications involving boundary layers.

The Turbulent Energy Cascade Turbulent flows, as already mentioned, consist of motion across a wide range of spatial and temporal scales. This multi-scale nature, already evident in the fluctuating stresses and fluxes discussed earlier, plays a central role in how turbulence transports momentum and energy. Phenomenologically, turbulent motion can be viewed as a composition of vortices of various sizes, where larger eddies successively break down into smaller structures. This hierarchical breakdown process is commonly referred to as the energy cascade, illustrated in Fig. 4.4. In this cascade, part of the kinetic energy originating from the mean flow is transferred into the motion of large-scale eddies characterized by an integral length scale L. This scale is typically of the same order as the characteristic flow dimension $\mathscr{L}$, and the velocity associated with it is comparable to $\mathscr{U}$. Consequently, the Reynolds number for the flow problem and the integral scale are of the same order of magnitude.[1] At these large scales, viscous effects are negligible, and inertial forces dominate the dynamics.

Through predominantly inviscid processes, these large turbulence structures break up into smaller eddies of higher frequency. As depicted in Fig. 4.4, this energy transfer continues down to the smallest eddy scale η, known as the Kolmogorov scale. At this scale, viscous forces become significant, and the turbulent energy is dissipated into internal energy.

While dissipation occurs at the smallest scale at the end of the cascade process (Pope 2000), under the assumption of equilibrium, the dissipation rate ε can be estimated based on the energy transfer initiated at the integral scale at the beginning of the sequence. The dissipation rate corresponds to the energy transfer rate per unit mass, which scales as $\varepsilon \sim \mathscr{U}^3/\mathscr{L}$.

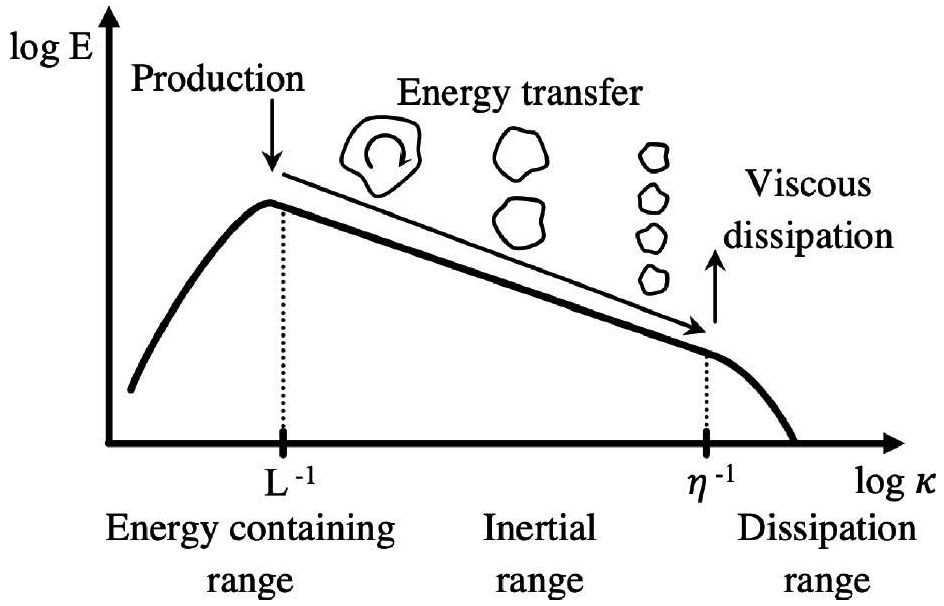


Fig. 4.4 Schematic illustration of production, energy cascade, and dissipation in the energy spectrum of turbulence

The **energy spectrum** $E(\kappa)$ is a function of the wavenumber $\kappa = 2\pi/\ell$, where ℓ is the wavelength, and it relates to the turbulence kinetic energy as

$$k_t = \int_0^\infty E(\kappa)\, d\kappa \ . \tag{4.35}$$

This integral represents the total kinetic energy per unit mass contained in the turbulent flow. The energy spectrum $E(\kappa)$ can be interpreted as the distribution of kinetic energy across the wavenumber band $0 \leq \kappa < \infty$, effectively serving as the turbulent kinetic energy density over these scales.

The **dissipation rate of turbulent kinetic energy** ε arises from the diffusion of velocity fluctuations at the smallest scales. It can be

expressed in terms of the energy spectrum (Pope 2000) as

$$\varepsilon = 2\nu \int_0^\infty \kappa^2 E(\kappa)\, d\kappa \ . \tag{4.36}$$

Kolmogorov's Hypotheses Kolmogorov proposed three hypotheses for turbulent flows at high Reynolds numbers, allowing to quantify the notion of the energy cascades (Pope 2000).

1. **Isotropy of Small-Scale Motions** The first hypothesis states that locally, small-scale turbulent motions are statistically isotropic, irrespective of the anisotropy of the larger-scale flow. In consequence, the statistical form of small-scale motions becomes self-similar in every high Re turbulent flow when scaled by the Kolmogorov scales η, u_η, τ_η, estimated in the following.
2. **Similarity Hypothesis for the Dissipation Scale** The statistics of the smallest eddies, in the dissipation range, are determined solely by the dissipation rate ε and the kinematic viscosity ν. This hypothesis reflects the idea that at these scales, the flow is dominated by viscous effects, and larger-scale dynamics are irrelevant. The corresponding dimension matrix yields

---

Table

From this, the characteristic scales are derived to

$$\eta \sim \left(\frac{\nu^3}{\varepsilon}\right)^{1/4} \ , \quad u_\eta \sim (\nu\varepsilon)^{1/4} \ , \quad \tau_\eta \sim \left(\frac{\nu}{\varepsilon}\right)^{1/2} \ . \tag{4.37}$$

These are the Kolmogorov length, velocity, and time scales, respectively. Applying the earlier considered dissipation rate $\varepsilon \sim \mathscr{U}^3/\mathscr{L}$ and integral scale Reynolds number $\mathrm{Re}_L = \mathscr{U}\mathscr{L}/\nu$, the ratio of the integral to dissipation length scale can be estimated to

$$\frac{L}{\eta} \sim (\mathscr{U}\mathscr{L}/\nu)^{3/4} = \mathrm{Re}_L^{3/4}. \tag{4.38}$$

Thus, resolving the dissipation scale in three-dimensional flows via direct numerical simulation (DNS) requires a spatial grid resolution of $\sim \mathrm{Re}_L^{9/4}$, making DNS computationally expensive for high Reynolds numbers.

3. **Similarity Hypothesis for the Inertial Subrange** In the inertial subrange, where eddies are significantly larger than the Kolmogorov scale η but smaller than the integral scale L, the flow statistics are uniquely determined by the energy dissipation rate ε and are independent of the viscosity ν (Pope 2000). This hypothesis highlights that inertial effects dominate in this range. The dimension matrix for energy spectrum $E(\kappa)$ depending on wave number κ and the energy dissipation rate ε reads

Table

From this, the energy spectrum follows a power law with

$$E(\kappa) = C\varepsilon^{2/3}\ \kappa^{-5/3}\ , \tag{4.39}$$

where $C \approx 1.5$ is a dimensionless constant determined experimentally (Pope 2000). The $-5/3$ exponent implies that the amount of energy in high wave numbers, with $\kappa \in [\kappa, \infty)$ is $\sim \kappa^{-2/3}$, meaning the bulk of energy resides at large scales. The dissipation for low wave numbers $\kappa \in [0, \kappa]$ is $\sim \kappa^{4/3}$, so that the bulk of dissipation dominates at the smallest scales.

Example 4.1 As an example, consider air ($\nu = 1.5 \times 10^{-5}\,\mathrm{m^2/s}$) flowing over a flat plate at $\mathscr{U} = 5\,\mathrm{m/s}$. At $x = 60\,\mathrm{cm}$, where $\mathrm{Re} \approx 10^5$, the boundary layer thickness is approximately $\delta \approx 10\,\mathrm{mm}$, emitting eddies of comparable integral length scale $L \sim \delta$. The eddies continuously break down to the dissipation length scale in the order of $\eta = (\nu^3\delta/\mathscr{U}^3)^{1/4} \approx 0.02\,\mathrm{mm}$.

Prandtl Mixing Length Model As discussed earlier, eddy viscosity models approximate the effect of turbulence by introducing a turbulent viscosity ν_t, which relates the Reynolds stresses to mean velocity gradients. One of the most intuitive formulations in this class is the mixing length model. Proposed by Prandtl, this model introduces a characteristic length scale, the **mixing length** ℓ_m, which represents the characteristic distance a fluid element travels laterally to the main flow direction before mixing with the surrounding fluid.

For illustration, consider a flow where the main direction is aligned with the *x*-axis, with a velocity gradient in the *y*-direction, similar to the boundary layer flow in Fig. 4.2. A fluid element at position *y* with velocity $u(y)$ in *x*-direction, moves laterally by ℓ_m, reaching a position $y + \ell_m$ with velocity $u(y + \ell_m)$. The velocity difference can be approximated as

$$u(y + \ell_m) - u(y) \approx \ell_m \frac{\partial u}{\partial y} \quad . \tag{4.40}$$

The velocity difference between both locations $u(y + \ell_m) - u(y) \approx \ell_m(\partial u/\partial y)$, provides an estimate for the fluctuation component of the *x*-velocity $u' = \mathcal{O}(\ell_m(\partial u/\partial y))$. The magnitude of v' conceptually follows by applying continuity, where two fluid elements with different speeds in *x*-direction would collide and consequently move laterally, giving $v' = \mathcal{O}(\ell_m(\partial u/\partial y))$. Since u' and v' are negatively correlated, that is a positive u' corresponds to a negative v' and vice versa, resulting in $u'v' \leq 0$. Using this approximation for velocity fluctuations, the turbulent shear stress can be expressed as

$$\tau_t = \rho u'v' = \rho \ell_m^2 \left| \frac{\partial u}{\partial y} \right| \frac{\partial u}{\partial y} \quad . \tag{4.41}$$

This shows that turbulent stresses scale with the square of the velocity gradient. The corresponding eddy viscosity is

$$\nu_t = \ell_m^2 \left| \frac{\partial u}{\partial y} \right| \quad , \tag{4.42}$$

indicating its dependence on the velocity gradient. The mixing length ℓ_m itself varies with the specific flow configuration and is generally a function of the *y*-coordinate normal to the main flow.

The Prandtl mixing length model is an algebraic turbulence model, notable for its straightforward physical interpretation, making it easier to argue sensible modeling assumptions. As any other algebraic model, it only depends on the local mean velocity field and, unlike with higher-order Reynolds stress models, cannot depict the history of the velocity field (Spurk 1996). Despite these limitations, the mixing length model has been successfully applied to a wide range of turbulent flows. It has proven particularly accurate for wall-bounded turbulent flows, such as boundary layers and pipe flows, and has also been utilized for free turbulent flows, including jets and wakes.

Near Wall Shear Flow For near-wall turbulent flows, valuable insights can be obtained by examining a simple shear flow, specifically the steady unidirectional flow between two parallel plates. In this configuration, the lower plate is stationary $u(0) = 0$, while the upper plate moves at a constant speed $u(h) = U$. The case of fully laminar flow under zero pressure gradient is known as **Couette flow**, governed by the simplified *x*-momentum equation

$$0 = \mu \frac{d^2u}{dy^2} \quad . \tag{4.43}$$

Integrating this equation once reveals that the total shear stress is constant throughout the fluid, corresponding to the wall shear stress $\tau_{xy} = \tau_w = \mu du/dy = \text{const.}$. A second integration yields a linear velocity profile $u \sim y$.

To analogously analyze turbulent wall-bounded flows, we consider the same flow configuration. However, we now focus on the mean velocity u and include the turbulent shear stress $u'v'$. The *x*-momentum equation for turbulent flow simplifies to

$$0 = \frac{d}{dy}\left(\mu \frac{du}{dy} - \rho u'v'\right) \quad . \tag{4.44}$$

Integration shows that the shear stress remains constant throughout the flow, leading to the relationship $\tau_w = \mu du/dy - \rho u'v'$, where τ_w is the wall shear stress. The mean velocity u is again solely a function of the wall-normal coordinate y, determined by the wall shear τ_w and the material properties ρ and ν. In terms of mean velocity, the shear stress can be expressed as

$$\frac{\tau_w}{\rho} = \nu \frac{du}{dy} - u'v' \ . \tag{4.45}$$

To nondimensionalize this relation, the friction velocity $u_\tau = \sqrt{\tau_w/\rho}$ is introduced, allowing the dimensionless velocity to be defined as $u^+ = u/u_\tau$. The viscous length scale ν/u_τ is well suited for nondimensionalizing the wall-normal distance, yielding $y^+ = yu_\tau/\nu$. In these terms, the shear stress can be rewritten as

$$1 = \frac{du^+}{dy^+} - \frac{u'v'}{u_\tau^2} \ . \tag{4.46}$$

Since the left-hand side is constant, both terms on the right-hand side must be functions of the dimensionless wall distance y^+, thus

$$u^+ = \frac{u}{u_\tau} = f(y^+) \ , \quad \frac{u'v'}{u_\tau^2} = g(y^+) \ . \tag{4.47}$$

The physical insight for the **law of the wall**, attributed to Prandtl and von Kármán, probably represents one of the most significant results in the study of turbulence. Beyond identifying the functional dependence of the velocity profile on the wall-normal distance, they deduced that the near-wall profile can be divided into three distinct regions, illustrated in Fig. 4.5.

1. **Viscous or Laminar Sublayer** ($0 < y^+ < 5$) In the immediate vicinity of the wall, the flow is dominated by molecular viscous shear. This region is associated with the first term on the right-hand side of Eq. (4.46) and exhibits a linear velocity profile, similar

to laminar flow. The influence of turbulence is negligible in this range.

2. **Outer Layer** ($y^+ > 30$) At larger wall distances, turbulent shear dominates the flow. This region corresponds to the second term on the right-hand side of Eq. (4.46). As detailed below, the velocity profile in this range follows a logarithmic law, which reflects the influence of turbulence on momentum transfer.

3. **Buffer Zone** ($5 < y^+ < 30$) Between the viscous sublayer and the outer layer lies the buffer zone, where both viscous and turbulent shear contribute to the flow dynamics. This region serves as a transitional layer, blending the characteristics of the viscous and turbulent regions.

These three regions together provide comprehensive regions for understanding and modeling the near-wall behavior of turbulent flows.

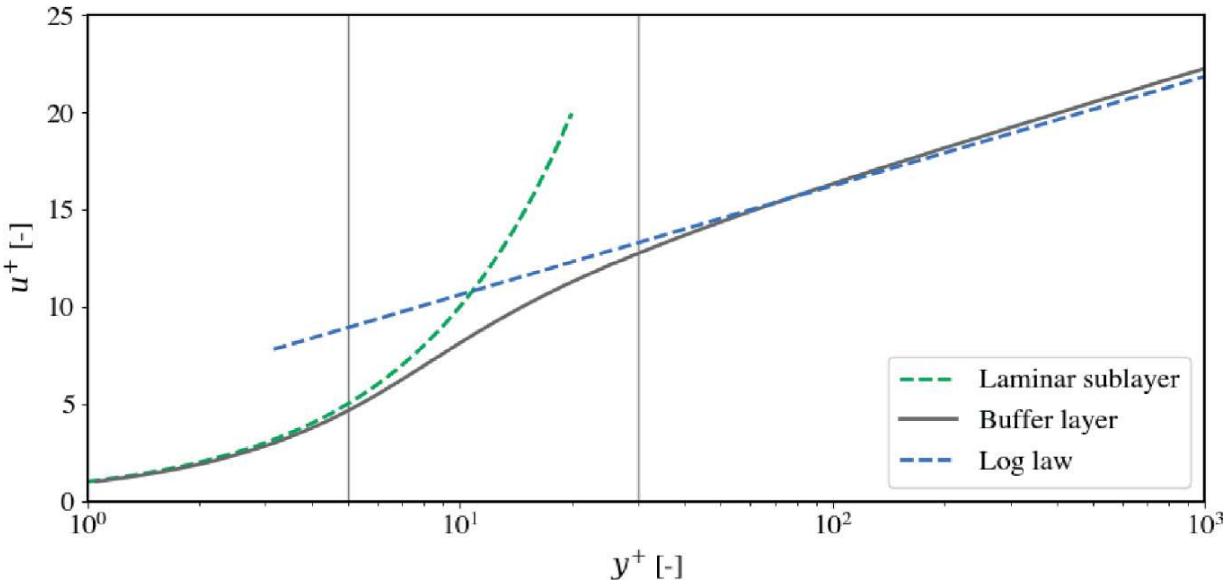


Fig. 4.5 Near-wall velocity profiles for viscous sublayer for $y^+ < 5$, buffer layer $5 \leq y^+ \leq 30$ and logarithmic wall layer $y^+ > 30$

Viscous Sublayer Directly adjacent to the wall, as $y^+ \to 0$, the turbulent shear stress diminishes, allowing the functional dependency

$f(y^+)$ to be derived using a Taylor expansion around $y^+ = 0$. Following Spurk (1996, 195f), the expansion for u^+ near $y^+ = 0$ is expressed as

$$u^+ = \frac{du^+}{dy^+}\bigg|_0 y^+ + \frac{d^2u^+}{dy^{+2}}\bigg|_0 \frac{y^{+2}}{2} + \dots \ . \tag{4.48}$$

The first-order coefficient is determined from Eq. (4.46), where $u'v'|_0 = 0$, leading to $du^+/dy^+|_0 = 1$. The higher-order coefficients are derived by differentiating Eq. (4.46) and evaluating them at $y^+ = 0$. The second-order coefficient evaluates to

$$\frac{d^2u^+}{dy^{+2}}\bigg|_0 = \frac{1}{u_\tau^2}\frac{d(u'v')}{dy}\frac{dy}{dy^+} = \frac{\nu}{u_\tau^3}\left[\frac{\partial u'}{\partial y}v' + u'\frac{\partial v'}{\partial y}\right]_0 = 0 \ , \tag{4.49}$$

where the terms in brackets vanish because $u'|_0 = v'|_0 = 0$. The third-order coefficient is expanded to

$$\frac{d^3u^+}{dy^{+3}}\bigg|_0 = \frac{\nu^2}{u_\tau^4}\left[\frac{\partial^2 u'}{\partial y^2}v' + 2\frac{\partial u'}{\partial y}\frac{\partial v'}{\partial y} + u'\frac{\partial^2 v'}{\partial y^2}\right]_0 = 0 \ . \tag{4.50}$$

Here, the first and third terms vanish because the fluctuation velocities are zero at the wall. Furthermore, the *x*- and *z*-directions align with the wall's native surface coordinates, so the gradients of the fluctuation velocities in these directions are also zero at the wall. By the continuity equation, it follows $\partial v'/\partial y = 0$ at the wall, ensuring that the entire third-order coefficient vanishes. The fourth-order coefficient evaluates to

$$\frac{d^4u^+}{dy^{+4}}\bigg|_0 = \frac{\nu^3}{u_\tau^5}\left[3\frac{\partial u'}{\partial y}\frac{\partial^2 v'}{\partial y^2}\right]_0 \ , \tag{4.51}$$

which cannot be further simplified without specific knowledge of the turbulent fluctuation profiles. From the Taylor expansion, it follows that in the immediate vicinity of the wall, that is $y^+ \to 0$, the turbulent fluctuations influence the velocity profile only at the order of $\mathcal{O}(y^{+4})$. Consequently, the velocity profile can be approximated as

(4.52)

$$u^+ = y^+ + \mathcal{O}({y^+}^4) \ .$$

In this region, the flow behaves essentially laminar, with a linear velocity profile analogous to the Couette flow described at the beginning of this section. The velocity profile is shown in Fig. 4.5. Note that because the *x*-axis is logarithmically scaled, the linear curve does not appear as a straight line.

The Logarithmic Wall Layer For larger distances from the wall with $y^+ > 30$, the viscous shear term du^+/dy^+ in Eq. (4.46) becomes negligible, leaving the turbulent fluctuations as the dominant factor. To model the turbulent shear stress, Prandtl's mixing length model from Eq. (4.41) is employed.[2] Substituting the mixing length model into Eq. (4.46) gives

$$1 = -\frac{u'v'}{u_\tau^2} = \ell_m^2 \left(\frac{du^+}{dy} \right)^2 \ . \tag{4.53}$$

To estimate the mixing length ℓ_m, it is reasonable to assume a linear relationship $\ell_m = \kappa y$, since the turbulent shear stress must vanish at the wall. The constant κ is named after von Kármán, who proposed a linear relation for the mixing length investigating smooth and rough pipe flows. Substituting the linear relation simplifies the shear relation to $1 = \kappa y^+ (du^+/dy^+)$. Integrating this equation by separation of variables results in the well-known logarithmic wall profile

$$u^+ = \frac{1}{\kappa} \ln y^+ + B \ . \tag{4.54}$$

This velocity profile is valid for many near-wall turbulent flows, including pipe, channel, and boundary layer flows. The von Kármán constant κ and the constant B are determined empirically. For the range $y^+ > 30$, experimental results suggest $\kappa \approx 0.41$ and $B \approx 5.0$, consistent with classical measurements of turbulent flows in smooth pipes by Nikuradse (1933a), discussed further in Sect. 5.3.2. In Fig. 4.5, the logarithmic scaling of the *x*-axis causes the profile to appear as a straight line.

The transition between the linear viscous sublayer ($y^+ < 5$) and the logarithmic profile ($y^+ > 30$) is continuous and forms a buffer layer ($5 \leq y^+ \leq 30$). To represent this transition, Spalding (1961) proposed the following expression, which blends the two regions

$$y^+ = u^+ + e^{\kappa B}\left(e^{\kappa u^+} - 1 - \kappa u^+ - \frac{(\kappa u^+)^2}{2} - \frac{(\kappa u^+)^3}{6}\right) . \tag{4.55}$$

This formula provides a unified description of the entire near-wall region, as shown in Fig. 4.5.

The Effect of a Pressure Gradient In many technical applications, a pressure gradient $\partial p/\partial x$ along the flow direction is present, particularly in pipe and channel flows where it is the primary driving force. In the presence of a pressure gradient, the momentum equation in Eq. (4.44) governing the shear flow extends to

$$\begin{aligned} 0 &= -\frac{\partial p}{\partial x} + \frac{d}{dy}\left(\mu \frac{du}{dy} - \rho u'v'\right) , \\ 0 &= -\frac{\partial p}{\partial y} + \frac{d}{dy}\left(-\rho v'v'\right). \end{aligned} \tag{4.56}$$

Following Spurk (1996), we analyze the dependency of the pressure gradient $\partial p/\partial x$. From the y-momentum equation, the combination $p + \rho v'v'$ must be independent of y and therefore can only be a function of x. Since the Reynolds stress term $\rho v'v'$ varies with y alone, its derivative with respect to x vanishes. This implies that the derivative of the pressure $\partial p/\partial x$ must depend on x only.

Furthermore, because the second term in the x-momentum equation does not depend on x, the gradient $\partial p/\partial x$ must be constant. Integrating the shear stress in the x-momentum equation, as given by Eq. (4.45), yields a linear relationship between shear stress and pressure gradient over y to

$$\tau = \frac{\partial p}{\partial x} y + \text{const.} \tag{4.57}$$

At the wall at $y = 0$, the shear stress matches the wall shear stress and thus $\tau(y = 0) = \tau_w$. As an example, consider a channel flow. Due to symmetry at the centerline of the channel where $y = h$, the shear stress becomes zero. This leads to a linear distribution of shear stress across the channel height, given by $\tau = \tau_w(1 - y/h)$. Near the wall, as $y \to 0$, the shear stress approaches a constant value equal to τ_w. In this region, the effect of the pressure gradient is minimal, and the assumptions underlying the derivation of the law of the wall in Eq. (4.45) remain applicable. Although a pressure gradient is present, it does not significantly influence the velocity profiles in the viscous sublayer or the buffer layer. Its effect becomes noticeable only at larger wall distances, typically when $y^+ \gtrsim 350$, where deviations from the logarithmic velocity profile begin to appear.

The effects of wall surface roughness on turbulent wall profiles, including deviations from the law of the wall, are discussed in the context of pipe flow in Sect. 5.3.2.

4.2.6 Free-Surface Flows

Free-surface flows involve fluid systems with an interface subject to zero parallel shear stress, such as the interface between air and water. Since the interface plays a crucial role, the analysis extends beyond the governing field equations to include the appropriate boundary conditions at the interface, as outlined in Sect. 3.3. Here, we consider the flow of an incompressible viscous fluid with a free surface, influenced by surface tension σ and the presence of a gravitational field $\mathbf{g}$.

To evaluate the impact of gravity, we compare gravitational forces to inertial forces represented by the convective terms in Eq. (4.1). This ratio yields $\mathscr{U}^2/g\mathscr{L} = 1/\ \mathrm{Fr}^2$, where Fr is the **Froude number**, defined as

$$\mathrm{Fr} = \frac{\mathscr{U}}{\sqrt{g\mathscr{L}}} \ . \tag{4.58}$$

The Froude number is particularly relevant in applications such as water waves, hydraulic channel flows, and ship hydrodynamics, where inertial and gravitational forces are of comparable magnitude $\mathscr{O}(\mathrm{Fr}) \approx 1$. For $\mathrm{Fr} \to \infty$, the influence of gravitational forces becomes negligible compared to inertial effects.

Surface tension arises from molecular interactions and generally acts on much smaller length scales than gravity. The relative importance of gravitational and surface tension forces is quantified by the **Bond number** $\mathrm{Bo} = \rho g \mathscr{L}^2/\sigma$. When $\mathrm{Bo} = 1$, gravitational and surface tension forces are of comparable magnitude, defining the **capillary length** $\mathscr{L}_c = \sqrt{\sigma/\rho g}$. For an air-water surface the capillary length is approximately $\mathscr{L}_c \approx 2.7\,\mathrm{mm}$. This length provides a scale that differentiates the dominance of surface tension or gravity. The scale of the capillary length is relevant for phenomena such as raindrops, pendant drops hanging from ceilings, or water-walking insects. At large scales ($\mathscr{L} \gg \mathscr{L}_c$), gravity dominates, governing phenomena such as ocean waves, ship waves, and hydraulic flows. At small scales ($\mathscr{L} \ll \mathscr{L}_c$) surface tension becomes increasingly significant, influencing capillary waves, droplets, and thin films.

In microscale fluid systems, surface tension becomes dominant, and free-surface flows often involve interactions between inertia and viscosity. The induced pressure jump at the interface due to surface tension is proportional to the surface curvature, as described by Eq. (3.74). Considering an inertia-induced pressure difference $\Delta p = \mathscr{O}(\rho \mathscr{U}^2)$ and a surface tension term with $\mathscr{O}(\sigma/\mathscr{L})$, where $\mathscr{L}$ here denotes the characteristic curvature radius, the ratio yields the **Weber number**

$$\mathrm{We} = \frac{\rho \mathscr{U}^2 \mathscr{L}}{\sigma} \quad . \tag{4.59}$$

The Weber number becomes significant for small-scale free-surface processes where inertia and surface tension interact, commonly involving strongly curved surfaces, such as droplets or perturbed liquid sheets.

To describe processes where viscous forces and surface tension interact, the **Ohnesorge number** Frohn and Roth (2000) is used

$$\mathrm{Oh} = \frac{\mu}{\sqrt{\rho \sigma \mathscr{L}}} \ . \tag{4.60}$$

The Ohnesorge number is related to the Weber and Reynolds numbers by $\mathrm{Oh} = \sqrt{\mathrm{We}} / \mathrm{Re}$, and it represents the ratio of viscous forces to the square root of inertia and surface tension. Aside from the characteristic length, it depends only on material properties, making it useful for characterizing a fluid's behavior at a given scale. Both We and Oh are essential for analyzing droplet dynamics, such as droplet oscillation, breakup, or impact onto a wetted wall illustrated in Sect. 9.4.

Example 4.2 To exemplify the range of these dimensionless numbers, consider water droplets at approximately $20\,^{\circ}\mathrm{C}$, where the droplet diameter is used as the characteristic length. A $1\,\mathrm{mm}$ raindrop falls with a velocity of approximately $4\,\mathrm{m/s}$ corresponding to $\mathrm{We} \approx 220$, $\mathrm{Oh} \approx 3.7 \times 10^{-3}$. A $3\,\mathrm{mm}$ droplet falls with a velocity of approximately $8\,\mathrm{m/s}$, resulting in $\mathrm{We} \approx 2640$ and $\mathrm{Oh} \approx 2.1 \times 10^{-3}$. A very small $10\,\mu\mathrm{m}$ droplet exhibits $\mathrm{Oh} \approx 3.7 \times 10^{-2}$. Larger Ohnesorge numbers at the same diameter indicate a greater influence of viscosity or a reduced influence of surface tension in the disperse phase.

4.3 Simplified Equations

For specific flow regimes and configurations, the governing equations can often be substantially simplified, making analytical and numerical analysis more tractable. These simplifications arise by identifying key assumptions, such as negligible viscosity, low Reynolds numbers, or constrained flow geometry, and are particularly valuable for understanding flow behavior in specific applications. Importantly, such simplifications often alter the mathematical character of the governing partial differential equations, fundamentally changing how information propagates through the flow field and the type of boundary conditions

required for well-posed solutions (Munz and Westermann 2018; DuChateau and Zachmann 2002).

The full compressible Navier-Stokes equations exhibit a mixed hyperbolic, parabolic character. The mass conservation equation is hyperbolic, while the presence of viscous diffusion and heat conduction introduces parabolic terms into the momentum and energy equations. Depending on the dominant physical processes, these mixed characteristics may reduce to purely hyperbolic, parabolic, or elliptic equations in specific flow regimes.

This section explores key simplifications, beginning with the boundary layer equations, which account for viscous effects near solid surfaces while leveraging the thin-layer approximation to reduce complexity. It then addresses inviscid flows governed by the Euler equations, which apply to compressible flows where viscosity and thermal diffusion are negligible. A special subclass of inviscid flows, potential flows, is introduced for irrotational conditions, where the governing equations reduce to the Laplace equation. Finally, creeping flows are discussed, characterized by the Stokes equations that govern highly viscous flows at very low Reynolds numbers. These simplified formulations reveal how distinct flow regimes enable tailored mathematical models to effectively capture the essential physics of fluid motion.

4.3.1 Boundary Layer Flow Equations

Even at very large Reynolds numbers ($\mathrm{Re} \gg 1$), the viscous term remains significant near boundaries where no-slip conditions apply, as discussed in Sect. 3.3. Within the boundary layer, viscosity cannot generally be neglected. However, the significant difference in orders of magnitude between the boundary layer thickness δ_u and the streamwise directed length scale $\mathscr{L}$ allows for simplifications of the governing equations. Here, we consider the boundary layer approximations for incompressible laminar flow over a flat plate, starting with the system of equations for an incompressible fluid given in Eq. (4.1), expressed in 2D Cartesian coordinates.

To simplify the equations, we introduce the length scale ratio $\varepsilon = \delta/\mathscr{L} \ll 1$, which is used to estimate the order of magnitude of the various terms in the governing equations. The change of the velocity components in *x*-direction is of $\mathscr{O}(1)$, while their change in *y*-direction is of $\mathscr{O}(\varepsilon)$, where $\varepsilon \ll 1$. The velocity components *u* and *v* exhibit stronger variations in wall-normal *y*-direction than in the streamwise *x*-direction, so that $\partial/\partial x \ll \partial/\partial y$ within the boundary layer. The continuity equation from Eq. (4.1) ensures that $\partial u/\partial x$ and $\partial v/\partial y$ are of the same order of magnitude. With $u = \mathscr{O}(1)$, it follows that $v = \mathscr{O}(\varepsilon)$, confirming that $v \ll u$.

In the *x*-momentum equation, the diffusion term $\partial^2 u/\partial x^2$ can be neglected, as it is smaller by a factor ε^2 compared to $\partial^2 u/\partial y^2$. The *y*-momentum equation reduces to $\partial p/\partial y \approx 0$, indicating that the pressure gradient normal to the wall is nearly zero within the boundary layer. Consequently, the pressure can be assumed independent of the wall-normal coordinate *y* and equal to the free-stream pressure $p(x) = p_\infty(x)$. Formally, the streamwise pressure gradient becomes an ordinary derivative, thus $\partial p/\partial y = dp/dx$. At the boundary layer interface with the free stream, the velocity and shear no longer vary in the *y*-direction, so that $\partial/\partial y \to 0$. The pressure gradient then simplifies to $dp/dx = -\rho U_\infty dU_\infty/dx$.

In the energy equation, the diffusion term $\partial^2 T/\partial x^2$ is negligibly small, and only the $\partial u/\partial y$ term is relevant for dissipation. Introducing these estimates into the governing equations in Eq. (4.1) and neglecting terms of smaller magnitude leads to the simplified boundary layer equations as follows

$$\begin{aligned}
\frac{\partial u}{\partial x} + \frac{\partial v}{\partial y} &= 0 \ , \\
\frac{\partial u}{\partial t} + u\frac{\partial u}{\partial x} + v\frac{\partial u}{\partial y} &= u_\infty \frac{du_\infty}{dx} + \nu \frac{\partial^2 u}{\partial y^2} \ , \\
\frac{\partial T}{\partial t} + u\frac{\partial T}{\partial x} + v\frac{\partial T}{\partial y} &= \frac{k}{\rho c_p}\frac{\partial^2 T}{\partial y^2} + \frac{\nu}{c_p}\left(\frac{\partial u}{\partial y}\right)^2 \ .
\end{aligned} \tag{4.61}$$

While these equations are derived for planar Cartesian coordinates, they remain valid for curved surfaces provided the boundary layer thickness is small compared to the wall's radius of curvature (White 1991, p. 231).

This equation set is parabolic, forming a mixed initial-boundary value problem. Conditions in the *y*-direction are specified at $y = 0$ and $y \to \delta_u$, respectively $\to \delta_T$. Conditions in *x* and *t* are only one-sided and semi-infinite. Due to the parabolic nature of the equations the flow history is propagated through the boundary layer along the characteristic velocity in the *x*-direction. In Sect. 5.2.1, the solution of the boundary layer equations is discussed for laminar flow over a flat plate. For a more detailed treatment of complex flow regimes, including compressible and turbulent flows, readers are referred to Kays et al. (2005).

4.3.2 Euler Equations

At high Reynolds numbers for $\mathrm{Re} \to \infty$, viscous and thermal diffusion are often negligible, particularly in the free-stream region outside thin boundary layers. By neglecting shear stresses, thus $\mu \to 0$ and heat conduction $\lambda \to 0$, the compressible Navier-Stokes equations from Eq. (4.5) reduce to the so-called Euler equations, which represent the fundamental equations of gas dynamics, expressed as

$$\begin{aligned} \frac{\partial \rho}{\partial t} + \nabla \cdot (\rho \mathbf{u}) &= 0 \ , \\ \frac{\partial}{\partial t}(\rho \mathbf{u}) + \nabla \cdot (\rho \mathbf{u}\mathbf{u}^\top) + \nabla p &= 0 \ , \\ \frac{\partial}{\partial t}\rho(e + \mathbf{u}^2/2) + \nabla \cdot \big(\rho \mathbf{u}(e + \mathbf{u}^2/2 + p)\big) &= 0 \ , \\ p = p(\rho, T) \ , \quad e &= e(\rho, T) \ . \end{aligned} \tag{4.62}$$

Here $p(\rho, T)$ and $e(\rho, T)$ define the state relations for pressure and internal energy. External body forces are omitted, as they are often negligible in compressible flows. In most practical applications for compressible flow analysis, these state relations are specified using the perfect gas law and the associated expressions for internal energy and

enthalpy, as detailed in Eq. (3.16). The Euler equations lose the highest-order diffusive terms present in the Navier-Stokes equations. This reduction simplifies the system to a hyperbolic form that describes the propagation of information in the medium. For a one-dimensional flow, as discussed in Munz and Westermann (2018), the equations can be reformulated as a first-order transport system

$$\frac{\partial \mathbf{q}}{\partial t} + \frac{d\mathbf{F}(\mathbf{q})}{d\mathbf{q}} \frac{\partial \mathbf{q}}{\partial \mathbf{x}} = 0 \ , \tag{4.63}$$

where $\mathbf{q}$ is the vector of conserved quantities, and $\mathbf{F}$ represents the corresponding fluxes with

$$\mathbf{q} = \begin{pmatrix} \rho \\ \rho u \\ \rho\left(e + u^2/2\right) \end{pmatrix}, \quad \mathbf{F} = \begin{pmatrix} \rho u \\ \rho u^2 + p \\ u\left(\rho e + \rho u^2/2 + p\right) \end{pmatrix} . \tag{4.64}$$

The flux Jacobian matrix $\mathbf{F}'(\mathbf{q})$ has three eigenvalues $\lambda_{1,2} = u \pm a,\ \ \lambda_3 = u$, where a is the speed of sound. Since all eigenvalues are real, the Euler equations form a strictly hyperbolic system, describing nonlinear wave propagation. In the physical interpretation, the eigenvalues represent the characteristic wave speeds $u \pm a$, the propagation velocities of pressure waves and u the flow velocity. If $|u| > a$, the flow is supersonic, and all eigenvalues are positive. Consequently, information propagates only downstream.

The Euler equations are typically solved as an initial value problem. Initial conditions specify the state of conserved variables at $t = 0$, while boundary conditions depend on the setup of the problem. For example, open boundaries may be used to allow waves to exit the domain, while closed walls cause waves to reflect back into the domain. The hyperbolic nature of the equations ensures that solutions evolve in space and time along characteristics, which are determined by the eigenvalues. These characteristics depend on the solution itself, making their paths nonlinear and generally not straight lines (Munz and Westermann 2018; DuChateau and Zachmann 2002).

When characteristics corresponding to the same eigenvalue intersect, a discontinuity forms in the solution, physically corresponding to a shock wave. Across such shocks, entropy increases due to dissipation at the discontinuity. However, in smooth regions of the flow, entropy remains constant as entropy-generating diffusive mechanisms are neglected. The behavior of shocks and the associated entropy changes are further discussed in Sect. 5.1.3.

4.3.3 Potential Flow

For incompressible flow with constant fluid properties, the momentum and energy equations are decoupled. To simplify the momentum equation, the nonlinear convective term can be decomposed using the vector identity

$$(\mathbf{u}\cdot\nabla)\cdot\mathbf{u} = \nabla\mathbf{u}^2/2 - \mathbf{u}\times\boldsymbol{\omega}\ , \tag{4.65}$$

where $\boldsymbol{\omega} = \nabla\times\mathbf{u}$ denotes the vorticity vector, as introduced in Eq. (3.25). Additionally, using the vector identity and recognizing that for incompressible flow the velocity field is solenoidal ($\nabla\cdot\mathbf{u}=0$), the momentum equation from Eq. (4.1) simplifies to

$$\rho\tfrac{\partial\mathbf{u}}{\partial t} + \nabla\left(p + \rho\tfrac{\mathbf{u}^2}{2} + \rho\mathbf{g}\mathbf{z}\right) = \rho\mathbf{u}\times\boldsymbol{\omega} - \mu\nabla\times\boldsymbol{\omega}\ . \tag{4.66}$$

A special class of flows, referred to as **potential flow** or ideal flow, arises when the velocity field is not only solenoidal but also irrotational ($\boldsymbol{\omega} = \nabla\times\mathbf{u} = 0$). Under these conditions, there exists a scalar potential Φ such that $\mathbf{u} = \nabla\Phi$. Knowledge of the scalar potential field is sufficient to determine all flow variables.

For irrotational flow, the convective terms simplify to represent only the kinetic energy, and the right-hand side of the momentum equation in Eq. (4.66) vanishes. Upon integration, this leads to the unsteady Bernoulli equation $\rho\partial\Phi/\partial t + p + \rho\mathbf{u}^2/2 + \rho g z = \text{const.}$, which is further discussed for quasi-one-dimensional flow in Sect. 5.1.

Potential flows are governed by the elliptic Laplace equation $\nabla^2\Phi = 0$ and are posed as boundary value problems. Unlike the compressible Euler equations, potential flows exhibit fundamentally different characteristics. In the case of the Laplace equation, any change within the flow field or at the boundary conditions instantaneously affects the entire domain. There is no history of motion retained in potential flows, and changes affect both upstream and downstream regions simultaneously. The solution of a potential flow problem requires specifying conditions along a closed contour that encloses the solution domain (White 1991).

The geometry of the flow domain primarily dictates the behavior of potential flows. The streamlines of a potential flow around a body, or through a duct or channel, are determined by the geometry of the boundaries. Mathematically, potential flows represent a versatile solution class due to the linearity of the governing equation and boundary conditions. By applying the principle of superposition, it is possible to construct complex flow patterns by combining elementary solutions such as uniform flow, point sources, and point vortices. This approach enables the modeling of flows in corners, through orifices, around spheres, and around airfoils.

However, it is crucial to recognize the limitations of potential flow. Since all vorticity-generating mechanisms are ignored, potential flow cannot satisfy the no-slip condition at walls. The only boundary condition imposed is that the velocity normal to the wall must vanish. Consequently, the boundary of an object effectively aligns with a streamline of the flow. Despite these limitations, potential flow often provides an excellent approximation for the free-stream flow outside thin boundary layers, as the effects of viscosity are concentrated within the boundary layer itself.

The mathematical framework of potential flow was extensively developed in the nineteenth century, and significant foundational work can be found in classic fluid mechanics treatises, such as those by Lamb (1932) and Milne-Thomson (1968).

4.3.4 Creeping Flow

After considering flow characterized by large Reynolds numbers, we now turn to the regime of small Re. Such conditions arise when the regarded length scales are extremely small, or for very viscous liquids, or for flows with comparatively low velocities. This flow regime is dominated by viscous forces, and referred to as creeping or **Stokes flow**.

To formalize the assumptions, we examine the nondimensionalized equations of motion. Here, we use the tilde $\tilde{q}$ to indicate the nondimensionalized form of a quantity or operator scaled by appropriate characteristic values. Since viscosity dominates in this regime, the pressure is nondimensionalized using the viscous scale $\mu\mathscr{U}/\mathscr{L}$ rather than the dynamic pressure scale $\rho\mathscr{U}^2/2$. The nondimensional equations of motion become

$$\begin{aligned} \tilde{\nabla}\tilde{\mathbf{u}} &= 0 \ , \\ \mathrm{Re}\left(\tfrac{\partial\tilde{\mathbf{u}}}{\partial\tilde{t}} + \tilde{\mathbf{u}}\cdot\tilde{\nabla}\tilde{\mathbf{u}}\right) &= -\tilde{\nabla}\tilde{p} + \tilde{\nabla}^2\tilde{\mathbf{u}} \ . \end{aligned} \tag{4.67}$$

In the limiting case of $\mathrm{Re}\to 0$, inertial terms can be neglected. The resulting equations, known as the Stokes equations, are linear and describe a balance between viscous and pressure forces

$$\nabla\cdot\mathbf{u} = 0 \ , \quad \nabla p = \mu\nabla^2\mathbf{u} \ . \tag{4.68}$$

Applying the gradient to the momentum equation, and using the fact that the velocity field is solenoidal, it follows that $\nabla^2 p = 0$. The velocity field also satisfies the biharmonic equation, with $\nabla^4\mathbf{u} = 0$. The pressure can be eliminated by taking the curl of the momentum equation, yielding $\nabla^2\nabla\times\mathbf{u} = \nabla^2\boldsymbol{\omega} = 0$, where $\boldsymbol{\omega}$ is the vorticity. Thus, in creeping flow, both the pressure and vorticity satisfy Laplace's equation (White 1991).

In the special case of Stokes flow in the Cartesian (x, y)-plane, the velocity field $\mathbf{u}$ has vorticity only in the z-direction, and the stream function $\Psi(x, y)$ is related to the vorticity by $\omega = -\nabla^2\Psi$. The

Laplacian for vorticity $\nabla^2\omega = 0$ can then be rewritten to $\nabla^4\Psi = 0$. This implies that Ψ satisfies the biharmonic equation, reducing the two-dimensional Stokes equations to a single linear equation.

In Sect. 5.2.2, we will apply these concepts to derive the drag on a sphere at low Reynolds numbers, offering insights into the physical implications of creeping flow. The analysis also forms the foundational basis for extending the validity range to flows at higher Reynolds numbers.

4.4 Similarity in Fluid Systems

The concept of **similitude** is fundamental in the analysis and modeling of thermo-fluid systems, as it establishes the conditions under which different flows, physical configurations, or entire systems exhibit equivalent behavior. Similitude enables the transfer of insights from a simplified or scaled system to a full-scale counterpart, ensuring that experimental, numerical, or theoretical results remain valid across different scenarios. This principle plays a crucial role, in situations where direct experimentation on full-scale systems is often impractical.

In the previous sections, we introduced various dimensionless groups, serving as **basic descriptors** of flow behavior across different regimes. As discussed in the course of Sect. 4.2, the applicability of these groups depends on the specific flow regime in question. Similitude provides the unifying framework that governs these diverse phenomena, ensuring that different systems exhibiting the same set of governing dimensionless parameters will follow analogous physical laws.

At its core, similitude addresses the question of when two geometrically similar systems will also exhibit physically similar behavior, meaning that the flow streamlines, temperature distributions, and other relevant physical quantities follow analogous patterns. Such similarity ensures that the fundamental governing equations retain the same form across different scales, making it possible to transfer experimental, numerical, or theoretical findings from one setup to

another. It ensures that the fundamental physical behavior of one system can be mapped onto another, regardless of differences in absolute size or operating conditions.

The formal foundation of similitude is established through the Π-theorem, introduced in Sect. 2.2. Given a set of relevant physical quantities $x_1, x_2, \ldots, x_n$, the theorem allows the formulation of a set of dimensionless groups $\Pi_1, \ldots, \Pi_d$ that encapsulate the underlying physics. If two systems share the same functional relationships among these Π-groups and their boundary conditions are matched, they will exhibit equivalent behavior. Mathematically, the governing relationship is expressed as $f(\Pi_1, \ldots, \Pi_d)$. Thus, two systems governed by the same dimensionless formulation will yield the same solutions under matched dimensionless parameters and boundary conditions.

While **complete similarity**, where all nondimensional groups are exactly matched, is the ideal case, it is often impractical in engineering applications. Instead, **partial similarity** is typically employed, where only the dominant effects are preserved while secondary effects are either minimized or accounted for as corrections. For example, Reynolds similarity ensures dynamically similar flows in inertia-viscosity dominated regimes, such as boundary layer and turbulent flows. Mach number similarity is required when compressibility effects and shock waves become significant. The Ohnesorge number and Weber number ensure equivalent free-surface behaviors in flows where viscous, inertial, and surface tension forces interact, as seen in droplets, multiphase flows, atomization, and spray processes. The appropriate dominant similarity criterion depends on the specific process under investigation.

While similitude provides a powerful analytical framework, its application requires careful attention. Matching boundary conditions is just as crucial as maintaining dimensionless group consistency, as any discrepancies can introduce significant errors when extrapolating results. In practice, scaling is rarely perfect, since material properties, gravitational effects, or surface roughness may not scale exactly, and therefore requiring to determine which deviations are negligible and

which must be corrected. Additionally, the validity of similarity principles is often limited to specific conditions. For instance, Reynolds number similarity may hold at moderate flow speeds, but at higher speeds, compressibility effects become dominant, necessitating adjustments to account for changing flow behavior.

Similitude is widely applied in engineering and science, in modeling, design optimization, and experimental validation. In scale-model testing, it allows to study scaled prototypes in wind tunnels, or laboratory setups while preserving key dimensionless parameters, ensuring accurate transfer to full-scale performance. It constitutes the basis for the **transferability of empirical correlations**, such as drag coefficients and heat transfer relations from one configuration to another, which rely on dynamically similar conditions. In turbomachinery, similitude principles enable performance predictions, and design scaling through dimensionless groups as discussed in the following section.

4.4.1 Incompressible Flow Machines

Similitude considerations are fundamental in understanding the behavior of turbomachinery and are integral to its design, selection, and operational analysis. By applying similarity principles, engineers are able to transfer performance characteristics across various conditions and predict operating conditions such as speed, flow rate, or working fluid. Machinery design engineers can develop families of related machines, ensuring scalable designs across different performance requirements. They furthermore help in the selection of optimal configurations during the machine design phase or when identifying a suitable machine type for a specific operating requirements range, such as axial, mixed-flow, or radial machinery designs.

We consider a generic turbomachine that modifies the fluid state through energy transfer, from a purely dimensional analysis perspective following Dixon and Hall (2013). Consider a turbomachine that performs either supply work (e.g., pump, compressor) or

extraction work (e.g., turbine) with power $P = \dot{m}gH = Q\Delta p$ to alter the fluid state from an inlet to an outlet condition $1 \to 2$. The machine operates at a speed of rotation Ω and processes a volumetric flow rate Q, both of which shall be considered as **control variables**.[3] We use the number of revolutions per unit time rotational speed n equivalently to Ω in this text.[4] The volumetric flow rate Q and the pressure head $\Delta p/\rho = gH$ constitute **duty parameters** demanded by operational requirements. The fluid properties ρ and μ characterize the working medium. The rotational speed Ω and the characteristic length scale D represent **design variables**, and dictate the machine's performance and operational behavior.

The machine operates with efficiency η, and the converted shaft work corresponds to a change in fluid energy. For incompressible fluids, the state change is expressed as $\Delta p = \rho g H$, where H denotes the head, corresponding to the height equivalent of the added potential energy. A characteristic length for the flow path is typically the impeller diameter D or a characteristic flow cross-section. The machine geometry is described by a set of length scales $\ell_1, \ell_2, \cdots$, as well as characteristic clearances ε_c, and ε_r to characterize surface roughnesses.

For any turbomachine handling an incompressible fluid, the performance parameters can thus be expressed by functional relations with variables of the form

$$\Delta p, \;\; \eta, \;\; P = f(Q, \Omega, D, \rho, \mu, \ell_1, \ell_2, \ldots \varepsilon_r, \varepsilon_c) \;\; , \tag{4.69}$$

that shall be expressed in nondimensional form in the following. Similitude across a family of machines requires ensuring both geometric and dynamic similarity. Geometric similarity is ensured when the length ratios $\ell_1/D, \ell_2/D, \ldots$ remain the same, thus the entire machine is geometrically scaled. However, surface roughness and clearances ε/D are commonly excluded from strict similarity conditions since their manufacturability is limited by fabrication techniques. The kinematic or dynamic similarity in turbomachine design is described by the established nondimensional groups

$$\Phi = \frac{Q}{\Omega D^3} \quad , \quad \Psi = \frac{\Delta p/\rho}{\Omega^2 D^2} \quad , \quad \tilde{P} = \frac{P/\rho}{\Omega^3 D^5} \quad . \tag{4.70}$$

Here, Φ is the **flow coefficient**, Ψ is the **pressure coefficient**, and $\tilde{P}$ is the **power coefficient**. Dynamic similarity prevails when these groups are constant, which from a flow topological perspective implies the geometrical similarity of streamline patterns relative to the blades (Dixon and Hall 2013). The nondimensionalisation of these groups is chosen such that the key variables Q, Δp, and $\tilde{P}$ enter linearly. With the definition of the effective power the relations connecting all three variables follow to $\tilde{P} = \Phi\Psi$. The machine efficiency η is already nondimensional. For a pump it relates to shaft power by $\tilde{P} = \eta \tilde{P}_{\text{shaft}}$. For general turbomachinery, the efficiency definitions are detailed in Sect. 5.1.4. Another relevant nondimensional group appears in the form of the machine Reynolds number $\mathrm{Re} = \Omega D^2/(\mu/\rho)$, where ΩD can be interpreted as characteristic scale for the blade speed.

In nondimensional terms, a turbomachine's performance can be characterized by general parametric relations of the form

$$\Psi = f_1\big(\Phi, \mathrm{Re}, \tfrac{\varepsilon}{D}\big) \quad , \quad \eta = f_2\big(\Phi, \mathrm{Re}, \tfrac{\varepsilon}{D}\big), \quad \tilde{P} = f_3\big(\Phi, \mathrm{Re}, \tfrac{\varepsilon}{D}\big). \tag{4.71}$$

While the functions are distinct, they depend on the same set of arguments. Similitude is achieved when all nondimensional groups remain equal, that is the geometry is uniformly scaled, while the dimensionless duty numbers (Φ, Ψ), and Reynolds number are maintained.

For high Reynolds numbers ($\mathrm{Re} > 2e5$), the influence of Re on overall performance is small, as boundary layers are typically thin and turbulent, having little effect on the overall flow field (Dixon and Hall 2013). However, Re can still influence efficiency, which tends to increase by a few percentage points as Re grows by an order of magnitude. For example, for turbomachines with water as working fluid, Re is typically large, and its effects may be neglected in first-order approximations.

As mentioned, the effects of surface finish and clearances described by ε/D are commonly excluded from the similarity, as the feasibility of geometrical scaling is limited by manufacturing processes. However, neglecting the respective terms may result in deviations of perfect similitude. Generally, increased relative clearances lead to loss in efficiency. At high Re, increased surface roughness leads to higher skin friction and efficiency losses. At lower Re, roughness effects can be more complex, potentially influencing transition to turbulence.

In case that Reynolds numbers are high enough that Re effects can be neglected and ε/D effects are considered secondary, the functional dependencies reduce to only Φ, thus

$$\Psi = f_1(\Phi) \ , \quad \eta = f_2(\Phi), \quad \tilde{P} = f_3(\Phi). \tag{4.72}$$

The functional forms of f_1, f_2, and f_3 are typically determined experimentally, but for certain machine types, they may be partially derived analytically, as exemplified for pumps in Sect. 10.2.

One key application of similitude is in the use of performance curves, which is particularly relevant for understanding and optimizing machine operation. By utilizing scaling laws, engineers can infer the operating conditions of a given turbomachine, simplifying performance characterization and ensuring reliable extrapolation to various operating conditions, as illustrated in Example 4.3. Additionally, similitude plays a crucial role in the design phase of machinery families, allowing for the development of scaled versions that meet varying duty requirements with reduced engineering effort and cost. This approach not only streamlines the design process but also enables direct comparison between machines under different operating conditions, as demonstrated in Example 4.4.

Example 4.3 A key application of similitude theory in turbomachinery is the prediction of performance at different operating speeds for a given machine. When a turbomachine operates at different rotational speeds n_A and n_B, dynamic similarity implies that all

dimensionless performance coefficients remain unchanged. In consequence the performance data represented in terms of nondimensional groups collapse into a single characteristic curve.

To illustrate, consider a single pump operating with the same working fluid at two different rotational speeds. Since the machine itself remains unchanged, the geometrical scale factor $M_D = D_B/D_A = 1$ is unity, and all fluid property scale factors remain constant. The only changing parameter is the rotational speed, represented by the scale factor $M_n = n_B/n_A$. Given that dynamic similarity is assumed, the flow coefficient remains unchanged, thus $M_\Phi = 1$, and the head coefficient also remains equal with $M_\Psi = 1$. These conditions lead to the fundamental scaling relations, that is the volumetric flow rate scales linearly with rotational speed, $M_Q = M_n$, while the pressure rise varies quadratically, $M_{\Delta p} = M_n^2$. Since the impeller diameter remains constant, the Reynolds number scales as $M_{\mathrm{Re}} = M_n$, meaning that perfect similitude in Re is not achievable. However, for sufficiently high Reynolds numbers, this effect can often be neglected. The power input scales as $M_{\tilde{P}} = M_n^3$.

Figure 4.6 illustrates a typical performance curve for a single pump at different operating conditions. In dimensional terms, each speed setting results in a distinct operating curve. However, by applying similarity laws, all data collapse onto a single nondimensional performance curve, as shown on the right-hand side of Fig. 4.6.

It is important to note that dynamic similitude holds strictly only in steady-state operation, where the flow field is well established. Neglecting Re, dynamic similarity prevails when both (Ψ, Φ) are constant, so for a specific pump yields $Q \sim n$ and $H \sim n^2$. Lines of constant (Ψ, Φ) thus correspond to parabolas in the *QH*-diagram as indicated on the left-hand side of Fig. 4.6.

It should be further noted that at high flow rates and rotational speeds, cavitation effects can lead to deviations from the expected performance curve, as observed in Fig. 4.6. Deviations from similitude in steady operations can also be an indicator for machine degradation.

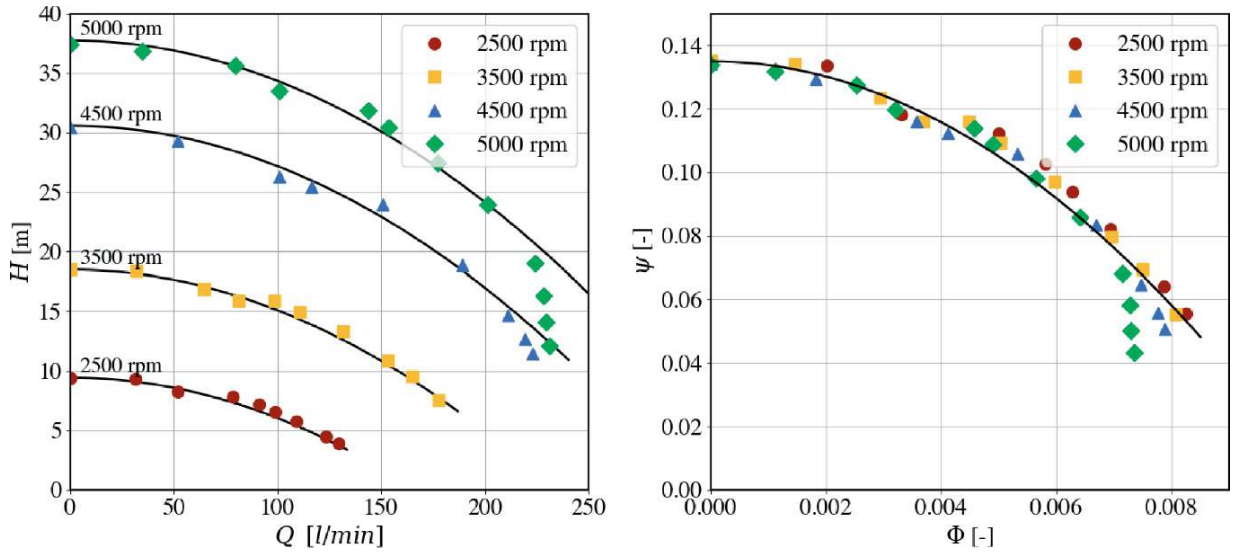


Fig. 4.6 Pump with $D = 0.1\,\mathrm{m}$ and design speed of $n = 3500\,\mathrm{rpm}$ in (Q, H) on the left and (Φ, Ψ) on the right. Reference data adapted from Dixon and Hall (2013)

Example 4.4 Scaling laws are widely applied not only to infer performance at different speeds for the same machine but also to compare performance characteristics across different but geometrically similar machines. In this example inspired by Lewis (1996), Fig. 4.7 illustrates the application of similitude-based scaling for comparing the performance of two geometrically similar pumps.

Pump A has an impeller diameter of $D_A = 0.1\,\mathrm{m}$ and operates at $n_A = 3500\,\mathrm{rpm}$. Pump B, which is a scaled-up version of Pump A, has a larger impeller diameter of $D_B = 0.15\,\mathrm{m}$ and runs at a lower speed of $n_B = 2500\,\mathrm{rpm}$. The left side of Fig. 4.7 shows the performance curves in dimensional terms, where the different scales for H and Q reflect the differences in machine size and operating speed. The right side presents the same data in nondimensional terms, where both the head coefficient Ψ and efficiency η collapse onto similar characteristic curves, demonstrating similitude scaling.

While the scaling laws provide an effective means for performance prediction and comparison, deviations from perfect similitude may arise due to differences in surface finish, tip clearance, or other secondary geometric effects that do not scale exactly in practice. These discrepancies can lead to variations in efficiency and overall

performance. However, across a wide range of operating conditions, the similarity laws remain a powerful tool for understanding machine behavior.

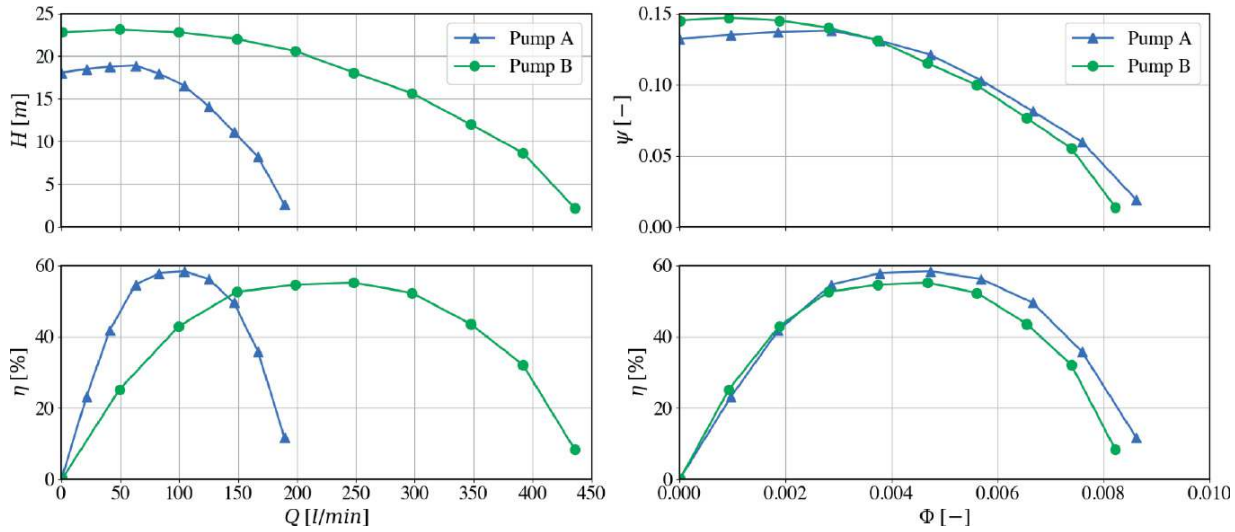


Fig. 4.7 Pump A with $D_A = 0.1\,\text{m}$ operating at $n_A = 3500\,\text{rpm}$ and Pump B with $D_B = 0.15\,\text{m}$ operating at $n_B = 2500\,\text{rpm}$ on the left in dimensional and on the right in nondimensional terms. Reference data adapted from Lewis (1996)

4.4.2 Compressible Flow Machines

So far, we have considered incompressible fluids, which are relevant for low-speed turbomachinery. However, for high-speed machines, compressibility effects become significant and must be accounted for in the analysis. In this section, we regard the case of a perfect gas as the working fluid.

In compressible flow analysis, due to density changes large variations in the values of volume flow rate Q may arise, and so it is replaced by the more suitable mass flow rate $\dot{m}$. Similarly, instead of using a constant density ρ, the stagnation density at the inlet ρ_{t1} is considered. As discussed in more detail in Sect. 5.1.3, instead of the pressure change Δp, it is more meaningful to analyze the specific isentropic stagnation enthalpy change Δh_{ts}. Additionally, two more parameters must be incorporated to account for compressibility effects, that is, the ratio of specific heats γ according to Eq. (3.7), and the speed of sound from Eq. (3.8) at the inlet stagnation state a_{t1}. The

characterization of component and flow geometry remains analogous to the incompressible case.

Thus, for a compressible flow turbomachine, the relevant variables are adapted as follows

$$\Delta h_{ts},\ \eta\ , P = f(\dot{m}, \Omega, D, \rho_{t1}, \mu, a_{t1}, \gamma, \ell_1, \ell_2, \ldots \varepsilon_r, \varepsilon_c)\ . \tag{4.73}$$

As in the incompressible case, we assume geometric similarity and focus the discussion on dynamic similarity. By forming nondimensional groups, the performance parameters can be expressed as

$$\frac{\Delta h_{ts}}{a_{t1}^2},\ \eta,\ \frac{P}{\rho_{t1} a_{t1}^3 D^2} = f\left(\frac{\dot{m}}{\rho_{t1} a_{t1} D^2}, \frac{\Omega D}{a_{t1}}, \frac{\rho_{t1} a_{t1} D}{\mu}, \gamma \right)\ . \tag{4.74}$$

Here, we use the speed of sound a_{t1} as a more meaningful velocity reference instead of the blade tip speed ΩD. The term $\Omega D / a_{t1}$ can be interpreted as a blade Mach number.

Applying the state and process equations for a perfect gas allows the nondimensional groups to be rewritten in terms of the more convenient stagnation pressures and temperatures at machine in- and outlet. Using the stagnation speed of sound and the isentropic relations, discussed in Sects. 5.1.1 and 5.1.3, the nondimensional enthalpy change can be rewritten as

$$\frac{\Delta h_{ts}}{a_{t1}^2} = \frac{1}{\gamma - 1} \left[\left(\frac{p_{t2}}{p_{t1}} \right)^{(\gamma-1)/\gamma} - 1 \right] = f\left(\frac{p_{t2}}{p_{t1}}, \gamma \right)\ . \tag{4.75}$$

Thus, the enthalpy change can be expressed in terms of the total pressure ratio p_{t2}/p_{t1}. Similarly, the nondimensional mass flow rate and power coefficient transform to

$$\begin{aligned} \hat{m} &= \frac{\dot{m}}{\rho_{t1} a_{t1} D^2} = \frac{\dot{m} \sqrt{\gamma R T_{t1}}}{\gamma D^2 p_{t1}}, \\ \tilde{P} &= \frac{P}{\rho_{t1} a_{t1}^3 D^2} = \hat{m} \frac{c_p (T_{t2} - T_{t1})}{a_{t1}^2} = \frac{\hat{m}}{(\gamma - 1)} \frac{\Delta T_t}{T_{t1}}\ . \end{aligned}$$

For a perfect gas, Eq. (4.74) can then be rewritten as

$$\frac{p_{t2}}{p_{t1}},\ \eta,\ \frac{\Delta T_t}{T_{t1}} = f\left(\frac{\dot{m}\sqrt{c_p R T_{t1}}}{D^2 p_{t1}}, \frac{\Omega D}{\sqrt{\gamma R T_{t1}}}, \mathrm{Re}, \gamma\right) . \tag{4.76}$$

Thus, the relevant nondimensional groups are expressed in terms of stagnation pressures and temperatures. If only a single gas is considered, the heat capacity ratio γ can be omitted, as it remains constant. Additionally, if the machine operates within a narrow speed range or at high Reynolds numbers, the Reynolds number Re can also be neglected. The fundamental scaling relations then reduce to

$$\frac{p_{t2}}{p_{t1}},\ \eta,\ \frac{\Delta T_t}{T_{t1}} = f\left(\frac{\dot{m}\sqrt{c_p T_{t1}}}{D^2 p_{t1}}, \frac{\Omega D}{\sqrt{R T_{t1}}}\right) . \tag{4.77}$$

The nondimensional mass flow $\hat{m}$ corresponds to the flow capacity introduced in the context of compressible isentropic flows in Eq. (5.29). Unlike incompressible turbomachinery, where performance parameters can be expressed as univariate relationships as shown in Eq. (4.72), compressible fluid machines require two independent variables to characterize performance. It shall be emphasized that the inlet total state explicitly appears in the nondimensional groups and plays a crucial role in ensuring dynamic similarity.

The derived groups provide valuable insight into the fundamental behavior of compressible flow machines. In practical applications, such as performance maps illustrated in Fig. 4.8, constants like D, γ, and R are often omitted to simplify the representation. Although this removes perfect dimensional consistency, it preserves the functional relationships. In the Sects. 5.1.1 and 5.1.4 further refinements beyond similarity are considered, based on first-principles equations.

Characteristic Compressor Map Fig. 4.8 shows a typical performance map for a compressor, depicting total pressure ratio, mass flow, and efficiency across various operating conditions. The map plots the total pressure ratio p_{t2}/p_{t1} against the normalized compressor entry mass flow $\dot{m}\sqrt{T_{t1}}/p_{t1}$. Multiple speed lines, representing different values of $\Omega/\sqrt{T_{t1}}$, are included, normalized to the design-point speed. The diagram also features contour lines indicating

compressor isentropic efficiency, which reaches its maximum near the design point.

Each speed line describes the variation in total pressure ratio across the mass flow range. On the lower mass flow side, the speed lines terminate at the **surge line**, where the flow stalls, meaning the airflow can no longer follow the blade passages smoothly. This leads to flow separation within the compressor, causing an oscillatory or reversed flow, ultimately resulting in unstable operation.

At high rotational speeds and mass flow rates, the speed lines become nearly vertical. Here, further increases in flow rate are not possible because the flow reaches sonic condition, thus $\mathrm{Ma} = 1$, at some point in the machine which is a phenomenon known as **choking**. The physics of choked flow, where the Mach number reaches unity at the narrowest cross-section, limiting further mass flow, is discussed in more detail in Sect. 5.1.3.

While the compressor can operate below the surge line, operation is typically constrained to an **operating line** to ensure stable performance. The operating line is set with sufficient margin below the surge line to prevent instability.

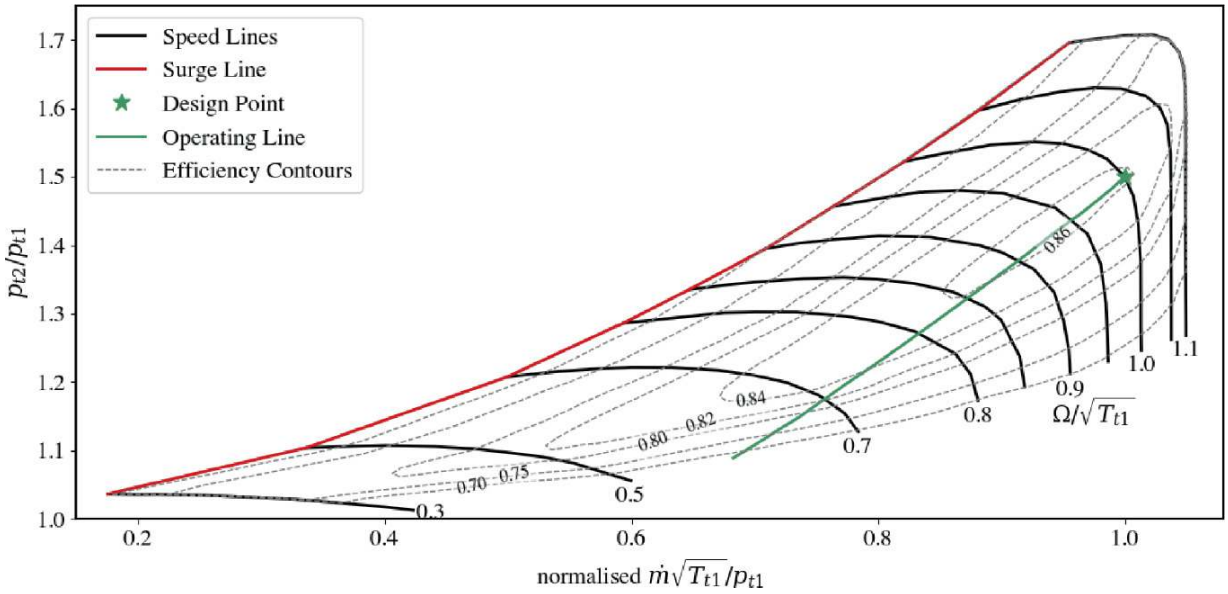


Fig. 4.8 Characteristic map of aeroengine fan showing total pressure ratio, normalized mass flow, speed lines, and efficiency contours and surge line indicated, adapted from Dixon and Hall (2013) and Cornell (1975)

Example 4.5 Scaling laws are widely applied not only to infer performance at different speeds for the same machine but also to design and adapt turbomachinery for varying operational conditions and to develop machine families. In the following, we illustrate their application in the context of more complex turbomachinery, specifically heavy-duty gas turbines used for electricity generation.

A gas turbine operates by first compressing air in the compressor, increasing its pressure before it enters the combustion chamber, where fuel is added and burned, significantly raising the temperature. The resulting high-enthalpy gas expands through the turbine, driving both the compressor and an external load, such as an electrical generator. In a simple cycle power generation system, the gas turbine generates power solely by driving a generator, which operates at a fixed grid frequency of either $50\,\mathrm{Hz}$ or $60\,\mathrm{Hz}$, depending on the region. To optimize design and manufacturing costs, a single baseline machine is developed, and the scaled counterpart design baseline is derived through similitude principles.

Consider the case of scaling a gas turbine designed for $50\,\mathrm{Hz}$ operation to an equivalent $60\,\mathrm{Hz}$ machine, while assuming the same total inlet conditions. It is further assumed that the compressor pressure ratio remains constant, as it is typically constrained by material temperature limits. Since grid frequency dictates turbine rotational speed, the rotational speed scaling factor is given by $M_n = 60/50 = 1.2$. To ensure dynamic similarity, we must preserve both the blade speed similarity, expressed by the dimensionless parameter $\Omega D/\sqrt{RT_{t1}}$, and the nondimensional mass flow $\dot{m}\sqrt{RT_{t1}}/(D^2 p_{t1})$. From the first condition, the characteristic diameter must scale inversely with rotational speed, yielding the diameter scale factor $M_D = 1/M_n$. Thus, the scaled machine runs 20% faster but is also physically smaller. The mass flow rate follows from preserving the nondimensional mass flow, leading to the scale factor $M_{\dot{m}} = 1/M_D^2 \approx 0.694$. For power output scaling, we employ Eq. (4.74) to obtain $M_P = 1/M_D^2 \approx 0.694$.

To illustrate, consider the Siemens SGT5-8000H gas turbine, which operates at $50\,\mathrm{Hz}$ with a pressure ratio of approximately 20. In simple cycle operation, it delivers $450\,\mathrm{MW}$ with an exhaust mass flow of $935\ \mathrm{kg/s}$. Applying the derived scaling factors, the $60\,\mathrm{Hz}$ variant yields a power output of $312.5\,\mathrm{MW}$ and an exhaust mass flow of $649.3\ \mathrm{kg/s}$. These values closely match published ratings for the Siemens SGT6-8000H, with deviations below 1% Siemens Energy (2024). While the overall physical dimensions scale accordingly, external casing dimensions may not strictly follow similitude due to structural, cooling, and installation constraints.

4.4.3 Flow Machine Classification

Interestingly, applying similitude principles also allows classification of machine designs based on the identified nondimensional groups. The classification is based on observing how different types of turbomachines align in the nondimensional parameter space. Specifically, the nondimensional groups (Φ, Ψ) or their alternative forms, the specific speed $\tilde{n}$ and specific diameter $\tilde{D}$, provide a systematic way to distinguish ranges for axial, mixed-flow, and radial (centrifugal) machine designs. This classification is valuable for both turbomachinery designers during the early design phase and engineers selecting appropriate machines for specific operational requirements, ensuring optimal performance across varying conditions.

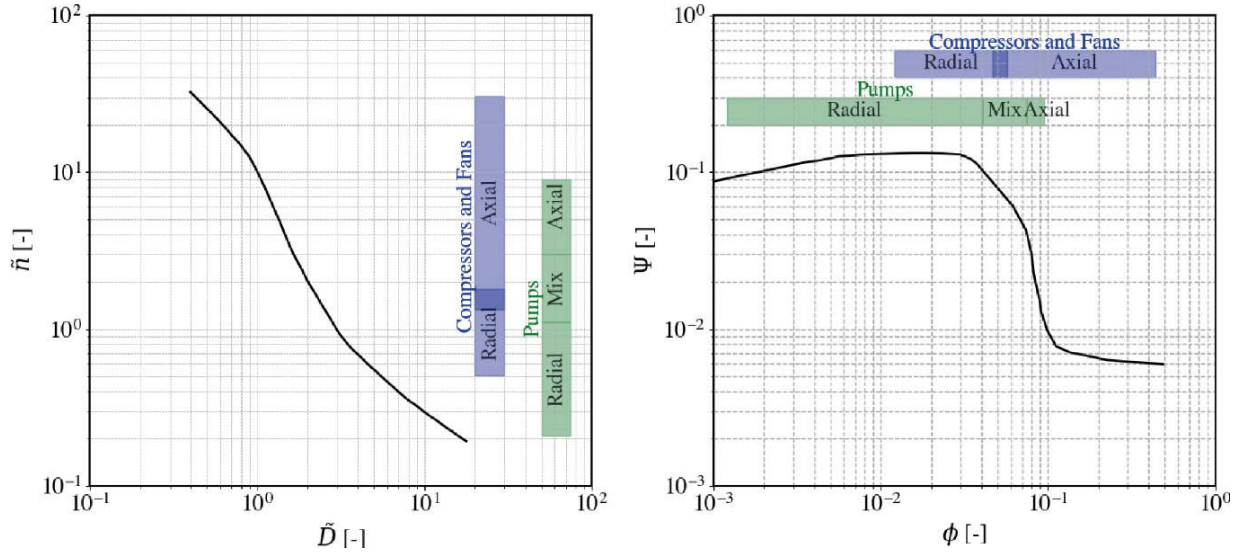


Fig. 4.9 Cordier diagram for pumps and fans, illustrating the classification of turbomachines based on specific speed and specific diameter

The specific speed $\tilde{n}$ and specific diameter $\tilde{D}$ are nondimensional parameters that characterize the fundamental shape and operating characteristics of a turbomachine. Specific speed $\tilde{n}$ eliminates the diameter D, providing a direct relationship between machine speed, flow rate, and head. It effectively serves as a shape factor, helping designers select a machine type that optimally balances duty requirements. Similarly, specific diameter $\tilde{D}$ eliminates the rotational speed, offering insight into the geometric scaling of the machine. Their practical significance lies in their ability to classify different machine types independently of absolute size, making them useful for both design and selection processes. They are related to the pair (Φ, Ψ) by

$$\tilde{n} = \frac{nQ^{1/2}}{(gH)^{3/4}} = \frac{\Phi^{1/2}}{\Psi^{3/4}} \quad , \quad \tilde{D} = \frac{D(gH)^{1/4}}{Q^{1/2}} = \frac{\Psi^{1/4}}{\Phi^{3/4}} \quad . \tag{4.78}$$

The inverse relations express the nondimensional duty groups in terms of $(\tilde{n}, \tilde{D})$

$$\Phi = \frac{1}{\tilde{n}\tilde{D}^3} \quad , \quad \Psi = \frac{1}{\tilde{n}^2\tilde{D}^2} \quad . \tag{4.79}$$

The **Cordier diagram** (Cordier 1953), illustrated on the left side of Fig. 4.9, provides an empirical correlation between specific speed $\tilde{n}$ and specific diameter $\tilde{D}$, based on a broad range of machines. This chart categorizes turbomachines by flow path designs, allowing engineers to quickly identify the most appropriate machine type for a given set of performance requirements. Generally, low specific speed values correspond to radial machines, which generate high pressure at low flow rates, while high specific speed values indicate axial machines, optimized for high flow rates with lower pressure rise. The right-hand side of the figure maps the relation onto the (Φ, Ψ) plane. Importantly, the data points in the Cordier diagram correspond to design conditions that exhibit the highest efficiency for each respective machine. This means that, while machines could operate outside of these ranges, the diagram effectively highlights the configurations that yield optimal performance in terms of energy conversion and efficiency.

This formulation enables a direct interpretation of machine performance characteristics. Centrifugal (radial) machines inherently operate at higher Ψ due to the strong centrifugal effects driving the pressure increase, but they exhibit lower Φ values because of inlet restrictions. In contrast, axial machines allow for handling higher flow rates at lower pressure heads, making them suited for applications requiring large volumetric throughput. Mixed-flow machines represent a compromise, blending characteristics of both axial and radial designs.

For centrifugal pumps and fans, the head coefficient Ψ generally falls within the range of $\Psi \approx 0.1$, consistent with their dominant pressure generation mechanism. Axial machines, in contrast, typically operate with lower head coefficients, ranging from $\Psi = 0.005$ to 0.5, but support significantly higher flow rates. Mixed-flow designs cover a narrower performance band, likely due to practical considerations such as design complexity and manufacturability, as noted by Lewis (1996). It is worth mentioning that the value ranges of Ψ in different sources may vary due to differences in defining rotational speed. Some formulations express speed in terms of angular velocity ω instead of

revolutions per unit time, introducing a factor of 2π, so that Ψ lies in the order of ≈ 5.

It should be noted that, in practice, a large dataset of experimentally tested machine specifications would not produce a single thin curve but rather a scatter plot or corresponding regions around the Cordier line. This spread accounts for variations in design optimization, efficiency, and secondary effects such as blade shape and surface roughness. Despite these variations, the underlying principles of similitude remain a powerful tool for both designing and selecting turbomachines. By leveraging these nondimensional groupings, engineers can systematically approach the selection of turbomachinery, ensuring optimal performance and efficiency while minimizing trial-and-error design iterations. Most manufacturers use their own adaptations of the Cordier diagram tailored to their specific product lines, yet they adhere to the same fundamental classification methodology (Dixon and Hall 2013).

It should be further noted that the Cordier diagram applies specifically to single-stage turbomachines, as it represents design conditions that yield optimal efficiency for individual stages. Many practical applications require significantly higher pressure ratios than those achievable with a single stage, leading to the use of **multistage** configurations, where multiple compressor stages are arranged in series to progressively increase pressure while managing aerodynamic and structural constraints.

In centrifugal compressors, single-stage pressure ratios typically range from 4–8, limited by mechanical stress and temperature constraints. To achieve higher pressure ratios, multiple stages are combined, often incorporating interstage cooling to reduce the temperature rise of the working fluid. Multistage centrifugal compressors commonly reach pressure ratios of 15–25 or higher and are widely used in applications such as the chemical process industry and pipeline compression stations, where continuous high-pressure operation is essential.

In contrast, axial compressors exhibit lower single-stage pressure ratios, generally between 1.1–1.5, due to their reliance on aerodynamic pressure rise rather than centrifugal effects. However, axial compressors are inherently suited for multistage operation, with each stage gradually increasing the pressure while preserving efficient flow characteristics. This allows axial compressors to achieve total pressure ratios of 20–50, with 12–16 stages being common in high-performance applications. A prime example of multistage axial compressors can be found in jet engines, where high-pressure ratios are critical for efficient propulsion. The Rolls-Royce Trent 1000, for instance, employs a 1-stage fan, 8-stage intermediate-pressure compressor (IPC), and 6-stage high-pressure compressor (HPC), reaching an overall pressure ratio of approximately ≈ 50 (Rolls-Royce 2025). Similarly, the General Electric GEnx engine features a 1-stage fan, 4-stage IPC, and 10-stage HPC, achieving pressure ratios of about 44–58 (Aerospace 2025). Multistage axial compressors are also prevalent in industrial gas turbines, where high efficiency and robust performance are essential for power generation. Large-frame gas turbines, such as the Siemens SGT5-8000H and GE 9HA, employ 14-stage axial compressors, delivering pressure ratios in the range of approximately 20–22 (Siemens Energy 2024).

4.4.4 Local Flow Parameters

The nondimensional parameters introduced so far have primarily been used to describe the overall performance of a turbomachine. However, for a more detailed analysis of the internal flow dynamics within individual stages, additional nondimensional groups are relevant particularly in turbomachinery design. Among these, the **flow coefficient** φ and **stage loading coefficient** ψ are well-established parameters. These parameters are directly related to the velocity triangles, which describe the relative motion of the flow with respect to the blades, as illustrated in later text for example in Fig. 5.9. By considering these nondimensional groups, engineers gain a more refined understanding of stage losses, efficiency, and optimal blade geometries.

The **flow coefficient** φ is a nondimensional measure of the throughflow velocity relative to the blade speed and is defined as

$$\varphi = \frac{c_m}{U} = \frac{c_m}{\Omega r} \ , \tag{4.80}$$

where c_m denotes the meridional velocity component, that corresponds to the axial velocity component in an axial machine, and $U = \Omega r$ represents the mean blade speed. The flow coefficient is independent of absolute velocities and instead depends on velocity ratios or angles, making it a fundamental similarity parameter for turbomachinery. The flow coefficient is used to define the geometric characteristics of the machine, directly influencing aerodynamic losses and efficiency. A larger flow coefficient enables increased volumetric flow rates but can also lead to shorter blade lengths, which may increase secondary losses at low flow rates.

For incompressible machines, the flow coefficient φ is directly proportional to the global flow parameter Φ, introduced in Sect. 4.4.1, since the volumetric flow rate scales as $Q \sim D^2 c_m$, and the blade speed scales as $U \sim \Omega D$. Consequently, for incompressible flows, the flow coefficient alone suffices to determine the operating condition, as indicated by Eq. (4.72). However, in compressible turbomachinery, where density variations significantly impact flow behavior, φ becomes a bivariate function of the nondimensional groups presented in Eq. (4.77).

In an operating turbomachine, the absolute flow velocity *c* is dictated by the inlet conditions and flow rate, so that the flow coefficient φ is determined by the ratio of volumetric flow rate to rotational speed. Consequently, φ is not only a design parameter but also an operational parameter and is commonly used to characterize the performance of machines in service. Typical design-point values of the flow coefficient range from $\varphi = 0.35 - 1$ for compressors and $\varphi = 0.35 - 1.2$ for turbines, depending on the machine type and application (Leitner 2004).

The **stage loading coefficient** ψ provides a nondimensional measure of the energy transfer per stage, normalized by the blade kinetic energy

$$\psi = \frac{\Delta h_t}{U^2} \quad , \tag{4.81}$$

where Δh_t is the specific stagnation enthalpy change across the stage. The stage loading coefficient quantifies the energy addition in compressors, or extraction in turbines per unit of blade kinetic energy. Unlike the flow coefficient, which is based on local velocity components, the stage loading coefficient requires knowledge of the total specific enthalpy change across the stage. In practical applications, ψ is often approximated using the enthalpy change of an isentropic reference process. As with the flow coefficient, the stage loading coefficient is directly related to the velocity triangle angles. For the compressible case, ψ can be expressed as a bivariate function of the nondimensional mass flow and blade speed, as indicated in Eq. (4.74). Thus, once both nondimensional parameters are fixed, the stage loading coefficient is determined. In practice, ψ is often used as an alternative to the power coefficient $\Delta T_t / T_t$, particularly in aerodynamic performance analysis (Dixon and Hall 2013).

The stage loading coefficient resembles the head coefficient introduced in Sect. 4.4.1, but it is important to distinguish that the stage loading coefficient is based on the actual stagnation enthalpy change in a given stage, whereas the head coefficient refers to the maximum isentropic energy conversion potential in a hydraulic machine (Dixon and Hall 2013).

Typical stage loading values vary by machine type. For axial compressors, ψ typically ranges from $0.4 - 1$, whereas radial compressors can reach values of up to $\psi \approx 1.5$. For axial turbines, where larger energy extraction per stage is common, ψ generally falls within $2 - 6$, while centrifugal turbines, designed for high-enthalpy extraction, operate at values of $\psi = 8 - 12$ (Leitner 2004).

Another key nondimensional parameter in stage analysis is the **stage reaction** *R*, which describes the distribution of static enthalpy change between the stator and rotor of a compressor or turbine stage. It is defined as

$$R = \frac{\Delta h_{\text{rotor}}}{\Delta h_{\text{stage}}} \quad , \tag{4.82}$$

where Δh_{rotor} represents the stagnation enthalpy change across the rotor and Δh_{stage} is the total stage enthalpy change. In incompressible flows, *R* can be approximated using pressure changes as $R \approx \Delta p_{\text{rotor}} / \Delta p_{\text{stage}}$. The reaction coefficient is central to defining the velocity triangle shape and aerodynamic loading of the stage. A reaction of $R = 0.5$ indicates that the enthalpy change is equally distributed between the stator and rotor, which leads to symmetrical velocity triangles and is a common design choice to balance aerodynamic loading. A reaction of $R \to 1$ implies that the entire enthalpy change occurs in the rotor (highly loaded rotor), while $R \to 0$ indicates that the stator carries the full enthalpy change (highly loaded stator) and is referred to as an impulse stage.

References

Anderson JD (2016) Fundamentals of aerodynamics. McGraw-Hill Education,

Batchelor GK (1953) The theory of homogeneous turbulence. Cambridge University Press, Cambridge science classics

Cordier O (1953) Ähnlichkeitsbedingungen für Strömungsmaschinen BWK Bd 6(10):337–340

Cornell WG (1975) Experimental quiet engine program. Technical Report NASA-CR-2519, National Aeronautics and Space Administration

Dixon SL, Hall C (2013) Fluid mechanics and thermodynamics of turbomachinery. Elsevier

DuChateau P, Zachmann DW (2002) Applied partial differential equations. Dover Books on Mathematics, Dover Publications

Frohn A, Roth N (2000) Dynamics of droplets, engineering online library. Springer [https://doi.org/10.1007/978-3-662-04040-9]

GE Aerospace. GEnx Aircraft Engines, 2025. www.geaerospace.com. Accessed March 2025

Hunt JK (2009) Lecture notes on applied mathematics: methods and models. University of California, Davis, Department of Mathematics

International Association for the Properties of Water and Steam. Revised Release on the IAPWS Industrial Formulation (1997) for the thermodynamic properties of water and steam (IAPWS-IF97). Switzerland, Technical report, IAPWS, Lucerne, p 1997

Kays WM, Crawford ME, Weigand B (2005) Convective heat and mass transfer. McGraw-Hill series in mechanical engineering. McGraw-Hill,

Lamb H (1932). Hydrodynamics. The University Press,

Leitner M (2004) Vorlesung Turbomaschinen I Lecture notes

Lewis RI (1996) Turbomachinery performance analysis. Butterworth-Heinemann

Milne-Thomson LM (1968) Theoretical hydrodynamics. Macmillan [https://doi.org/10.1007/978-1-349-00517-8]

Munz C-D, Westermann T (2018) Numerische Behandlung gewöhnlicher und partieller Differenzialgleichungen: Ein anwendungsorientiertes Lehrbuch für Ingenieure. Springer,

Nikuradse J (1933) Gesetzmäßigkeiten der turbulenten Strömung in glatten Rohren. VDI-Forschungsheft 356:1

Panton RL (1996) Incompressible flow. Wiley

Pope SB (2000) Turbulent flows. Cambridge University Press [https://doi.org/10.1017/CBO9780511840531]

Rolls-Royce (2025) Civil aerospace, 2025. www.rolls-royce.com. Accessed March 2025

Schlichting H, Truckenbrodt E (2001) Aerodynamik des Flugzeugs, Teil 1. Springer [https://doi.org/10.1007/978-3-642-56911-1]

Siemens Energy. Siemens energy official website, 2024. www.siemens-energy.com. Accessed July 2024

Spalding DB (1961) A single formula for the “law of the wall.” J Appl Mech 28(3):455–458

Spurk J (1996) Strömungslehre: Einführung in die Theorie der Strömungen. Springer,

Weigand B, Kohler J, von Wolfersdorf J (2016) Thermodynamik kompakt, 4th edn. Springer, Berlin [https://doi.org/10.1007/978-3-662-49703-6]

White FM (1991) Viscous fluid flow, 2nd edn. McGraw-Hill

Footnotes

1 In specific cases, such as boundary or shear layer flows, the integral length scale L can be further refined to the layer thickness δ_u.

2 Spurk (1996) demonstrates that the underlying differential equation for the logarithmic velocity profile can also be derived using a purely dimensional analysis, without relying on Prandtl's mixing length model.

3 As noted by Dixon and Hall (2013), the choice of independent variables is somewhat arbitrary. An alternative selection would be to use the shaft torque τ instead of P or Ω.

4 The speed of rotation represents an angular velocity Ω, measured in the unit $\mathrm{rad} \,/\, \mathrm{min}$. The number of revolutions per unit time rotational speed n is commonly with the unit $\mathrm{rev} \,/\, \mathrm{min}$. They are related by $n = 2\pi\Omega$ and so while they are equivalent from a dimensional analysis perspective, their numerical values differ by a factor of 2π.

© The Author(s), under exclusive license to Springer Fachmedien Wiesbaden GmbH, part of Springer Nature 2026
H. Gomaa, *Modeling with Knowledge and Data*, Mathematical Engineering
https://doi.org/10.1007/978-3-658-50679-7_5

5. Basic Flow Cases

Hassan Gomaa[1] ✉
(1) Strategic Projects Co-Innovation, Cognite, Oslo, Norway

This chapter presents a selection of fundamental flow configurations that serve as basic and illustrative examples. These basic cases illustrate how the general conservation laws introduced earlier manifest in practical applications and provide a foundation for more complex modeling. Each case emphasizes a specific physical mechanism, such as compressibility, boundary layer formation, or internal friction, and shows how the governing equations can be simplified or complemented by subscale models.

This chapter begins with quasi-one-dimensional flow, including effects like area variation, friction, and heat transfer. It then addresses external flows over immersed bodies, focusing on boundary layers and flow-induced forces. Finally, it examines internal flows in pipes and ducts, highlighting the development of velocity and temperature profiles, as well as pressure losses due to friction and geometric features.

5.1 Quasi-One-Dimensional Flow

The study of steady one-dimensional flow provides a practical approach to understanding fundamental flow phenomena across various technical applications. By reducing the dimensionality of the system, the governing equations become mathematically more manageable, allowing for an isolated examination of key physical mechanisms and their interactions. The flow is modeled along a streamline, where flow variables vary only along a single independent streamline direction, denoted as s, and derivatives are expressed as d/ds.

Although the flow is conceptually one-dimensional, the cross-sectional area of the flow tube can change, introducing some aspects of two-dimensional

behavior. However, the results derived under this approximation remain valid as long as the area variations are continuous and moderate. The flow variables represent cross-sectional averages, yet the underlying physical phenomena often involve higher-dimensional effects. For instance, in a viscous fluid flowing through a pipe, the no-slip boundary condition at the pipe wall induces a velocity profile, such as the Hagen-Poiseuille profile in laminar flow discussed in Sect. 5.3.1, where frictional effects vary according to the velocity gradient across the cross-section.

Variables that are indeed functions of the cross direction in higher-dimensional considerations are represented by corresponding subscale models as discussed in Sect. 5.1.5. Physical terms that act across the cross-section, such as viscous friction, heat transfer, and similar are represented by lower-dimensional subscale models that mimic the physical effect. These models often combine first-principle derivations with empirical correlations, as will be highlighted in later discussions. One-dimensional governing equations can, in principle, be derived by integrating the general field equations. However, to avoid excessive mathematical complexity, the equations are instead formulated based on the fundamental conservation principles outlined in Sect. 3.2.1, applied to the control volume shown in Fig. 5.1. The one-dimensional formulation is developed for both incompressible and compressible flows with constant specific heat, incorporating the following physical effects

- Cross-sectional area variations,
- Shear friction at the no-slip wall,
- Drag exerted by internal bodies,
- Gravitational body forces,
- External shaft work input or extraction,
- Heat transfer through the walls,
- Mass injection into the main stream.

For compressible flows including the effects of variable specific heat, phase change, and chemical reactions, the reader is referred to Shapiro (1953, Chap. 8).

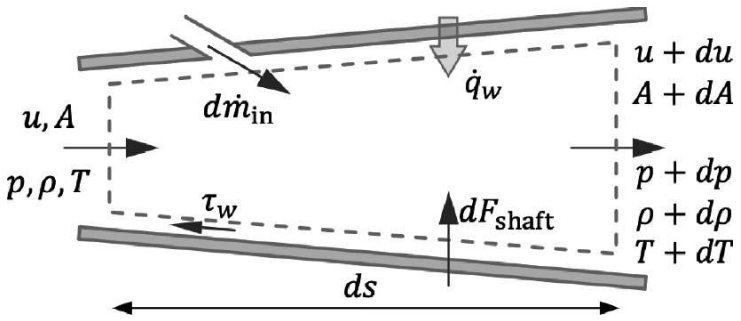


Fig. 5.1 Control volume for one-dimensional stream tube with addition of mass, momentum, and energy (Shapiro 1953)

The system boundary is defined by outer streamlines, which are tangent to the local velocity vectors, ensuring that no fluid crosses the boundary. Unless otherwise stated, the outer surface is treated as a solid wall where the no-slip condition applies. The mass flow rate through the tube is given by $\dot{m} = \rho u A$, and the governing equations must account for a continuously varying cross-sectional area $A(s)$ along the streamline direction. Additionally, mass injection into the flow is considered, so that in line with Eq. (3.37) the **continuity equation** reads

$$d(\rho u A) = d\dot{m}_{\text{in}} \ . \tag{5.1}$$

The **momentum balance** is formulated in the streamline-aligned direction s. Using Eq. (3.38), it accounts for body forces such as gravity, as well as other forces collectively denoted by dF. The balance must also include the pressure force $-pdA$ acting on the flow tube surface, and the momentum flux associated with mass injection, which enters with its projected velocity component in the s-direction. This results in the momentum balance

$$d(\dot{m}u) = -d(pA) - pdA + dF + dF_{\text{shaft}} - \rho g dz + u_{\text{in}} d\dot{m}_{\text{in}} \ . \tag{5.2}$$

Here, dF_{shaft} represents the shaft force associated with external shaft work $\dot{W}$, related via $\dot{W} = u \ dF_{\text{shaft}}$. The term $dF = -\tau_w dA_w + dF_d$ accounts for wall shear stress τ_w and drag forces dF_d from stationary internal objects such as struts, vanes, or flow orifices. The specific mathematical expressions for these forces require additional subscale modeling, discussed in Sect. 5.1.5. Although only gravitational body forces are included here, extensions to centrifugal forces are straightforward. Gravity acts through its vertical projection dz. Expanding the inertia term and using the continuity equation, the momentum equation simplifies to

$$(\rho u du + dp + \rho g dz)A = -\tau_w dA_w + dF_d + dF_{\text{shaft}} + (u_{\text{in}} - u) d\dot{m}_{\text{in}} \ , \tag{5.3}$$

where the final term consolidates the influence of injected mass, accounting for its relative velocity difference with the main stream.

For **energy conservation**, the balance follows from Eq. (3.40), including heat transfer $d\dot{Q}$ into the control volume and shaft work $d\dot{W}$ leading to

$$d\big(\dot{m}\big(h + u^2/2 + gz\big)\big) = d\dot{Q} + d\dot{W} + \big(h + u^2/2 + gz\big)_{\text{in}} d\dot{m}_{\text{in}} \ . \tag{5.4}$$

Heat exchange occurs through the control volume surface, expressed as an area-specific heat transfer rate $d\dot{Q} = \dot{q}_w dA_w$. Shaft work is expressed per unit mass as $d\dot{W} = \dot{m}\ dw_{\text{shaft}}$. A positive shaft work term corresponds to work input, as for example by the compressor blades. A negative term represents work extraction such as for a turbine rotor. Notably, wall shear stress and drag forces do not perform work, as they act at a no-slip boundary where velocity is zero (White 1991). Internal shear stresses contribute to F_d and dissipate momentum as heat, but since this conversion occurs within the control volume, it does not alter the overall energy balance (Spurk 1996). Applying the continuity equation and simplifying the injected mass contributors leads to

$$\dot{m}(dh_t + gdz) = \dot{q}_w dA_w + \dot{m}\ dw_{\text{shaft}} + (h_{t_{in}} - h_t) d\dot{m}_{\text{in}}\ , \tag{5.5}$$

where $h_t = h + u^2/2$ is the specific stagnation enthalpy, discussed in detail in the next section.

For cases **without mass injection**, thus $\dot{m}_{\text{in}} = 0$, the governing equations simplify to

$$\begin{aligned} d(\rho\ u\ A) &= 0\ , \\ (\rho u du + dp + \rho g dz)A &= dF + dF_{\text{shaft}}\ , \\ \dot{m}(de + \tfrac{dp}{\rho} + u du + g dz) &= d\dot{Q} + d\dot{W}\ . \end{aligned} \tag{5.6}$$

Integrating the equation between two locations $1 \rightarrow 2$ of a streamline provides

$$\begin{aligned} \dot{m}_2 - \dot{m}_1 &= 0\ , \\ \left[(\rho u^2 + p + gz)A\right]_2 - \left[(\rho u^2 + p + gz)A\right]_1 &= \int_1^2 dF + \int_1^2 dF_{\text{shaft}}\ , \\ \dot{m}(h_{t2} - h_{t1} + g(z_2 - z_1)) &= \int_1^2 d\dot{Q} + \int_1^2 d\dot{W}\ . \end{aligned} \tag{5.7}$$

5.1.1 Stagnation State

The **stagnation state**, interchangeably referred to as **total state**, is widely used to characterize technical flow applications. The stagnation state refers to the condition that the fluid attains if it were brought to rest without transfer of heat or work. While the fluid is not actually decelerated to a stagnation state, the concept rather can be seen as a thought experiment. With the kinetic energy reduced to zero, the state indicates the total enthalpy content of the fluid. As such, it serves as a reference state, allowing for the characterization of energy transfer and losses in flow processes (Greitzer et al. 2007, p. 41). The definitions

of total enthalpy and total pressure can be interpreted as invariants of the momentum and energy equations. In the absence of body forces for an adiabatic flow with no external work transfer the energy equation (5.5) simplifies to $dh + u du = 0$, so that the **total enthalpy** defined as

$$h_t = h + \tfrac{1}{2} u^2 \ , \tag{5.8}$$

remains constant along a streamline, meaning $dh_t = 0$. However, between adjacent streamlines the total enthalpy remains constant only if they originate from the same uniform flow conditions, such as a homogeneous free flow.

The definition of the **total pressure** is more restrictive. If in addition to the previous assumptions, the flow is also lossless, the momentum equation (5.3) simplifies to $dp + \rho u \, du = 0$. Since an adiabatic flow without added work, reduced to its stagnation state in a reversible manner corresponds to an isentropic process (Greitzer et al. 2007), the total pressure $dp_t = dp + \rho u \, du$ remains invariant along a streamline. However, the specific mathematical expression for total pressure depends on the fluid model, such as constant-density or ideal-gas behavior, which will be derived below.

Since the stagnation state is defined in a thermodynamically consistent manner, the fundamental thermodynamic relations remain valid. For instance, the Gibbs equation (3.9) remains valid to describe entropy changes in terms of total quantities

$$T_t \ ds = dh_t - \tfrac{dp_t}{\rho_t} \ , \tag{5.9}$$

where static and total entropy are identical (Greitzer et al. 2007).

The total enthalpy remains invariant along a streamline between two locations $1 \to 2$, as long as the flow is adiabatic and no work is performed, regardless of reversibility, that is $h_{t2} = h_{t1}$. Considering entropy production due to irreversibilities, following Eq. (3.62) we established that for an adiabatic flow, $ds \geq 0$. Using Eq. (5.9) with $dh_t = 0$ leads to $dp_t \leq 0$. Between two points in the flow, we therefore obtain $p_{t2} \leq p_{t1}$. In the special case of an isentropic flow ($ds = 0$), total pressure remains constant, meaning $p_{t2} = p_{t1}$. However, total pressure generally varies between adjacent streamlines, even if they originate from identical initial conditions, due to differing exposure to irreversibility along the path. For example, in viscous flows, streamlines near a wall experience stronger shear forces and are thus exposed to greater entropy generation than those in free flow.

The interpretation of the total state differs in nuance between incompressible and compressible flows. For incompressible flows, where the momentum and energy equations are decoupled due to constant density, the stagnation state primarily concerns the conservation of mechanical energy, manifesting in total enthalpy h_t and total pressure p_t. In contrast, for compressible flows, where momentum and energy conservation are tightly coupled, the total state quantities reflect both mechanical and thermal energy conservation. Besides total enthalpy and pressure, the total temperature T_t and total density ρ_t become relevant, as detailed in the following.

For an **incompressible fluid**, the caloric state relations are given by

$$de = c\ dT\ , \quad dh = c\ dT + \tfrac{1}{\rho}\ dp\ , \quad ds = \tfrac{c}{T}\ dT\ . \tag{3.23}$$

For isentropic incompressible flow it follows that $dT = 0$. Using the enthalpy definition, total pressure follows to $dp_t = \rho dh_t$. The **total pressure** thus relates to the static state by

$$p_t = p + \tfrac{\rho}{2} u^2\ . \tag{5.10}$$

As previously discussed in the context of incompressible flow equations (4.1), pressure appears only in derivative form and is thus determined up to an arbitrary reference value. Consequently, both static and total pressure are often considered relative to a reference value, which does not affect the flow (Panton 1996, p. 206). Since density and temperature are independent of velocity for an incompressible fluid, no meaningful total temperature or total density can be defined, so that for practical purposes they can be assumed the same. As the pressure is determined by the momentum equation, it represents a mechanical quantity rather than a thermodynamic variable. The total pressure serves as a measure of mechanical energy content, making total pressure losses a common metric for flow losses, as detailed in Sect. 5.3.3.

As mentioned, the total pressure is constant along an isentropically propagated streamline. The integration constant that arises from integration along the streamline generally varies from streamline to streamline. But one can show that the underlying invariance is valid even for unsteady flows as long as the flow is irrotational (White 1991, p. 89), thus possesses zero vorticity $\boldsymbol{\omega} = \mathbf{0}$. For derivation, the momentum equation (4.1) is considered for incompressible fluids, substituting gravity as body force and applying the vector identities

(5.11)

$$
\begin{aligned}
(\mathbf{u}\cdot\nabla)\mathbf{u} &= \nabla(\mathbf{u}^2/2) - \mathbf{u}\times\boldsymbol{\omega}\ , \\
\nabla^2\mathbf{u} &= \nabla(\nabla\cdot\mathbf{u}) - \nabla\times\boldsymbol{\omega}\ .
\end{aligned}
$$

Simplifying with $\nabla\cdot\mathbf{u}=0$ for incompressible flow the momentum equation reduces to

$$
\rho\tfrac{\partial\mathbf{u}}{\partial t} + \nabla\big(p + \tfrac{1}{2}\rho\mathbf{u}^2 + \rho g z\big) = \rho\mathbf{u}\times\boldsymbol{\omega} - \mu\nabla\times\boldsymbol{\omega}\ . \tag{5.12}
$$

For irrotational flows with $\boldsymbol{\omega}=\mathbf{0}$ the right-hand side vanishes, and a velocity potential ϕ exists such that $\mathbf{u}=\nabla\phi$. Integration yields the well known **Bernoulli equation** to

$$
\rho\tfrac{\partial\phi}{\partial t} + p + \tfrac{1}{2}\rho\mathbf{u}^2 + \rho g z = \text{const.}\ . \tag{5.13}
$$

For irrotational flows, such as found in inviscid potential flows, this relation applies throughout the entire flow field, not just along a streamline. Here the integration constant is the same throughout the entire field and the Bernoulli equation is valid between two locations of the flow field. Note that in the absence of heat and any thermal effects, the energy equation reduces to its mechanical terms that coincide with the dot product of $\mathbf{u}$ with the differential momentum equation, and potentially subsequent integration. Accordingly, in literature one also finds derivations based on the energy equation. Integrating the Bernoulli Eq. (5.13) in streamwise direction and substituting the stagnation pressure results in $(p_{t2}-p_{t1})/\rho + g(z_2-z_1)=0$. In turbomachinery applications, where incompressible working fluids are considered, the quantity $z+p_t/(\rho g)$ is known as **head** (Dixon and Hall 2013, p. 13). It represents the pressure rise in terms of the height a fluid could be lifted by that pressure increase, making head loss a common representation of total pressure losses.

The considerations so far allow us to characterize trends in the total state change for an incompressible fluid between two locations $1\to2$ under different conditions. In an **isentropic flow**, total enthalpy and total pressure remain constant along a streamline, meaning $h_{t1}=h_{t2}$ and $p_{t1}=p_{t2}$. Since there are no irreversible losses, energy is conserved, and the static temperature remains unchanged. In an **adiabatic but non-isentropic flow** without added work, such as a viscous flow through a rough pipe, total enthalpy remains unchanged ($h_{t1}=h_{t2}$), while total pressure decreases due to frictional dissipation ($p_{t1}>p_{t2}$). The mechanical energy lost to friction results in a small increase in static temperature, which, however, is usually negligible in practical applications (see Sects. 4.2.4 and 9.1). For an **adiabatic flow with added work**, such as a pipe

flow with a pump, external work input increases both total enthalpy and total pressure, leading to $h_{t2} > h_{t1}$ and $p_{t2} > p_{t1}$. Conversely, in a system where work is extracted, such as a turbine, both total enthalpy and total pressure decrease accordingly. In a **flow with heat addition**, total enthalpy increases ($h_{t2} > h_{t1}$), causing a rise in static temperature. If the process is idealized as lossless, total pressure remains unchanged. However, in practical scenarios, frictional losses may lead to a simultaneous decrease in total pressure.

For a calorically **perfect gas**, the thermal state variables p, ρ, T are directly coupled, meaning that converting a fluid element to its total state affects all three variables simultaneously. The relations can be directly deduced from the caloric state equations for an ideal gas, given in Eq. (3.17) and Eq. (3.20) to

$$de = c_v \; dT \;, \quad dh = c_p \; dT \;, \quad ds = -\frac{R}{p} \; dp + \frac{c_p}{T} \; dT \;. \tag{5.14}$$

Using $h_t = c_p T_t$ and the total enthalpy definition in Eq. (5.8), the relation between static and **total temperature** is obtained as

$$T_t = T + \frac{c_p}{2} u^2. \tag{5.15}$$

Here, only the assumption of adiabaticity, but not necessarily reversibility, has been made. Consequently, the total temperature remains constant along an adiabatic streamline and is also uniform across streamlines if they originate from the same uniform flow conditions.

As previously noted and illustrated in Fig. 5.2, defining the total pressure presumes reversibility, so that the total state for pressure and correspondingly density follows by applying the isentropic relations to

$$\frac{p_t}{p} = \left(\frac{T_t}{T} \right)^{\frac{\gamma}{\gamma-1}} \;, \qquad \frac{\rho_t}{\rho} = \left(\frac{T_t}{T} \right)^{\frac{1}{\gamma-1}} . \tag{5.16}$$

It is emphasized that the Bernoulli equation (5.13) is no longer valid for compressible fluids, as it is derived based on an incompressible fluid model.

Analogous to the incompressible case, we analyze changes in the total state between two locations $1 \to 2$ along a streamline for different flow scenarios. In an **isentropic flow**, total pressure, total enthalpy, and total temperature remain constant, so that $p_{t1} = p_{t2}$, $h_{t1} = h_{t2}$, and $T_{t1} = T_{t2}$. Now consider an **adiabatic but non-isentropic flow** without external work input, such as a high-speed flow in a duct with friction. Similar to the incompressible case, total enthalpy and total temperature remain unchanged ($h_{t1} = h_{t2}$), while entropy production leads to a

reduction in total pressure ($p_{t1} > p_{t2}$). Next, we examine an **adiabatic flow with added work**, such as flow through a **compressor** or **turbine**, which will be explored in more detail in Sect. 5.1.4. In a compressor, external work input increases total enthalpy, total pressure, and total temperature, leading to $h_{t2} > h_{t1}$, $p_{t2} > p_{t1}$, and $T_{t2} > T_{t1}$. Conversely, in a turbine, where work is extracted, all three quantities decrease, resulting in $h_{t2} < h_{t1}$, $p_{t2} < p_{t1}$, and $T_{t2} < T_{t1}$. While the incompressible case follows a similar trend for pressure and enthalpy, temperature variations in compressible flow play a crucial role, as they directly influence density and velocity. Finally, consider a **flow with heat addition** that is otherwise lossless. Heat input increases total enthalpy ($h_{t2} > h_{t1}$) and raises the total temperature ($T_{t2} > T_{t1}$). According to Eq. (5.16), this also leads to an increase in total pressure and density, such that $p_{t2} > p_{t1}$ and $\rho_{t2} > \rho_{t1}$.

Unlike in incompressible flow, where total pressure primarily serves as a measure of mechanical losses, compressible flow involves a more intricate interplay between heat, work, and flow dynamics. In particular, the relationship between total and static quantities depends on the Mach number, a dependency that will be further explored in Sect. 5.1.3.

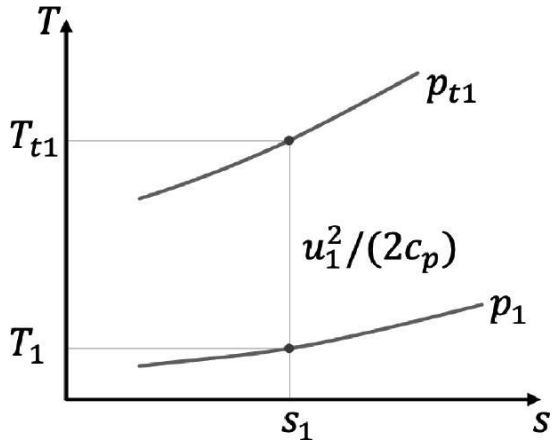


Fig. 5.2 Relation between total and static quantities on a *T*, *s*-diagram

5.1.2 Flow with Variable Cross-Section

To explore the influence of a varying flow cross-sectional area, we consider the continuity equation from Eq. (5.7), which states that the mass flow rate remains constant, given by $\dot{m} = \rho u A$ within the flow tube. Taking the logarithmic derivative of this conservation equation yields

$$\frac{d\rho}{\rho} + \frac{du}{u} + \frac{dA}{A} = 0 \ . \tag{5.17}$$

For **incompressible flow**, where density remains constant ($d\rho = 0$), the relation simplifies to

$$\frac{du}{u} = -\frac{dA}{A} \ , \tag{5.18}$$

which has a straightforward interpretation. A decrease in the cross-sectional area ($dA < 0$) results in an acceleration of the flow ($du > 0$), while an increase in area ($dA > 0$) leads to flow deceleration ($du < 0$).

For **compressible flows**, the behavior is more intricate due to density variations. As a reference, we consider the speed of sound, which governs the propagation of small pressure disturbances, as defined in Eq. (3.8). These disturbances propagate through the fluid as isentropic density variations, allowing us to introduce the speed of sound via the relation $a^2 = \partial p / \partial \rho|_s$. Substituting this into the differential form of the continuity equation gives

$$\frac{1}{a^2}\frac{dp}{\rho} + \frac{du}{u} + \frac{dA}{A} = 0 \ . \tag{5.19}$$

The relationship between pressure and velocity is governed by the momentum equation, which, for isentropic flow along a streamline, simplifies to $-dp = \rho u du$. Substituting into the equation above yields

$$-\frac{u}{a^2}du + \frac{du}{u} + \frac{dA}{A} = 0 \ . \tag{5.20}$$

Substituting the Mach number $\mathrm{Ma} = u/a$ according to Eq. (4.6) and rearranging, we obtain

$$(\mathrm{Ma}^2 - 1)\frac{du}{u} = \frac{dA}{A} \ . \tag{5.21}$$

This expression provides valuable insights into the flow behavior. The term $(\mathrm{Ma}^2 - 1)$ determines how velocity responds to changes in the cross-sectional area.

For subsonic flow ($\mathrm{Ma} < 1$), the behavior is similar to incompressible flow, where a decreasing cross-sectional area ($dA < 0$) leads to an increase in velocity ($du > 0$), and vice versa. For supersonic flow ($\mathrm{Ma} > 1$), the relationship is reversed. A decrease in area ($dA < 0$) causes a velocity decrease ($du < 0$), while an increasing area ($dA > 0$) results in acceleration ($du > 0$). At $\mathrm{Ma} = 1$, the prefactor $(\mathrm{Ma}^2 - 1)$ vanishes, implying that $dA = 0$ corresponds to an extremum in the cross-sectional area. Note that the prefactor is valid for

isentropic flow conditions and changes under the effect of viscosity or heat transfer.

Based on this understanding, generating a supersonic flow in a duct requires a converging-diverging geometry. To accelerate a subsonic flow ($\mathrm{Ma} < 1$) toward sonic conditions ($\mathrm{Ma} \to 1$), the cross-sectional area must decrease. To further accelerate the flow beyond $\mathrm{Ma} = 1$ into the supersonic regime ($\mathrm{Ma} > 1$), the cross-sectional area must then increase, so that a transition from subsonic to supersonic flow necessitates a minimum in the cross-sectional area. The precise location of $\mathrm{Ma} = 1$ depends on the pressure difference applied across the duct. As discussed in the next Sect. 5.1.3, the inlet to outlet pressure ratio must satisfy the condition

$$\frac{p_{\mathrm{in}}}{p_{\mathrm{out}}} \geq \left(\frac{\gamma+1}{2}\right)^{\gamma/(\gamma-1)} , \tag{5.22}$$

which for air is approximately 1.894 (Spurk 1996).

5.1.3 Compressible Flow Phenomena

Isentropic Flow The total state of a perfect gas flow, discussed in Sect. 5.1.1, can be conveniently expressed in terms of the Mach number Ma. For a perfect gas, the Mach number is defined as $\mathrm{Ma} = u/\sqrt{\gamma R T}$ so that, using the enthalpy relation $h = c_p T$, the stagnation enthalpy from Eq. (5.8) becomes

$$h_t = c_p T_t = c_p T + \frac{u^2}{2} = c_p T + \frac{\gamma R T}{2}\,\mathrm{Ma}^2 \ . \tag{5.23}$$

Using Eq. (5.15) and the specific heat relation $c_p = \gamma R/(\gamma - 1)$, the total temperature follows as

$$\frac{T_t}{T} = 1 + \frac{\gamma-1}{2}\,\mathrm{Ma}^2 \ . \tag{5.24}$$

Since the total pressure and density were derived under the assumption of an isentropic process, substituting Eq. (5.24) into the isentropic relations of Eq. (5.16) yields

$$\frac{p_t}{p} = \left(1 + \frac{\gamma-1}{2}\,\mathrm{Ma}^2\right)^{\frac{\gamma}{\gamma-1}} , \qquad \frac{\rho_t}{\rho} = \left(1 + \frac{\gamma-1}{2}\,\mathrm{Ma}^2\right)^{\frac{1}{\gamma-1}} . \tag{5.25}$$

The variations of these properties over the Mach number are plotted in Fig. 5.3 for air.

As established in Sect. 5.1.2, the fluid reaches $\mathrm{Ma} = 1$ at the narrowest cross-section, provided the stagnation pressure is sufficiently large. This state, called the **critical state**, satisfies the following relations

$$\frac{T^*}{T_t} = \frac{2}{\gamma+1} \ , \qquad \frac{p^*}{p_t} = \left(\frac{2}{\gamma+1}\right)^{\frac{\gamma}{\gamma-1}} \ , \qquad \frac{\rho^*}{\rho_t} = \left(\frac{2}{\gamma+1}\right)^{\frac{1}{\gamma-1}} \ . \tag{5.26}$$

For air with $\gamma = 1.4$, these evaluate to

$$\frac{T^*}{T_t} = 0.833 \ , \qquad \frac{p^*}{p_t} = 0.528 \ , \qquad \frac{\rho^*}{\rho_t} = 0.634 \ . \tag{5.27}$$

If the total pressure exceeds the critical value p^*, sonic conditions emerge at the narrowest cross-section. To further accelerate the gas to supersonic velocities, the nozzle geometry must follow a specific shape, determined by applying the continuity equation for the flow tube in reference to the critical state (Weigand et al. 2016). Using the continuity equation $\dot{m} = \rho u A = \rho^* u^* A^*$, where u^* corresponds to the speed of sound, and solving for the area ratio yields

$$\left(\frac{A^*}{A}\right)^2 = \frac{1}{\mathrm{Ma}^2}\left(\frac{2}{\gamma+1}\left(1 + \frac{\gamma-1}{2}\,\mathrm{Ma}^2\right)\right)^{-\frac{\gamma+1}{\gamma-1}} \ . \tag{5.28}$$

This area ratio is plotted in Fig. 5.3 and describes the nozzle shape, called the **Laval nozzle**, required to develop supersonic flow. In accordance with the discussion in Sect. 5.1.2, the nozzle geometry follows a convergent-divergent shape, with subsonic flow conditions in the converging section, $\mathrm{Ma} = 1$ at the throat, and supersonic flow in the diverging section, thus $A^*/A < 1$.

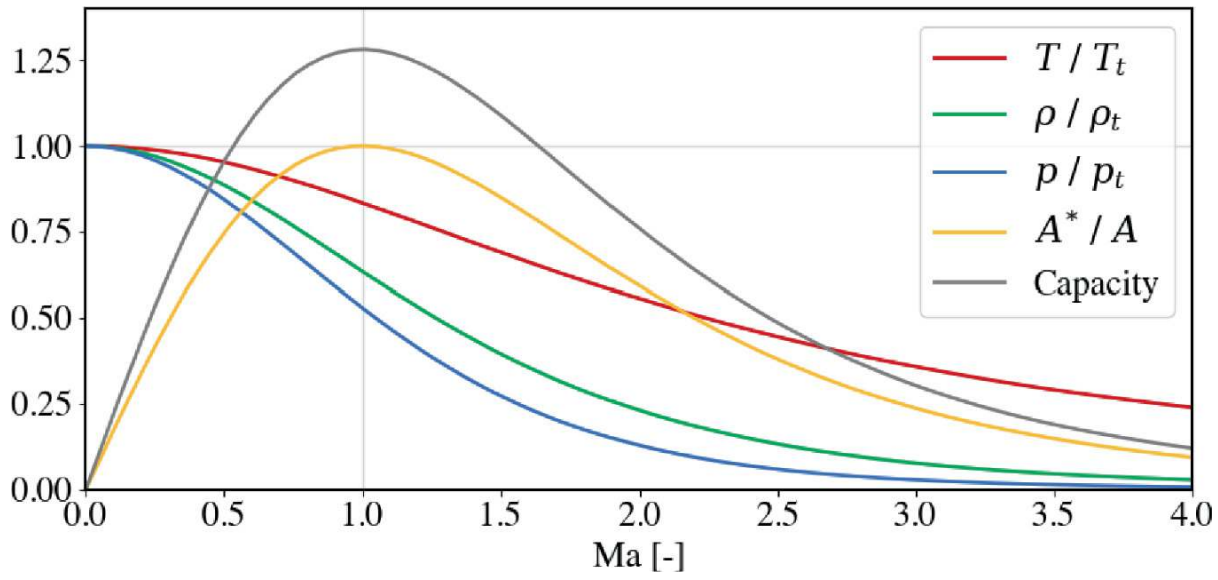


Fig. 5.3 State variables as function of Mach number Ma for air with $\gamma = 1.4$

The area ratio also corresponds to the local area-specific mass flow $\dot{m}/A = \rho u$ referenced to the critical state, thus $(\rho u)(\rho^* u^*) = (A^*)(A)$. In the subsonic regime, the area-specific mass flow increases with the Mach number, as the velocity u increases more rapidly than the density decreases (Dixon and Hall 2013). The maximum is reached at $\mathrm{Ma} = 1$. Beyond this, in the supersonic regime, the trend reverses, and the mass flux per unit area decreases with increasing Ma. Combining the cross-section and the fluid's total state allows to derive the nondimensional mass flow rate, often called **capacity**, yields

$$\frac{\dot{m}\sqrt{c_p T_t}}{A^* p_t} = \frac{\gamma \mathrm{Ma}}{\sqrt{\gamma - 1}} \left(1 + \frac{\gamma - 1}{2}\,\mathrm{Ma}^2\right)^{-\frac{1}{2}\frac{\gamma+1}{\gamma-1}}. \tag{5.29}$$

The relation is also plotted in Fig. 5.3. The quantity is central in turbomachinery design and operation, commonly used in performance maps, discussed in Sect. 4.4. As shown, the nondimensional mass flow reaches its maximum at $\mathrm{Ma} = 1$, leading to the important consequence that once sonic conditions are reached at the throat, the mass flow cannot be further increased without changing the total conditions, a phenomenon known as **choked flow** (Dixon and Hall 2013).

The isentropic flow Eqs. (5.24) and (5.25) accurately describe the Laval nozzle flow only if the ambient pressure at the nozzle exit, p_a, matches the computed exit pressure, p_e, from Eq. (5.25), as shown in Case *a* of Fig. 5.4. Different back pressures p_e at fixed inlet total pressure p_t are considered. In Case *b* the ambient back pressure is slightly increased compared to the calculated exit pressure, thus $p_a > p_e$. A **shock wave** forms inside the nozzle, that represents an abrupt compression of the fluid that decelerates the flow from supersonic to subsonic speed, and will be detailed in the following paragraph. As the ambient back pressure p_a increases, the shock wave shifts upstream (Case *c*), becoming weaker. In Case *d*, the back pressure is too high, and the critical pressure ratio is no longer reached in the throat, so that the flow remains subsonic in the entire nozzle.

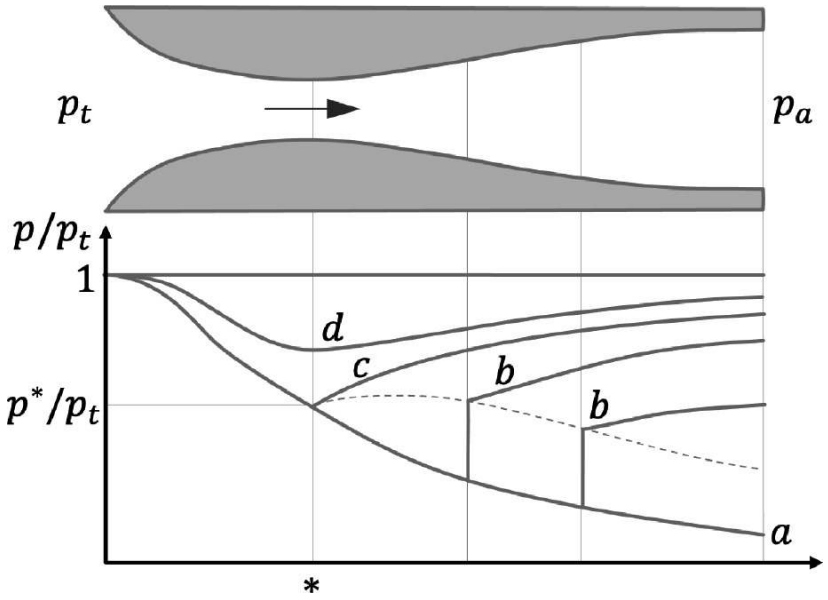


Fig. 5.4 Pressure distribution in Laval nozzle at different ambient exit pressures p_a

Shockwaves Contrary to incompressible flows, where flow properties vary smoothly and continuously, supersonic flows characteristically feature shock waves. A **shock wave** is an abrupt, discontinuous, and irreversible change of the flow variables, due to a rapid compression taking place over an extremely thin region on the order of $\mathcal{O}(10^{-7}\,\mathrm{m})$. Depending on the flow configuration, shock waves can be either normal, that is, perpendicular to the flow, or oblique at an angle to the flow. Across a **normal shock**, the flow decelerates from supersonic to subsonic conditions, while behind an **oblique shock**, the flow can remain supersonic but at a reduced Mach number (Anderson 2016). Shock waves occur in both external flows, such as transonic wing flows, and internal flows, such as those in nozzles and ducts discussed in the previous Sect. 5.1.3. Here, we analyze the state change across a normal shock.

A normal shock is so thin that no heat is exchanged with the surroundings, allowing us to treat the process as adiabatic. The state change across the shock is irreversible and involves no external work transfer. Consequently, the total enthalpy remains constant ($h_{t2} = h_{t1}$), while due to the irreversibility the entropy increases ($s_2 > s_1$). According to Eq. (5.9), this implies a decrease in total pressure ($p_{t2} < p_{t1}$), as entropy production causes mechanical energy dissipation. To describe the compression across the shock, the one-dimensional governing equations are formulated in a shock wave centered reference frame to

(5.30)

$$\begin{aligned} \rho_1 u_1 &= \rho_2 u_2 \ , \\ \rho_1 u_1^2 + p_1 &= \rho_2 u_2^2 + p_2 \ , \\ h_1 + \tfrac{u_1^2}{2} &= h_2 + \tfrac{u_2^2}{2} \ . \end{aligned}$$

The static enthalpy difference across the shock follows by eliminating the velocity terms to

$$h_2 - h_1 = \tfrac{1}{2}(p_2 - p_1)\left(\tfrac{1}{\rho_1} + \tfrac{1}{\rho_2}\right) \ . \tag{5.31}$$

This equation, known as the **Hugoniot equation**, describes the thermodynamic constraints of a shock induced compression for any fluid. For a given fluid model with known caloric and thermal state equations the relation allows deriving the state change over the shock wave. For a perfect gas, the specific enthalpy can be expressed as $h = \frac{\gamma}{\gamma-1}(p/\rho)$ and substituting into Eq. (5.31) yields

$$\frac{p_2}{p_1} = \frac{\frac{\gamma+1}{\gamma-1}\frac{\rho_2}{\rho_1} - 1}{\frac{\gamma+1}{\gamma-1} - \frac{\rho_2}{\rho_1}} \ , \tag{5.32}$$

The equation provides the relation between pressure and density ratio in front of and after the shock wave as plotted in Fig. 5.5. The function has an asymptote for a density ratio $\rho_2/\rho_1 = (\gamma+1)/(\gamma-1)$, for which the pressure ratio approaches infinity. The asymptote represents the maximum physically possible density ratio, that for a diatomic gas with $\gamma = 1.4$ is calculated to $\rho_2/\rho_1 = 6$. As the pressure ratio p_2/p_1 increases, the shock strengthens, eventually reaching this limiting density ratio. Figure 5.5 also shows the isentropic relation $p/\rho^\gamma = \text{const.}$ for reference, to show that for small pressure ratios $p_2/p_1 \to 1$ Eq. (5.32) approaches a reversible adiabatic.

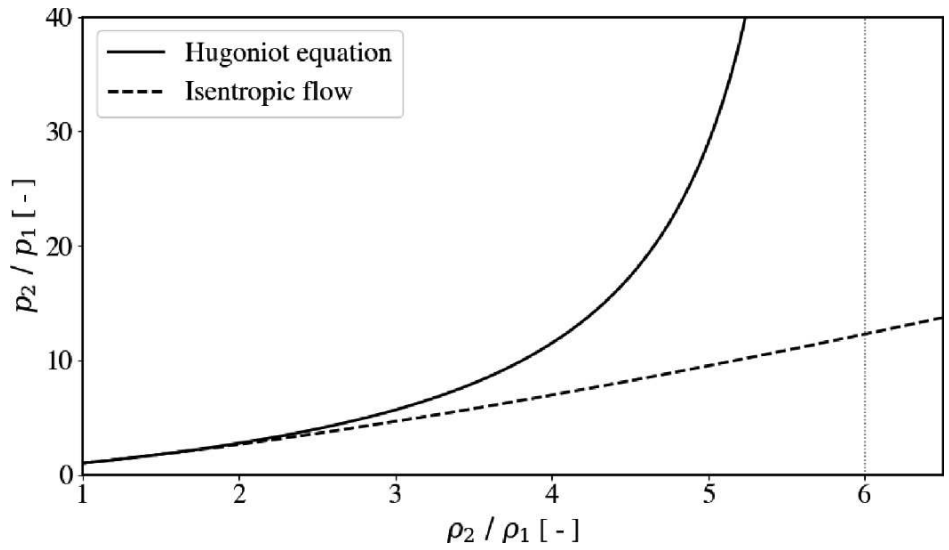


Fig. 5.5 Hugoniot equation and isentropic relation for perfect gas with $\gamma = 1.4$

The state change across the shock wave can be formulated for a calorically perfect gas as a function of the upstream Mach number $\mathrm{Ma}_1 = u_1/a_1$, using the upstream speed of sound $a_1 = \gamma R T_1$. For this purpose, the critical state is introduced as a reference on both sides of the shock wave, leading to the handy relation $a^{*2} = u_1 u_2$.

After some transformations the downstream Mach number Ma_2 follows to Anderson (2016, p. 576)

$$\mathrm{Ma}_2^2 = \frac{(\gamma-1)(\mathrm{Ma}_1^2-1)+(\gamma+1)}{2\gamma(\mathrm{Ma}_1^2-1)+(\gamma+1)} \quad . \tag{5.33}$$

As can be seen in Fig. 5.6 the flow behind a normal shock is subsonic with $\mathrm{Ma}_2 < 1$. For increasing upstream Mach numbers Ma_1 the shock wave successively becomes stronger and the downstream Ma_2 monotonically decreases. In the limit of large $\mathrm{Ma}_1 \to \infty$ the downstream Mach number Ma_2 converges toward $\sqrt{(\gamma-1)/2\gamma}$ which results to $\mathrm{Ma}_2 = 0.378$ for $\gamma = 1.4$.

Utilizing the governing normal shock equations (5.30) allows to derive the changes of the static thermal state over the shock. With the aid of the critical reference state the continuity equation yields the density ratio ρ_2/ρ_1 and the momentum equation yields the pressure ratio p_2/p_1. The temperature ratio follows either through the thermal state equation for an ideal gas or the enthalpy equation, so that the state change is described by

(5.34)

$$
\begin{aligned}
\frac{\rho_2}{\rho_1} &= \frac{(\gamma+1)\mathrm{Ma}_1^2}{2+(\gamma-1)\mathrm{Ma}_1^2} \ , \\
\frac{p_2}{p_1} &= 1 + \frac{2\gamma}{\gamma+1}\left(\mathrm{Ma}_1^2 - 1\right) \ , \\
\frac{T_2}{T_1} &= \left[1 + \frac{2\gamma}{\gamma+1}\left(\mathrm{Ma}_1^2 - 1\right)\right] \frac{2+(\gamma-1)\mathrm{Ma}_1^2}{(\gamma+1)\mathrm{Ma}_1^2} \ .
\end{aligned}
$$

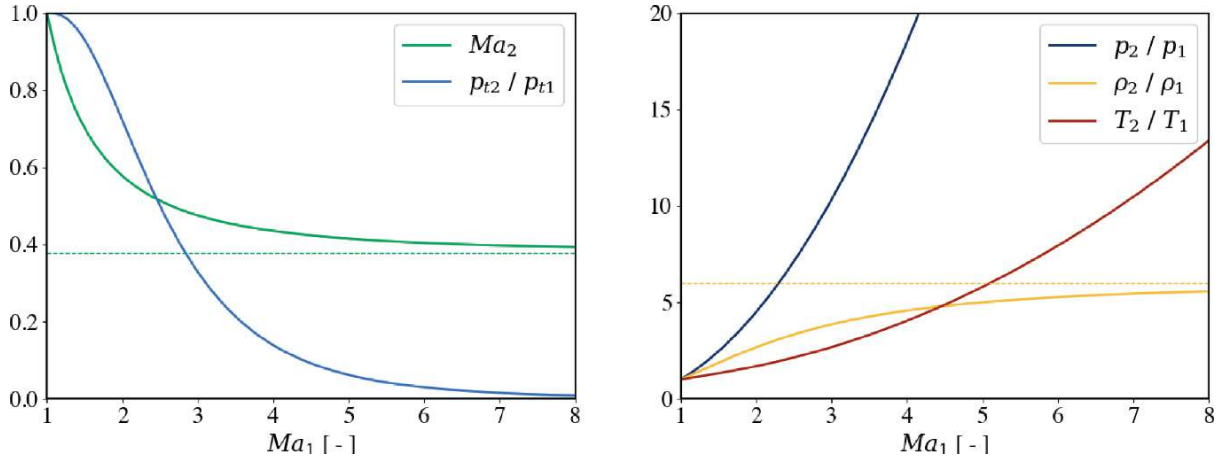


Fig. 5.6 Mach number, total pressure ratio, and static pressure, density, and temperature ratios across a normal shock as a function of upstream Mach number Ma_1 for a perfect gas with $\gamma = 1.4$

The ratios in Fig. 5.6 illustrate that the magnitude of the discontinuous changes across the shock wave increases as the upstream Mach number Ma_1 rises. As discussed earlier, the density ratio asymptotically approaches $\rho_2/\rho_1 \to (\gamma+1)/(\gamma-1)$, which evaluates to $\rho_2/\rho_1 = 6$ for $\gamma = 1.4$. Meanwhile, both the pressure and temperature ratios continue to increase indefinitely as $\mathrm{Ma}_1 \to \infty$. The entropy increase across the shock can be determined by substituting the static state changes for pressure and temperature from Eq.(5.34) directly into

$$
s_2 - s_1 = c_p \ln\left(\frac{T_2}{T_1}\right) - R \ln\left(\frac{p_2}{p_1}\right) \ . \tag{3.22}
$$

As described in Sect. 5.1.1, since the total state is defined in a thermodynamically consistent manner, the entropy difference can also be expressed in terms of total state properties. With constant total temperature across the shock ($T_{t2} = T_{t1}$), solving for the total pressure ratio yields

$$
\frac{p_{t2}}{p_{t1}} = -e^{\frac{s_2 - s_1}{R}} \ . \tag{5.35}
$$

Since entropy increases across the shock wave ($s_2 - s_1 \geq 0$), the total pressure always decreases ($p_{t2} < p_{t1}$). Equality holds only in the limiting case of $\mathrm{Ma}_1 = 1$, where the shock disappears and transitions into a continuous, isentropic flow of unchanged properties. For all $\mathrm{Ma}_1 > 1$, the entropy increase leads to a monotonic decrease in total pressure, approaching zero as $\mathrm{Ma}_1 \to \infty$, as shown in Fig. 5.6. In conclusion, it is remarkable that the shock relations depend solely on the upstream Mach number, making them fundamental for characterizing compressible flow behavior.

5.1.4 Turbomachinery

Lower-dimensional approaches are commonly used to characterize the primary flow in turbomachinery. Mean-line analysis considers flow conditions at the mean radius, typically at the inlet and outlet of each vane and blade row, and is widely applied during the early design phases. Higher-dimensional approaches become necessary to capture variations in the cross-stream direction, secondary flows, and losses due to wall friction and leakage. These methods also account for circumferential profiling and detailed loss mechanisms, including profile friction, secondary flows, and clearance flows.

Here, we will apply the governing equations for the control volume of a generic turbomachine, as illustrated in Fig. 5.7. We adopt the standard turbomachinery velocity notation, where *c* denotes the absolute velocity, that is, relative to to the stationary frame, *w* represents the velocity relative to the rotating blade, and *U* is the blade speed.

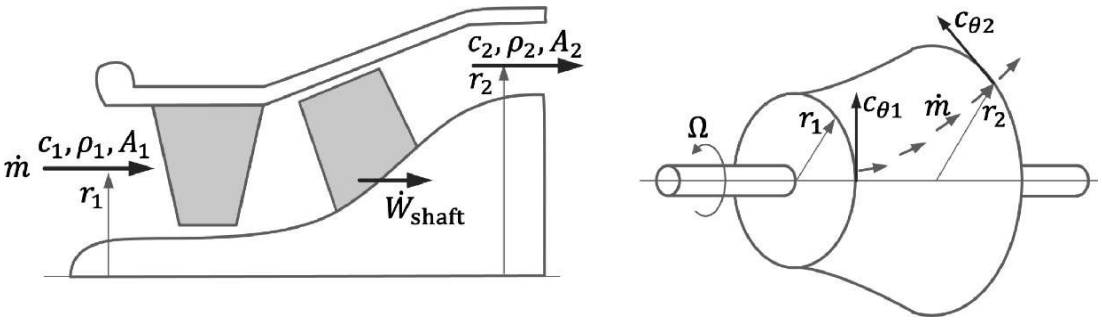


Fig. 5.7 Control volume for a turbomachine with meridional flow cross-section (left). Streamtube flowing along the surface of revolution (right)

The work transfer in turbomachines is achieved through the conversion of the fluid's kinetic energy into mechanical shaft work, as well as the transformation of the fluid's enthalpy, or pressure differences, into kinetic energy and vice versa. The pressure changes in the working fluid result from varying its velocity as it moves through converging or diverging ducts formed by the

blading. To analyze this process, we examine the transfer of shaft work using the **one-dimensional energy equation for steady flow**. This equation describes the energy conversion between the rotor and the fluid in turbomachinery. Since most turbomachinery flows are nearly adiabatic, heat transfer effects can be neglected, thus $\dot{Q} = 0$, and potential energy changes are often insignificant. Applying the steady flow energy equation from Eq. (5.7), between machine entry to exit $1 \rightarrow 2$ we obtain

$$\frac{\dot{W}_{\text{shaft}}}{\dot{m}} = (h_2 + c_2^2/2) - (h_1 + c_1^2/2) = h_{t2} - h_{t1} \ . \tag{5.36}$$

Compressors and pumps convert mechanical shaft work into an increase in fluid pressure, so that with the sign convention used here $\dot{W}_{\text{shaft}} > 0$. Conversely, turbines extract energy from the fluid and convert it into mechanical work, so that$\dot{W}_{\text{shaft}} < 0$.

In real machines, the efficiency suffers due to mechanical and hydraulic losses. This means that compressors require more work than the theoretical minimum, and turbines extract less work than an ideal expansion would yield. Given the actual machine inlet and outlet states $1 \rightarrow 2$, the real shaft work is determined by Eq. (5.36). The ideal reference state depends on the assumed idealized process (Dixon and Hall 2013). But once defined, the **efficiency** is thus defined by comparing the actual work with the ideal work. Here, we focus only on flow-related losses, neglecting mechanical losses in components like bearings or couplings. For a compressor, the hydrodynamic efficiency is given by

$$\eta_C = \frac{\text{ideal minimal work input}}{\text{actual work input}} \ , \tag{5.37}$$

while for a turbine, the efficiency compares actual work output to the ideal maximum work available in the fluid

$$\eta_T = \frac{\text{actual work output}}{\text{ideal maximal work output}} \ . \tag{5.38}$$

Both efficiencies satisfy $0 < \eta < 1$.

Turbomachinery handling **incompressible fluids** is often referred to as hydraulic machinery. In such machines, pumps convert shaft work into increased fluid pressure, while hydraulic turbines extract energy from the fluid to produce mechanical work. At ideal energy conversion, the work input required by a pump is minimized, and the work output from a hydraulic turbine is maximized, both corresponding to an isentropic process. Following the discussion of the total

state of an incompressible fluid with Eq. (3.23) an isentropic flow $ds = 0$ implies $dT = 0$. At ideal conversion the internal energy remains equal, so that total enthalpy difference corresponds to the total pressure difference, thus $\Delta h_{t_{12}} = \Delta p_{t_{12}}$. The corresponding **ideal work for an incompressible fluid** becomes

$$\frac{\dot{W}_{\text{shaft}}}{\dot{m}} = (p_2/\rho + c_2^2/2) - (p_1/\rho + c_1^2/2) = (p_{t2} - p_{t1})/\rho = g(H_2 - H_1) \ . \quad (5.39)$$

As previously mentioned, the hydraulic head *H* is defined as $gH = p/\rho + c^2/2 + gz$, representing the height to which the liquid can be moved against gravity. The hydrodynamic efficiency for a pump and a hydraulic turbine is then given by

$$\eta_P = \frac{\dot{m}g(H_2 - H_1)}{\dot{W}_{\text{shaft}}}, \quad \eta_T = \frac{-\dot{W}_{\text{shaft}}}{\dot{m}g(H_1 - H_2)} \ . \quad (5.40)$$

For turbomachinery operating with **compressible fluids**, the energy conversion process involves changes in both density and temperature. In a compressor the volume of the fluid is reduced, so that both density and temperature of the working fluid are increased. Conversely, in a turbine, the working fluid expands, increasing in volume while experiencing a corresponding decrease in density and temperature. Following the estimate in Sect. 4.2 the gravitational terms can usually be neglected in the context of of compressible flows, so that the actual specific shaft work simplifies to

$$\frac{\dot{W}_{\text{shaft}}}{\dot{m}} = h_{t2} - h_{t1} = h_2 - h_1 + \frac{1}{2}\left(c_2^2 - c_1^2\right) \ . \quad (5.41)$$

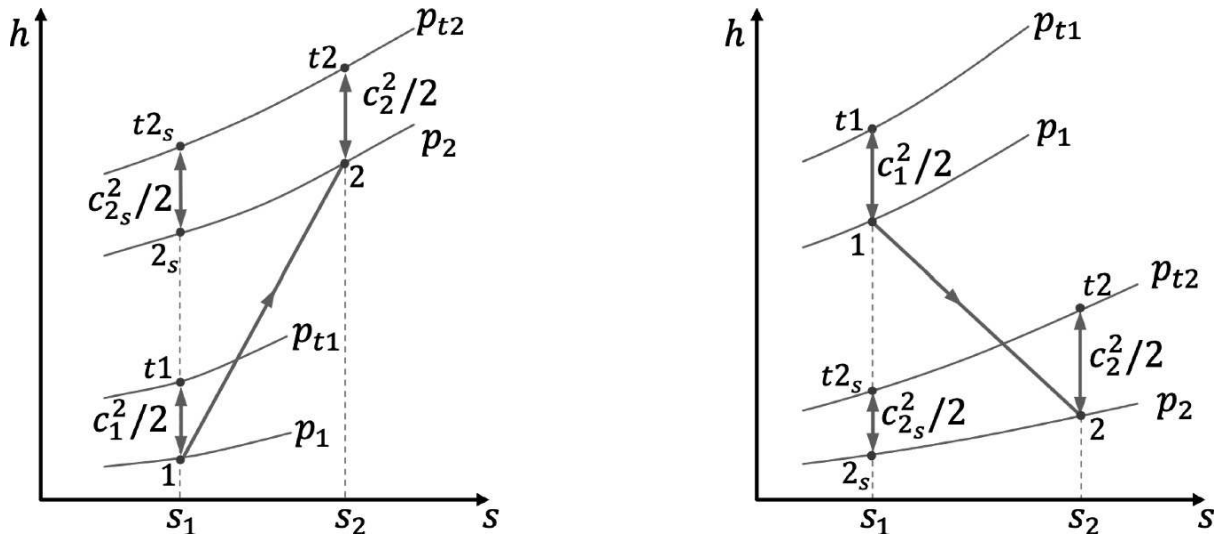


Fig. 5.8 $h - s$ diagram for flow through adiabatic compressor and turbine real and ideal reference state

To define the ideal work output, a reference process is introduced in which the exit static pressure p_2 and total pressure p_{2t} are reached through an isentropic process $1 \rightarrow 2s$, as sketched in Fig. 5.8. The ideal specific work output then results to

$$\frac{\dot{W}_{\text{ideal}}}{\dot{m}} = h_{t2_s} - h_{t1} = h_{2_s} - h_1 + \frac{1}{2}\left(c_{2_s}^2 - c_1^2\right) \ . \tag{5.42}$$

The efficiency definitions for both compressors and turbines relate the total enthalpy differences, providing a measure of how effectively energy is converted in real converted in real machines, and are given by

$$\eta_C = \frac{h_{t2_s} - h_{t1}}{h_{t2} - h_{t1}} \ , \quad \eta_T = \frac{h_{t1} - h_{t2}}{h_{t1} - h_{t2_s}} \ . \tag{5.43}$$

These definitions account for internal losses within the machinery and allow for performance evaluation based on deviations from the ideal isentropic process. An important consideration in defining the ideal reference state for turbines is whether the kinetic energy at the turbine exit is usefully employed. As discussed by Dixon and Hall (2013, p. 23), the appropriate efficiency definition depends on whether the kinetic energy at the exhaust contributes to useful work or is lost as waste. In cases where the exhaust kinetic energy can be recovered, such as in multistage turbines, a total-to-total efficiency definition is appropriate. This is also relevant for the final stage of a jet engine, where the exit velocity directly contributes to thrust. However, in mid-sized power turbines, where the exhaust air exits into the ambient environment and its kinetic energy dissipates without

performing useful work, it is more appropriate to exclude the kinetic energy term $c_{2_s}^2/2$ from the ideal maximum work calculation.

To gain deeper insights into the mechanisms of energy transfer in turbomachines, it is useful to move beyond energy conservation at the stage level and examine the **conservation of angular momentum** at the blade and vane level. The conservation of angular momentum states that the sum of external torques τ about an arbitrary axis is equal to the time rate of change of angular momentum, thus

$$\tau = \frac{d}{dt}\left(mrc_\theta\right) \ . \tag{5.44}$$

Consider the control volume of an elementary stream tube passing through the turbomachine $1 \rightarrow 2$, as illustrated on the right-hand side of Fig. 5.7. The fluid enters the control volume at a radius r_1 with a tangential velocity component $c_{\theta 1}$ and exits at a radius r_2 with a tangential velocity component $c_{\theta 2}$. By balancing the external torque with the rate of angular momentum flux, we obtain $\tau = \dot{m}(r_2 c_{\theta 2} - r_1 c_{\theta 1})$. For an adiabatic turbomachine rotating at an angular velocity Ω, applying the steady flow energy equation leads to the power transfer equation

$$\begin{aligned} \dot{W} &= \tau\Omega \\ &= \dot{m}\Omega(r_2 c_{\theta 2} - r_1 c_{\theta 1}) \\ &= \dot{m}(U_2 c_{\theta 2} - U_1 c_{\theta 1}) \ , \end{aligned} \tag{5.45}$$

with $U = \Omega r$. Expressing the work transfer per unit mass flow, we obtain the specific work equation

$$\Delta w_{12} = U_2 c_{\theta 2} - U_1 c_{\theta 1} \ ,$$

which is known as the **Euler work equation**. It represents the fundamental relationship governing work transfer in turbomachinery. It applies to both viscous and inviscid flows under steady-state conditions. However, it does not account for changes in angular momentum caused by frictional effects at the hub and casing, which can influence real machine performance (Dixon and Hall 2013).

Euler's work equation can also be expressed in terms of total enthalpy as $\Delta(h_t - Uc_\theta) = 0$, which indicates that the quantity $h_t - Uc_\theta$, referred to as **rothalpy**, is conserved through a stage. For a stationary blade row, the stator where $U = 0$, this equation simplifies to $h_t = \text{const.}$, meaning that the total

enthalpy remains unchanged across the stator. Since energy transfer occurs only in the rotor, where the blades move with speed *U*, it is useful to reformulate Euler's equation in terms of the relative velocity component $w = c - U$. Substituting into Euler's work equation gives

$$h_t - U c_\theta = h + \tfrac{1}{2} w^2 - \tfrac{1}{2} U^2 = h_{t,\mathrm{rel}} - \tfrac{1}{2} U^2 \ , \tag{5.46}$$

where $h_{t,\mathrm{rel}} = h + w^2/2$ is the **relative stagnation enthalpy**. It follows that the quantity $h_{t,\mathrm{rel}} - U^2/2$ remains constant over the rotor. For a constant blade speed, the relative stagnation enthalpy $h_{t,\mathrm{rel}}$ remains conserved throughout the rotor. The formulation provides a deeper thermodynamic interpretation of the energy transfer process in a rotating frame of reference and is particularly useful for analyzing flow behavior in compressors and turbines, as shown in the following.

Axial Compressor An axial compressor increases the pressure of air by passing it through alternating rows of rotating blades, called rotors, and stationary vanes, called stators. Each compressor stage consists of a rotor-stator pair, where the rotor transfers energy to the working fluid, increasing its total enthalpy and velocity, while the stator diffuses the flow, converting a portion of the kinetic energy into increased static pressure. To achieve higher pressure ratios, axial compressors are typically configured as multistage machines, where multiple rotor-stator pairs are arranged in series. As the working medium flows through successive stages, its density and temperature increase due to compression. To maintain a nearly constant axial velocity, the annular flow area between the rotor shaft and the stator casing gradually decreases along the compressor's length.

Since axial compressors operate under a positive and thus adverse pressure gradient, they are inherently prone to flow separation and instability. Unlike turbines, where the flow benefits from a favorable pressure gradient, compressors must carefully control blade loading and diffusion rates to prevent boundary layer separation, which can lead to surge conditions. In addition to pressure recovery, the stator vanes correct the flow direction, ensuring that the fluid exits at the correct angle to enter the subsequent rotor stage, thereby maintaining efficient compression throughout the machine.

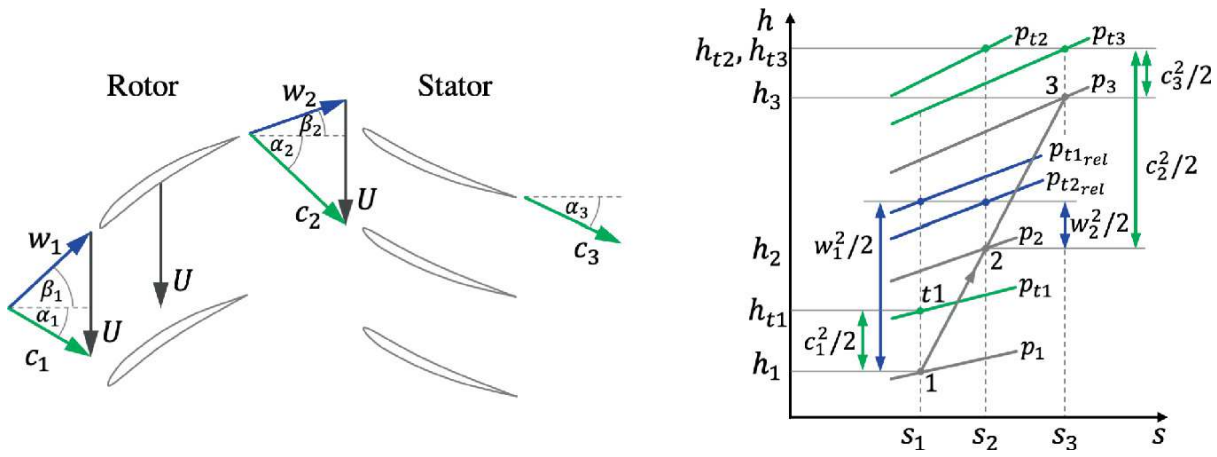


Fig. 5.9 Velocity triangles for a compressor stage (left) and the corresponding $h - s$ diagram (right)

The flow behavior within each stage can be analyzed using velocity triangles, which describe how the flow interacts with the blades in both absolute and relative frames of reference. The left-hand side of Fig. 5.9 illustrates these velocity triangles, while the corresponding enthalpy changes are represented in the $h - s$ diagram on the right-hand side. The $h - s$ diagram further depicts the isentropic reference process $1 \rightarrow 3$, representing an idealized, loss-free stage. Additionally, it is possible to construct isentropic reference states for a loss-free rotor or stator, which correspond to the intersections of the vertical isentropic line with the respective isobars. For a perfect gas, the isentropic efficiency of the compressor, derived from Eq. (5.37), simplifies to

$$\eta_C = \frac{\Delta h_{t_s}}{\Delta h_t} = \frac{(p_{t3}/p_{t1})^{\gamma/(\gamma-1)} - 1}{(T_{t3} - T_{t1})/T_{t1}} \ . \tag{5.47}$$

Applying Euler's work equation to an axial compressor stage, where the radial displacement of streamlines is negligible, results in

$$\Delta w_{13} = h_{t3} - h_{t1} = U(c_{\theta 3} - c_{\theta 1}) \ , \tag{5.48}$$

where it is assumed that for an axial machine, the blade speed remains approximately constant across the rotor, so that $U = U_1 \approx U_2$ (Dixon and Hall 2013).

At the rotor inlet (station 1), the fluid enters with an absolute velocity c_1 at an inflow angle α_1. In the rotating frame, where the blade moves at speed U, the corresponding relative velocity is w_1, with an associated relative flow angle β_1. As the fluid passes through the rotor, the specific work Δw_{13} is transferred from the rotor to the fluid, reducing the relative velocity to w_2 and adjusting the flow angle to β_2. In the absolute frame of reference, this corresponds to an exit

velocity c_2 at an outflow angle α_2. Since U is assumed constant, the total relative enthalpy remains conserved in the rotor, and we obtain the relation

$$h_1 + \frac{w_1^2}{2} = h_2 + \frac{w_2^2}{2} \ . \tag{5.49}$$

After exiting the rotor, the flow enters the stator, where it undergoes diffusion. The stator reduces the absolute velocity from c_2 to c_3 while increasing the static pressure. Across the stator, the total enthalpy remains constant, leading to the equation

$$h_2 + \frac{c_2^2}{2} = h_3 + \frac{c_3^2}{2} \ . \tag{5.50}$$

In a multistage compressor, a repeating stage configuration is often employed, where the stator exit velocity satisfies $c_3 = c_1$ and the exit flow angle satisfies $\alpha_3 = \alpha_1$. The cyclic flow pattern ensures that the compressor operates efficiently across multiple stages while maintaining stable and predictable aerodynamic conditions.

Axial Turbine An axial turbine extracts energy from the working fluid as it expands through alternating rows of stationary vanes, called nozzles or nozzle guide vanes (NGVs), and rotating blades. Each turbine stage consists of a stator-rotor pair, where the stator accelerates the flow, converting pressure energy into kinetic energy, while the rotor extracts work, reducing the fluid's total enthalpy and velocity, thereby transferring energy to the shaft. To accommodate the increasing specific volume due to expansion, the annular flow area between the rotor shaft and casing gradually increases in the direction of the main flow.

Unlike compressors, axial turbines operate under a favorable pressure gradient, meaning the flow experiences a gradual pressure drop. The favorable condition allows turbines to achieve high efficiency even with large pressure drops across a stage. As a result, fewer stages are required to achieve comparable pressure ratios in a turbine than in a compressor. Additionally, the levels of flow turning in a turbine are generally higher than in a compressor, influencing blade design and aerodynamic considerations.

The velocity triangles describing turbine flow are similar to those used for compressors but reflect the opposite energy conversion process. The left-hand side of Fig. 5.10 illustrates these velocity triangles, while the right-hand side presents the corresponding $h - s$ diagram, showing the enthalpy decrease associated with the expansion process. The isentropic reference process $1 \rightarrow 3s$ represents the idealized, loss-free turbine stage. As in compressors, one can define isentropic reference states for an ideal stator or rotor, found at the

intersections of the vertical isentropic line with the respective isobars. For a perfect gas, the isentropic efficiency of the turbine, derived from Eq. (5.37), simplifies to

$$\eta_T = \frac{\Delta h_t}{\Delta h_{t_s}} = \frac{(T_{t3} - T_{t1})/T_{t1}}{(p_{t1}/p_{t3})^{(\gamma-1)/\gamma} - 1} \ . \tag{5.51}$$

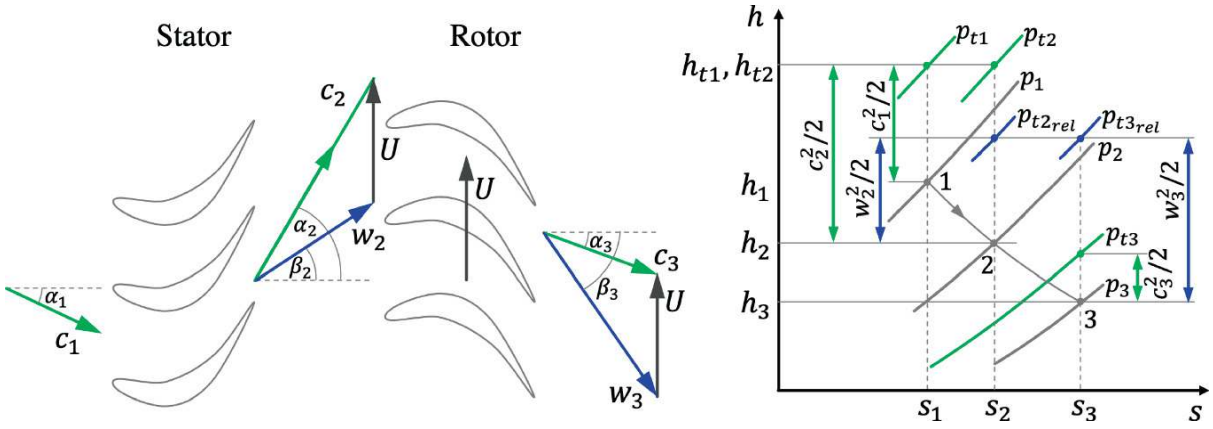


Fig. 5.10 Velocity triangles for a turbine stage (left) and the corresponding $h - s$ diagram (right)

The design of turbine blades must account for aerodynamic losses, secondary flows, and cooling requirements, particularly in high-temperature applications such as gas turbines. The sources of losses in a turbine stage that can be resolved in two-dimensional analysis include blade boundary layer effects, trailing edge mixing, flow separation, and shock waves. In contrast, three-dimensional losses encompass tip leakage flows, secondary endwall flows, and coolant flow for cooled turbine stages (Dixon and Hall 2013).

Across the stator, the total enthalpy remains constant, yielding $h_{t1} = h_{t2}$. Applying Euler's work equation for an axial turbine stage yields the same equation as for a compressor but with a negative sign, since the turbine extracts work from the fluid.

$$\Delta w_{13} = h_{t1} - h_{t3} = U(c_{\theta 1} + c_{\theta 3}) \ . \tag{5.52}$$

Note that in accordance with Fig. 5.10 the tangential velocity components $c_{\theta 3}$ are added. As in axial compressors, the blade speed U remains approximately constant. However, the turbine extracts energy, resulting in a decrease in total enthalpy. Again assuming no significant radial displacement of streamlines, the relative total enthalpy remains constant within the rotor, giving the relation

(5.53)

$$h_2 + \frac{w_2^2}{2} = h_3 + \frac{w_3^2}{2} \ .$$

Centrifugal Compressor or Pump A centrifugal compressor increases the pressure of the working fluid by converting angular momentum into static pressure. A centrifugal compressor typically consists of a single or double-sided impeller followed by a diffuser and a collector. The working fluid is drawn into the impeller eye, where the high-speed rotation of the impeller transfers energy to the flow. Due to the centrifugal action, the fluid is accelerated radially outward toward the impeller tip, leading to an increase in both velocity and static pressure. The high-velocity flow then enters the ring of diffuser vanes, where it is decelerated, converting kinetic energy into increased static pressure. Finally, the flow is collected in the collector and exits through the outlet pipe.

As discussed in Sect. 4.4.3, compared to axial compressors, centrifugal compressors can achieve significantly higher pressure ratios per stage but are generally limited in terms of mass flow capacity. They tend to be more robust and less sensitive to inlet flow distortions, making them preferable for applications requiring moderate to high-pressure ratios in a compact design.

The velocity diagrams for a centrifugal compressor differ from those of an axial compressor due to the radial acceleration of the fluid. The left-hand side of Fig. 5.11 illustrates the velocity triangles for a centrifugal machine, while the right-hand side presents the corresponding $h - s$ diagram.

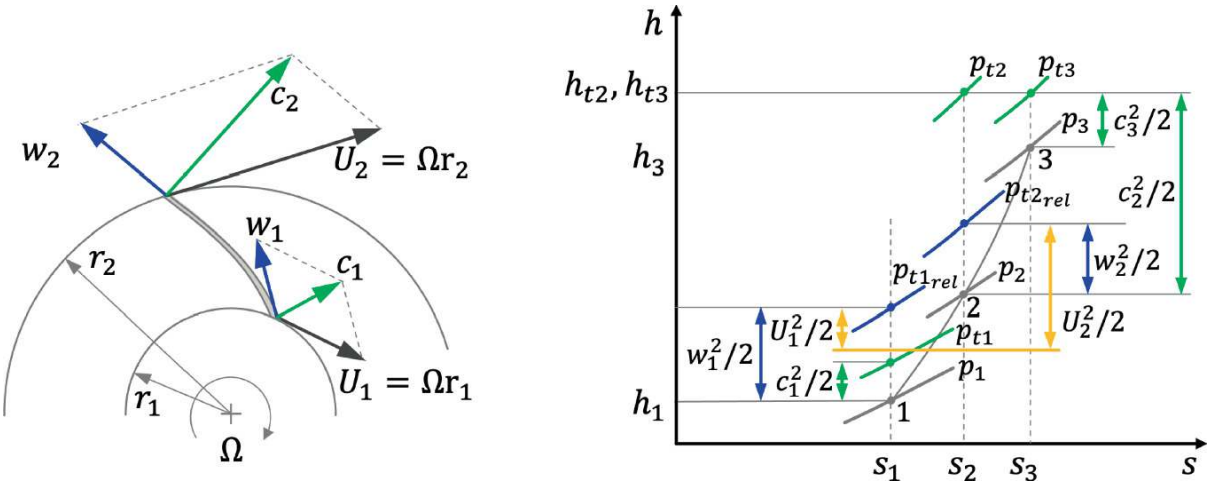


Fig. 5.11 Velocity diagrams for a centrifugal compressor stage (left) and the corresponding $h - s$ diagram (right)

For centrifugal compressors and pumps, it is common for the flow to enter the impeller without prerotation, meaning that the absolute tangential velocity component at the inlet is negligible, thus $c_{\theta 1} = 0$. Applying Euler's work

equation, the specific work transfer per unit mass for a centrifugal compressor simplifies to

$$\Delta w_{12} = h_{t2} - h_{t1} = U_2 c_{\theta 2} \ . \tag{5.54}$$

For an incompressible pump, the work transfer is related to the hydraulic head as $\Delta w_{12} = gH$.

Across the impeller, the quantity $h_{t,\mathrm{rel}} - U^2/2$ remains constant. Unlike axial compressors, where the blade speed is nearly constant, a centrifugal impeller exhibits a significant increase in blade speed from the hub to the tip, given by $U_2/U_1 = r_2/r_1$. This variation in blade speed influences the velocity triangles and contributes to the overall enthalpy rise. The enthalpy change across the impeller is given by

$$h_2 - h_1 = \tfrac{1}{2}\left(U_2^2 - U_1^2\right) + \tfrac{1}{2}\left(w_1^2 - w_2^2\right) \ . \tag{5.55}$$

This equation highlights why the static enthalpy rise in a centrifugal compressor is generally larger than that in a single-stage axial compressor. The second term, $(w_1^2 - w_2^2)/2$, represents the contribution from the diffusion of relative velocity, which also appears in axial compressors. However, the first term $(U_2^2 - U_1^2)/2$, resulting from the increase in blade speed due to the centrifugal effect, provides an additional mechanism for enthalpy rise unique to centrifugal compressors (Dixon and Hall 2013). After leaving the impeller, the flow enters the diffuser, where its velocity is reduced, and its kinetic energy is converted into pressure. Across the diffuser, from station $2 \rightarrow 3$, the total enthalpy remains constant.

5.1.5 Subscale Modeling

In practical thermo-fluid systems, physical phenomena often take place on spatial or temporal scales that exceed the resolution intended in a lower-dimensional framework. To account for such effects, **subscale models** are applied. These models abstract the detailed behavior of unresolved physical processes and represent their impact on the mean flow quantities. They commonly appear as additional source terms in the governing equations, or as boundary conditions representing averaged interactions across unresolved interfaces.

As introduced in Sect. 5.3, duct or channel flows are often treated as one dimensional, where variables are averaged across the cross-section. However, some key effects, such as wall friction, heat transfer, or flow-feature induced disturbances, arise due to gradients in the cross-stream direction and cannot be

resolved directly. Subscale models are used to account for these unresolved effects, enabling their impact to be represented in the respective system-level equations.

The development and application of subscale models is a key example of combining first-principles physics with empirical or data-driven correlations. While conservation laws ensure that the governing equations remain physically consistent, the subscale phenomena are introduced through quantities derived from theory, experiments, or high-fidelity simulations. This approach enables accurate modeling of essential physical mechanisms while avoiding the computational cost of resolving all scales explicitly. Throughout this chapter, we highlight several such models, with an emphasis on wall friction and convective heat transfer. Their broader development and applications are exemplified in Part III.

Wall Friction In both internal and external flows, momentum loss due to viscous forces at solid boundaries is a major physical effect. In the quasi-one-dimensional momentum equation (5.3), this appears as a sink term associated with the wall shear stress τ_w, which acts along the wetted area dA_w of the control volume. The wall shear stress is commonly nondimensionalized via the **skin-friction coefficient** c_f, defined by

$$c_f = \frac{\tau_w}{\frac{1}{2}\rho u^2} \ , \tag{5.56}$$

which compares the wall shear to the dynamic pressure of the flow. The total wall friction force can then be written as

$$\tau_w \, dA_w = \frac{2 c_f \, \rho u^2 A}{d_h} \, ds \ , \tag{5.57}$$

where the **hydraulic diameter** d_h generalizes the concept of a diameter for noncircular ducts and is defined as

$$d_h = \frac{4A}{P} \ , \tag{5.58}$$

with A the cross-sectional area and P the wetted perimeter. As detailed in Sect. 5.3 the hydraulic diameter provides a generalized length scale that allows internal flow correlations to be extended to noncircular ducts (White 1991, p. 123).

The friction coefficient c_f depends on a range of factors, including the Reynolds number, surface roughness, and the state of flow development, that is whether the flow is laminar or turbulent, developing or fully developed.

Geometrical features such as cross-sectional shape, area variation, such as converging or diverging segments, and internal fittings like bends, orifices, or ribbed walls further influence the effective wall friction. Numerous empirical correlations for c_f exist, typically in the form $c_f = f(\mathrm{Re}, \mathrm{Geometry})$, of which a few selected cases are discussed in Sect. 5.3.3.

In the literature, several alternative but equivalent forms of friction factor representation are commonly used. A widely applied definition in internal flow analysis is the **Darcy friction factor** f given by

$$f = \frac{\Delta p}{\rho \bar{u}^2/2} \frac{d_h}{\ell} \ , \tag{5.59}$$

where Δp is the pressure drop over a segment of length ℓ, $\bar{u}$ is the mean flow velocity, and d_h is the hydraulic diameter. The Darcy friction factor is standard in engineering pressure loss calculations and for instance commonly used in the Moody diagram. An alternative definition, more common in the heat transfer literature, is the **Fanning friction factor** f_F. It is defined as one-quarter of the Darcy friction factor and corresponds directly to the friction coefficient c_f introduced earlier (White 1991)

$$f_F = \frac{f}{4} = c_f \ . \tag{5.60}$$

Unless otherwise noted, the following text adopts the Darcy friction factor f, consistent with its widespread use in internal flow modeling and pressure drop calculations.

For localized losses caused by abrupt changes in geometry, such as expansions, contractions, or valves, it is often convenient to introduce a **loss coefficient** ζ, which relates the pressure drop to the dynamic pressure via

$$\Delta p = \zeta \, \frac{1}{2} \rho u^2 \ . \tag{5.61}$$

In distributed systems, ζ can be related to the Darcy friction factor by

$$\zeta = f \, \frac{\ell}{d_h} \ , \tag{5.62}$$

providing a unified view of pressure losses whether due to wall shear or discrete disturbances.

In external flows, the combined effects of viscous and pressure forces acting on a body surface give rise to aerodynamic drag. This drag generally includes two components, first the **skin-friction drag**, resulting from viscous shear along the

surface, and **form drag** or pressure drag, caused by pressure differences due to flow separation or bluff body effects. The total effect is captured by the nondimensional **drag coefficient** c_D, defined as

$$c_D = \frac{F_D}{\frac{1}{2}\rho u_\infty^2 A_{\text{ref}}} \ , \tag{5.63}$$

where F_D is the total drag force, u_∞ is the free-stream approach velocity, and A_{ref} is a reference area, typically the projected frontal area of the body. Friction factors such as c_f, f_F, and f primarily represent viscous losses due to wall shear skin friction, and do not directly account for pressure drag arising from flow separation or bluff body effects. Such form drag is typically modeled separately using a drag coefficient c_D for external flows, or a loss coefficient ζ for localized disturbances in internal flows.

The drag coefficient c_D depends on the body shape, Reynolds number, surface roughness, and flow regime, including effects such as laminar-to-turbulent transition, flow separation, and wake dynamics. In quasi-one-dimensional models, distributed drag forces arising from embedded components such as struts, screens, or porous media can be incorporated using a drag formulation analogous to Eq. (5.63), contributing to the internal body force term dF_d in the momentum equation.

Convective Heat Transfer In convective heat transfer, the wall heat transfer arises due to temperature gradients normal to the boundary and is modeled using the convective heat transfer coefficient *h* introduced in Eq. (3.77). In nondimensional form, heat transfer is typically expressed using the **Nusselt number** Nu, defined in Eq. (4.21), which characterizes the ratio of convective to conductive heat transfer. For forced convection, correlations of the form $\mathrm{Nu} = f(\mathrm{Re}, \mathrm{Pr})$ are commonly used. The Nusselt number depends on the flow regime (i.e., laminar or turbulent), surface geometry, and thermal boundary conditions. For noncircular ducts, the hydraulic diameter d_h is again employed to ensure compatibility across different geometries. The wall heat transfer then becomes

$$\dot{q}_w \, dA_w = h(T_w - T_\infty) = \frac{\mathrm{Nu}\, k}{d_h} (T_w - T_\infty) \, dA_w = \frac{\mathrm{Nu}\, k}{d_h} (T_w - T_\infty) \, \frac{4A}{d_h} \, ds \ , \tag{5.64}$$

where *k* is the thermal conductivity of the fluid.

As with wall friction, convective heat transfer can be enhanced by modifying the geometry via flow features. Techniques such as surface roughening, ribbing, or the inclusion of turbulators are used to enhance convective transport, by

disrupting the boundary layer and thus increasing local heat transfer. Modeling these enhancements often requires geometry-specific empirical correlations specific to the flow feature in question.

In systems with distributed heat transfer interfaces, such as porous media, finned heat exchangers, or packed beds, a **volumetric heat transfer coefficient** can be introduced. In such cases, the heat exchange is modeled in terms of the rate per unit volume as

$$\dot{q}_v = h_v \, a_s \, (T_s - T_f) \ , \tag{5.65}$$

where T_s and T_f denote the solid and fluid temperatures, respectively, and a_s is the specific surface area (also called surface area density), defined as the available surface area for heat transfer per unit volume. The coefficient h_v then characterizes the local convective interaction at the solid-fluid interface, while a_s reflects the geometrical configuration of the medium. This volumetric formulation is particularly useful in homogenized or volume-averaged energy models, where detailed surface geometry is not resolved, but its thermal effect is captured through $h_v a_s$.

Turbomachinery In turbomachinery, the interaction between rotating blades and the working fluid occurs on spatial and temporal scales that are not resolved within a one-dimensional streamtube model. The cumulative effect of blade work is incorporated into the governing equations via the shaft work term dF_{shaft} in the momentum equation, or equivalently dw_{shaft} in the energy equation (5.5). The corresponding total pressure rise in hydraulic machines and total enthalpy change in compressible machines, as discussed in Sect. 5.1.4, can also be interpreted as subscale models. These quantities are coupled to the local flow conditions through performance maps, discussed in Sect. 4.4. These maps relate work input or extraction to local flow conditions and form another important class of subscale models, combining empirical knowledge with system-level conservation laws.

Further applications of subscale models arise in the context of turbulence modeling and multiphase flows, where unresolved transport processes are captured through models for mass, momentum, and energy exchange rates. Examples of such models are presented in Part III.

5.2 External Flow

External flows involve fluid motion over immersed bodies, where the domain extends into a free stream and the boundaries are defined by the object surface.

They are typically characterized by boundary layer development, flow separation, and wake formation, with behavior governed by geometry, Reynolds number, and surface conditions. The boundary layer model and the use of drag coefficients for bluff bodies, such as spheres, represent typical examples of subscale modeling used to capture complex flow behavior in a simplified form.

This section begins with the laminar boundary layer equations and their solution over a flat plate, continues with simplified modeling of flow around a sphere, as an example of how external flow effects can be captured through reduced-order modeling.

5.2.1 Laminar Boundary Layer Equations

In Sect. 4.3.1, the simplified boundary layer equations were derived for steady, laminar, incompressible flow. Here, we apply them to the classic case of external flow over a flat plate. The flow is assumed to be steady, laminar, and two-dimensional, with constant material properties. The free-stream velocity u_∞ is taken to be constant in the streamwise direction, so that the pressure gradient in the x-direction is zero. In the energy equation, viscous dissipation is neglected, corresponding to $\mathrm{Ec} \ll 1$. Body forces such as gravity are also neglected. Under these assumptions, the boundary layer equations (5.66) reduce to

$$\begin{aligned} \frac{\partial u}{\partial x} + \frac{\partial v}{\partial y} &= 0 \ , \\ u\frac{\partial u}{\partial x} + v\frac{\partial u}{\partial y} &= \nu\frac{\partial^2 u}{\partial y^2} \ , \\ u\frac{\partial T}{\partial x} + v\frac{\partial T}{\partial y} &= \alpha\frac{\partial^2 T}{\partial y^2} \ . \end{aligned} \tag{5.66}$$

At the wall, the no-slip condition applies, and the wall is assumed to have constant temperature. The boundary conditions are thus

$$\begin{aligned} y = 0: &\qquad u = 0, \qquad v = 0, \qquad T = T_w = \text{const.} \\ y \to \infty: &\qquad u = u_\infty, \qquad\qquad T = T_\infty = \text{const.} \end{aligned} \tag{5.67}$$

Blasius Solution for a Flat Plate As discussed in Sect. 4.1, for an incompressible flow, the momentum and energy equations are decoupled and can therefore be solved sequentially. We start with the velocity field. Since the semi-infinite flat plate lacks a characteristic length scale in the streamwise direction, it is reasonable to assume that the velocity profiles are self-similar (Simon et al. 2017), meaning they can be mapped onto a single, dimensionless profile via a transformation rule. The corresponding similarity variable is defined as

(5.68)

$$\eta = y\sqrt{\frac{u_\infty}{2\nu x}} \ ,$$

which combines the spatial coordinates *x* and *y* into a single spatial variable. This transformation reduces the continuity and momentum equations from two partial differential equations in (x, y) to a single ordinary differential equation in η. As introduced in Sect. 3.2.3, a stream function $\psi(x, y)$ is introduced to identically satisfy the continuity equation with

$$u = \frac{\partial \psi}{\partial y}, \quad v = -\frac{\partial \psi}{\partial x} \ . \tag{5.69}$$

The use of a stream function eliminates the continuity equation, but increases the differential order of the system. Associated with η, a nondimensional stream function $f(\eta)$ is defined with

$$f(\eta) = \frac{\psi}{y\sqrt{2\nu u_\infty x}} \ . \tag{5.70}$$

With the Reynolds number $\mathrm{Re}_x = u_\infty x/\nu$, the velocity components become

$$\frac{u}{u_\infty} = f' \ , \quad \frac{v}{u_\infty} = \frac{1}{\sqrt{2\mathrm{Re}_x}}(\eta f' - f) \ . \tag{5.71}$$

Substituting these expressions into the momentum equation, and applying the boundary conditions, yields the classical **Blasius equation**

$$\begin{aligned} f''' + ff'' &= 0 \ , \\ \eta = 0: \quad f &= 0, \quad f' = 0 \ , \\ \eta \to \infty: \quad f' &= 1 \ . \end{aligned} \tag{5.72}$$

This third-order nonlinear ordinary differential equation (ODE), subject to two boundary conditions at $\eta = 0$ and one at $\eta \to \infty$, forms a boundary value problem for which no closed-form analytical solution exists. A standard numerical approach is to rewrite it as a first-order system with $\mathbf{y} = (f'', f', f)^\top = (y_1, y_2, y_3)^\top$ and $\mathbf{y}' = (-ff'', f'', f')^\top = (-y_1 y_3, y_1, y_2)^\top$. A shooting method is then used to iterate on $f''(0)$ such that $f'(\eta \to \infty) \to 1$, with $\eta = 10$ typically providing sufficient approximation instead of $\eta \to \infty$. The resulting value is $f''(0) \approx 0.46960$. Figure 5.12 shows the numerical solution obtained using a fifth-order Runge-Kutta method.

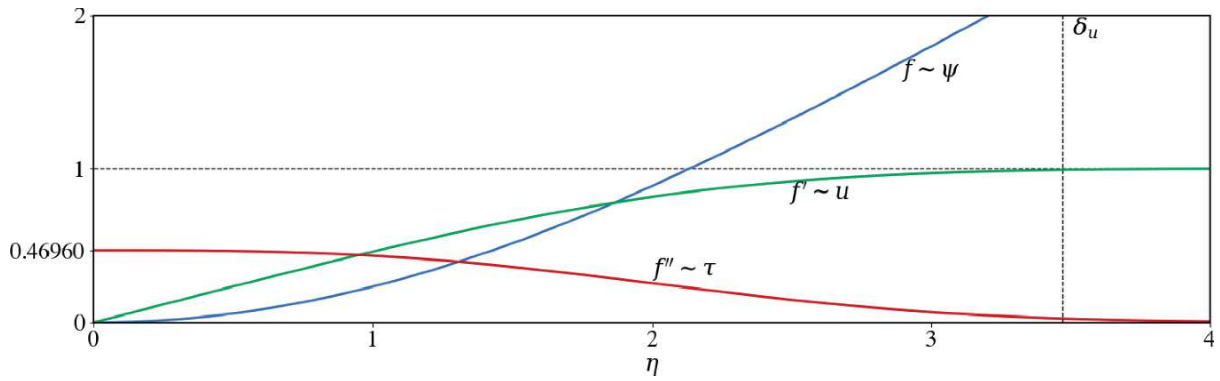


Fig. 5.12 Blasius solution for flat plate boundary layer flow. Shown are $f''(\eta)$, $f'(\eta)$ and $f(\eta)$ as functions of the similarity variable η

The boundary layer thickness δ_u, defined as the distance from the wall at which the velocity reaches 99% of the free-stream value, i.e., where $f' = 0.99$ occurs at $\eta \approx 3.5$. Back-substituting the similarity variable yields

$$\delta_u \approx \sqrt{\frac{2\nu x}{u_\infty}} \quad \text{or} \quad \frac{\delta_u}{x} = \frac{5.0}{\sqrt{\mathrm{Re}_x}} \ . \tag{5.73}$$

This result aligns with the scale estimate derived in Sect. 4.3.1. The wall shear stress, obtained from the velocity gradient at the wall, is evaluated by computing the value of $f''(0)$ from the Blasius solution. Using the definition of shear stress and substituting the similarity variable, the wall shear stress and the associated friction coefficient become

$$\tau_w = \mu \frac{\partial y}{\partial \eta}\Big|_w = \frac{\mu u_\infty f''(0)}{\sqrt{2\nu x/u_\infty}} \quad \text{or} \quad c_f = \frac{2\tau_w}{\rho u_\infty^2} \approx \frac{0.664}{\sqrt{\mathrm{Re}_x}} \ . \tag{5.74}$$

The drag coefficient over a plate of length L is obtained by integrating c_f along x to

$$C_D = \frac{1}{L}\int_0^L c_f \, dx = \frac{1.328}{\sqrt{\mathrm{Re}_L}} \ , \tag{5.75}$$

consistent with the scaling analysis of Sect. 4.3.1.

Pressure Gradient The flat plate boundary layer assumes a vanishing pressure gradient along the wall, that is $\partial p/\partial x = 0$, which simplifies the momentum equation as shown in Eq. (5.66). However, in most practical external flows, the geometry of the body induces a varying external velocity $U_\infty(x)$, resulting in a nonzero pressure gradient. Inside the boundary layer, the pressure must match that of the inviscid outer flow, and therefore the pressure gradient $\partial p/\partial x$ is imposed directly by the external flow. As derived in Sect. 4.3.1, the

pressure gradient can be expressed in terms of the external velocity as $dp/dx = -\rho U_\infty dU_\infty/dx$. For steady flow the boundary layer momentum equation in Eq. (5.66) simplifies to

$$u\frac{\partial u}{\partial x} + v\frac{\partial u}{\partial y} = U_\infty \frac{dU_\infty}{dx} + \nu\frac{\partial^2 u}{\partial y^2} \ , \tag{5.76}$$

At the wall, using the no-slip condition $u = 0$ at $y = 0$, the equation reduces to $U_\infty dU_\infty/dx + \nu\partial^2 u/\partial y^2 = 0$, meaning that the curvature of the velocity profile at the wall is directly determined by the streamwise pressure gradient. A favorable pressure gradient, corresponding to acceleration ($dU_\infty/dx > 0$), implies $\partial^2 u/\partial y^2 < 0$, indicating increased near-wall shear. An adverse pressure gradient, associated with deceleration ($dU_\infty/dx < 0$), leads to $\partial^2 u/\partial y^2 > 0$, signifying reduced wall shear and the potential onset of flow reversal.

Further insight is gained by differentiating the momentum equation with respect to *y*

$$\frac{\partial u}{\partial y}\frac{\partial u}{\partial x} + u\frac{\partial^2 u}{\partial x \partial y} + v\frac{\partial^2 u}{\partial y^2} + \frac{\partial v}{\partial y}\frac{\partial u}{\partial y} = \nu\frac{\partial^3 u}{\partial y^3} \ . \tag{5.77}$$

At the wall, where $u = v = 0$ and $\partial v/\partial y = 0$, this simplifies to show that $\partial^2 u/\partial y^2$ must attain an extremum at the wall. In the presence of an adverse pressure gradient, the velocity profile may develop a point of inflection, where the curvature of the profile changes sign. Qualitatively, this means that instead of smoothly bending toward the free-stream velocity, the velocity curve develops an S-shape, first curving upward steeply, then bending back toward the free stream with a flatter slope. Such a profile lacks the smooth convexity typical of favorable pressure gradient flows and is an early indicator of instability and risk of separation. As the adverse gradient intensifies, the wall shear stress $\tau_w = \mu(\partial u/\partial y)|_{y=0}$ diminishes and may ultimately vanish. Once reversed flow appears near the wall, boundary layer separation occurs.

Similarity solutions such as the Falkner-Skan family incorporate pressure gradients by prescribing a power-law external velocity profile $U_\infty(x) \sim x^m$, embedding the pressure gradient into the boundary layer formulation. These solutions allow systematic treatment of accelerating ($m > 0$) and decelerating ($m < 0$) flows and enable estimates of the critical conditions for separation. A comprehensive discussion is provided in White (1991) and Kays et al. (2005).

Blasius Flat Plate Thermal Solution for Constant Wall Temperature With the velocity profile known, we turn to the thermal boundary layer. The energy equation from Eq. (5.66) is used, with temperature boundary conditions from

Eq. (5.67). Again, viscous dissipation is neglected ($\mathrm{Ec} \to 0$), and both wall and free-stream temperatures are constant. We define the nondimensional temperature as

$$\theta(\eta) = \frac{T - T_w}{T_\infty - T_w} \ . \tag{5.78}$$

For the case of a self-similar solution, θ is only a function of η only. Substituting into the energy equation gives

$$\begin{aligned} \theta'' + \mathrm{Pr} \ f(\eta)\theta' = 0 \ , \\ \theta(\eta = 0) = 0, \quad \theta(\eta \to \infty) = 1 \ . \end{aligned} \tag{5.79}$$

This is a linear ODE, where $f(\eta)$ is taken from the Blasius solution and the Prandtl number Pr enters as a parameter. The temperature equation can be solved exactly by separation of variables (White 1991), yielding

$$\theta(\eta) = \frac{\displaystyle\int_0^\eta \exp\left(-\mathrm{Pr}\int_0^s f(t)\,dt\right) ds}{\displaystyle\int_0^\infty \exp\left(-\mathrm{Pr}\int_0^s f(t)\,dt\right) ds} \ . \tag{5.80}$$

The temperature profile can thus be evaluated by integrating the stream function, and is plotted in Fig. 5.13 for different Prandtl numbers. The thermal boundary layer thickness δ_T is identified by the η value at which $\theta \to 1$. The profiles are consistent with the interpretation of the Prandtl number as the ratio of flow to thermal boundary layer thickness discussed in Sect. 4.3.1. For $\mathrm{Pr} = 1$, the flow and thermal boundary layers correspond at $\eta \approx 3.5$. For $\mathrm{Pr} \gg 1$, viscous effects dominate over thermal diffusion, resulting in $\delta_T < \delta_u$. Conversely, for $\mathrm{Pr} \ll 1$, thermal diffusion dominates, leading to $\delta_T > \delta_u$. The ratio δ_T/δ_u is approximated by $\delta_T/\delta_u \approx \mathrm{Pr}^{-0.4}$, as shown in Fig. 5.14 (White 1991).

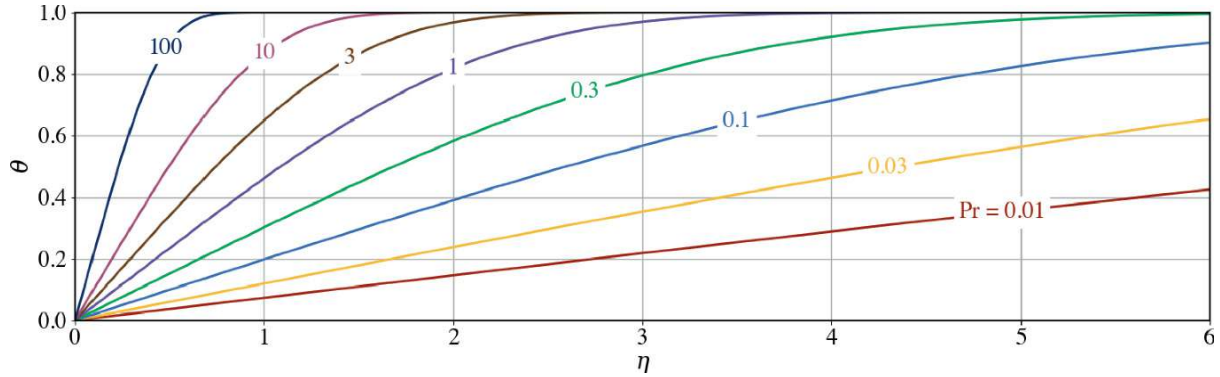


Fig. 5.13 Nondimensional temperature profiles $\theta(\eta)$ for various Prandtl numbers Pr over a flat plate with constant wall temperature

Following Fourier's law, the wall heat transfer $\dot{q}_w$ is given by the temperature gradient at the wall

$$\dot{q}_w = -k \frac{\partial T}{\partial y}\Big|_{y=0} = -k(T_\infty - T_w)\theta'(0)\sqrt{\frac{u_\infty}{2\nu x}} \ . \tag{5.81}$$

In nondimensional terms

$$\mathrm{Nu}_x = \frac{hx}{k} = \frac{\theta'(0)}{\sqrt{2}}\ \mathrm{Re}_x^{1/2} \ , \tag{5.82}$$

where the wall gradient is evaluated by

$$\theta'(0) = \frac{1}{\displaystyle\int_0^\infty \exp\left(-\,\mathrm{Pr}\int_0^\eta f ds\right) d\eta} \ . \tag{5.83}$$

It is remarkable that for all similarity solutions, the relation $\mathrm{Nu}_x\,/\sqrt{\mathrm{Re}_x} = \text{const.}$ holds, with the constant depending on Pr, that is $\mathrm{Nu}_x\,/\sqrt{\mathrm{Re}_x} = f(\mathrm{Pr})$. For $\mathrm{Pr} = 1$, the nondimensional temperature and velocity profiles coincide. A widely used approximation is $\theta'(0)/\sqrt{2} \approx 0.332\ \mathrm{Pr}^{1/3}$, which satisfies the correct gradient at $\mathrm{Pr} = 1$, leading to the classical correlation

$$\mathrm{Nu}_x = 0.332\ \mathrm{Pr}^{1/3}\ \sqrt{\mathrm{Re}_x} \ . \tag{5.84}$$

The correlation is plotted in Fig. 5.14 along with the computed wall gradients. For $\mathrm{Pr} = 1$, it satisfies the matching nondimensional velocity gradient at the wall as described by Eq. (5.74) and is valid for Prandtl numbers close to unity. For $\mathrm{Pr} > 0.2$, it matches the exact solution within about $\pm 5\%$. Variants of the correlation for extended Pr ranges are discussed in Sect. 9.3.

As an alternative approach to evaluating the integral solution, the numerical formulation of the Blasius system can be extended. The solution vector is expanded to $\mathbf{y} = (y_1, y_2, y_3, y_4, y_5)^\top = (f'', f', f, \theta', \theta)^\top$ and the ODE system to integrate becomes $\mathbf{y}' = (-y_1 y_3, y_1, y_2, -\,\mathrm{Pr}\ y_3 y_4, y_4)^\top$. Solving with a shooting method for the boundary condition $\theta(\infty) = 1$ requires adjusting the integration domain, especially for small $\mathrm{Pr} < 1$, where the thermal boundary layer exceeds the velocity boundary layer. In these cases, the numerical integration domain

must be extended beyond the typical range (e.g., $\eta = 10$) to ensure the solution captures the asymptotic behavior of the temperature profile.

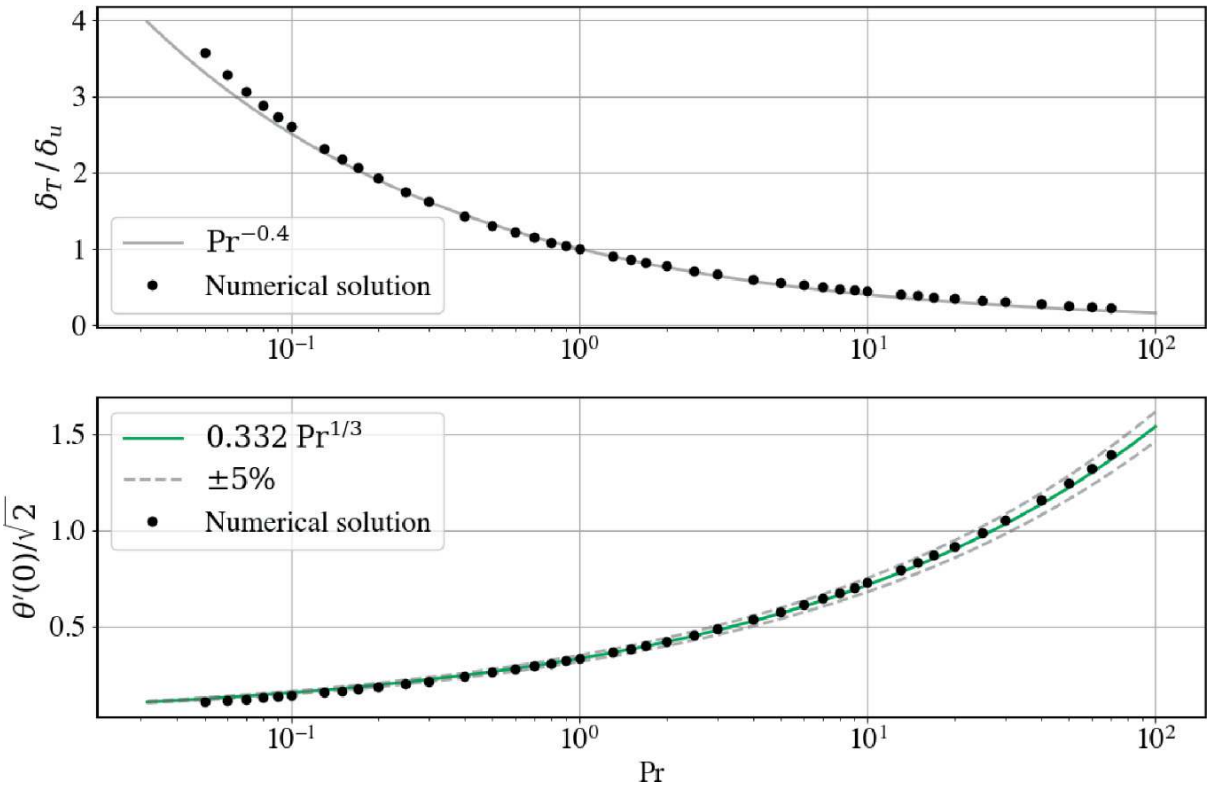


Fig. 5.14 Ratio of the thermal boundary layer thickness to flow boundary layer thickness δ_T/δ_u over the Prandtl number Pr (top). Nondimensional temperature gradient at the wall $\theta'(0)$ (bottom)

Reynolds Analogy The similarity between the momentum and energy equations in boundary layer theory leads to the classical **Reynolds analogy**, which relates heat and momentum transfer. For laminar flow over a flat plate with $\mathrm{Pr} = 1$, the momentum and energy equations take the same form. As a result, the nondimensional momentum and thermal boundary layers exhibit self-similarity and can be mapped onto each other. As discussed above, the hydrodynamic and thermal boundary layer thicknesses are equal when $\mathrm{Pr} = 1$. The analogy regards the direct proportionality between the wall heat transfer and the wall shear stresses

$$\frac{|\dot{q}_w|}{\tau_w} = \frac{k(\partial T)/(\partial y)_w}{\mu(\partial u)/(\partial y)_w} \approx \frac{k}{\mu}\left|\frac{dT}{du}\right|_w , \tag{5.85}$$

which links the thermal and velocity gradients at the wall. In nondimensional terms, this leads to a relation between the Stanton number $\mathrm{St} = \mathrm{Nu}_x/(\mathrm{Re}_x \mathrm{Pr})$, and the local skin-friction coefficient, $c_f = \tau_w/(\rho u_\infty^2/2)$, as

$$\mathrm{St} = \frac{c_f}{2}. \tag{5.86}$$

This result shows that knowing the skin-friction coefficient is sufficient to estimate the heat transfer rate. A similar relation can also be derived for turbulent flow, making the Reynolds analogy a useful tool for estimating the heat transfer coefficient, especially in early-stage analysis (Kays et al. 2005).

The classical form of the Reynolds analogy holds best for $\mathrm{Pr} \approx 1$, where the velocity and thermal boundary layers have similar structures. For other Prandtl numbers or more complex flow geometries, empirical corrections are necessary. For instance, in stagnation-point flow over a flat surface, the analogy is modified to $\mathrm{St}\ /(c_f/2) \approx 0.23\ \mathrm{Pr}^{-0.6}$, valid in the range $0.1 < \mathrm{Pr} < 10$ for planar boundary layers (White 1991). While not exact, the Reynolds analogy remains a valuable engineering tool for estimating convective heat transfer based on known momentum transfer, particularly in laminar boundary layers over simple geometries.

5.2.2 Flow Past a Sphere

An illustrative example of external flow around a body is the steady flow of a viscous fluid past a sphere. The formulation of the drag acting on a sphere in free flow dates back to the mid-nineteenth century, originally motivated by the need to better understand the motion of pendulums in air, which was crucial for improving clock accuracy (Michaelides 1997). Since then, the flow around a sphere has become a classical benchmark problem in fluid dynamics, with numerous applications across disciplines. The problem has been extensively studied, and the fundamental behavior is well understood.

We consider a rigid sphere of diameter D immersed in an otherwise steady and uniform flow of velocity U_∞. To begin, we focus on the regime of low Reynolds number $\mathrm{Re}_D \ll 1$, where viscous forces dominate over inertial effects. The Reynolds number based on the sphere diameter is defined as $\mathrm{Re}_D = \rho U_\infty D/\mu$. In this creeping flow regime, the Navier-Stokes equations simplify considerably, as discussed in Sect. 4.3.4. The analytical solution for this case is known as the classical Stokes solution, and its derivation is detailed in Appendix B.2. In that derivation, a sphere of radius $R = D/2$ is considered and spherical coordinates are used to utilize the axial symmetry. Here, we present the main physical results of that analysis and discuss their implications.

Creeping Flow Solution Under the assumption of axisymmetry and steady, incompressible, creeping flow, the velocity components in spherical coordinates are derived in Eq. (5.87) to

(5.87)

$$
\begin{aligned}
u_r &= U_\infty \cos\theta \left(1 - \tfrac{3R}{2r} + \tfrac{R^3}{2r^3}\right) \,, \\
u_\theta &= -U_\infty \sin\theta \left(1 - \tfrac{3R}{4r} - \tfrac{R^3}{4r^3}\right) \,.
\end{aligned}
$$

As expected, the velocity field tends asymptotically to the uniform free-stream flow for $r \to \infty$. The inverse powers of r describe the perturbation induced by the sphere and show that the effect of viscous retardation extends well beyond the immediate vicinity of the surface. Notably, at a radial distance $r = D$, the flow velocities remain at $\approx 0.5 U_\infty$ and at $r = 5D$ distance still at $\approx 0.9 U_\infty$. The pressure field associated with the Stokes flow is given by Eq. (5.88) to

$$
p(r,\theta) = p_\infty - \tfrac{3}{2} \tfrac{\mu U_\infty R}{r^2} \cos\theta \,. \tag{5.88}
$$

The pressure difference relative to p_∞ is positive at the front and negative at the back of the sphere (White 1991), creating a net pressure-induced drag along the flow direction. At the surface of the sphere ($r = R$), the pressure distribution simplifies to

$$
\Delta p = -\tfrac{3}{2} \tfrac{\mu U_\infty}{R} \cos\theta \,. \tag{5.89}
$$

The shear stress on the sphere's surface, due to viscous effects, is proportional to the tangential velocity gradient and given by

$$
\tau_w = \tfrac{3}{2} \tfrac{\mu U_\infty}{R} \sin\theta \,. \tag{5.90}
$$

A cross-sectional visualization of the velocity field, streamlines, and surface stresses is shown in Fig. 5.15. This planar section is aligned with the flow direction and passes through the center of the sphere.

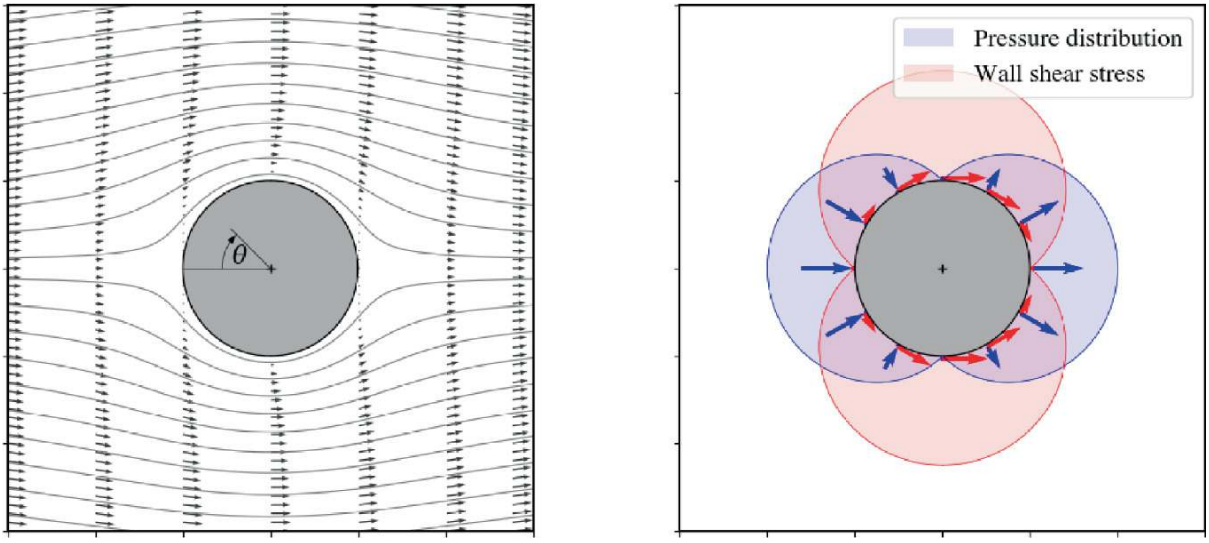


Fig. 5.15 Steady flow of a viscous fluid past a sphere for $\mathrm{Re}_D \ll 1$ (left). Pressure and shear stress on the surface of a sphere (right)

At very low Reynolds numbers, the flow pattern is symmetric about the free-stream axis and front-to-back with respect to the sphere. The no-slip condition ensures zero velocity at the surface, while the flow transitions smoothly to the uniform stream at infinity. The viscous shear stress is largest at the equator ($\theta = \pi/2$), where the surface velocity gradient is greatest, and vanishes at the front and rear stagnation points. The pressure distribution exhibits perfect symmetry as well, with a high-pressure region at the front ($\theta = 0$) and a low-pressure region at the back ($\theta = \pi$).

The **total drag force** on the sphere is the result of both pressure and viscous shear contributions. Projecting the stress tensor onto the flow direction and integrating over the sphere surface, as derived in Appendix B.2, yields the drag force

$$F_D = 3\pi\mu U_\infty D \ . \tag{5.91}$$

This classical result is known as **Stokes' law**, and shows that the drag force is linearly proportional to the fluid viscosity μ, the free-stream velocity U_∞, and the sphere diameter D. Of this total drag, $1/3$ is contributed by the pressure force and $2/3$ by the viscous shear. The corresponding nondimensional drag coefficient is defined as

$$C_D = \frac{F_D}{\frac{1}{2}\rho U_\infty^2 \pi R^2} = \frac{24}{\mathrm{Re}_D} \ , \tag{5.92}$$

which is known as the **Stokes formula** for the drag coefficient. The drag coefficient decreases inversely with the Reynolds number in this creeping flow regime, reflecting the dominance of viscous effects at small scales. The variation of C_D with Reynolds number is illustrated in Fig. 5.17, and the changes in flow structure for increasing Re_D are discussed in the following sections.

Despite the presence of viscosity, the streamline pattern in creeping flow appears superficially similar to that of inviscid potential flow discussed in Sect. 4.3.3. The idealized flow around a sphere can be constructed by superposing a uniform stream with a source-sink pair (Lamb 1932). Both flows exhibit axial symmetry and a smooth pattern of streamlines. However, the resemblance is limited. In potential flow, the velocity remains finite at the surface and no-slip is not enforced, whereas in creeping flow the velocity vanishes on the boundary. Moreover, the pressure distribution in inviscid flow is symmetric, resulting in zero net force on the sphere, while in viscous flow the asymmetry in pressure, combined with shear stress, produces a finite drag. Despite the similarity in streamline patterns, the respective flows exhibit fundamentally different force balances and boundary behavior.

Regimes at Higher Reynolds Numbers So far, we have considered the case of steady flow past a sphere in the creeping flow regime, where the Reynolds number $\mathrm{Re}_D \ll 1$ and the Stokes solution applies. In this section, we extend the discussion to regimes of higher Reynolds numbers, where inertial effects become increasingly significant and lead to changes in the observed flow patterns, as discussed by Southard (2006) or White (1991).

As the Reynolds number increases from very small values, the assumptions of creeping flow remain valid for some time. In the range $\mathrm{Re}_D \ll 1$, the flow belongs to Regime A in Fig. 5.16. As discussed in the previous section, in this regime the streamlines are symmetric, and the entire flow field is dominated by viscous effects. The flow is steady, axisymmetric, and extends smoothly outward over many diameters. Despite the presence of viscosity, the streamline pattern is qualitatively similar to that of inviscid potential flow, apart from the fact that the no-slip condition enforces zero velocity on the surface of the sphere.

As the Reynolds number increases to approximately $\mathrm{Re}_D \approx 1$, the solution still satisfies the creeping flow equations, but subtle asymmetries begin to appear. The streamlines diverge more rapidly on the upstream side and converge more slowly downstream. Although there is still no flow separation, the pressure field is no longer perfectly symmetric. The velocity disturbance continues to extend far from the sphere, and Stokes' law provides a reasonable approximation for the drag, though deviations begin to grow.

With further increase to $\mathrm{Re}_D \approx$ 10-100, the first signs of separation occur, as sketched in Regime B in Fig. 5.16. A ring vortex, that is a closed recirculating flow region, forms immediately behind the sphere. This eddy is attached to the surface and remains steady and axisymmetric. Outside the eddy, the streamlines deviate from the surface, indicating the onset of separation. The presence of the ring vortex signifies a shift in the drag mechanism. Pressure effects now contribute significantly to the form drag, so that the total drag begins to deviate noticeably from the Stokes prediction. The overall flow remains laminar and stable, and there is no unsteadiness in the wake.

As the Reynolds number increases further to $\mathrm{Re}_D \approx$ 100-150, the flow enters Regime C of Fig. 5.16, in which the previously steady ring vortex becomes unsteady and oscillates in space. The oscillation may involve shifting of the vortex center or subtle time-periodic deformations of the recirculating region. This is the beginning of unsteady behavior in the wake, although vortex shedding has not yet fully developed. The flow remains largely laminar, but temporal effects are now present, leading to fluctuating forces on the sphere. These oscillations are precursors to the periodic vortex shedding that will dominate the next regime.

When Re_D reaches approximately 150 or above, the flow is characterized by the periodic shedding of ring vortices from the rear of the sphere, sketched as Regime D in Fig. 5.16. These vortices form near the separation point, then detach and are carried downstream by the flow, creating a time-periodic pattern in the wake. This vortex shedding process is analogous to the von Kármán vortex street observed behind cylinders, but occurs in three dimensions. The wake becomes increasingly turbulent as the Reynolds number rises within this range (up to about $\mathrm{Re}_D \approx 10^4$), although the boundary layer on the sphere front side typically remains laminar. The drag force now includes significant contributions from both pressure drag and unsteady wake interactions, and the flow is no longer symmetric or steady.

At even higher Reynolds numbers, in the range $\mathrm{Re}_D \approx 10^3$–$2.5 \times 10^5$, the flow transitions to Regime E. In this regime, the wake is fully turbulent, and its structure becomes increasingly irregular and chaotic. The separation point remains relatively fixed at $\approx 70^\circ$–80° from the front stagnation point but becomes less sharply defined due to the turbulent nature of the flow. Although the boundary layer on the sphere remains laminar, it is now very thin and susceptible to transition. The drag is dominated by form drag resulting from the large wake, while viscous shear contributions are minimal. The drag coefficient

stabilizes in this range at $C_D \approx 0.4$–0.45 and is relatively insensitive to further increases in Re_D, often referred to as the drag plateau.

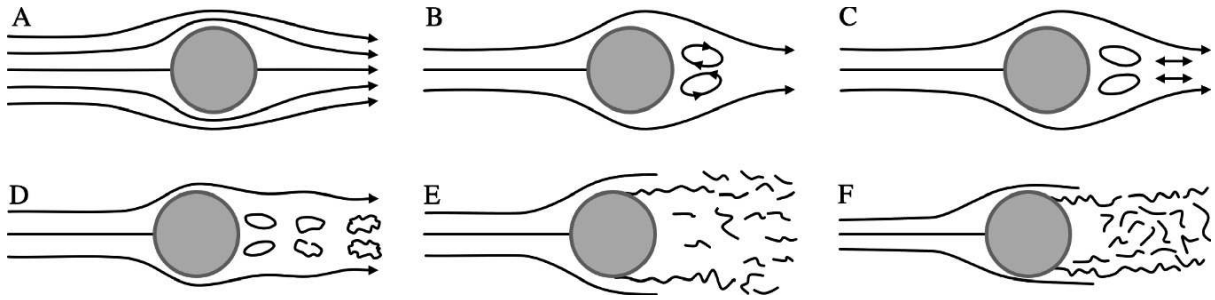


Fig. 5.16 Schematic patterns of flow around a sphere for several values of Reynolds number for increasing Re_D, adapted from Southard (2006)

Finally, at Reynolds numbers beyond $\mathrm{Re}_D \approx 2.5 \times 10^5$, corresponding to Regime F in Fig. 5.16, the boundary layer undergoes transition from laminar to turbulent *before* separation occurs. In laminar separation (as seen in Regime E), the adverse pressure gradient near the rear of the sphere causes earlier detachment of the boundary layer, resulting in a wide wake and large pressure drag. However, in Regime F, the turbulent boundary layer, being more resistant to adverse pressure gradients due to enhanced momentum transport, remains attached longer. As a result, separation is delayed and occurs farther downstream, typically at an angular position of $\approx 120^\circ$–130° from the front stagnation point. This downstream shift in the separation point has two important effects. First, the low-pressure region behind the sphere becomes narrower, reducing the overall contribution of pressure drag. Second, the pressure on the rear surface of the sphere increases significantly due to better flow attachment, improving pressure recovery. The net result is an abrupt and significant reduction in total drag. The drag coefficient C_D, which remained nearly constant at around 0.4 in Regime E, now drops sharply to values as low as $C_D \approx 0.1$ in Regime F, a phenomenon commonly known as the **drag crisis**. The drag crisis is highly sensitive to disturbances in the flow and to surface properties of the sphere. A perfectly smooth sphere in a low turbulence free-stream flow may experience the drag crisis at higher Reynolds numbers than a rough sphere or one exposed to upstream turbulence. Surface roughness, in particular, can trigger earlier boundary layer transition and thus cause an earlier drag crisis.

The flow in Regime F is fully turbulent, both in the wake and in the boundary layer prior to separation. Despite the turbulence, the flow field is more compact and streamlined compared to the wide, detached wake of Regime E. As Re_D

increases further beyond the drag crisis, the drag coefficient gradually begins to rise again due to increasing skin friction, but it remains well below the 0.4 plateau.

It is noteworthy that the successive flow regimes, from creeping motion with symmetric streamlines to turbulent separation with dramatically reduced drag, are all governed primarily by the Reynolds number, though the exact transition ranges are approximate and as mentioned depend sensitively on secondary properties such as surface roughness, free-stream turbulence, and upstream disturbances.

Drag Correlations Beyond the creeping flow regime, where Stokes' law accurately predicts the drag force on a sphere, the drag behavior becomes increasingly complex and must be described empirically. As detailed by Clift et al. (2005), numerous empirical correlations have been developed to capture the steady-state drag coefficient over different ranges of the Reynolds number Re_D, each with varying degrees of accuracy depending on the flow regime. The experimentally observed variation of the drag coefficient with Reynolds number (White 1991), along with selected empirical correlations discussed below, is shown in Fig. 5.17.

For practical purposes, the drag force acting on a sphere is typically expressed in the standard form

$$\mathbf{F}_D = \tfrac{1}{2}\rho C_D A U_\infty^2 \ , \tag{5.93}$$

where C_D is the nondimensional drag coefficient, ρ is the fluid density, U_∞ is the free-stream velocity, and $A = \pi D^2/4$ is the projected frontal area of the sphere.

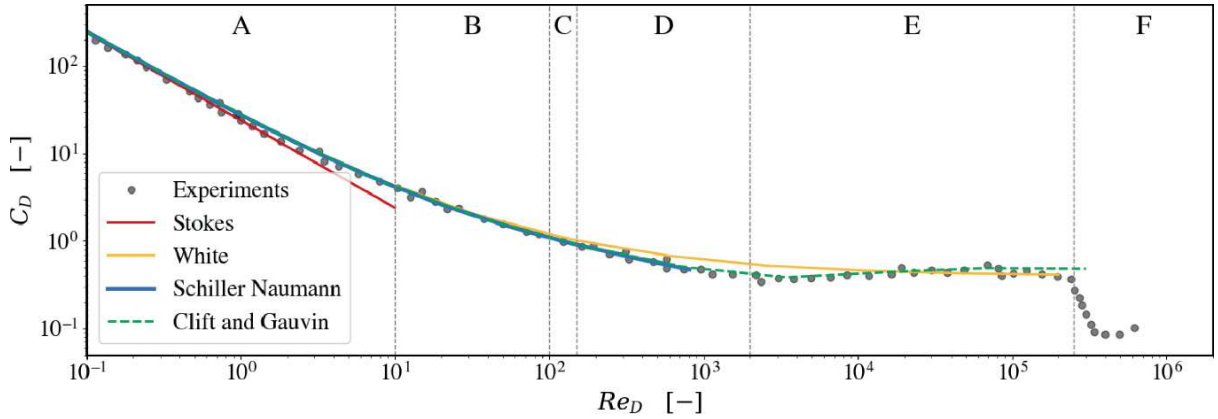


Fig. 5.17 Drag coefficient of a sphere over the Reynolds number for experimental data (White 1991) and selected empirical correlations

In the creeping flow regime ($\mathrm{Re}_D \ll 1$), the drag coefficient follows directly from the analytical solution derived in Appendix B.2, yielding $C_D = 24/\ \mathrm{Re}_D$. The expression reflects the dominance of viscous, that is, skin-friction forces, arising from the no-slip condition along the sphere surface. As discussed in the previous section, as the Reynolds number increases, inertial effects begin to modify the flow field. In particular, flow separation and wake formation introduce increasing contributions from pressure drag, which eventually dominates the total drag. To capture these effects while preserving the inverse scaling of Stokes' law, many empirical correlations have been proposed in the form

$$C_D = \frac{24}{\mathrm{Re}_D}\ g(\mathrm{Re}_D)\ , \tag{5.94}$$

where $g(\mathrm{Re}_D)$ is a Reynolds number dependent correction function that accounts for inertial influences. One of the most widely used correlations was introduced by Schiller and Naumann (1933), valid for moderate Reynolds numbers up to approximately $\mathrm{Re}_D < 800$ with

$$g(\mathrm{Re}_D) = 1 + 0.15\ \mathrm{Re}_D^{0.687}\ . \tag{5.95}$$

This correlation is plotted in Fig. 5.17. It remains accurate to within a few percent over its validity range and provides a simple yet effective extension to the Stokes drag formula. To improve accuracy over a broader range, particularly in the regime approaching the drag crisis, Clift and Gauvin (1970) extended the Schiller-Naumann formula by introducing an additional inertial term with

$$g(\mathrm{Re}_D) = 1 + 0.15\ \mathrm{Re}_D^{0.687} + \frac{0.0175\mathrm{Re}_D}{1+4.25\times10^4\mathrm{Re}_D^{-1.16}} \quad \text{for} \quad \mathrm{Re}_D < 3\times10^5\ . \tag{5.96}$$

As shown in Fig. 5.17, the extended formulation improves agreement with experimental data, capturing the gradual transition from laminar to unsteady and eventually turbulent wake flow.

An alternative expression is presented by White (1991), who added terms to account separately for viscous drag at low Reynolds numbers and form drag dominating at higher Reynolds numbers with

$$C_D = \frac{24}{\mathrm{Re}_D} + \frac{6}{1+\sqrt{\mathrm{Re}_D}} + 0.4 \qquad \text{for} \quad \mathrm{Re}_D < 2\times10^5\ . \tag{5.97}$$

This additive fit transitions smoothly from the Stokes regime at low Re_D to the asymptotic value $C_D \approx 0.4$ observed in the turbulent wake regime. It is accurate

within about 10% across its range and is particularly useful for covering intermediate flow regimes with low complexity.

As discussed in the previous section, increasing Reynolds number leads to a sequence of flow transitions, the onset of separation, unsteady wake dynamics, vortex shedding, and finally turbulent boundary layer separation. These transitions manifest as sharp variations in the drag coefficient, culminating in the well-known drag crisis around $\mathrm{Re}_D \approx 2.5 \times 10^5$. In this regime, the boundary layer becomes turbulent before separation, significantly improving rear pressure recovery and reducing the overall drag to a minimum of approximately $C_D \approx 0.1$. Note that the abrupt drop in drag associated with the drag crisis is not captured by the empirical correlations presented here, which remain valid only up to the onset of this regime.

5.3 Internal Flow

Internal flows are characterized by the fluid motion constrained by solid boundaries, like ducts, pipes, or channels. In contrast to external flows, where the boundary layers develop freely into an unconfined domain, internal flows are confined by walls on all sides, and the flow domain is entirely bounded. The presence of enclosing surfaces makes all friction and heat transfer inherently important features of internal flows.

A significant feature of internal flow is the development of velocity and temperature profiles from the entrance region toward a fully developed state. Near the entrance, the velocity distribution evolves from its initial form under the effect of viscosity. Over a certain entry length, the boundary layers merge, and the flow reaches a steady distribution that no longer changes in the streamwise direction. In this fully developed region, the velocity profile remains invariant along the main flow axis, and analytical solutions become possible for simple geometries. However, in practical systems, the flow is often influenced by geometrical features such as fittings, bends, expansions, and contractions. These features introduce complex phenomena such as flow separation, secondary flows, and additional pressure losses, which require modeling beyond the fully developed approximation.

In this section we begin with fully developed laminar pipe flow, described by the classic Hagen-Poiseuille solution. It then addresses heat transfer in circular ducts, considering both constant wall heat flux and constant wall temperature boundary conditions, and extensions to noncircular ducts are considered. The analysis proceeds to the turbulent regime, where empirical correlations for friction and velocity profiles are examined, including the influence of surface

roughness. The final part of the section reviews localized flow features such as pipe entrances, sudden expansions, and contractions, emphasizing their impact on pressure loss and the necessity of empirical loss coefficients. Throughout the section, internal flow models are formulated within the quasi-one-dimensional framework introduced earlier, where wall effects are represented by subscale models. These models allow wall shear stress and convective heat transfer to be incorporated as effective source terms, ensuring a consistent system-level treatment of momentum and energy transport.

5.3.1 Circular Pipe Flow

Incompressible internal flows through pipes and ducts can be effectively analyzed within the quasi-one-dimensional framework introduced earlier, where the effects of viscosity are captured through a pressure drop along the flow direction. Instead of resolving the detailed velocity gradients in the cross-section, wall friction is modeled as a reduction in total pressure, expressed through a nondimensional loss coefficient $\zeta = \Delta p_t / (\rho u^2/2)$. The formulation applies to both continuous and localized losses, where **continuous pressure losses** arise due to shear stresses at the wall and the resulting velocity gradients in fully developed pipe or duct flow. **Localized losses** occur at geometrical discontinuities such as expansions, contractions, bends, or fittings, where complex flow phenomena like separation or vortex shedding introduce additional dissipation.

To analyze losses, we begin with a case where the velocity profile can be derived analytically, that is, the **fully developed laminar flow** in a circular pipe, known as Hagen-Poiseuille flow. This case serves as a foundational example to illustrate how wall friction manifests as pressure loss, and how it can be quantified in a reduced-order model.

Hagen-Poiseuille Flow Consider the steady, incompressible, fully developed laminar flow through a straight, horizontal circular pipe of radius $R = d/2$. The pipe is assumed to be infinitely long in the streamwise direction, with the flow aligned along the *x*-axis in cylindrical coordinates (r, φ, x). The flow is symmetric in the circumferential direction, so that $\partial/\partial\varphi = 0$. For a fully developed flow the axial velocity does not vary along the pipe, so that $\partial u/\partial x = 0$. The radial and circumferential velocity components vanish, thus $u_r = u_\varphi = 0$, and the only nonzero velocity component is in the axial direction, that is $u_x = u$. Along the pipe wall, the no-slip boundary condition applies, so that $u(R) = 0$. Expanding the continuity and momentum equations in cylindrical coordinates, as

provided in Appendix A, and applying the above simplifications, the governing equations reduce to

$$\begin{aligned} \frac{\partial u}{\partial x} &= 0 \ , \\ 0 &= \frac{\partial p}{\partial r} \ , \\ 0 &= -\frac{\partial p}{\partial x} + \mu\left(\frac{\partial^2 u}{\partial r^2} + \frac{1}{r}\frac{\partial u}{\partial r} \right) \ . \end{aligned} \tag{5.98}$$

From the continuity equation, the condition $\partial u/\partial x = 0$ together with $u_r = 0$ implies that the axial velocity depends only on the radial coordinate, thus $u = u(r)$. The second equation confirms that the pressure is uniform in the radial direction, so that $p = p(x)$. The *x*-momentum equation describes the axial velocity profile, with pressure gradient acting as the driving force. Since the pressure gradient $\partial p/\partial x$ does not depend on *x*, it needs to be constant. That implies that the pressure decreases linearly along the pipe length, so that $\partial p/\partial x = -\Delta p/\ell$, with ℓ denoting the pipe length. The axial velocity profile can be obtained by integrating the *x*-momentum equation in Eq. (5.98) twice to

$$u(r) = \frac{dp}{dx}\frac{r^2}{4\mu} + c_1 \ln r + c_2 \ . \tag{5.99}$$

To ensure physical validity, the velocity must remain finite along the center line ($r = 0$), so we set $c_1 = 0$. Applying the no-slip boundary condition at the pipe wall $u(R) = 0$ determines c_2, yielding the velocity profile to

$$u(r) = \frac{R^2}{4\mu}\frac{dp}{dx}\left[1 - \left(\frac{r}{R}\right)^2\right] = \frac{\bar{u}}{2}\left[1 - \left(\frac{r}{R}\right)^2\right] \ . \tag{5.100}$$

This is the classic parabolic velocity distribution of Hagen-Poiseuille flow, with maximum velocity $u_{\max} = u(0) = 2\bar{u}$ at the centerline. The mean velocity $\bar{u}$ is obtained by averaging over the cross-section

$$\bar{u} = \frac{1}{\pi R^2}\int_0^R u(r) 2\pi r \, dr = \frac{R^2}{8\mu}\frac{dp}{dx} \ . \tag{5.101}$$

The corresponding volume flow rate is

$$Q = \bar{u}\pi R^2 = \frac{\pi R^4}{8\mu}\frac{dp}{dx} \ , \tag{5.102}$$

known as the **Hagen-Poiseuille equation**, which expresses the linear relationship between pressure gradient and volume flow rate in fully developed

laminar pipe flow. The equation highlights the strong dependence of flow rate on pipe radius, scaling with $Q \sim R^4$, as experimentally confirmed with high accuracy for the laminar regime (Spurk 1996, p. 162).

The relation can be rearranged to $dp/dx = 8\mu\bar{u}/R^2$ to provide a direct expression for the pressure gradient in terms of the mean flow velocity. To express the pressure loss in nondimensional form, the pipe diameter based Reynolds number is defined employing the mean velocity $\bar{u}$ to $\mathrm{Re}_d = \rho d\bar{u}/\mu$. The dimensionless friction coefficient for laminar flow can then be derived to

$$f = \frac{dp}{dx}\frac{2R}{\rho\bar{u}^2/2} = \frac{64}{\mathrm{Re}_d} \ . \tag{5.103}$$

The loss coefficient ζ represents the nondimensional pressure loss with

$$\zeta = \frac{\Delta p}{\rho\bar{u}^2/2} = \frac{64\mu\ell}{\rho\bar{u}d^2} = \frac{\ell}{d}\frac{64}{\mathrm{Re}_d} \ . \tag{5.104}$$

The friction coefficient and the loss coefficient are related by $\zeta = f\ell/d$, indicating that the pressure loss depends on the two nondimensional numbers Re_d and ℓ/d. At fixed Reynolds number, the pressure loss increases linearly with pipe length ℓ and decreases with increasing diameter d. For short pipes, flow friction and the resulting pressure losses are typically negligible, but as the pipe length increases, friction becomes increasingly significant.

The viscous shear induces mechanical **energy dissipation**, converting kinetic energy into internal energy, and can be calculated with Eq. (3.57) employing the determined velocity field (Bejan 1995). Rewriting in cylindrical coordinates, the local dissipation per unit volume follows to

$$\Phi = \mu\left(\frac{\partial u}{\partial r}\right)^2 = 64\mu\frac{\bar{u}^2}{d^2}\left(\frac{r}{R}\right)^2 \ . \tag{5.105}$$

This function has a parabolic shape, peaking near the wall where velocity gradients are steepest, and vanishing at the centerline. The total rate of energy dissipation over a length ℓ is obtained by integrating over the cross-sectional area to

$$\dot{E}_{\mathrm{diss}} = \int_0^\ell \int_0^R \Phi \ 2\pi r \, dr \, dx = 8\pi\mu\bar{u}^2\ell \ . \tag{5.106}$$

Alternatively, the same result can be obtained by employing the energy balance along the pipe boundaries at inlet and exit. Due to continuity the velocity at inlet

and outlet remain equal, while the static pressure drops by Δp. The dissipated energy amounts to

$$\dot{E}_{\mathrm{diss}} = \dot{m}\frac{\Delta p}{\rho} = \zeta \dot{m}\frac{\bar{u}^2}{2} \quad , \tag{5.107}$$

where $\dot{m} = \rho Q = \rho \pi R^2 \bar{u}$. Substituting the pressure drop from the Hagen-Poiseuille equation (5.102) confirms the previous result obtained from the velocity field based calculation. Rearranging the expression also allows the loss coefficient ζ to be interpreted as the ratio of dissipated energy to the kinetic energy flow $\zeta = \dot{E}_{\mathrm{diss}}/\dot{E}_{\mathrm{kin}}$. Note that the loss does not affect the kinetic energy, which remains constant for flow through a pipe of uniform diameter, but instead reduces the static pressure. Assuming the pipe is otherwise perfectly adiabatic, the dissipated energy manifests as a temperature increase at the outlet, given by $\Delta T = \dot{E}_{\mathrm{diss}}/(\dot{m}c)$. However, this temperature rise is typically negligibly small, as illustrated in the following example.

Example 5.1 Consider an $\ell = 10\,\mathrm{m}$ long horizontal pipe of diameter $d = 10\,\mathrm{mm}$, with a mean velocity $\bar{u} = 1\,\mathrm{m/s}$. Water and air are compared as two fluids, using standard material properties from Table 3.2. With a ratio $\ell/d = 1000$, the fully developed flow assumption is justified. The Reynolds numbers are $\mathrm{Re}_{d,\mathrm{water}} = 998$ and $\mathrm{Re}_{d,\mathrm{air}} = 657$, confirming the flow is laminar for both. The resulting loss coefficients are $\zeta_{\mathrm{water}} = 64.1$ and $\zeta_{\mathrm{air}} = 97.3$, indicating a high multiple of the kinetic energy flow is dissipated when the fluid passes through the pipe. The required pressure difference between pipe in- and outlet in order to facilitate the mean velocity follows from Eq. (5.102) to $\Delta p = 8\mu Q\ell/(\pi R^4)$ to $\Delta p_{water} = 32 \times 10^3\,\mathrm{Pa}$ and only $\Delta p_{air} = 58\,\mathrm{Pa}$. The resulting temperature rise due to dissipation is marginally small with $\Delta T_{\mathrm{water}} \approx 7.7 \times 10^{-3}\,\mathrm{K}$ and $\Delta T_{\mathrm{air}} \approx 5.7 \times 10^{-5}\,\mathrm{K}$.

Finally, we also want to examine the **wall shear stress**, which is the physical origin of the pressure drop described above. The frictional losses in fully developed laminar pipe flow are entirely due to the viscous shear acting at the pipe wall. The momentum balance for a cylindrical fluid element of radius R yields $dp/dx = 2\tau_w/R$, allowing the wall shear stress to be determined from the velocity profile in Eq. (5.100) as

$$\tau_w = \frac{R}{2}\frac{dp}{dx} = -\mu \frac{\partial u}{\partial r}\bigg|_w = \frac{4\mu\bar{u}}{R} \quad . \tag{5.108}$$

The wall shear stress is directly proportional to the mean velocity and inversely proportional to the pipe radius, capturing the viscous resistance exerted at the boundary. As the driving mechanism behind pressure loss in laminar pipe flow, it provides a direct link between the velocity distribution and the pressure gradient. Nondimensionalizing the wall shear stress with the dynamic pressure yields the **skin-friction coefficient**.

$$c_f = \frac{\tau_w}{\rho \bar{u}^2/2} = \frac{16}{\mathrm{Re}_d} \ . \tag{5.109}$$

This compact expression is a defining result of fully developed laminar pipe flow. It reveals that the wall friction scales inversely with the Reynolds number, and unlike in turbulent flow, is entirely governed by viscous effects. In this regime, the friction factor is independent of pipe roughness, highlighting the dominance of molecular viscosity over inertial or surface effects as will be discussed in more depth in Sect. 5.3.2.

Temperature Profiles In the following, we examine the temperature distribution for fully developed laminar flow inside a smooth circular tube. We assume constant thermophysical properties and a symmetric configuration, so that $\partial/\partial\varphi = 0$. The velocity profile is taken from the previously derived fully developed Hagen-Poiseuille flow, as given in Eq. (5.100), where the radial and azimuthal velocity components vanish ($u_r = u_\varphi = 0$), and only the axial component $u_x = u(r)$ remains. For thermal analysis, we begin with the energy equation for steady, incompressible flow without axial conduction, which is justified for flows with high Peclet number (Kays et al. 2005, Chap. 8). The resulting energy equation simplifies to

$$u \frac{\partial T}{\partial x} = \alpha \frac{1}{r} \frac{\partial}{\partial r} \left(r \frac{\partial T}{\partial r} \right) \ , \tag{5.110}$$

where $\alpha = k/(\rho c_p)$ is the thermal diffusivity of the fluid. Unlike velocity, which is fully developed once its profile becomes invariant along the tube axis, the concept of a fully developed temperature profile is more nuanced. In the thermal context, the profile is considered fully developed when its shape remains constant along the flow direction. That is, the nondimensional temperature profile becomes invariant with respect to *x*. As a reference quantity for the temperature profile, we define the mass-averaged or **bulk temperature** $T_m(x)$ as

$$T_m(x) = \frac{\int_A T \rho u \, dA}{\int_A \rho u \, dA} = \frac{\int_0^R T \rho u \ 2\pi r \, dr}{\int_0^R \rho u \ 2\pi r \, dr} \ , \tag{5.111}$$

which represents the average fluid temperature weighted by the mass flux and serves as a reference for convective heat transfer. To analyze the thermal behavior independently of absolute temperatures, we introduce the nondimensional temperature

$$\Theta(r,x) = \frac{T_w(x) - T(r,x)}{T_w(x) - T_m(x)} \quad , \tag{5.112}$$

which compares the local fluid temperature to the driving temperature difference between the wall and bulk at position *x*. This form ensures that $\Theta = 0$ at the wall and $\Theta = 1$ for $T = T_m$. The description of the heat transfer coefficient is adapted to the bulk temperature as reference to

$$\dot{q} = h(T_w(x) - T_m(x)) = -k \frac{\partial T}{\partial r}\Big|_{r=R} \quad , \tag{5.113}$$

that balances the heat conduction through the tube wall at $r = R$.

For a **thermally fully developed flow**, the dimensionless temperature profile $\Theta(r,x)$ must be independent of *x*, thus $\partial\Theta/\partial x = 0$. Differentiating the definition of Θ gives

$$\frac{\partial T}{\partial x} = \frac{T - T_m}{T_w - T_m}\frac{dT_w}{dx} + \frac{T_w - T}{T_w - T_m}\frac{dT_m}{dx} \quad , \tag{5.114}$$

which shows how the temperature gradient depends on the relative position in the profile and on the rates of change of T_w and T_m. Since Θ is independent of *x*, its radial derivative $\partial\Theta/\partial r$ must also be independent of *x*, implying that the radial gradient of temperature remains fixed in shape along the flow direction. This leads to a constant wall gradient $\partial T/\partial r|_w$, and hence a constant heat transfer coefficient *h*, provided that *k* is constant. This insight explains why, under fully developed conditions, *h* becomes independent of *x*, which is supported by experimental data for certain boundary conditions (Kays et al. 2005).

In the following, the temperature profile and corresponding heat transfer coefficient are derived for two classical wall boundary conditions, a uniform wall temperature $T_w = \text{const.}$ and a constant wall heat flux $\dot{q}_w$. The qualitative variations of the bulk fluid temperature $T_m(x)$ and the wall temperature $T_w(x)$ along the tube axis are illustrated in Fig. 5.18. For the case of constant wall temperature, the fluid gradually heats up and the bulk temperature asymptotically approaches T_w. In contrast, for a constant wall heat flux, both T_m and T_w increase linearly with *x*, maintaining a constant temperature difference.

The corresponding radial temperature distributions are analyzed in the following, based on the derivations presented by Kays et al. (2005).

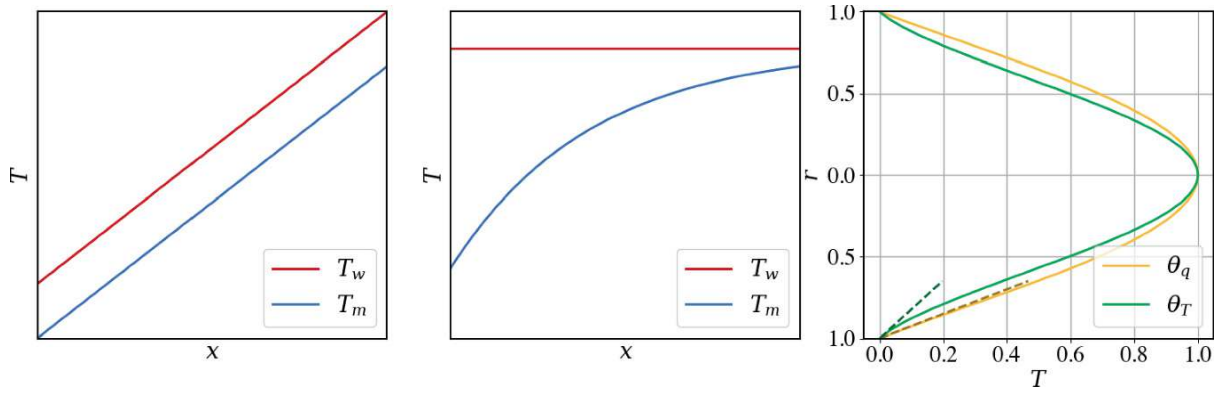


Fig. 5.18 Qualitative variation of bulk temperature T_m and wall surface temperature T_w over tube axis coordinate *x* for the two considered boundary conditions for constant wall heat flux (left) and uniform wall temperature (middle). For both boundary conditions the normalized radial temperature profiles and the temperature gradient (right)

Constant Wall Heat Flux In this case, the wall heat flux shall be constant along the pipe, thus $\dot{q}_w = \text{const.}$, implying a constant rate of energy input per unit area. Since $\dot{q}_w = h(T_w - T_m)$ is constant, and *h* is constant for a fully developed temperature profile, it follows that $(T_w - T_m)$ must also remain constant over *x*. Therefore, both $T_m(x)$ and $T_w(x)$ increase linearly with *x*, with the same slope, as sketched in Fig. 5.18 .

With Eq. (5.114) it follows that the linear growth implies that $\frac{\partial T}{\partial x} = dT_m/dx$ is spatially uniform across the cross-section, and thus simplifies the energy equation (5.110). A differential energy balance over a control volume of length *dx* yields the rate of bulk temperature increase as

$$\dot{q}_w = \frac{\rho c_p \bar{u} R}{2} \frac{dT_m}{dx} \ , \tag{5.115}$$

relating the heat flux at the wall to the streamwise gradient of T_m. With $u(r)$ from Eq. (5.100) and the expression for $dT/\partial x$, the energy equation (5.110) becomes

$$\begin{aligned} u(r)\frac{dT_m}{dx} &= \alpha \frac{1}{r}\frac{d}{dr}\left(r\frac{dT}{dr}\right) \ , \\ r = 0: \quad \frac{dT}{dr} &= 0 \ , \\ r = R: \quad T &= T_w \ . \end{aligned} \tag{5.116}$$

Substituting the velocity profile and assuming a fully developed temperature distribution allows the equation to be separated and integrated over the radial

direction, yielding the temperature profile of the fully developed pipe flow to

$$T(r) = T_w - \frac{\bar{u}R^2}{\alpha}\frac{dT_m}{dx}\left(\frac{1}{8}\left(\frac{r}{R}\right)^4 - \frac{1}{2}\left(\frac{r}{R}\right)^2 + \frac{3}{8}\right) \ . \tag{5.117}$$

The expression reveals that the temperature distribution, like the velocity field, has a parabola like shape, however with r^4. Its dominant curvature is determined by the balance between axial convection, driven by the mean flow velocity $\bar{u}$, and radial conduction, governed by the thermal diffusivity α. The presence of the streamwise bulk temperature gradient dT_m/dx as a prefactor indicates that the temperature field scales directly with the wall heat flux added to the flow.

To determine the actual bulk temperature T_m, mass-flux-weighted averaging over the pipe cross-section is carried out according to Eq. (5.111), yielding

$$T_m = T_w - \frac{11}{48}\frac{\rho c_p \bar{u} R^2}{k}\frac{dT_m}{dx} \ . \tag{5.118}$$

The expression still depends on the streamwise gradient dT_m/dx as a measure of the added heat rate and was deduced to be constant earlier. The heat transfer coefficient can be determined according to its defining equation Eq. (5.113) and use of the pipe segment energy balance from Eq. (5.115), resulting in

$$h = \frac{48}{11}\frac{k}{D} \approx 4.364\frac{k}{D}, \qquad \mathrm{Nu} = \frac{hD}{k} = 4.364 \ , \tag{5.119}$$

which is the classical result for thermally fully developed laminar flow in a pipe with constant wall heat flux. The Nusselt number is constant and does not vary with axial position, Reynolds number, or Prandtl number. This reflects the special nature of fully developed laminar flow under constant wall heat flux, where the temperature field reaches a repeating pattern, and the wall to fluid heat transfer becomes independent of position. The corresponding temperature profile and wall gradient are sketched in Fig. 5.18, illustrating the characteristic curvature and thermal behavior.

Constant Wall Temperature In the case where the wall temperature is held constant, thus $T_w = \mathrm{const.}$, the axial derivative of the wall temperature vanishes, $dT_w/dx = 0$. As a result, the axial temperature gradient simplifies according to Eq. (5.114) to

$$\frac{\partial T}{\partial x} = \frac{T_w - T}{T_w - T_m}\frac{dT_m}{dx} \ . \tag{5.120}$$

Substituting this relation into the energy equation and using the fully developed axial velocity profile from Eq. (5.100), we obtain the governing differential

equation for the radial temperature distribution to

$$\begin{aligned} u(r)\,\tfrac{T_w-T}{T_w-T_m}\,\tfrac{dT_m}{dx} &= \alpha\,\tfrac{1}{r}\,\tfrac{\partial}{\partial r}\left(r\,\tfrac{\partial T}{\partial r}\right)\ , \\ r=0: \qquad \tfrac{\partial T}{\partial r} &= 0\ , \\ r=R: \qquad T &= T_w\ . \end{aligned} \tag{5.121}$$

The differential equation remains nonlinear due to the dependence of both *u* and *T* on *r*, and an analytical solution in closed form is not available. However, due to the axisymmetry of the geometry and boundary conditions, the temperature profile can be expressed as a power series of even *r*-powers. That series automatically satisfies the symmetry condition at $r = 0$ and reflects the smooth behavior of the solution across the cross-section. Following the formulation presented by Kays et al. (2005), a solution was provided by Bhatti in the form of an infinite series

$$\tfrac{T_w-T}{T_{\text{centerline}}} = \sum_{n=0}^{\infty} C_{2n}\left(\tfrac{r}{R}\right)^{2n}. \tag{5.122}$$

where $T_{\text{centerline}}$ is the fluid temperature at the pipe centerline. The coefficients C_{2n} are determined recursively (Kays et al. 2005, Chap. 8), based on the eigenvalue λ_0 of the solution, which characterizes the decay rate of temperature from the centerline to the wall. The series coefficients are given by

$$\begin{aligned} \lambda_0 &= 2.704364\ , \\ C_0 &= 1\ , \quad C_2 = -\tfrac{1}{4}\lambda_0^2 \approx -1.828\ , \\ C_{2n} &= \left(\tfrac{\lambda_0}{2n}\right)^2 (C_{2n-4} - C_{2n-2})\ . \end{aligned} \tag{5.123}$$

Using this solution structure, the Nusselt number can be evaluated from the wall gradient of the temperature profile to

$$\text{Nu} = \tfrac{hD}{k} = \tfrac{1}{2}\lambda_0^2 = 3.657\ , \tag{5.124}$$

which is slightly lower than the value obtained for the case of constant wall heat flux. This difference reflects the nature of the thermal boundary condition, that is, for a constant wall temperature, the temperature difference between wall and fluid decreases along the pipe, reducing the local driving force for heat transfer, especially near the outlet. The solution yields a smooth, symmetric temperature profile that decreases from the wall toward the centerline. Although no closed-

form solution exists, the series converges rapidly and captures the essential behavior of the temperature distribution. The normalized temperature profile and wall gradient are illustrated in Fig. 5.18, highlighting the reduced temperature difference and slightly flatter gradient at the wall compared to the constant heat flux case.

Noncircular Duct Flow While circular tubes are often used for analytical treatment due to their symmetry, many practical internal flow systems involve ducts with noncircular cross-sections, such as rectangular, square, or triangular geometries. These geometries are particularly common in compact heat exchangers, cooling channels, or HVAC systems. In such cases, the wall shape and the presence of corners significantly influence both the velocity and temperature fields. Nevertheless, under fully developed laminar conditions, analogous expressions for wall friction and convective heat transfer can still be obtained.

The analysis of fully developed laminar flow in ducts of arbitrary cross-section follows the same foundational assumptions, that is, the flow field is steady, incompressible with no axial variation in velocity or temperature field. The governing equations for momentum and energy retain their general form, but must be solved over a domain with modified geometry. The axial velocity and temperature profiles satisfy the two-dimensional elliptic equations

$$0 = -\frac{\partial p}{\partial x} + \mu \nabla^2 u(y,z) \ , \qquad u(y,z)\frac{\partial T}{\partial x} = \alpha \nabla^2 T(y,z) \ , \tag{5.125}$$

subject to no-slip and prescribed thermal boundary conditions on the duct walls. Closed-form solutions are generally not available for arbitrary geometries, but the fields can be obtained via series expansions or numerical integration. Once the profiles are known, cross-sectional integration yields the mean velocity and bulk temperature, from which the pressure drop and convective heat transfer rate follow.

As a classic example, the flow between two infinite parallel plates represents one of the simplest geometries, and leads to the classical plane Poiseuille flow. The velocity profile depends only on the lateral coordinate and forms a simple parabola across the channel height. The temperature profile, under uniform wall heat flux or constant wall temperature conditions, can also be derived analytically, making this configuration a standard reference case for internal laminar flow (White 1991).

Table 5.1 Fully developed laminar flow parameters for various duct geometries (Kays et al. 2005; Shah and London 1978)

In contrast, rectangular ducts, where flow is confined in both lateral directions, exhibit more complex behavior. Solving the momentum equation using separation of variables yields a Fourier series solution (Kays et al. 2005; White 1991). The resulting velocity profile is flatter in the center of the duct and shows steeper gradients near the walls, particularly along the narrower dimension. As in other cases, the pressure drop arises from viscous shear at the boundary. The corresponding friction factor remains well defined, but depends on the duct's aspect ratio and must typically be obtained from tables or numerical results. Values for selected geometries are summarized in Table 5.1. For a more comprehensive overview of duct shapes and boundary conditions, the reader is referred to Shah and London (1978).

For fully developed conditions, the key results can be expressed compactly using two nondimensional quantities. The first is the friction factor f_F, defined here in terms of the Fanning formulation, which relates pressure drop to mean velocity via $dp/dx = -4f_F\rho\bar{u}^2/(2d_h)$. The second is the Nusselt number $\mathrm{Nu} = hd_h/k$, characterizing the relative strength of convective to conductive heat transfer. In both expressions, the hydraulic diameter $d_h = 4A/P$ is used as the characteristic length, where A is the cross-sectional area and P the wetted perimeter, as introduced in Sect. 5.1.5. The hydraulic diameter provides a unified geometric scale that allows comparison between different duct shapes, and allows results from circular pipe flow to be extended to noncircular configurations.

For laminar, thermally and hydrodynamically fully developed flow with constant material properties, both $f_F\,\mathrm{Re}$ and Nu are constants, independent of Reynolds and Prandtl numbers, and depend solely on the duct geometry and thermal boundary conditions. Table 5.1 summarizes values for a selection of duct geometries. It includes both constant wall heat flux (Nu_H) and constant wall temperature (Nu_T) boundary conditions, and the product $f_F\,\mathrm{Re}$, sometimes referred to as the Poiseuille number[1]. It further lists the dimensionless entrance length L^+, which characterizes the streamwise development length required to reach fully developed flow, scaled by d_h. The circular duct values listed in the table match the analytical expressions derived in Eqs. (5.119) and (5.124). Likewise, the friction factor given in Eq. (5.103) gives $f\,\mathrm{Re} = 64$, corresponding to Fanning formulation $f_F\,\mathrm{Re} = 16$ in the table.

As seen from Table 5.1, rectangular ducts with large aspect ratios, representing wide rectangular channels, exhibit higher Nusselt numbers due to their increased surface to volume ratio, which enhances convective heat transfer. However, this often comes at the cost of increased pressure losses. Conversely,

ducts with sharp corners, such as triangular geometries, tend to show lower heat transfer performance, as local stagnation zones form in the corners where temperature gradients and wall heat flux decrease. The dimensionless hydrodynamic entrance length $L^+ = L/(d_h\,\mathrm{Re})$ indicates the scaled streamwise distance L, required for the velocity and temperature profiles to reach their fully developed form. In short ducts, entrance effects can dominate, necessitating corrections or use of developing flow models.

The results summarized here are widely applied in reduced-order flow models. When incorporated as **subscale closures** for wall friction and heat transfer, they enable noncircular ducts to be treated within a quasi-one-dimensional modeling framework, while preserving physical accuracy in predictions of pressure drop and thermal transport. For extensions to developing flow, non-uniform heating, or mixed convection the reader is referred to specialized references such as Kays et al. (2005) and Shah and London (1978).

5.3.2 Turbulent Flow

The laminar flow regime, characterized by a linear relationship between pressure drop and volumetric flow rate, is only valid up to moderate Reynolds numbers, typically $\mathrm{Re}_{crit} \approx 2300$. For $\mathrm{Re} > \mathrm{Re}_{crit}$, the flow transitions to a turbulent regime, marked by chaotic, three-dimensional velocity fluctuations. These fluctuations enhance mixing and momentum diffusion, resulting in significantly higher resistance to flow, as discussed in Sect. 4.2. In the turbulent regime, the pressure drop increases roughly with the square of the mean velocity, $\Delta p \sim \bar{u}^2$. In the following, we first consider turbulent flow along **smooth walls**, where surface roughness does not significantly affect the flow. We then extend the discussion to **rough walls**, where surface texture alters the near-wall behavior and modifies the overall resistance to flow.

Smooth Walls Unlike laminar flow, turbulent flow cannot be described entirely by theoretical analysis. However, extensive experimental studies and scaling arguments have led to practical engineering correlations. For the **turbulent flow in smooth pipes**, in early investigations (Blasius 1913) applied similarity arguments and fitted data of the body of experiments available at that time. For laminar flow he found the previously discussed relation $f = 64/\,\mathrm{Re}$ and for turbulent flow obtained the empirical relation

$$f = \frac{0.3164}{\mathrm{Re}^{1/4}}\ , \tag{5.126}$$

that is valid for Reynolds numbers up to about 1×10^5. To extend the characterization to higher Reynolds numbers, Nikuradse (1933a) conducted

detailed experiments, covering Re up to 3×10^6, as shown in Fig. 5.21. Building on Prandtl's mixing length theory, discussed in Sect. 4.2.5, Nikuradse proposed the following implicit relation for smooth pipes

$$\frac{1}{\sqrt{f}} = 2 \log_{10} \left(\mathrm{Re}_d \sqrt{f} \right) - 0.8 = -2 \log_{10} \left(\frac{2.51}{\mathrm{Re}_d \sqrt{f}} \right) , \tag{5.127}$$

commonly known as Prandtl's friction law. As shown in Fig. 5.21, it agrees well with Blasius' formula at lower Re_d, but provides improved accuracy at higher Reynolds numbers. Besides the friction factor, Nikuradse (1933a) also reported detailed measurements of turbulent velocity profiles for Reynolds numbers ranging from 4×10^3 to 3.24×10^6. In Fig. 5.19, a selection of these profiles is shown for illustration, nondimensionalized by the respective maximum velocity $u_{\max}$. For comparison, the laminar velocity distribution from Eq. (5.100) is also included. The figure illustrates how, with increasing Reynolds number, the velocity profile becomes increasingly flattened in the core region, while near-wall gradients steepen significantly. This trend reflects the redistribution of momentum in turbulent flow, where enhanced mixing pushes high-speed fluid toward the wall, resulting in stronger shear stresses near the boundary. As a result, the velocity profile evolves from the parabolic shape of laminar flow to a plug-like distribution, with a thin high shear layer near the wall.

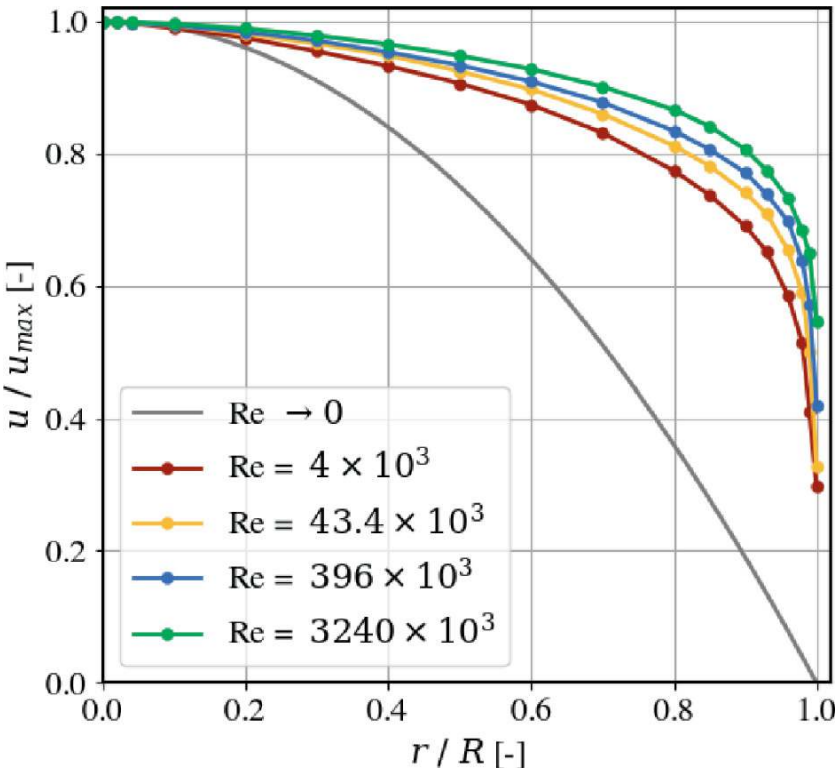


Fig. 5.19 Laminar and turbulent velocity distribution in a smooth pipe at different Reynolds numbers according to Nikuradse (1933a)

From Blasius' friction law in Eq. (5.126), Prandtl deduced that the near-wall velocity profile in turbulent flow follows a power law of the form $u \sim y^{1/7}$, where $y = R - r$ denotes the distance from the pipe wall. This scaling arises from relating the friction factor to the wall shear stress. As detailed by Nikuradse (1933a), applying the definition of the friction coefficient to the wall shear stress in Eq. (5.108) yields $\tau_w = f\rho\bar{u}^2/8$. Substituting the Blasius friction factor from Eq. (5.126) into this relation, and solving for the mean velocity $\bar{u}$, leads to the expression $\bar{u} \sim (\tau_w/\rho)^{4/7}(R/\nu)^{1/7}$. Assuming a fixed ratio $u_{\max}/\bar{u}$ and replacing R by the wall distance y, and $u_{\max}$ by u, the local velocity near the wall follows to $u \sim (\tau_w/\rho)^{4/7}(y/\nu)^{1/7}$. This proportionality was later quantified by Schlichting and Truckenbrodt (2001, p. 246) as $u/u_\tau = 8.74(yu_\tau/\nu)^{1/7}$. Thus, the $1/4$ exponent in the Reynolds number dependence of the Blasius friction law, according to Eq. (5.126), translates into a $1/7$ power law for the velocity profile near the wall. This connection reveals how the friction behavior is directly reflected in the structure of the velocity field. As shown in Fig. 5.21, experimental data indicate that the slope of the smooth-wall friction curve decreases slightly at very high Reynolds numbers. For $\mathrm{Re} \approx 3 \times 10^6$, the friction factor's Reynolds number exponent approaches $1/7$, which corresponds to a velocity profile with $u \sim y^{1/10}$ near the wall (Nikuradse 1933a).

An alternative to the power-law velocity distribution is given by the analytically founded logarithmic wall function, discussed in detail in Sect. 4.2.5. Based on his experimental data, Nikuradse (1933a) determined the following empirical fit for the near-wall velocity profile

$$u^+ = 5.5 + 5.75 \log_{10}\left(y^+\right) \ , \tag{5.128}$$

which corresponds to the general log-law form in Eq. (4.54) with the corresponding von Kármán constant $\kappa = 0.40$ and intercept $B = 5.5$. As shown in Fig. 5.20, this logarithmic velocity law exhibits very good agreement with Nikuradse's measured data in the range $y^+ \geq 70$, where the logarithmic layer dominates.

In a subsequent analysis, Lindgren (1965) extended the experimental resolution closer to the wall, enabling direct comparison with the viscous sublayer model described by Eq. (4.52). The combined data, also shown in Fig. 5.20, reveal consistent agreement with the expected linear behavior $u^+ = y^+$ within the viscous sublayer for $y^+ \leq 5$, as well as with the transitional

buffer region defined in Eq. (4.55) for $5 \leq y^+ \leq 70$. Together, these datasets confirm the classical three-layer structure of wall-bounded turbulence and support the use of universal wall functions in turbulent flow modeling.

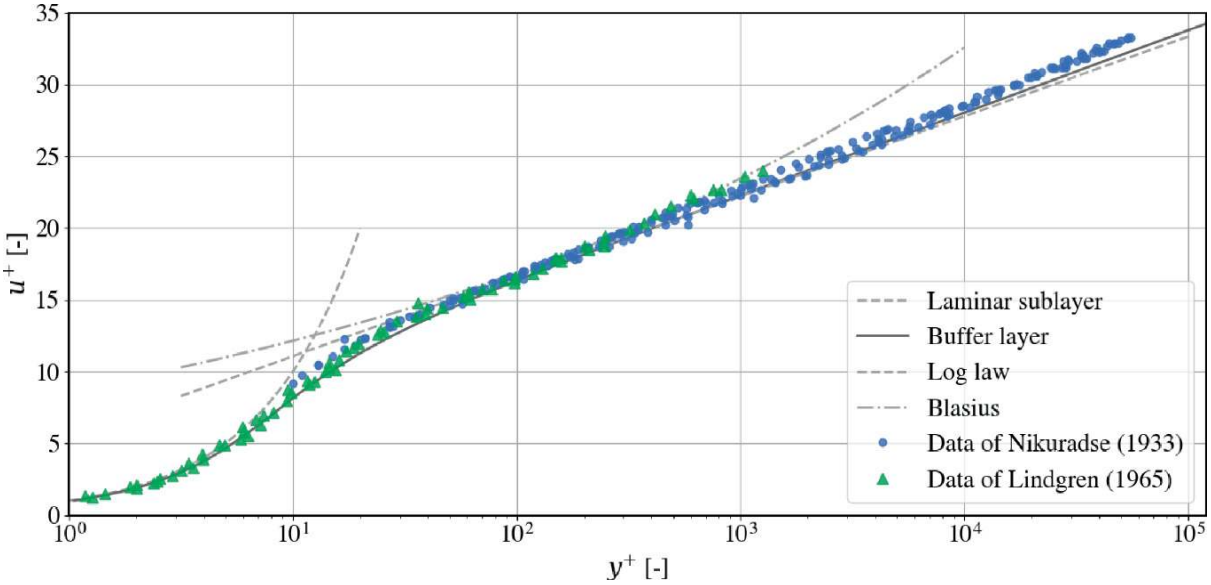


Fig. 5.20 Universal velocity distributions compared to experiments according to Nikuradse (1933a) for $4 \times 10^3 \leq \mathrm{Re} \leq 3.24 \times 10^6$ and Lindgren (1965) for $6.1 \times 10^3 \leq \mathrm{Re} \leq 49 \times 10^3$

Rough Walls While the previous discussion focused on hydraulically smooth pipes, most practical systems involve surfaces with some degree of **surface roughness**, typically characterized by the average roughness height k_s. Even small deviations from smoothness can alter flow resistance in the turbulent regime. The influence of such roughness on turbulent pipe flow was systematically investigated by Nikuradse (1933b), whose detailed measurements are presented in Fig. 5.21.

While at laminar flow conditions the surface roughness barely shows any effect, in turbulent flow the roughness can have a significant impact on the pressure drop, as evident from the data shown in Fig. 5.21 for lower Reynolds numbers. The decisive factor turns out to be the roughness height k_s relative to the viscous length ν/u_τ, which is captured by the nondimensional ratio $k_s^+ = u_\tau k_s/\nu$. This parameter allows the classification of surface roughness effects into three regimes (Schlichting and Truckenbrodt 2001, p. 249).

For **hydraulically smooth walls**, defined by $k_s^+ \leq 5$, the roughness elements remain entirely within the viscous sublayer, which was discussed in Sect. 4.2.5. In this regime, the influence of roughness is negligible, and the wall behaves as if it were perfectly smooth. The resulting friction factor $f = f(\mathrm{Re}_d)$ depends solely on the Reynolds number, and matches the values obtained for a smooth pipe.

If the roughness height is comparable to the viscous sublayer thickness, entering the range $5 \leq k_s^+ \leq 70$, the roughness elements begin to penetrate the **buffer layer**, which lies between the viscous sublayer and the logarithmic region. In this transitionally rough regime, the friction factor becomes a function of both the Reynolds number and the relative roughness k_s/R, so that $f = f(\mathrm{Re}_d, k_s/R)$. Compared to a smooth wall at the same Reynolds number, the friction coefficient increases due to the added form drag associated with the exposed roughness elements.

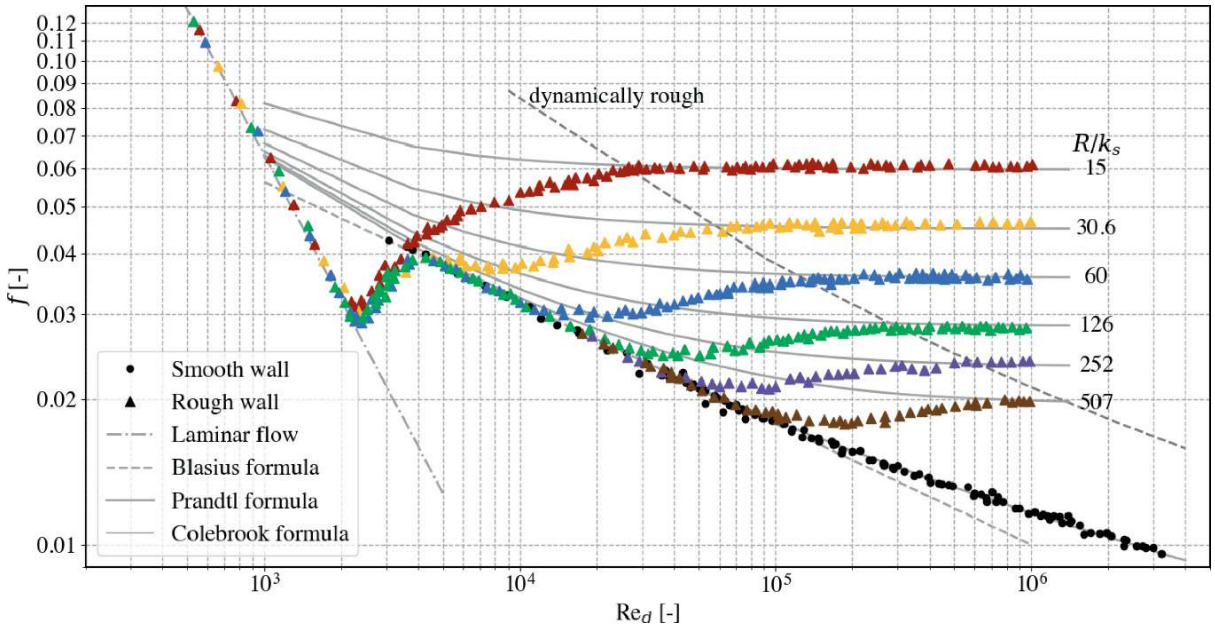


Fig. 5.21 Friction coefficient f over Re_d for smooth and rough wall. Measurements for smooth wall according to Nikuradse (1933a) and data for rough wall with different surface roughness k_s/R from Nikuradse (1933b)

For $k_s^+ \geq 70$, the roughness substantially reaches into the logarithmic layer. In this case, referred to as the **dynamically completely rough surface**, the viscous effects near the wall are negligible. The resulting friction is dominated by the surface roughness, and the dependence on Reynolds number vanishes. In this fully rough regime, the friction factor follows the von Kármán relation

$$\frac{1}{\sqrt{f}} = 1.74 - 2\,\log_{10}\left(\frac{k_s}{R}\right)\,, \tag{5.129}$$

which expresses the friction solely as a function of the relative roughness k_s/R. This asymptotic behavior is observed as a plateau in experimental friction curves at high Reynolds numbers, where the resistance is determined entirely by the surface texture.

It is important to note that the von Kármán relation in Eq. (5.129) is independent of the Reynolds number. In the literature, this expression appears in slightly different forms, sometimes with the empirical constants incorporated into the logarithmic argument or expressed using different logarithmic bases. As the relative roughness k_s/R decreases, the predicted friction factors approach those of a hydraulically smooth wall, gradually transitioning back toward the Reynolds-dependent regime. Conversely, as the Reynolds number increases, the viscous length scale ν/u_τ decreases, meaning that the same physical roughness becomes more prominent in nondimensional terms. As a result, the threshold at which a surface is considered fully rough shifts toward smaller values of k_s/R, that is, larger values for R/k_s. This transition behavior is reflected in the boundary curve shown in Fig. 5.21, which separates the transition region from the fully rough regime. Beyond this limiting boundary, the friction factor reaches a plateau for each fixed R/k_s, as described by Eq. (5.129). To derive the location of this plateau curve, the roughness Reynolds number threshold is substituted into Eq. (5.129), using the relation $u_\tau = \bar{u}\sqrt{f/8}$ (Spurk 1996).

To bridge the transition between smooth and rough wall behavior across a wide range of Reynolds numbers, Colebrook et al. (1937) proposed the following empirical correlation

$$\frac{1}{\sqrt{f}} = 1.74 - 2\log_{10}\left(\frac{k_s}{R} + \frac{18.7}{\mathrm{Re}_d\sqrt{f}}\right) . \tag{5.130}$$

The formula blends the smooth-wall behavior captured by Prandtl's relation in Eq. (5.127) with the fully rough limit of the von Kármán law in Eq. (5.129). For vanishing relative roughness $k_s/R \to 0$, the expression simplifies to the smooth-pipe friction relation. At the opposite extreme, when $\mathrm{Re}_d \to \infty$, viscous effects vanish, the second term in the logarithmic argument becomes negligible, and the relation reduces to the von Kármán fully rough limit. The combined behavior predicted by Colebrook's formula is shown in Fig. 5.21, plotted alongside the experimental measurements of Nikuradse (1933b).

5.3.3 Incompressible Pipe Flow

So far, we have considered flow and the associated pressure losses only in straight ducts of constant cross-section. However, real-world piping systems typically consist of multiple segments with varying diameters and a range of flow-modifying components, such as valves, bends, expansions, and contractions. These components serve operational purposes, such as directing the flow, regulating pressure, or facilitating flow transitions, but they also introduce

additional sources of energy dissipation. In addition to the continuous friction losses along the length of straight duct segments, described by the Darcy friction factor *f*, there are discrete losses caused by geometric changes or internal components. These localized losses are commonly characterized by the dimensionless **loss coefficient** ζ, which quantifies the pressure drop across a device or feature in terms of the upstream dynamic pressure

$$\Delta p_L = \zeta \tfrac{\rho}{2} u_1^2 \ . \tag{5.131}$$

Here, u_1 denotes the upstream reference velocity. For components involving area changes, the velocity is often expressed in terms of the known volume flow rate $Q = uA$, allowing pressure losses to be linked directly to flow conditions. In a piping system comprising multiple flow segments *j* of different lengths and diameters, and various flow-affecting features *k*, the total pressure loss in incompressible flow can be computed by summing all individual contributions to

$$\Delta p_L = \tfrac{\rho}{2} \left(\sum_j f_j \tfrac{\ell_j}{d_{hj}} u_j^2 + \sum_k \zeta_j u_k^2 \right) \ . \tag{5.132}$$

Following Sect. 5.3.1 for a straight duct segment of constant cross-section *A*, the friction-induced pressure loss can be rewritten in terms of a corresponding loss coefficient using $\zeta = f\ell/d_h$. For ducts with variable cross-sectional area $A(s)$ along the streamwise direction, the total pressure loss due to wall friction can be obtained by integrating local contributions to

$$\zeta = \int_1^2 \left(\tfrac{A_1}{A(s)} \right)^2 \tfrac{f(s)}{d_h(s)} \ ds \ . \tag{5.133}$$

In most cases, the complex flow phenomena within flow devices, such as turbulence, separation, and secondary flows, make it unfeasible to derive ζ from first principles. As such, loss coefficients for common components are based on measurements or manufacturer specifications. In the following, we examine a few key scenarios involving flow development, expansions, and contractions. For a comprehensive overview of component-specific loss coefficients, the reader is referred to Rennels (2022), Richter (1962).

The approach can also be transferred to turbomachinery applications. As discussed in Sect. 5.1.4, pumps and turbines introduce shaft work into the system, thereby raising or lowering the pressure of the working fluid. In one-dimensional flow models, the effect of these hydraulic machines is captured by a

pressure change term related to the shaft power $\dot{W}_{\text{shaft}}$. Rewriting Eq. (5.40), the pressure rise or drop associated with pumps and turbines is expressed as

$$\Delta p_P = \frac{\eta_P \dot{W}_{\text{shaft}}}{uA}, \quad \Delta p_T = \frac{\dot{W}_{\text{shaft}}}{\eta_T uA} \ . \tag{5.134}$$

Here, the sign of $\dot{W}_{\text{shaft}}$ distinguishes whether energy is added (positive, pump) or extracted (negative, turbine). The efficiencies η_P and η_T are generally functions of operating conditions such as rotational speed and flow rate.

While this section focuses on selected cases of incompressible flow, readers seeking a more general treatment, including compressible flows and networked systems, are referred to Glück (1988) and Rennels (2022), which beyond the current scope also provide methods for handling gas-dynamic piping systems.

Expansions Diffusers are designed to slow down a flow and increase its static pressure. For subsonic flows, this is achieved by a gradual widening of the cross-section. Assuming ideal, frictionless conditions, the pressure gain between inlet and outlet $1 \to 2$ is obtained from Bernoulli's equation

$$\Delta p_{\text{ideal}} = \frac{\rho}{2} \bar{u}_1^2 \left(1 - \frac{A_1^2}{A_2^2}\right) \ . \tag{5.135}$$

In real flows, however, adverse pressure gradients can cause boundary layer separation. As the flow slows and static pressure rises, the momentum near the wall may not be sufficient to overcome the increasing pressure, leading to stagnation and even local flow reversal. These recirculation zones increase turbulence and dissipate energy. As a result, the actual pressure gain is reduced to

$$\begin{aligned} \Delta p_{\text{real}} &= \Delta p_{\text{ideal}} - \Delta p_L = \frac{\rho}{2} \bar{u}_1^2 \left(1 - \frac{A_1^2}{A_2^2} - \zeta\right) \\ &= \frac{\rho}{2} \bar{u}_1^2 \, \eta_D \left(1 - \frac{A_1^2}{A_2^2}\right) \ , \end{aligned} \tag{5.136}$$

where η_D denotes the **diffuser efficiency** that relates to the loss coefficient via

$$\zeta = (1 - \eta_D)\left(1 - (A_1/A_2)^2\right) \ . \tag{5.137}$$

To minimize the risk of separation, the diffuser opening angle is typically kept below $\delta < 8\,^\circ$, where δ is the half-opening angle. Experiments show that separation can occur as early as $\delta \approx 10\,^\circ$ in rectangular ducts (Spurk 1996). A uniform inlet velocity profile with thin boundary layers is also desirable.

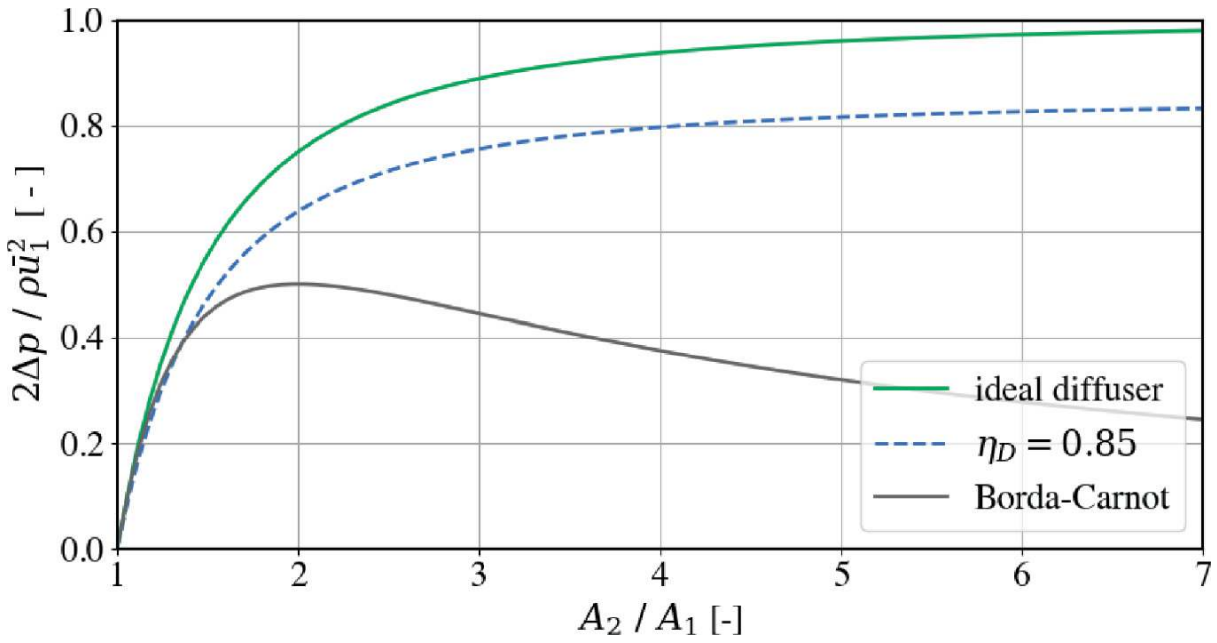


Fig. 5.22 Comparison of pressure increase in an ideal to a real diffuser with $\eta_D = 0.8$ and the increase though a sudden flow expansion

Figure 5.22 illustrates the relationship between pressure recovery and area ratio. While theoretically the pressure gain increases with $A_2/A_1 \to \infty$, most of the gain is already achieved for $A_2/A_1 \approx 3$ – 4. Beyond that, gains are marginal, and longer diffusers, needed to maintain a small angle, introduce additional friction losses. For well-designed, non-separated diffusers, efficiencies around $\eta_D \approx 0.85$ are achievable (Spurk 1996).

In the case of a **sudden expansion** , the flow separates immediately at the sharp edges, forming a recirculation zone, as shown in Fig. 5.23. In the momentum balance along the flow direction, we consider the net change in momentum flux and pressure forces between inlet and outlet. The total force acting on the control volume is given by $F = \rho(u_1^2 A_1 - u_2^2 A_2) + p_1 A_1 - p_2 A_2$. Here, we neglect the contribution of wall shear, assuming the flow element is short and shear effects are minimal. The net force *F* must balance the pressure force exerted by the expanding channel walls. Since the walls exert a pressure p_1 over the area increment $(A_2 - A_1)$, this yields $F = -(A_2 - A_1)p_1$. Applying mass conservation to express u_2 in terms of u_1 and the area ratio, the resulting pressure difference across the expansion becomes

$$(p_2 - p_1)_{\text{real}} = \rho u_1^2 \frac{A_1}{A_2}\left(1 - \frac{A_1}{A_2}\right) \ . \tag{5.138}$$

This relation is known as the **Borda-Carnot equation**. The associated pressure loss relative to the ideal case is

$$\Delta p_L = (p_2 - p_1)_{\text{ideal}} - (p_2 - p_1)_{\text{real}} = \frac{\rho}{2}(u_1 - u_2)^2 = \rho \frac{u_1^2}{2}\left(1 - \frac{A_1}{A_2}\right)^2 \quad .(5.139)$$

As a limiting case, if the pipe discharges into an open reservoir ($A_2/A_1 \to \infty$), the entire kinetic energy is dissipated, thus $\Delta p_L = \rho u_1^2/2$.

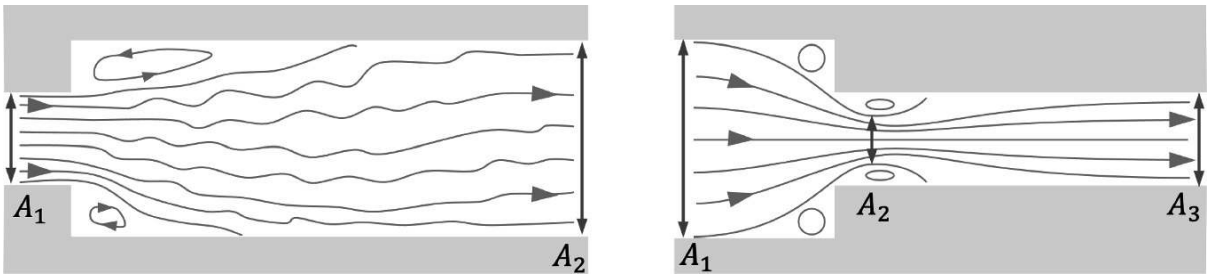


Fig. 5.23 Flow through a sudden expansion (left) and contraction (right)

Contractions For the flow through a nozzle, the fluid accelerates while its static pressure decreases. In incompressible flow, this acceleration is caused by a reduction in flow area from the inlet to the outlet $1 \to 2$. Beyond this basic geometrical contraction, nozzles play a key role in many technical systems, for example in turbomachinery stator vanes or rotor blade channels, where they serve to convert pressure energy into kinetic energy, as discussed in Sect. 5.1.4.

Nozzles are typically short, such that the flow does not reach a fully developed profile, and viscous effects play only a minor role. The pressure difference $\Delta p = p_1 - p_2$ across the nozzle acts as the driving force, and follows from the combination of continuity and Bernoulli's equation (5.13). Expressed in terms of the nozzle exit velocity, the pressure drop becomes

$$\Delta p = \frac{\rho}{2}\bar{u}_2^2\left[1 - \left(\frac{A_2}{A_1}\right)^2\right] \quad , \qquad u_2 = \sqrt{\frac{2\Delta p/\rho}{1-(A_2/A_1)^2}} \quad . \qquad (5.140)$$

In the case of a sudden, step-like contraction of the flow path, separation can occur both upstream and downstream of the sharp transition. As illustrated in Fig. 5.23, the flow does not immediately fill the narrower section. Instead, it contracts to a smaller effective area $A_3 = \alpha A_2$ due to recirculation zones forming along the walls just downstream of the edge. After a short distance, the flow gradually reexpands to occupy the entire duct area.

The contraction coefficient α, defined as the ratio of the effective flow area to the actual pipe area, typically lies in the range $0.5 \leq \alpha \leq 1$ (Truckenbrodt 1968). Since the major pressure loss occurs during this reexpansion from A_3 to A_2, the loss can be estimated using the Borda-Carnot equation (5.138)

$$\Delta p_L = \rho \frac{u_3^2}{2} \left(1 - \frac{A_3}{A_2}\right)^2 = \rho \frac{u_2^2}{2} \left(\frac{1-\alpha}{\alpha}\right)^2 , \tag{5.141}$$

which corresponds to a loss coefficient of $\zeta = (1 - \alpha/\alpha)^2$. Note that in this case, the downstream velocity u_2 is used as the reference for defining the loss coefficient.

Entrance Flow In the previous sections, the analysis of laminar and turbulent duct flow was based on the assumption of fully developed velocity profiles. That is, beyond a certain distance from the inlet, the profile becomes invariant in the streamwise direction. However, at the entrance of a duct, the incoming flow often exhibits a nearly uniform velocity distribution, and requires a finite length to transition into the fully developed state. This entrance region is characterized by the formation and growth of boundary layers along the duct walls, which eventually merge to fill the entire cross-section, as sketched in Fig. 5.24.

This distribution is reached asymptotically. The **entrance length** l_e is typically defined as the distance from the inlet at which the centerline velocity reaches 99% of its fully developed value. Empirical correlations for the entrance length (Spurk 1996), based on the Reynolds number, are given by

$$\frac{l_e}{d} = \begin{cases} 0.056\ \mathrm{Re} & \text{for laminar flow} \\ 0.39\ \mathrm{Re}^{1/4} & \text{for turbulent flow} \end{cases} \tag{5.142}$$

At comparable Reynolds numbers, turbulent flows develop significantly faster than laminar ones, requiring shorter entrance lengths. During the entrance region, as the velocity profile evolves, an additional pressure loss occurs. This loss arises because a uniform velocity profile carries less kinetic energy than a non-uniform, fully developed one at the same mean velocity. The difference in kinetic energy is quantified by the **kinetic energy correction factor** α, defined by

$$\alpha = \frac{\int u^3 \, dA}{A \bar{u}^3} , \tag{5.143}$$

which accounts for the energy content of the actual velocity distribution compared to a flat profile (Truckenbrodt 1968, p. 190). For a perfectly uniform profile it follows $\alpha = 1$, while for non-uniform profiles $\alpha > 1$. For example, the parabolic laminar profile described by Eq. (5.100) yields $\alpha = 2$, whereas a turbulent profile based on a 1/7-th power law gives $\alpha \approx 1.058$, much closer to unity. The pressure loss associated with the development of the velocity profile can be estimated as $\Delta p = \rho/2(\alpha_1 - \alpha_2)\bar{u}^2$, where α_1 and α_2 refer to the values at the inlet and at the end of the entrance region, respectively. Empirical values for the loss coefficient ζ_{l_e} associated with this developing region (Truckenbrodt 1968) are in the range of

$$\zeta_{l_e} = \begin{cases} 1.16 - 1.41 & \text{for laminar flow} \\ 0.07 & \text{for turbulent flow} \end{cases} \tag{5.144}$$

As noted by Glück (1988), the total entrance loss also includes the local loss at the **pipe inlet**. When flow enters from a large reservoir or open domain, the inlet acts effectively as a sudden contraction with $A_2/A_1 \to 0$. For a sharp-edged entrance, the loss coefficient can be as high as $\zeta_i \approx 0.4$, while a slightly rounded inlet reduces this to $\zeta_i \approx 0.25$. Very large and carefully designed inlets can achieve significantly lower losses, in the range $\zeta_i \approx 0.06 - 0.10$ (Truckenbrodt 1968).

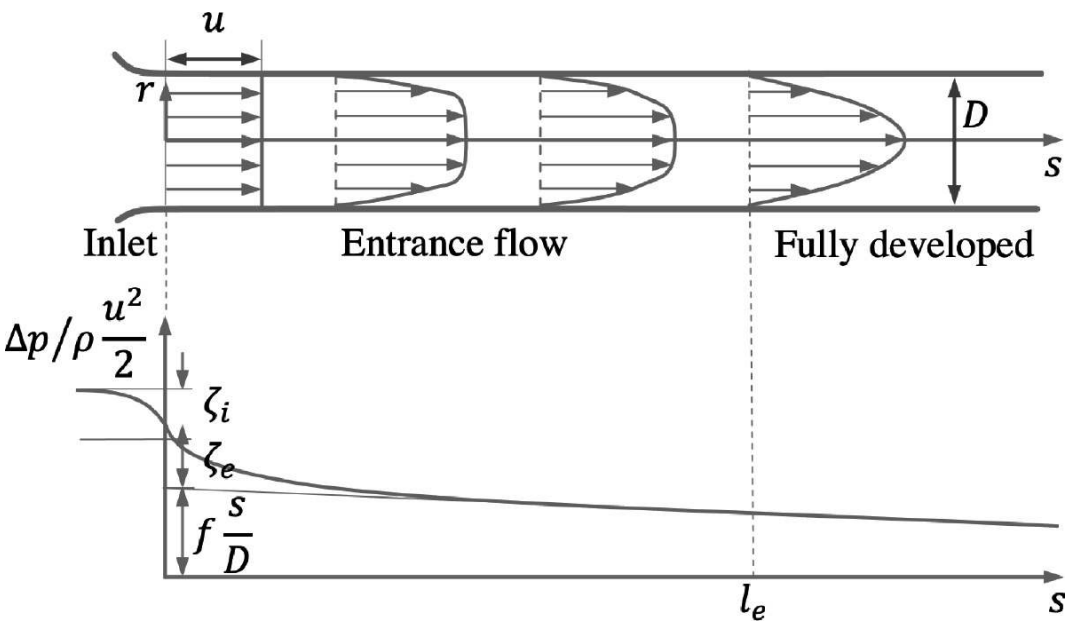


Fig. 5.24 Development of velocity and pressure profiles in entrance flow

The total pressure drop from inlet to the end of the entrance region thus consists of the inlet loss, the developing profile loss, and the frictional loss over the length ℓ, according to Eq. (5.132), resulting to

$$\Delta p_L = \left(f \frac{\ell}{d} + \zeta_{l_e} \right) \frac{\rho}{2} u^2 \ . \tag{5.145}$$

Once the fully developed region is reached, the pressure drop continues linearly with distance according to the wall friction, as discussed before. The required entrance length also depends on the cross-sectional geometry of the duct as outlined by the dimensionless development length L^+ for various noncircular geometries listed in Table 5.1.

References

Anderson JD (2016) Fundamentals of aerodynamics. McGraw-Hill Education

Bejan A (1995) Entropy generation minimization: the method of thermodynamic optimization of finite-size systems and finite-time processes. Mechanical and aerospace engineering series. Taylor & Francis

Blasius H (1913) Das Ähnlichkeitsgesetz bei Reibungsvorgängen in Flüssigkeiten. In *Mitteilungen über Forschungsarbeiten auf dem Gebiete des Ingenieurwesens*. Springer, pp 1–41

Glück B (1988) Hydrodynamische und gasdynamische Rohrströmung: Druckverluste. Verlag für Bauwesen

Clift R, Gauvin WH (1970) On the motion of particles in turbulent gas streams. Proc Chemeca 1:14–28

Clift R, Grace JR, Weber ME (2005) Bubbles, drops, and particles. Dover

Colebrook CF, White CM, Taylor GI (1937) Experiments with fluid friction in roughened pipes. Proc Royal Soc Lond. Ser A - Math Phys Sci 161(906):367–381

Dixon SL, Hall C (2013) Fluid mechanics and thermodynamics of turbomachinery. Elsevier

Greitzer EM, Tan CS, Graf MB (2007) Internal flow: concepts and applications. Cambridge engine technology series. Cambridge University Press

Kays WM, Crawford ME, Weigand B (2005) Convective heat and mass transfer. McGraw-Hill series in mechanical engineering. McGraw-Hill

Lamb H (1932) Hydrodynamics. The University Press

Lindgren ER (1965) Experimental study on turbulent pipe flows of distilled water. Technical Report Report AD621071, Oklahoma State University

Michaelides EE (1997) The transient equation of motion for particles, bubbles and droplets. ASME J Fluids Engin 119:233–247
[https://doi.org/10.1115/1.2819127]

Nikuradse J (1933b) Strömungsgesetze in rauhen Rohren VDI-Forschungsheft 361:1

Nikuradse J (1933) Gesetzmäßigkeiten der turbulenten Strömung in glatten Rohren. VDI-Forschungsheft 356:1

Panton RL (1996) Incompressible flow. Wiley

Rennels DC (2022) Pipe flow: a practical and comprehensive guide. Wiley

Richter H (1962) Rohrhydraulik, 4th edn. Springer

Schiller L, Naumann AZ (1933) Über die grundlegenden Berechnungen bei der Schwerkraftaufbereitung. Z VDI 77:318–320

Schlichting H, Truckenbrodt E (2001) Aerodynamik des Flugzeugs, Teil 1. Springer

Shah RK, London AL (1978) Laminar flow forced convection in ducts: a source book for compact heat exchanger analytical data. Advances in heat transfer. Academic Press, New York

Shapiro AH (1953) The dynamics and thermodynamics of compressible fluid flow, engineering special collection, vol 1. Wiley

Simon V, Weigand B, Gomaa H (2017) Dimensional analysis for engineers: mathematical engineering. Springer

Southard J (2006) Introduction to fluid motions, sediment transport, and current-generated sedimentary structures. ocw.mit.edu, 2006. Course notes, MIT OpenCourseWare

Spurk J (1996) Strömungslehre: Einführung in die Theorie der Strömungen. Springer

Truckenbrodt E (1968) Strömungsmechanik: Grundlagen und technische Anwendungen. Springer, Berlin

Weigand B, Kohler J, von Wolfersdorf J (2016) Thermodynamik kompakt, 4th edn. Springer, Berlin

White FM (1991) Viscous fluid flow, 2nd edn. McGraw-Hill

Footnotes

1 As introduced in Sect. 5.1.5, we adopt the Darcy friction factor f, while this subsection uses the Fanning friction factor f_F, which is one fourth of the Darcy value, $f_F = f/4$. Care should be taken when comparing with external references, as some sources, such as Shah and London (1978), primarily report results in the Fanning form.

Part II
Uncertainty, Data, and Learning

© The Author(s), under exclusive license to Springer Fachmedien Wiesbaden GmbH, part of Springer Nature 2026
H. Gomaa, *Modeling with Knowledge and Data*, Mathematical Engineering
https://doi.org/10.1007/978-3-658-50679-7_6

6. Probability Theory

Hassan Gomaa[1] ✉
(1) Strategic Projects Co-Innovation, Cognite, Oslo, Norway

Probability theory plays an essential role in modeling for two main reasons. First, it provides a way to quantify and reason about uncertainty, allowing us to estimate outcomes and support decisions when knowledge is incomplete. Second, it offers a practical tool for reducing the complexity of systems that are too intricate to analyze exactly by enabling meaningful approximations. The importance of probability in addressing uncertainty and complexity has long been recognized. The earliest known work that touches on probability and statistics can be traced back to the eighth century. At that time, the Arab linguist Al-Farahidi wrote the first known book on cryptography. He applied permutations and combinations to compile a comprehensive list of all possible Arabic words. The roots of modern probability theory trace back to gambling analysis in the sixteenth century, notably through the work of Cardano, a mathematician and seasoned gambler who provided the first systematic treatment of chance. In the seventeenth century, a gambling problem posed by Chevalier de Méré to Pascal sparked a correspondence with Fermat, leading to the concept of expected value, considered as the foundation of classical probability. Progress continued with Bernoulli's early formulation of the law of large numbers in 1713 and de Moivre's work on the central limit theorem in 1730, both of which were later expanded by Laplace in his **Théorie Analytique des Probabilités** (1812). In 1809, Gauss introduced core statistical tools including the method of least squares, maximum likelihood estimation, and the normal distribution. By 1919, von Mises formalized the frequentist interpretation of probability, and in 1933, Kolmogorov's axiomatic framework provided the rigorous mathematical foundation that underpins modern probability theory, especially for infinite outcome spaces. Reflecting this historical development, different paths are usually chosen to introduce

probability theory. These include the classical definition originating from Laplace's approach, the frequentist definition by von Mises, and the modern axiomatic definition by Kolmogorov.

The **classical definition** of probability, as commonly taught in school curricula, originates in the attempt to quantify gambling chances. It is based on two basic assumptions. The first is that the number of possible outcomes is finite. The second is that every outcome occurs with equal probability. For instance, an ideal coin toss has two possible outcomes, which are heads and tails. The question to answer focuses on a particular combination of outcomes. For example, we may ask what the chance is of getting heads every time when tossing the coin three times. Estimating the probability becomes a combinatorial counting exercise in which the number of favorable outcomes is compared to the total number of possible outcomes. For this example, there is one favorable outcome and 2^3 possible outcomes. The respective probability is therefore $1/8$. A brief summary of the common combinatorial cases is given in Sect. 6.3. Strictly speaking, the classical definition is insufficient to define probability in general because it is limited to cases where the outcomes have equal probability. However, for symmetrical problems with discrete uniform distributions, it serves the purpose well.

In contrast, the **frequentist definition** interprets probability as a measurable quantity that can be empirically determined through experimentation. A random experiment is conducted n times, from which the outcome A is observed n_A times. This results in the relative frequency n_A/n, which lies within the interval [0, 1]. The frequentist definition of probability is introduced as the limiting frequency for infinitely many experiments, that is

$$P(A) = \lim_{n\to\infty} \frac{n_A}{n} \quad .$$

As discussed later in Sect. 6.4, the law of large numbers states that the sample average of the conducted experiment converges, with virtual certainty, toward the expected value and tends to get closer as more trials are performed. As will become apparent in Chap. 8, the frequentist approach to probability proves practical and is highly relevant in engineering disciplines, e.g., for flow field measurements, machine reliability, and lifetime estimation.

The third, **axiomatic approach** is motivated by embedding probability theory within mathematics as a formal discipline. Three axioms form the basis for a mathematically sound definition of probability, allowing the deduction of a comprehensive theoretical framework that generalizes both the classical and

frequentist definitions. Furthermore, it ensures the validity of the empirical limit value from a frequentist perspective. The axiomatic definition extends the classical approach from a finite number of outcomes to countably infinite outcomes, while allowing for non-uniform probabilities of each outcome. The axioms are based on Lebesgue measure and integration theory, within which probabilities are standardized measures. Measure theory generalizes elementary geometrical terms such as the length of an interval and allows the concept of probability to transition from discrete to continuous domains and from finite to countably infinite domains.

As detailed further in the text, to introduce the axioms, a sample space Ω is defined that covers all possible outcomes of the regarded experiment. Furthermore, an event *A* is defined as a subset of Ω representing a combination of different outcomes. The probability *P* is introduced as a measure over all events that satisfies the following conditions

1. Each event is assigned a non-negative real number

$$P(A) \geq 0 \ .$$

2. The sample space Ω covers all possible outcomes. Therefore, the probability of the entire space is equal to one, thus

$$P(\Omega) = 1 \ .$$

3. For any finite or countable collection of mutually exclusive events A_i the probability of their union is the sum of their individual probabilities, that is

$$P(\cup_i A_i) = \sum_i P(A_i) \ .$$

This means that the probability of an event consisting of several disjoint sub-events can be calculated by summing the probabilities of the individual sub-events $P(A_i)$. This third axiom extends the classical definition from finite outcomes with equal probability to countably infinite outcomes with variable probabilities. The axiomatic approach allows the direct determination of the probability of any event if the underlying subset probabilities $P(A_i)$ are known via $\sum_i P(A_i)$, or equivalently through probabilities of complements via

$1 - \sum_j P(A_j^c)$. If neither is known, the experimental path following the frequentist definition remains available.

After this brief overview of the development of probability theory, the following sections will successively develop the concept from the axiomatic point of view. The given introduction follows the approaches of Argyris et al. (2017), striking a balance between clarity and specificity, combined with the depth of the manuscripts by Ross (2012) and Moeschlin (2012).

6.1 Fundamentals of Probability

In this section, we introduce the key building blocks for describing random experiments mathematically, including the sample space, events, and the event space.

6.1.1 Random Experiments

A random experiment describes any well-defined and repeatable procedure with an uncertain outcome. It does not matter whether the uncertainty arises from inherent randomness or from unknown conditions under which the experiment is conducted. We introduce two examples to illustrate the terminology that follows

E1 In the first random experiment we roll two dice.

E2 In the second experiment we measure the lifetime of a pump.

Mathematically, a random experiment is described by a **probability space** that consists of three parts

1. The sample space Ω, which is a nonempty set containing all possible outcomes of the experiment.
2. The event space $\mathscr{A}$, which is a system of subsets of Ω, where each event represents a set containing zero or more outcomes.
3. The probability map P, which assigns probabilities to events. It is defined as $P : \mathscr{A} \to \mathbb{R}$ and satisfies the conditions detailed in the following Sect. 6.2.

The probability space is also referred to as the probability tuple $(\Omega, \mathscr{A}, P)$. In the following, we introduce each of these elements.

Sample Space To describe a random experiment, it is necessary to specify all possible outcomes. These outcomes represent the actual results of the experiment and are denoted as ω_1, ω_2, and so on. The collection of all possible outcomes forms the sample space, written as $\Omega = \{\omega_1, \omega_2, \cdots, \omega_n\}$, where $n \in \mathbb{N}$. The sample space has the following properties

- The outcomes in the sample space are mutually exclusive. If the outcome of an experiment is ω_i, it cannot at the same time be ω_j with $j \neq i$ for any $j \in \mathbb{N}$.
- The outcomes in the sample space are collectively exhaustive. This means that any possible outcome ω_i must belong to Ω.

The outcomes can be either discrete or continuous in nature. In the first example **E1**, each die has six possible discrete values, and assuming fair dice each value is equally probable. In the second example **E2**, the lifetime of the pump is a continuous variable that can take any positive value. The probability that a continuous variable takes on an exact value, for instance that the lifetime is exactly $t = 42\,000\,\mathrm{h}$, is effectively zero. To handle this, continuous spaces are divided into intervals. Mathematically, this reduces the problem from infinitely many uncountable elements to a countable collection of intervals. The probability question then becomes whether the value lies within a particular interval rather than matching an exact value. The sample spaces for our two examples are as follows

E1 $\Omega_1 := \{(i, j) \in \mathbb{N} \times \mathbb{N} \mid 1 \leq i, j \leq 6\}$,

E2 $\Omega_2 := \{t \in \mathbb{R} \mid t \geq 0\}$.

6.1.2 Events and Event Spaces

Typically, we are interested not in individual outcomes but in combinations of outcomes, which are called **events**. An event represents a set of possible outcomes for a given experiment and therefore forms a subset of the sample space. Once the experiment is performed and the outcome is known, we can determine whether the event has occurred.

For our two illustrative examples, typical events of interest could be as follows

E1 The event that the sum of the two dice exceeds eight. This corresponds to the set $\{(i, j) \in \Omega_1 \mid i + j > 8\}$.

E2 The event that the pump breaks after a lifetime between $60\,000$ and $70\,000$ operating hours. This corresponds to the set

$\{t \in \Omega_2 \mid 60\,000 \leq t \leq 70\,000\}$.

The complement of any event A is the event $A^c = \{\omega_i \in \Omega \mid \omega_i \notin A\}$. This represents the event that A does not occur. The events A and A^c are mutually exclusive and collectively exhaustive. If $A = \Omega$, meaning it covers all possible outcomes of the sample space, then its complement is the empty set $A^c = \emptyset$. The empty set $\emptyset$ is itself considered an event, although it never occurs. When an event contains only a single outcome, that is $A = \{\omega_i\}$, it is called an **elementary event**.

Event Relations and Operations Since events are sets, their relations and operations follow the standard rules of set theory. To illustrate, consider two events A and B. If A is contained in B, that is

$$A \subseteq B \ , \tag{6.1}$$

then every elementary event from A, meaning each $\omega \in A$, is also contained in B, so $\omega \in B$. For a performed experiment, this means that if A occurs, then B occurs as well.

If two events A and B contain exactly the same elementary events, then they are considered **equal**, written as

$$A = B \ . \tag{6.2}$$

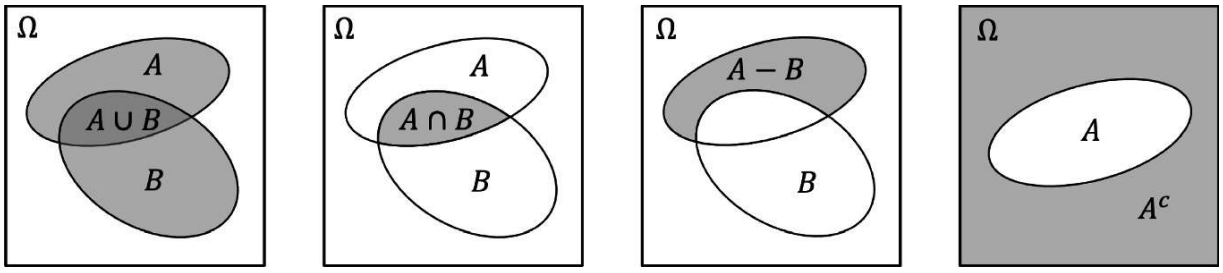


Fig. 6.1 Visual representation of basic set operations on events within a sample space. The figure shows the union $A + B$, the intersection AB, the difference $A - B$ and the complement A^c (Argyris et al. 2017)

Operations on sets apply in the same way to events, as depicted in Fig. 6.1. The **union** $A + B$ describes the event that occurs if either A or B occurs, and represents the event that covers all outcomes that are either in A or in B, expressed as

$$A \cup B = \{\omega \in \Omega \,|\, \omega \in A \text{ or } \omega \in B\} \ . \tag{6.3}$$

The product of A and B, also called the **intersection**, represents the event that covers all outcomes that are in both A and B, written as

$$A \cap B = \{\omega \in \Omega \,|\, \omega \in A \text{ and } \omega \in B\} \ . \tag{6.4}$$

The **difference** of A and B represents the event that covers all outcomes that are in A but not in B, expressed by

$$A - B = A \setminus B = \{\omega \in \Omega \,|\, \omega \in A \text{ and } \omega \notin B\} \ . \tag{6.5}$$

The **complement** of an event A represents the event that A does not occur. This is the set of all outcomes that are in Ω but not in A, thus

$$A^c = \{\omega \in \Omega \,|\, \omega \notin A\} \ . \tag{6.6}$$

Finally, if A and B have no elementary events in common, they are called **disjoint** or mutually exclusive events, written as

$$A \cap B = \emptyset \ . \tag{6.7}$$

Event Space As mentioned, the sample space Ω contains all possible outcomes of an experiment. From these elementary outcomes, we can form different combinations, which are called events. The event space, denoted by $\mathscr{A}$, consists of all possible events that can be formed. This means that the event space contains all subsets of Ω, including the empty set $\emptyset$ and the full sample space Ω itself.

When the sample space Ω is discrete and finite, the event space can be described using the power set of Ω. The power set is the set of all subsets of Ω. For example, if Ω contains n elements, the power set contains 2^n subsets, which represent all possible event combinations. In our first example, where we roll two distinguishable dice, the sample space Ω_1 contains 36 elements. The corresponding event space $\mathscr{A}_1$ therefore contains 2^{36} possible events. A summary of common combinations and permutations can be found in Sect. 6.3.

In cases where the sample space contains continuous outcomes, as in the example of the pump lifetime, the situation becomes more complicated. In this case, the event space cannot simply be described by the power set. Instead, we use what is called a sigma algebra for $\mathscr{A}$, that represents a collection of subsets of the sample space that satisfies specific conditions required for probability measures. The sigma algebra must satisfy the following properties

1. It contains the sample space itself, so $\Omega \in \mathscr{A}$.

2. It is closed under taking complements, meaning that if $A \in \mathscr{A}$, then $A^c \in \mathscr{A}$. So if an event is in the event space, so is its complement.
3. It is closed under countable unions, so that if $A_1, A_2, A_3, \ldots \in \mathscr{A}$, then $\cup_n A_n \in \mathscr{A}$. This ensures that the union of any countable sequence of events is also an event.

The sigma algebra ensures that the event space is closed under the basic operations needed in probability theory. It is no longer practical to list all elements of the sigma algebra when the sample space is continuous. Instead, it is described through a generating set. A common example is the Borel sigma algebra, which is generated by the open and closed sets of real numbers and allows probability measures to be applied on $\mathbb{R}$.

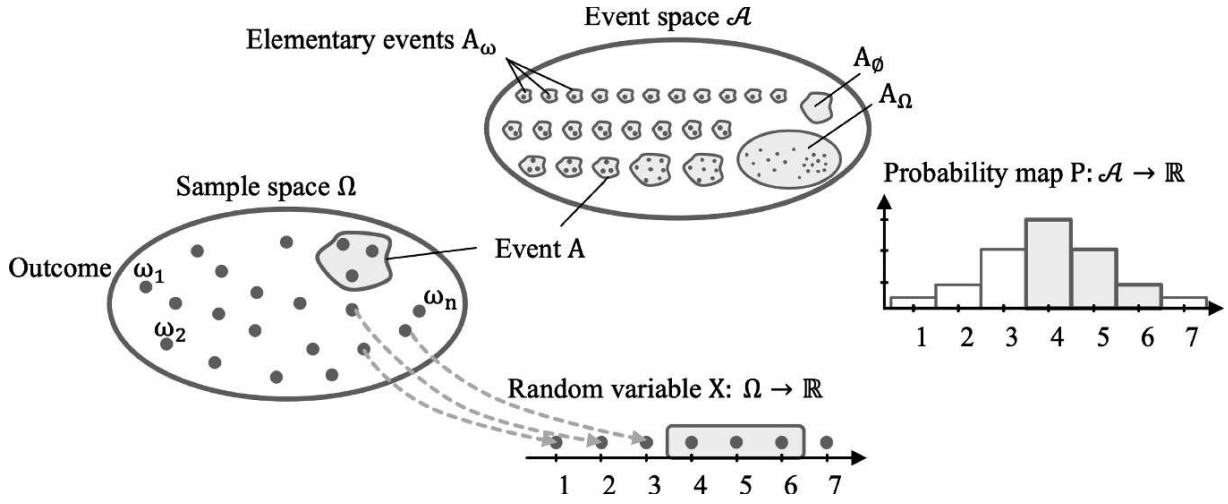


Fig. 6.2 Schematic overview of a probability space. The figure illustrates the relationship between outcomes, the sample space Ω, the event space $\mathscr{A}$, random variables and the probability map *P*

6.2 Probability Distributions

The sample space Ω captures all possible outcomes of an experiment, and the event space $\mathscr{A}$ represents the combinations of these outcomes that we can consider. These subsets allow us to divide the domain into mutually exclusive parts. Outcomes can be qualitative, for example heads or tails, the color of a ball, or the suit of a card. They can also be quantitative, for example the number on a die or the lifetime of a pump. To develop a quantitative theory of probability, we must assign numbers to these outcomes. This is the role of the random variable,

which defines the domain for the probability function. The random variable and the probability function are closely connected, as the choice of random variable determines how we describe and compute probabilities.

6.2.1 Random Variable

To define the domain for a probability function, we assign a numerical value to each elementary event. This mapping is called a random variable and is illustrated in Fig. 6.2. The term random variable can be misleading because it is neither a variable nor random. It is a measurable mapping that defines the domain to which the probability measure is applied. A random variable $X(\omega)$ maps the elements of the sample space Ω to numeric values. In this text, we focus on real-valued random variables, so the mapping is $X : \Omega \to \mathbb{R}$. A random variable can be either discrete or continuous depending on the nature of the outcomes it describes.

A random variable must be measurable. This means that for any real number x the set of outcomes for which $X(\omega) \leq x$ holds must belong to the event space $\mathscr{A}$, thus

$$\forall x \in \mathbb{R} \quad \{\omega \mid X(\omega) \leq x\} \in \mathscr{A} \ . \tag{6.8}$$

This condition ensures that the structure of the sample space is preserved when mapping to the domain of real numbers. It also guarantees that probabilities can be assigned in a consistent way.

The probability that the random variable X takes a value in a subset S of the real numbers is written as

$$P(X \in S) \ . \tag{6.9}$$

This is a compact form of the equivalent and more formal expression

$$P(\{\omega \in \Omega \mid X(\omega) \in S\}) \ , \tag{6.10}$$

that is the probability of the set of all outcomes ω in the sample space Ω for which the random variable X takes a value in the set S. If the random variable is discrete, the set S consists of specific numbers. If it is continuous, the set S consists of intervals. This distinction reflects whether we sum over discrete values or integrate over continuous ranges when computing probabilities.

The choice of random variables influences how we approach a problem and how easily we can analyze it. If the outcomes of an experiment are already numerical, we could simply define the random variable as the identity function.

This means the random variable maps each outcome to itself without any transformation. For example, in experiment **E1** where two dice are rolled, we can define the sample space as $\Omega = \{(i,j) \mid 1 \leq i,j \leq 6\}$ where each pair (i,j) represents the numbers rolled on the two dice. Assuming fair dice, every outcome has equal probability. The probability measure is therefore uniform with $P(\omega) = 1/36$ for all $\omega \in \Omega$ and the event space is the power set of Ω.

However, it is often helpful to define a random variable that simplifies the analysis or better reflects the question of interest. For instance, if we are interested in the sum of the numbers rolled, we can define a new random variable $T : \Omega \to \Omega' \quad \text{with } T(i,j) = i + j$, where the new sample space is $\Omega' = \{2, 3, \cdots, 12\}$, and the event space is the power set of Ω'. For any event A' in Ω' we can define the corresponding set $S(A') = \{(i,j) \in \Omega \mid T(i,j) \in A'\}$, which consists of all outcome pairs in the original space that lead to sums in A'. The probability of the event A' is then given by $P'(A') = P(S(A'))$. Since the original probability measure is uniform, this becomes $P'(A') = |S(A')|/36$. For example, if $A' = \{4\}$, then $S(\{4\}) = \{(1,3), (2,2), (3,1)\}$ and the probability is $P'(\{4\}) = 3/36$. The random variable and its resulting probability distribution are strongly linked. For the identity mapping, the distribution is uniform over all pairs (i,j), while for the sum $T(i,j) = i + j$ the distribution follows a binomial-like form.

So far we have assigned a single random variable to each outcome. In general it is also possible to assign multiple random variables to the same elementary event. For instance, in experiment **E2**, where we observe the lifetime of a pump, we might also record additional characteristics such as the number of on–off switches, the operating conditions, or if we are studying a fleet of pumps, the pump size and the type of fluid being pumped. In this case we define several random variables on the same sample space. If ω represents an elementary outcome, we might have random variables $X_1(\omega),\ X_2(\omega),\ \cdots,\ X_n(\omega)$, where each X_i describes a different feature of interest for the same outcome.

A linear combination of random variables such as $\alpha_1 X_1 + \alpha_2 X_2$ is itself a random variable. The same holds for the product $X_1 X_2$, the quotient X_1/X_2 as long as X_2 is not zero, and any mapping $\phi(X_1(\omega))$ where ϕ is a function.

Random variables are also of central importance in applied statistics and data-driven modeling, as they correspond to the features in a data set, as will be discussed in Sect. 8.1. Their properties, such as distribution, moments, and dependencies discussed in the following, are essential for statistical analyses.

6.2.2 Probability Map

Equipped with the defined random variable, we are now ready to introduce the corresponding probability map *P*. The probability map $P : \mathscr{A} \to \mathbb{R}$ assigns a number to each element $A \in \mathscr{A}$, thus returning the probability of the event *A*. The map satisfies the three fundamental axioms introduced at the beginning of this chapter

1. **Non-negativity** $P(A) \geq 0 \quad (A \in \mathscr{A})$,
2. **Unitarity** $P(\Omega) = 1$,
3. σ**-additivity** For any countable sequence of disjoint, that is mutually exclusive, events A_i,

$$P\big(\cup_{i=1}^{\infty} A_i\big) = \sum_{i=1}^{\infty} P(A_i) \ .$$

The non-negativity axiom ensures that probabilities are never negative, reflecting their interpretation as measures of likelihood. Unitarity states that the probability of the entire sample space is one, meaning that some outcome in Ω will certainly occur. The axiom of σ-additivity ensures that if we consider any countable sequence of disjoint events, the probability of their union is simply the sum of their individual probabilities. Together, these axioms apply both to finite discrete systems and to systems with countably infinite or continuous outcomes.

Monotonicity From these axioms, we immediately see that the probability of any event lies within the interval [0, 1]. The empty set $\emptyset$ represents the impossible event, so $P(\emptyset) = 0$. The second axiom guarantees that the probability of the entire sample space is one, so that $P(\Omega) = 1$. Furthermore, the probability is monotonic. If *A* is a subset of *B*, then the probability of *A* cannot exceed the probability of *B*, that is

$$A \subseteq B \quad \Rightarrow \quad P(A) \leq P(B) \ . \tag{6.11}$$

Complementary Probability Every event *A* has a complement A^c consisting of all outcomes in Ω that are not in *A*. Since *A* and A^c are disjoint and together form the entire sample space, we have

$$P(A^c) = 1 - P(A) \ , \tag{6.12}$$

expressing that the probability of an event not occurring is simply one minus the probability that it does occur.

Addition Law of Probability For two events *A* and *B* that are not disjoint, the probability that at least one of them occurs is given by

$$P(A \cup B) = P(A) + P(B) - P(A \cap B) \ . \tag{6.13}$$

This formula subtracts the overlap $P(A \cap B)$ to avoid double counting. If *A* and *B* are disjoint, meaning $A \cap B = \emptyset$, this simplifies to $P(A \cup B) = P(A) + P(B)$.

Conditional Probability Conditional probability describes the probability of an event *A* given that another event *B* has occurred. Provided $P(B) > 0$, it is defined as

$$P(A|B) = \frac{P(A \cap B)}{P(B)} \ . \tag{6.14}$$

This leads directly to the multiplication rule

$$P(A \cap B) = P(A|B)P(B) = P(B|A)P(A) \ , \tag{6.15}$$

showing that the joint probability of *A* and *B* can be obtained by multiplying the probability of one event by the conditional probability of the other event given that the first has occurred. **Bayes' theorem** naturally follows. For two events *A* and *B* with $P(A) > 0$ and $P(B) > 0$, we have

$$P(B|A) = \frac{P(A|B)P(B)}{P(A)} \ . \tag{6.16}$$

Bayes' theorem enables the reversal of conditional probabilities and is particularly useful when *P*(*A*|*B*) is easier to determine than *P*(*B*|*A*). In Bayesian inference, this relation is used to update prior beliefs *P*(*B*) into posterior probabilities *P*(*B*|*A*) as new evidence *A* is observed.

Independence Two events *A* and *B* are said to be independent if the occurrence of one does not affect the probability of the other, and in that case

$$P(A \cap B) = P(A)P(B) \ . \tag{6.17}$$

For example, consider our earlier illustrative experiments where we roll two dice in **E1** and observe the lifetime of a pump in **E2**. The time at which the pump fails is completely independent of whatever numbers appear on the dice. This

means that the probability that the pump fails after 3000 h and the dice show two sixes equals the probability that the pump fails after 3000 h multiplied by the probability that the dice show two sixes. A more relevant example can be found in a manufacturing process where both the temperature of a furnace and the rotational speed of a cooling fan are monitored. If the furnace temperature and the fan speed are controlled by independent systems with no shared feedback or coupling, the probability that the temperature exceeds a certain threshold and that the fan operates at a given speed equals the probability that the temperature exceeds the threshold multiplied by the probability that the fan operates at that speed.

6.2.3 Probability Distribution and Density Function

For a given random experiment and a defined random variable *X*, we often want to determine the probability that *X* takes a value within a certain range. Let this range be [*a*, *b*] with $a < b$. First, we identify all outcomes that lie within the specified range

$$\{a < X(\omega) \leq b\} = \{\omega \,|\, a < X(\omega) \leq b\} \ . \tag{6.18}$$

By applying the axiom of σ-additivity, we can express the probability of the event as the sum of the individual probabilities of the elementary outcomes with

$$P(a < X(\omega) \leq b) = \textstyle\sum_{\omega_i \in A} P(\omega_i) \ . \tag{6.19}$$

Probability Distribution The random variable orders the outcomes over the real line $\mathbb{R}$, enabling us to map the probability distribution as a function of the variable. This mapping is referred to as the **cumulative distribution function** (cdf) and illustrated in Fig. 6.3. The cdf expresses the probability that *X* takes a value less than or equal to *x*. In terms of the cdf, the probability of the interval $a < X \leq b$ becomes

$$P(a < X \leq b) = F(b) - F(a) \ . \tag{6.20}$$

By definition, the cumulative distribution function is monotonically increasing. Its limits at the boundaries of the real line are $\lim_{x \to -\infty} F(x) = 0$ and $\lim_{x \to +\infty} F(x) = 1$ reflecting that probabilities accumulate from zero up to one as we move along the real line.

Density Distribution If the random variable is discrete, the sample space consists of distinct outcomes ω_i, and the random variable maps these outcomes

to discrete points along $\mathbb{R}$. If the random variable is continuous, we work with intervals $[a, b] \subset \mathbb{R}$ rather than individual points. The formal transition from discrete to continuous probability replaces summation in Eq. (6.19) with integration

$$P(a < X \leq b) = \int_a^b f(x)\, dx \ , \tag{6.21}$$

where $f(x)$ is the **probability density function** (pdf), shown in Fig. 6.3. The pdf relates to the cdf through

$$F(x) = P(X \leq x) = \int_{-\infty}^{x} f(\xi)\, d\xi \quad \forall x \in \mathbb{R} \ , \tag{6.22}$$

and conversely

$$f(x) = \frac{d}{dx} F(x) \ . \tag{6.23}$$

The pdf satisfies the two essential properties, that it is non-negative everywhere and integrates to unity over the entire real line

$$f(x) \geq 0 \quad \text{and} \quad \int_{-\infty}^{+\infty} f(x)\, dx = 1 \ . \tag{6.24}$$

The mathematical transition from discrete to continuous distributions can also be described using the Dirac δ-function. Let $x_1, \ldots, x_n$ be the discrete values of the random variable and their associated probabilities $p_1, \ldots, p_n$. The delta function is defined by $\delta(x - x_i) = 0$ for all $x \neq x_i$ and satisfies the property $\int_{x_i-\epsilon}^{x_i+\epsilon} \delta(x - x_i)\, dx = 1$ for any small $\epsilon > 0$. The corresponding probability density is then $f(x) = \sum_i p_i\, \delta(x - x_i)$ where the sum of probabilities satisfies $\sum_i p_i = 1$. Integration yields the cumulative distribution $F(x) = \sum_i p_i \int_{-\infty}^{x} \delta(\xi - x_i)\, d\xi$.

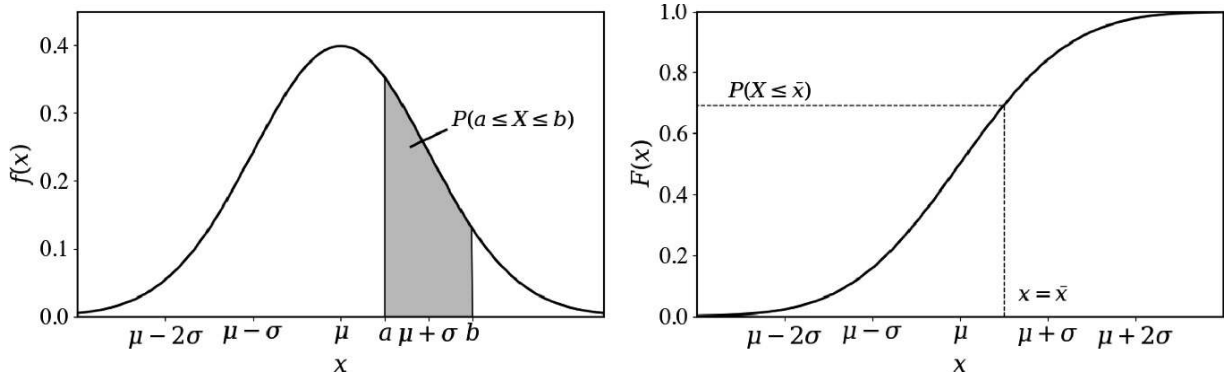


Fig. 6.3 Probability density function and cumulative distribution function

6.2.4 Distribution Parameters

The properties of a random variable *X* are directly accessible through its pdf. Assuming the pdf is given, it can be characterized by a number of distribution measures.

Expected Value The expected value of a random variable *X* with pdf *f*(*x*) is defined as the probability-weighted average of the possible values that *X* can take. For discrete distributions, it is calculated as

$$\mathrm{E}\left[X\right] = \langle X \rangle = \sum_n x_n f(x_n) \tag{6.25}$$

and for continuous distributions, the expected value follows through integration as

$$\mathrm{E}\left[X\right] = \langle X \rangle = \int_{-\infty}^{+\infty} x\, f(x)\, dx \ . \tag{6.26}$$

The expected value is also referred to as the first moment of *X* or the mean, denoted $\mathrm{E}\left[X\right] = \mu$. Since the expected value is solely determined by the pdf, all random variables sharing the same pdf have the same expected value. To illustrate the expected value, we reconsider our example

E1 In the random experiment of throwing two dice, the probability of each outcome in the sample space $\Omega = \{(i,j) \in \mathbb{N} \times \mathbb{N} \mid 1 \leq i,j \leq 6\}$ is uniformly distributed. As we are interested in the total sum of numbers, we define the random variable $T : \Omega \to \Omega'$, where $\Omega' = \{2, \cdots, 12\}$ and $T(i,j) = i + j$. The expected value becomes

$$\mathrm{E}\left[T\right] = \sum_{m \in T(\Omega)} m\, P(T = m) \ , \tag{6.27}$$

where $P(T = m)$ corresponds to the probability of obtaining the sum *m*. With the probabilities as introduced in Sect. 6.2.1, we obtain

$$\begin{aligned} \mathrm{E}\left[T\right] \ &= 2\,\tfrac{1}{36} + 3\,\tfrac{2}{36} + 4\,\tfrac{3}{36} + 5\,\tfrac{4}{36} + 6\,\tfrac{5}{36} + 7\,\tfrac{6}{36} \\ &\quad + 8\,\tfrac{5}{36} + 9\,\tfrac{4}{36} + 10\,\tfrac{3}{36} + 11\,\tfrac{2}{36} + 12\,\tfrac{1}{36} = 7 \ . \end{aligned} \tag{6.28}$$

The expected value has several important properties that are useful for further developments in probability and statistics.

Linearity of Expectation The expectation operator is linear. For a random variable *X* and real constants $a, b \in \mathbb{R}$, we have

$$\mathrm{E}\left[aX + b\right] = a\,\mathrm{E}\left[X\right] + b\ . \tag{6.29}$$

In addition, the expectation of the sum of two random variables satisfies

$$\mathrm{E}\left[X + Y\right] = \mathrm{E}\left[X\right] + \mathrm{E}\left[Y\right]\ . \tag{6.30}$$

This property extends to the sum of any finite number of random variables, provided their expectations exist.

Chain of Expectation If a random variable *X* always takes a constant value $c \in \mathbb{R}$, then its expected value is simply that constant, thus $\mathrm{E}\left[X\right] = c$. This leads to the property known as the chain of expectation. For any random variable *X* with a well-defined expectation, taking the expectation of its expected value gives the same result, that is

$$\mathrm{E}\left[\mathrm{E}\left[X\right]\right] = \mathrm{E}\left[X\right]\ . \tag{6.31}$$

This reflects that once the expected value is computed, applying the expectation operator again does not change it.

Generalized Argument In many cases, we are interested not in the expected value of the random variable itself, but in the expected value of some function of it. Let $g(X)$ be a function applied to the random variable *X*. The expected value of $g(X)$ is given by

$$\mathrm{E}\left[g(X)\right] = \langle g(X) \rangle = \textstyle\sum_n g(x_n) f(x_n)\ , \tag{6.32}$$

for a discrete random variable, where the sum runs over all possible values x_n weighted by their probabilities $f(x_n)$. For a continuous random variable, the expected value is expressed as an integral

$$\mathrm{E}\left[g(X)\right] = \langle g(X) \rangle = \int_{-\infty}^{+\infty} g(x) f(x)\, dx\ . \tag{6.33}$$

This formulation allows us to compute expectations for transformations of *X*, such as powers, exponentials, or other functions, by weighting each possible value according to its probability.

Variance, Skewness, and Kurtosis The generalized quantity $\mathrm{E}\left[X^k\right]$, with $k \in \mathbb{N}$, is referred to as k^{th} moment and for discrete and continuous distributions respectively reads

$$\mathrm{E}\left[X^k\right] = \langle X^k \rangle = \textstyle\sum_n x_n^k f(x_n) \ , \tag{6.34}$$

$$\mathrm{E}\left[X^k\right] = \langle X^k \rangle = \int_{-\infty}^{+\infty} x^k \, f(x) \, dx \ . \tag{6.35}$$

Shifting X by its mean yields the so-called k^{th} central moments $E\Big[\left(X - \mathrm{E}\left[X\right]\right)^k\Big]$. The first central moment is by definition zero, thus

$$\mathrm{E}\left[\left(X - \mathrm{E}\left[X\right]\right)\right] = 0 \ . \tag{6.36}$$

The second central moment defines the **variance** with

$$\mathrm{Var}\left(X\right) = \mathrm{E}\left[\left(X - \mathrm{E}\left[X\right]\right)^2\right] = \mathrm{E}\left[X^2\right] - \mathrm{E}\left[X\right]^2 \ . \tag{6.37}$$

The variance $\mathrm{Var}\left(X\right) = \sigma^2$ measures the average squared deviation from the mean and is sometimes referred to as the dispersion. Its positive square root, σ is the standard deviation. Both quantities describe the statistical spread of the outcomes. A small variance indicates that values are tightly concentrated around the mean, while a large variance corresponds to a broader distribution with values more widely spread out. In line with the linearity of expectation, it is worth noting that variance is additive for independent random variables, that is $\mathrm{Cov}\left(X, Y\right) = 0$, so that $\mathrm{Var}\left(X + Y\right) = \mathrm{Var}\left(X\right) + \mathrm{Var}\left(Y\right)$. The standard deviation does not share this property since in general $\sigma(X + Y) \neq \sigma(X) + \sigma(Y)$.

The third central moment captures asymmetry in the distribution with

$$\mathrm{E}\left[\left(X - \mathrm{E}\left[X\right]\right)^3\right] = \mathrm{E}\left[X^3\right] - 3\,\mathrm{E}\left[X\right]\mathrm{E}\left[X^2\right] + 2\,\mathrm{E}\left[X\right]^3 \ . \tag{6.38}$$

From this, the **skewness** can be defined as

$$\mathrm{S}\left(X\right) = \frac{\mathrm{E}\left[\left(X - \mathrm{E}[X]\right)^3\right]}{\sigma^3} = \mathrm{E}\left[\frac{X - \mu}{\sigma}\right]^3 \ . \tag{6.39}$$

Skewness quantifies the degree of asymmetry. It is zero for symmetric distributions, positive when the distribution has a longer right tail, and negative when the left tail is longer, as shown in Fig. 6.4.

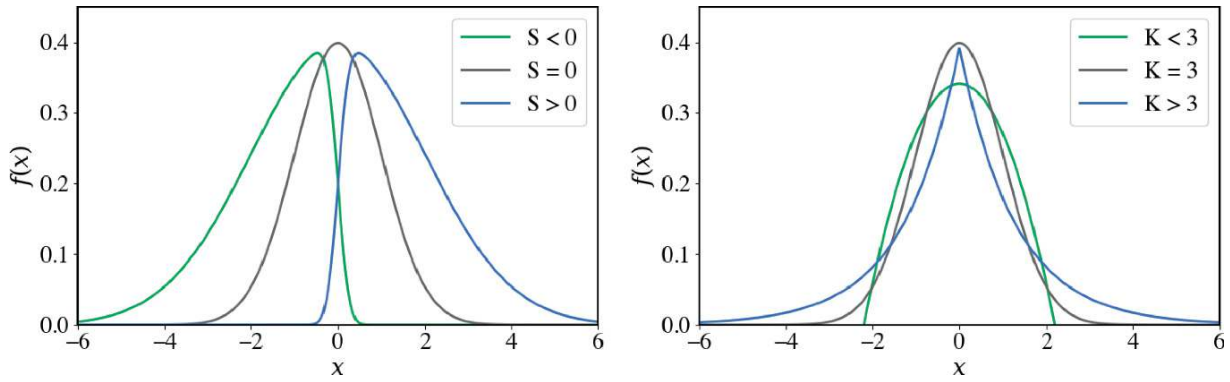


Fig. 6.4 Illustration of skewness (left) and kurtosis (right) using representative probability density functions

The fourth central moment leads to the **kurtosis**, defined by

$$\mathrm{K}\,(X) = \frac{\mathrm{E}\left[(X-\mathrm{E}[X])^4\right]}{\sigma^4} = \mathrm{E}\left[\frac{X-\mu}{\sigma}\right]^4 . \tag{6.40}$$

Kurtosis, like skewness, is a measure of the shape of a distribution. It describes how peaked the distribution is around the mean and how heavy its tails are. The kurtosis is often compared to that of a univariate normal distribution where $\mathrm{K} = 3$, discussed in Sect. 6.3. Distributions with greater K show stronger deviations from the mean due to heavier tails or sharper peaks, as depicted in Fig. 6.4.

In this section, probability densities were characterized by various measures and moments. It shall be mentioned that in the case where all moments exist, the corresponding probability density $f(x)$ can be fully described by the so-called generating or **characteristic function**, which provides an alternate analytical route.

Multiple Random Variables So far, we have limited the expected value to univariate functions, where a single random variable X maps outcomes to real numbers. In many applications, however, we encounter scenarios where several random variables are defined on the same probability space, for example when describing multiple features of a physical system. Extending the concept of expectation to such cases allows us to analyze the joint behavior of these variables. Consider two random variables X and Y defined on the same probability space. Let $f(x, y)$ denote the corresponding joint probability distribution function. This function describes the likelihood that X takes the

value x and Y simultaneously takes the value y. The expected value of a general function $g(X, Y)$ of these variables is given by applying the joint distribution to

$$\langle g(X,Y) \rangle = \int_{-\infty}^{+\infty} \int_{-\infty}^{+\infty} g(x,y)\, f(x,y)\, dx\, dy \ , \tag{6.41}$$

where the integration is over the domain of X and Y. This integral sums the contributions of all possible pairs of values, weighted by their joint probability density.

For the case of discrete random variables, where X and Y can take values $\{x_i\}$ and $\{y_j\}$ respectively, the expectation becomes

$$\langle g(X,Y) \rangle = \sum_i \sum_j g(x_i, y_j) f(x_i, y_j) \ , \tag{6.42}$$

where $f(x_i, y_j)$ is the joint probability mass function giving the probability that $X = x_i$ and $Y = y_j$. A common quantity of interest is the expected value of the product of two random variables

$$\langle XY \rangle = \int_{-\infty}^{+\infty} \int_{-\infty}^{+\infty} xy\, f(x,y)\, dx\, dy \ , \tag{6.43}$$

for continuous random variables, or equivalently

$$\langle XY \rangle = \sum_i \sum_j x_i y_j f(x_i, y_j) \ , \tag{6.44}$$

for discrete random variables. This quantity plays a central role in measuring the relationship between X and Y, as discussed in the context of the covariance and correlation in the next section.

6.2.5 Independence, Uncorrelatedness, and Covariance

A central concept in probability theory is the independence of events. Intuitively, two events A and B are independent if the occurrence of A has no influence on the occurrence of B, and vice versa. In this case, knowing that A has occurred does not change the probability of B occurring. Mathematically, this is expressed through conditional probability in Eq. (6.14). If $P(A) > 0$, then

$$P(B|A) = \frac{P(A \cap B)}{P(A)} = P(B) \ , \tag{6.45}$$

so that the conditional probability equals the unconditional probability of *B*. This leads directly to the defining condition for **independence** of two events

$$P(A \cap B) = P(A)P(B) \ , \tag{6.46}$$

meaning the probability that both events occur is simply the product of their individual probabilities. This definition naturally generalizes to multiple events. The events $A_1, A_2, \cdots, A_n$ are independent if for any subset of these events, the joint probability of all of them occurring is the product of their individual probabilities, that is

$$P\left(\cap_{i=1}^{n} A_i\right) = \prod_{i=1}^{n} P(A_i) \ . \tag{6.47}$$

We extend the concept of independence from events to random variables. Random variables $X_1, X_2, \cdots, X_n$ are independent if for all values $x_1, x_2, \cdots, x_n$ their probabilities follow

$$P(X_1 = x_1, \cdots, X_n = x_n) = P(X_1 = x_1)P(X_2 = x_2) \cdots P(X_n = x_n) \ , \tag{6.48}$$

so their joint probability factors into the product of the individual probabilities. For continuous random variables, the same principle applies to their joint probability density function. Two random variables *X* and *Y* are independent if

$$f(x, y) = f_x(x) f_y(y) \ , \tag{6.49}$$

where *f*(*x*, *y*) is the joint pdf and $f_x(x)$ and $f_y(y)$ are the respective pdfs of *X* and *Y*.

Beyond full independence, two random variables may still exhibit no linear relationship even though they are dependent. Two random variables *X* and *Y* are called **uncorrelated** if

$$\langle XY \rangle = \langle X \rangle \langle Y \rangle \ , \tag{6.50}$$

which means that their joint expectation equals the product of their individual expectations, reflecting the absence of a linear relationship between them. While independence implies uncorrelatedness, the reverse is not true. Two variables can be uncorrelated but still dependent in a nonlinear way, as illustrated in the example at the end of this section. The fact that independence implies uncorrelatedness can be illustrated by writing out the expectation explicitly. If *X* and *Y* are independent, their joint pdf factorizes with

$$\begin{aligned}\langle XY\rangle &= \int_{-\infty}^{+\infty}\int_{-\infty}^{+\infty} xy\, f(x,y)\, dx\, dy \\ &= \int_{-\infty}^{+\infty} x f_x(x)\, dx \int_{-\infty}^{+\infty} y f_y(y)\, dy = \langle X\rangle\langle Y\rangle \ ,\end{aligned} \tag{6.51}$$

confirming that independence leads to uncorrelatedness.

Random variables *X* and *Y* are said to be **orthogonal** if

$$\langle XY\rangle = 0 \ . \tag{6.52}$$

Orthogonality and uncorrelatedness are related but distinct concepts. Orthogonality directly imposes $\langle XY\rangle = 0$, independent of the means of *X* and *Y*, whereas uncorrelatedness requires that $\langle (X - \langle X\rangle)(Y - \langle Y\rangle)\rangle = 0$ equivalent to $\langle XY\rangle = \langle X\rangle\langle Y\rangle$. If both variables have zero mean, orthogonality and uncorrelatedness coincide. In general, however, they impose different conditions, that is, orthogonality concerns the expectation of the product itself, while uncorrelatedness concerns how the variables deviate jointly from their means.

For the case where *X* and *Y* are not independent and may exhibit statistical dependence, we introduce the **covariance** as a way to quantify their linear relationship

$$\operatorname{Cov}\left(X,Y\right) = \operatorname{E}\left[(X - \operatorname{E}\left[X\right])(Y - \operatorname{E}\left[Y\right])\right] \ , \tag{6.53}$$

which represents the expected product of the deviations of *X* and *Y* from their means. Using linearity of expectation, this can be expanded to

$$\operatorname{Cov}\left(X,Y\right) = \operatorname{E}\left[XY\right] - \operatorname{E}\left[X\right]\operatorname{E}\left[Y\right] \ ,$$

where we have used that constants can be factored out of the expectation. The covariance quantifies how much *X* and *Y* vary together, compared to what would be expected if they were independent. The common form of the covariance can be obtained by expanding the second-order central moment and applying the linearity property of expectation.

$$\begin{aligned}\operatorname{Cov}\left(X,Y\right) &= \operatorname{E}\left[(X - \operatorname{E}\left[X\right])(Y - \operatorname{E}\left[Y\right])\right] \\ &= \operatorname{E}\left[XY - X\operatorname{E}\left[Y\right] - \operatorname{E}\left[X\right]Y + \operatorname{E}\left[X\right]\operatorname{E}\left[Y\right]\right] \\ &= \operatorname{E}\left[XY\right] - \operatorname{E}\left[X\right]\operatorname{E}\left[Y\right] \ .\end{aligned} \tag{6.54}$$

where we have used the fact that expectation of a constant times a random variable equals the constant times the expectation of the random variable.

The covariance of a variable with itself recovers the variance, thus

$$\text{Cov}\,(X,X) = \text{Var}\,(X)\ , \tag{6.55}$$

measuring the average squared deviation of *X* from its mean. For continuous random variables, the covariance can be computed as

$$\text{Cov}\,(X,Y) = \int_{-\infty}^{+\infty}\int_{-\infty}^{+\infty}(x-\mu_X)(y-\mu_Y)f(x,y)\,dx\,dy\ , \tag{6.56}$$

where $\mu_X = \text{E}\,[X]$ and $\mu_Y = \text{E}\,[Y]$. For discrete random variables, the integrals are replaced by summations, as previously discussed in Sect. 6.2.4.

To obtain a dimensionless measure of linear dependence, we define the **correlation coefficient** to

$$\rho(X,Y) = \frac{\text{Cov}(X,Y)}{\sigma(X)\sigma(Y)} = \frac{\langle XY\rangle - \langle X\rangle\langle Y\rangle}{\sigma(X)\sigma(Y)}\ , \tag{6.57}$$

where $\sigma(X)$ and $\sigma(Y)$ are the standard deviations of *X* and *Y*. The correlation coefficient satisfies $-1 \le \rho(X,Y) \le 1$. A value of $\rho = 1$ indicates perfect positive linear correlation, $\rho = -1$ perfect negative linear correlation, and $\rho = 0$ no linear correlation. If *X* and *Y* are independent, then

$$\text{Cov}\,(X,Y) = 0 \quad \text{and} \quad \rho(X,Y) = 0\ , \tag{6.58}$$

confirming that independence implies that the variables are uncorrelated. However, the converse is not generally true. Uncorrelated random variables may still be dependent through nonlinear relationships.

Example 6.1 This simple example highlights that uncorrelatedness, as indicated by zero covariance, reflects only the absence of a linear relationship between *X* and *Y*. It does not rule out other forms of dependence such as quadratic or higher-order relationships. Let *X* be a random variable uniformly distributed on the interval $[-1,1]$, and define $Y = X^2$. Clearly, *Y* is completely determined by *X*, so the variables are dependent. However, since *X* is symmetric about zero, its mean is $\langle X\rangle = 0$. The covariance becomes

$$\text{Cov}\,(X,Y) = \langle XY\rangle - \langle X\rangle\langle Y\rangle = \langle X^3\rangle - 0\langle Y\rangle = 0$$

because the odd moment $\langle X^3 \rangle$ is zero due to symmetry. Thus, *X* and *Y* are uncorrelated even though they are clearly dependent.

6.3 Special Distributions

There exists an extensive list of probability distributions, commonly categorized by whether the random variables are discrete or continuous, as well as by the domain of definition, that is, whether their support is on finite, half-infinite, or the whole real line. After laying the foundation and properties of distribution functions, we are now ready to explore some selected probability distributions to exemplify and illustrate their properties. We will start with discrete probability distributions and proceed to continuous distributions. We begin the discussion with a brief review of basic combinatorial considerations, as these are fundamental to quantifying probabilities in discrete uniform distributions, that is, equally likely outcomes.

6.3.1 Uniform Distribution

The uniform distribution describes the case where all outcomes on the support are equally likely. We consider both the discrete and continuous cases.

Discrete Uniform Distribution The discrete uniform distribution $\mathscr{U}\{a, b\}$ describes the case where all integer values in the interval [*a*, *b*] are equally likely, where $b \geq a$. The support set therefore consists of $n = b - a + 1$ discrete values. For each value within the support set, that is for $k \in \{a, a+1, \cdots, b-1, b\}$, the probability is equal. The probability distribution reads

$$\mathscr{U}\{a, b\} = \frac{1}{b-a+1} \quad . \tag{6.59}$$

The expected value is given by

$$\mathrm{E}\left[X\right] = \frac{a+b}{2} \quad , \tag{6.60}$$

and the variance is

$$\mathrm{Var}\left[X\right] = \frac{n^2-1}{12} \quad . \tag{6.61}$$

Enumerative Combinatorics For discrete sample spaces, the formulation of the event space involves variations of permutations and combinations. Quantifying the probability of a particular event in a discrete space with uniform outcome probabilities can be directly achieved by counting the number of favorable events and comparing this to the total number of possible events. This approach corresponds exactly to the classical definition of probability introduced earlier, where probability is expressed as the ratio of favorable to total outcomes for experiments with equally likely possibilities.

Consider a set *A* consisting of *n* elements from which *k* elements are drawn. The resulting cases depend on whether order matters, referred to as **permutations**, or whether order does not matter, referred to as **combinations**. It further depends on whether elements can be repeated or not. This is illustrated below using a simple example where the set is $\{1, 2, 3\}$, thus $n = 3$, and we draw $k = 2$ elements.

In the case of permutations without repetition, the number of possibilities is given by

$$\frac{n!}{(n-k)!} \quad , \tag{6.62}$$

which for our example corresponds to the 6 possibilities $\{(1, 2), (1, 3), (2, 1), (2, 3), \quad (3, 1), (3, 2)\}$. When repetition is allowed, the number of permutations is

$$n^k \quad , \tag{6.63}$$

which for our example returns the 9 possibilities $\{(1, 1), (1, 2), (1, 3), (2, 1), (2, 2), (2, 3), \quad (3, 1), (3, 2), (3, 3)\}$. For combinations without repetition, where order does not matter, the number of possibilities is

$$\binom{n}{k} = \frac{n!}{k!(n-k)!} \quad , \tag{6.64}$$

which in our example set gives the 3 possibilities $\{(1, 2), (1, 3), (2, 3)\}$. Finally, when repetition is allowed and order does not matter, the number of combinations is

$$\binom{n+k-1}{k} = \frac{(n+k-1)!}{k!(n-1)!} \quad , \tag{6.65}$$

which for our example gives the 6 possibilities $\{(1,1),(1,2),(1,3),(2,2),(2,3),(3,3)\}$. With these cases, most typical classical problems characterized by finite outcomes and equally likely possibilities can be solved by comparing the number of favorable events to the number of possible events in a uniformly distributed discrete sample space.

Continuous Uniform Distribution Similar to the discrete case, the continuous uniform distribution $\mathscr{U}(a,b)$ describes the situation where all values within the continuous interval $[a, b]$ with $-\infty < a < b < \infty$ are equally likely. The probability density is constant across the support interval, so that

$$\mathscr{U}(a,b) = \tfrac{1}{b-a} \quad . \tag{6.66}$$

The mean of the distribution is

$$\mathrm{E}\left[X\right] = \tfrac{a+b}{2} \quad , \tag{6.67}$$

and the variance is

$$\mathrm{Var}\left[X\right] = \tfrac{(b-a)^2}{12} \quad . \tag{6.68}$$

6.3.2 Binomial Distribution

The binomial distribution is a discrete distribution that arises in random experiments consisting of n independent draws, each with binary outcomes $\{\omega_0, \omega_1\}$, as shown in Fig. 6.5. Such trials are referred to as binomial or Bernoulli trials. The central question is about the probability of obtaining outcome ω_1 exactly k times in n draws. We introduce a random variable X that assigns $X = 0$ for ω_0 and $X = 1$ for ω_1. Let the probability of ω_1 be p, so that the probability of ω_0 is $1 - p$. The corresponding individual probabilities to obtain k times $X = 1$ and therefore $n - k$ times $X = 0$ are p^k and $(1-p)^{n-k}$, respectively. Since the draws are independent, the probability of any particular sequence of outcomes is given by the product

$$p^k (1-p)^{n-k} \quad . \tag{6.69}$$

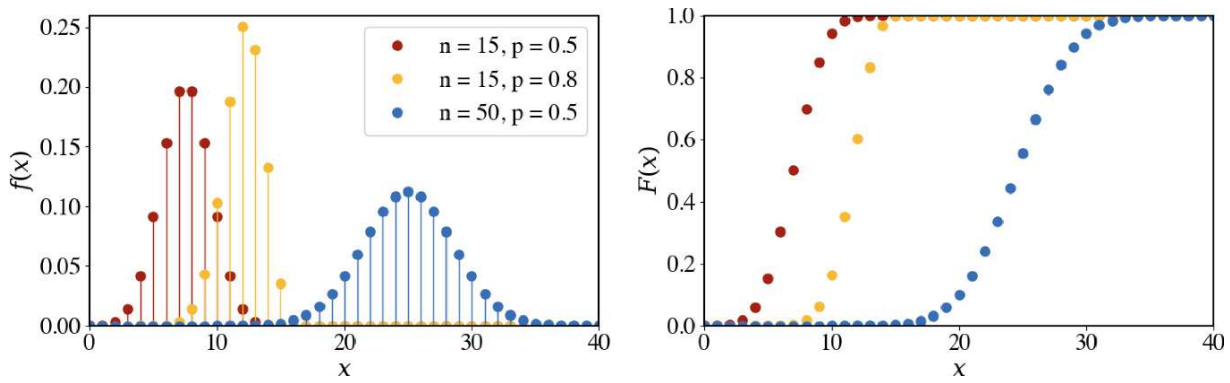


Fig. 6.5 Binomial pdf and cdf for different parameters

Because the order of the draws is not considered, there are $\binom{n}{k}$ different ways to arrange k outcomes of ω_1 among n trials. This yields the binomial distribution

$$\mathscr{B}(n,p) = \binom{n}{k} p^k (1-p)^{n-k} \ . \tag{6.70}$$

The mean of the binomial distribution is

$$\mathrm{E}\left[X\right] = np \ , \tag{6.71}$$

and its variance is

$$\mathrm{Var}\left[X\right] = np(1-p) \ . \tag{6.72}$$

6.3.3 Poisson Distribution

The Poisson distribution is a discrete distribution that serves as a useful approximation to the binomial distribution when the number of independent trials n is very large, the probability of success p is very small, and the product np remains moderate (Fig. 6.6). The product $\lambda = np$ represents the expected number of successes and becomes the defining parameter of the distribution, typically determined empirically. The distribution can be formally obtained as the limiting case $\lim_{n\to\infty} \mathscr{B}(n,p)$ which results in

$$\mathscr{P}(\lambda) = \frac{\lambda^k}{k!} \exp^{-\lambda} \ . \tag{6.73}$$

Typical examples where the Poisson distribution arises include the number of misprinted letters in a book, the number of pumps that fail immediately at first use, or the probability of an event occurring at a specific point in time within a given interval. Both the expected value and the variance of the Poisson distribution are equal to λ, thus

$$\mathrm{E}\left[X\right] = \lambda \ , \tag{6.74}$$

and

$$\mathrm{Var}\left[X\right] = \lambda \ . \tag{6.75}$$

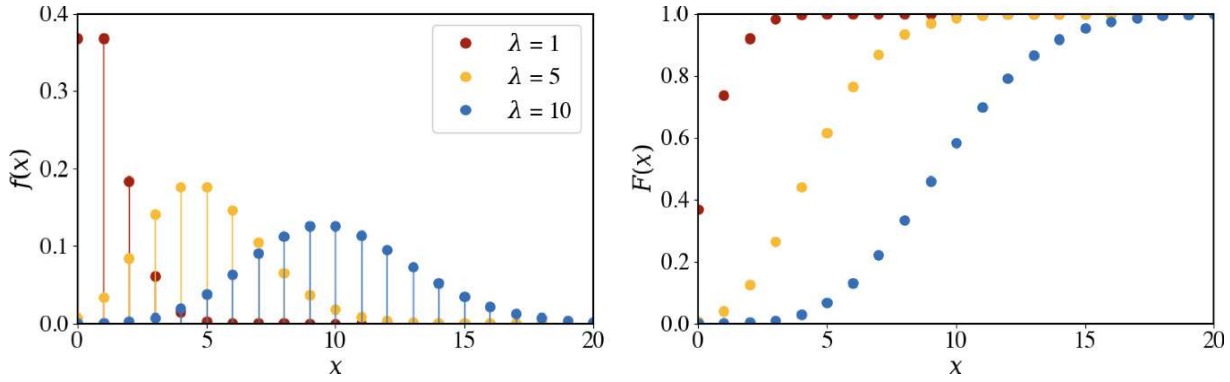


Fig. 6.6 Poisson pdf and cdf for different values of the parameter λ

6.3.4 Normal Distribution

The normal distribution is of particular importance in the natural and engineering sciences. It characterizes many processes either exactly or, at least in good approximation, and plays a central role in the central limit theorem as discussed later in Sect. 6.4. The normal distribution arises as the limiting case of the binomial distribution for $n \to \infty$ after appropriate normalization.[1]

The probability density function is symmetrically bell-shaped around the mean μ, with

$$\mathcal{N}(\mu, \sigma) = \frac{1}{\sqrt{2\pi\sigma^2}} \, \exp\left(-\frac{(x-\mu)^2}{2\sigma^2}\right) \ . \tag{6.76}$$

Here, the mean μ represents the location parameter, and the standard deviation σ acts as a scale parameter. The smaller σ, the larger the maximum value of the pdf at its mean μ and the steeper the slope of the bell, as visible in Fig. 6.7. The cumulative distribution function of the random variable X is obtained by integrating the density function

$$P(X < x) = F(x) = \frac{1}{\sqrt{2\pi\sigma^2}} \int_{-\infty}^{x} \exp\left(-\frac{(\xi-\mu)^2}{2\sigma^2}\right) d\xi = \frac{1}{2}\left(1 + \operatorname{erf}\left(\frac{x-\mu}{\sqrt{2}\sigma}\right)\right) . \tag{6.77}$$

The mean μ and variance σ^2 serve as the parameters of the distribution. Since the normal distribution is symmetric about its mean, the skewness is zero. The kurtosis of the normal distribution is $K = 3$.

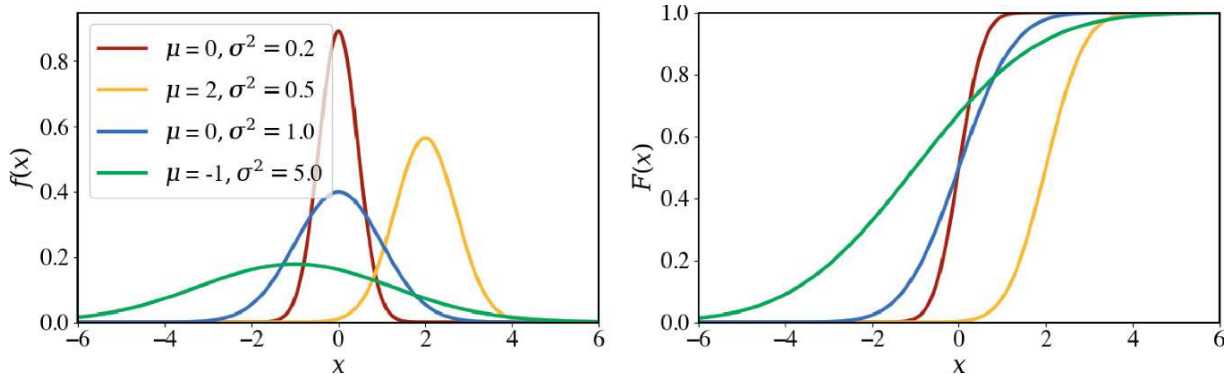


Fig. 6.7 Normal pdf and cdf for different values of mean μ and variance σ^2

6.3.5 Lognormal Distribution

The lognormal distribution describes the distribution of a random variable X in the case where $Z = \ln(X)$ is normally distributed, that is $Z \sim \mathcal{N}(\mu, \sigma)$. The lognormal distribution can thus be constructed via the normal distribution with $X = e^Z$. The support of X is $x \in (0, +\infty)$, with $\mu \in (-\infty, +\infty)$ and $\sigma > 0$. The corresponding probability density function is

$$\mathscr{L}(\mu, \sigma) = \frac{1}{x\sqrt{2\pi\sigma^2}} \exp\left(-\frac{(\ln x - \mu)^2}{2\sigma^2}\right) . \tag{6.78}$$

The cumulative distribution function is

$$F(x) = \frac{1}{2}\left(1 + \operatorname{erf}\left(\frac{\ln x - \mu}{\sqrt{2}\sigma}\right)\right) . \tag{6.79}$$

The mean of the lognormal distribution is

$$\mathrm{E}[X] = \exp\left(\mu + \frac{\sigma^2}{2}\right) , \tag{6.80}$$

and the variance is

(6.81)

$$\text{Var}\left[X\right] = \left(\exp\left(\sigma^2\right) - 1\right) \exp\left(2\mu + \sigma^2\right) \ .$$

Since the lognormal distribution is asymmetric, the median and mode no longer coincide with the mean. The median is

$$\text{median}\left[X\right] = \exp\left(\mu\right) \ , \tag{6.82}$$

and the mode is

$$\text{mode}\left[X\right] = \exp\left(\mu - \sigma^2\right) \ . \tag{6.83}$$

The skewness, reflecting the asymmetry, is nonzero and given by the expression

$$\text{S}\left[X\right] = \left(\exp\left(\sigma^2\right) + 2\right)\sqrt{\exp\left(\sigma^2\right) - 1} \ . \tag{6.84}$$

For $\sigma \ll 1$, the lognormal distribution is very narrow and closely resembles a normal distribution. As the standard deviation σ increases, the distribution becomes increasingly skewed, with a longer right tail representing rare but large events, as can be seen in Fig. 6.8.

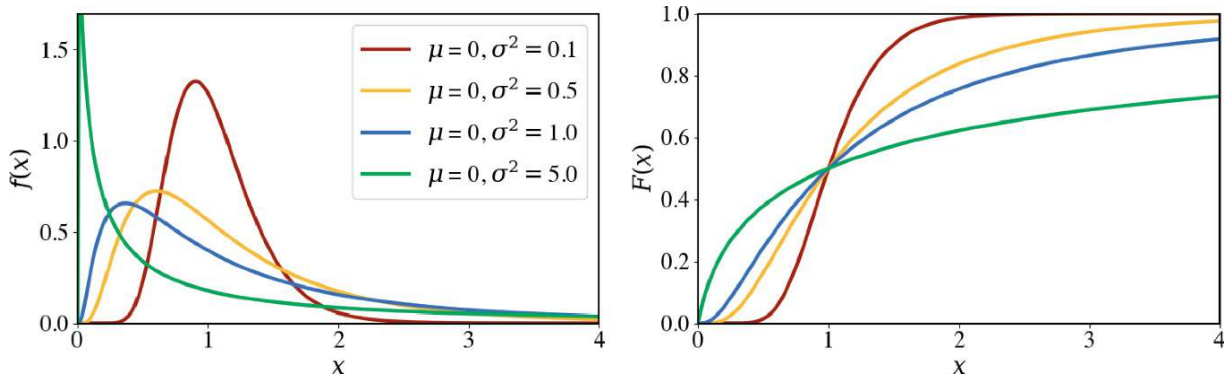


Fig. 6.8 Lognormal pdf and cdf for different values of variance σ^2

6.3.6 Weibull Distribution

The Weibull distribution is versatile in its application and widely used in engineering disciplines. It is commonly employed in reliability engineering for failure and survival analysis, for instance to describe failures due to mechanical or thermal fatigue in materials. For $x \in [0, +\infty)$ the cumulative Weibull distribution has the form

$$F(x, \lambda, k) = \begin{cases} 1 - \mathrm{e}^{-(x/\lambda)^k} & x \geq 0 \\ 0 & x < 0 \end{cases} \tag{6.85}$$

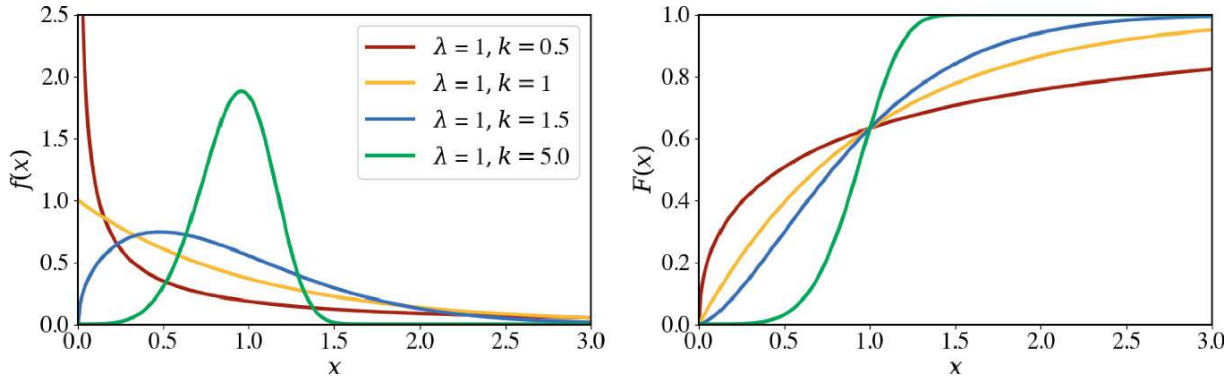


Fig. 6.9 Weibull pdf and cdf for different values of the shape parameter k

A random variable following this cumulative distribution is called a Weibull random variable. The corresponding probability density function follows from differentiation to

$$f(x, \lambda, k) = \begin{cases} \frac{k}{\lambda}\left(\frac{x}{\lambda}\right)^{k-1} \mathrm{e}^{-(x/\lambda)^k} & x \geq 0 \\ 0 & x < 0 \end{cases} \tag{6.86}$$

Here, $k \in (0, +\infty)$ is the shape parameter and $\lambda \in (0, +\infty)$ is the scale parameter of the distribution (Fig. 6.9). In practice, various parameterizations exist, often including a location parameter to shift x. For $k = 1$ the Weibull distribution reduces to the exponential distribution $F(x) = 1 - \mathrm{e}^{-x/\lambda}$. In reliability engineering, the random variable X typically represents a time to failure. The Weibull distribution then models a time-dependent failure rate that follows a power law. When $k < 1$, the failure rate decreases over time. When $k = 1$, the failure rate remains constant. When $k > 1$, the failure rate increases over time.

The mean and variance of the distribution are

$$\mathrm{E}\left[X\right] = \lambda\,\Gamma\left(1 + \tfrac{1}{k}\right)\ , \tag{6.87}$$

$$\mathrm{Var}\left(X\right) = \lambda^2\left[\Gamma\left(1 + \tfrac{2}{k}\right) - \left(\Gamma\left(1 + \tfrac{1}{k}\right)\right)^2\right]\ , \tag{6.88}$$

where Γ is the Gamma function. Since the Weibull distribution is not symmetric, the skewness is nonzero, given by

(6.89)

$$\mathrm{S}= \frac{\Gamma\left(1+\frac{3}{k}\right)\lambda^3-3\mathrm{E}[X]\mathrm{Var}(X)-(\mathrm{E}[X])^3}{\mathrm{Var}(X)^{3/2}} \ .$$

For nonsymmetric distributions, the median, that is the value *x* for which $F(x) = 0.5$, no longer coincides with the mean. The median of the Weibull distribution is

$$\text{median}= \lambda(\ln\, 2)^{1/k} \ . \tag{6.90}$$

The location of the maximum of the density, called the mode, is

$$\text{mode}= \begin{cases} 0 & k \leq 1 \\ \lambda\left(\frac{k-1}{k}\right)^{1/k} & k > 1 \end{cases} \tag{6.91}$$

6.4 Limit Theorems

The limit theorems, which include the law of large numbers (LLN) and the central limit theorem (CLT), are among the most fundamental results in probability theory. They describe the asymptotic behavior of sample averages and sums of independent random variables. Let $X_1, X_2, \ldots X_n$ be a sequence of independent and identically distributed random variables, each with a finite mean $\mathrm{E}\left[X_i\right] = \mu$. The key object of interest is the **sample mean**

$$\overline{X}_n = \tfrac{1}{n}\textstyle\sum_{j=1}^{n} X_j \ . \tag{6.92}$$

The LLN states that under certain conditions, the sample mean converges to the expected value as $n \to \infty$. The CLT states that, under appropriate conditions, the standardized sum of a large number of independent and identically distributed random variables converges in distribution to a normal distribution.

6.4.1 Law of Large Numbers

The law of large numbers (LLN) establishes conditions under which the sample mean $\overline{X}_n$ converges to the true expected value μ. There are two versions, the weak law of large numbers, which expresses convergence in probability, and the strong law of large numbers, which states almost certain convergence. To understand the LLN, we first introduce two fundamental probability inequalities that provide estimation bounds based on the mean and variance of a distribution.

The first, called **Markov's inequality**, provides an upper bound on the probability that a non-negative random variable *X* exceeds a given threshold $a > 0$ in terms of its expectation

$$P(X \geq a) \leq \frac{\mathrm{E}[X]}{a} \quad . \tag{6.93}$$

This bound is useful when only the expectation is known. To prove the inequality, an indicator function *I* is introduced that indicates whether the inequality $X \geq a$ holds with

$$I = \begin{cases} 1 & \text{if } X \geq a \\ 0 & \text{otherwise, thus } X < a \end{cases}$$

The motivation for introducing *I* is that it allows us to express the probability $P(X \geq a)$ as an expectation, that is $\mathrm{E}\left[I\right] = P(X \geq a)$. Since $X \geq a$, dividing by *a* gives $X/a \geq I$. Taking expectations on both sides yields $\mathrm{E}\left[X\right]/a \geq \mathrm{E}\left[I\right]$. Since $\mathrm{E}\left[I\right] = P(X \geq a)$, it follows that $P(X \geq a) \leq \mathrm{E}\left[X\right]/a$, completing the proof, shown here to illustrate the reasoning behind the inequality.

When both expectation and variance are known, **Chebyshev's inequality** provides a sharper bound

$$P(|X - \mu| \geq k\sigma) \leq \frac{1}{k^2} \quad . \tag{6.94}$$

Since $(X - \mu)^2$ is a non-negative random variable, we apply Markov's inequality with $a = (k\sigma)^2$ to obtain $P\left((X - \mu)^2 \geq (k\sigma)^2\right) \leq \mathrm{E}\left[(X - \mu)^2\right]/(k\sigma)^2$. Since $(X - \mu)^2 \geq (k\sigma)^2$ is equivalent to $|X - \mu| \geq k\sigma$, and given that $\mathrm{E}\left[(X - \mu)^2\right] = \sigma^2$, we obtain Chebyshev's inequality as stated. The inequality is only useful if $k > 1$, since for $k \leq 1$ the inequality reduces to the trivial statement that the probability is ≤ 1. A direct consequence of Chebyshev's inequality is that if $\mathrm{Var}\left(X\right) = 0$, then $P(X = \mathrm{E}\left[X\right]) = 1$, indicating that a probability of 1 is associated with zero variance.

Both inequalities are independent of the actual distributions, therefore the estimated bounds are not expected to be close to the actual probabilities. They can be significantly refined with knowledge of the specific underlying probability distribution, as illustrated in the following example.

Example 6.2 Suppose that the lifetime of a certain type of industrial pump, measured in operating hours, is a random variable X with mean $\mathrm{E}[X] = 10\,000\,\mathrm{h}$.

a. What can be said about the probability that a pump will last more than $12\,000\,\mathrm{h}$? By applying Markov's inequality with $a = 12\,000\,\mathrm{h}$, it follows that

$$P(X \geq 12\,000\,.) \leq \frac{\mathrm{E}[X]}{a} = \frac{10\,000\,.}{12\,000\,.} \approx 83.3\% \ .$$

b. Assume the population standard deviation is known to be $\sigma = 1000\,\mathrm{h}$. What can be said about the probability that a pump's lifetime will be between $8000\,\mathrm{h}$ and $12\,000\,\mathrm{h}$?

The interval $[8000\,, 12\,000\,]$ corresponds to $|X - 10\,000\,| < 2000\,.$ With $2000 = 2\sigma$, we apply Chebyshev's inequality with $k = 2$ and obtain

$$P(|X - 10\,000\,.| \geq 2000\,.) \leq \frac{1}{4} \ .$$

Therefore, the probability that X is within this range is

$$P(|X - 10\,000\,.| < 2000\,.) \geq 1 - \frac{1}{4} = \frac{3}{4} = 75\% \ .$$

c. If the pump lifetime is normally distributed as $X \sim \mathcal{N}(\mu = 10\,000\,, \sigma = 1000\,)$, how do the probabilities compare?

The probability that a pump lasts more than $12\,000\,\mathrm{h}$ is

$$P(X > 12\,000\,.) = 1 - P(X \leq 12\,000\,.) \approx 2.28\%.$$

The probability that the pump lifetime lies within $[8000\,, 12\,000\,]$ is

$$P(8000\,. \leq X \leq 12\,000\,) \approx 95.45\% \ .$$

The corresponding probability density function and cumulative distribution function sketches illustrating these estimates can be found in Fig. 6.10. This demonstrates that Markov's and Chebyshev's inequalities give much looser bounds than the true probabilities when the distribution is in fact known.

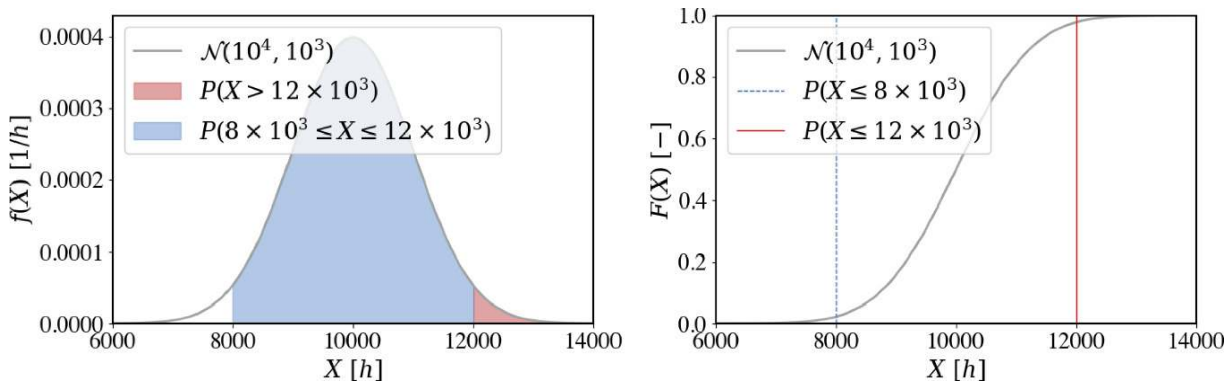


Fig. 6.10 Pdf and cdf of the pump lifetime X modeled as a normal distribution, with indication of $P(X > 12\,000\,\text{h}$ and $P(8000\,\text{h} \leq X \leq 12\,000\,\text{h})$

Using Chebyshev's inequality, the **weak law of large numbers** can be stated as

$$P\left(\left|\overline{X}_n - \mu\right| \geq \epsilon\right) \to 0 \quad \text{as } n \to \infty \ \forall \epsilon > 0 \ . \tag{6.95}$$

It follows under the assumption of a finite variance σ^2 with

$$\mathrm{E}\left[\frac{X_1 + \cdots + X_n}{n}\right] = \mu \ , \text{and } \mathrm{Var}\left[\frac{X_1 + \cdots + X_n}{n}\right] = \frac{\sigma^2}{n} \ ,$$

so that applying Chebyshev's inequality from Eq. (6.94) yields

$$P\left(\left|\overline{X}_n - \mu\right| \geq \epsilon\right) \leq \tfrac{\sigma^2}{n\epsilon^2} \ . \tag{6.96}$$

This result shows that as n increases, the probability of deviations from μ becomes arbitrarily small. The **strong law of large numbers** strengthens this result, with

$$P\left(\lim_{n\to\infty} \overline{X}_n = \mu\right) = 1 \ . \tag{6.97}$$

This means that the sample mean almost surely converges to μ, ensuring that individual sequences behave predictably in the long run. A sufficient condition for the strong LLN is $\sum_i^\infty \mathrm{Var}\,[X_i]/i^2 < \infty$.

Unlike classical sequences studied in calculus, probability theory rarely allows for absolute statements about the convergence of a sequence of random outcomes. The reason is that in a sequence of random trials, such as the

repeated rolls of a fair die discussed in Example 6.3, there exists the possibility of extreme cases, such as rolling a sequence of only ones. For such a sequence, the arithmetic mean does not converge to the expected value, violating the law of large numbers. However, while these extreme sequences are theoretically possible, they constitute an almost impossible event, that is their probability is zero in an infinite sequence of trials. The strong law of large numbers guarantees that for almost all sequences of random outcomes, the sample average will eventually converge to the true mean.

As shown in Example 6.3, one commonly observes a decrease in standard deviation following a $\sigma/\sqrt{n}$ trend, which is a direct consequence of the properties of the sample mean. For a sequence of independent and identically distributed random variables with finite variance σ^2, the variance of the sample mean $\overline{X}_n$ is given by $\operatorname{Var}\left(\overline{X}_n\right) = \sigma^2/n$, leading to a standard deviation of $\sigma/\sqrt{n}$. As the sample size increases, the sample mean exhibits decreasing fluctuations around the true mean, as predicted by the law of large numbers. Consequently, the probability of significant deviations from the expected value diminishes, leading to more precise estimates in empirical observations.

Example 6.3 To illustrate the LLN, we consider rolling a fair six-sided die multiple times. The outcome of each roll, denoted by X_i, follows a discrete uniform distribution $X_i \sim \mathscr{U}([1,6])$, where each outcome appears with equal probability $1/6$. The theoretical expected value of a single roll is given by $\mu_0 = 3.5$. To observe the behavior predicted by the LLN, we conduct a sequence of 1200 independent rolls and compute the running sample mean $\overline{X}_n$.

The top plot in Fig. 6.11 displays the observed outcomes for each of the 1200 rolls over two independent experiments, showcasing the randomness of individual realizations. The bottom plot tracks the evolution of the sample mean $\overline{X}_n$, revealing its convergence to the expected value $\mu_0 = 3.5$. As anticipated, $\overline{X}_n$ initially exhibits significant fluctuations due to the randomness inherent in small samples. However, as the number of rolls increases, the fluctuations diminish, and the sample mean stabilizes near the theoretical expectation. For large n, the probability that $\overline{X}_n$ significantly deviates from μ_0 becomes arbitrarily small.

To further analyze the rate of convergence, we extend the data set to 100 independent experiments, each consisting of n die rolls, and evaluate the normalized absolute deviation from the mean $|\overline{X}_n - \mu_0|/\mu_0$.
Figure 6.12 presents these deviations on a log-log scale, along with the

theoretical convergence bound $\sigma_0/\sqrt{n}$. This result confirms that, in accordance with the LLN, the probability of significant deviations decreases as n grows. The rare instances where deviations exceed the theoretical bound illustrate that while convergence is not monotonic, to the largest extent it follows the expected trend.

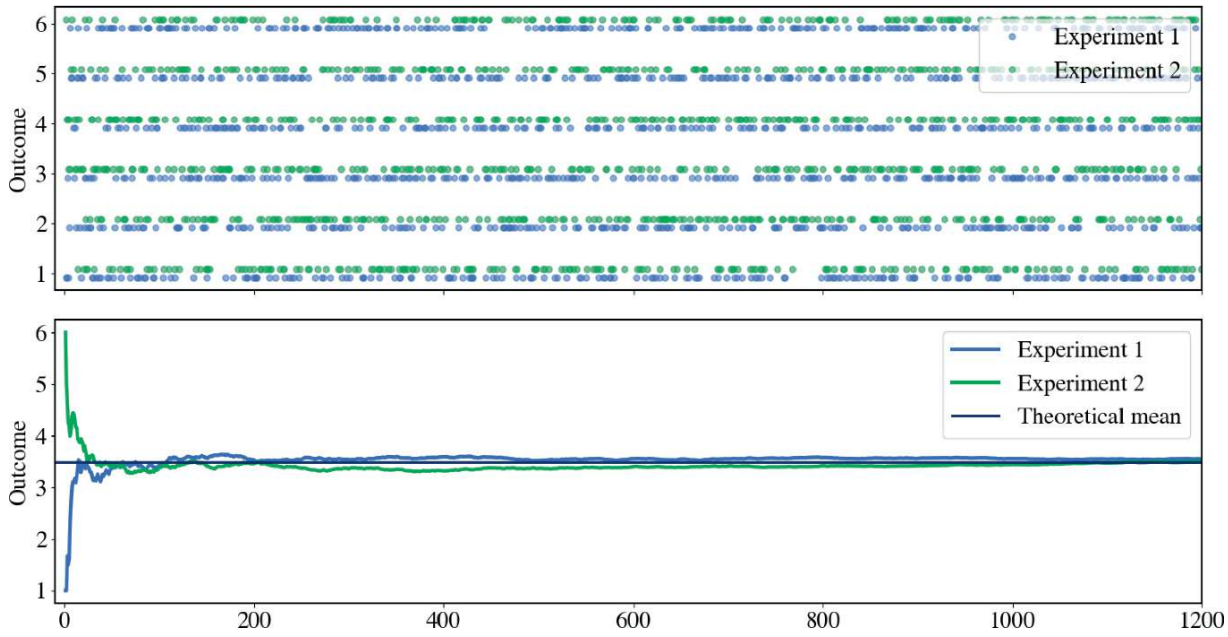


Fig. 6.11 The top plot shows the outcomes of rolling a fair die 1200 times for two independent experiments. The bottom plot displays the running sample mean $\overline{X}_n$, demonstrating convergence toward the expected value $\mu_0 = 3.5$ as n increases

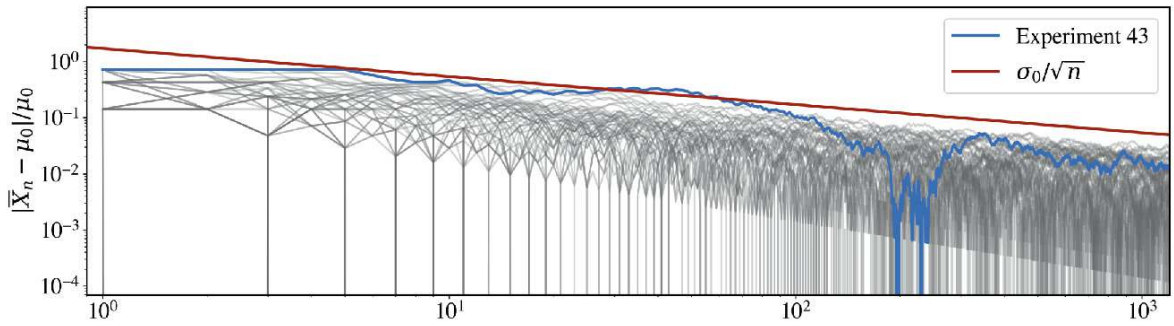


Fig. 6.12 Log-log plot of the normalized deviation $|\overline{X}_n - \mu_0|/\mu_0$ for 100 independent experiments. The reference line $\sigma_0/\sqrt{n}$ represents the typical expected decay in fluctuations, however occasionally one may observe the unlikely case such as experiment 43 here that the bounds is exceeded

6.4.2 Central Limit Theorem

The central limit theorem (CLT) provides a theoretical foundation for the empirical observation that many real-world random phenomena exhibit normal

distributions. The CLT states that the distribution of the sum (or mean) of a large number of independent random variables tends to a normal distribution, regardless of the underlying individual distribution.

Consider a sequence of independent and identically distributed random variables $X_1, \ldots, X_n$ each with mean μ and variance σ^2. The **central limit theorem** states that as $n \to \infty$ the distribution of

$$\frac{X_1+\ldots+X_n-n\mu}{\sigma\sqrt{n}} \ , \tag{6.98}$$

tends to the standard normal distribution $\mathcal{N}(0,1)$. This statement can be equivalently reformulated in terms of the standardized sample mean, defined as

$$Z_n = \frac{\overline{X}_n-\mu}{\sigma/\sqrt{n}} \ . \tag{6.99}$$

In other words, for any real number $a \in (-\infty, \infty)$ we have

$$P(Z_n \leq a) \to \frac{1}{\sqrt{2\pi}} \int_{-\infty}^{a} \mathrm{e}^{-x^2/2} \ dx \quad \text{for} \quad n \to \infty \ . \tag{6.100}$$

This result implies that regardless of the shape of the original distribution, the sum (or mean) of a sufficiently large number of independent and identically distributed random variables approximates a normal distribution. Consequently, for large enough *n*, the distribution of $\overline{X}_n$ is arbitrarily close to a normal distribution with mean μ and standard deviation $\sigma/\sqrt{n}$. The key significance of the theorem is that the distribution of the properly scaled deviation $\sqrt{n}(\overline{X}_n - \mu)$ approaches normality, even when the original variable is not normally distributed. While the CLT holds for all distributions with finite variance, the rate at which normality is attained depends significantly on the shape and symmetry of the original distribution, as illustrated for a uniform distribution in Example 6.4.

Example 6.4 To further illustrate the Central Limit Theorem, we consider the case of rolling a fair six-sided die. The outcome of a single roll, denoted by X_i, follows a discrete uniform distribution $X_i \sim \mathcal{U}([1,6])$, where each value has an equal probability of $1/6$. Applying the expected value and variance of a single roll for a discrete uniform distribution from Sect. 6.3.1 resulting in a mean $\mu_0 = 3.5$ and $\sigma_0 = (6^2-1)/12 = 35/12$. Now, consider the sum of *n* independent dice rolls, defined as $S_n = X_1 + X_2 + \ldots + X_n$. Using the

linearity of expectation and variance, we obtain $\mathrm{E}\left[S_n\right] = n\mu_0$ and $\mathrm{Var}\left(S_n\right) = n\sigma_0^2$.

To examine how the distribution of S_n evolves with increasing *n*, we conduct a set of random experiments similar to Example 6.3 in which we generated independent realizations of the random variables $X_1, X_2, \ldots, X_n$, corresponding to rolling *n* fair dice. Each experiment consists of drawing *n* independent values from $\mathscr{U}(\llbracket 1, 6 \rrbracket)$ and computing their sum. This process is repeated 1200 times for different values of *n* to generate an empirical dataset. Figure 6.13 illustrates the empirical distribution of S_n for three different cases $n = 1$, $n = 2$, and $n = 10$ compared with the corresponding normal approximation $\mathscr{N}(n\mu_0, \sqrt{n}\sigma_0)$.

For $n = 1$, the distribution remains discrete and uniform, as expected from the underlying process. When summing two independent rolls, that is $S_2 = X_1 + X_2$, the resulting distribution begins to take a bell-shaped form, though it still exhibits a discrete nature. For $n = 10$, the empirical distribution of S_{10} closely follows a normal distribution, demonstrating the convergence predicted by the CLT. The value range of the distributions move with *n* to [*n*, 6*n*]. Alternatively, one might present the standardized sum $Z_n = (S_n - n\mu_0)/(\sqrt{n}\sigma_0)$, which accordingly converges in distribution to the standard normal distribution $\mathscr{N}(0, 1)$.

It is worth noting that the quick convergence observed in this example is partly due to the fact that the original discrete uniform distribution $\mathscr{U}(\llbracket 1, 6 \rrbracket)$ is symmetric around its mean. Distributions that are symmetric tend to exhibit faster convergence under the CLT, as their skewness is zero, ensuring that deviations from the mean occur with equal probability in both directions. In consequence, even for relatively small values of *n*, the sum S_n closely approximates a normal distribution. In contrast, if the original distribution were asymmetric, such as an exponential distribution or another highly skewed discrete distribution, convergence to normality would generally require a larger number of summands. For small to moderate values of *n*, the sum would still exhibit some degree of skewness before gradually approaching the normal distribution.

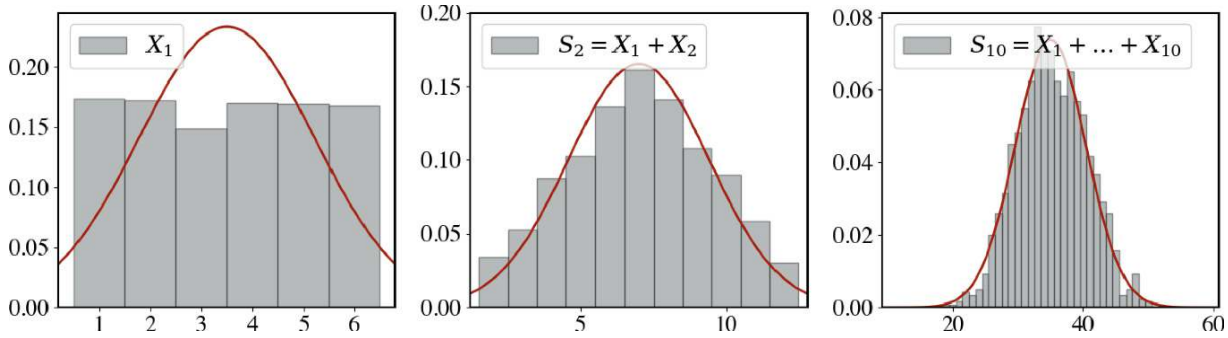


Fig. 6.13 Illustration of the CLT. The histograms shows summed distribution random variables $S_n = X_1, \ldots, X_n$ compared to normal distributions $\mathcal{N}(n\,\mu_0, \sqrt{n}\,\sigma_0)$ for $n = 1$ on the left, $n = 2$ in the middle and $n = 10$ on the right

References

Argyris JH, Faust G, Haase M, Friedrich R (2017) Die Erforschung des Chaos: Eine Einführung in die Theorie nichtlinearer Systeme, 3rd edn. Springer Vieweg

Moeschlin O (2012) Wahrscheinlichkeitstheorie. Lecture Notes

Ross SM (2012) A first course in probability, 9th edn. Pearson

---

Footnotes

1 Applying Stirling's approximation $n! \approx \sqrt{2\pi n}\, n^n e^{-n}$ to the binomial coefficient and expanding around the mean $\mu = np$ gives

$$P(X = k) \approx \frac{1}{\sqrt{2\pi np(1-p)}} \exp\left(-\frac{(k-np)^2}{2np(1-p)}\right)$$

which is the density of the normal distribution with mean np and variance $np(1-p)$.

© The Author(s), under exclusive license to Springer Fachmedien Wiesbaden GmbH, part of Springer Nature 2026
H. Gomaa, *Modeling with Knowledge and Data*, Mathematical Engineering
https://doi.org/10.1007/978-3-658-50679-7_7

7. Statistical Methods for Data Analysis

Hassan Gomaa[1] ✉
(1) Strategic Projects Co-Innovation, Cognite, Oslo, Norway

Generally speaking, the subject of statistics is concerned with analyzing and interpreting data to effectively support data-driven decision-making. Statistical techniques are applied extensively in many sectors where increasingly larger amounts of data are available. A significant part of statistical analysis involves **descriptive statistics**, which are applied to structure, summarize, and present information based on observed or measured data sets. Another essential part is **inferential statistics**, which focuses on using data from limited sample observations to infer information and properties about a larger entirety, called the population.

Statistical reasoning is fundamental in engineering and natural sciences, where measurements are often subject to variability, noise, and uncertainty. The ability to draw reliable conclusions from incomplete or imperfect data is key for designing models, making predictions, and ultimately supporting decision-making in the presence of uncertainty. In hybrid modeling, where prior knowledge and data are combined, statistical methods provide the tools to quantify confidence in our estimates, assess model fit, and validate assumptions about the underlying physical processes.

We will start this chapter by introducing the basic terminology and essential descriptive tools that allow us to accurately describe the characteristics and properties of an observed data set. Subsequently,

we will explore confidence intervals and hypothesis tests that allow us to quantify the accuracy and reliability of the conclusions drawn. For further reading, Illowsky and Dean (2013) offer a comprehensible introduction to statistics. For the connoisseurs, the classic by Box et al. (2005) is highly recommended.

Samples and Population In the last chapter on probability, we mainly argued from a position where the random variable is known and we are evaluating the corresponding distribution to derive properties and characteristics. We assumed that the information describing the entirety of objects, for instance a probability distribution, is readily available. However, in practical scenarios where the probability distribution describes collected or measured data, accessing the complete data set is rarely practical. The complete data set containing the entirety of all objects or measurements in question is, in most cases, a theoretical construct referred to as a **population**. Usually, data exist only for a small subset of a population, called a **sample**, illustrated in Fig. 7.1.

To illustrate, consider a manufacturer assessing the reliability of centrifugal pumps. The population consists of all pumps produced and operated in the field. Since monitoring every pump continuously is impractical, data are collected from a representative sample operating under various conditions. The aim is to infer population properties, such as the mean time between failures or failure rate, from this sample. The validity of such conclusions depends on the sample being representative. Drawing conclusions from a sample inevitably introduces uncertainty, which inferential statistics seeks to quantify and manage using tools such as confidence intervals and hypothesis testing.

In Chap. 6, we introduced several measures used to characterize and quantify probability distributions, such as the mean or median, referred to as **parameters** when describing a population. The corresponding quantities computed from a sample are called **statistics**. In inferential statistics, parameters are generally unknown and need to be estimated from sample data. A statistic provides the best available

estimate of an unknown parameter, and we will explore methods to quantify the accuracy and reliability of such estimates.

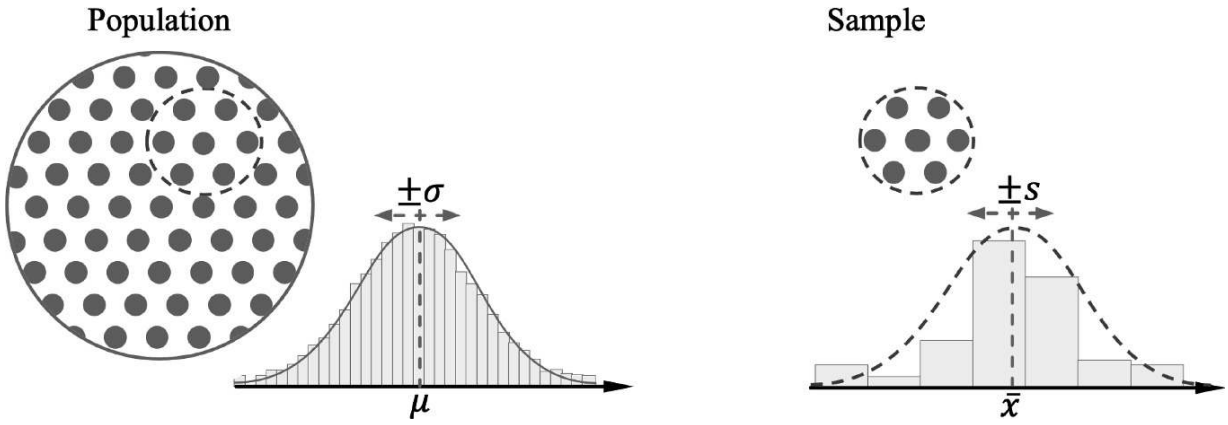


Fig. 7.1 Illustration of a population and a representative sample

7.1 Descriptive Statistics and Data Visualization

The aim of descriptive statistics is to structure, summarize, and present sample data in a meaningful way. In this section we will review key methods for quantitative summary statistics as well as common graphical tools used for data visualization. A **statistic** reduces an aspect of a sample data set to a single aggregated number. Depending on what feature of the data is captured, statistics can be grouped into measures of location, dispersion, shape, or correlation. These statistics are the sample-based analogues of the distribution parameters introduced in Sect. 6.2.4, providing empirical estimates of those theoretical quantities.

A good starting point is to recall the distinction of data types and their corresponding measurement scales as introduced in Sect. 1.5. Each scale allows specific mathematical operations, which determine the set of meaningful descriptive methods that can be applied. These relationships are summarized in Fig. 7.2.

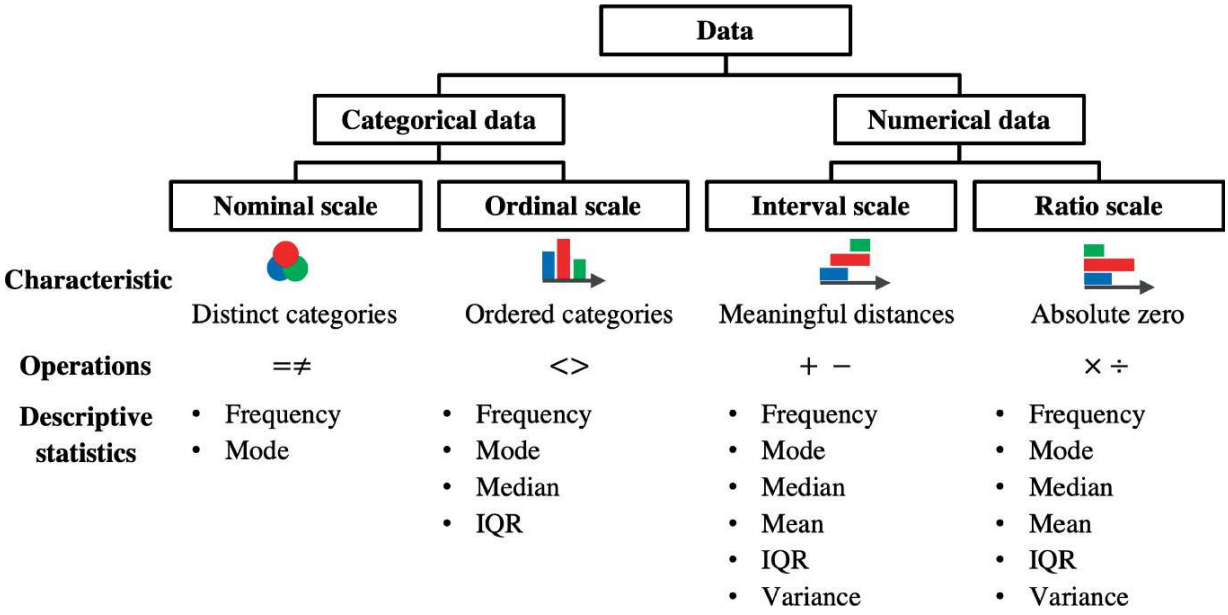


Fig. 7.2 Overview of descriptive statistics and suitable methods for different data scales

Categorical data can be organized by grouping elements into categories and counting their frequencies. For data on a nominal scale, a good first choice for visual display is a **bar chart**, which allows easy comparison of category frequencies. Sorting the bars from largest to smallest results in a **Pareto chart**, which improves readability when category order is not inherent. For ordinal data, the categories follow a natural order, so Pareto charts may obscure the underlying sequence. Quantitative data are most commonly represented using **histograms**, which show how data are distributed across intervals while respecting the order of values, as illustrated in Fig. 7.3.

For quantitative data, categories are commonly not predefined. To construct a histogram, the values must first be divided into intervals, called **classes**. Once classes are established, frequency and relative frequency can be computed for each class, similar to categorical data. This process is also illustrated in Fig. 7.3, where numerical data are grouped into classes for visualization.

The choice of the number of classes affects how patterns in the data are revealed and should be adjusted to the context of the analysis. A common rule of thumb is to use roughly the square root of the sample size, with a practical range of about 5 to 30 bins, and sometimes up to

50 for very large datasets. The class width is then determined by dividing the data range by the chosen number of classes. Each class should ideally contain several data points to ensure the histogram reflects meaningful patterns rather than random noise.

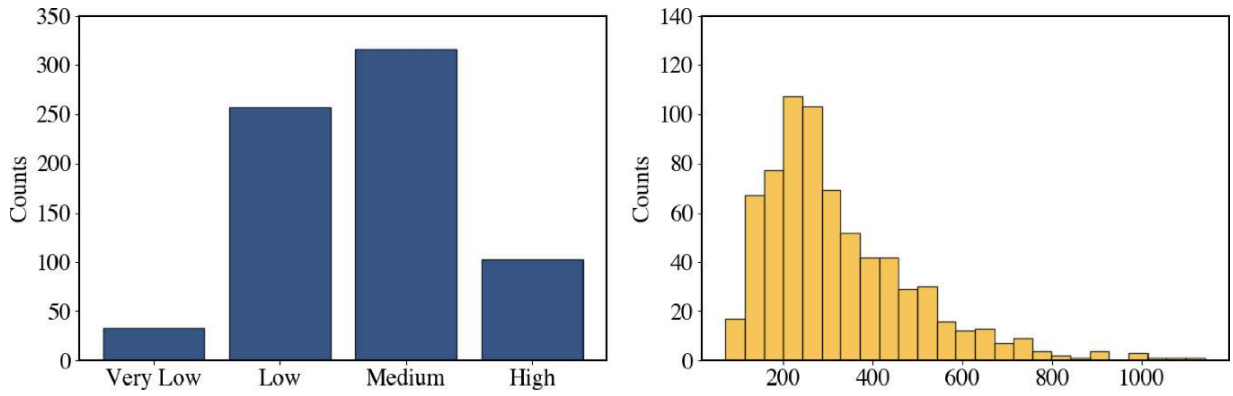


Fig. 7.3 Examples of histograms for numerical and categorical data

7.1.1 Location Statistics

Location statistics aim to describe where the center of a data set lies. They provide a measure of what might be considered a typical or central value. The most common measures of location are the **mode**, the **mean**, and the **median**. The choice of the most appropriate measure depends on the characteristics of the data. When the data distribution is perfectly symmetric, these three measures are equal. In contrast, for skewed distributions, they differ, where the mean is influenced by extreme values or outliers, while the median remains more stable and is therefore often preferred when outliers are present.

Mode The mode is the value or category that occurs most frequently in a data set. For categorical data, it is simply the category with the highest count. The mode provides a useful summary when identifying the most common or typical category. For continuous data, a discretization into classes is required to determine the mode, as exact duplicates of numerical values are rare. Distributions with two or more local maxima are called bimodal or multimodal, respectively. Recognizing such patterns can provide important information about the underlying processes that generated the data.

Mean The mean represents the average of the data and corresponds to the expected value of a random variable, as discussed in Chap. 6. It is widely used because of its mathematical properties, particularly its connection to many statistical models. Several forms of the mean are used in practice, each suited to different kinds of data and applications. The **arithmetic mean** is the sum of all sample values divided by their number

$$\bar{x} = \frac{1}{n} \sum_{i=1}^{n} x_i \ . \tag{7.1}$$

The **harmonic mean** is useful when averaging rates, ratios or quantities defined per unit, such as speeds or densities

$$\left(\frac{1}{n} \sum_{i=1}^{n} x_i^{-1} \right)^{-1} \ . \tag{7.2}$$

The **geometric mean** is appropriate when the data represent multiplicative processes or growth rates

$$\left(\prod_{i=1}^{n} x_i \right)^{1/n} = \exp \left(\frac{1}{n} \sum_{i=1}^{n} \ln x_i \right) \ . \tag{7.3}$$

The geometric mean is especially meaningful for data that span several orders of magnitude or follow a lognormal distribution.

Median The median is the middle value of a data set when the data are ordered from smallest to largest. It divides the data into two equal halves, with half of the data points lying below the median and half lying above. The median is especially valuable when the data contain outliers or are skewed, as it is not affected by extreme values. It is calculated as

$$\text{median}(x) = \begin{cases} x_{\left(\frac{n+1}{2}\right)} \ , & \text{for odd } n \\ \frac{1}{2} \left(x_{\frac{n}{2}} + x_{\frac{n}{2}+1} \right) \ , & \text{for even } n \end{cases} \tag{7.4}$$

In a probability distribution, the median corresponds to the point where the cumulative distribution function equals 0.5, also known as the 50th percentile. This makes it a natural measure of the central point of the distribution.

7.1.2 Dispersion and Shape Statistics

Dispersion statistics provide an estimate of how concentrated or spread out data points are around a typical value. They help quantify the variability within a data set, offering insight into its structure beyond the central tendency.

Variance The variance measures the average squared deviation of data points from the mean. It is computed as

$$s^2 = \frac{1}{n-1} \sum_{i=1}^{n} \left(x_i - \bar{x}\right)^2 \ , \tag{7.5}$$

and is related to the sample standard deviation *s*, which is the square root of the variance. Squaring the deviations gives greater weight to points that lie farther from the mean. The use of $n - 1$ rather than *n* in the denominator is known as Bessel's correction. This correction accounts for the fact that calculating the mean from the sample uses up one degree of freedom, because the mean itself depends on the data. As a result, using *n* in the denominator would systematically underestimate the true variance on average, producing a biased estimator. Bessel's correction adjusts for this bias, ensuring an unbiased estimate of variance when sampling from a population. For large sample sizes, the difference between using *n* and $n - 1$, however, becomes negligible.

Variance and standard deviation are also commonly used to assess whether individual data points deviate significantly from the typical values of the distribution. In normally distributed data, values that lie more than two standard deviations away from the mean are often regarded as unusual. Such points represent $\approx 5\%$ of the data if the distribution is truly normal. Data points that are farther than three

standard deviations from the mean are typically considered outliers, as they fall in the extreme tails of the distribution and occur with very low probability, approximately 0.3%. This approach to identifying outliers assumes the data are approximately normal and that variance is an appropriate measure of spread. When the data contain outliers or are not normally distributed, a more robust alternative is to use the interquartile range (IQR) as the basis for detecting unusually large or small values. The IQR focuses on the spread of the middle 50% of the data and is less sensitive to extreme values at the boundaries, as discussed further below.

Range The range is the simplest measure of spread, defined as the difference between the largest and smallest values in the data set. While easy to compute, it provides no information about the distribution of values between these extremes and is of course highly sensitive to outliers. *Median Absolute Deviation* The median absolute deviation (MAD) is a robust estimator of dispersion, calculated as

$$\text{MAD} = \text{median}(|x_i - \text{median}(x)|) \ . \tag{7.6}$$

Like the median, the MAD is insensitive to extreme values and is useful for describing variability when outliers are present.

Percentiles and Quartiles Percentiles provide information about the cumulative distribution of data. The *k*-th percentile P_k indicates the value below which *k*% of data points fall. Percentiles are determined by ordering the data from smallest to largest and identifying the value at the desired cumulative position. Quartiles are specific percentiles that divide the data into four equal parts $Q_1 = P_{25}$, $Q_2 = P_{50}$, that is the median, and $Q_3 = P_{75}$.

Interquartile Range The interquartile range (IQR) captures the spread of the middle 50% of the data $\text{IQR} = Q_3 - Q_1$. The IQR is often used to detect outliers. Data points are typically considered outliers if they lie outside the interval $[Q_1 - 1.5\,\text{IQR},\ Q_3 + 1.5\,\text{IQR}]$. This approach provides a robust alternative to standard deviation-based methods, as it is less influenced by extreme values.

7.1.3 Normalization

When data sets cover vastly different ranges it becomes difficult to compare their distributions directly. In such cases it is beneficial to normalize the data to a common scale so that patterns and relationships can be more easily detected. Normalization is not only useful for visual analysis or descriptive statistics. It is often an essential step in preparing data for modeling and prediction. Many modeling methods work under the assumption that input variables are on comparable scales. This applies to techniques that rely on distances or variances, such as linear regression or principal component analysis, discussed in Chap. 8. For example, consider a data set that contains both temperature and pressure measurements. Without normalization, a variable that happens to have larger numerical values, such as pressure measured in Pa, might dominate the model simply because of its scale rather than its actual importance in explaining the outcome. Normalization ensures that each variable contributes fairly to the model and that differences in scale do not distort the results.

The two most common normalization methods are z-score normalization and range scaling. Each of these methods is suited to different types of data and different analysis purposes. The ***z*-score** transformation shifts the data set *x* by subtracting its mean and scales it by its standard deviation. This results in

$$z = \frac{x - \bar{x}}{s} \quad , \tag{7.7}$$

where $\bar{x}$ is the sample mean and *s* is the sample standard deviation. After z-score normalization, the data are centered at zero and have unit standard deviation. This method is particularly well suited when the data are approximately normally distributed. It is also preferable when outliers may be present, because it does not restrict the data to a fixed interval and preserves the relative distances between points.

Range scaling, also called **min-max scaling**, rescales the data to fit within a specified interval, commonly [0, 1]. The transformation is defined as

$$z = \frac{x - \min(x)}{\max(x) - \min(x)} \quad . \tag{7.8}$$

This method is straightforward and effective when the data do not contain significant outliers. However, it is sensitive to extreme values because the minimum and maximum values determine the scaling range. A single outlier at either end can distort the scaling of the remaining data points. The method can also be adapted to map the data to a different interval, such as $[-1, 1]$. This can be useful when zero has a meaningful interpretation in the data or when the sign of the value carries information.

7.1.4 Graphical Summarization of Data

Graphical representations are powerful tools for summarizing and communicating key characteristics of data. They help reveal patterns, identify outliers, and compare groups in ways that numerical summaries alone may not. Aside from the histograms discussed earlier, two widely used and informative graphical methods in descriptive statistics are boxplots and quantile-quantile plots. These provide compact visual summaries of data distributions and make it easier to detect structure and differences between groups.

Boxplots A boxplot provides a compact visual summary of the central tendency and variability of a data set. It combines information about location and dispersion statistics in a single figure. The boxplot shown in Fig. 7.4 illustrates how data are grouped and how their distributions can be compared across categories. The central element of a boxplot is the box itself. The box spans the interquartile range (IQR), which represents the middle 50% of the data between the first quartile Q_1 and the third quartile Q_3. A line inside the box marks the median. This helps identify where the center of the data lies and whether the distribution is symmetric or skewed.

The so-called whiskers extend from the edges of the box to cover data points that fall within a certain distance from the quartiles. By convention, the whiskers extend to the smallest and largest data points that are no more than 1.5 times the IQR below Q_1 or above Q_3. Any

data points beyond this range are considered potential outliers and are plotted individually as separate markers. This makes it easy to visually detect unusually large or small values in the data.

Boxplots are particularly useful when comparing distributions across different groups or categories. They provide a quick way to assess differences in medians, variability, and the presence of outliers between groups.

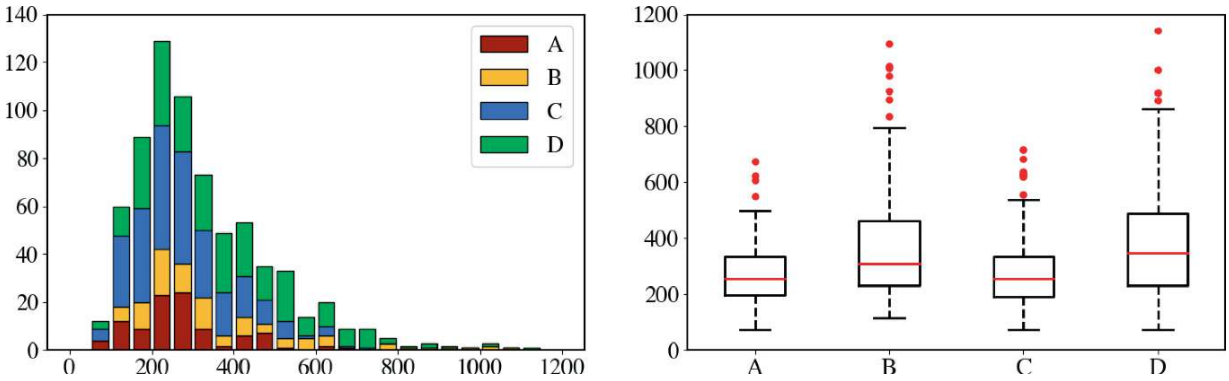


Fig. 7.4 Breakdown of histogram in Fig. 7.3 into groups and corresponding boxplots for each group

Quantile-Quantile Plots Quantile-quantile plots, often abbreviated as QQ-plots, provide a graphical method to compare the distributions of two data sets or to compare a sample distribution to a theoretical reference distribution. A QQ-plot is created by plotting the quantiles of one distribution on the vertical axis against the quantiles of the other distribution on the horizontal axis. If the distributions are similar, the points will approximately follow the diagonal line where the two quantiles are equal.

QQ-plots are often used to assess whether a data set follows a specific theoretical distribution, such as the normal distribution. When comparing to a normal distribution, a QQ-plot helps detect deviations from normality which could manifest as skewness or heavy tails. If the data match the theoretical distribution well, the points will lie close to the diagonal line. Any systematic deviation from this line indicates differences in the distributional shape and provides visual evidence for departures from the assumed model. Figure 7.5 shows an example

where two sample sets are compared to a standard normal distribution. The upper row shows Sample A that follows a normal distribution quite closely. This is indicated by the alignment of the points along the diagonal line. On the lower row Sample B is illustrated, that is skewed as reflected by the curvature of the points away from the diagonal especially at the distribution tails.

Before creating a QQ-plot, it is often beneficial to normalize or standardize the data so that differences in location or scale do not obscure the comparison of shapes. QQ-plots are a valuable tool for checking assumptions in statistical modeling and for assessing goodness of fit. In later sections we will introduce formal statistical tests that complement the visual insight provided by QQ-plots.

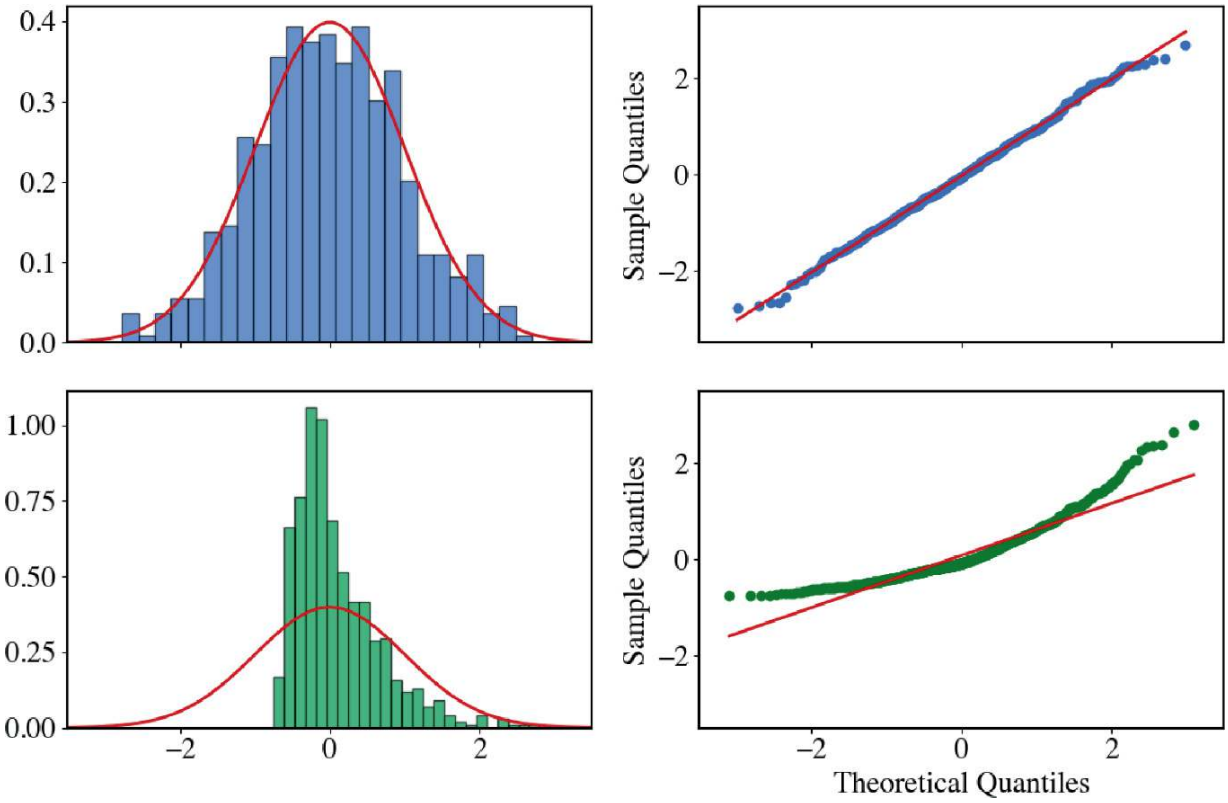


Fig. 7.5 Quantile-quantile plots comparing two sample distributions to a standard normal distribution

7.2 Distributions for Inference

Inferential statistics use sample data to estimate unknown characteristics of a population, such as its mean or standard deviation. Since data sets covering the entire population are rarely available, these population parameters are typically unknown. Before turning to estimation methods in Sect. 7.3 and hypothesis testing in Sect. 7.4, we introduce three distributions essential for inferential statistics, that is the *t*-distribution, the χ^2-distribution, and the *F*-distribution.

7.2.1 *t*-Distribution

The *t*-distribution plays a central role in statistical inference, particularly when estimating the population mean μ or testing related hypotheses in cases where the population standard deviation σ is unknown, as we will see in Sects. 7.3 and 7.4.

Assume we draw a sample $x_1, \ldots, x_n$ from a normal distribution $\mathcal{N}(\mu, \sigma)$. The sample mean $\bar{x}$ is normally distributed with mean μ and variance σ^2/n. Thus, the standardized variable $\bar{x} - \mu/(\sigma/\sqrt{n})$ follows a standard normal distribution $\mathcal{N}(0, 1)$.

In practice, since σ is unknown, we replace it with the sample standard deviation *s*. This yields the statistic

$$\frac{\bar{x}-\mu}{s/\sqrt{n}} = \frac{\sqrt{n}\,(\bar{x}-\mu)}{\sqrt{\sum_{i=1}^{n}(x_i-\bar{x})^2/(n-1)}}\,, \tag{7.9}$$

which no longer follows a normal distribution. Instead, it follows the so-called *t*-distribution, given the hypothesized mean μ is correct. The *t*-distribution is symmetric, and similar to the normal distribution, but is heavier on its tails, as it accounts for the spread of possible true variances. The distribution shape depends on the degrees of freedom $n - 1$, where *n* is the sample size.[1] The *t*-distribution-distribution converges toward the normal distribution for increasing degrees of freedom, as depicted in Fig. 7.6. For sample sizes of $n > 30$, a difference between the two distributions is hardly recognizable. The distribution and its derivation are not presented here, but the interested reader is referred to statistics textbooks (Ross 2012).

7.2.2 χ^2-Distribution

The χ^2-distribution is fundamental in statistical inference, particularly for analyzing variances and assessing goodness of fit. It is used to construct confidence intervals for the standard deviation of a normally distributed population, as discussed in Sect. 7.3, and to evaluate how well observed frequencies match expected frequencies in goodness-of-fit tests, as detailed in Sect. 7.4.

If $x_1, \ldots, x_n$ are independent samples from a normal distribution, the scaled sum of squared deviations

$$\frac{1}{\sigma^2} \sum_{i=1}^{n} (x_i - \bar{x})^2 \ , \tag{7.10}$$

follows a χ^2-distribution with $n - 1$ degrees of freedom, as illustrated in Fig. 7.7. Equivalently, if z_i are independent standard normal variables, then $\sum_{i=1}^{n} Z_i^2$ is χ^2-distributed with n degrees of freedom. This can be interpreted as the squared distance from the origin in n-dimensional space when coordinates follow independent standard normals.

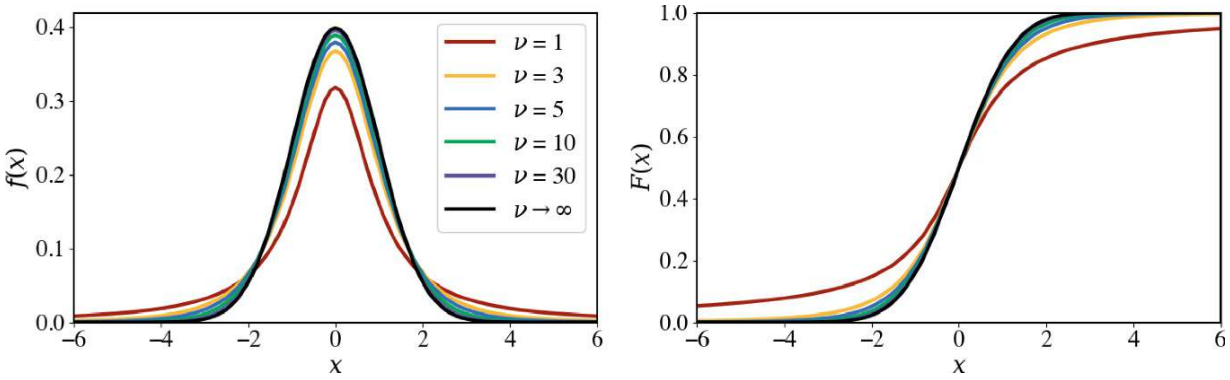


Fig. 7.6 Comparison of *t*-distributions with different degrees of freedom to the standard normal distribution

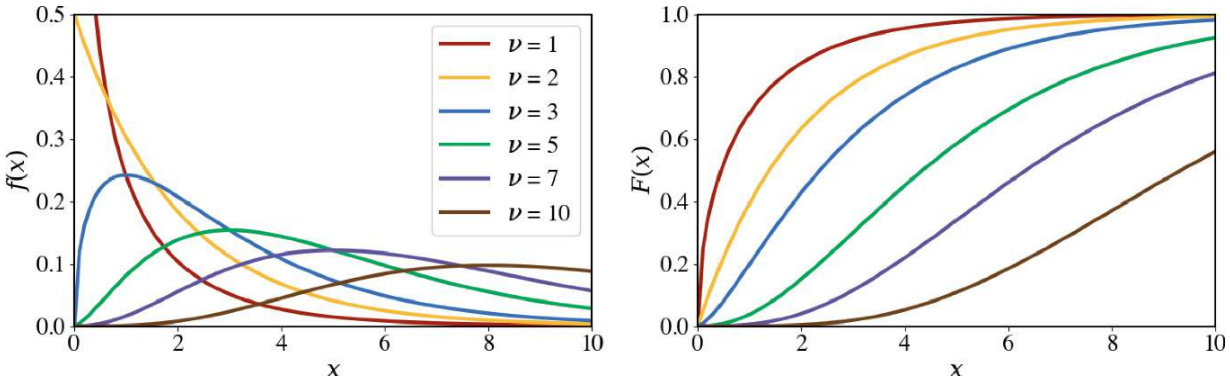


Fig. 7.7 χ^2-distribution for various degrees of freedom *n*

7.2.3 *F*-Distribution

The *F*-distribution, plays a key role in the analysis of variances. It is commonly used to compare the variances of two independent samples and underlies procedures for testing whether multiple population means are equal.

The *F*-distribution arises as the ratio of two scaled, independent χ^2-distributed variables. Let *X* and *Y* be independent random variables, where $X \sim \chi^2(d_1)$ and $Y \sim \chi^2(d_2)$ with d_1 and d_2 degrees of freedom, respectively. Then the random variable

$$F(d_1, d_2) = \frac{(X/d_1)}{(Y/d_2)} \quad , \tag{7.11}$$

follows an *F*-distribution with d_1 and d_2 degrees of freedom. The *F*-distribution is positive-valued and asymmetric, with its exact shape depending on both d_1 and d_2. As the degrees of freedom increase, the distribution becomes more symmetric and approaches a normal-like shape. The probability density and cumulative distribution functions for selected combinations of degrees of freedom are illustrated in Fig. 7.8. The *F*-distribution is particularly sensitive to differences between sample variances, making it a powerful tool for comparing variability across groups.

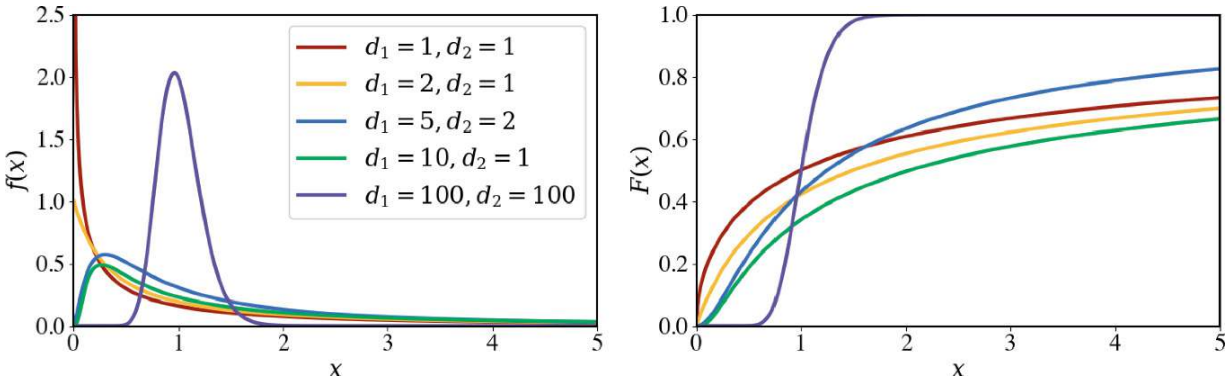


Fig. 7.8 The *F*-distribution for selected combinations of numerator degrees of freedom d_1 and denominator degrees of freedom d_2

7.3 Confidence Intervals

Inferential statistical estimators for population characteristics, such as the mean or variance, are derived from sample data. The sample mean $\bar{x}$ serves as a **point estimator** for the population mean μ, providing a single best guess. However, it is unlikely that a single point estimate perfectly represents the true population parameter. **Confidence intervals** provide an **interval estimate** that specifies a plausible range in which the true, yet unknown parameter lies. The interval is centered at the point estimate and extends in both directions by a margin of error, for example $\bar{x} \pm \text{margin of error}$.

The margin of error is associated with a **confidence level** that specifies the proportion of similarly constructed intervals that would contain the true parameter if the experiment were repeated many times. A commonly used confidence level is 95%, corresponding to the area under the normal distribution within approximately two standard deviations of the mean. Depending on the criticality of the case, other levels such as 90 or 99% may also be used. In the following discussion we focus on the 95% case.

In its interpretation a 95% confidence interval means that 95% of all intervals computed from repeated sampling under identical conditions would cover the true population parameter, such as the population mean, variance, or a similar quantity. It does not mean there is a 95% chance that the specific computed interval contains the true

parameter. The true parameter is fixed, and the interval either contains it or not. Similarly, it does not imply that 95% of the data lie within the interval.

The width of the confidence interval depends primarily on the chosen confidence level and the sample size. A higher confidence level or a smaller sample size leads to a wider interval.

Confidence Interval for the Mean with Unknown Variance When the population variance σ^2 is unknown, which is typically the case, we use the *t*-distribution to compute the confidence interval for the mean of a normally distributed population. We define the confidence level CL and the corresponding reverse probability $\alpha = 1 - \mathrm{CL}$. Since the *t*-distribution is symmetric, the interval is split equally, placing $\alpha/2$ in each tail. With $t_{\frac{\alpha}{2},n-1}$ denoting the *t*-value corresponding to the $\alpha/2$ quantile and $n-1$ degrees of freedom, the confidence interval satisfies

$$P\left(t_{\frac{\alpha}{2}} \leq \frac{\bar{x}-\mu}{n/\sqrt{n}} \leq t_{1-\frac{\alpha}{2}}\right) = \mathrm{CL} \ , \tag{7.12}$$

where due to symmetry $t_{\frac{\alpha}{2}} = t_{1-\frac{\alpha}{2}}$. Accordingly, the confidence interval for the mean is given by

$$\bar{x} - t_{\frac{\alpha}{2}} \frac{s}{\sqrt{n}} \leq \mu \leq \bar{x} + t_{\frac{\alpha}{2}} \frac{s}{\sqrt{n}} \ . \tag{7.13}$$

To simplify the notation, the degrees of freedom $n-1$ as *t*-distribution parameter is not explicitly stated in the given expressions.

Confidence Interval for the Mean with Known Variance In case the population variance σ^2 is known, the drawn sample follows the normal distribution. Constructing the interval is analogous, only that now the z-score is used to construct the confidence interval, resulting in

$$\bar{x} - z_{\frac{\alpha}{2}} \frac{\sigma}{\sqrt{n}} \leq \mu \leq \bar{x} + z_{\frac{\alpha}{2}} \frac{\sigma}{\sqrt{n}} \ . \tag{7.14}$$

Confidence Interval for the Standard Deviation Just as for the mean, the estimation of the standard deviation determined from sample data is subject to uncertainty. When estimating the population standard

deviation from a sample, the confidence interval is derived from the χ^2-distribution as

$$s\sqrt{\frac{n-1}{\chi^2_{\frac{\alpha}{2}}}} \leq \sigma \leq s\sqrt{\frac{n-1}{\chi^2_{1-\frac{\alpha}{2}}}} \ , \tag{7.15}$$

where the χ^2-distribution for the given confidence level is applied with $n-1$ degrees of freedom. Note that the χ^2-distribution is not symmetric, so the bounds must be evaluated separately for both the lower and upper interval bounds.

It is emphasized that these confidence intervals assume that the population is normally distributed. Even when justified by the central limit theorem, practical application requires sufficiently large sample sizes, typically $n > 30$, and at least a visual or statistical check for approximate normality in the sample data.

7.4 Hypothesis Testing

Generally speaking, when we explore data, our intuition alone is often insufficient to reliably distinguish between patterns that arise from genuine effects and those that occur by random chance. **Hypothesis testing** provides a formal framework of statistical inference that helps us evaluate whether the patterns we observe in our data are statistically significant or simply the result of natural variability.

A **hypothesis** represents an initial claim or conjecture about a population parameter. This claim is typically based on theoretical considerations, prior studies, or rational deduction. A hypothesis test uses the information in sample data to assess the validity of this claim, quantifying the strength of evidence in its favor or against it. In general, hypothesis tests follow a standard sequence of steps

- Formulate two opposing assumptions about a population parameter. One represents our claim, the other its logical alternative.
- Design and perform an experiment or collect sample data that is appropriate for testing these assumptions.

- Analyze the data by computing a test statistic and comparing it to a reference distribution that describes expected outcomes under the baseline assumption.
- Conclude whether the data provide sufficient evidence to reject the baseline assumption.

7.4.1 Hypothesis Testing Terminology

Hypothesis tests can be classified according to several criteria, depending on the structure of the data and the type of population characteristic being tested. In this section, we follow the terminology and structure as outlined by Skipper (2016).

First, hypothesis tests differ based on the type of sample data considered, that is tests for categorical data and for continuous data, with implications on applicable scale and statistics according to Sects. 1.5.1 and 7.1.

Second, hypothesis tests are distinguished by the number of sample sets involved. **One-sample tests** compare data from a single sample to a hypothesized value for the population characteristic. **Two-sample tests** compare data from two distinct samples, typically to test whether they originate from populations with the same characteristic. **Multigroup tests**, such as analysis of variance (ANOVA), extend this comparison to more than two sample sets.

Third, tests are categorized by the population characteristic they are designed to assess. **Distribution tests** target the underlying probability distribution of the population. They are used to determine whether the data are consistent with a specific distribution, e.g., normality tests, or whether two samples share the same distribution. **Location tests** focus on parameters that describe the central tendency of the population, such as the mean or median, for example the *t*-test. **Dispersion tests** assess variability within the population. The χ^2-test, for instance, can be used to evaluate claims about the variance.

Although there exists a wide variety of statistical tests corresponding to these distinctions, they all share a common underlying structure and terminology. The essential aim of this section

is to enable the reader to formulate hypotheses, select suitable tests, and interpret the resulting outputs, rather than to compute test statistics by hand. Established software packages provide reliable implementations of the various tests. For readers seeking a deeper mathematical treatment of test statistics, references such as (Illowsky and Dean 2013) are recommended.

To help demonstrate the testing procedure and the interpretation of results in a practical context, we revisit the example of pump lifetime introduced in Chap. 6 and apply a one-sample *t*-test on continuous data.

Hypotheses are formulated in pairs, the **null hypothesis** H_0 and the **alternative hypothesis** H_a. These are opposing and mutually exclusive statements about a population parameter. The null hypothesis H_0 represents the baseline assumption, typically asserting equality, for example that a population parameter equals a hypothesized value. H_0 generally represents the position of no effect or no difference and is the hypothesis we aim to test, that is the hypothesis to be disproved and rejected. So H_0 usually represents the argument of statistical insignificance, corresponding to random chance being responsible for an observed difference. The alternative hypothesis H_a contradicts the null hypothesis. It reflects the possibility of a genuine effect or difference, that is, the observation is due to some underlying pattern that manifests in an inequality ($\neq$), greater than (>), or less than (<) a reference value.

Example 7.1 Suppose we want to investigate the lifetime of pumps produced by a manufacturer advertising a mean lifetime of 8000 h. We want to assess whether the observed mean lifetime differs significantly from this claim or whether any observed difference could reasonably be attributed to random chance. We may have an intuition that there is a significant difference in lifetime between observation and claim. We formulate the null hypothesis to state, there exists no difference between observed and claimed lifetime, so that the observed population has the claimed population mean, thus $H_0 : \mu = 8000$. The assumption thus attributes any observed differences between samples

to population mean to random chance. The corresponding alternate hypothesis contradicts H_0 stating there exists a genuine difference of lifetime between observation and claim, thus $H_a : \mu \neq 8000$.

Based on the evidence provided by the sample data, we can draw one of two possible **conclusions**

1. Reject H_0 and thereby support H_a.
2. Fail to reject H_0 because the evidence is insufficient to conclude a significant difference, and thus not support H_a.

Importantly, our conclusion relies on sample data rather than full population set. Due to the incomplete nature of available information, we **cannot** prove or support a statement to be true, and therefore never prove that H_0 or H_a is true. We can only evaluate whether the evidence is strong enough to reject H_0. For that reason, the conjecture is typically presented as the alternative hypothesis.

Along with the incompleteness of information comes the possibility that the inferred conclusion might be erroneous. It is distinguished between two types of errors. A **Type I error** occurs when we wrongly reject H_0 even though it is true. The probability of making a Type I error is denoted by α, the **significance level** of the test. Typical values for α are 5%, sometimes also 10% or 1%, depending on the consequences of a false positive. A **Type II error** occurs when we fail to reject H_0 even though H_a is true. The probability of a Type II error is denoted by β. The quantity $1 - \beta$ is called the **power** of the test and reflects the probability of correctly rejecting H_0 when H_a is true.

To decide between H_0 and H_a, we compute a **test statistic**. This is a quantity derived from the sample data that reduces the evidence to a single numerical value. The distribution of this statistic under H_0 is known or can be approximated, enabling us to compute the so-called ***p*-value**. The *p*-value represents the probability of observing data as extreme as (or more extreme than) the actual sample, assuming that H_0 is true. A small *p*-value indicates that the observed data are unlikely

under H_0, and thus provides evidence against it. If the *p*-value is smaller than the pre-set significance level α, we reject H_0.

Conceptually, the test statistics and reference distributions used in hypothesis tests are closely related to those introduced earlier for confidence intervals. For example, the *z*-score, *t*-score, and χ^2-statistic introduced in Sect. 7.1 reappear here. The main difference is that, in hypothesis testing, we assume a particular population parameter value (from H_0) and assess whether the sample is consistent with this assumption.

For illustration, let us consider testing a claim about the population mean μ when the population is assumed normal but its variance is unknown. In this case, we use a one-sample *t*-test, computing $t = (\bar{x} - \mu_0)/(s/\sqrt{n})$, where $\bar{x}$ is the sample mean, *s* the sample standard deviation, *n* the sample size, and μ_0 the mean specified by H_0. The case is illustrated for the example in Fig. 7.9. The *p*-value corresponds to the tail area(s) beyond the computed *t* in the reference distribution, depending on whether we conduct a one- or two-tailed test.

Example 7.2 Returning to our pump lifetime example, we assume a normal distribution of lifetime around the population mean μ_0. Suppose we collect data on lifetimes and since variance is unknown, we compute the *t*-score and utilize the *t*-distribution. We set $\alpha = 0.05$ and calculate a *p*-value of $p = 0.48$. This indicates a 48% probability of observing such a sample (or more extreme) under H_0. Since *p* is much larger than α, we do not reject H_0. The available evidence is insufficient to claim that the mean lifetime differs from 8000 h.

To summarize, the standard steps in hypothesis testing are

1. Formulate H_0 and H_a.
2. Choose the significance level α.
3. Collect and analyze the sample data.

4. Compute the test statistic and corresponding p-value.
5. Draw a conclusion, if $p < \alpha$ reject H_0 and support H_a, else do not reject H_0.

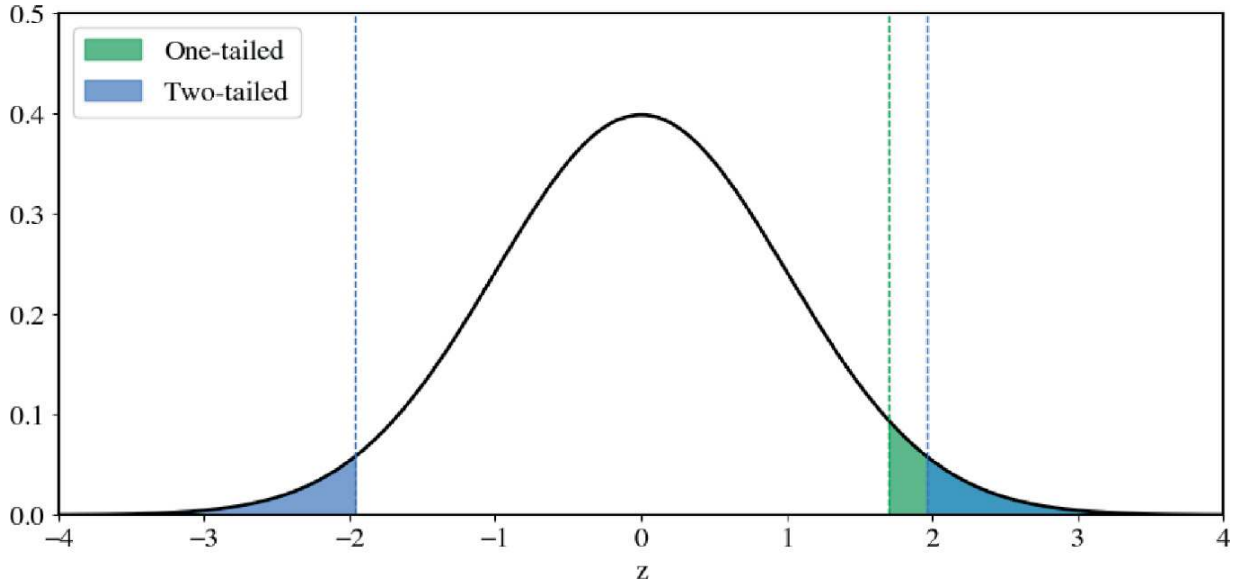


Fig. 7.9 Illustration of one-tailed and two-tailed hypothesis tests. The blue areas show critical regions for a two-tailed test at $\alpha = 0.05$, while the green area shows the p-value of a one-tailed test

One- and Two-Tailed Tests The formulation of H_a determines whether we perform a one- or two-tailed test. If H_a states that the parameter is simply different, for example $\mu \neq \mu_0$, we perform a two-tailed test. The significance α is split symmetrically between the two tails of the distribution.

If H_a specifies a direction, for example $\mu > \mu_0$ or $\mu < \mu_0$, we perform a one-tailed test, placing all of α in one tail. A **right-tailed test** is used when H_a claims the parameter is greater, while a **left-tailed test** is used when H_a claims the parameter is smaller. The p-value corresponds to the area in the specified tail beyond the observed test statistic.

Figure 7.9 illustrates both one- and two-tailed tests under the standard normal distribution. The central curve shows the probability density of the standard normal distribution $Z \sim \mathcal{N}(0, 1)$. The shaded blue regions indicate the rejection zones in a two-tailed test at a 5% significance level. These areas correspond to the outer 2.5% in each tail, cut off at $z = \pm 1.96$, beyond which the null hypothesis is rejected. In contrast, the green region shows the *p*-value for a one-tailed test, where the test statistic $z = 1.7$ is marked and the *p*-value corresponds to the area to its right. A one-tailed test places the entire significance level α in one tail, depending on the direction specified in H_a.

The choice of an appropriate hypothesis test depends on the nature of the data and the question being asked. At a high level, one must consider whether the sample data are continuous or categorical, whether a single sample is compared to a fixed reference or to another sample, and whether the aim is to assess characteristics such as distribution shape, central tendency, or variability. In this and the following sections, we introduce common types of hypothesis tests, organized by the type of population characteristic they assess. We begin with distribution tests, which evaluate whether a data set plausibly follows a given distribution or whether two samples originate from the same distribution.

7.4.2 Distribution Tests

Distribution tests provide a way to quantify whether sample data originate from a population with a particular distribution. Among these, normality tests are probably most well-known. They are used to check whether the underlying population can reasonably be assumed to follow a normal distribution. Normality tests play a crucial role when applying other hypothesis tests, such as the *t*-test, which rely on the assumption of normality. Beyond that, normality tests are also useful for evaluating residuals in linear regression or other models, as part of checking model assumptions. If residuals are not approximately normally distributed, this may indicate that the model does not fully

capture all relevant variables or relationships, or that the functional form of the model is inadequate.

One-sample distribution tests, such as the **Anderson-Darling** test or the **Kolmogorov-Smirnov** test, assess whether data are consistent with a specific hypothesized distribution. In these tests, the null hypothesis H_0 states that the sample comes from the specified distribution, i.e., normal or other distribution. These tests allow us to evaluate whether the data plausibly follow the assumed distribution or whether significant deviations are present.

To compare whether two samples come from the same distribution, two-sample distribution tests are used. An example is the **two-sample Kolmogorov-Smirnov test**, which assesses the hypothesis H_0, that both samples come from the same underlying distribution.

χ^2 Goodness-of-Fit The χ^2 goodness-of-fit test evaluates how well a statistical model fits a set of observations (Skipper 2016, Ch. 11). Here, the term statistical model may refer to a specified probability distribution or to a model predicting frequencies, such as a regression model applied to categorical outcomes. In this test, data are grouped into bins, and for each bin, both observed counts O_i and expected counts E_i are determined. The test compares how close these counts are across all categories. The hypotheses are formulated as

H_0 : The observed data follow the expected distribution.

H_a : The observed data do not follow the expected distribution.

The test statistic is computed as

$$\chi^2 = \sum_{i=1}^{n} \frac{(O_i - E_i)^2}{E_i} \quad , \tag{7.16}$$

where here *n* is the number of categories. This statistic measures the overall discrepancy between observed and expected counts. If the observed counts match the expected counts perfectly, the test statistic is zero. Since the differences are squared, the test statistic is always non-negative, making this a one-sided test. For sufficiently large counts,

the test statistic approximately follows a χ^2-distribution, discussed in Sect. 7.2.

The *p*-value corresponds to the area in the right tail of the χ^2-distribution beyond the calculated test statistic. This *p*-value represents the probability of observing a discrepancy at least as large as the one found, assuming H_0 is true. The larger the difference between observed and expected counts, the larger the test statistic and the smaller the *p*-value. When $p < \alpha$, where α is the chosen significance level, we reject H_0 and conclude that the data do not fit the expected distribution.

Test for Independence The same χ^2 test statistic can also be used to test whether two categorical variables are independent (Skipper 2016, Ch. 11). In this context, the data are arranged in a **contingency table**, where one categorical variable defines the rows and the other defines the columns. Each cell of the table contains the observed count O_{ij} for that combination of categories. The hypotheses are formulated as

H_0 : The two categorical variables are independent.

H_a : The two categorical variables are dependent.

The expected counts E_{ij} are calculated under the assumption of independence to

$$E_{\text{ij}} = \frac{(\text{row total})_i \, (\text{column total})_j}{n} \quad , \tag{7.17}$$

where *n* is the total number of observations.

The χ^2 test statistic is then calculated in the same way as for the goodness of fit

$$\chi^2 = \sum \frac{(O_{\text{ij}} - E_{\text{ij}})^2}{E_{\text{ij}}} \quad . \tag{7.18}$$

Again, for large sample sizes, the test statistic approximately follows a χ^2-distribution. The *p*-value corresponds to the probability, under H_0, of observing a test statistic as large as, or larger than, the one computed. A small *p*-value indicates that the variables are unlikely to be

independent. When $p < \alpha$, we reject H_0 and conclude that the variables are statistically dependent.

7.4.3 Location Tests

Location tests are used to evaluate claims about the central tendency of a population, typically its mean, under an assumed distribution. In the following we review the one-sample *z*-test and *t*-test, as well as their extensions to two-sample cases. Both tests assume that the data originate from a normally distributed population *X*. Thanks to the central limit theorem, many test statistics are approximately normally distributed, which makes these tests widely applicable. However, the assumption of normality should always be verified for the specific case at hand, either by visual inspection or through distribution tests as discussed earlier.

As mentioned in Sect. 7.2, the distinction between *z*- and *t*-tests lies in the knowledge of the population variance. The *z*-test applies when the population variance is known, while the *t*-test is used in the more common case where the population variance is unknown and must be estimated from the sample itself.

***z*-Test** When the population variance σ^2 is known, the **one-sample *z*-test** is used to test a claim about a population mean μ_0. The null hypothesis asserts $H_0 : \mu = \mu_0$ and the alternative hypothesis is typically $H_a : \mu \neq \mu_0$ indicating a two-tailed test. The test statistic is the *z*-score

$$z = \frac{\bar{x} - \mu_0}{\sigma / \sqrt{n}} \quad , \tag{7.19}$$

where *n* is the sample size. Under H_0, this statistic follows the standard normal distribution $\mathcal{N}(0, 1)$.

For a two-tailed test, the *p*-value corresponds to the combined area in both tails beyond the calculated *z* value $p = 2P(Z > |z|)$, where *Z* is a standard normal random variable. If $p < \alpha$, we reject H_0. The test can also be formulated as a one-tailed test if H_a specifies a direction, for

example $H_0 : \mu \geq \mu_0$ versus $H_a : \mu < \mu_0$. In that case, the *p*-value corresponds to the area in the appropriate tail.

***t*-Test** In the more typical situation where the population variance is unknown, we use the **one-sample *t*-test**. The assumptions and hypotheses are the same as for the *z*-test, but the test statistic is

$$t = \frac{\bar{x} - \mu_0}{s/\sqrt{n}} \ , \tag{7.20}$$

where now we apply *s*, that is the sample-based standard deviation. Under H_0, this statistic follows the *t*-distribution with $n - 1$ degrees of freedom. The *p*-value is determined similarly to the *z*-test, but using the *t*-distribution.

As mentioned above, two-sample tests are used to compare two data sets and determine whether their differences are statistically significant. A key distinction here is whether the two samples are **independent** or **paired**. Independent samples come from separate populations, and no natural linkage exists between individual observations in one sample and those in the other. In contrast, paired samples are related in a meaningful way, often through repeated measurements on the same subjects before and after a treatment or under two different conditions. Both independent and paired sample tests follow the same conceptual steps as one-sample tests. In the following, we illustrate the testing procedure based on the *t*-test for the more common case where population variances are unknown and are estimated from sample data.

Independent Two-Sample *t*-Test In the case of independent samples, we compare the means of two populations with $H_0 : \mu_1 = \mu_2$ and $H_a : \mu_1 \neq \mu_2$, where μ_1 and μ_2 are the respective population means. Assuming the population variances are unknown and may not be equal, we use Welch's *t*-test, for which the test statistic is

$$t = \frac{(\bar{x}_1 - \bar{x}_2) - (\mu_1 - \mu_2)}{\sqrt{s_1^2/n_1 + s_2^2/n_2}} \ , \tag{7.21}$$

where $\bar{x}_1, \bar{x}_2$ are the sample means, s_1^2, s_2^2 are the sample variances, and n_1, n_2 are the sample sizes. The calculation of degrees of freedom for Welch's test involves s_1^2, s_2^2, n_1, n_2 and is rather complicated and beyond the present scope and is commonly handled by statistical software, for example (Illowsky and Dean 2013). The *p*-value is obtained from the *t*-distribution with these degrees of freedom.

Paired Two-Sample *t*-Test Now we consider the case where two data sets arise from repeated measurements on the same subjects or entities, observed before and after experiencing some change or treatment. In this case, we are examining the same underlying random variable at two different states, denoted here as state 1 and state 2. The goal is to determine whether the process has introduced a statistically significant difference in the population mean. Since the two samples are inherently linked, the analysis proceeds by considering the difference between paired observations.

For each pair, we compute the difference $d_i = x_{2,i} - x_{1,i}$. This transforms the problem into a one-sample test on the set of differences d_i. The null hypothesis is that the population mean of these differences is zero, that is $H_0 : \mu_d = 0$. The alternative hypothesis states that $\mu_d \neq 0$, indicating a systematic change. The test statistic is then given by

$$t = \frac{\bar{d}}{s_d/\sqrt{n}} \ , \tag{7.22}$$

where $\bar{d}$ is the sample mean of the differences, s_d is their standard deviation, and *n* is the number of paired observations. Under H_0, this statistic follows a *t*-distribution with $n - 1$ degrees of freedom. The corresponding *p*-value quantifies the probability of observing a mean difference at least as extreme as $\bar{d}$, assuming no true effect is present.

7.4.4 Dispersion Tests

Dispersion tests are used to evaluate claims about the variability of a population, such as its variance. In the following, we describe two commonly used tests, the one-sample χ^2 variance test and the two-

sample *F*-test. Both assume that the underlying populations are normally distributed.

χ^2 Variance Test The χ^2 variance test assesses whether the variance of a normally distributed population equals a specified value σ_0^2. The hypotheses assert $H_0 : \sigma^2 = \sigma_0^2$ and $H_a : \sigma^2 \neq \sigma_0^2$. The test statistic is

$$T = (n-1)\left(\frac{s}{\sigma_0}\right)^2 \ , \tag{7.23}$$

where *n* is the sample size, s^2 is the sample variance, and σ_0^2 is the hypothesized population variance. Under H_0, this statistic follows a χ^2-distribution with $n-1$ degrees of freedom. The *p*-value corresponds to the probability of observing a test statistic at least as extreme as *T*, assuming H_0 is true. Large deviations between the observed variance and the hypothesized variance result in large values of *T*, shifting the statistic further into the right tail of the distribution and yielding smaller *p*-values. If the *p*-value falls below the chosen significance level α, we reject H_0 and conclude that the variance differs from the hypothesized value.

Two-Sample *F*-Test The two-sample *F*-test compares the variances of two independent, normally distributed populations. The hypotheses are $H_0 : \sigma_1^2 = \sigma_2^2$ and $H_a : \sigma_1^2 \neq \sigma_2^2$. The test statistic is defined as the ratio of the two sample variances

$$F = \frac{s_1^2}{s_2^2} \ , \tag{7.24}$$

where s_1^2 and s_2^2 are the sample variances from samples of sizes n_1 and n_2, respectively. Under H_0, the *F* statistic follows an *F*-distribution with $(n_1 - 1)$ and $(n_2 - 1)$ degrees of freedom. The *p*-value represents the probability of observing such an *F* value, or a more extreme one, if H_0 is true. If the sample variances are similar, the *F* statistic will be close to 1, leading to a high *p*-value. The greater the difference between sample variances, the further *F* deviates from 1, and the smaller the *p*-value

becomes. Again, when $p < \alpha$, we reject H_0 and conclude that the population variances differ significantly and cannot be explained by random chance.

References

Box GEP, Hunter JS, Hunter WG (2005) Statistics for experimenters: design, innovation, and discovery. Wiley Series in Probability and Statistics. Wiley

Illowsky B, Dean SL (2013) Introductory statistics. Rice University, OpenStax College

Ross SM (2012) A first course in probability, 9th edn. Pearson

Skipper D (2016) Lecture Notes for introductory statistics

Footnotes

1 We represent a sample of *n* independent observations as the random vector $\mathbf{x} = (x_1, \ldots, x_n)^\top$, where each component is a scalar-valued random variable on the same probability space $(\Omega, \mathscr{A}, P)$. If we denote the sample mean by $\bar{x}$, then the deviations from the mean are given by $\mathbf{x} - \bar{x}$. These deviations satisfy the constraint $\sum_{i=1}^{n}(x_i - \bar{x}) = 0$, which leaves $n - 1$ degrees of freedom.

© The Author(s), under exclusive license to Springer Fachmedien Wiesbaden GmbH, part of Springer Nature 2026
H. Gomaa, *Modeling with Knowledge and Data*, Mathematical Engineering
https://doi.org/10.1007/978-3-658-50679-7_8

8. Machine Learning and Prediction

Hassan Gomaa[1] ✉
(1) Strategic Projects Co-Innovation, Cognite, Oslo, Norway

An early and widely cited description of machine learning is attributed to Arthur Samuel, who described it as "*the field of study that gives computers the ability to learn without being explicitly programmed*". A more formal and operational definition is provided by Tom Mitchell, stating "*A computer program is said to learn from experience E with respect to some class of tasks T and performance measure P, if its performance at tasks in T, as measured by P, improves with experience E*". In essence, machine learning refers to a class of methods that allow systems to infer patterns from data and use these patterns to make predictions. The learning process is based on data, and the quality of learning is typically evaluated by how well the resulting model performs on tasks of interest.

Machine learning problems are broadly categorized into supervised and unsupervised learning, depending on the availability and nature of the data labels. In **supervised learning**, the model is trained on a labeled data set, meaning that for each data instance the corresponding output value is known. The aim is to learn a functional mapping *f* that relates the input *x* to the output *y*, such that $y = f(x)$. Once trained, this model *f* can be used to make predictions for new inputs that have not been seen before. Within supervised learning, problems are further distinguished by the type of the output variable *y*. When *y* is a numerical quantity, either continuous or discrete but ordered, the task is called a **regression** problem. Regression problems are discussed in detail in Sect. 8.1. When *y* is a categorical variable, representing a discrete class label with no intrinsic ordering, the task is referred to as a **classification** problem, which we address in Sect. 8.2.

In contrast to supervised learning, **unsupervised learning** addresses problems where the data set contains inputs *x* but no associated output labels *y*. The objective here is to uncover hidden structures, patterns, or relationships within the data itself. This may involve identifying groupings of similar instances, detecting unusual or anomalous examples, or reducing the complexity of the data representation while preserving its essential features. The following sections will discuss some of the most widely used unsupervised learning approaches. These include **clustering**, covered in Sect. 8.3, where the goal is to group similar data instances into distinct clusters. **Dimensionality reduction**, introduced in Sect. 8.4, seeks to reduce the number of input variables while retaining the structure of the data. Finally, **anomaly detection** in Sect. 8.5 deals with identifying data points that deviate significantly from the majority of the data and may correspond to rare events or faults.

8.1 Regression

The objective in regression problems is to determine a **hypothesis function** $h : X \to Y$ that accurately maps a set of **input variables** $x \in X$ to a corresponding output $y \in Y$. As introduced in Sect. 1.2.1, the output *y* is also referred to as the dependent variable or response, while the input *x* is referred to as the independent variable or feature set. When the input variables are continuous, they are also called covariates. If they are categorical, they are referred to as factors.

The defining characteristic of a regression problem is that the target variable *y* is continuous. This allows the hypothesis function to produce numerical predictions that vary over a real-valued range, so we have $y \in \mathbb{R}$. To formalize the problem, we consider a training set that contains *m* **observations**, and *n* input variables, also referred to as **features**. Each observation consists of a measured output value $y^{(i)} \in \mathbb{R}$ and a corresponding **feature vector** $\mathbf{x}^{(i)} \in \mathbb{R}^n$, where the superscript denotes the *i*-th observation in the data set, with $i = 1 \dots m$. The feature vector can be written as

$$\mathbf{x}^{(i)} = \begin{bmatrix} x_1^{(i)} & x_2^{(i)} & \dots & x_n^{(i)} \end{bmatrix} . \tag{8.1}$$

Each component $x_j^{(i)}$ represents the value of the *j*-th feature measured for the *i*-th observation, with $j = 1 \dots n$. Grouping all *m* observations together yields the **target vector** and the **feature matrix**. The output values are collected into the target vector $\mathbf{y} \in \mathbb{R}^m$, written as

$$\mathbf{y} = \begin{bmatrix} y^{(1)} \\ y^{(2)} \\ \vdots \\ y^{(m)} \end{bmatrix} . \tag{8.2}$$

In parallel, the *m* observed input vectors are combined into the **feature matrix** $\mathbf{X} \in \mathbb{R}^{m \times n}$, which collects the full set of training data. The feature matrix $\mathbf{X}$ can be expressed both row-wise, collecting transposed feature vectors for each observation, and column-wise, collecting all samples of each individual feature, as

$$\mathbf{X} = \begin{bmatrix} \left(\mathbf{x}^{(1)}\right)^\top & \left(\mathbf{x}^{(2)}\right)^\top & \dots & \left(\mathbf{x}^{(m)}\right)^\top \end{bmatrix} = \begin{bmatrix} \mathbf{x}_1 & \mathbf{x}_2 & \dots & \mathbf{x}_n \end{bmatrix} . \tag{8.3}$$

The feature matrix thus has *m* rows and *n* columns. Throughout the text, we will use both the row-wise view, which emphasizes individual data samples $\mathbf{x}^{(i)}$, and the column-wise view, which focuses on individual input variables $\mathbf{x}_j$.

Data-driven problems considered here are generally characterized by $m \gg n$, meaning there are more observations than input variables. Assuming the number of model parameters is in the same order as the number of variables, this implies that the system is overdetermined and that there are fewer model parameters than data points. Such problem classes are typically addressed using estimation procedures such as least squares regression, which aim to determine the parameters that best fit the observed data, as discussed in the following.

Example 8.1 As an example, consider a data set obtained from a measurement campaign investigating the drag force on a sphere. The experiments are conducted for varying sphere diameters and different fluids, resulting in a range of physical conditions. For each observation,

the target variable *y* is the measured drag force. The corresponding input variables include the free-stream velocity *u*, the sphere diameter *D*, the fluid density ρ, and the dynamic viscosity μ, giving $n = 4$ input variables in total. Each observation is represented by a feature vector $\mathbf{x}^{(i)} = \begin{bmatrix} u^{(i)} & D^{(i)} & \rho^{(i)} & \mu^{(i)} \end{bmatrix}^\top \in \mathbb{R}^4$. Suppose the campaign collects $m = 100$ such measurements. The full training set then consists of 100 feature vectors and 100 corresponding target values, assembled into a feature matrix $\mathbf{X} \in \mathbb{R}^{100 \times 4}$.

8.1.1 Linear Regression for Linear Hypothesis

To begin with linear regression, we consider the case where the relationship between the input variables and the output is assumed to be linear. This means that the **hypothesis function** $h_{\boldsymbol{\theta}} : \mathbb{R}^n \to \mathbb{R}$ models the output as a weighted sum of the input features. The hypothesis is parameterized by the **model parameter vector** $\boldsymbol{\theta} \in \mathbb{R}^{n+1}$, which contains the coefficients of the linear model. The function is defined as

$$h_{\boldsymbol{\theta}}(\mathbf{x}) = \boldsymbol{\theta}^\top \mathbf{x} = \theta_0 + \theta_1 x_1 + \theta_2 x_2 + \ldots + \theta_n x_n \ . \tag{8.4}$$

This expression corresponds to a hyperplane in *n*-dimensional space, where each parameter θ_j defines the slope in the direction of the *j*-th feature. The term θ_0 represents the intercept and determines the value that the hyperplane takes at the origin, where all input features are zero.

In order to include the intercept term θ_0 within the vector notation, the feature vector $\mathbf{x} \in \mathbb{R}^n$ is extended with an artificial zeroth feature $x_0 = 1$. Consequently, the extended feature vector becomes $(n+1)$-dimensional. This adjustment allows the linear hypothesis to be expressed compactly as a dot product with the parameter vector $\boldsymbol{\theta} \in \mathbb{R}^{n+1}$. Even though the number of true input features remains *n*, this notational shift is standard and convenient for analysis and implementation.

Cost Function To train the linear regression model, the aim is to determine the model parameters $\boldsymbol{\theta}$ such that the predicted output $h_{\boldsymbol{\theta}}(\mathbf{x})$ closely matches the actual target values *y*. In order to quantify how well the model fits the data, we define a **cost function** $J(\boldsymbol{\theta})$ that measures the discrepancy between the predicted and actual outputs. A widely used cost function for regression is the **mean squared error** (MSE). It computes the average of the squared residuals over all *m* training samples. The MSE is given by

$$J(\boldsymbol{\theta}) = \text{MSE}\,(\boldsymbol{\theta}) = \frac{1}{m} \sum_{i=1}^{m} \left(h_{\boldsymbol{\theta}}(\mathbf{x}^{(i)}) - y^{(i)} \right)^2, \tag{8.5}$$

where each residual $\varepsilon^{(i)} = h_{\boldsymbol{\theta}}(\mathbf{x}^{(i)}) - y^{(i)}$ represents the prediction error for the *i*-th training sample. The MSE corresponds to the squared Euclidean distance between the vector of predicted outputs and the vector of true outputs. This can be interpreted as an L_2-norm squared. Alternative metrics exist that may be more appropriate in certain settings. For instance, the mean absolute error corresponds to the L_1 norm, and the maximum absolute deviation corresponds to the L_∞ norm. These alternative norms may be preferred in the presence of outliers or for robustness considerations.

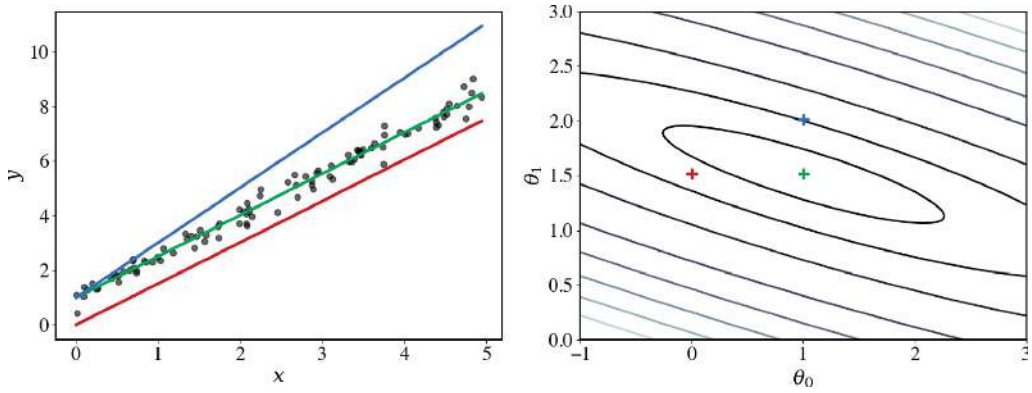


Fig. 8.1 Linear regression with varying parameters on the left and the cost function on the right. The optimal parameters are $\hat{\theta}_0 = 1.07$ and $\hat{\theta}_1 = 1.48$

Nevertheless, the MSE is often a suitable and convenient choice. Minimizing it leads to the **optimal parameter vector $\hat{\boldsymbol{\theta}}$**, defined by

$$\min_{\boldsymbol{\theta} \in \mathbb{R}^{n+1}} J(\boldsymbol{\theta}) \ . \tag{8.6}$$

To visualize this process, consider the univariate case where there is only a single input feature x_1, so the hypothesis becomes $h_{\boldsymbol{\theta}}(x_1) = \theta_0 + \theta_1 x_1$. Figure 8.1 illustrates this setup. On the left, the training data is shown along with three different linear hypotheses, each corresponding to a different choice of parameters. On the right, the cost function $J(\boldsymbol{\theta})$ is plotted over the parameter space spanned by θ_0 and θ_1. The plot includes isocontour lines of the cost function, which represent parameter combinations yielding equal cost. These contours take the shape of ellipses, increasing in value as one moves away from the optimum. The cost function reaches its minimum at a specific parameter combination, here $\hat{\boldsymbol{\theta}} = (1.07, 1.48)^\top$. This point corresponds to the hypothesis that best fits the training data in terms of mean squared error. Any deviation from these optimal parameters leads to an increased cost, indicating a poorer fit to the data.

Convexity of the Cost Function The MSE cost function for linear regression is a **convex quadratic function** of the model parameters $\boldsymbol{\theta}$. To see this, consider the linear hypothesis $h_{\boldsymbol{\theta}}(\mathbf{x}) = \boldsymbol{\theta}^\top \mathbf{x}$, so that the residuals are linear and the squared residuals are quadratic. As a result, $J(\boldsymbol{\theta})$ is a quadratic form in $\boldsymbol{\theta}$ and can be written as

$$J(\boldsymbol{\theta}) = \tfrac{1}{m} |\mathbf{X}\boldsymbol{\theta} - \mathbf{y}|^2 = \tfrac{1}{m} (\mathbf{X}\boldsymbol{\theta} - \mathbf{y})^\top (\mathbf{X}\boldsymbol{\theta} - \mathbf{y}) \ , \tag{8.7}$$

where $\mathbf{X} \in \mathbb{R}^{m \times (n+1)}$ is the extended feature matrix containing the extended input vectors. Expanding yields

$$J(\boldsymbol{\theta}) = \tfrac{1}{m} \left(\boldsymbol{\theta}^\top \mathbf{X}^\top \mathbf{X} \boldsymbol{\theta} - 2 \boldsymbol{\theta}^\top \mathbf{X}^\top \mathbf{y} + \mathbf{y}^\top \mathbf{y} \right) \ . \tag{8.8}$$

This is a quadratic function in $\boldsymbol{\theta}$ with a symmetric positive semi-definite Hessian matrix $\frac{2}{m} \mathbf{X}^\top \mathbf{X}$. When the matrix $\mathbf{X}$ has full rank, the Hessian is positive definite. This implies that $J(\boldsymbol{\theta})$ is strictly convex, and therefore has a unique global minimum. This convexity ensures that any local minimum is also the global minimum, which makes training linear regression models particularly well-behaved and numerically robust. While the MSE cost function is both convex and smooth, alternative norms such as the mean absolute L_1 norm and the maximum absolute

L_∞ norm also yield convex cost functions. However, these are not necessarily smooth and are generally not differentiable everywhere.

Model Verification Once a linear regression model has been trained, it is good practice to verify whether the underlying assumptions that motivated the model are satisfied by the data. For linear regression, the central assumption is that the data can be well represented by a linear relation, meaning that the true target values lie approximately on an *n*-dimensional hyperplane defined by the model hypothesis. A second assumption is that the residuals, representing the differences between predicted and actual values, are independently and normally distributed with zero mean and constant variance. In formal terms, this means that the residuals $\varepsilon^{(i)} = h_{\boldsymbol{\theta}}(\mathbf{x}^{(i)}) - y^{(i)}$ should satisfy

$$\mathrm{E}\left(\varepsilon^{(i)}\right) = 0 \quad \text{and} \quad \mathrm{Var}\left(\varepsilon^{(i)}\right) = \sigma^2 \quad \text{for all } i \in \{1, \ldots, m\} \ . \tag{8.9}$$

These assumptions are not just theoretical conveniences. They form the foundation for many useful statistical properties of the estimator, including the derivation of confidence intervals and hypothesis tests on parameters. Therefore, verifying the distribution and behavior of the residuals is a crucial step in practical applications of linear regression.

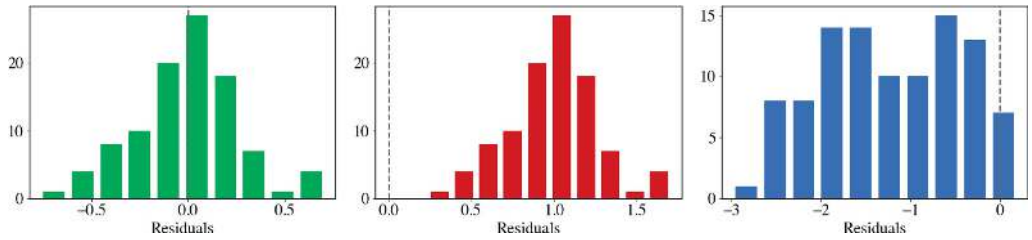


Fig. 8.2 Residuals for the three θ variations from Fig. 8.1

Figure 8.2 illustrates the residuals for the three parameter variations shown previously in Fig. 8.1. Visual inspection of the residuals can reveal whether the model is systematically biased, or whether the variance appears to change with the magnitude of the prediction. Such patterns would indicate that the assumptions of independence or constant variance may be violated.

Beyond numerical metrics, visual inspection plays a critical role in assessing the validity of a regression model. To illustrate this, Fig. 8.3 shows the famous example known as **Anscombe's quartet**. The figure displays four different data sets that share nearly identical descriptive statistics. For each set, the mean and variance of *x* and *y* are the same, the correlation coefficient between *x* and *y* is nearly equal, and the linear regression results in an identical best-fit line with $\hat{\boldsymbol{\theta}} = (3.0, 0.5)^\top$. However, when the data sets are plotted, their structure and the appropriateness of a linear model differ dramatically. This shall serve as an example that statistical summaries, while informative, can obscure underlying structure. A regression line alone does not tell the full story. Model verification should include a combination of numerical diagnostics and graphical inspection to ensure that the learned model not only fits the data but also captures the nature of the underlying process.

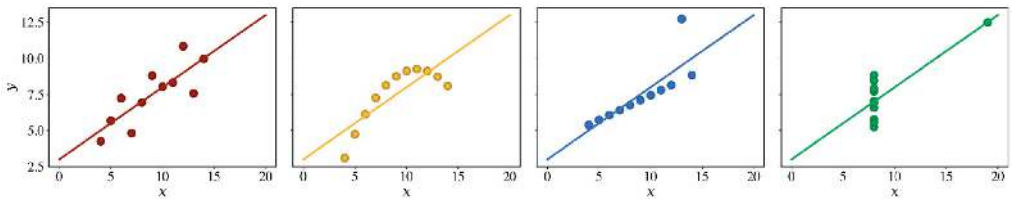


Fig. 8.3 All four sets are identical when examined using simple summary statistics, but vary considerably when plotted

The linear regression model is not only used for inference but also serves as a practical method for quickly identifying dominant trends in data. Even when the true relationship is not linear, a linear model often provides a useful first approximation. It is computationally efficient, easy to interpret, and can serve as a valuable baseline against which more complex models are compared.

8.1.2 Solution Approach

The linear regression problem considered here can be expressed as a system of *m* linear equations with $n+1$ unknowns, due to the inclusion of the intercept term. Since $m \gg n$, there are more equations than unknowns, and the system is overdetermined. This means that, in general, no choice of parameters satisfies all *m* equations exactly. Instead, we determine the parameters that provide the best fit by minimizing the sum of squared residuals.

The Normal Equation The normal equation provides a closed-form expression for the model parameters $\boldsymbol{\theta}$ that minimize the least squares cost function. Specifically, we aim to find the vector $\boldsymbol{\theta}$ that minimizes the Euclidean distance between the predicted outcomes $\mathbf{X}\boldsymbol{\theta}$ and the actual outcomes $\mathbf{y}$, that is

$$\min_{\boldsymbol{\theta} \in \mathbb{R}^{n+1}} \|\mathbf{X}\boldsymbol{\theta} - \mathbf{y}\|_2^2 \ . \tag{8.10}$$

Here, we use the column form of $\boldsymbol{\theta}$ and matrix-vector multiplication to express the hypothesis function compactly over all *m* observations. As shown in Appendix C.1, the minimum of the mean square error results at the parameter vector $\hat{\boldsymbol{\theta}} \in \mathbb{R}^{n+1}$ given by

$$\hat{\boldsymbol{\theta}} = (\mathbf{X}^\top \mathbf{X})^{-1} \mathbf{X}^\top \mathbf{y} \ . \tag{8.11}$$

This expression is known as the normal equation. It involves computing the inverse of the matrix $\mathbf{X}^\top \mathbf{X} \in \mathbb{R}^{(n+1)\times(n+1)}$. However, the inverse only exists if this matrix is nonsingular. A necessary condition for this is that the feature matrix $\mathbf{X}$ has full column rank, meaning $\text{rank}\ (\mathbf{X}) = n+1$. If two or more features are linearly dependent, then $\mathbf{X}^\top \mathbf{X}$ becomes singular and cannot be inverted. This situation can arise easily in practice, for example by mistakenly including redundant features that encode the same information. To overcome this issue, the inverse is replaced by the Moore-Penrose pseudoinverse, which exists for any matrix and yields a least squares solution even when $\mathbf{X}^\top \mathbf{X}$ is not invertible, as detailed in Appendix C.1.

While the normal equation provides an exact solution, it requires matrix inversion, which has a computational complexity of approximately $\mathcal{O}(n^3)$. This becomes a significant burden when the number of features *n* is large, for instance in the range of 10^4 to 10^5 or more. In such cases, the normal equation becomes computationally inefficient and iterative solution methods are preferable. However, in many engineering problems of interest, the number of input features

n typically ranges from a few tens to possibly a few hundreds. In this regime, the normal equation remains very practical and provides a fast and interpretable solution. It is furthermore especially useful during early stages of model development or as a benchmark to validate iterative optimization algorithms on smaller-scale problems.

Iterative Solver Gradient descent represents a first-order iterative optimization method used to find a local minimum of a cost function. It proceeds by following the direction of steepest descent, determined by the negative gradient of the function. Starting from an initial guess $\boldsymbol{\theta}^0 \in \mathbb{R}^{n+1}$, the algorithm generates a sequence of parameter vectors $\boldsymbol{\theta}^k$ according to the iterative rule

$$\boldsymbol{\theta}^{k+1} = \boldsymbol{\theta}^k - \alpha^k \nabla_{\boldsymbol{\theta}} J(\boldsymbol{\theta}^k), \quad k = 0, 1, \dots \ . \tag{8.12}$$

Here, the quantity $\alpha^k > 0$ is the step size in the *k*-th iteration, often referred to as the learning rate. The gradient vector of the cost function at step *k* is given by

$$\nabla_{\boldsymbol{\theta}} J(\boldsymbol{\theta}^k) = \begin{bmatrix} \frac{\partial}{\partial \theta_0} & \frac{\partial}{\partial \theta_1} & \dots & \frac{\partial}{\partial \theta_n} \end{bmatrix}^\top J(\boldsymbol{\theta}^k) \ . \tag{8.13}$$

This gradient determines the direction in the parameter space along which the cost function $J(\boldsymbol{\theta})$ increases most rapidly. Moving in the opposite direction, the algorithm descends toward a minimum of the function. For the linear regression problem considered here, the cost function is the mean squared error, given by

$$J(\boldsymbol{\theta}) = \text{MSE}\ (\boldsymbol{\theta}) = \tfrac{1}{m} |\mathbf{X}\boldsymbol{\theta} - \mathbf{y}|^2 \ . \tag{8.14}$$

The gradient of this cost function with respect to $\boldsymbol{\theta}$ can be derived analytically as the expression

$$\nabla_{\boldsymbol{\theta}} J(\boldsymbol{\theta}) = \tfrac{2}{m} \mathbf{X}^\top (\mathbf{X}\boldsymbol{\theta} - \mathbf{y}) \ . \tag{8.15}$$

This analytical gradient can now be substituted into the iteration rule to perform each update step. Gradient descent will generally converge to a local minimum, and the result depends on the initial parameter vector $\boldsymbol{\theta}^0$. However, as mentioned above for the linear regression with a convex cost function, there exists only one global minimum. In that case, gradient descent is guaranteed to converge to the correct minimum, provided that the learning rate α is chosen appropriately.

Since gradient descent relies on the gradient direction to navigate the parameter space, it is sensitive to the relative scaling of the input features. Consider a case with two input features representing pressures, and one is measured in Pa and the other in bar. The resulting scale difference of about $\mathcal{O}(10^5)$ causes the optimization surface to be strongly elongated. As a result, convergence becomes slow at best and perhaps oscillatory. A practical remedy is to normalize the input features so that they are of comparable magnitude. Doing so significantly improves the convergence rate of the algorithm.

The learning rate α plays a central role in determining the efficiency and reliability of convergence. If α is chosen too small, the algorithm will converge very slowly. If it is too large, the update steps may overshoot the minimum, causing the method to diverge. As illustrated in Fig. 8.4, a suitable learning rate lies between these extremes, enabling stable and efficient convergence.

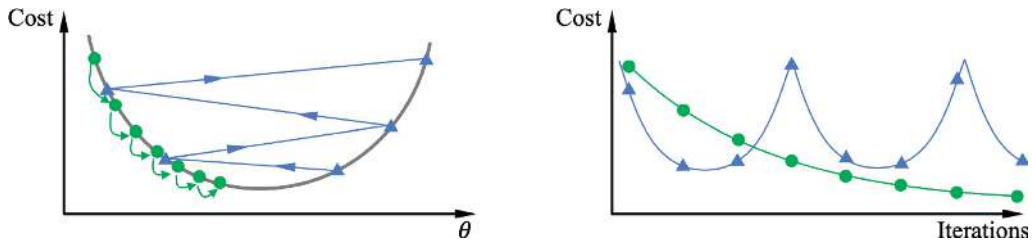


Fig. 8.4 Convergence behavior of gradient descent for different learning rates α showing stable progress with moderate α and divergence with excessive α (Géron 2019)

Gradient descent follows a common structure shared by many numerical solvers. To determine when to stop the iteration, a convergence criterion is applied. A typical condition is that the change in the cost function or parameter vector, that is, the relative residual, falls below a threshold, often chosen around $\mathcal{O}(10^{-4})$. The computational complexity of each gradient descent step is approximately $\mathcal{O}(n^2)$, which is significantly lower than the complexity of computing a matrix inverse as required by the normal equation. This makes gradient descent well suited for problems with a large number of features, typically in the range of $n > 10^4$.

While gradient descent is illustrated as a prototypical iterative method, in practice, it is recommended to use optimization algorithms that are available in scientific computing libraries. These implementations are more advanced, thoroughly tested, and optimized for performance and stability. Typically, such solvers require as input the cost function, an initial guess for $\boldsymbol{\theta}$, and parameters that control convergence. Some algorithms also allow the user to supply a closed-form expression for the cost gradient. This avoids the need to numerically approximate the gradient through repeated cost function evaluations, which reduces computational effort.

8.1.3 Nonlinear Hypothesis

Despite its name, linear regression does not require the hypothesis function to be linear in the input variables. The term 'linear' refers instead to linearity in the model parameters $\boldsymbol{\theta}$, not necessarily in the inputs $\mathbf{x}$. As long as the parameters enter the hypothesis in a linear form, the model is classified as a linear regression, even if the inputs appear in nonlinear terms.

This flexibility allows for a broad class of hypothesis functions that are nonlinear in the inputs but still linear in the parameters. A general form of such a hypothesis reads

$$h_{\boldsymbol{\theta}}(\mathbf{x}) = \boldsymbol{\theta}^{\top}\mathbf{f}(\mathbf{x}) = \theta_0 + \sum_{k=1}^{p} \theta_k f_k(x_1, \ldots, x_n) \ , \tag{8.16}$$

where each function $f_k : \mathbb{R}^n \to \mathbb{R}$ represents a nonlinear transformation of the input variables $x_1, \ldots, x_n$. The resulting transformed inputs form an extended feature vector $\mathbf{f}(\mathbf{x})$, which enters the hypothesis function linearly through its inner product with the parameter vector $\boldsymbol{\theta}$. The number of such features *p* may differ from the original number of input variables *n*. Through this transformation, a rich variety of nonlinear patterns can be captured using the linear regression framework.

This construction makes linear regression a very flexible modeling tool. A few illustrative examples help to clarify. One common extension is to use **polynomials** of the input variables. In this case, the model is often referred to as polynomial regression. For a single input variable x_1, a polynomial hypothesis of degree *p* reads

$$h_{\boldsymbol{\theta}}(x_1) = \sum_{k=0}^{p} \theta_k x_1^k = \theta_0 + \theta_1 x_1 + \theta_2 x_1^2 + \ldots + \theta_p x_1^p \ . \tag{8.17}$$

This formulation remains a linear model with respect to the parameters θ_k, although the input appears with nonlinear powers. The idea can also be extended to multiple input variables. For example, a second-order polynomial in two variables leads to the following hypothesis

$$h_{\boldsymbol{\theta}}(x_1, x_2) = \theta_0 + \theta_1 x_1 + \theta_2 x_2 + \theta_3 x_1 x_2 + \theta_4 x_1^2 + \theta_5 x_2^2 \ . \tag{8.18}$$

This defines a general quadratic surface, or a two-dimensional quadric. The concept generalizes naturally to higher-order polynomials and to more input variables. For instance, a second-order polynomial in *n* variables includes all products $x_i x_j$ for $i, j = 1, \ldots, n$, as well as all linear terms and a constant offset. Such a function can be written compactly as

$$h_{\boldsymbol{\theta}}(\mathbf{x}) = \textstyle\sum_{i=0}^{n} \sum_{j=0}^{n} \theta_{k(i,j)} x_i x_j \ , \tag{8.19}$$

where index zero incorporates the intercept term, that is for $x_0 = 1$. With this convention, the linear terms arise from the mixed products $x_0 x_j$ and $x_j x_0$ for $j = 1, \ldots, n$, and the constant term corresponds to $x_0 x_0 = 1$. The parameter indices θ_k are assigned according to the order in which the corresponding features $x_i x_j$ are added[1].

More elaborate features may also be constructed by combining inputs through mathematical operations such as addition, multiplication, or nonlinear functions. For instance

$$h_{\boldsymbol{\theta}}(x_1, x_2) = \theta_0 + \theta_1 (x_1 + x_2) + \theta_2 (x_1 x_2)^{3/2} \ ,$$

$$h_{\boldsymbol{\theta}}(x_1) = \theta_0 + \theta_1 x_1 + \theta_2 e^{-x_1} \cos\left(x_1\right) + \theta_3 \ln\left(x_1\right) \ .$$

In each of these examples, the hypothesis remains a linear combination of features, and therefore fits within the framework of linear regression.

It is important to recognize which models fall outside this class. The key requirement is that the parameters must appear linearly in the hypothesis. The following are illustrative examples of models that are **not linear** in parameters

$$h_{\boldsymbol{\theta}}(x_1) = \theta_0 + \theta_1 e^{\theta_2 x_1} \ , \quad h_{\boldsymbol{\theta}}(x_1) = \exp\left(\theta_0 + \theta_1 x_1\right) \ .$$

The second example, however, can be transformed into a linear form by taking the logarithm of both sides, which is a common trick in modeling. The ability to construct custom features is particularly valuable when prior knowledge about the system is available, as discussed in the examples in Chapters 9 and 10. For example, if the underlying functional form is known from physical modeling or dimensional analysis, it can be encoded directly into the regression. In such cases, the regression is used to calibrate parameters of a known model structure. When creating new features, feature scaling becomes especially important. As discussed earlier, differences in the magnitude of inputs can lead to slow convergence. Normalization ensures that all features contribute comparably during model training, which is even more critical when higher-order or nonlinear terms are involved.

8.1.4 Overfitting and Regularization

With the previously introduced hypothesis functions, we now have the ability to construct highly flexible models. By expanding the feature space, we can fit increasingly complex functions to the training data. However, this flexibility introduces the risk of overfitting. **Overfitting** occurs when a model is too closely adapted to the training data. It results in excellent prediction performance on the training set but poor generalization to new, unseen data. The opposite case is referred to as **underfitting**, which arises when the model is too simple to capture the underlying data structure. Both concepts apply not only to linear regression but also to classification problems, as discussed later in Sect. 8.2.

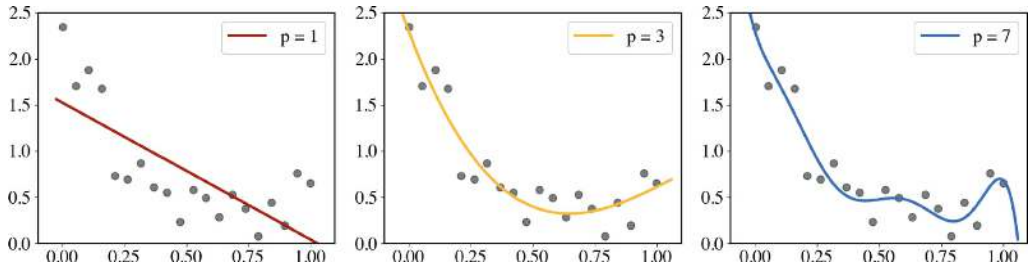


Fig. 8.5 Polynomial fit for polynomial orders $p = 1$, $p = 3$ and $p = 7$

To illustrate the problem, Fig. 8.5 shows polynomial fits of increasing order for a data set with nonlinear structure. The leftmost plot shows a linear model $y = \theta_0 + \theta_1 x$ fitted to the training data. The trend of the data is not captured well, and the model underfits. In the center plot, the polynomial order is increased to $p = 3$, and the fit begins to represent the structure of the data more accurately. In the plot on the right, a 7th order polynomial is used. Although the model passes through every training point, it produces unnatural oscillations that are unlikely to reflect the true data structure. This model is overfitting and is too closely tuned to the peculiarities of the training set, failing to generalize beyond it.

A characteristic symptom of overfitting in high-order polynomial models is the emergence of model coefficients θ_i that grow rapidly in magnitude and alternate in sign. This behavior can be understood by analyzing the structure of the polynomial itself. As the model attempts to pass through all training points, especially when they do not follow a smooth underlying pattern, each new polynomial term is tasked with correcting slight deviations introduced by previous terms. This results in a cascade where one term overcompensates, and the next term must then reverse or bend the function back, leading to alternating signs and increasing amplitudes in θ_i. The effect is most pronounced when fitting unconstrained polynomials of high degree to data with limited or uneven structure. These large and oscillating parameter values stem directly from the algebraic form of the hypothesis. This is a strong indication of overfitting and lack of generalization.

One possible approach to avoid overfitting is to reduce the number of features, either manually or using automatic feature selection techniques, as will be discussed in Sect. 8.4. An alternative and perhaps more elegant method is to use regularization.

Regularization Regularization is a widely used technique to improve the generalizability of a model. It works by adding a penalty term to the cost function, which discourages large parameter values. This results in simpler hypothesis functions that are less likely to overfit.

To illustrate, consider the 7th order polynomial model in Fig. 8.5, given by

$$y = \theta_0 + \theta_1 x + \theta_2 x^2 + \ldots + \theta_7 x^7 \ .$$

If the higher-order terms θ_4 to θ_7 lead to unwanted oscillations, we can reduce their influence by artificially increasing their cost. For example, by modifying the cost function to include a large penalty on these parameters

$$J(\boldsymbol{\theta}) = \frac{1}{2}\sum_{i=1}^{m}\left(h_\theta(x^{(i)}) - y^{(i)}\right)^2 + 1000\ \left(\theta_4^2 + \ldots + \theta_7^2\right)\ .$$

Minimizing this new cost function leads to small values for θ_4 through θ_7, making the associated polynomial terms negligible.

A general and systematic way to regularize models is to penalize the parameter vector using a norm. The most common approach is known as Tikhonov regularization or **ridge regression**, which adds an L_2 penalty term to the cost function

$$J(\boldsymbol{\theta}) = \text{MSE}\ (\boldsymbol{\theta}) + \frac{\lambda}{2}\sum_{k=1}^{n}\theta_k^2\ . \tag{8.20}$$

Here, $\lambda \geq 0$ is the regularization parameter that controls the strength of the penalty. For $\lambda = 0$, we recover the original unregularized MSE cost function from Eq. (8.5). As λ increases, the penalty discourages large parameter values, thereby reducing model complexity. However, if λ becomes too large, meaningful features may be suppressed, leading to underfitting.

Figure 8.6 illustrates how regularization affects model behavior. The plots on the left display both the cost function and the magnitude of the parameter vector as functions of λ. When λ is small, the model tends to overfit. It closely follows the training data, resulting in minimal cost, but the parameter values become large and oscillatory. As λ increases, the penalty term starts to influence the optimization. The parameter magnitudes begin to shrink and eventually settle on a stable plateau, often near $\mathcal{O}(1)$ when the data set is normalized. At the same time, the cost increases, reflecting a looser fit to the training points. The plot on the right in Fig. 8.6 shows the corresponding regression results. For moderate values of λ, such as those between 1×10^{-4} and 1×10^{-2}, the model still captures the main trend in the data while avoiding overfitting. For larger values of λ, the regularization becomes dominant and the fit degrades. The parameter vector becomes very small, and the model begins to flatten. In the extreme case where $\lambda = 1 \times 10^{2}$, the result is nearly a constant bias term that no longer reflects the shape of the data. To choose a meaningful value for λ, one typically considers both model complexity and fit quality. A good choice corresponds to a region where the cost remains acceptably low while the parameter magnitudes have stabilized at a reasonable level.

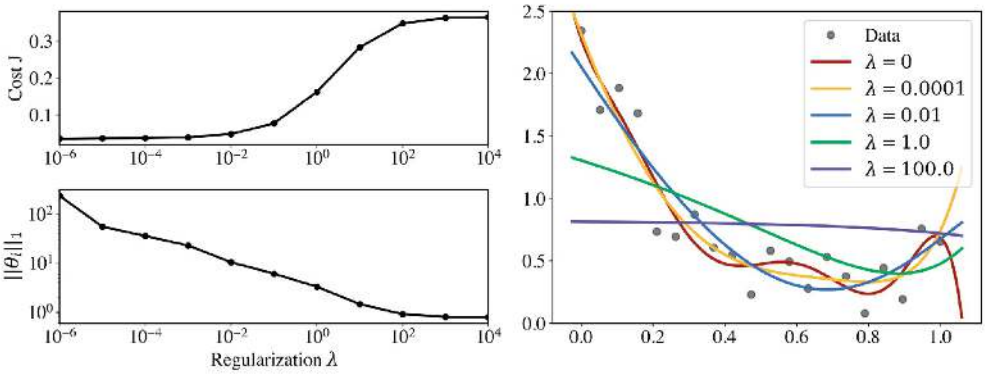


Fig. 8.6 Effect of regularization shown by cost and parameter magnitudes versus λ (left) and regression fits (right)

To compute the regularized parameters $\hat{\boldsymbol{\theta}}$, we can continue to use iterative solvers such as gradient descent, simply by applying them to the modified cost function. In the specific case of ridge regression, a closed-form solution also exists. It is obtained by adapting the normal equation, discussed in Sect. 8.1.2, and takes the form

$$\hat{\boldsymbol{\theta}} = \left(\mathbf{X}^\top \mathbf{X} + \lambda \mathbf{A}\right)^{-1} \mathbf{X}^\top \mathbf{y}. \tag{8.21}$$

In this expression, the matrix $\mathbf{A} \in \mathbb{R}^{(n+1)\times(n+1)}$ is the identity matrix with its first entry set to zero. This ensures that the bias term θ_0 is not penalized by the regularization.

8.2 Classification

In many engineering problems, the goal is not to predict a continuous value but to assign an input to a specific category, a task known as classification. Examples include identifying whether pipe flow is laminar or turbulent, predicting whether a droplet impact will deposit or splash, detecting faults in machinery, determining equipment operating modes, or identifying anomalies in measured signals. Unlike regression, which outputs continuous values, classification assigns inputs to discrete labels such as normal or faulty, stable or unstable, or one of several operating states. As in regression, models are trained on labeled examples, but here the aim is to correctly classify new inputs and generalize to unseen cases. We begin with binary classification, involving only two possible outcomes, before extending to multiclass problems.

8.2.1 Logistic Regression

The classification problem is conceptually similar to regression, with the shared objective of learning from labeled examples to train a model that maps an input *x* to an output *y*. However, in classification, the output variable *y* takes on a finite number of discrete values rather than being continuous. We begin by addressing **binary classification**, where the output can only assume two possible values, $y \in \{0, 1\}$, and generalize to multiclass problems later. As in linear regression, we organize the input data into a feature matrix $\mathbf{X} \in \mathbb{R}^{m\times(n+1)}$, where each row corresponds to one input instance and each column to one feature, including a bias, following the structure introduced in Sect. 8.1.

Hypothesis Representation Since the output variable is binary, we modify the hypothesis function $h_\theta(x)$ such that its range is constrained to $0 \leq h_\theta(x) \leq 1$. The function remains continuous and is interpreted probabilistically. For example, a value $h_\theta(x) = 0.9$ indicates a 90% predicted probability that $y = 1$ and a 10% probability that $y = 0$. More generally, we express this as

$$h_\theta(x) = P(y = 1 \mid x) = 1 - P(y = 0 \mid x) \quad \text{with} \quad P(y = 0) + P(y = 1) = 1 \ . \tag{8.22}$$

To assign the final class label, we apply a simple threshold at 0.5, rounding the probability to the nearest class, that is

$$\begin{aligned} h_\theta(x) \geq 0.5 \quad &\Rightarrow \quad y = 1 \ , \\ h_\theta(x) < \quad 0.5 \quad &\Rightarrow \quad y = 0 \ . \end{aligned} \tag{8.23}$$

To define such a function, we apply the **sigmoid function**, also known as the logistic or activator function. The sigmoid maps any real-valued input to the interval [0, 1] and is defined by

$$\text{sigmoid}\,(x) = \tfrac{1}{1+e^{-x}}\ . \tag{8.24}$$

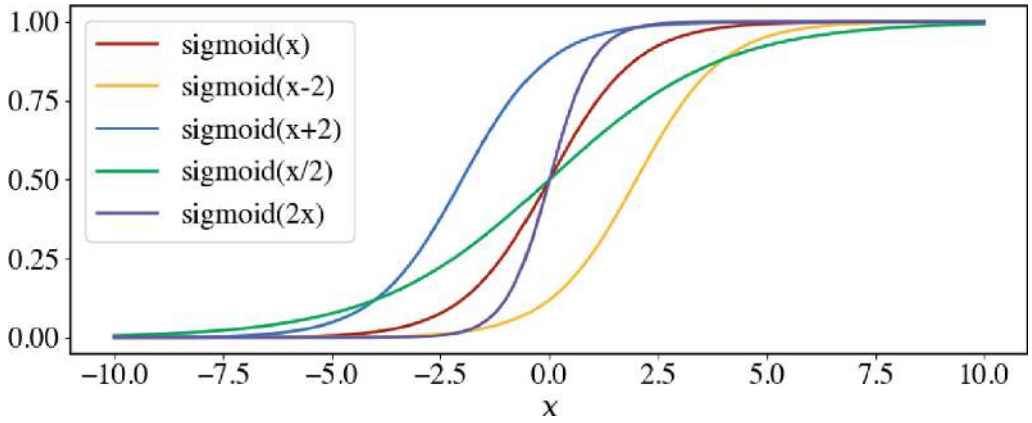


Fig. 8.7 Variations of the sigmoid function under shifts and scaling, showing how translation and slope changes affect the transition region

As shown in Fig. 8.7, the sigmoid function smoothly transitions between the two classes. Its asymptotic behavior is characterized by

$$\begin{aligned} x \to -\infty: &\quad \text{sigmoid}\,(x) \to 0 \\ x = 0: &\quad \text{sigmoid}\,(x) = 0.5 \\ x \to \infty: &\quad \text{sigmoid}\,(x) \to 1 \end{aligned} \tag{8.25}$$

This makes the sigmoid function particularly suitable for binary classification, as it naturally interpolates between class 0 and class 1. In its basic form, however, the sigmoid transitions at $x = 0$, which means the decision boundary is fixed. To make the boundary adaptable to the input data, we use a linear model as the input to the sigmoid. This follows the same structure introduced earlier in the context of linear regression in Sect. 8.1. Specifically, we use the inner product $\boldsymbol{\theta}^\top \mathbf{x}$ as the argument of the sigmoid function, leading to the hypothesis function

$$h_{\boldsymbol{\theta}}(\mathbf{x}) = \text{sigmoid}\,(\boldsymbol{\theta}^\top \mathbf{x}) = \tfrac{1}{1+e^{-\boldsymbol{\theta}^\top \mathbf{x}}}\ . \tag{8.26}$$

This composition enables us to learn a flexible boundary between the classes. The decision rule is determined by the threshold value of 0.5, which corresponds to $\boldsymbol{\theta}^\top \mathbf{x} = 0$. That is, the boundary between class 0 and class 1 is defined by

$$h_{\boldsymbol{\theta}}(\mathbf{x}) \geq 0.5 \quad \Rightarrow \quad \boldsymbol{\theta}^\top \mathbf{x} \geq 0\ . \tag{8.27}$$

This yields the classification rule

$$\begin{aligned} y = 0, &\quad \text{if } \boldsymbol{\theta}^\top \mathbf{x} < 0 \\ y = 1, &\quad \text{if } \boldsymbol{\theta}^\top \mathbf{x} \geq 0 \end{aligned} \tag{8.28}$$

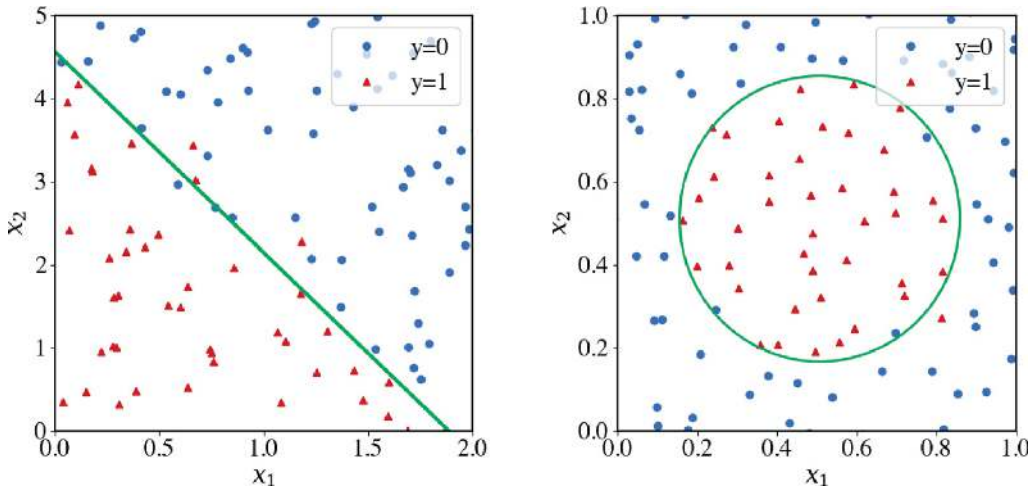


Fig. 8.8 Illustrative examples for binary classification problems modeled by a linear hypothesis (left) and a second-order polynomial hypothesis (right)

As discussed in Sect. 8.1.3, the expression $\boldsymbol{\theta}^\top \mathbf{x}$ does not have to be purely linear in the input variables. By extending the feature vector $\mathbf{x}$ to include nonlinear terms such as x_1^2 or $x_1 x_2$, we can model more complex decision boundaries. For example, the right-hand side of Fig. 8.8 shows a circular boundary that emerges from a quadratic hypothesis of the form $z = \theta_0 + \theta_1 x_1^2 + \theta_2 x_2^2$. This flexibility allows logistic regression to represent a wide variety of decision boundaries, including highly nonlinear shapes, as long as the hypothesis remains linear in the model parameters.

Cost Function To train the logistic regression model, we require a cost function that appropriately penalizes incorrect predictions. Since the output y is binary, the cost is defined conditionally based on the actual class label

$$\text{cost}(h_{\boldsymbol{\theta}}(\mathbf{x}), y) = \begin{cases} -\log\left(1 - h_{\boldsymbol{\theta}}(\mathbf{x})\right) & \text{if } y = 0 \\ -\log\left(h_{\boldsymbol{\theta}}(\mathbf{x})\right) & \text{if } y = 1 \end{cases} \tag{8.29}$$

This formulation is constructed to reward correct predictions and severely penalize wrong ones. For example, if the true label is $y = 1$, the cost is $-\log\left(h_{\boldsymbol{\theta}}(\mathbf{x})\right)$. When the model predicts class 1, meaning $h_{\boldsymbol{\theta}}(\mathbf{x}) \to 1$, the logarithm approaches zero and so does the cost, since $\log(1) = 0$. On the other hand, if the model wrongly predicts a value close to zero, then $h_{\boldsymbol{\theta}}(\mathbf{x}) \to 0$, and $-\log\left(h_{\boldsymbol{\theta}}(\mathbf{x})\right) \to \infty$, making the cost very large. This imposes a strong penalty on incorrect predictions that are made with high confidence. The behavior is symmetric for $y = 0$, where the cost becomes $-\log\left(1 - h_{\boldsymbol{\theta}}(\mathbf{x})\right)$. Again, the cost approaches zero when $h_{\boldsymbol{\theta}}(\mathbf{x}) \to 0$, which is a correct and confident prediction, and it diverges when $h_{\boldsymbol{\theta}}(\mathbf{x}) \to 1$, meaning the model wrongly predicts class 1 with high certainty. In both cases, the logarithmic form ensures that uncertain predictions, that is, values close to 0.5, incur moderate cost, while confident but wrong predictions are heavily penalized. This encourages the model to not only be correct, but to be correct with higher certainty. Figure 8.9 illustrates how the cost behaves for both classes as a function of the predicted value.

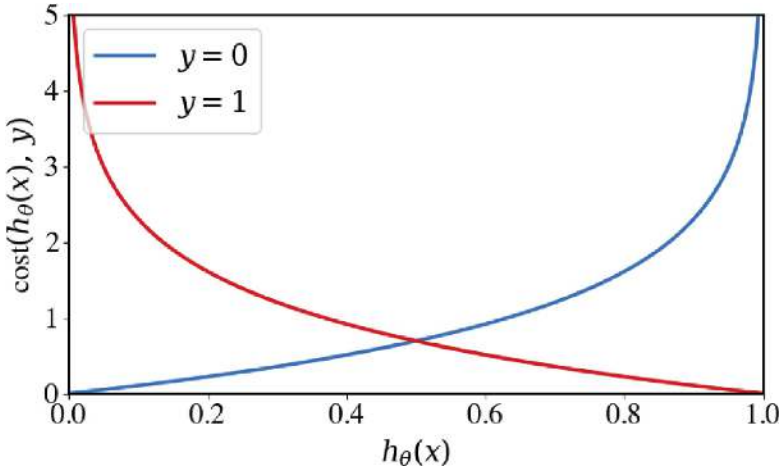


Fig. 8.9 The cost as a function of the hypothesis value $h_{\boldsymbol{\theta}}(\mathbf{x})$ for $y = 0$ and $y = 1$

This piecewise definition can be written in a more compact and unified form with

$$\text{cost}(h_{\boldsymbol{\theta}}(\mathbf{x}), y) = -y \log\left(h_{\boldsymbol{\theta}}(\mathbf{x})\right) - (1 - y) \log\left(1 - h_{\boldsymbol{\theta}}(\mathbf{x})\right) \ . \tag{8.30}$$

This expression combines both cases $y = 0$ and $y = 1$ into a single equation, and works because only one of the two terms is active depending on the discrete value of y. If $y = 1$, then the first term becomes $-\log\left(h_{\boldsymbol{\theta}}(\mathbf{x})\right)$ and the second term vanishes, since $1 - y = 0$, and thus returns the cost for predicting class 1. If $y = 0$, then the second term becomes $-\log\left(1 - h_{\boldsymbol{\theta}}(\mathbf{x})\right)$ and the first term disappears, since $y = 0$, returning the cost for predicting class 0. This compact formulation is particularly useful for implementation and for deriving gradients and is referred to as the binary cross-entropy or log loss. To compute the total cost over the training set, we take the average over all m training examples

$$\begin{aligned} J(\boldsymbol{\theta}) = & \ \frac{1}{m} \sum_{i=1}^{m} \text{cost}(h_{\boldsymbol{\theta}}(\mathbf{x}^{(i)}), y^{(i)}) \\ = & \ -\frac{1}{m} \sum_{i=1}^{m} \left[y^{(i)} \log\left(h_{\boldsymbol{\theta}}(\mathbf{x}^{(i)})\right) + (1 - y^{(i)}) \log\left(1 - h_{\boldsymbol{\theta}}(\mathbf{x}^{(i)})\right) \right] \ . \end{aligned} \tag{8.31}$$

Minimizing this cost function allows us to learn the parameter vector $\boldsymbol{\theta}$ that best classifies the training data. Unlike in linear regression, there is no closed-form solution such as the normal equation. However, the cost function is convex, which ensures that optimization algorithms such as gradient descent can reliably converge to the global minimum, provided the algorithm is properly configured. The gradient of the cost function with respect to $\boldsymbol{\theta}$ can again be derived in closed form, and is given by

$$\nabla_{\boldsymbol{\theta}} J(\boldsymbol{\theta}) = \frac{1}{m} \sum_{i=1}^{m} (h_{\boldsymbol{\theta}}(\mathbf{x}^{(i)}) - y^{(i)}) \mathbf{x}^{(i)} \ . \tag{8.32}$$

This gradient has the same structural form as in linear regression, enabling us to apply the same iterative solvers.

Overfitting and Regularization Logistic regression models, just like those in linear regression discussed in Sect. 8.1, are prone to overfitting. This is especially the case when the

hypothesis includes high-order polynomial terms. Regularization helps address this issue by controlling model complexity and improving generalization. Since the underlying principles are very similar to those in linear regression, here we summarize only the key ideas.

The effect of underfitting and overfitting in logistic regression is shown in Fig. 8.10. The patterns closely resemble those observed in regression. Simple models fail to capture important trends in the data. In contrast, models that are too complex tend to follow the noise in the training data too closely, which harms their ability to generalize. To mitigate overfitting, we can modify the cost function by adding a regularization term that again penalizes large parameter values, and discourages excessively flexible hypothesis functions and encourages simpler models. Using the Tikhonov regularization, the cost function becomes

$$J(\boldsymbol{\theta}) = -\frac{1}{m}\sum_{i=1}^{m}\left[y^{(i)}\,\log\left(h_\theta(x^{(i)})\right) + (1-y^{(i)})\,\log\left(1-h_\theta(x^{(i)})\right)\right] + \frac{\lambda}{2m}\sum_{j=1}^{n}\theta_j^2 \ . \quad (8.33)$$

The regularization parameter λ controls the strength of the penalty. A small value of λ results in behavior similar to unregularized logistic regression, while larger values increasingly constrain the model complexity. It is important to note that the regularization sum excludes the bias term θ_0, allowing the model to shift the decision boundary freely without penalty.

Regularization is particularly valuable when working with expanded feature sets, such as polynomial features or high-dimensional data. It stabilizes the training process, improves numerical conditioning, and enhances the model's ability to generalize to unseen data.

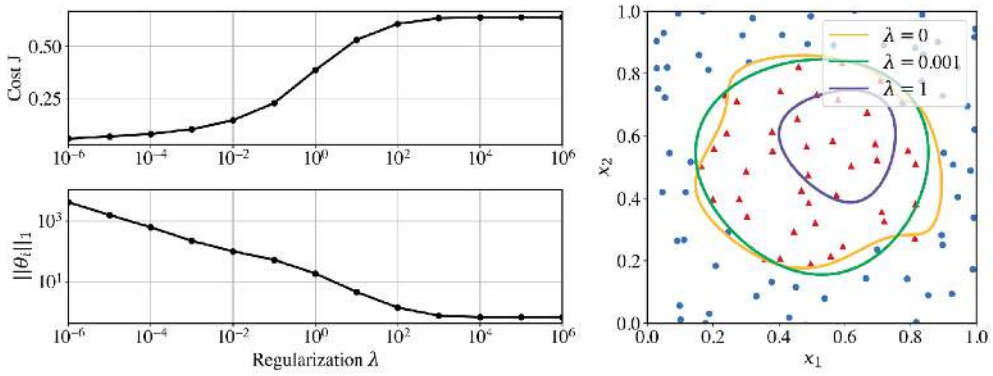


Fig. 8.10 Regularized logistic regression, showing the effect of varying λ on the cost, parameter norm, and resulting decision boundary

8.2.2 Performance Measures

To evaluate the quality of a classifier, one might be tempted to simply report the **accuracy**, which is the proportion of correctly predicted labels. While this measure may seem intuitive, it can be misleading for imbalanced data sets. For example, in a scenario where 95% of data points belong to one class, a naive classifier that always predicts this majority class would achieve 95% accuracy, despite being practically useless.

To address such shortcomings, more informative performance metrics have been developed. In the following, we will examine two key tools for classifier evaluation, that is, the **confusion matrix** and the **ROC curve**. These allow us to quantify the predictive quality of a classifier in a more nuanced and robust manner. Note that, as with regression models, cross-validation

techniques apply to classification tasks as well and should always be employed to obtain reliable performance estimates.

Confusion Matrix The confusion matrix is a tabular summary that compares predicted class labels with the true labels on a validation data set. It provides a detailed view of the model's performance by showing how often predictions match the actual outcomes. This is especially useful when dealing with imbalanced data, where accuracy alone can be misleading. The concept is similar to the types of statistical error discussed in Sect. 7.4, and we briefly revisit it here to introduce the key performance metrics of **precision**, **recall**, and the combined F_1**-score**.

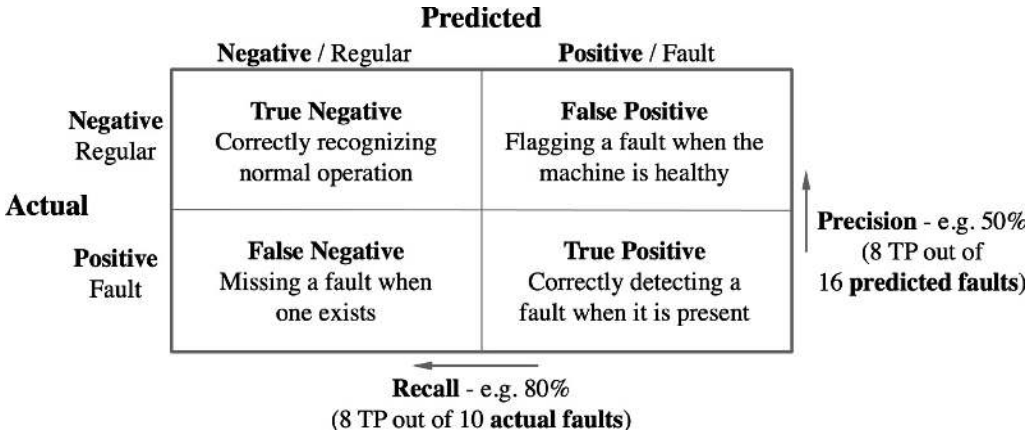


Fig. 8.11 Confusion matrix for machinery fault detection, showing correct classifications (TP, TN), misclassifications (FP, FN), and examples for recall and precision

In the confusion matrix each row corresponds to the predicted class and each column to the actual class, or vice versa. For binary classification problems, as illustrated in Fig. 8.11, we count the number of correctly and incorrectly classified instances, namely the number of True Positives (TP), False Positives (FP), True Negatives (TN), False Negatives (FN). These values are then arranged in table form. An ideal classifier would yield a confusion matrix with nonzero entries only along the diagonal, indicating no misclassifications. Based on the entries in the confusion matrix, targeted performance metrics can be derived.

Precision is the ratio of true positive predictions to all positive predictions made by the model. It reflects how many of the predicted positives were actually correct

$$\mathrm{P} = \frac{\mathrm{TP}}{\mathrm{TP}+\mathrm{FP}} \ . \tag{8.34}$$

Recall is the ratio of true positives to all actual positive instances. It quantifies how many of the actual positives the model correctly identified

$$\mathrm{R} = \frac{\mathrm{TP}}{\mathrm{TP}+\mathrm{FN}} \ . \tag{8.35}$$

Recall is sometimes referred to as sensitivity or true positive rate. A perfect classifier would achieve both $\mathrm{P} = 1$ and $\mathrm{R} = 1$. To combine these two measures into a single score, the F_1**-score** is introduced as the harmonic mean of precision and recall as

$$\mathrm{F}_1 = \frac{2}{\frac{1}{\mathrm{P}}+\frac{1}{\mathrm{R}}} = 2\frac{\mathrm{P}}{\mathrm{P}+\mathrm{R}} \ . \tag{8.36}$$

This score balances the trade-off between precision and recall. A high F_1 score is only achieved when both precision and recall are simultaneously high. If either $\mathrm{P} = 0$ or $\mathrm{R} = 0$, the F_1 score vanishes. Only if both precision and recall are perfect, $\mathrm{F}_1 = 1$ is reached.

The F_1 score is especially useful when precision and recall are equally important. However, this balance does not always reflect the priorities of a given application. Consider a health monitoring system that raises an alarm if an uncritical component is predicted to be at risk of failure ($y = 1$). In this case, we may only want to trigger an alert when we are highly confident, to avoid unnecessary maintenance actions or planned downtime. This means we prioritize high precision, even if it results in a lower recall and some potential faults being missed. In contrast, consider a failure detection system for a safety-critical application, such as an aircraft engine. Missing an actual failure (FN) could have catastrophic consequences. In this case, we aim to detect as many true positives as possible, even at the cost of some false alarms, thus prioritizing a high recall.

Unfortunately, both precision and recall cannot usually be increased simultaneously. Enhancing one often leads to a reduction in the other. In the following, we explore this trade-off in more detail through the use of the ROC curve.

Precision Recall Trade-Off To understand the trade-off between precision and recall, let us revisit the modeling approach in logistic regression. The hypothesis $0 \leq h_\theta(x) \leq 1$ represents a prediction probability that the output y belongs to class 1. To convert this continuous prediction into a binary class label, we apply a **decision threshold**, assigning the predicted class according to

$$y = \begin{cases} 1 & \text{if } h_\theta(x) \geq \text{threshold} \\ 0 & \text{if } h_\theta(x) < \text{threshold} \end{cases} \tag{8.37}$$

Up to this point we have used a decision threshold of 0.5, without further justification. However, the choice of threshold has a direct influence on the classifier's behavior. By increasing the threshold, we require the model to be more confident before predicting a positive class. This leads to fewer predicted positives and more negatives. As a consequence, precision increases while recall decreases. Conversely, lowering the threshold leads to more predicted positives and fewer negatives, which increases recall but reduces precision. This inverse relationship is illustrated on the left side of Fig. 8.12. The right-hand plot in Fig. 8.12 shows the **precision-recall** (PR) curve, which plots precision as a function of recall over a range of decision thresholds. This representation is particularly useful for comparing different classifiers. The closer the curve is to the upper right corner of the plot, the better the classifier performs. The PR curve is especially effective when dealing with imbalanced data sets, where the positive class is underrepresented.

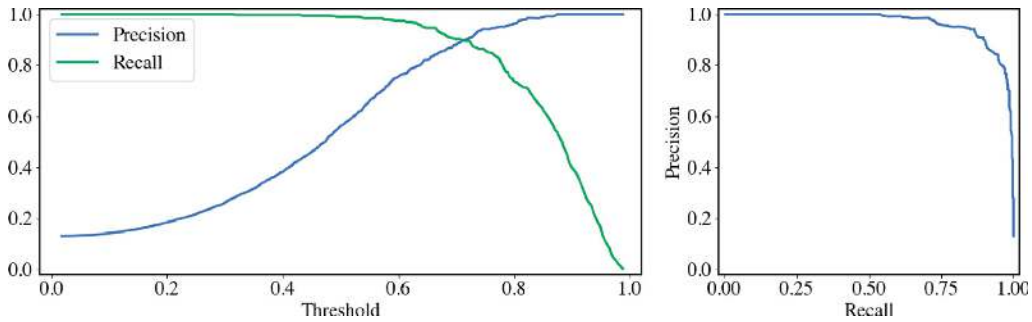


Fig. 8.12 Relationship between precision, recall, and the decision threshold (left) with the corresponding precision–recall trade-off curve (right)

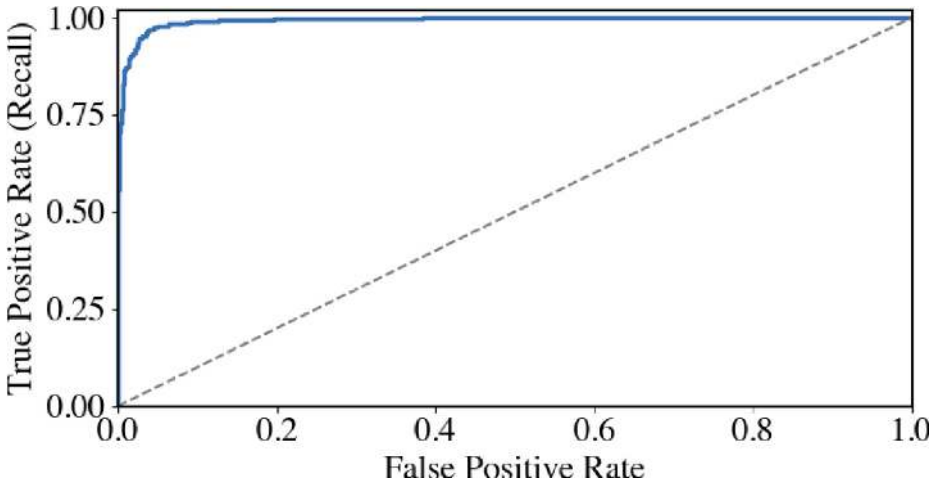


Fig. 8.13 The ROC curve plots the false positive rate against the true positive rate for different thresholds

The choice of decision threshold needs to be tailored to the specific modeling objective. In some applications, high precision is desired to avoid false positives, while in others, high recall is critical to minimize false negatives. The balance depends on the consequences of prediction errors and must be determined case by case.

ROC Curve Another common tool to assess classifier performance is the **Receiver Operating Characteristic** (ROC) curve. Similar to the PR curve, the ROC curve evaluates the model over a range of decision thresholds. However, instead of plotting precision against recall, it plots the true positive rate (TPR) against the false positive rate (FPR), with

$$\mathrm{TPR} = \mathrm{R} = \frac{\mathrm{TP}}{\mathrm{TP+FN}} \ , \quad \mathrm{FPR} = \frac{\mathrm{FP}}{\mathrm{FP+TN}} \ . \tag{8.38}$$

An example is shown in Fig. 8.13. Each point on the ROC curve corresponds to a different decision threshold. The diagonal dashed line represents the performance of a random classifier. The further the curve is from this diagonal, the better the classifier. A ROC curve that closely aligns with the top-left corner indicates strong predictive performance. As a scalar measure, the **area under the ROC curve** (AUC) is often used to summarize performance. An AUC of 1 corresponds to a perfect classifier, while an AUC of 0.5 corresponds to random guessing. The AUC is especially useful when comparing the overall performance of multiple classifiers.

8.2.3 Multiclass Classification

Having established the framework for binary classification with $y \in \{0, 1\}$, we now extend the discussion to multiclass problems, where the target variable y can take on K distinct values. That is, $y \in \{0, 1, \ldots, K-1\}$. In this section we introduce two widely used strategies to handle multiclass classification, that is, the **one-versus-all** approach and **multinomial logistic regression**, also known as softmax regression.

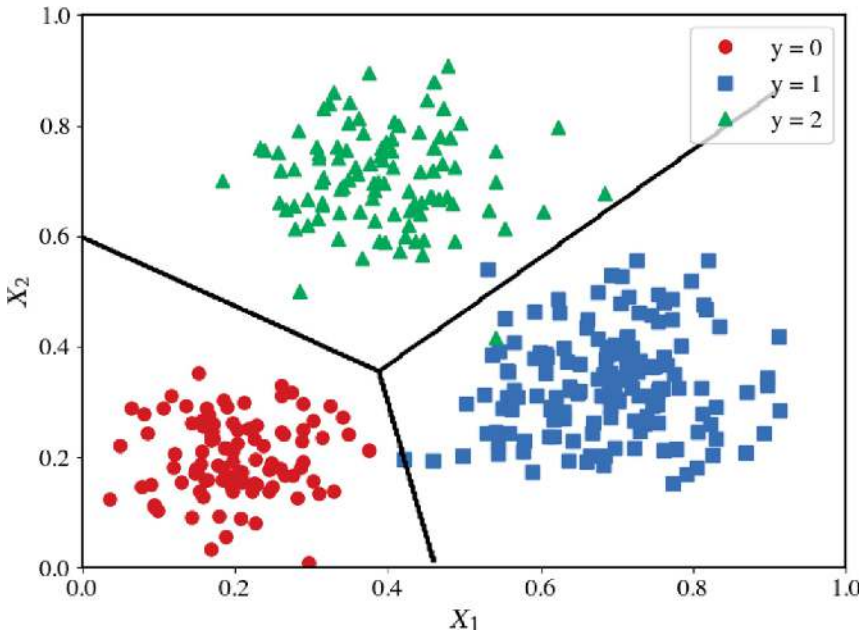


Fig. 8.14 One-versus-all classification setup. Each class is separated from the remaining classes by an individual logistic classifier

One Versus All A natural strategy for handling multiple classes is to decompose the problem into K separate binary classification tasks, where K is the total number of distinct classes. In each task, one class k is treated as the positive class, while all other classes are grouped together as the negative class. A logistic regression model $h_{\boldsymbol{\theta}}^k(\mathbf{x})$ is then trained to distinguish class k from the rest. This setup is illustrated in Fig. 8.14 for a three-class problem.

Just like in binary classification, each classifier $h_{\boldsymbol{\theta}}^k(\mathbf{x})$ yields a prediction between 0 and 1, which we interpret as the estimated probability that the instance $\mathbf{x}$ belongs to class k. Since one classifier is trained per class, we obtain K predicted values. These form a set of binary outputs that must be combined into a single multiclass prediction. To do so, we evaluate all classifiers and choose the class with the highest predicted probability

$$y_{\text{pred}} = \text{argmax}_k \; h_{\boldsymbol{\theta}}^k(\mathbf{x}) \; . \tag{8.39}$$

This approach is simple and widely used in practice. However, a limitation is that each binary classifier is trained independently, so the resulting probability estimates may not be well calibrated with respect to one another.

Multinomial Logistic Regression An alternative to the one-versus-all strategy is to extend logistic regression directly to handle multiple classes in a unified way. This approach is known as multinomial logistic regression or **softmax regression**. Assume we have K distinct classes, and we want to model the probability that a given input $\mathbf{x}$ belongs to class k for each $k = 1, \ldots, K$. The softmax function is used to convert raw prediction scores into class

probabilities that lie between 0 and 1 and sum to one. The probability that the input belongs to class *k* is defined as

$$p(y = k) = \frac{\exp(\boldsymbol{\theta}_k^\top \mathbf{x})}{\sum_{i=1}^{K} \exp(\boldsymbol{\theta}_i^\top \mathbf{x})} \ . \tag{8.40}$$

Each class *k* has its own parameter vector $\boldsymbol{\theta}_k$, and the softmax function normalizes the exponential scores across all classes. The predicted class is then selected as the one with the highest probability. To train the model, we adjust the parameter vectors $\boldsymbol{\theta}_k$ so that the predicted probabilities match the true class labels as closely as possible. A natural extension of the binary logistic loss is the **cross-entropy loss**, which serves as the cost function

$$J(\boldsymbol{\theta}) = -\frac{1}{m} \sum_{i=1}^{m} \sum_{k=1}^{K} y_k^{(i)} \log \left(p_k^{(i)}\right) \ . \tag{8.41}$$

Here, $y_k^{(i)}$ is an indicator variable that equals 1 if instance *i* belongs to class *k*, and 0 otherwise. The quantity $p_k^{(i)}$ is the model's predicted probability that instance *i* belongs to class *k*.

As in binary logistic regression, we use gradient-based optimization to minimize the cost function. The gradient with respect to the parameter vector $\boldsymbol{\theta}_k$ for class *k* is given by

$$\nabla_{\boldsymbol{\theta}_k} J(\boldsymbol{\theta}) = \frac{1}{m} \sum_{i=1}^{m} (p_k^{(i)} - y_k^{(i)}) \mathbf{x}^{(i)} \ , \tag{8.42}$$

and reflects the average difference between the predicted and actual class assignments, weighted by the input features. Its structure mirrors that of the binary case, which allows for efficient optimization using familiar algorithms.

8.3 Clustering

Clustering falls under the category of unsupervised learning. The objective is to organize unlabeled data instances into discrete groups or **clusters**, such that instances within the same cluster are by some measure more similar to each other than to instances in different clusters. This allows us to uncover hidden structure or groupings in the data set, when no prior labels are provided.

Similar to the classification problems discussed in Sect. 8.2, we begin with a set of input features represented by the data matrix $\mathbf{X}$. The matrix $\mathbf{X} \in \mathbb{R}^{m \times n}$ contains *m* observations, each described by *n* input features. Each row $x^{(i)}$ corresponds to one observation, so that $x^{(i)} \in \mathbb{R}^n$ for $i = 1, \ldots, m$. However, unlike in supervised learning, no output labels $\mathbf{y}$ are available. The task is to infer a meaningful grouping of the *m* unlabeled data points based on their location in the *n*-dimensional feature space.

A wide range of clustering techniques exist, which are generally categorized into three families, that is hierarchical, partitional, and probabilistic clustering algorithms. **Hierarchical clustering** builds a multilevel structure of nested clusters. These methods can proceed in a top-down fashion, where the entire data set is recursively split into smaller clusters, or in a bottom-up fashion, where each point starts as its own cluster, and clusters are successively merged based on similarity. The process continues until all data points belong to a single cluster or

some stopping criterion is met. The result is often represented as a tree-like structure that visualizes the merging or splitting steps. **Partitional clustering** methods, by contrast, assign all data points into a fixed number of clusters in a single step. These approaches aim to optimize a specific clustering criterion, such as minimizing the variance within each cluster. A widely used example is K-means clustering, which will be discussed in the following. The method partitions the data into K clusters such that the distances between points and their assigned cluster centers are minimized. **Bayesian clustering** or probabilistic mixture models assume that the data are generated from a mixture of underlying probability distributions. Each cluster is associated with one such distribution. A prominent example is the Gaussian Mixture Model, which models the dataset as a superposition of several multivariate normal distributions and infers the likelihood that a given point belongs to each cluster.

Clustering techniques vary in their assumptions, flexibility, and computational cost. While many approaches exist, in this chapter we focus on K-means clustering, as a prototypical method, that is widely used in practice. It is conceptually simple, computationally efficient, and well suited for exploring structure in large data sets. More advanced algorithms, such as DBSCAN or Gaussian Mixture Models, can handle more complex cluster shapes or overlapping groups. DBSCAN, for example, is a density-based algorithm that identifies clusters as regions where data points are closely packed together, making it particularly effective for discovering clusters of arbitrary shape and filtering out noise. These methods, however, are computationally more expensive and often require additional parameter tuning. They are not discussed in detail here, but are mentioned to clarify the scope and limitations of K-means. For an accessible overview of alternative techniques, the reader is referred to Géron (2019).

8.3.1 K-means Algorithm

The K-means algorithm is a widely used method for partitional clustering. It organizes data into K clusters by iteratively refining a set of cluster centers based on the spatial distribution of the data. The goal is to assign each data point to the cluster whose center is closest in terms of Euclidean distance, thereby minimizing the total within-cluster variance. Despite its simplicity, K-means is effective in practice and forms a useful starting point for understanding clustering behavior. The method assumes that the number of clusters K is known in advance and performs best when clusters are roughly spherical and of similar size. As with many clustering algorithms, it can be sensitive to outliers and the initial placement of cluster centers.

For a predefined number of clusters K, the K-means algorithm assumes that each cluster is associated with a center, called a **centroid**. Each instance is assigned to the closest centroid based on the Euclidean L_2 distance. Since differences in feature scale can distort distance-based measures, input features should be scaled or mean-normalized as a preprocessing step.

The cluster assignment is described by the cluster index $c^{(i)} \in \{1, \dots, K\}$, which labels each instance $x^{(i)} \in \mathbb{R}^n$ to a cluster. The centroid $\mu_k \in \mathbb{R}^n$ of each cluster $k = 1, \dots, K$ is computed as the mean of the points assigned to it. The algorithm optimizes both the cluster assignments and centroid positions such that the overall cost function, computed by

$$J\big(c^{(1)}, \dots, c^{(m)}, \mu_1, \dots, \mu_K\big) = \tfrac{1}{m} \textstyle\sum_{i=1}^{m} \left\| x^{(i)} - \mu_{c^{(i)}} \right\|_2^2 \tag{8.43}$$

is minimized.

The algorithm proceeds iteratively, alternating between the two key steps

1. Assign each instance $x^{(i)}$ for $i = 1, \ldots, m$ to the cluster with the closest centroid.

2. Recompute the centroids μ_k for $k = 1, \ldots, K$ as the mean of the samples assigned to each cluster.

The iteration is repeated until a cost minimum is reached, at which point the cluster assignments no longer change and the centroid locations have converged. This process is illustrated on the left of Fig. 8.15, which shows the result of applying K-means with $K = 3$ clusters. The figure visualizes the trajectories of the three centroids as they move through the feature space during successive iterations. The final positions of the centroids are indicated, and data points are labeled according to their cluster membership in the final iteration. Note that the *K*-means algorithm is sensitive to the initial placement of cluster centroids. Since the algorithm proceeds by iteratively refining these centroids to minimize the within-cluster variance, a poor initialization can cause it to converge to a local rather than a global minimum. To mitigate this sensitivity, it is common practice to use smarter initialization strategies that spread out the initial centroids in the feature space. Such approaches improve both convergence speed and the quality of the resulting clustering.

Since cluster membership is assigned using the Euclidean distance, the resulting clusters tend to be spherical and of similar size. Consequently, *K*-means does not perform well for non-spherical clusters or clusters of strongly varying diameter. The standard K-means version assigns each instance to a single cluster, referred to as hard clustering. In contrast, so-called soft clustering methods, such as Gaussian Mixture Models, allow each instance to belong to multiple clusters with a certain probability.

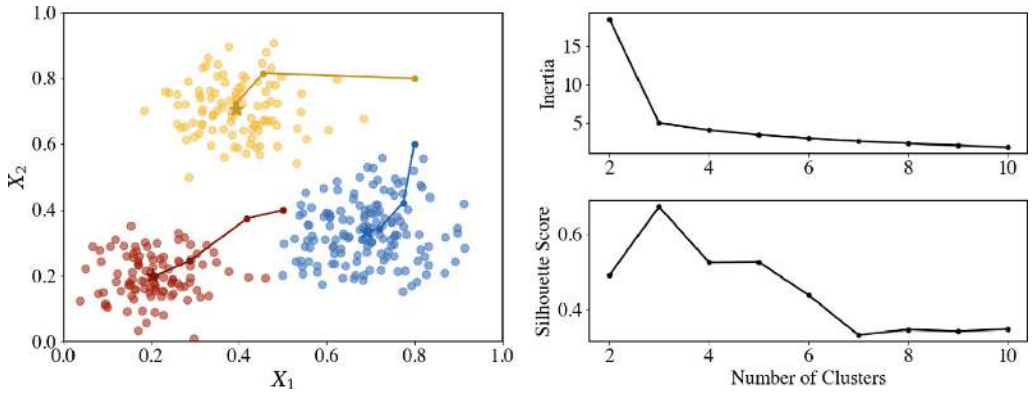


Fig. 8.15 Centroid traces over iterations (left). Inertia and silhouette score for varying number of clusters (right)

One drawback of *K*-means is that the number of clusters *K* must be set manually. Often, a good choice for *K* is not obvious. In such cases, running *K*-means with different values of *K* and evaluating the resulting cost or cluster compactness can provide helpful guidance. A commonly used approach to determine the number of clusters is known as the **elbow method**. As the number of clusters *K* increases, the total cost decreases monotonically because more centroids can better fit the data. However, the rate of improvement typically slows down after a certain point. The value of *K* at which this slowdown becomes noticeable marks the so-called elbow in the cost curve. This point is considered a good candidate for the optimal number of clusters. In Fig. 8.15, the elbow appears at $K = 3$.

A more quantitative and widely recommended metric for selecting the number of clusters K is the **silhouette score**. This score measures how well each data point fits within its assigned cluster compared to its similarity to other clusters. For a given point, the silhouette coefficient is defined as $(b - a)/\max(a, b)$, where a is the average distance to all other points in the same cluster and b is the average distance to points in the nearest neighboring cluster. The resulting value lies in the interval $[-1, +1]$. A coefficient close to $+1$ indicates that the point is well matched to its own cluster and clearly distinct from others. A value near -1 suggests that the point may be misclassified. Averaging the silhouette coefficients over all data points yields the silhouette score. As shown in Fig. 8.15, selecting the value of K that maximizes this score provides a more objective and interpretable criterion for choosing the number of clusters.

8.4 Dimensionality Reduction

In Chapter 2, we introduced an algebraic method to reduce the number of independent variables by exploiting physical dimensional consistency. This approach, based on the Π-Theorem, yields a minimal set of nondimensional groups that capture the governing behavior of a system from a physics-based perspective. In this section, we now consider dimensionality reduction from a data-driven viewpoint. Engineering data sets often arise from systems with complex dynamics, multiple sensors, or coupled subsystems. This typically leads to high-dimensional feature spaces, where each observation may contain tens or hundreds of input variables, including physical measurements, derived signals, or control parameters. Yet, only a subset of these variables may be relevant to the dominant modes of behavior or to the predictive task at hand.

Let the original data set consist of m observations and n input features, such that the feature matrix $\mathbf{X} \in \mathbb{R}^{m \times n}$. The goal is to transform this high-dimensional representation into a lower-dimensional form $\mathbf{X}_{\text{red}} \in \mathbb{R}^{m \times d}$ with $d < n$, in a way that retains the essential structure and informative content of the original data. This process is referred to as **dimensionality reduction**.

As the number of input features increases, data becomes extremely sparse in the surrounding space. This phenomenon is often referred to as the **curse of dimensionality**. In high-dimensional settings, most data points are far from one another, and almost every point appears to be an outlier in some direction. The idea of a local neighborhood becomes meaningless because even the nearest points may be separated by large distances. As a result, distance-based methods such as clustering or nearest neighbor classification become unreliable, since they depend on the assumption that nearby points share meaningful similarities.

In addition to geometric challenges, high-dimensional data are also more prone to overfitting. Models may capture spurious patterns or noise, leading to poor generalization. Dimensionality reduction helps mitigate these issues by projecting the data into a lower-dimensional subspace where structure is more concentrated, neighborhoods are more meaningful, and patterns are easier to model and interpret.

Reducing the number of features simplifies the modeling task, especially when inputs are noisy, redundant, or irrelevant. It improves numerical stability, reduces the risk of overfitting, and makes models easier to interpret, validate, and maintain. In the context of engineering problems, dimensionality reduction serves two complementary purposes. First, it addresses computational and statistical challenges associated with high-dimensional data. Second, it often

reveals latent structure in the system response, such as dominant modes, conserved quantities, or intrinsic low-dimensional behavior, that links naturally to physical understanding and supports the development of simplified or hybrid models. Furthermore, dimensionality reduction plays a valuable role in visualization. Lower-dimensional projections allow complex data sets to be represented in two or three dimensions, making patterns, clusters, or trends more readily observable and interpretable.

There are various dimensionality reduction approaches, which can be broadly categorized along different criteria. One distinction lies between **linear** and **nonlinear** methods, as outlined by van der Maaten et al. (2009). Pudil and Novovicov (1998) distinguish methods based on **feature selection** versus **feature extraction**. Géron (2019) further differentiates between **projection techniques** and **manifold learning** approaches. In the following, we will explore one of the most well-established and widely applied linear projection methods, that is the Principal Component Analysis (PCA).

8.4.1 Principal Component Analysis

Principal Component Analysis (PCA) is a method that transforms a data set into a new coordinate system to simplify its structure. The idea is to change the basis of the feature space such that the greatest variance in the data lies along the first coordinate axis, called the first principal component. The second principal component is chosen orthogonal to the first and captures the second largest variance, and so on. Applying the approach implicitly assumes that directions in which the data vary most are also the most informative for understanding or predicting the system's behavior. The transformation is analogous to the familiar principal axis transformation known from mechanics, used to identify the natural axes of rotation for a rigid body. In both cases, the transformation reveals a coordinate system aligned with the intrinsic structure of the system, where cross-coupling terms vanish and the system's behavior can be described more simply.

PCA is widely used to compress data by projecting it onto the first few principal components that retain most of the data's variation. By omitting the remaining components, the original data can be approximated with significantly fewer dimensions, often without sacrificing much information. The principal components are linear combinations of the original features, so PCA is fundamentally a linear transformation.

Mathematically, the principal components correspond to the eigenvectors of the data's covariance matrix, introduced in Sect. 6.2.5. To compute this matrix, we start with the feature matrix $\mathbf{X} \in \mathbb{R}^{m \times n}$, where each of the m rows is an observation and each of the n columns corresponds to a feature. We interpret each column $X_i \in \mathbb{R}^m$ as a random variable consisting of m samples. The expected value of the data is computed column-wise, yielding the mean vector

$$\mu_{\mathbf{X}} = \mathrm{E}\left[\mathbf{X}\right] = \left(\mathrm{E}\left[X_1\right], \mathrm{E}\left[X_2\right], \ldots, \mathrm{E}\left[X_n\right]\right). \tag{8.44}$$

The covariance matrix, also called the auto-covariance matrix, captures how each pair of features co-varies across the observations. It is defined as

$$\mathrm{Cov}\left(\mathbf{X}, \mathbf{X}\right) = \mathrm{E}\left[\left(\mathbf{X} - \mu_{\mathbf{X}}\right)^{\top}\left(\mathbf{X} - \mu_{\mathbf{X}}\right)\right] = \mathrm{E}\left[\mathbf{X}^{\top}\mathbf{X}\right] - \mu_{\mathbf{X}}^{\top}\mu_{\mathbf{X}} \ . \tag{8.45}$$

In expanded form, the covariance matrix is a symmetric $n \times n$ matrix given by

$$\operatorname{Cov}(\mathbf{X}, \mathbf{X}) = \begin{bmatrix} \operatorname{Var}(X_1) & \operatorname{Cov}(X_1, X_2) & \cdots & \operatorname{Cov}(X_1, X_n) \\ \operatorname{Cov}(X_2, X_1) & \operatorname{Var}(X_2) & \cdots & \operatorname{Cov}(X_2, X_n) \\ \vdots & \vdots & \ddots & \vdots \\ \operatorname{Cov}(X_n, X_1) & \operatorname{Cov}(X_n, X_2) & \cdots & \operatorname{Var}(X_n) \end{bmatrix} = \tag{8.46}$$

$$\begin{bmatrix} \mathrm{E}\left[(X_1 - \mu_{X_1})^2\right] & \mathrm{E}\left[(X_1 - \mu_{X_1})(X_2 - \mu_{X_2})\right] & \cdots & \mathrm{E}\left[(X_1 - \mu_{X_1})(X_n - \mu_{X_n})\right] \\ \mathrm{E}\left[(X_2 - \mu_{X_2})(X_1 - \mu_{X_1})\right] & \mathrm{E}\left[(X_2 - \mu_{X_2})^2\right] & \cdots & \mathrm{E}\left[(X_2 - \mu_{X_2})(X_n - \mu_{X_n})\right] \\ \vdots & \vdots & \ddots & \vdots \\ \mathrm{E}\left[(X_n - \mu_{X_n})(X_1 - \mu_{X_1})\right] & \mathrm{E}\left[(X_n - \mu_{X_n})(X_2 - \mu_{X_2})\right] & \cdots & \mathrm{E}\left[(X_n - \mu_{X_n})^2\right] \end{bmatrix}$$

To apply the PCA, the data needs to be centered by subtracting the mean of each feature so that the resulting feature matrix has zero mean, that is $\mu_{\mathbf{X}} = \mathbf{0}$. This preprocessing step simplifies the expression for the covariance matrix to

$$\operatorname{Cov}(\mathbf{X}, \mathbf{X}) = \mathrm{E}\left[\mathbf{X}^\top \mathbf{X}\right] = \tfrac{1}{m} \mathbf{X}^\top \mathbf{X} = \tfrac{1}{m} \sum_{i=1}^{m} x^{(i)} \left(x^{(i)}\right)^\top . \tag{8.47}$$

Furthermore, it is recommended to standardize the features if they vary in scale. Otherwise, features with large numerical ranges would dominate the principal components and bias the result.

To extract the principal components, one could directly compute the eigenvectors of the covariance matrix $\operatorname{Cov}[\mathbf{X}]$. A common alternative is to perform a **Singular Value Decomposition** (SVD) of $\mathbf{X}$, which has the advantage of providing both the eigenvectors and eigenvalues in one procedure, and is also numerically more robust. As detailed in Appendix C.2, the SVD decomposes $\mathbf{X} \in \mathbb{R}^{m \times n}$ into $\mathbf{X} = \mathbf{U}\Sigma\mathbf{V}^\top$, where the matrices $\mathbf{U} \in \mathbb{R}^{m \times m}$ and $\mathbf{V} \in \mathbb{R}^{n \times n}$ are orthogonal, and $\Sigma \in \mathbb{R}^{m \times n}$ is a diagonal matrix containing the singular values $\sigma_1, \sigma_2, \ldots, \sigma_p$ with $p = \min(m, n)$. These singular values are ordered in decreasing magnitude, and the squared singular values σ_i^2 correspond to the eigenvalues of the covariance matrix. Each eigenvalue quantifies the variance explained by the associated principal component. The columns of $\mathbf{V} = (V_1, V_2, \ldots V_n)$ are the principal components.

Dimensionality reduction is achieved by keeping only the first $d < n$ principal components. These form the reduced basis matrix $\mathbf{B} = (V_1, V_2, \ldots V_d) \in \mathbb{R}^{n \times d}$. The projection of the original data $\mathbf{X} \in \mathbb{R}^{m \times n}$ to its low-dimensional representation $\mathbf{X_B} \in \mathbb{R}^{m \times d}$ is then given by

$$\mathbf{X_B} = \mathbf{X}\ \mathbf{B}\ . \tag{8.48}$$

This transformation retains the dominant directions of variance while filtering out lower-variance components, which are typically considered as noise or redundant information. Similarly, an individual data sample $x^{(i)} \in \mathbb{R}^n$ can be projected to its reduced form via

$$x_{\mathbf{B}}^{(i)} = \mathbf{B}^\top x^{(i)}\ . \tag{8.49}$$

The resulting features can be used directly for visualization or as inputs to machine learning models (Fig. 8.16). Importantly, since PCA is a linear method, it is best suited for problems where the dominant structure in the data lies along linear directions.

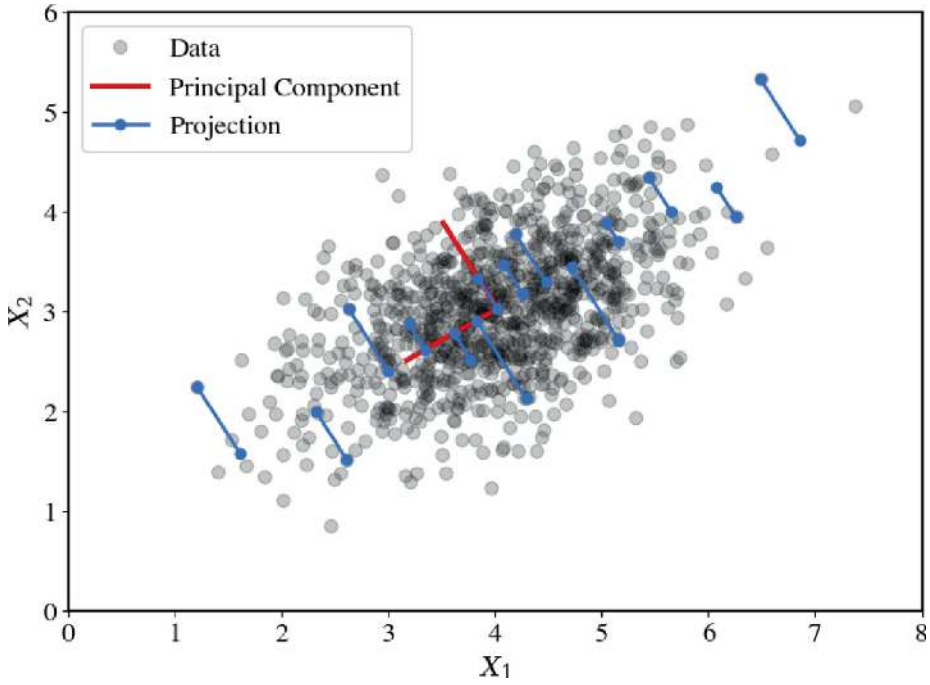


Fig. 8.16 Principal components for data set and projection to first principal component

Choosing the Number of Principal Components As discussed, the principal components are ordered by the amount of variance they capture from the data. This makes the **retained variance** a natural criterion for deciding how many components to keep. A reduced-dimensional representation should preserve most of the original structure while discarding less informative directions. The mean squared projection error from dimensionality reduction is given by $\frac{1}{m}\sum_{i=1}^{m}\|x^{(i)} - x_{\mathbf{B}}^{(i)}\|_2^2$, while the total variance in the data is $\frac{1}{m}\sum_{i=1}^{m}\|x^{(i)}\|_2^2$. The ratio of these two quantities indicates the fraction of variance that is lost. To retain a desired portion of the original variance, the criterion can be expressed as

$$\frac{\sum_{i=1}^{m}\|x^{(i)} - x_{\mathbf{B}}^{(i)}\|^2}{\sum_{i=1}^{m}\|x^{(i)}\|^2} \leq \Delta_{\text{var}} \ , \tag{8.50}$$

where Δ_{var} defines the tolerated fraction of variance loss. For instance, setting $\Delta_{\text{var}} = 0.2$ ensures that at least 80% of the original variance is retained in the reduced representation.

As an example, Fig. 8.17 illustrates the outcome of a PCA performed on the turbofan data set FD001, discussed in Sect. 10.4. The top plot shows both the individual and cumulative explained variance per principal component. In this case, the first three components capture roughly 81% of the total variance. The bottom plot highlights how strongly each original signal contributes to the first five principal components, offering insight into the linear combination of sensors entering the PCs.

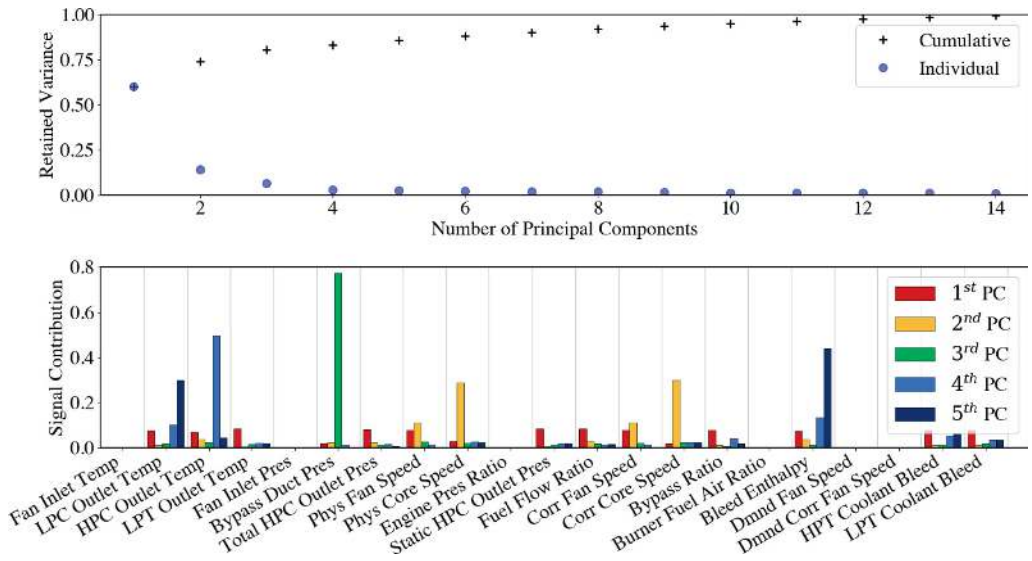


Fig. 8.17 PCA of the turbofan dataset FD001 from Chapter 10.4, showing individual and cumulative explained variance (top) and component-wise signal contributions (bottom)

When using SVD, the variance contribution of each principal component is directly linked to its corresponding singular value. The cumulative variance retained by the first d components can be computed as $\sum_{i=1}^{d} \sigma_i / \sum_{i=1}^{n} \sigma_i$. Plotting this ratio as a cumulative curve, as shown above, provides a helpful visual guide. The retained variance criterion then simplifies to the form

$$\frac{\sum_{i=1}^{d} \sigma_i}{\sum_{i=1}^{n} \sigma_i} \geq 1 - \Delta_{\text{var}} \ , \tag{8.51}$$

making it straightforward to determine the number of principal components needed to achieve a desired variance retention threshold.

Practical Aspects To apply PCA as a preprocessing or transformation step within a modeling pipeline, it is essential to retain all information related to centering and scaling. That is, the mean and standard deviation used to normalize the training data must be stored and applied consistently to any new data before projection. This ensures that the new observations are transformed into the same feature space that the principal components were derived from.

PCA is particularly useful for data compression. By retaining only the top d principal components, the dimensionality of the data is reduced while preserving the corresponding variance. If needed, the original data can be approximately reconstructed by projecting back into the original space using the inverse transformation $x^{(i)} \approx \mathbf{B} x_{\mathbf{B}}^{(i)}$. However, this reconstruction will lack the information contained in the discarded components. The lost variance cannot be recovered, and the reconstructed data is a lower-rank approximation of the original input. Nevertheless, this trade-off is often acceptable, especially when the reduced dimensions in fact capture the dominant behavior of the system.

As previously mentioned, PCA is also often used for visualization of high-dimensional data sets. Reducing a data set to $d = 3$, $d = 2$, or even $d = 1$ dimensions enables a visual representation of complex relationships and structure. Clusters, outliers, or patterns that may

not be visible in the full feature space often become more apparent in the principal component space.

8.5 Anomaly Detection

The objective of anomaly detection is to identify rare observations that deviate significantly from the majority of the data set. Such observations are commonly referred to as anomalies, but may also be called outliers or exceptions. Accordingly, anomaly detection is often used interchangeably with outlier detection. The problems addressed by anomaly detection are typically characterized by a strong class imbalance, where only a small fraction of the data differs from the dominant pattern. The goal is to identify those few unusual instances that may indicate a different underlying process. According to Hawkins (1980), "*an outlier is an observation which deviates so much from the other observations as to arouse suspicions that it was generated by a different mechanism*".

The conceptual foundation of anomaly detection is rooted in a simplified perspective of data behavior. It assumes that observations are generated by a single, dominant process and that anomalies are rare deviations from this norm. This basic intuition works well in univariate settings, where an observation that lies several standard deviations from the mean can be flagged as unusual. However, real-world data is rarely so simple. In industrial contexts especially, systems are influenced by a wide range of interacting variables. The data is inherently multivariate, and observations may result from a variety of underlying mechanisms. Different operating modes, transitional states, or fault conditions can all generate distinct patterns that deviate from what is considered nominal. As a result, anomalies may not be isolated points, but rather form coherent clusters that reflect alternative yet structured behavior. A strict assumption of a single normal-generating process may therefore miss broader patterns of deviation.

Anomaly detection is of particular importance in industrial applications, where it serves as a core component in condition monitoring, predictive maintenance, and process safety. It is used to detect unusual system behavior that may signal faults, degradation, or changes in process dynamics. Common examples include unexpected shifts in vibration levels, temperature anomalies, or irregularities in sensor readings that precede equipment failure. Detecting such changes early enables timely interventions and helps prevent unplanned downtime, costly repairs, or safety hazards.

Despite its value, anomaly detection remains a fundamentally challenging task. Although system behavior may be governed by physical principles and bounded within an expected operating envelope, the high dimensionality and strong interdependence among features complicate the identification of abnormal patterns. Noise, drift, and contextual variability can obscure the simplest distinction between normal and anomalous behavior. Moreover, anomalies may be subtle or evolve gradually, making them difficult to detect using static thresholds or simple statistical models. In practice, human expertise often remains essential. Domain experts are frequently required to interpret alerts, assess whether a deviation reflects a genuine issue, and differentiate between harmful anomalies and benign fluctuations caused by changes in environment, operating conditions, or adjacent processes.

There exists a broad variety of methods developed for anomaly detection. A comprehensive overview on statistical and data-mining-based methods is given by Zimek and Filzmoser (2018). One major distinction they draw is between supervised, semi-supervised and unsupervised

approaches. **Supervised approaches** require that the data is labeled, meaning that each instance is explicitly labelled as either *normal* or *anomalous*. A classifier is then trained to distinguish between the two groups. These approaches are typically more accurate when labels are available, as the training process is guided by known outcomes. However, acquiring high-quality labels for anomaly detection is often difficult and costly. Accurate labeling may require expert knowledge or detailed insight into the underlying mechanisms producing the data. In practice, most anomaly detection tasks are carried out in settings where labels are not available.

Unsupervised approaches assume that the majority of the data is normal. Anomalies are then identified based on their deviation from the common patterns in the data. These methods do not require labeled examples and are particularly suited for applications where no prior information about anomalies exists. **Semi-supervised approaches** operate in between. They rely on training data that only contains examples from the normal class. A model is learned to capture the structure of the normal data, and new instances are evaluated based on how well they fit into this learned structure. Instances with low compatibility are considered anomalous.

The authors further distinguish anomaly detection approaches based on the scope of the detection. In **global anomaly detection**, the outlier is identified in relation to the full data distribution, whereas in **local anomaly detection**, the outlier status is determined relative to a local neighborhood. Another criterion is the form of the algorithm output. Some methods return a binary decision for each instance, indicating whether it is anomalous or not, while others assign a continuous score reflecting the degree of anomaly.

A further important classification considers the underlying detection technique. **Statistical tests** operate under the assumption that normal data follows a known distribution, and anomalies are those observations that deviate significantly from that distribution. In Sect. 7.4 we discussed statistical hypothesis testing, and in Sect. 7.1 we introduced box plots as a simple graphical tool to identify outliers in univariate normally distributed data. **Distance-based approaches** evaluate each instance by its proximity to other instances in the data set. The underlying idea is that normal instances are surrounded by many similar observations, forming dense regions in feature space. In contrast, outliers tend to be isolated and lie far from their neighbors. There exist various distance-based scoring methods, ranging from counting neighbors within a fixed radius to evaluating distances to the K nearest neighbors. **Density-based methods**, such as the Local Outlier Factor (LOF), extend this idea by evaluating the local density around each point and comparing it to the densities of nearby regions. An instance is flagged as an outlier if its local density is significantly lower than that of its neighbors. In that sense, the method identifies points that are located in sparser regions than expected.

In the following, we illustrate a simple statistical testing approach using a multivariate normal distribution as a baseline model, chosen for both its clarity and practical relevance. The multivariate normal distribution provides an interpretable and analytically tractable framework for introducing the basic principles of statistical anomaly detection in multidimensional feature spaces. It generalizes the familiar one-dimensional 3σ rule, commonly used to assess whether a value lies unusually far from the mean, to higher dimensions. In this setting, the distance of a point from the mean is evaluated relative to the shape and orientation of the data distribution, as encoded by the covariance matrix. This results in elliptical probability contours rather than simple intervals and enables consistent thresholding based on confidence regions under the multivariate distribution. In particular, the model captures essential aspects such as correlations between features through the off-diagonal elements of the covariance matrix. Even approximate Gaussian assumptions can in real-world industrial systems yield reasonable

performance for initial anomaly screening, especially when supported by domain knowledge or applied to well-controlled subsystems.

8.5.1 Multivariate Gaussian

As a practical baseline, we now consider a statistical testing approach based on the multivariate normal distribution. Despite its simplicity, this model captures important characteristics of real-world data, such as feature correlations, and offers a clear probabilistic framework for detecting anomalies. The core idea is that normal observations are expected to fall within high-probability regions of the distribution, while anomalies lie in low-probability regions. Detection thresholds can be set using statistical confidence intervals, extending the familiar 3σ rule to higher dimensions.

In the multivariate setting, distance from the mean is evaluated not only by magnitude but also relative to the data's covariance structure. This leads to elliptical probability contours that reflect the orientation and spread of the distribution in feature space. An observation is flagged as anomalous if it falls outside a chosen threshold.

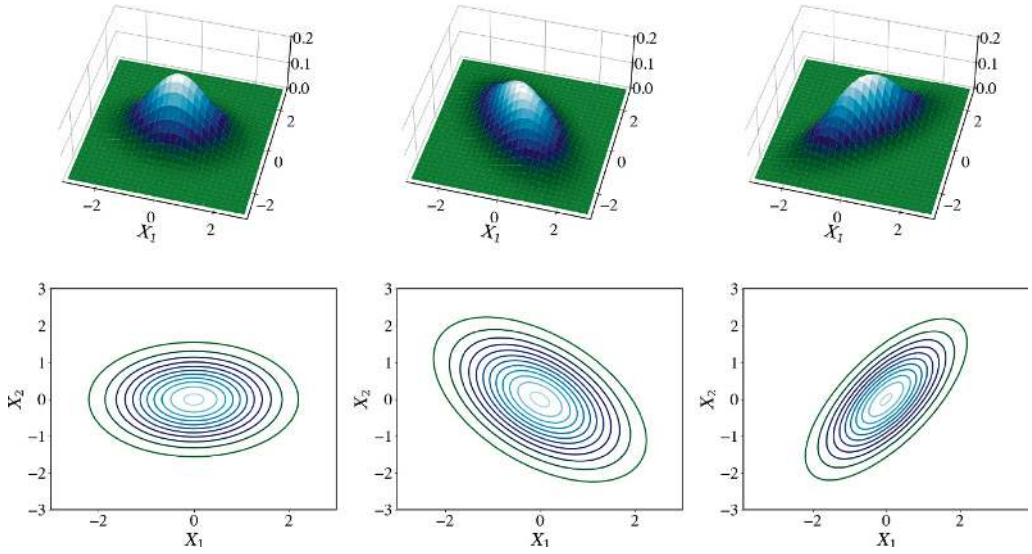


Fig. 8.18 Multivariate Gaussian distributions with $\mu = \left[\begin{smallmatrix} 0 \\ 0 \end{smallmatrix}\right]$ for all and covariance matrices from left to right $\mathbf{S} = \left[\begin{smallmatrix} 1 & 0 \\ 0 & 0.5 \end{smallmatrix}\right]$, $\mathbf{S} = \left[\begin{smallmatrix} 1 & -0.5 \\ -0.5 & 1 \end{smallmatrix}\right]$, $\mathbf{S} = \left[\begin{smallmatrix} 1 & 0.7 \\ 0.7 & 1 \end{smallmatrix}\right]$

The multivariate normal probability density function is given by

$$p(\mathbf{x}, \mu, \mathbf{S}) = \frac{1}{\sqrt{(2\pi)^n |\mathbf{S}|}} \exp\left(-\frac{1}{2}(\mathbf{x} - \mu)^\top \mathbf{S}^{-1} (\mathbf{x} - \mu)\right) , \tag{8.52}$$

where $\mu \in \mathbb{R}^n$ is the mean vector, $\mathbf{S} \in \mathbb{R}^{n \times n}$ is the covariance matrix, and n is the number of features. For the inverse $\mathbf{S}^{-1}$ to exist, the number of observations m must exceed n to ensure that the covariance matrix is full rank. Given a training set $\mathbf{X} = \left(x^{(1)}, x^{(2)}, \ldots, x^{(m)}\right)^\top \in \mathbb{R}^{m \times n}$, the parameters of the distribution are fitted by estimating the empirical mean and covariance as

$$\mu = \frac{1}{m} \sum_{i=1}^{m} x^{(i)} \quad , \quad \mathbf{S} = \frac{1}{m} \sum_{i=1}^{m} \left(x^{(i)} - \mu\right)\left(x^{(i)} - \mu\right)^\top . \tag{8.53}$$

In this multivariate formulation the features are not assumed to be statistically independent. Thus the covariance matrix may contain nonzero off-diagonal terms that capture correlations between features. This is illustrated in Fig. 8.18, where different structures in the covariance matrix correspond to different orientations and shapes of the probability contours. If the covariance matrix $\mathbf{S}$ is diagonal, this implies that the features are statistically independent under the model, meaning there are no linear correlations between them. In this case, the multivariate Gaussian reduces to a product of univariate Gaussian distributions, one for each feature, thus

$$p(x) = \prod_{j=1}^{n} p\left(x_j\,,\,\mu_j, \sigma_j^2\right)\ . \tag{8.54}$$

This formulation reflects a situation where the variables vary independently, and the probability density along each axis can be evaluated separately. When the covariance matrix contains nonzero off-diagonal entries, this indicates the presence of linear dependencies between features, and the full multivariate form must be retained to capture the joint structure of the data.

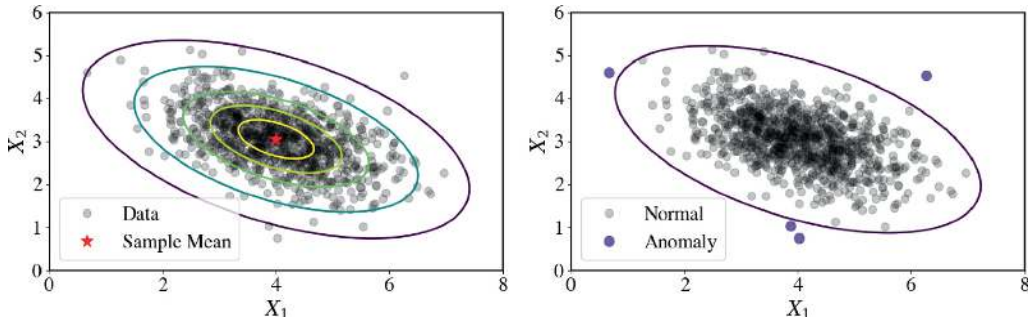


Fig. 8.19 Confidence ellipses of the multivariate Gaussian with sample mean (left), and anomalies flagged by the Mahalanobis threshold (right)

The quadratic form $(\mathbf{x}-\mu)^\top \mathbf{S}^{-1}(\mathbf{x}-\mu)$ appearing in the exponent of the pdf is known as the squared **Mahalanobis distance**. It generalizes the notion of distance by incorporating the feature correlations encoded in $\mathbf{S}$. The Mahalanobis distance between a sample *x* and the mean μ is denoted by

$$D_M(x,\mu)^2 = (\mathbf{x}-\mu)^\top \mathbf{S}^{-1}(\mathbf{x}-\mu)\ . \tag{8.55}$$

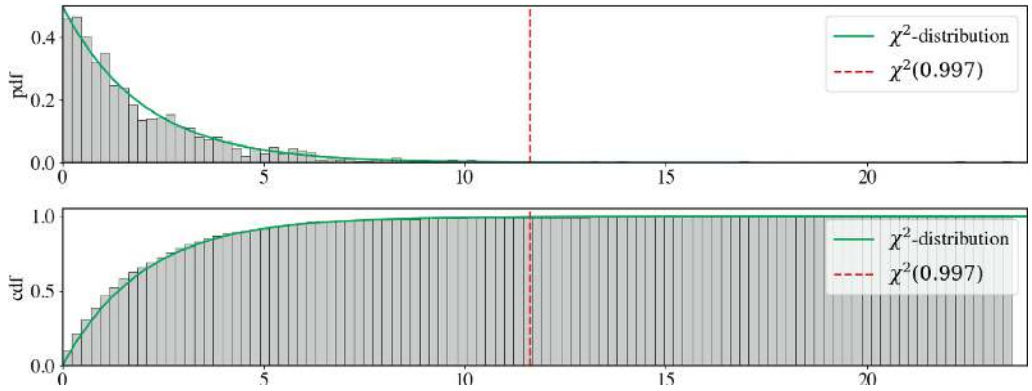


Fig. 8.20 χ^2 probability density function (top) and cumulative distribution function (bottom) with threshold at the 99.7% confidence level

It measures the number of standard deviations a point is away from the mean in the transformed space defined by the covariance structure. The Mahalanobis distance follows a χ^2-distribution with *n* degrees of freedom. This provides a natural way to set a detection threshold. A point is flagged as an anomaly if

$$D_M(x, \mu)^2 > \varepsilon \ , \tag{8.56}$$

with ε set as a quantile of the χ^2-distribution. A common choice is $\varepsilon = \chi^2(0.997)$, corresponding to a confidence region of approximately 3σ for normally distributed data. Figure 8.19 on the left illustrates a sample distribution and its Mahalanobis-based confidence ellipses and on the right shows how points beyond the confidence threshold are classified as anomalies.

While the above approach yields a binary decision whether an instance is anomalous or not, the output can be generalized to a continuous score. For example, instead of thresholding the Mahalanobis distance, we may interpret the anomaly score as the probability under the model, and define the anomaly score as $1 - p(\mathbf{x})$. This allows ranking observations by degree of abnormality and adjusting the detection threshold depending on the specific application context. The associated probability density and cumulative distribution of the χ^2-distribution used for thresholding are shown in Fig. 8.20.

References

Géron A (2019) Hands-on machine learning with Scikit-Learn, Keras, and TensorFlow: concepts, tools, and techniques to build intelligent systems, 2nd ed. O'Reilly Media

Hawkins DM (1980) Identification of outliers. Chapman and Hall, Monographs on Applied Probability and Statistics

Pudil P, Novovicov J (1998) Novel methods for feature subset selection with respect to problem knowledge. In: Liu H, Motoda H (eds) The Springer international series in engineering and computer science, vol 453. Springer

van der Maaten L, Postma E, van den Herik J (2009) Dimensionality reduction: a comparative review. J Mach Learn Res 10:66–71

Zimek A, Filzmoser P (2018) There and back again: outlier detection between statistical reasoning and data mining algorithms. Wiley Interdisc Rev: Data Mining Knowl Discov 8(6)

Footnotes

[1] This expression can also be written in the familiar form $\sum_{i,j=1}^{n} a_{ij}x_i x_j + 2\sum_{i=1}^{n} b_i x_i + c = 0$, which represents a general quadric surface and is equivalent to a second-order hypothesis linear in parameters.

Part III
Engineering Applications Modeling

© The Author(s), under exclusive license to Springer Fachmedien Wiesbaden GmbH, part of Springer Nature 2026
H. Gomaa, *Modeling with Knowledge and Data*, Mathematical Engineering
https://doi.org/10.1007/978-3-658-50679-7_9

9. Modeling Isolated Physical Processes

Hassan Gomaa[1] ✉
(1) Strategic Projects Co-Innovation, Cognite, Oslo, Norway

This chapter presents a series of isolated physical processes that serve as instructive examples to illustrate how hybrid modeling strategies can be applied to concrete engineering problems. These examples are drawn from classical mechanics, thermodynamics, and fluid mechanics, and they are selected to showcase the step-by-step development of models rooted in physical reasoning, while being complemented, where necessary, by data-driven refinement.

The modeling efforts in this chapter follow the framework introduced in Sect. 1.3. Each example begins with a well-defined modeling **purpose** that explains the motivation for constructing the model. This purpose may involve gaining insight into a physical mechanism, supporting a simplification in a larger system model, or developing a reduced-order surrogate that can be embedded in simulation toolchains. The modeling **objective** defines the specific physical mechanism to be captured, identifies the input-output behavior of interest, and clarifies the scope within which the model should operate. The modeling **strategy** then integrates physical knowledge and data into a coherent workflow that reflects the model requirements. These requirements may include dimensional consistency, computational efficiency, or predictive accuracy, and are considered in the context of the intended application.

The physical processes selected for this chapter are sufficiently constrained and isolated to allow a detailed and transparent presentation of the modeling steps. Because these processes can be studied independently of external system interactions, boundary conditions can be specified precisely and the relevant variables can be directly controlled or measured. This level of isolation simplifies the modeling effort and supports a clear connection between the underlying physics, the assumptions made, and the resulting model structure. It also provides an ideal setting for demonstrating how physical reasoning and data complement one another in the development of hybrid models. This degree of isolation is a key distinction from the examples to be discussed in Chapter 10, where system-level interactions and operational complexity play a central role in shaping the modeling approach.

From the perspective of hybrid modeling, all examples presented in this chapter fall within the white-box to gray-box spectrum. The model structures are primarily informed by first principles, with parameters either derived from theory or inferred using data

where theoretical knowledge is incomplete or where calibration is required for practical accuracy. The relationships between primary variables in these models typically stem from nondimensional groups, which capture the balance of governing forces and support validity and transferability across different regimes. Early examples, such as the damped pendulum, rely entirely on first principles and demonstrate the direct connection between physical laws and model form. As this chapter progresses, cases such as heat transfer in boundary layers or droplet impact on wetted surfaces introduce empirical terms or closure relations where data is needed to extend model fidelity and practical applicability. These examples show how data complements physical understanding and enables models to meet the demands of engineering applications. This chapter concludes with turbulence modeling using the eddy viscosity concept, where data begins to influence both model parameters and structure.

9.1 Damped Pendulum Motion

This first example focuses on modeling the motion of a spherical pendulum surrounded by a viscous fluid. It serves as a classical example for describing a mechanical system governed by basic principles of dynamics and fluid resistance. The problem illustrates the interaction between a moving solid and an external viscous flow, and is often found in introductory discussions on mathematical modeling.

Within the hybrid modeling framework introduced in Sect. 1.1.2, the damped pendulum represents a **white-box** case, in which both the model structure and the parameters are derived from physical laws and domain knowledge. In this case, no empirical or data-driven correction is required. The focus lies on physical interpretability, mechanistic understanding, and analytical accessibility.

The **purpose** of this modeling effort is to understand and describe the transient behavior of the pendulum as it returns to equilibrium under the influence of gravity and viscous damping. This includes predicting the system motion over time, as well as assessing the corresponding energy transfers between kinetic, potential, and dissipative mechanisms.

The **objective** is to develop a mathematical model that represents the angular motion of the pendulum as a function of time. In particular, the model should predict the deflection amplitude, oscillation frequency, and energy dissipation over time, based on a known set of initial conditions.

The **strategy** follows a typical modeling flow based on known physical principles. The approach begins with the constitutive and balance equations, here represented by Newton's second law. Physically motivated simplifications are then introduced, including the small-angle approximation and creeping flow assumptions. These steps lead to a linear second-order differential equation that can be solved analytically and supports physical interpretation. The damping force is modeled using Stokes' law for viscous flow around a sphere, as discussed in Sect. 5.2.2. The general analytical closed-form solution for a harmonic oscillator is derived and discussed in Appendix B.1.

9.1.1 Governing Equation and Motion

To develop the model, we begin by analyzing the forces acting on the pendulum along its arc of motion. As illustrated in Fig. 9.1, the subject of investigation is a spherical mass of diameter D and density ρ, suspended from a massless rigid rod of length ℓ, fully immersed in an incompressible Newtonian fluid with dynamic viscosity μ. It is free to oscillate in a vertical plane under the influence of gravity, starting from an initial angular deflection. The configuration is treated as two-dimensional, and effects such as rod drag or added mass from the fluid are neglected. After being initially deflected, the pendulum swings back and forth under the influence of gravity while subjected to frictional forces from the surrounding fluid.

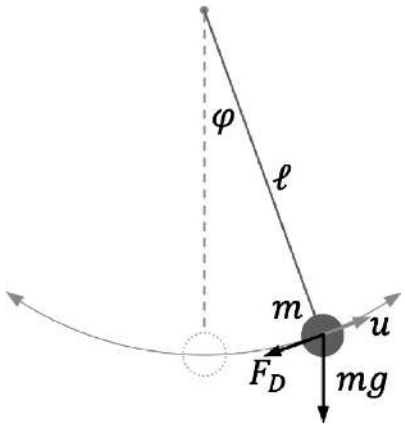


Fig. 9.1 Schematic of a spherical pendulum oscillating in a viscous fluid

The angular deflection of the pendulum, denoted by the angle φ, determines the arc length s. This relationship allows for a direct formulation of the velocity and acceleration along the pendulum arc

$$\begin{aligned} s &= \ell\varphi \ , \\ u &= \dot{s} = \ell\dot{\varphi} \ , \\ a &= \ddot{s} = \ell\ddot{\varphi} \ . \end{aligned} \tag{9.1}$$

Applying Newton's second law to the tangential direction along the pendulum arc results in a balance between the acting forces. The gravitational force component contributes to restoring motion, while the drag force acts in opposition. The resulting equation of motion, along with general initial conditions, is given by

$$m\ell\ddot{\varphi} - F_D + mg\sin\varphi = 0 \ , \qquad \varphi(t=0) = \varphi_0 \ , \qquad \dot{\varphi}(t=0) = \dot{\varphi}_0 \ . \tag{9.2}$$

Here, φ_0 denotes the initial angular deflection of the pendulum measured from the vertical, and $\dot{\varphi}_0$ is the initial angular velocity. Together, they define the starting state of the system.

To simplify the analysis, we assume creeping flow conditions where the Reynolds number approaches zero, $\mathrm{Re} \to 0$, as discussed in Sect. 5.2.2. In this regime, inertial

effects in the surrounding fluid are negligible compared to viscous forces. The drag force acting on a sphere under such conditions is described by Stokes' law. The resulting expression, derived in Appendix B.2, is $F_D = -3\pi\mu D u$, which shows that the drag is directly proportional to the pendulum speed u.

We further simplify the system by considering small deflection angles $\varphi \lesssim 15\,^\circ$. In this regime, the gravitational restoring force $\sin\varphi$ may be approximated by φ with an associated error below 1.2 %. This approximation transforms the nonlinear term into a linear spring-like force. Introducing these simplifications into the equation of motion results in a linear second-order ordinary differential equation representing a damped harmonic oscillator

$$\ddot{\varphi} + 2\delta\omega_0\dot{\varphi} + \omega_0^2\varphi = 0 \;, \quad \text{with} \quad \omega_0 = \sqrt{\tfrac{g}{\ell}} \;, \quad \delta = \tfrac{3\pi\mu D}{2\,m\omega_0} = \tfrac{9\mu}{\rho D^2\omega_0} \;. \tag{9.3}$$

Here ω_0 represents the natural angular frequency of the undamped pendulum, and δ is the nondimensional damping ratio. This formulation captures the competing effects of inertia, gravitational restoring force, and fluid drag. The analytical solution to this equation, along with its classification into underdamped, critically damped, and overdamped regimes, is derived in Appendix B.1.

9.1.2 Oscillatory Behavior

The mathematical solutions to the damped oscillator equation show that the system behavior depends on the value of the damping ratio δ. For the range $0 < \delta < 1$, the motion is classified as underdamped. In this case, the pendulum oscillates with a decaying amplitude that decreases exponentially over time. The presence of the damping force modifies the oscillation period compared to the undamped case.

For a system without damping, that is $\delta = 0$, the natural oscillation period is given by $T = 2\pi/\omega_0$. With damping, this period increases and becomes

$$T = \tfrac{2\pi}{\omega_0\sqrt{1-\delta^2}} \;, \tag{9.4}$$

so that the oscillation slows as the damping increases. For small damping ratios $\delta \ll 1$, the frequency only slightly deviates from the undamped natural frequency. In the case of critical damping, where $\delta = 1$, the pendulum returns to its steady state without oscillating and does so in the shortest possible time. This defines a sharp boundary between oscillatory and non-oscillatory regimes.

To illustrate these different behaviors, the analytical solution is evaluated for varying values of δ. Figure 9.2 shows the deflection amplitude over time (left) and the corresponding phase diagram (right), which plots the nondimensional pendulum speed over its angular deflection. For the cases shown, the pendulum is initially deflected from rest, so that $\dot{\varphi}_0 = 0$. In the undamped case $\delta = 0$, the pendulum retains a constant amplitude, and its phase trajectory forms a closed elliptical curve. With damping, such as $\delta = 0.05$, the amplitude decays exponentially, and the phase portrait exhibits a visible

spiral that converges toward the origin, indicating the loss of mechanical energy over time. At $\delta = 1$, the motion decays to equilibrium in the shortest time without oscillations, while for $\delta = 1.5$ the decay is slower, reflecting the overdamped regime.

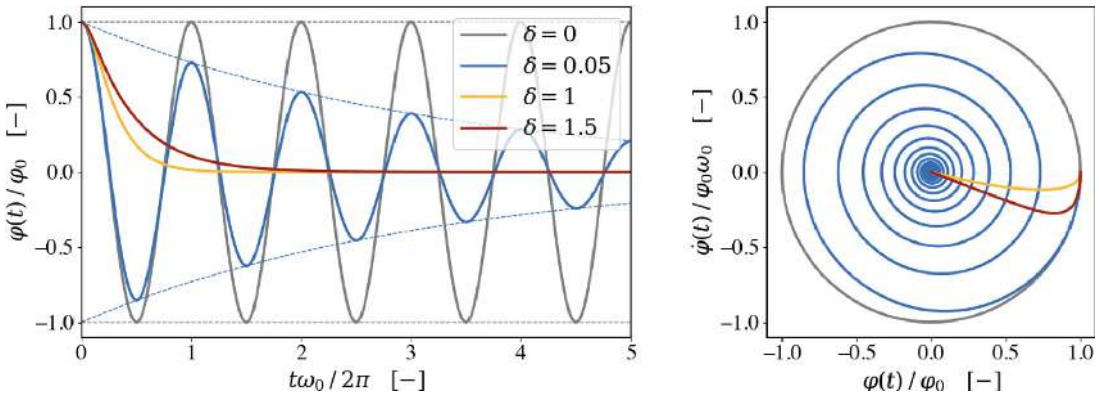


Fig. 9.2 Deflection amplitude over time (left) and non dimensional pendulum speed over deflection (right) for different damping ratios δ

9.1.3 Energy Balance and Dissipation

To gain further insight into the pendulum dynamics, we now examine the corresponding energy transformations. The kinetic energy of the pendulum mass is given by $E_{\text{kin}} = mu^2/2$, where the velocity $u = \ell\dot{\varphi}$, and the potential energy due to gravity is $E_{\text{pot}} = mg\ell(1 - \cos\varphi)$.

In order to ensure consistency between the energy balance and the momentum equation, we need to apply the small-angle assumption to the potential energy term. Applying a second-order Taylor expansion of the cosine term yields

$$\cos\varphi \approx 1 - \frac{\varphi^2}{2} \quad , \tag{9.5}$$

so that the potential energy simplifies to $E_{\text{pot}} = mg\ell\varphi^2/2$. Figure 9.3 shows the time evolution of kinetic and potential energy, along with the total mechanical energy $E_{\text{tot}} = E_{\text{kin}} + E_{\text{pot}}$. In the idealized undamped case $\delta = 0$, the total energy remains constant over time. The motion is therefore fully reversible and conserves mechanical energy.

When viscous damping is present, as represented by a damping ratio $\delta > 0$, the pendulum loses mechanical energy during its motion. This energy is dissipated into the surrounding fluid as internal energy, effectively warming the medium due to viscous shear. The dissipated energy is cumulative and increases more rapidly when the pendulum has higher kinetic energy. This behavior is consistent with the model, since the damping force is proportional to the velocity, and thus the power loss scales with the square of speed.

Figure 9.3 illustrates this process by plotting the cumulative dissipated energy alongside the mechanical energy terms. While kinetic and potential energies are interchangeable and reversible within the system, the dissipated energy represents an

irreversible loss, consistent with entropy generation. The viscous shear converts the pendulum's mechanical energy into the ambient internal energy, which is an irreversible thermodynamic process. The energy loss per oscillation cycle can be quantified by considering the decay in amplitude due to damping. For a cycle starting at time t_0, using the exponential decay relationship $\varphi(t_0+T)/\varphi(t_0) = e^{-\delta\omega_0 T}$, the change in potential energy per cycle becomes

$$\Delta E_{\text{diss}}\big|_{t_0}^{t_0+T} = \frac{mg\ell\varphi(t_0)^2}{2}\left(1-e^{-2\delta\omega_0 T}\right) \ . \tag{9.6}$$

For completeness, it should be noted that an alternative approach to quantifying the dissipated energy is to evaluate the velocity field in the surrounding fluid and compute the viscous dissipation via the corresponding expression for viscous power loss, as outlined in Eq. (3.64), and then integrate over the entire fluid domain.

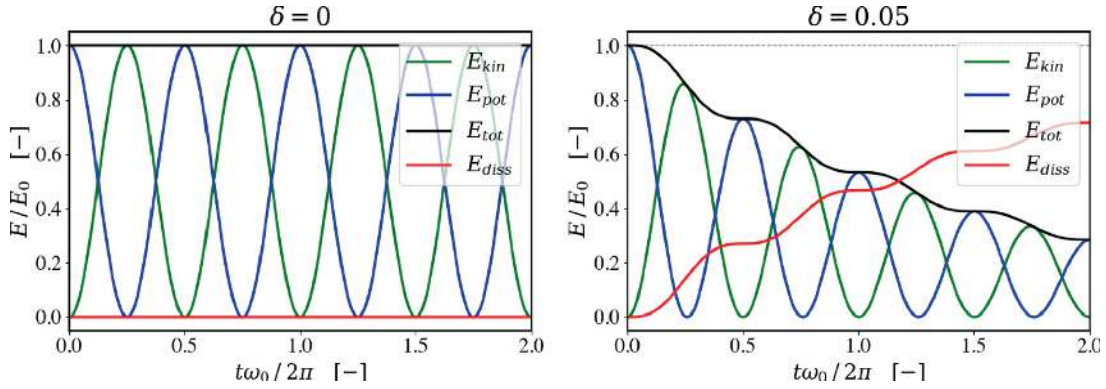


Fig. 9.3 Energy terms and balance for undamped $\delta = 0$ and underdamped oscillation $\delta = 0.05$

9.2 Relaxation Behavior of a Spherical Particle

This second example considers the motion of a rigid spherical particle that is suddenly exposed to an ambient flow. It provides a simple example to study the interplay between particle inertia and drag forces in a fluid medium, and illustrates how characteristic time scales arise from this interaction. The problem offers a useful setting to examine how a particle relaxes to ambient flow conditions.

Within the hybrid modeling framework discussed in Sect. 1.1.2, this case lies firmly on the **white-box** end of the modeling spectrum. The model structure and governing relationships are entirely derived from physical reasoning and analytical formulations. In particular, no data-driven components or empirical parameter tuning are applied. Instead, the physical model is based on Newton's laws and idealized drag correlations, such as Stokes' law or Putnam's correlation, to describe the forces acting on the particle.

The **purpose** of the model is to gain physical insight into how a particle responds dynamically to sudden flow disturbances. This includes quantifying the velocity relaxation process, identifying the time scales over which momentum exchange occurs, and understanding how different regimes of drag affect particle behavior. Such

understanding provides a basis for evaluating droplet or particle dynamics in practical applications such as spray systems, particle-laden flows, or shock-laden environments.

The **objective** is to derive and analyze a mathematical model that predicts the temporal evolution of a spherical particle's velocity and position as it adjusts to a change in relative flow. The analysis focuses on characterizing the velocity decay, the associated penetration depth, and how these depend on key quantities such as particle diameter, density ratio, and Reynolds number.

The **strategy** begins by formulating the equation of motion for the particle based on Newton's second law, balancing the particle inertia against the aerodynamic drag. For this, both the creeping flow regime and moderate Reynolds number regimes are considered. In the first part of the analysis, the Stokes drag formulation is applied under the assumption of low particle Reynolds numbers, which leads to a first-order differential equation with exponential decay behavior. This case supports closed-form analytical solutions for both velocity and position, offering clarity into the relaxation scale and characteristic penetration depth. To extend the model into more realistic operating regimes, the second part of the analysis introduces and adopts the drag correlation proposed by Putnam (1961), which is valid for $\mathrm{Re}_D < 10^3$. This correction introduces a Reynolds number dependence into the drag formulation while preserving integrability of the equation of motion. The resulting solution reveals how the simplifications of Stokes drag become inaccurate for moderate Reynolds number flows, and highlights the effect of increased drag on the relaxation time and penetration distance. This progression from low to moderate Reynolds number formulations not only provides a broader understanding of relaxation behavior but also illustrates the modeling implications of drag regime assumptions.

Overall, this example uses an idealized model to explore how particles respond dynamically in a fluid. It provides a controlled setting to study parameter effects, and characterize flow regimes in particle or droplet-laden systems. An application is the modeling of liquid dynamics in water spray cooled compressors, where droplet relaxation, impact, and film formation play a critical role (Gomaa 2014).

9.2.1 Governing Equation and Motion

The motion of a rigid spherical particle immersed in a continuous fluid is governed by Newton's second law. To determine the particle trajectory, we consider the balance of external forces acting on the particle as it adjusts to the surrounding flow. Neglecting gravity and other body forces, the dominant contribution is the aerodynamic drag exerted by the fluid. The resulting momentum equation is expressed as

$$m_D \dot{\mathbf{u}}_D = \mathbf{F}_D \ , \tag{9.7}$$

where m_D denotes the particle mass and $\dot{\mathbf{u}}_D$ is its acceleration. The drag force $\mathbf{F}_D$ depends on the relative motion between the particle and the ambient fluid and is generally modeled as

(9.8)

$$\mathbf{F}_D = \tfrac{1}{2}\rho_G C_D A |\mathbf{u}_r| \mathbf{u}_r \,,$$

where ρ_G is the ambient fluid density, A is the projected cross-sectional area of the particle, and $\mathbf{u}_r = \mathbf{u}_G - \mathbf{u}_D$ is the relative velocity between the ambient flow $\mathbf{u}_G$ and the particle velocity $\mathbf{u}_D$. The drag coefficient C_D describes the dependency of the drag force on the particle Reynolds number, defined as

$$\mathrm{Re}_D = \frac{|\mathbf{u}_r| D}{\nu_G} \,, \tag{9.9}$$

with D denoting the particle diameter and ν_G the kinematic viscosity of the gas phase. A discussion of the drag coefficient $C_D(\mathrm{Re}_D)$ and various drag regimes is provided in Sect. 5.2.2.

To analyze the particle relaxation behavior, we introduce a simplified flow setup. A spherical particle is assumed to be suddenly released into a uniform ambient flow field of constant velocity $\mathbf{u}_G$. The particle may initially be at rest, or have a different initial velocity $\mathbf{u}_{D0}$. The resulting mismatch in velocity $\mathbf{u}_r(t=0) = \mathbf{u}_G - \mathbf{u}_{D0}$ generates an aerodynamic drag that causes the particle to accelerate until it gradually aligns with the ambient flow. While idealized, the setup captures the essential mechanisms governing the interaction between particle inertia and aerodynamic resistance. It also provides a useful framework for assessing the behavior of particles exposed to velocity gradients, as often encountered in shear flows or stratified flow fields.

When paired with an appropriate drag correlation $C_D(\mathrm{Re}_D)$, the governing Eq. (9.7) supports analytical solutions that describe both the velocity evolution $u_D(t)$ and the trajectory $x_D(t)$ of the particle. These solutions provide direct access to characteristic time and length scales of the relaxation process. Assuming one-dimensional motion along the direction of flow, and introducing the particle mass $m_D = \pi/6 \rho_L D^3$ and cross-sectional area $A = \pi/4 D^2$, the equation of motion reduces to

$$\dot{u}_D = \frac{3\rho_G}{4 D \rho_L} C_D(\mathrm{Re}_D)(u_G - u_D)|u_G - u_D| \,. \tag{9.10}$$

This expression represents a first-order nonlinear ordinary differential equation, where the drag coefficient C_D depends on the relative velocity via the particle Reynolds number $\mathrm{Re}_D = |u_G - u_D| D/\nu_G$. Assuming $u_G = \text{const}$, the relative velocity is $u_r = u_G - u_D$, and we can reformulate Eq. (9.10) in terms of u_r as

$$\dot{u}_r = -\frac{3\rho_G}{4 D \rho_L} C_D(\mathrm{Re}_D) u_r |u_r| \,, \tag{9.11}$$

with initial condition $u_r(0) = u_{r0} = u_G - u_{D0}$. Integrating the governing equation provides an implicit expression for the particle velocity as a function of time. Rearranging and separating variables yields

(9.12)

$$\int_{u_{r0}}^{u_r(t)} \frac{1}{C_D(\mathrm{Re}_D) u_r |u_r|}\, du_r = -\frac{3\rho_G}{4D\rho_L} t \ .$$

This equation describes the evolution of the relative velocity $u_r = u_G - u_D$ over time as governed by the applied drag law $C_D(\mathrm{Re}_D)$. For arbitrary C_D, this integral requires numerical evaluation. However, for specific forms of $C_D(\mathrm{Re}_D)$, such as the Stokes drag law, closed-form analytical solutions are available. Once the time-dependent relative velocity $u_r(t)$ is known, the particle position can be determined by time integration of the velocity, thus

$$x_D(t) = \int_0^t u_D(\tau)\, d\tau = \int_0^t (u_G - u_r(\tau))\, d\tau \ . \tag{9.13}$$

This formulation provides the foundation for analyzing relaxation dynamics across different Reynolds number regimes, as discussed in the following.

9.2.2 Creeping Flow Relaxation

In the low Reynolds number limit, the drag force can be approximated using Stokes' law, for which the drag coefficient is given by $C_D = 24/\ \mathrm{Re}_D$. Substituting this expression into the general formulation yields a closed-form solution for the particle relaxation process. The relative velocity and particle position evolve as

$$\frac{u_r}{u_{r0}} = e^{-\frac{t}{t_D}} \ , \qquad \frac{x_r}{D} = \frac{\mathrm{Re}_D}{18}\frac{\rho_L}{\rho_G}\left(1 - e^{-\frac{t}{t_D}}\right) \ , \tag{9.14}$$

where t_D is the characteristic relaxation time with

$$t_D = \frac{\rho_L D^2}{18\mu_G} \ . \tag{9.15}$$

Here, x_r denotes the particle displacement in a gas-fixed frame of reference, that is relative to a coordinate system moving with the ambient flow velocity u_G. The particle velocity and trajectory in the lab frame are accordingly

$$\begin{aligned} u_D &= u_G - (u_G - u_{D0}) e^{-\frac{t}{t_D}} \ , \\ x_D &= u_G t + t_D (u_G - u_{D0}) \left(1 - e^{-\frac{t}{t_D}}\right) \ . \end{aligned} \tag{9.16}$$

The relaxation time t_D characterizes the time scale over which the particle velocity approaches the ambient velocity. In the Stokes regime, the relative velocity reduces to about 37% of its initial value after one relaxation time, that is $u_r(t_D) \approx 0.37 u_{r0}$.

To capture this behavior more accurately across a wider range of flow conditions, the Reynolds number dependency of the drag must be considered. As illustrated in Fig. 9.4,

Stokes' law underestimates the drag for moderate to higher Re_D, resulting in overly slow predicted relaxation.

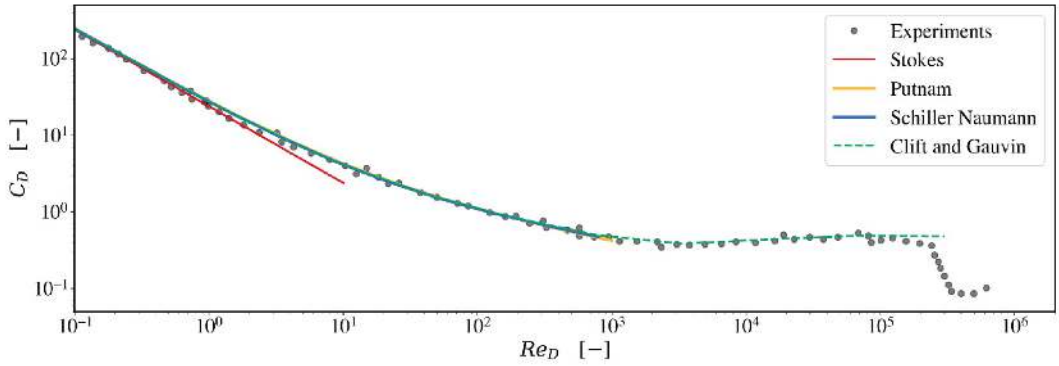


Fig. 9.4 Drag coefficient of a sphere over the Reynolds number for experimental data (White 1991) and selected empirical correlations including (Putnam 1961)

9.2.3 Moderate Reynolds Flow Relaxation

At moderate Reynolds numbers Stokes drag model becomes inaccurate because it underestimates the drag force. As a result, it overpredicts both the relaxation time and the penetration depth. To better capture the particle behavior in this regime, a Reynolds-dependent drag formulation is required.

As presented in Sect. 5.2.2 and illustrated in Fig. 9.4, several refined correlations are available that account for the Reynolds number dependence of the drag coefficient and provide improved agreement with experimental data across a broad range of flow regimes. These include the widely used Schiller-Naumann correlation, valid up to $\mathrm{Re}_D \approx 800$, and the extended formulation by Clift-Gauvin, which remains accurate up to $\mathrm{Re}_D \approx 3 \times 10^5$. However, introducing these correlations to the previously derived equation of motion in Eq. (9.10), leads to differential equations that are no longer analytically integrable and instead require a numerical solution. While such approaches are feasible, they limit the analytical insight and make it more difficult to isolate the influence of key parameters such as particle diameter, fluid properties, or initial conditions.

To retain analytical accessibility and preserve a closed-form solution, we employ the drag correlation introduced by Putnam Putnam (1961),

$$C_D = \frac{24}{\mathrm{Re}_D}\left(1 + \frac{1}{6}\,\mathrm{Re}_D^{2/3}\right) , \qquad \text{for} \quad \mathrm{Re}_D < 10^3 , \tag{9.17}$$

also plotted in Fig. 9.4. While slightly less accurate than the Clift-Gauvin or Schiller-Naumann correlations in reproducing experimental drag data, due to the adjusted Reynolds exponent, Putnam's formulation retains the advantage of allowing analytical integration of Eq. (9.12). This leads to closed-form expressions for the particle velocity and position, which clarify the influence of key nondimensional parameters on the relaxation process. For this reason, the Putnam correlation is adopted here as a balance

between physical accuracy and analytical accessibility. Using this correlation, the equation of motion can again be integrated, yielding the following solution for the velocity relaxation

$$\frac{u_r}{u_{r0}} = \frac{u_G - u_D}{u_G - u_{D0}} = \left[\left(1 + \mathrm{Re}_D^{2/3}/6\right)\mathrm{e}^{2t/3t_D} - \mathrm{Re}_D^{2/3}/6\right]^{-3/2} . \tag{9.18}$$

This formulation smoothly recovers the Stokes solution as $\mathrm{Re}_D \to 0$. The two solutions agree closely up to $\mathrm{Re}_D \approx 1$, beyond which Putnam's formulation captures the increased drag observed experimentally. Figure 9.5 illustrates the normalized velocity decay for various initial Reynolds numbers. It is observed that while $u_r(t_D) \approx 0.37 u_{r0}$ for Stokes flow, it reduces to less than 1% of u_{r0} for $\mathrm{Re}_D = 10^3$, indicating a significantly faster relaxation in this regime.

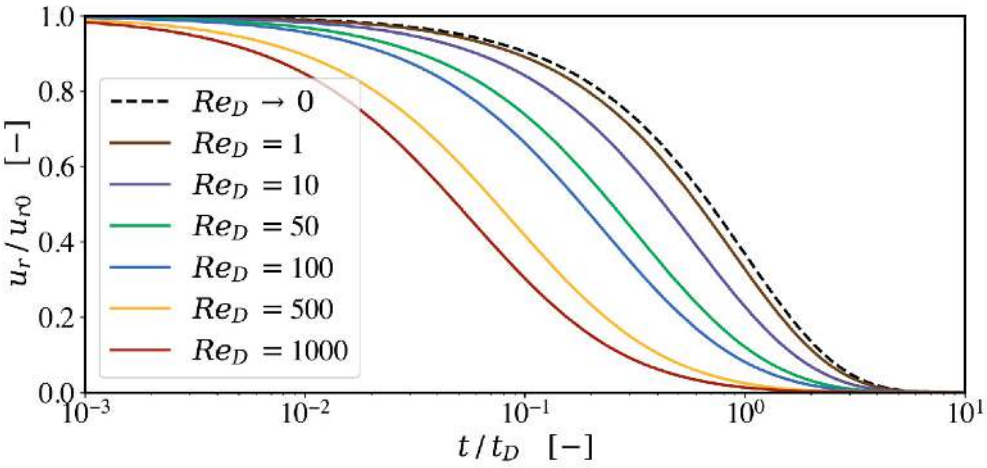


Fig. 9.5 Normalized relative velocity u_r/u_{r0} relaxation over nondimensional time t/t_D using Putnam drag coefficients for different Reynolds numbers

The corresponding particle trajectory is obtained via a second integration

$$x_D = u_G t + \frac{d\mathrm{Re}_D^{1/3}\rho_L}{\rho_G}\left[1 - (u_r/u_{r0})^{1/3} - \sqrt{6}\,\mathrm{Re}_D^{-1/3}\tan^{-1}\left(\sqrt{6}\,\mathrm{Re}_D^{-1/3}\,\frac{1-(u_r/u_{r0})^{1/3}}{(u_r/u_{r0})^{1/3} + 6\mathrm{Re}_D^{-2/3}}\right)\right] . \tag{9.19}$$

In the limit $u_r \to 0$, this reduces to the penetration depth relative to the gas-fixed frame

$$\Delta x_D = x_D - u_G t = D\frac{\rho_L}{\rho_G}\left[\mathrm{Re}_D^{1/3} - \sqrt{6}\,\tan^{-1}\left(\frac{\mathrm{Re}_D^{1/3}}{\sqrt{6}}\right)\right] . \tag{9.20}$$

As expected and shown in Fig. 9.6, the increased drag force in the moderate Re_D regime leads to a noticeable reduction in penetration depth. Compared to the Stokes regime, both

the relaxation time and the required distance to match the ambient velocity decrease by roughly one order of magnitude for $\mathrm{Re}_D \approx 10^3$.

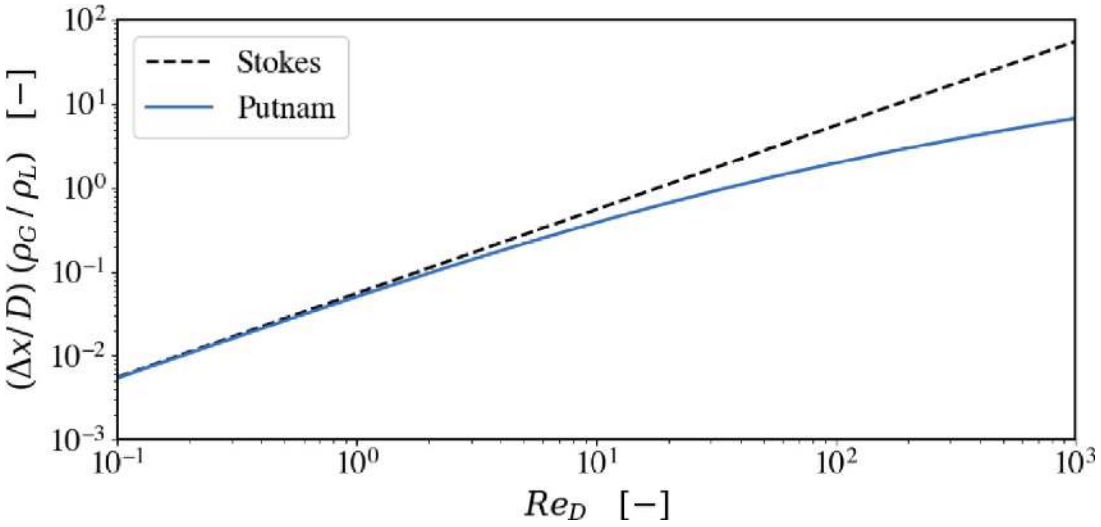


Fig. 9.6 Predicted nondimensional particle penetration depth $\Delta x_D/D$ for varying Reynolds numbers using Stokes and Putnam drag coefficients

9.3 Heat Transfer in External Boundary Layer Flow

We now consider convective heat transfer from a flat plate to a steady, uniform free-stream flow. In this classical configuration, a semi-infinite flat plate is maintained at a constant surface temperature, and a uniform fluid flows with the constant velocity u_∞ over it. As the flow develops, a thermal boundary layer forms along the plate. Conduction dominates heat transfer near the wall, and advection carries the heated fluid through the boundary layer toward the free stream. The arrangement is illustrated in Fig. 9.7.

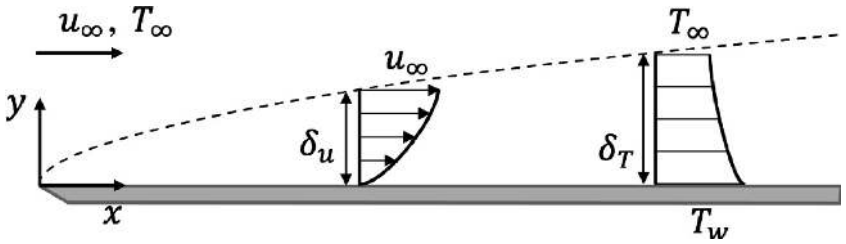


Fig. 9.7 Velocity and thermal boundary layer development over a flat plate, with thicknesses δ_u and δ_T relative to the free-stream velocity u_∞ and temperature T_∞

This problem represents a prototypical case in thermo-fluid dynamics, and serves as a controlled setting to study coupled transport processes and model simplification strategies. In the context of the hybrid modeling framework introduced in Sect. 1.1.2, the present case exemplifies a **light-gray-box** model. Here, the model structure is derived from first principles, but its calibration across a broad range of parameters leverages

numerically generated data, serving as a surrogate for experimental or high-fidelity simulation data. In doing so, the approach combines theoretical modeling with targeted numerical augmentation, reflecting the modeling flow introduced in Sect. 1.3.3.

The modeling **purpose** is to predict convective heat transfer from a flat plate with constant wall temperature in laminar flow, in a form that is physically interpretable and computationally efficient. This setup supports applications such as early-stage thermal system design or model embedding in optimization frameworks. The **objective** is to describe the local wall heat flux through a Nusselt correlation that remains accurate across a wide range of Prandtl numbers, specifically over $1 \times 10^{-3} \leq \mathrm{Pr} \leq 1 \times 10^{3}$, with a target deviation below 1%. This requirement includes correct scaling behavior in the asymptotic limits $\mathrm{Pr} \ll 1$ and $\mathrm{Pr} \gg 1$.

The modeling **strategy** begins with the classical analysis presented in Sect. 5.2.1, where the thermal boundary layer is described using a similarity solution of the energy equation. In that formulation, the Blasius velocity profile enters as a known input, and the Prandtl number Pr appears as the key parameter governing thermal diffusion. The resulting ordinary differential equation is solved numerically, leading to a nondimensional temperature gradient at the wall. Via Fourier's law, this gradient directly links to the dimensional wall heat flux. The result is expressed through a Nusselt number that scales with $\sqrt{\mathrm{Re}_x}$ and depends on Pr through the term $\theta'(0)$, as

$$\mathrm{Nu}_x = \frac{hx}{k} = \frac{\theta'(0)}{\sqrt{2}}\, \mathrm{Re}_x^{1/2} \ . \tag{9.21}$$

Fixing the Reynolds number scaling, the model structure reduces to a relation of the form

$$\mathrm{Nu}_x \ / \ \mathrm{Re}_x^{1/2} = \frac{\theta'(0)}{\sqrt{2}} = f(\mathrm{Pr}) \ . \tag{9.22}$$

Thus, the core modeling task becomes to accurately correlate the wall temperature gradient $\theta'(0)$ as a function of the Prandtl number. As outlined in Sect. 5.2.1, a commonly used approximation is $\theta'(0)/\sqrt{2} \approx 0.332\ \mathrm{Pr}^{1/3}$, which is based on matching the behavior near $\mathrm{Pr} = 1$ and approximates the similarity solution with reasonable accuracy across moderate Pr values.

To enhance model accuracy and ensure consistency with asymptotic physical behavior, the modeling strategy adopted here proceeds by explicitly incorporating the limiting cases $\mathrm{Pr} \ll 1$ and $\mathrm{Pr} \gg 1$. In the limit $\mathrm{Pr} \to 0$, it is further assumed that the Peclet number remains large, that is $\mathrm{Pe} \gg 1$, so that lateral heat conduction term in the energy equation can be neglected (Kays et al. 2005; Weigand 2015). Closed-form asymptotic solutions are first derived under appropriate simplifications of the boundary layer profiles. Based on these, surrogate models are constructed using analytical ansatz functions whose parameters are informed by physical reasoning and curve-fitted using high-resolution numerical data. This approach preserves the interpretability and scaling properties of a white-box model while achieving the flexibility and precision typically

associated with data-informed models, thus providing a representative example of a light-gray-box approach.

9.3.1 Numerical Solution and Classical Correlation

As outlined in Sect. 5.2.1, data points for $\theta'(0)$ can be obtained either by numerically evaluating the integral in Eq. (5.83) or by solving the extended boundary layer ODE system. In the present case, the latter approach is applied. The considered Prandtl number range $1 \times 10^{-3} \leq \mathrm{Pr} \leq 1 \times 10^{3}$ is discretized into approximately 80 values distributed on a logarithmic scale to ensure adequate resolution across the entire domain. For each Prandtl number, the extended boundary layer system is solved numerically using a shooting method. The solution vector is defined as $\mathbf{y} = (f'', f', f, \theta', \theta)^\top$, and the integration domain is adjusted to satisfy the boundary condition $\theta(\infty) = 1$. This adjustment is especially important for low Prandtl numbers, where the thermal boundary layer becomes significantly thicker than the velocity boundary layer.

According to the Nusselt number formulation, the wall temperature gradient is normalized to $\theta'(0)/\sqrt{2}$. The top of Fig. 9.8 shows the computed values across the regarded Pr number range. For validation, reference data from Kays et al. (2005, p. 152) and White (1991, p. 241) are included and show agreement up to the reported digits. Also plotted is the classical correlation $\theta'(0)/\sqrt{2} \approx 0.332\ \mathrm{Pr}^{1/3}$, which was derived based on the solution behavior near $\mathrm{Pr} = 1$.

The lower part of Fig. 9.8 shows the relative deviation of this classical correlation from the numerical solution. The correlation and the dataset intersect near $\mathrm{Pr} \approx 1$, consistent with the underlying derivation. The fact that the error does not vanish exactly at this point reflects the rounding in the prefactor 0.332 of the correlation. As expected, deviations increase in the asymptotic regimes. At $\mathrm{Pr} = 1000$, the correlation underpredicts the wall gradient by approximately 2%. At the lower end, for $\mathrm{Pr} = 0.001$, the relative error increases significantly to an overprediction of nearly 90%. While the classical expression performs well near and above $\mathrm{Pr} \approx 1$, it fails to accurately capture the behavior for low Prandtl number fluids such as liquid metals. This motivates the development of a more general correlation that remains accurate across all regimes of interest.

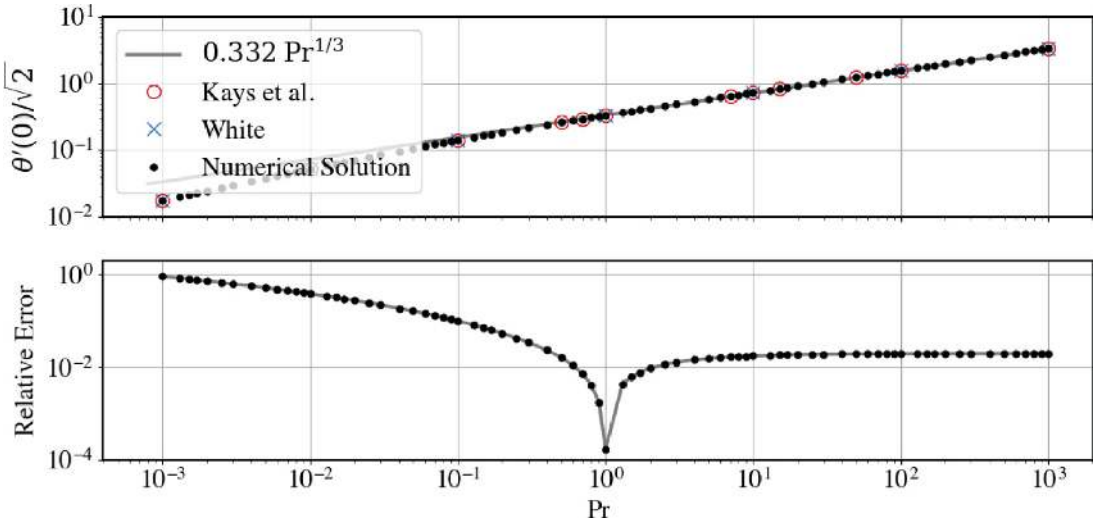


Fig. 9.8 Numerical solution of the wall temperature gradient $\theta'(0)/\sqrt{2}$ over the regarded Prandtl number range compared to the classical correlation $0.332\ \mathrm{Pr}^{1/3}$. Reference data from Kays et al. (2005, p. 152) and White (1991, p. 241) are included for validation (top). Relative deviation of the classical correlation from the numerical solution (bottom)

9.3.2 Asymptotic Behavior of Wall Temperature Gradient

Instead of relying on the classical correlation developed to match the similarity solution around $\mathrm{Pr}= 1$, we now consider the asymptotic behavior in the limits $\mathrm{Pr}\gg 1$ and $\mathrm{Pr}\ll 1$. As discussed in Sect. 4.3.1, the Prandtl number Pr expresses the ratio of momentum to thermal diffusivity, and thereby indicates the relative thickness of the velocity and thermal boundary layers. Specifically, for $\mathrm{Pr}\gg 1$ the thermal boundary layer is thinner than the velocity boundary layer, while for $\mathrm{Pr}\ll 1$ it becomes significantly thicker. This distinction by asymptotic regimes allows for simplified physical assumptions in each regime that can be leveraged to derive closed-form analytical expressions.

For $\mathrm{Pr}\gg 1$, the thermal boundary layer develops entirely within the inner region of the velocity boundary layer. In this regime, the velocity profile can be approximated as linear over the thickness of the thermal boundary layer. From the Blasius solution, the velocity gradient at the wall is $f''(0) \approx 0.46960$ (see Sect. 5.2.1), which corresponds to a stream function of the form $f(\eta) = 0.4696\eta^2/2$ in the thermal layer. Substituting this approximation into the energy Eq. (5.79), the resulting ODE can be solved directly, leading to the closed-form expression (Kays et al. 2005, p. 153)

$$\frac{\mathrm{Nu}_x}{\mathrm{Re}_x^{1/2}} = 0.339 Pr^{1/3} \quad \text{for } \mathrm{Pr}\gg 1\ . \tag{9.23}$$

For $\mathrm{Pr}\ll 1$, the thermal boundary layer extends far beyond the velocity boundary layer. In this case, the velocity is approximately equal to the free-stream velocity throughout the thermal boundary layer, implying $f' = 1$ across the domain of interest. Substituting into the differentiated form of the energy equation and applying the additional boundary condition $\theta''(0) = 0$, as shown by Kays et al. (2005, p.153), leads to a solvable ODE of the form $(g''/g')' + \mathrm{Pr}= 0$. After triple integration, the closed-form solution is

(9.24)

$$\frac{\mathrm{Nu}_x}{\mathrm{Re}_x^{1/2}} = 0.565 Pr^{1/2} \quad \text{for } \mathrm{Pr} \ll 1 \ .$$

For large Prandtl numbers, the asymptotic result in Eq. (9.23) is close to the classical correlation and differs mainly in the prefactor. However, the asymptotic slope in the low Pr regime is steeper, with an exponent of $n = 1/2$ instead of $n = 1/3$. Figure 9.9 shows both asymptotic approximations plotted against the numerical data, with their relative deviations shown in the lower panel. For $\mathrm{Pr} = 100$ to 1000, the $\mathrm{Pr} \gg 1$ asymptote agrees within 0.1% error and remains within 10% down to about $\mathrm{Pr} = 0.1$. Conversely, the $\mathrm{Pr} \ll 1$ asymptote shows a deviation of about 3% at $\mathrm{Pr} = 0.001$, which increases gradually to about 10% at $\mathrm{Pr} = 0.01$.

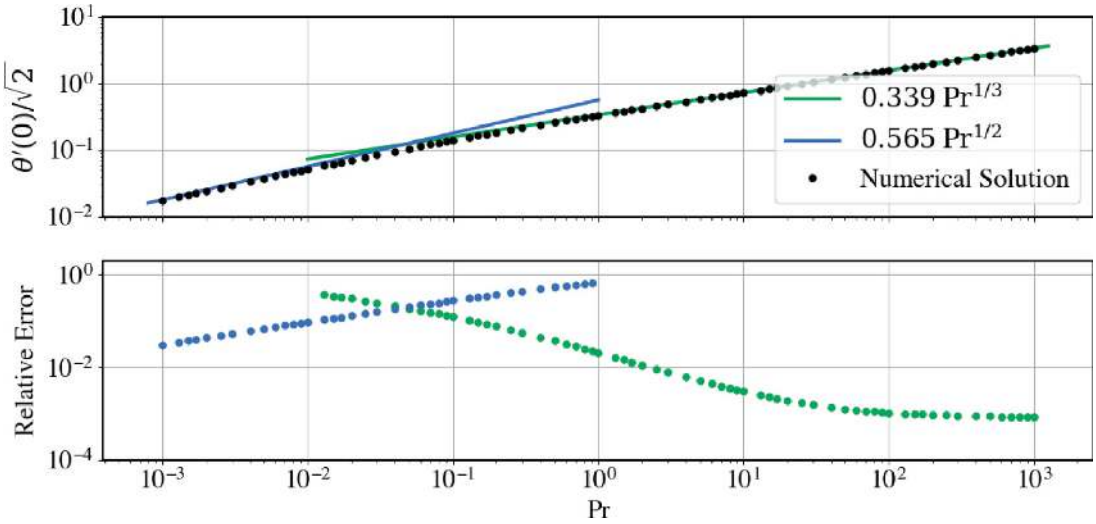


Fig. 9.9 Comparison of asymptotic approximations for $\mathrm{Pr} \gg 1$ and $\mathrm{Pr} \ll 1$ against numerical data (top). Relative deviation of the asymptotes from the numerical solution (bottom)

9.3.3 Extending Asymptotic Limits Into a Unified Correlation

To describe the entire regarded range of Prandtl numbers, a natural idea is to construct a blending function that transitions smoothly between the two asymptotic approximations given in Eqs. (9.24) and (9.23). However, this direct approach proves too stiff to achieve the desired accuracy across multiple decades in Pr. Instead, we model the power-law exponent directly, allowing for a smooth and physically consistent transition between the asymptotic limits.

Since both the Prandtl number and the wall gradient $\theta'(0)/\sqrt{2}$ span several orders of magnitude, the modeling is performed in double-logarithmic space. In this representation, the slope of the curve corresponds to the exponent of a power-law relation. The objective is therefore to construct a smooth transition of this exponent n from $n = 1/2$ for $\mathrm{Pr} \ll 1$ to $n = 1/3$ for $\mathrm{Pr} \gg 1$. To extract the slope, the logarithm to base 10 is applied to both axes, and the local exponent is computed using central differences. The resulting values of n are shown in Fig. 9.10, along with the asymptotic limits $n = 1/2$ and $n = 1/3$ as references. The numerical slope confirms what was already suggested by the deviations in Fig. 9.9. Over the range $\mathrm{Pr} = 10$–1000, the slope

remains close to $1/3$ and then gradually transitions toward $1/2$ as Pr decreases. However, the limit $n = 1/2$ is not fully reached within the regarded range, which reflects the slower convergence in the low Prandtl regime.

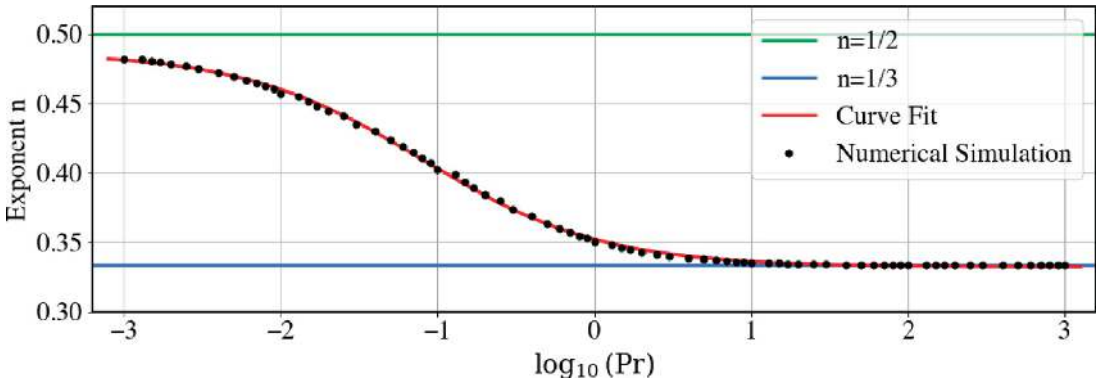


Fig. 9.10 Power-law exponents computed from double-logarithmic slope of $\theta'(0)/\sqrt{2}$ over Pr with asymptotic limits $n = 1/2$ for $\mathrm{Pr} \ll 1$ and $n = 1/3$ for $\mathrm{Pr} \gg 1$

To model the smooth transition of the exponent n $\log\,(\mathrm{Pr})$, a scaled logistic function is employed,

$$h(x) = a + \frac{b}{1+\exp(-(cx+d))} \ , \tag{9.25}$$

where $x = \log\,(\mathrm{Pr})$. This form corresponds to a sigmoid function scaled by *b* and vertically shifted by *a*. As introduced in Sect. 8.2, the parameters *c* and *d* govern the steepness and horizontal shift of the transition. In the limit $x \to -\infty$, the function approaches *a*, and for $x \to \infty$, it approaches $a + b$. Given the desired asymptotic behavior, we expect $a \approx 1/2$ and $a + b \approx 1/3$, implying $b \approx -1/6$. Fitting the logistic form to the computed slope yields the parameters $(a = 0.487, b = -0.154, c = 1.736, d = 1.904)$, which are also shown in Fig. 9.10. The resulting curve accurately reproduces the observed slope transition and aligns with the expected asymptotic values.

To reconstruct the modeled temperature gradient, the fitted slope is integrated to obtain the corresponding logarithmic expression for $\theta'(0)/\sqrt{2}$ to

$$H(x) = ax + \frac{b}{c}\,\log\,(1+\,\exp\,(d+cx)) + e \ , \tag{9.26}$$

where *e* is an integration constant that shifts the curve vertically. For the fitted case, $e = -0.298$ is selected to match the curve mean. Here again, *x* represents $\log\,(\mathrm{Pr})$. To revert to the original scale, the prediction is expressed as $\theta'(0)/\sqrt{2} = 10^{H(\log(\mathrm{Pr}))}$.

The resulting model is evaluated in Fig. 9.11, which shows the predicted wall gradients alongside the numerical data and includes both train and test datasets. The training set corresponds to the original dataset introduced earlier, based on the range $1 \times 10^{-3} \ \leq \mathrm{Pr} \leq 1 \times 10^{3}$, and is used for the curve fit. To assess extrapolation and

generalization, a new test set is created in the same manner but extends the range to $1 \times 10^{-4} \leq \mathrm{Pr} \leq 1 \times 10^{4}$, and is discretized into approximately 100 logarithmically spaced points that differ from those in the training set. For $1 \times 10^{-3} \leq \mathrm{Pr} \leq 1 \times 10^{3}$, the relative error remains below 0.2% on both the training and test sets. In the extended range, the error approaches 1% only at the lowest point $\mathrm{Pr} = 1 \times 10^{-4}$, which can be attributed to the fitted value of *a*. If needed, this parameter can be further adjusted or fixed based on the known asymptotic limits.

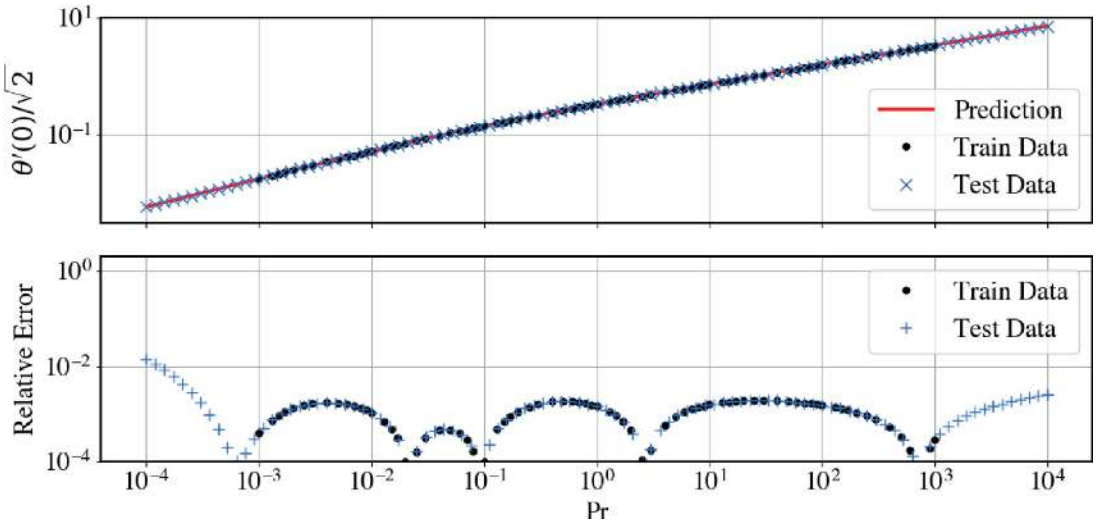


Fig. 9.11 Comparison of fitted model with training and extended test data for $\theta'(0)/\sqrt{2}$ over Pr (top). Relative deviation between model and data (bottom)

9.4 Impact of a Drop on a Wetted Surface

This example explores the fluid dynamics of droplet impacts on wetted surfaces, a phenomenon relevant in a wide range of technical applications such as fuel injection, surface cooling, spray coating, as well as wall-bounded spray flows in general. Since the early experimental studies by Worthington (1908), this topic has attracted extensive attention across experimental, numerical, and theoretical domains. Despite these efforts, a generally applicable predictive description of drop impact outcomes is not yet available. Key distinctions include single versus multiple droplet impacts, dry versus wetted targets, and the presence or absence of heat transfer (Ashgriz 2011; Yarin 2006; Moreira et al. 2010).

The present modeling effort follows the framework introduced in Sects. 1.1.2. The **purpose** here is to develop a model that predicts the splashing threshold for droplet impacts on wetted surfaces, supporting the simulation of turbomachinery components exposed to spray ingestion. The **objective** is to provide a closure model that captures the onset of splashing in a form that is both physically interpretable and computationally efficient, enabling its integration into engineering flow solvers. The **strategy** adopted combines prior knowledge from fluid dynamics, scaling laws, and conservation principles

with data generated through high-fidelity direct numerical simulations (DNS), forming a representative example of a light-gray-box hybrid modeling approach.

This example focuses on single droplet impacts onto thin liquid films without heat transfer. Of particular interest is the so-called splashing threshold, which separates impacts that result in smooth deposition from those that lead to secondary droplet ejection. The splashing threshold depends on the interplay of inertial, viscous, and capillary forces. A hybrid approach combining theoretically grounded parameters and DNS is applied to infer model coefficients.

The simulation campaign systematically varies droplet diameter, impact velocity, and film thickness to characterize the splashing threshold for conditions relevant to the technical application of spray ingestion in stationary gas turbines. As described in detail in Gomaa (2014), water injection into stationary gas turbines can be used to temporarily increase power output, for example helping to balance electricity grid fluctuations. As the injected water evaporates through the compressor it cools the flow and reduces the required compression work which boosts net power by up to 12%. However, spray droplets can impact compressor blades forming a wall film and causing liquid backsplash into the flow which can lead to erosion damage. To accurately simulate these processes in flow solvers simple and efficient models are needed that capture the key droplet dynamics and liquid film interactions without excessive computational cost. Here the partial process aspect of a splashing limit is considered, as described below. The aim is to provide a physics-based closure model for wall impact phenomena that captures the splashing onset and bridges fundamental understanding and engineering application.

Despite progress in theoretical understanding, a fully resolved physically grounded model for splashing does not exist. For example, theoretical models for droplet impact, such as the inviscid and capillary-free framework by Yarin and Weiss (1995), provide analytical insights into the lamella dynamics and crown formation. These models are extended to include viscous effects (Trujillo and Lee 2001), oblique impacts (Roisman and Tropea 2002), and thin sheet ejection (Thoroddsen 2002), but do not yet offer a generalized predictive model for the onset of splashing or the generation of secondary droplets. Most practical approaches are either empirical, correlating spray impact data to specific outcomes, or assume independence of individual droplet impacts. While the former are limited in generalizability, the latter ignore inter-droplet interactions. This motivates the present modeling effort, which seeks to evaluate single droplet impacts on thin films under well-controlled conditions and to develop a parameterized model based on DNS results.

9.4.1 Physics and Dimensional Analysis of Splashing

The conditions of a normal impact are mainly determined by the droplet diameter d, the velocity at impact v and the thickness of the liquid film h, as illustrated in Fig. 9.12. These variables can be expressed using nondimensional numbers that capture the balance of forces during impact. The initial state is typically described by the Weber number, Ohnesorge number, nondimensional film thickness and Reynolds number

(9.27)

$$\mathrm{We}=\frac{\rho_L v^2 d}{\sigma}\,,\qquad \mathrm{Oh}=\frac{\mu_L}{\sqrt{\rho_L d\sigma}}\,,\qquad \delta=\frac{h}{d}\,,\qquad \mathrm{Re}=\frac{\rho_L d v}{\mu_L}=\frac{\sqrt{\mathrm{We}}}{\mathrm{Oh}}\,.$$

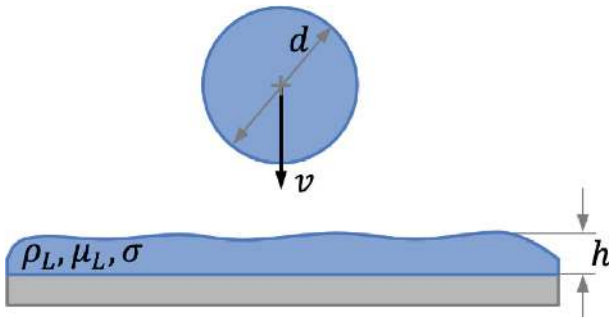


Fig. 9.12 Schematic of a single droplet impacting a thin liquid film on a wetted surface

The impact process evolves over a characteristic nondimensional time $T = tv/d$ starting from the instant the droplet makes contact with the film. The outcome depends on the interaction between inertia, viscosity and surface tension. At lower impact momentum the droplet simply merges with the film in a process referred to as **deposition**. When the momentum is sufficiently high the impact may produce a crown and the ejection of secondary droplets which defines the **splashing** regime.

The sequence of events during splashing can be structured into distinct phases as described by Cossali et al. (1997). The initial stage features the impact itself and the outward motion of a thin lamella. If the impact momentum is large and the local viscosity is small enough a narrow sheet or neck, known as the ejecta sheet (Thoroddsen 2002), is launched that can break up into very fine secondary droplets referred to as prompt splash. The second stage is marked by the emergence of the crown and formation of a central cavity. The crown rim becomes unstable in the third stage generating fingers and cusps that lead to further droplet ejection. The final stage occurs as the crown collapses back onto the film. For thicker films the impact can also produce rebound effects in this phase.

To gain insight into the scaling of splashing it is useful to consider simplified conservation equations. Following Yarin and Weiss (1995), a one-dimensional height averaged formulation in cylindrical coordinates (r, ϕ) can describe the radial growth of the crown. Although this model neglects viscous and capillary contributions it serves to identify key variables for later correlation work. Following the curvilinear formulation from Appendix A with scale factors $h_1 = 1$, $h_2 = r$ and restricting to axisymmetry ($\partial/\partial\phi = 0$, $u_\phi = 0$) the mass and momentum balances with a crown source term q take the form

$$\frac{\partial(hr)}{\partial t}+\frac{\partial(hru)}{\partial r}=q\frac{\delta(r-r_C)}{2\pi}\,,$$

(9.28)

$$\rho_L\left(\frac{\partial(hru)}{\partial t}+\frac{\partial(hru^2)}{\partial r}\right)=-\mu_L r\frac{\partial u}{\partial n}+\sigma r\frac{\partial}{\partial r}\left(h\frac{\partial^2 h}{\partial r^2}\right)+\rho_L uq\frac{\delta(r-r_C)}{2\pi}\ .$$

For splashing to occur inertial forces must strongly outweigh viscous and capillary forces. A dimensional estimate of the relevant balance can be obtained from the momentum equation. The inertial term scales with $\rho_L dv^2$. The viscous contribution scales as $\mu_L dv/h_\mu$ where h_μ is a characteristic viscous length. The surface tension term scales as $\sigma h^2/d^2$. Following the reasoning of Pasandideh Fard et al. (1996) the viscous length is of order $h_\mu \sim d/\sqrt{\mathrm{Re}}$ based on similarity to a stagnation-point boundary layer. The resulting condition $1 \gg \frac{1}{\sqrt{\mathrm{Re}}}+\frac{\delta^2}{\mathrm{We}}$ leads to $\mathrm{We}\sqrt{\mathrm{Re}} \gg \delta^2$ which defines a **dimensionless impact factor**

$$K=\sqrt{\mathrm{We}\sqrt{\mathrm{Re}}}>\delta\ . \tag{9.29}$$

This group K provides a useful measure for the transition between deposition and splashing. In the literature, similar combinations of We, Re or Oh are used to describe splashing onset (Mundo et al. 1998; Cossali et al. 1997; Josserand and Zaleski 2003). The threshold is often written as $K > K_{\mathrm{crit}}$ where K_{crit} denotes a critical value depending on conditions. Equivalent threshold conditions appear in alternative forms, such as raising both sides of the expression to the power $8/5$ resulting in the frequently used $K^{8/5}=\mathrm{WeOh}^{-2/5}$ (Cossali et al. 1997; Mundo et al. 1995; Yarin and Weiss 1995). These expressions are mathematically equivalent, differing only by algebraic rearrangement, and reflect the same underlying scaling among inertial, viscous, and surface tension effects.

When K is below the threshold, deposition occurs while splashing is expected above it. For thin films the threshold K_{crit} depends mainly on δ and increases roughly linearly as the film becomes thicker. This means higher impact momentum is needed to produce splashing as δ increases though the relationship holds only for thin films. A comprehensive overview of thresholds under various conditions is given by Moreira et al. (2010). Of particular relevance are the experiments of Cossali et al. (1997) who studied millimetric droplets impacting films of varying thickness and viscosity. Their data span $200 \leq \mathrm{We} \leq 1600$, $2.2\times10^{-3} \leq \mathrm{Oh} \leq 0.141$ and $0.08 \leq \delta \leq 1$. They proposed the correlation

$$K_{\mathrm{crit}}^{8/5}=2100\,.+5880\,.\,\delta^{1.44}\ . \tag{9.30}$$

This relation aligns with prior studies on individual film thicknesses (Walzel 1980; Yarin and Weiss 1995). As the film thickness δ approaches zero the threshold reduces to values consistent with dry wall impacts (Coghe et al. 1994; Mundo et al. 1995; Stow and Hadfield 1981) where surface roughness plays a key role and K_{crit} lies between 50 and 140. The upper end corresponds to smooth surfaces which are less prone to splashing.

The present numerical investigation aims to capture the small-scale dynamics associated with splashing and to determine the splashing threshold for conditions

representative of spray ingestion in gas turbines. The parameter space explored includes droplet diameters from 10 to 100 µm, impact velocities up to 150 m/s and nondimensional film thicknesses in the range $0.1 \leq \delta \leq 1.0$. The corresponding kinematic conditions span Weber numbers up to $\mathrm{We} \leq 3.1 \times 10^4$ and Ohnesorge numbers between $9.4 \times 10^{-3} \leq \mathrm{Oh} \leq 3 \times 10^{-2}$. Compressibility effects are negligible at the scales relevant to this study. Following the argument of Weiss and Yarin (1999), compressibility becomes significant only at spatial and temporal scales far smaller than those of interest. Therefore, it is appropriate to consider incompressible flows in this context, and the numerical code FS3D, which is designed for incompressible multiphase flows, is well suited for the simulations presented here and is briefly introduced in the following.

9.4.2 DNS-Based Data Generation

The numerical investigation is conducted using the research code Free Surface 3D (FS3D) developed at the Institute of Aerospace Thermodynamics at the University of Stuttgart for simulating free-surface multiphase flows involving incompressible and immiscible fluids. The governing Navier-Stokes equations are solved using direct numerical simulation to achieve high accuracy with minimal reliance on subscale models. The approach employs fine spatial resolution to resolve small-scale structures such as liquid ligaments and turbulent fluctuations. The governing equations solved in FS3D are the incompressible Navier-Stokes equations with constant material properties in each phase. Since heat transfer and evaporation are not part of the present study, the energy equation is omitted although FS3D includes capabilities for such processes. The simulations focus on mass and momentum conservation formulated in a single field representation. Surface tension is modeled as a volume force using the Continuum Surface Stress method (Lafaurie et al. 1994) in which the capillary force is written as the divergence of a stress tensor. The surface tension coefficient is assumed constant along the interface. The interface between liquid and gas is tracked using the Volume of Fluid method (Hirt and Nichols 1981) with Piecewise Linear Interface Calculation reconstruction Rider and Kothe (1998) to maintain a sharp interface. The conservation equations are discretized using second-order finite volume methods on a staggered Cartesian grid. Advection terms are treated with upwind Godunov schemes, while diffusive terms are approximated by second-order central differences. The momentum equations are integrated in two steps following the projection method. The velocity field is first advanced without the pressure gradient then corrected by solving a Poisson equation for pressure using a multigrid solver with Red-Black Gauss-Seidel smoothing (Rieber 2004). FS3D has been applied to simulate and validate a wide range of multiphase dynamic processes (Eisenschmidt et al. 2016; Ertl et al. 2013; Gomaa et al. 2010, 2011; Roth et al. 2010). Specifically for droplet wall impact the numerical results have been validated by comparison to experimental evidence as shown in Geppert et al. (2014), Gomaa (2014), Rieber and Frohn (1999).

Simulation Campaign and Data Generation The simulation campaign systematically varies droplet diameter, impact velocity, and film thickness to map the splashing threshold for conditions representative of spray ingestion in gas turbines. The

droplet diameters range from 10 to 100 µm, impact velocities reach up to 150 m/s, and nondimensional film thicknesses δ vary between 0.1 and 1.0. All simulations are carried out for water as the liquid. The use of nondimensional numbers in presenting the results does not imply validity for other liquids, but is adopted here for convenience in modeling and interpretation. The computational domain represents a liquid droplet impacting normally onto a solid surface covered by a water film, with quiescent air as the surrounding gas phase. To reduce computational effort, symmetry in two planes is exploited so that only one-quarter of the domain is simulated. The solid surface is modeled as no-slip, and zero-gradient open boundaries are applied at the remaining sides.

The base domain extends $5d$ in each direction. For thicker films where δ approaches unity, the domain is enlarged to $10d$ to fully capture crown dynamics. The standard grid uses 128 cells per direction, with refinement concentrated near the liquid film and wall to resolve the key dynamics. Outer regions that do not influence the outcome are coarsened to reduce computational cost. This setup resolves the droplet diameter with about 50 cells near the impact area, corresponding to a typical local cell size of $0.02d$. For larger domains, the relative resolution decreases by about a factor of two. Simulations are run until the crown evolution is complete, which corresponds to nondimensional times between $T = 15$ and $T = 250$ depending on impact conditions.

For the formulation of the splashing threshold, the **critical velocity** that distinguishes deposition from splashing for different combinations of droplet diameter d and film thickness δ needs to be determined. The parameter space is defined by a grid of ten droplet diameters and six film thicknesses. For each combination, the critical velocity is identified through an iterative algorithm that automatically sets up simulations at varying impact velocities and evaluates the outcome based on the amount of disintegrated liquid. Using nested intervals, the critical velocity is successively refined, typically requiring about ten simulations per parameter combination. An initial automatic labeling classifies the outcome as splashing or deposition. However, because it is difficult to define a distinct numerical criterion for splashing and the overall topology must be assessed, the final classification and determination of the critical velocity are performed manually for each case once the narrowed velocity range has been simulated. The overall parameter variation comprises about 600 direct numerical simulations, yielding 60 data points for correlation of the critical velocity. These results form the basis for the model development in the following.

9.4.3 Hybrid Correlation Development for Splashing Onset

The critical velocities for the 60 correlation points at different droplet diameters at various wall film thicknesses are shown in Fig. 9.13. For each wall thickness, the critical velocity decreases as the droplet diameter increases, which is intuitive since larger droplets have greater momentum. This relationship aligns well with the dimensional argument introduced in the previous section for the impact factor *K*. When analyzing the data in a double-logarithmic plot, the slope is approximately -0.58, which is consistent with the scaling $v_{\mathrm{crit}} \sim d^{-3/5}$ derived from the impact factor *K*. This scaling is used in

Fig. 9.13 to connect the data points for each δ, and the agreement supports the use of K to capture the underlying relation between v_{crit} and d. The figure also illustrates that, as the film thickness increases, the required impact velocity for splashing generally rises.

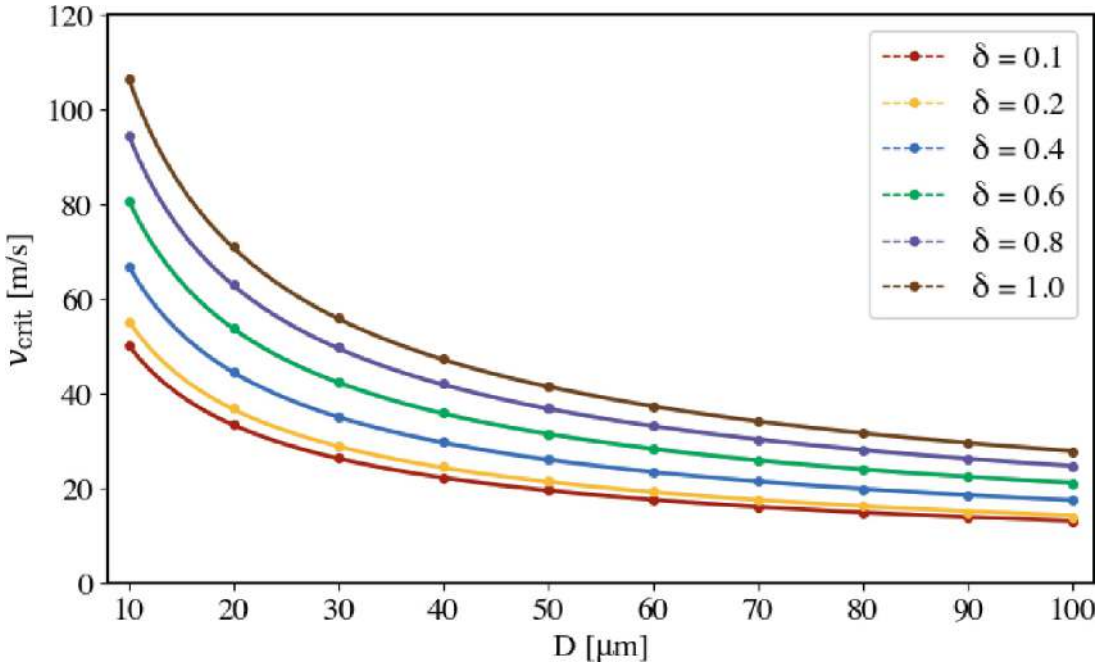


Fig. 9.13 Critical velocity as a function of droplet diameter for different film thicknesses

By applying the impact factor K as a relation between velocity and diameter, the dimensionality of the parameter space is reduced. This is illustrated in Fig. 9.14, where $1/\ \mathrm{Oh}^2$ is used as a proxy for the droplet diameter for comparability with Fig. 9.13. With this formulation, we implicitly assume that for a given film thickness the critical impact factor K_{crit} is constant. The data demonstrate that this is a reasonable approximation, although deviations from the constant value are evident and increase as conditions vary. These deviations reflect the limitations of K in fully collapsing the parameter space.

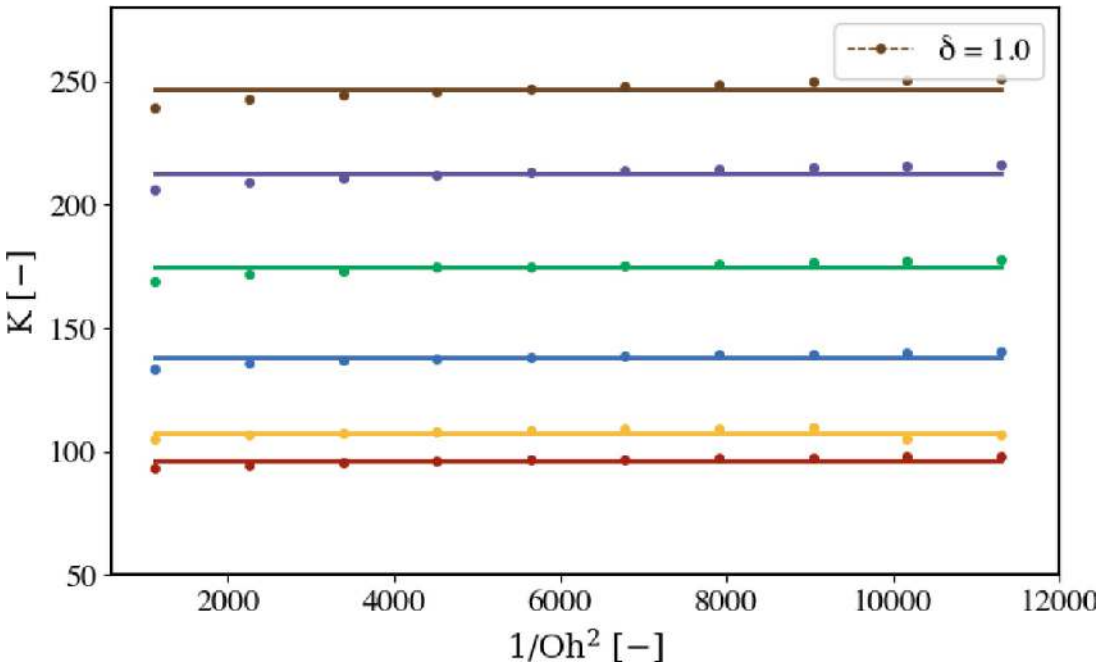


Fig. 9.14 Critical impact factor K over $1/\ \mathrm{Oh}^2$ for different film thicknesses

The good overall agreement between the simulation results and this nondimensional formulation justifies proposing a simple model hypothesis of the form $K_{\mathrm{crit}} = f(\delta)$. Since no data are available for $\delta \to 0$, the range for dry wall impacts discussed earlier, that is $50 < K_{\mathrm{crit}} < 140$, provides guidance. A power-law expression is applied to fit the data, yielding the correlation (Gomaa 2014) to

$$K_{\mathrm{crit}} = 85 + 163\delta^{1.2}\,. \tag{9.31}$$

The extrapolated limit for $\delta \to 0$ lies near the center of the surface roughness dependent range for dry walls. Although surface roughness is not explicitly included in this model, it is known that rougher surfaces lower the splashing threshold, while smoother surfaces correspond to the upper end of the range.

Figure 9.15 shows the simulation results alongside the proposed correlation and the expression from Cossali et al. (1997). For each film thickness, the predicted K_{crit} values match the simulation data well, supporting the suitability of the impact factor to describe the splashing threshold. However, a systematic offset of about $\Delta K \approx 30$ toward lower impact factors is observed when compared to the reference correlation. Several factors may contribute to this difference. From a numerical standpoint, insufficient resolution can cause premature lamella rupture, leading to an underestimation of the threshold (Gomaa 2014). On the experimental side, the reference data were obtained for millimetric droplets and more viscous glycerol mixtures, so exact similarity cannot necessarily be expected.

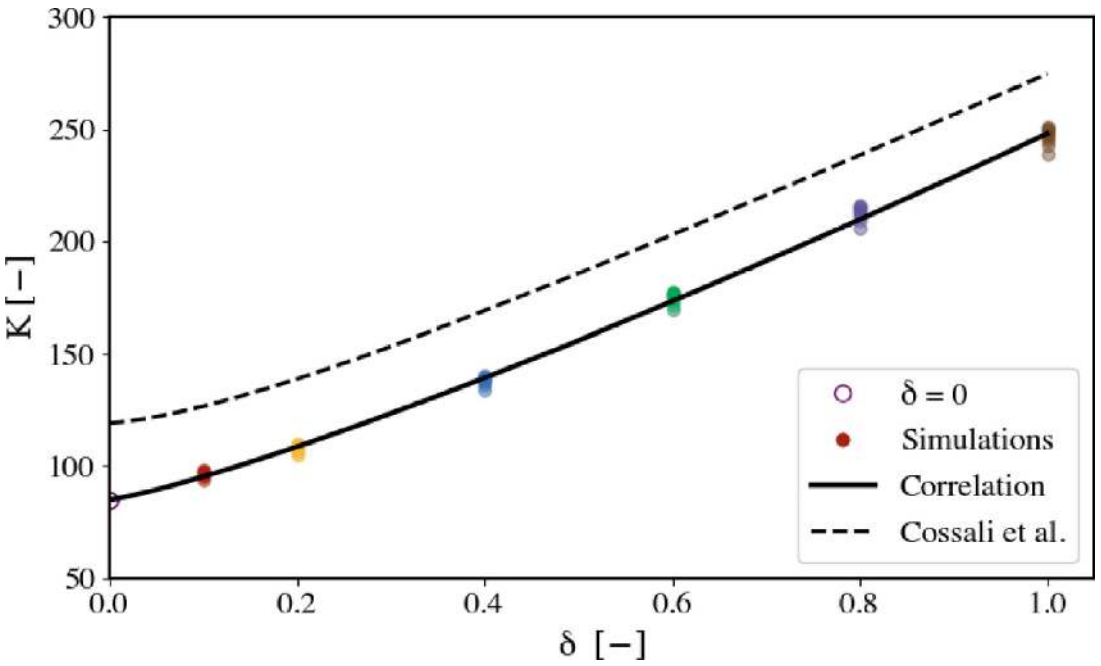


Fig. 9.15 Comparison of simulation results, proposed correlation, and reference expression from Cossali et al. (1997) in nondimensional form

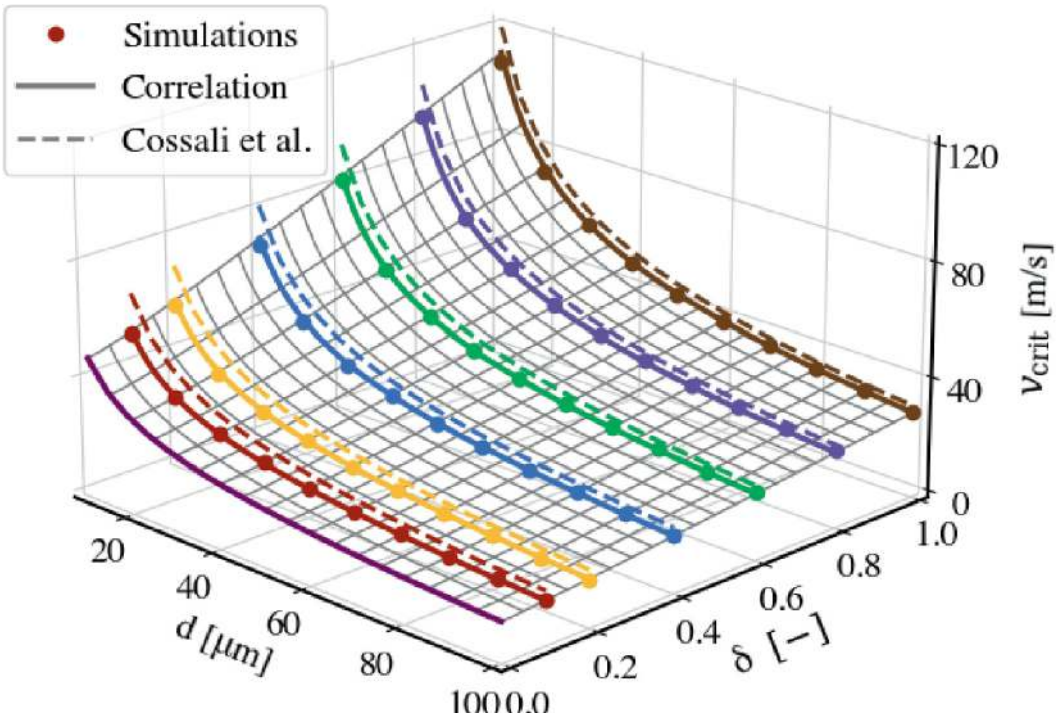


Fig. 9.16 Comparison of simulation results and correlation in dimensional form

Figure 9.16 presents the same comparison in dimensional form across the investigated parameter range. For clarity, the reference correlation is plotted only for selected film thicknesses. The difference between the correlation and the simulation results corresponds to a mean deviation of approximately 13%, with a maximum

deviation of about 20% at the smallest δ. Overall, these differences are within acceptable limits for engineering applications. The deviation is quantified using the normalized root-mean-square error

$$\mathrm{RMS}_x = \sqrt{\frac{1}{n}\sum_{i=1}^{n}\left(\frac{x_i^S - x_i^C}{x_i^S}\right)^2} \tag{9.32}$$

where x_i^S are the simulation results and x_i^C the corresponding values from the correlation for n cases. For the present data, this yields $\mathrm{RMS}_{K_{\mathrm{crit}}} = 0.02$, confirming the robustness of the proposed correlation.

9.5 Eddy Viscosity Turbulence Model

This example explores the use of data-driven approaches to improve eddy viscosity turbulence models, introduced in Sect. 4.2.5. The focus is on constructing a predictive surrogate for the eddy viscosity ν_t that enhances predictive capability beyond classical formulations while remaining compatible with established RANS frameworks. Classical eddy viscosity models are widely used in commercial CFD applications for their robustness and computational efficiency. However, they rely on the Boussinesq hypothesis and empirical coefficients, which are not universally valid and may fail in complex or anisotropic flow conditions. These structural limitations motivate the development of more flexible approaches that retain physical relevance.

As a canonical case, turbulent flow through a planar channel is considered. This configuration provides a well-defined and controlled setting in which high-fidelity DNS data is available for model development and evaluation. It offers a clear physical structure that facilitates the construction of input features and supports meaningful model validation. In the present example, we adopt a hybrid modeling strategy that combines physically motivated features with a data-driven mapping learned from DNS. No explicit hypothesis for the eddy viscosity is assumed. Instead, the closure is inferred directly from high-fidelity data using a regression model. The feature set is constructed from turbulence quantities grounded in dimensional reasoning, enabling transferability across Reynolds numbers, which is achieved by using normalized and physically interpretable input variables.

The model is trained on data from a single Reynolds number and is subsequently evaluated across a broader range to assess its generalization capabilities. This setup reflects the characteristics of a dark-gray-box model in which the inputs and physical context are well defined while the functional form of the closure is not specified analytically but learned from data. The objective is not to achieve optimal predictive performance but rather to demonstrate how physical understanding and data-driven techniques can be combined to support model development. Recent work has shown that realizable and scale-consistent data-driven closures can be constructed using modular regression strategies that infer individual model components (Mandler and Weigand

2022). At the same time, Mandler and Weigand (2024) highlight fundamental limits to the generalization of data-driven turbulence models across diverse flow regimes, particularly when models are tailored to specific phenomena. These findings underscore both the potential and the constraints of modeling approaches.

9.5.1 Optimal Eddy Viscosity from DNS

One step toward a data-informed turbulence model is the so-called concept of **optimal eddy viscosity** (Wu et al. 2018, 2019). As introduced in Sect. 4.2.5, linear eddy viscosity models are based on the Boussinesq hypothesis, which assumes that the turbulent stress tensor $\boldsymbol{\tau}_t$ is aligned with the mean strain rate tensor $\overline{\mathbf{S}}$. This assumption allows the turbulent stresses to be modeled in analogy to viscous stresses using a scalar eddy viscosity. Given a direct numerical simulation (DNS) result, the Boussinesq form can be used in reverse to determine the value of the eddy viscosity that best matches the true Reynolds stress field. This is done by projecting the exact Reynolds stress tensor obtained from DNS onto the mean strain rate tensor. The projection isolates the component of the stress that is aligned with the strain and returns the scalar eddy viscosity required to reproduce it. Mathematically, this leads to the relation

$$\boldsymbol{\tau}_t : \overline{\mathbf{S}} + \tfrac{2}{3} k \mathbf{I} : \overline{\mathbf{S}} = 2\nu_t \overline{\mathbf{S}} : \overline{\mathbf{S}} \ , \tag{9.33}$$

where the $:$ operator denotes the double scalar product of two tensors[1] yielding a scalar. For incompressible flow, the second term on the left-hand side vanishes identically since $\mathrm{tr}\,(\overline{\mathbf{S}}) = 0$, and the equation simplifies to

$$\nu_t^{\mathrm{opt}} = \tfrac{1}{2} \frac{\boldsymbol{\tau}_t : \overline{\mathbf{S}}}{\overline{\mathbf{S}} : \overline{\mathbf{S}}} = \tfrac{1}{2} \frac{\boldsymbol{\tau}_t : \overline{\mathbf{S}}}{|\overline{\mathbf{S}}|^2} \ . \tag{9.34}$$

This definition represents the optimal eddy viscosity in the sense that it reproduces the stress component aligned with the mean strain. It can also be expressed in terms of the production rate of turbulent kinetic energy P_k which describes the rate at which energy is transferred from the mean flow to turbulent fluctuations, resulting to

$$\nu_t^{\mathrm{opt}} = \tfrac{1}{2} \frac{P_k}{|\overline{\mathbf{S}}|^2} \ , \text{with } P_k = \boldsymbol{\tau}_t : \overline{\mathbf{S}} \ . \tag{9.35}$$

Although this approach yields an optimal eddy viscosity within the constraints of the Boussinesq hypothesis, it does not overcome its structural limitations, such as the inability to represent anisotropic stresses or non-aligned stress-strain relationships. It provides a best-case estimate for the eddy viscosity under the linear modeling assumption, and thus offers a valuable target for evaluating or calibrating turbulence models.

The model development proceeds in two conceptual steps referred to as **field inversion** and **inference**. Field inversion recovers a spatially resolved optimal eddy viscosity from high-fidelity data, while inference generalizes this field into a reusable

mapping defined over physically motivated input features. In the field inversion step, the spatial distribution of the optimal eddy viscosity is extracted from DNS data, as described above (Ling and Templeton 2015; Ling et al. 2016). However, this optimal viscosity field $\nu_t^{\text{opt}}(\mathbf{x})$ is known only at discrete spatial locations, is not transferable to other geometries, and cannot be computed during a RANS simulation without access to DNS data. Therefore, a second step is required. In the inference step, a surrogate model is trained to reproduce the optimal eddy viscosity as a continuous function of local flow features. This surrogate effectively replaces a traditional closure model with a data-informed functional relation. Unlike analytical closures, it is flexible enough to capture complex nonlinear dependencies embedded in the input features. The goal is to construct a mapping $h : \boldsymbol{\lambda}(\mathbf{x}) \rightarrow \nu_t^{\text{opt}}(\mathbf{x})$, where $\boldsymbol{\lambda}(\mathbf{x})$ denotes a vector of scalar input variables that can be computed from the mean flow within a RANS solver. This mapping enables general applicability across different flows without requiring DNS input. The chosen input features are physically motivated and reflect quantities commonly used in turbulence modeling. They include ratios of time scales, local gradients, and turbulence-related nondimensional groups. Table 9.1 presents a theoretically motivated set of such dimensionless quantities, providing a good starting point for inferring eddy viscosity in a physically consistent manner. While not exhaustive, the list serves as a practical basis for exploratory analysis, with each feature's relevance requiring careful assessment during the selection process.

Table 9.1 Raw input features $\boldsymbol{\lambda}_i$ used for eddy viscosity model inference

The input features listed in Table 9.1 are selected to balance physical interpretability and compatibility with established turbulence modeling practices. Most features are constructed from local mean flow quantities such as strain rate, rotation rate, turbulent kinetic energy, and dissipation-related time or length scales. These quantities are commonly available in standard RANS solvers and reflect core mechanisms of turbulence production, transport, and dissipation. All features are nondimensional and subsequently normalized to ensure numerical robustness and scale invariance during model inference. In the following, a selection of representative features is discussed in more detail to highlight their physical significance and modeling relevance.

The **specific dissipation rate** ω and the turbulent time scale τ appear in several feature expressions in Table 9.1. They are closely linked quantities that characterize the rate at which energy is transferred and dissipated in turbulent flows. Both arise naturally from the phenomenological description of the turbulent energy cascade described in Sect. 4.2.5, where kinetic energy injected at large scales cascades down to smaller eddies until it is dissipated at the Kolmogorov scale. In this cascade, the characteristic time over which energy is transferred from one scale to the next is given by $\tau^\star \sim k/\varepsilon$, where k is the turbulent kinetic energy and ε is the dissipation rate, described in Sect. 4.2.5. In the standard k–ω model, the specific dissipation rate ω is introduced as a primary variable that represents the rate of turbulent energy dissipation per unit kinetic energy. The

dissipation rate ε used in the energy cascade description can be related to ω through the modeled relation $\varepsilon = \beta^\star k\omega$ with $\beta^\star = 9/100$, a form consistent with the standard Wilcox formulation (Wilcox 2008). Substituting this into the definition of $\tau^\star$ yields

$$\tau^\star = \frac{k}{\varepsilon} = \frac{1}{0.09\,\omega} \quad . \tag{9.36}$$

This eddy turnover time appears in many feature expressions and underlies the classical eddy viscosity formulation $\nu_t = \beta^\star k\tau^\star = 0.09\,k^2/\varepsilon$. The interpretation of ω is discussed in the literature and is commonly associated with a characteristic turbulence frequency that reflects the rate at which energy-containing eddies decay and dissipate.

As described in Sect. 4.2.5, that picture changes near the end of the energy cascade. In the dissipation range, viscous effects dominate and the relevant dynamics are governed by the Kolmogorov time scale

$$\tau_K = 6.0\sqrt{\frac{\nu}{0.09\,k\,\omega}} \quad , \tag{9.37}$$

which reflects the lifetime of the smallest dynamically relevant eddies. To prevent the predicted turbulence scales from falling below the physically meaningful Kolmogorov limit (Durbin 1991; Menter et al. 2012; Weatheritt and Sandberg 2017), and to avoid overprediction of the eddy viscosity in such regions, a limiter is applied to $\tau^\star$ by enforcing

$$\tau = \frac{1}{0.09\,\omega}\ \max\left(1, \frac{\tau_K}{\tau^\star}\right) = \frac{1}{0.09\,\omega}\ \max\left(1, 6.0\sqrt{\frac{0.09\,\nu\,\omega}{k}}\right) \quad . \tag{9.38}$$

This ensures that τ transitions smoothly from an inertial-range turnover time to a dissipation-limited lifetime consistent with Kolmogorov's similarity hypothesis. The final time scale τ is then used to construct nondimensional features that remain robust across different turbulence regimes.

The rotation rate tensor $\mathbf{\Omega}$, introduced in Sect. 3.1.2, quantifies the local rigid-body-like rotation of fluid elements and appears in several feature expressions in Table 9.1. The three time scale ratios involving τ, $|\overline{\mathbf{S}}|$, and $|\overline{\mathbf{\Omega}}|$ offer important insight into the relative dominance of turbulence versus mean strain and rotation. The quantities $\tau|\overline{\mathbf{S}}|$ and $\tau|\overline{\mathbf{\Omega}}|$ measure how local mean deformation compares to the turbulence time scale, while the ratio $|\mathbf{S}|/|\mathbf{\Omega}|$ helps to identify strain-dominated versus vortical regions. Such quantities are useful for distinguishing flow topologies, especially in shear layers or near-wall regions.

The elliptic blending parameter φ accounts for wall effects that are not well captured by local turbulence quantities. In elliptic relaxation models, the parameter φ modulates the effective velocity scale, typically expressed as $u \sim \sqrt{\varphi\,k}$, to better capture turbulence suppression near solid boundaries, where k alone tends to overestimate turbulent activity. The last feature, labeled *SST model variable 2*, corresponds to the empirical expression $500\nu/(\omega y^2)$ used in the SST turbulence model to control the blending

between k–ω and k–ϵ formulations (Menter 1994). In this approach, a blending function is employed to transition smoothly from the k–ω model near the wall, where it performs well under strong shear and adverse pressure gradients, and to the k–ϵ model in the free-stream region, which is less sensitive to free-stream values of ω (Pope 2000).

9.5.2 DNS Data for Channel Flow

The simulation data is obtained from publicly available direct numerical simulation results of classical plane Poiseuille flow (Lab 2009), where a constant streamwise pressure gradient $\partial p/\partial x = \text{const.}$ drives the flow between two infinite parallel plates. The configuration corresponds to fully developed turbulent channel flow, as described in Sect. 5.3. The fluid is assumed incompressible, and the flow is statistically stationary and homogeneous in the streamwise and spanwise directions.

The computational domain employs periodic boundary conditions in the streamwise x- and spanwise z-directions, and no-slip conditions on the top and bottom channel walls. The incompressible Navier-Stokes and continuity equations are numerically solved using a finite difference scheme on a staggered grid. A fourth-order central difference scheme is used for spatial discretization in the streamwise and spanwise directions, while a second-order central difference scheme is applied in the wall-normal y-direction (Abe et al. 2001). Time integration of the viscous terms involving wall-normal derivatives is performed using a Crank-Nicolson scheme, while all remaining terms are advanced with a second-order Adams-Bashforth method (Seki et al. 2006; Kozuka et al. 2008).

The simulation is run in time until a statistically steady state is reached, as indicated by converged profiles of total shear stress and turbulent kinetic energy. Ensemble-averaged turbulence statistics are then collected over a sufficiently long period to ensure statistical convergence. The duration of averaging varies with the specific flow Reynolds number, with integration times corresponding to approximately 10 to 25 wash-out times based on the bulk velocity. The total averaging window spans from about 1300 to $14\,000$ nondimensional time units, where time is normalized by the viscous scale ν/u_τ^2, with $u_\tau = \sqrt{\tau_w/\rho}$ denoting the friction velocity based on the wall shear stress τ_w.

The dataset includes four configurations characterized by the friction Reynolds number $\mathrm{Re}_\tau = u_\tau (H/2)/\nu$, where H is the full channel height. For each case, the highest available spatial resolution (Lab 2009) is used. The computational domain size, mesh resolution, and corresponding bulk Reynolds number $\mathrm{Re}_{\mathrm{bulk}} = u_m H/\nu$ are listed in Table 9.2.

For each configuration, the dataset provides not only the mean velocity field and all components of the Reynolds stress tensor, but also a comprehensive set of turbulence statistics. These include wall-normal profiles of velocity fluctuations and Reynolds stress components, which are primarily used in the present study. In addition, the dataset includes detailed budgets of the transport equations for the turbulent stresses and turbulent kinetic energy, computed directly from the DNS fields. These budgets include contributions from production, dissipation, pressure-strain correlation, turbulent diffusion, molecular diffusion, and residual terms. This level of detail enables in-depth

analysis of turbulence dynamics and provides a valuable reference for the development and validation of turbulence models.

Table 9.2 DNS configurations used for model training and evaluation. All geometries are given in units of channel half-height $H/2$

Figure 9.17 presents wall-normal profiles of the normalized mean velocity, strain rate magnitude, and turbulent kinetic energy k over the half-channel height for four Reynolds numbers Re_τ. The mean velocity profiles are normalized by the maximum velocity at the channel centerline. They exhibit the classical shape of turbulent channel flow with a flattened core region and a sharp increase near the wall. As the Reynolds number increases, the wall-normal gradient of the velocity profile becomes steeper, indicating stronger wall shear and thinner near-wall layers. This trend reflects the enhanced momentum transport in the near-wall region consistent with the structure of wall-bounded turbulence discussed in Sect. 4.2.5.

The strain rate magnitude $|\overline{\mathbf{S}}^+|$, shown in wall units, corresponds to $|\overline{\mathbf{S}}^+| = |du^+/dy^+|/2$ for this flow configuration. It exhibits a pronounced peak near the wall, which intensifies with increasing Re_τ. The turbulent kinetic energy k vanishes at the wall due to the no-slip condition, which applies to both the mean and fluctuating velocity components. Moving away from the wall, k increases sharply and reaches a maximum near the wall. With increasing Reynolds number, this peak becomes sharper and shifts closer to the wall, reflecting a stronger concentration of turbulent energy in the near-wall region.

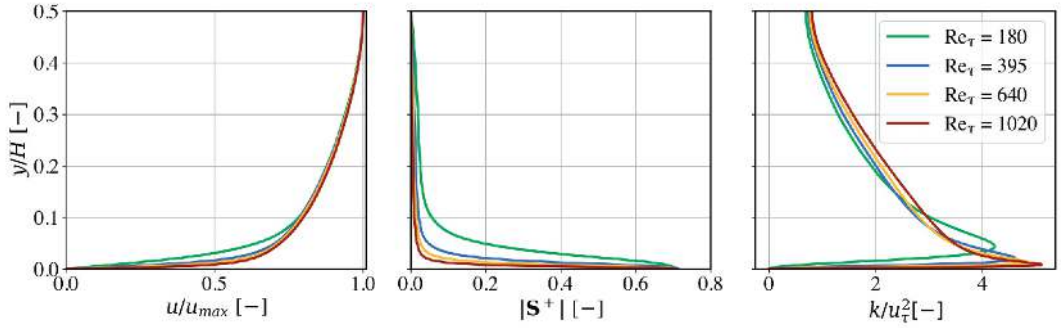


Fig. 9.17 Wall-normal profiles of mean velocity normalized by centerline velocity, strain rate magnitude $|\overline{\mathbf{S}}^+|$ in wall units, and turbulent kinetic energy k, shown for four Reynolds numbers Re_τ

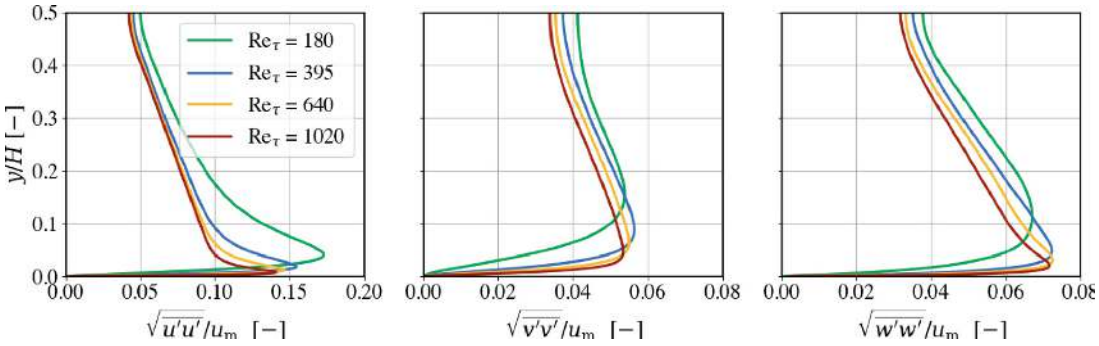


Fig. 9.18 RMS velocity fluctuations $\sqrt{\overline{u'^2}}$, $\sqrt{\overline{v'^2}}$, and $\sqrt{\overline{w'^2}}$ normalized by bulk velocity u_m. All quantities are plotted over the half-channel height for different Reynolds numbers Re_τ

Figure 9.18 shows the root-mean-square (RMS) velocity fluctuations in the streamwise $\sqrt{\overline{u'^2}}$, wall-normal $\sqrt{\overline{v'^2}}$, and spanwise $\sqrt{\overline{w'^2}}$ directions, all normalized by the bulk velocity u_m. All three fluctuation components vanish at the wall due to the no-slip condition and are symmetric about the channel centerline, resulting in zero wall-normal gradients at mid-height. The streamwise fluctuation $\sqrt{\overline{u'^2}}$ is the largest among the components, reaching around 15% of the bulk velocity. As it aligns with the main flow direction and is least constrained by the wall, it constitutes the dominant contribution to *k* and exhibits a spatial distribution similar to that of the turbulent kinetic energy. The wall-normal fluctuations $\sqrt{\overline{v'^2}}$ are directly impeded by the presence of the wall and reach their maximum farther from the wall than the streamwise or spanwise components with lower magnitude. The spanwise component $\sqrt{\overline{w'^2}}$ lies between the two in both magnitude and wall-normal location. Despite the nominally two-dimensional character of the mean flow, the presence of non-negligible spanwise fluctuations highlights the inherently three-dimensional nature of turbulence.

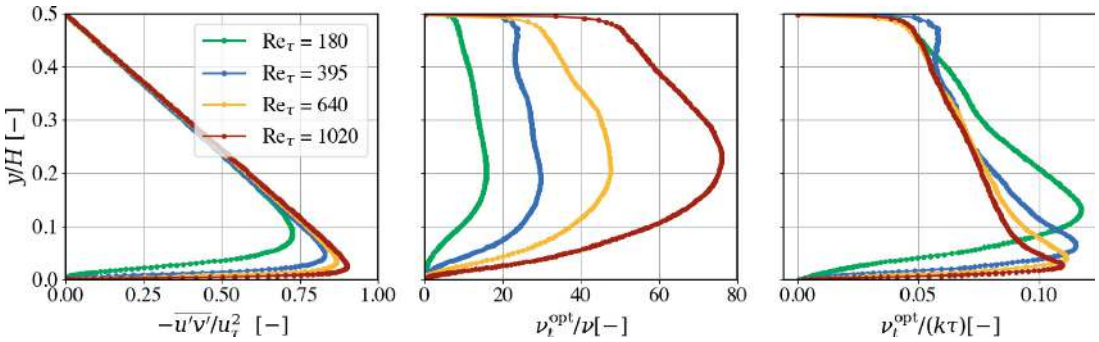


Fig. 9.19 Wall-normal profiles of Reynolds shear stress, optimal eddy viscosity, and normalized target quantity $\nu_t^{\mathrm{opt}}/(k\tau)$ for different Reynolds numbers Re_τ. Shear stress and eddy viscosity are normalized by wall units

For the present channel flow configuration, the mean velocity gradient is oriented in the wall-normal direction and the flow is primarily governed by shear. In this case, the Reynolds stress tensor simplifies, and the Boussinesq hypothesis reduces to a direct

relation between the shear stress and the mean strain. Accordingly, the optimal eddy viscosity becomes

$$\nu_t^{\mathrm{opt}} = \frac{1}{\sqrt{2}} \frac{\overline{u'v'}}{|\overline{\mathbf{S}}|} \ , \tag{9.39}$$

while the production term of turbulent kinetic energy simplifies to

$$P_k = \sqrt{2}\,|\overline{\mathbf{S}}|\,\overline{u'v'} \ . \tag{9.40}$$

As discussed in Sect. 4.2.5 and emphasized in Eq. (4.27), the Reynolds shear stress $-\overline{u'v'}$ plays a central role in RANS modeling. Figure 9.19 shows the wall-normal profiles of $-\overline{u'v'}/u_\tau^2$, the corresponding optimal eddy viscosity ν_t^{opt}/ν, and the normalized target variable $\nu_t^{\mathrm{opt}}/(k\tau)$ for the four Reynolds numbers. The shear stress $-\overline{u'v'}$ increases from zero at the wall, reaches a peak in the near-wall region, and vanishes at the centerline due to symmetry. The profile maintains a consistent shape across Reynolds numbers, although the peak magnitude increases and shifts toward the wall with increasing Re_τ.

The optimal eddy viscosity ν_t^{opt} exhibits its maximum around $y/H \approx 0.2$, and its magnitude increases significantly with Reynolds number. To reduce this sensitivity and improve generalization across flow regimes, a **normalized target variable** is introduced as

$$C_1 = \frac{\nu_t^{\mathrm{opt}}}{k\tau} \ , \tag{9.41}$$

which incorporates local turbulence scales to mitigate Reynolds dependence. As shown on the right of Fig. 9.19, the scaled profiles exhibit more consistent peak values across different Reynolds numbers. The normalization by $k\tau$ is physically motivated. As discussed earlier in this section, the eddy viscosity is commonly expressed in terms of the turbulent kinetic energy and a characteristic time scale through the relation $\nu_t \sim k\tau$. This scaling appears explicitly in standard models such as the k–ω formulation, where $\nu_t = \beta^\star k/\omega$ with $\beta^\star = 0.09$. While the location of the peak shifts slightly toward the channel interior with increasing Re_τ, the overall variation is significantly reduced. This improved consistency makes $\nu_t^{\mathrm{opt}}/(k\tau)$ a suitable modeling target for training our data-driven closure model.

9.5.3 Model Development and Evaluation

In the following, we present the development and evaluation of a data-informed surrogate model for the normalized eddy viscosity $\nu_t^{\mathrm{opt}}/(k\tau)$. The focus is on demonstrating the general modeling approach and assessing its qualitative performance. The objective is not to optimize the feature set, model complexity, or hyperparameters beyond what is required to illustrate the methodology.

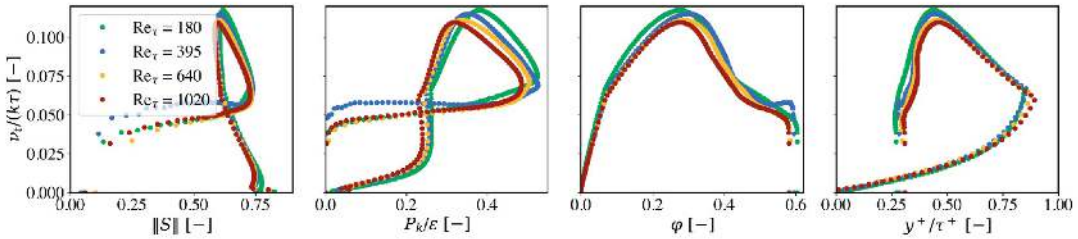


Fig. 9.20 Selected input features plotted against the normalized eddy viscosity target $\nu_t^{\text{opt}}/(k\tau)$ for all four Reynolds numbers Re_τ

Feature Selection In addition to the quantities directly available from the DNS dataset, several derived flow variables are computed to support the modeling and feature extraction process. These include the turbulent kinetic energy k and its gradient ∇k, the turbulent frequency ω, as well as the magnitudes of the mean strain rate tensor $|\overline{\mathbf{S}}|$ and the mean rotation rate tensor $|\overline{\mathbf{\Omega}}|$. These tensorial quantities are extracted from the local velocity gradient field according to their definitions given in Sect. 3.1.2. With these inputs, the raw feature set listed in Table 9.1 can be fully constructed from the DNS fields.

From this list, a subset of four features is manually selected for model development. The selection is based on the shape, spread, and distribution of the feature-target relationships, with the aim of representing the feature space in a physically diverse manner. The selected features are shown in Fig. 9.20, plotted against the normalized eddy viscosity target $\nu_t^{\text{opt}}/(k\tau)$. Each feature represents a distinct flow aspect, including local strain through $|\overline{\mathbf{S}}|$, turbulence production via the ratio $P_k\ /\varepsilon$, wall effects captured by the elliptic blending parameter φ, and the interaction between near-wall scaling and turbulence time scale expressed by y^+/τ.

All features are nondimensional and normalized across the dataset to ensure consistent scaling and numerical stability during model training. In selecting the subset, particular attention is given to the fact that these features exhibit qualitatively similar behavior across the regarded Reynolds number range. As seen in the plots, their distributions are largely similar, making them robust descriptors of turbulence mechanisms across flow regimes. Together, they exhibit meaningful correlation with the target variable across different Reynolds numbers. Individually, the features do not yield a unique mapping to the target, as their relationships are generally not bijective. This means that a single feature value can correspond to multiple different values of the target variable, depending on the flow context. However, taken together, they form a feature space that is sufficiently expressive to characterize the variability in the optimal eddy viscosity, and their joint variation supports the identification of nonlinear patterns required for constructing a robust regression model.

Model Training To develop a predictive surrogate for the normalized eddy viscosity $\nu_t^{\text{opt}}/(k\tau)$, a regularized polynomial regression model is employed. The training is performed exclusively on the highest Reynolds number dataset with $\text{Re}_\tau = 1020$, which inherently spans the widest range in wall units y^+ and turbulence time scale τ. This

ensures that the model is exposed to the broadest possible variability in flow conditions. Furthermore, as discussed earlier, restricting training to a single Reynolds number allows for a clear and controlled evaluation of model transferability by testing its performance on unseen Reynolds numbers.

Polynomial basis functions up to tenth order are initially considered to capture potential nonlinear dependencies in the feature-target relationship. To control model complexity and mitigate overfitting, Tikhonov regularization is applied. The regularization parameter λ is selected to balance predictive fidelity with smoothness of the solution by analyzing the trade-off between the training cost and the L_1 norm of the regression coefficients, as discussed in Sect. 8.1. Based on this analysis, a value of $\lambda = 10^{-2}$ is adopted. Further analysis shows that a second-order polynomial already captures the basic trends in the feature-target relationship and offers a reasonable approximation of the underlying behavior. However, to better resolve the distribution of the normalized eddy viscosity target $\nu_t^{\mathrm{opt}}/(k\tau)$, particularly in regions near the peak, a fourth-order polynomial is ultimately selected. This choice allows the model to represent localized variations more accurately while maintaining robustness and generalization across the domain. The final surrogate model thus applies a fourth-order polynomial in the selected four input features, resulting in a total of 17 regression coefficients.

Figure 9.21 compares the trained model against the DNS-based target for $\mathrm{Re}_\tau = 1020$. The results demonstrate that a fourth-order polynomial suffices to capture the main trends in the feature-target relationship. The trained model accurately reproduces the normalized eddy viscosity field, as evident from the close agreement between the predicted and target profiles. The model slightly underestimates the peak value of $\nu_t^{\mathrm{opt}}/(k\tau)$, indicating some local loss of resolution despite the higher-order basis. In the near-wall region, where local strain rates are high, the model predicts small negative values of eddy viscosity. Although numerically minor, these values are physically inadmissible, since eddy viscosity must remain non-negative. This outcome illustrates a typical limitation of unconstrained regression and points to the potential benefit of incorporating physical constraints or post-processing to enforce non-negativity.

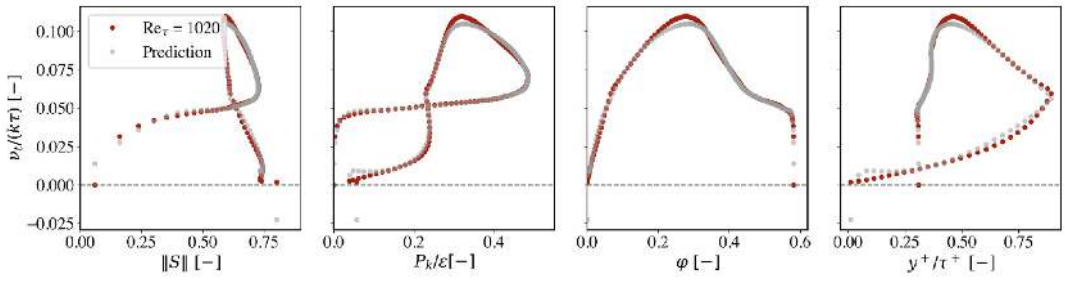


Fig. 9.21 Comparison of the predicted normalized eddy viscosity $\nu_t^{\mathrm{opt}}/(k\tau)$ from the fourth-order polynomial model with the DNS-based target for $\mathrm{Re}_\tau = 1020$

Evaluation The model is subsequently evaluated on the remaining DNS datasets for $\mathrm{Re}_\tau = 180, 395, 640, 1020$ to assess its generalization capabilities across the regarded

Reynolds number range. This evaluation is of particular interest, as the trained model relies on engineered and physically informed features to achieve Reynolds transferability. Figure 9.22 presents the predicted and DNS-derived profiles for the normalized eddy viscosity $\nu_t^{\text{opt}}/(k\tau)$, the nondimensional eddy viscosity ν_t^{opt}/ν, and the Reynolds shear stress $-\overline{u'v'}$, all shown over the channel half-height.

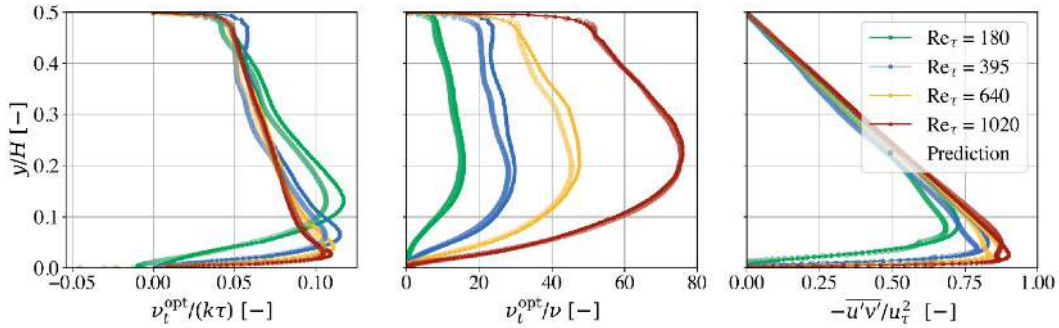


Fig. 9.22 Evaluation of the trained eddy viscosity model for $\mathrm{Re}_\tau = 180$, 395, 640, and 1020. Shown are the predicted and DNS-based profiles of the normalized eddy viscosity $\nu_t^{\text{opt}}/(k\tau)$, the nondimensional eddy viscosity ν_t^{opt}/ν, and the Reynolds shear stress $-\overline{u'v'}/u_\tau^2$ over the channel half-height

The normalized eddy viscosity profiles $\nu_t^{\text{opt}}/(k\tau)$ reveal that the near-wall peak is consistently underestimated, with this discrepancy becoming more pronounced at lower Reynolds numbers. Nonetheless, the predicted shift of the peak location toward the channel center as Reynolds number increases is captured well. Negative values of eddy viscosity are also observed near the wall. While small in magnitude, these values are physically meaningless and become even more prominent at lower Reynolds numbers. This behavior again highlights a limitation of the unconstrained regression model and must be critically addressed before applying the model in predictive settings.

The nondimensional eddy viscosity ν_t^{opt}/ν shows good agreement with DNS data for $\mathrm{Re}_\tau = 1020$ across the entire channel. For the lower Reynolds numbers, the model retains reasonable accuracy, although deviations become visible in the upper half of the channel, especially around $y/H \approx 0.3$ for $\mathrm{Re}_\tau = 395$ and 640. The distributions of the Reynolds shear stress $-\overline{u'v'}$ exhibit trends consistent with the previous observations. In particular, the peak magnitude is not fully captured, reflecting the model's tendency to underestimate turbulence production near the wall.

Of course, the results indicate potential areas for improvement, particularly in suppressing unphysical negative predictions of eddy viscosity near the wall and in resolving the peak magnitude of the target variable more accurately. Despite these limitations, the overall predictive performance remains fairly robust across the range of Reynolds numbers. The use of physically motivated features and normalization by $k\tau$ plays a central role in enabling this transferability. The evaluation results demonstrate that incorporating physical insight into the feature design and normalization process enhances the generalization capability of data-driven models. This hybrid modeling

approach offers a structured pathway to improve upon classical turbulence closures within their applicable regimes.

References

Abe H, Kawamura H, Matsuo Y (2001) Direct numerical simulation of a fully developed turbulent channel flow with respect to Reynolds number dependence. ASME J Fluids Eng 123:382–393
[https://doi.org/10.1115/1.1366680]

Ashgriz N (2011) Handbook of atomization and sprays: theory and applications, 1st edn. Springer

Coghe A, Cossali GE, Marengo M (1994) Single drop impingement on thin liquid film. In: Proceedings of the 2nd international conference on experimental fluid mechanics. Turin, Italy

Cossali GE, Coghe A, Marengo M (1997) The impact of a single drop on a wetted solid surface. Exp Fluids 22:463–472
[https://doi.org/10.1007/s003480050073]

Durbin PA (1991) Near-Wall turbulence closure modeling without "Damping Functions". Theoret Comput Fluid Dyn 3(1):1–13
[https://doi.org/10.1007/BF00271513]

Eisenschmidt K, Ertl M, Gomaa H, Kieffer-Roth C, Meister C, Rauschenberger P, Reitzle M, Schlottke K, Weigand B (2016) Direct numerical simulations for multiphase flows: an overview of the multiphase code FS3D. Appl Math Comput 272:508–517
[MathSciNet]

Ertl M, Roth N, Brenn G, Gomaa H, Weigand B (2013) Simulations and experiments on shape oscillations of Newtonian and Non-Newtonian liquid droplets. In: 25th European conference on liquid atomization and spray systems: ILASS Europe 2013

Geppert A, Gomaa H, Meister C, Lamanna G, Weigand B (2014) Droplet wall-film-interaction: impact morphology and splashing/deposition boundary of hyspin/N-hexadecane two-component system. In: ILASS Americas 26th

Gomaa H (2014) Modeling of liquid dynamics in spray laden compressor flows. Verlag Dr, Hut

Gomaa H, Kumar S, Huber C, Weigand B, Peters B (2011) Numerical comparison of 3D jet breakup using a compression scheme and an interface reconstruction based VOF-code. In: Proceedings ILASS-Europe

Gomaa H, Roth N, Schlottke J, Weigand B (2010) DNS calculations for the modeling of real industrial applications. Atom Sprays 20(4)

Hirt CW, Nichols BD (1981) Volume of Fluid (VOF) method for the boundaries of free surfaces. J Comput Phys 39:201–225
[https://doi.org/10.1016/0021-9991(81)90145-5]

Josserand C, Zaleski S (2003) Droplet splashing on a thin liquid film. Phys Fluids 15(6):1650–1657
[https://doi.org/10.1063/1.1572815]

Kawamura Lab (2025) DNS database of wall turbulence and heat transfer. www.rs.tus.ac.jp, 2009

Kays WM, Crawford ME, Weigand B (2005) Convective heat and mass transfer. McGraw-Hill Series in Mechanical Engineering. McGraw-Hill

Kozuka M, Seki Y, Kawamura H (2008) Direct numerical simulation of turbulent heat transfer with a high spatial resolution. In: Proceedings of the 7th international symposium on engineering turbulence modelling and measurements (ETMM7), vol 1, pp 163–168

Lafaurie B, Nardone C, Scardovelli R, Zaleski S, Zanetti G (1994) Modelling merging and fragmentation in multiphase flows with SURFER. J Comput Phys 113:134–147
[MathSciNet][https://doi.org/10.1006/jcph.1994.1123]

Ling J, Kurzawski A, Templeton J (2016) Reynolds averaged turbulence modelling using deep neural networks with embedded invariance. J Fluid Mech 807:155–166

[MathSciNet][https://doi.org/10.1017/jfm.2016.615]

Ling J, Templeton J (2015) Evaluation of machine learning algorithms for prediction of regions of high Reynolds averaged Navier Stokes uncertainty. Phys Fluids 27(8)

Mandler H, Weigand B (2024) Generalization limits of data-driven turbulence models. Flow, Turbulence and Combustion

Mandler H, Weigand B (2022) A realizable and scale-consistent data-driven non-linear eddy viscosity modeling framework for arbitrary regression algorithms. Int J Heat Fluid Flow 97

Menter FR, Garbaruk AV, Egorov Y (2012) Explicit algebraic Reynolds stress models for anisotropic wall-bounded flows. In: EUCASS Proceedings Series - advances in aeroSpace sciences, vol 3

Menter FR (1994) Two-equation Eddy-viscosity turbulence models for engineering applications. AIAA J 32(8):1598–1605 [https://doi.org/10.2514/3.12149]

Moreira ALN, Moita AS, Panao MR (2010) Advances and challenges in explaining fuel spray impingement: how much of single droplet impact research Is useful? Prog Energy Combust Sci 36(5):554–580 [https://doi.org/10.1016/j.pecs.2010.01.002]

Mundo C, Sommerfeld M, Tropea C (1995) Droplet-wall collisions: experimental studies of the deformation and breakup process. Int J Multiph Flow 21(2):151–173 [https://doi.org/10.1016/0301-9322(94)00069-V]

Mundo C, Sommerfeld M, Tropea C (1998) On the modeling of liquid sprays impinging on surfaces. Atom Sprays 8(6)

Pasandideh Fard M, Qiao YM, Chandra S, Mostaghimi J (1996) Capillary effects during droplet impact on a solid surface. Phys Fluids 8(3):650–659

Pope SB (2000) Turbulent flows. Cambridge University Press

Putnam A (1961) Integrable form of droplet drag coefficient. ARS J 31:1467–1468

Rider WJ, Kothe DB (1998) Reconstructing volume tracking. J Comput Phys 141:112–152 [MathSciNet][https://doi.org/10.1006/jcph.1998.5906]

Rieber M (2004) Numerische Modellierung der Dynamik Freier Grenzflächen in Zweiphasenströmungen. PhD thesis, Universität Stuttgart

Rieber M, Frohn A (1999) A numerical study on the mechanism of splashing. Int J Heat Fluid Flow 20:455–461 [https://doi.org/10.1016/S0142-727X(99)00033-8]

Roisman IV, Tropea C (2002) Impact of a drop onto a wetted wall: description of crown formation and propagation. J Fluid Mech 472:373–397 [MathSciNet][https://doi.org/10.1017/S0022112002002434]

Roth N, Gomaa H, Weigand B (2010) Droplet collisions at high weber numbers: experiments and numerical simulations. In: Proceedings of DIPSI workshop 2010 on droplet impact phenomena and spray investigation

Seki Y, Iwamoto K, Kawamura H, Prandtl number effect on turbulence quantities through high spatial resolution DNS of turbulent heat transfer in a channel flow. In: Hanjalić K, Nagano Y, Jakirlić S (eds) (2006) Turbulence, heat and mass transfer, vol 5. In: Proceedings of the 5th international symposium on turbulence, heat and mass transfer, pp 301–304

Stow CD, Hadfield MG (1981) An experimental investigation of fluid flow resulting from the impact of a water drop with an unyielding dry surface. Proc Royal Soc Lond. A. Math Phys Sci 373(1755):419–441

Thoroddsen ST (2002) The ejecta sheet generated by the impact of a drop. J Fluid Mech 451:373–381. ISSN 1469-7645

Trujillo MF, Lee CF (2001) Modeling crown formation due to the splashing of a droplet. Phys Fluids 13(9):2503–2516 [MathSciNet][https://doi.org/10.1063/1.1388541]

Walzel P (1980) Zerteilgrenze beim Tropfenaufprall. Chem-Ing-Tech 52(338)

Weatheritt J, Sandberg RD (2017) The development of algebraic stress models using a novel evolutionary algorithm. Int J Heat Fluid Flow 68:298–318
[https://doi.org/10.1016/j.ijheatfluidflow.2017.09.017]

Weigand B (2015) Analytical methods for heat transfer and fluid flow problems. Springer, Berlin Heidelberg
[https://doi.org/10.1007/978-3-662-46593-6]

Weiss DA, Yarin AL (1999) Single drop impact onto liquid films: neck distortion, jetting, tiny bubble entrainment, and crown formation. J Fluid Mech 385:229–254
[https://doi.org/10.1017/S002211209800411X]

White FM (1991) Viscous fluid flow, 2nd edn. McGraw-Hill

Wilcox DC (2008) Formulation of the k–omega turbulence model revisited. AIAA J 46(11):2823–2838
[https://doi.org/10.2514/1.36541]

Worthington AM (1908) A study of splashes. Green, and Co., Longmans

Wu J-L, Xiao H, Paterson E (2018) Physics-informed machine learning approach for augmenting turbulence models: a comprehensive framework. Phys Rev Fluids 3(7)

Wu J, Xiao H, Sun R, Wang Q (2019) Reynolds-averaged Navier-Stokes equations with explicit data-driven Reynolds stress closure can be Ill-conditioned. J Fluid Mech 869:553–586
[MathSciNet][https://doi.org/10.1017/jfm.2019.205]

Yarin AL (2006) Drop impact dynamics: splashing, spreading, receding, bouncing... Annu Rev Fluid Mech 38(1):159–192

Yarin AL, Weiss DA (1995) Impact of drops on solid surfaces: self-similar capillary waves, and splashing as a new type of kinematic discontinuity. J Fluid Mech 283:141–173
[https://doi.org/10.1017/S0022112095002266]

Footnotes

1 The double scalar product of two tensors is equivalent to the component sum of the element-wise multiplication of the two tensors.

© The Author(s), under exclusive license to Springer Fachmedien Wiesbaden GmbH, part of Springer Nature 2026
H. Gomaa, *Modeling with Knowledge and Data*, Mathematical Engineering
https://doi.org/10.1007/978-3-658-50679-7_10

10. Industrial System Modeling

Hassan Gomaa[1] ✉
(1) Strategic Projects Co-Innovation, Cognite, Oslo, Norway

The previous chapter focused on processes that can be studied in relative isolation, such as laboratory experiments or high-fidelity simulations. In those cases the key variables are directly measurable or controllable, boundary conditions can be prescribed with precision, and the use of nondimensional analysis provides a natural path to generalization. Under these circumstances the link between physical assumptions, model formulation, and supporting data can be established in a transparent way.

Industrial systems, by contrast, present a different set of challenges. They typically consist of multiple interacting subsystems and are influenced by neighboring processes through mass, work, and heat transfer. The system boundaries are shaped not only by engineering design but also by operational demands, with boundary conditions that may be uncertain, time-varying, and only partially observable. These characteristics make strict isolation impractical and often require hybrid strategies that combine physical reasoning with data-driven inference to capture system behavior in a meaningful and usable form.

The data available for industrial systems adds further complexity. Unlike the examples discussed in the previous chapter, where data may be collected specifically for modeling or validation purposes, industrial data are primarily gathered for operational monitoring, control, maintenance, and safety. As a result, the data typically reflect

operational priorities rather than modeling needs. This leads to challenges such as uneven coverage across the operating envelope, limited representation of off-design or transient conditions, and imbalanced datasets that may not fully span the scope of interest from a modeling perspective.

The examples in this chapter illustrate how these challenges shift the focus toward the contextualization of data and system behavior as a prerequisite for meaningful modeling. Rather than beginning with isolated equations or first-principles formulations, the modeling effort often starts with understanding and formalizing the system boundaries, operational conditions, and available data landscape. This contextualization integrates domain knowledge, physical principles, and operational data to create a coherent foundation for hybrid modeling. The focus lies on supporting decision-making in areas such as performance monitoring, reliability estimation, and maintenance planning. The cases include component-level models for pumps, system-level models for compressors, and data-centric analyses of complex assets such as turbofan engines.

10.1 Industrial Domain

Before turning to specific examples, we first take a closer look at the industrial domain in which these models are applied. Understanding the industrial context provides the necessary background for defining system boundaries, interpreting data, and embedding domain knowledge into modeling efforts. This section outlines the characteristics of industrial environments, the motivations for digital transformation, and the critical role of domain expertise in shaping practical and effective models.

10.1.1 Industrial Context

Industrial sectors such as oil and gas, the chemical process industry, and manufacturing are characterized by the use of large, capital-intensive machinery operating under complex physical, chemical, and

thermal conditions. These systems involve numerous interconnected components, such as compressors, pumps, heat exchangers, and turbines, often deployed in tightly coupled processes with high safety, reliability, and efficiency requirements. Operational sites such as offshore platforms, chemical plants, and power stations routinely monitor a vast number of physical variables and control parameters, with data acquired at rates of several thousand tags per second. These systems operate in highly regulated, safety-critical environments, where uptime and process stability are key performance indicators.

The physical technology in these domains is typically mature. Equipment design and process engineering are governed by established principles, and operational models have been refined over decades of use. As such, many of the improvement margins through traditional engineering means are already narrow. New opportunities for performance improvement often lie not within the hardware itself, but in optimization based on the intelligent use of data.

Economic Motivation The push toward digital transformation in heavy industry is primarily driven by classical economic value levers that cover

- **Improving operational efficiency and uptime** by minimizing unplanned downtime and improving asset utilization.
- **Reducing maintenance and lifecycle costs** by reducing maintenance, repair, and energy costs.
- **Minimizing health, safety, and environmental risks** improving safety, environmental compliance, and reducing failure-related consequences.
- **Extending asset life and capital productivity** extending the operational life of equipment and infrastructure.
- **Enhancing customer performance** improving reliability, availability, and service outcomes for clients.

The objectives remain the same as before, but digital technologies offer new, more efficient ways to reach them. Advances in sensing, data infrastructure, and computational modeling now provide insights that

were previously inaccessible or economically impractical. Lower-cost sensors, scalable storage, cloud computing, and modern open-source and commercial analytics tools make it possible to unlock value from previously fragmented data, supporting better asset management and more informed operational decision-making.

The Role of Industrial Analytics Industrial analytics sits at the intersection of operational domain expertise, data science, and digital infrastructure. It focuses on extracting actionable insights from vast and heterogeneous data sources, including sensor measurements, control systems, maintenance logs, simulation results, and more. The volume, velocity, variety, and veracity of this data demand scalable architectures and algorithms to convert it into operational value.

Industrial analytics refers to the use of data-driven methods to improve decision-making in the operation and maintenance of physical systems. Key application areas include condition monitoring and diagnostics, performance benchmarking, failure prediction, maintenance optimization, and operational forecasting. In this context, interpretability is essential, and analytics rarely replaces physics-based modeling. Instead, it **augments domain knowledge** through data-driven learning, particularly in areas where physical models fall short due to complexity, unknown parameters, or unmodeled dynamics. The hybrid approach leverages the strengths of both domains.

Human-Centered Decision Support Despite increasing levels of automation, critical decisions in industrial settings remain fundamentally human-centric. Operators, engineers, and managers are ultimately responsible for interpreting complex information, weighing trade-offs, and making judgments under uncertainty. The goal of industrial analytics is to elevate their capability providing them with clearer, timelier, and more actionable insights grounded in both data and domain knowledge.

Realizing this potential requires more than data and technical expertise. Implementation efforts must navigate organizational complexity and bridge across traditionally siloed functions such as operations, maintenance, data science, and IT, each with its own

vocabulary, priorities, and incentives. Effective collaboration demands not only technical integration, but also shared understanding and trust across disciplines. Successful transformation depends on multidisciplinary coordination, bringing together domain expertise, analytical methods, software engineering, and systems thinking. Analytics solutions must be technically sound, but also interpretable, usable, and well-aligned with operational workflows. Their role is to support, and not replace, human decision-making, particularly in environments shaped by uncertainty, safety constraints, and complex system interactions.

10.1.2 Industrial Domain Knowledge

As discussed in Sect. 1.4, domain knowledge refers to context-specific insights rooted in engineering practice, industry standards, and operational constraints. In contrast to theoretical or empirical knowledge, which often generalize across disciplines, domain knowledge is closely tied to particular industries, such as oil and gas, power generation, or manufacturing, and to the specific business domains and operational areas within them. It reflects the practical realities of how systems behave, degrade, and are managed in day-to-day operation. This knowledge plays a central role in defining modeling assumptions, setting boundary conditions, and interpreting sensor data, especially in system-level applications. The following aspects outline key elements of domain knowledge in industrial contexts. They are not intended to be exhaustive, as the diversity and complexity of industrial domains cannot be fully captured here.

A first key aspect of domain knowledge is an understanding of **industrial processes** and their associated **value chains**, particularly how they contribute to the production of the primary output, whether it be energy, chemicals, or refined materials. This includes not only the technical steps involved in creating the main product or maximizing yield, but also how these steps fit into broader industrial and economic contexts. At a high level, this means distinguishing between sectors such as oil and gas, power generation, manufacturing, or the chemical

process industry, each with its own regulatory landscape, operational demands, and value drivers. Within these sectors, domain knowledge becomes more specialized, branching into business domains such as upstream production, midstream transport, or downstream refining in the oil and gas industry, each defined by specific processes, asset types, and performance objectives.

At the facility level, domain knowledge involves understanding how plant sections and process units work together to deliver the intended product. This includes the arrangement and function of key units, their integration through thermal, chemical, or mechanical coupling, and how their local performance influences system-wide outcomes such as yield, efficiency, emissions, and product quality. For example, in a natural gas-fired power plant, this may involve combined-cycle configurations that optimize energy conversion, while in an ethylene production plant, it may include thermal cracking and separation units tuned for olefin yield, representing the primary building blocks for polymers.

In all cases, domain knowledge extends to operational constraints, control strategies, and trade-offs between competing objectives, all of which are necessary for interpreting data and evaluating model predictions in a meaningful context.

A second major aspect of domain knowledge is the **understanding of machinery**. This knowledge informs how equipment, such as pumps, compressors, turbines, and heat exchangers, operates under varying conditions, and how deviations in physical parameters may indicate inefficiencies, wear, or emerging faults. Importantly, this understanding applies not only at the level of individual equipment, but also within the context of coupled systems, where components interact through thermal, mechanical, or control linkages. It includes knowledge of how machines are operated in coordination with others through start-up and shutdown protocols, ramp rate limits, unit sequencing, and inter-unit coordination. It also encompasses equipment-specific constraints such as design limitations, failure modes, and maintenance requirements. Such insight is essential for identifying relevant variables

and embedding realistic assumptions into models. Closely related is the understanding of typical **operational profiles**, which are primarily shaped by the requirements of the surrounding process. Different process functions impose varying dynamic and temporal demands on the equipment involved. Some processes require stable, continuous operation, while others involve frequent transients, periodic multi-week cycles, or shifting loads. Domain knowledge includes recognizing these operational patterns, such as whether the system is expected to ramp quickly, maintain tight control margins, or operate flexibly across a range of conditions. These patterns strongly influence how equipment is monitored, maintained, and modeled. This also encompasses broader operational rhythms, including shift schedules, production planning, and maintenance cycles, all of which affect how the process is managed and how data is interpreted over time.

A further aspect is the understanding of **failure mechanisms** and degradation patterns, which form the foundation for diagnostics, condition monitoring, and reliability modeling. Industrial practitioners are familiar with how different components degrade under thermal, mechanical, or chemical stress, whether through corrosion, erosion, fouling, fatigue, or creep. These mechanisms have characteristic patterns in process data, often visible as subtle shifts in pressure drop, vibration, or temperature gradients. Curated datasets such as OREDA (Technology et al. 2015) provide empirically grounded statistics on failure rates, modes, and criticalities across a wide range of industrial components and environments, and offer useful context for typical failure probabilities in asset management and risk analysis.

Domain knowledge also encompasses familiarity with **industry standards** that enable interoperable data representation, a prerequisite for scalable analytics. Across industries, substantial efforts have been made to establish standards that ensure interoperability across different layers of the technology stack. For example, OP CUA (Foundation 2025) defines standard communication protocols for data exchange from field-level sensors to cloud-based applications. To name another example, DEXPI (e.V. 2025) facilitates consistent modeling of

piping and instrumentation diagrams for process design and operations. These are just two of many standards aimed at aligning data conventions across equipment, systems, and organizations. A particularly relevant example for our context is ISO 14224 (International Organization for Standardization 2016), which provides a comprehensive framework for collecting and exchanging reliability and maintenance data throughout the lifecycle of equipment in the petroleum, natural gas, and petrochemical sectors. It defines standardized taxonomies, failure modes, and information structures that enable harmonized data usage across organizations and platforms. These standards help formalize domain knowledge and ensure consistent, machine-interpretable representation of physical systems and events.

Altogether, domain knowledge combines formal standards, engineering practice, and operational experience. Its integration into modeling and analytics is essential for interpreting results, validating assumptions, and ensuring real-world relevance. It enables practitioners to recognize normal behavior, detect meaningful deviations, and understand interactions between components and neighboring systems.

Domain knowledge also shapes how KPIs are defined, which operational patterns are monitored, and what data resolutions and variables are most informative. It guides the required level of model detail, ensures alignment with actual system dynamics and constraints, and enables insights to be embedded within a framework grounded in physics, engineering logic, and operational context.

10.1.3 Industrial System Hierarchy

To clearly define the system under consideration, including its boundaries and internal structure, a structured classification of industrial systems and their hierarchies is essential. ISO 14224 (International Organization for Standardization 2016), developed for the petroleum, petrochemical, and natural gas industries, offers a widely recognized taxonomy that organizes industrial systems into

hierarchical levels based on both industrial context and equipment subdivision. While tailored to the oil and gas domain, the framework is broadly applicable and can be adapted to other industries and equipment types with similar structural logic. It provides a valuable basis for defining the model object and supports consistency and clarity in system representation. The full hierarchical classification is summarized in Table 10.1, which maps system elements from broad industrial context down to the individual part level, providing a reference for a structured representation of industrial systems.

Table 10.1 Hierarchical classification of industrial systems based on ISO 14224 (International Organization for Standardization 2016). The taxonomy organizes systems from broad industrial context to individual parts, supporting scalable modeling and data analysis

At the highest levels (1–5), the taxonomy captures the industrial context and use/location data, from the type of industry (e.g., oil and gas, petrochemical) and business category (e.g., petrochemical processing), down to plant and section levels. This categorization is independent of specific equipment and is useful for defining the modeling context, identifying economic drivers, and describing the operational environment.

At the lower levels (6–9), the taxonomy focuses on equipment decomposition in a parent-child structure. This includes the equipment class (e.g., compressors), subunits (e.g., lubrication system, control system), components (e.g., motors, valves), and individual parts (e.g., seals, bolts). This structure allows the system to be clearly organized, with model boundaries defined at appropriate levels of granularity. It supports precise system definition, consistent hierarchy modeling, and verification that the structure conforms to standard logic (e.g., parts within components, components within subunits, subunits within equipment, etc.). For levels 3–6, the standard provides comprehensive tables listing standardized entities for each hierarchical level. These will be discussed in more detail for specific applications in Sects. 10.2

and 10.3, where the system context and modeling boundaries for pumps and compressors are introduced.

System Boundary While the standard taxonomy was originally developed to standardize the recording and classification of failures within industrial environments, in the following we adopt and adapt this taxonomy as a structural framework to define system hierarchies and to ensure a consistent mapping of the equipment under consideration, including relevant subunits essential for its operation. An illustrative example of such a boundary definition is provided by the system diagram for a compressor system, shown in Fig. 10.1, adapted from ISO 14224 (International Organization for Standardization 2016). The figure shows the compressor system, which belongs to the *Equipment Class* level, corresponding to level 6 in the taxonomy hierarchy. The boundary includes *Subunits* and *Components* necessary for the compressor's core functionality. Elements such as inlet and outlet valves, the compressor driver with its associated auxiliaries, and interstage cooling units lie outside this boundary and, in accordance with the taxonomy, are treated as separate equipment classes.

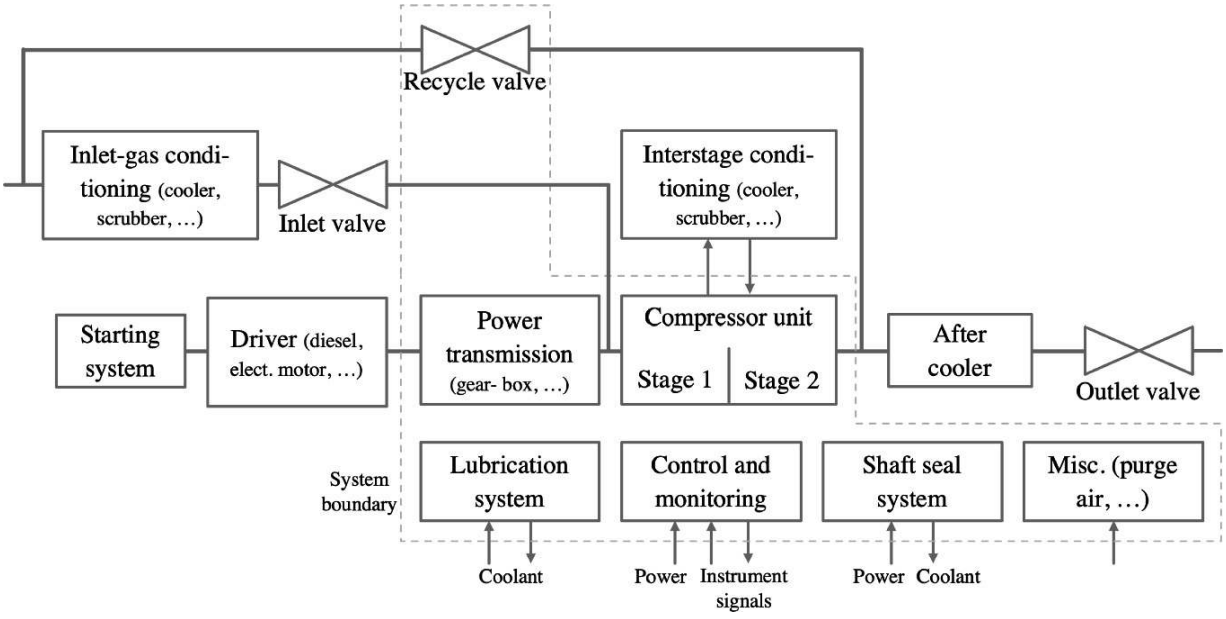


Fig. 10.1 System boundary definition for a compressor system from ISO 14224 (International Organization for Standardization 2016)

As detailed in Table 10.2, each subunit comprises multiple components. The compressor system encompasses several subunits, defined at level 7 of the taxonomy, including the compressor unit, power transmission, control and monitoring systems, lubrication system, shaft seal system, and miscellaneous. The compressor unit contains the core components responsible for gas compression, including the casing, rotor, radial, and thrust bearings, as well as the antisurge system, which protects the compressor from unstable operating conditions. The power transmission subunit connects the driver to the compressor, enabling the transfer of mechanical energy through elements like gearboxes and couplings. The control and monitoring system manages compressor operation by regulating process parameters and collecting sensor data for real-time control and diagnostics. The lubrication system supplies lubrication and cooling to rotating parts, minimizing friction, wear, and the risk of overheating. The shaft seal system prevents process gas leakage along the rotating shaft, typically using sealing technologies such as dry gas seals or oil seals to ensure containment and operational safety. The miscellaneous subunit comprises supporting structures and auxiliary components that do not fall within the primary functional subunits but are essential for installation, integration, and safe operation of the compressor system.

In cases where compressors consist of multiple stages or operate as part of a compressor train, the entire assembly is treated as a single inventory item within the defined boundary. The system boundary also specifies all interfaces where transfers of working fluid, coolant, or power occur across the system boundary. The component list is designed with sufficient generality to accommodate various compressor types, including centrifugal, reciprocating, screw, and axial compressors. However, this also implies that not all components listed are present in every compressor configuration.

Table 10.2 Components of subunits within the compressor *Equipment Class* according to ISO 14224 (International Organization for Standardization 2016)

It is important to note that in the ISO 14224 standard, sensors are formally assigned to the control and monitoring subunit. This convention aligns with the standard's primary objective of supporting accurate failure and maintenance data attribution. For our present purposes of system modeling and sensor data analysis, and to better reflect subunit-level granularity, we deviate from this convention by reassigning sensors to their respective functional subunits. This adjustment, as reflected in Table 10.2, allows for a more precise alignment between sensor readings and the physical components or subsystems they monitor.

In this book, the focus is on systems defined at the *Equipment Class* level and below, corresponding to level 6 and deeper within the taxonomy. Sensor data, primarily in the form of time series recordings, forms the basis for system modeling, operational performance analysis and condition monitoring. Depending on the complexity of the equipment and process, several dozen to hundreds of sensors may be involved, each monitoring specific aspects across subunits and components. A clearly defined system boundary and hierarchical structure not only ensure consistent system representation but also provide the framework for organizing and interpreting sensor data. To effectively apply this data in modeling and analysis, each sensor tag must be accurately linked to its physical and operational context, as discussed in the following.

10.1.4 Sensor Contextualization

For any given system, including its subunits and components, sensors can generally be categorized into control, process, condition, and support system sensors. **Control sensors** provide insight into the operational status of the system. These include variables such as setpoints, valve positions, rotor speed, and general operation status indicators. **Process sensors** measure key process parameters, often related to the working fluid. Examples include suction and discharge pressures, flow rates, temperatures, and other variables that describe

the thermodynamic or fluid dynamic state of the system. **Condition sensors** are used to monitor the health and integrity of equipment components. Typical examples include vibration sensors positioned at the drive and non-drive ends, as well as temperature sensors placed on axial and thrust bearings. These sensors are critical for detecting signs of wear, misalignment, or developing faults. **Support system sensors** are associated with auxiliary subunits, such as lubrication, cooling, or sealing systems, where they monitor variables like oil temperature, pressure, flow rates, or seal gas conditions to ensure proper operation of these supporting functions.

In many cases, sensor tags are not explicitly linked to a system map or hierarchy. To identify and associate sensors with their corresponding system elements, it is necessary to contextualize each sensor by enriching it with descriptive information that allows the inference of its physical and operational context. This includes

- **Physical quantity and units** by defining what the sensor measures, such as pressure, temperature, or flow rate, along with its unit of measurement, which is often extracted from the respective unit-of-measure conventions.
- **System mapping** by identifying the corresponding system hierarchy, subunit, and component within the system hierarchy to provide a clear understanding of the physical context and operational relevance.
- **Location and orientation** by specifying the sensor's position within the process, for example at the inlet or outlet, or mechanically at the drive end or non-drive end. For certain sensors, particularly those monitoring vibration, further detail such as axis direction (e.g., horizontal, vertical, or along specific coordinate axes) is important.
- **Associated fluid** by identifying whether the sensor is related to the working fluid, lubrication oil, coolant, or seal gas. This helps to map the sensor accurately to the relevant process or supporting system.

In practice, much of this descriptive information is not available in a structured format. It is often embedded within tag names or hidden in

unstructured textual descriptions found in instrumentation databases or other technical records. Extracting relevant contextual information relies on a combination of domain expertise and automated techniques. Methods such as Natural Language Processing can support the interpretation of naming conventions, the decoding of patterns, and the derivation of meaningful metadata that links sensors to their physical and operational context.

Beyond assigning static metadata to individual sensors, contextualization also extends to capturing how the system operates over time. This is achieved by deriving categorical time series that describe the machine's dynamic behavior, based primarily on control variable readings. Machinery exhibits distinct signal patterns across different operating states. From a data-driven perspective, explicitly labeling these operational modes as time-based intervals is essential for meaningful analysis. For instance, when aiming to detect efficiency drifts, it is important to focus only on periods when the machine operates under stable and regular conditions. If data from transitional phases such as start-up, shutdown, or idle states are included, it can introduce unnecessary variability and reduce the accuracy of the analysis. The same principle applies when calculating performance indicators. Metrics such as average monthly efficiency are meaningful only when they are based on consistent operational behavior. Including data from periods that do not represent regular operation would distort these calculations and lead to incorrect conclusions. To focus on the relevant operational conditions, the machine's operating state is provided as contextual information in the form of categorical time series, derived by labeling each time interval based on control variable readings.

Table 10.3 Hierarchical breakdown of total time for representation of availability states, operating ranges, and load conditions. Timeline definitions are adapted from ISO 14224 (International Organization for Standardization 2016)

The ISO 14224 standard (International Organization for Standardization 2016) provides a suitable foundation for defining such operational states through its structured timeline definition. Originally developed to accurately determine time-based reliability parameters, the framework is adapted here to describe operational modes for analytical purposes. As outlined in Table 10.3, total time is divided into **Up Time** and **Down Time**, distinguishing periods when the system is available or operating from those when it is not. During downtime, time series data are typically unavailable, and further differentiation, such as whether downtime was planned or due to an unexpected failure, must be extracted from maintenance records or operational logs.

Within uptime, the system transitions between several operating modes. The **Running** state refers to regular operation under load, while **Ramping** captures transient phases as the system starts up or shuts down. The **Idle** state indicates availability without load, and certain machinery may also support **Online Maintenance**, where specific maintenance tasks are performed without halting operation. These operating states can, in most cases, be inferred directly from control sensor readings through appropriate signal processing techniques.

Depending on the type of equipment and operational context, additional or modified labeling schemes may be required. For example, Table 10.3 also includes optional categorizations such as **Operating Region** and **Load Conditions**. The concept of operating regions, commonly applied in pump reliability, differentiates between the **Preferred Operating Region** (POR), **Acceptable Operating Region** (AOR), and **Not Allowed Operating Region** (NOR), reflecting whether machinery is running within optimal conditions, within acceptable limits, or outside of those limits. Similarly, load conditions distinguish between **Full Load** and **Part Load** operation. Both categorizations require the definition of appropriate threshold values to enable automated labeling based on sensor data.

By systematically labeling control variables in this way, large volumes of operational data can be structured to support accurate performance analysis, condition monitoring, and the effective

application of data-driven methods within clearly defined operational contexts.

10.1.5 System Coupling in Industrial Equipment

So far, we have focused on enriching individual sensors with metadata and capturing system dynamics through time-based labeling. We now turn to how sensors can reveal relationships within the system by reflecting the underlying **coupling** between components and processes. Industrial equipment and processes are characterized by varying degrees of coupling between components, subunits, and systems. In this context, coupling describes how closely the behavior of different sensors or system elements is interdependent, often observable through the similarity, synchronization, or causality within their sensor signal patterns over time.

Coupling can be viewed as a spectrum, from tightly coupled setups governed by clear physical laws to loosely coupled configurations where relationships arise from complex interactions, delays, or external influences. Recognizing the strength and nature of these couplings is helpful for choosing the right modeling approach. When behavior is dictated by well-defined physics, analytical models provide interpretability and transparency. In contrast, where system dynamics are too complex or uncertain to be captured explicitly, data-driven methods are better suited to uncover hidden patterns. For instance, coupling insights can inform the development of diagnostic tools, such as combining vibration analysis with physical constraints and machine learning-based anomaly detection.

Tight Coupling at the Component Level At the strongest end of the spectrum, redundant or co-located sensors measure identical or near-identical physical quantities. This is commonly seen in critical operational or process measurements, installed to ensure measurement reliability and fault tolerance. For example, multiple speed sensors along a compressor train monitor rotational speed at different points, ensuring consistent readings even if one sensor drifts or fails. Similarly, in condition monitoring, orthogonal vibration

sensors, mounted at 90-degree angles, capture multi-directional mechanical behavior. In these cases, sensor signals are expected to align closely, with only minor deviations caused by calibration offsets or measurement noise, making them well suited for cross-validating sensor integrity and enforcing strict physics-based constraints.

State Coupling through Shared Process Variables State coupling occurs when sensors measure different physical quantities that are intrinsically linked by governing physical laws. A typical example is the relationship between pressure and temperature at the same location, such as the compressor inlet, where both describe the same thermodynamic state of the working fluid. In such cases, sensor signals often exhibit similar patterns because they are connected through known equations or proportional relationships. Another example is found in rotating machinery, where speed and torque are analytically related. These forms of coupling allow for direct application of physical models to monitor system behavior and detect deviations from expected relationships, supporting both validation and anomaly detection in a transparent and interpretable way.

Process Coupling Across Locations Process coupling describes interactions within a single component but across different locations. For instance, the pressure and temperature difference between the inlet and outlet of a compressor reflects the underlying compression process, which can be characterized by polytropic relations. Similarly, vibration signals measured at the drive and non-drive ends of machinery show related patterns but may include phase shifts or amplitude differences due to mechanical dynamics. These couplings remain governed by physical principles but are influenced by process dynamics and structural behavior. While sensor signals remain strongly related, time lags and functional transformations may appear.

Subunit and System-Level Coupling At higher hierarchical levels, coupling emerges through the transfer of mass, energy, or mechanical work between subunits and interconnected systems. These relationships become more complex as they are shaped by control logic, auxiliary systems such as lubrication or cooling, and varying

operational states. For instance, the coupling between a compressor and its driver is immediate and mechanical, clearly reflected in correlated load and speed signals. In contrast, the interaction between a compressor and its lubrication system may only become apparent at the level of overall operational states, or when operational thresholds are breached, such as rising oil temperatures indicating possible wear. At this level, simple physical models are often insufficient to capture the full behavior. Data-driven methods can help reveal hidden patterns, while domain knowledge ensures that these correlations are interpreted within a meaningful physical and operational context.

Understanding the degrees of coupling within a system not only guides modeling choices and data organization but also plays a crucial role in enhancing interpretability and building trust in analytics outcomes. Tightly coupled systems are well suited for constraint-based models that enforce known physical laws, while loosely coupled systems benefit from data-driven methods to capture complex, less predictable behavior. Hybrid approaches bridge these domains by applying physical limits and using machine learning to model residual dynamics caused by factors like wear or unmodeled interactions, enhancing both accuracy and interpretability. Coupling insights also inform feature engineering by embedding system dynamics directly into the model. For redundant sensors in tightly coupled setups, discrepancies between signals can reveal sensor faults. In state coupling, features derived from ratios or combined variables track adherence to known physical relationships, flagging deviations as potential anomalies. For process coupling, expected values generated from physical equations can be used as reference values to be compared to actual measurements, with deviations serving as indicators of abnormal operation.

10.2 Component Level Modeling of a Centrifugal Pump

Pumps are used across most industrial processes, including oil and gas, power generation, chemical processing, and manufacturing. As essential devices for transporting fluids, they play a critical role in maintaining process continuity and efficiency. Most pumps, particularly centrifugal pumps, are driven by electric motors or other engines. Traditionally, centrifugal pumps operated at constant speeds with flow rates controlled by valves, which inherently result in losses due to increased flow resistance. With the availability of cheaper speed-controlled motors, regulating flow by adjusting speed has become more common, making pump operation more efficient even for smaller units (Gülich 2010; Isermann 2011).

From a reliability perspective, failures in centrifugal pumps usually originate from hydraulic issues where fluid flow affects performance or from mechanical parts that wear out over time. Reliability data for pump systems is comprehensively documented by OREDA, which follows the hierarchical system structure defined by ISO 14224, as discussed in Sect. 10.1.3. At the *Equipment Class* level 6, centrifugal pumps are treated as a distinct system, while failure statistics are further detailed down to *Component* level 8, referred to as *Maintainable Items*. Consistent with system boundary definitions, as illustrated for compressors in Fig. 10.1, elements such as the driver unit, inlet and outlet valves are outside the pump system boundary. Failure data are presented using three key aspects. The **failure mode** describes how a failure becomes visible as the observable effect on the system. The **failure mechanism** identifies the immediate cause of the failure, usually linked to the lowest identifiable subsystem level. **Maintainable items** are assemblies of parts that are serviced or replaced during maintenance and correspond to components on level 8 in the system hierarchy. Figure 10.2 summarizes reliability data for centrifugal pumps by highlighting the main contributors that account for the top $\sim 90\%$ of observed failures across these three aspects. In the presented statistic, some components have been grouped together compared to the more detailed breakdown available in OREDA (Technology et al. 2015). The failure mechanisms data show that various forms of wear

such as corrosion, erosion, blockage, and breakage are common, indicating that material degradation and deposit formation are frequent issues in pump operation. At the maintainable item level, after unknown components, instrumentation failures are among the leading contributors, followed by issues with seals. This is consistent with the reporting by Isermann (2011), who identified sliding ring seals as a frequent source of failure. Bearings, impellers, shafts, and casings, all affected by mechanical wear, also make up a significant part of reliability concerns.

As pointed out by Isermann (2011), the feasibility of pump supervision and fault detection strongly depends on the available instrumentation. In minimally instrumented setups, where only outlet pressure is monitored, only major deviations from normal operating conditions signal potential failures, typically when faults are already severe. The inclusion of flow rate measurement improves insight but still falls short of enabling precise fault diagnosis. Monitoring inlet pressure provides insight into cavitation risks by allowing observation of the Net Positive Suction Head (NPSH). However, these conventional supervision methods, primarily based on threshold checks, rarely support early fault detection or diagnosis. Well-instrumented pump systems monitor a broader set of parameters, including inlet and outlet pressures, flow rate, rotational speed, and bearing temperatures. While this allows for more comprehensive supervision, traditional limit-based monitoring still focuses on detecting significant deviations rather than enabling deeper diagnostics.

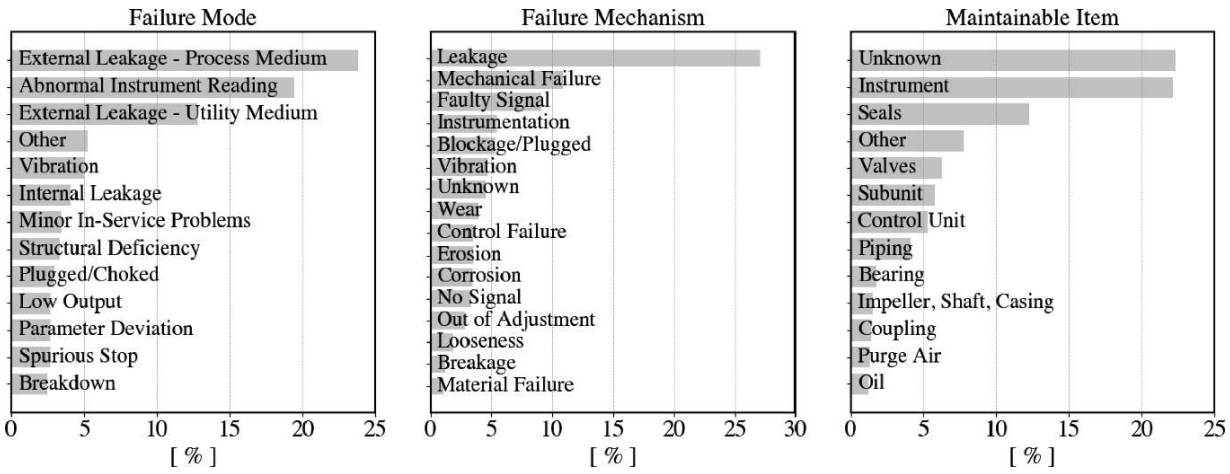


Fig. 10.2 Overview of reliability data for centrifugal pumps, showing the top contributors to failures categorized by Failure Mode, Failure Mechanism, and Maintainable Item, based on OREDA data (Technology et al. 2015)

10.2.1 Centrifugal Pump Characteristics

For the sake of simplicity, we consider a pump with constant speed operation and basic instrumentation, using flow rate and driving power measurements to estimate reliability and efficiency parameters. In Sect. 4.4.1, we considered incompressible flow machines from a dimensional analytical perspective, and in Sect. 5.1.4, we examined the Euler work equation in the context of centrifugal pumps. The general nondimensional groups that characterize machine performance were derived in Eq. (4.71). For the case of centrifugal pumps, these are now restated using the head H, with the respective variables inserted explicitly as

$$\frac{gH}{\Omega^2 D^2}, \quad \eta, \quad \frac{P}{\rho \Omega^3 D^5} = f\left(\frac{Q}{\Omega D^3}, \frac{\rho \Omega D^2}{\mu}, \frac{\varepsilon}{D}\right). \tag{10.1}$$

In this expression, the first term on the right-hand side is the flow coefficient $\Phi = Q/\Omega D^3$, which typically exhibits the most significant impact on pump performance. The second term represents the Reynolds number $\mathrm{Re} = \rho \Omega D^2/\mu$, while the third captures geometric ratios that influence performance, such as surface roughness and clearance gaps. The nondimensional groups were constructed such that the key physical quantities H, Q, and P each enter linearly in the

respective expressions. As derived in Sect. 5.1.4, the real pump power is given by $P = \rho g H Q / \eta$ and is related to the required torque through $P = \tau \Omega$. The Euler work equation derived in Eq. (5.54) allows further connection to the local flow turning within the impeller.

For purposes of operational modeling, we are interested in constructing a simplified functional form that describes pump behavior under varying flow and speed conditions. To this end, we disregard variables that remain constant during normal operation, such as characteristic length scale or fluid properties. Assuming the working fluid density ρ is constant, and also neglecting geometric effects represented by ε / D since, while important for long-term performance degradation, they are not directly measured during standard operation, leads to a reduced set of relations of

$$\frac{H}{\Omega^2}, \quad \eta, \quad \frac{P}{\Omega^3} = f\left(\frac{Q}{\Omega}, \Omega D^2\right). \tag{10.2}$$

This simplification limits the model's applicability to a **single pump design** or a tightly controlled family of machines with fixed impeller shape and size ratios. When modeling across broader populations, such as pumps of varying designs, diameters, or stage counts, the characteristic scale and geometry ratios can no longer be neglected, and their inclusion becomes essential to preserve predictive accuracy.

The machine performance curves describe unique values for head, efficiency, and power at every specific flow rate Q for a given design speed Ω. However, for practical modeling, we also want to incorporate the functional dependence on variable speed. To propose a meaningful ansatz function for the head-flow relation, we consider the scaling of H with respect to Q and Ω from a dimensional analytical perspective.

As discussed in Sect. 2.2.3 on single dimensionless products, dimensional analysis becomes particularly powerful when the system is governed by only one nondimensional group. In this case, that group must remain constant, and its dimensional structure determines the functional form, up to a proportionality constant. We begin by examining limiting behaviors. Holding the flow rate Q constant, the

head coefficient $\Psi = gH/\Omega^2 D^2$ implies $H \sim \Omega^2$. Conversely, at constant speed Ω, combining Ψ and Φ in a way that eliminates Ω yields $H \sim -Q^2$. This result would also directly follow from the specific speed and diameter relations in Eq. (4.78). To generalize further, we consider linear combinations of nondimensional groups. From Ψ and Φ we obtain $H \sim -\Omega Q$, and from Ψ and Re we get $H \sim -\Omega^3$. Assuming these terms contribute independently and additively, we propose the following ansatz function

$$H = \theta_0 + \theta_1 \Omega^2 - \theta_2 Q^2 - \theta_3 \Omega Q - \theta_4 \Omega^3. \tag{10.3}$$

The signs of the individual terms reflect their expected physical contributions. The term proportional to Ω^2 represents the ideal scaling of head with rotational speed and is expected to be positive. The Q^2 and ΩQ terms capture head loss effects due to increasing flow rate, both anticipated to reduce head and thus carry negative signs. The Ω^3 term, which arises from viscous loss mechanisms, is likewise expected to be negative. While these signs are physically motivated, the final coefficient values θ_i and their signs are empirical and can be obtained from data using linear regression, as illustrated below in Sect. 10.2.3. It is important to note that the assumption of a linear superposition of terms in Eq. (10.3), although dimensionally valid, rests on the modeling simplification that nonlinear interactions do not introduce significant cross or higher-order terms. This ansatz should therefore be understood as a first-order approximation rather than a complete physical description of pump behavior. As discussed in Sect. 4.4.1, the Reynolds number effects represented by the last term can often be omitted.

To construct an analogous ansatz function for power *P*, we may follow the same dimensional reasoning or directly apply the relation $P \sim HQ$. Substituting the head function, we obtain

$$P = \theta_0 Q + \theta_1 \Omega^2 Q - \theta_2 Q^3 - \theta_3 \Omega Q^2 - \theta_4 \Omega^3 Q \ . \tag{10.4}$$

In some cases, the torque τ may be available as a direct measurement. It is then convenient to construct an ansatz function in terms of τ, which follows analogously from $P = \tau\Omega$ and $P \sim HQ$, yielding $\tau \sim HQ/\Omega$. While the efficiency η is presented as a modeled output alongside head and power, in real-world operational applications it is not directly measurable. Instead, efficiency is typically inferred from simultaneous measurements of power and head, where instrumentation allows. This introduces potential measurement noise and bias, which must be considered when applying the model to real-world data.

Impact of Efficiency Degradation To assess how efficiency degradation affects pump performance, we begin by considering a non-degraded reference state where the pump delivers a head H_0 with power P_0 at efficiency η_0. Suppose that after field operation and mechanical wear, the efficiency drops to $\eta = \eta_0 - \Delta\eta$, while the speed and flow rate remain unchanged. We are interested in the resulting changes in head and power, denoted by $H = H_0 + \Delta H$ and $P = P_0 + \Delta P$, respectively. Starting from the basic power relation $P = \rho g H Q/\eta$, the degraded condition becomes

$$P_0 + \Delta P = \rho g Q \, \frac{H_0 + \Delta H}{\eta_0 + \Delta\eta} \quad . \tag{10.5}$$

Rewriting this expression in terms of relative deviations yields

$$\left(1 + \frac{\Delta P}{P_0}\right)\left(1 + \frac{\Delta\eta}{\eta_0}\right) = 1 + \frac{\Delta H}{H_0} \quad , \tag{10.6}$$

which allows a direct interpretation of how a given efficiency degradation manifests as either increased power demand, reduced head, or both. Since $\Delta\eta/\eta_0 < 0$, a drop in efficiency must be visible either through an increase in required power or a decline in delivered head. The relative impact depends on the degradation mechanism.

Typical degradation mechanisms can be of hydraulic or mechanical nature. Hydraulic degradation includes clearance gap wear, impeller erosion, and inlet deposits, each distinctly affecting the energy transfer

from impeller to fluid. Clearance wear increases leakage and recirculation, reducing head and efficiency while shifting the characteristic curves leftward. In single-stage pumps, this is often accompanied by increased disk friction losses. Impeller erosion, especially near the outlet, may initially lead to a slight increase in head due to sharper blade edges, but eventually reduces energy transfer efficiency. Deposits at the inlet obstruct incoming flow, resulting in reduced head and increased resistance, particularly at higher flow rates. Mechanical losses are typically caused by bearings, shaft seals, coupling to the driver, or auxiliary equipment connected to the pump shaft. These degradation effects appear as measurable shifts in head and power at constant speed and flow conditions, enabling early fault detection by tracking changes in characteristic curves, as discussed by Isermann (2011).

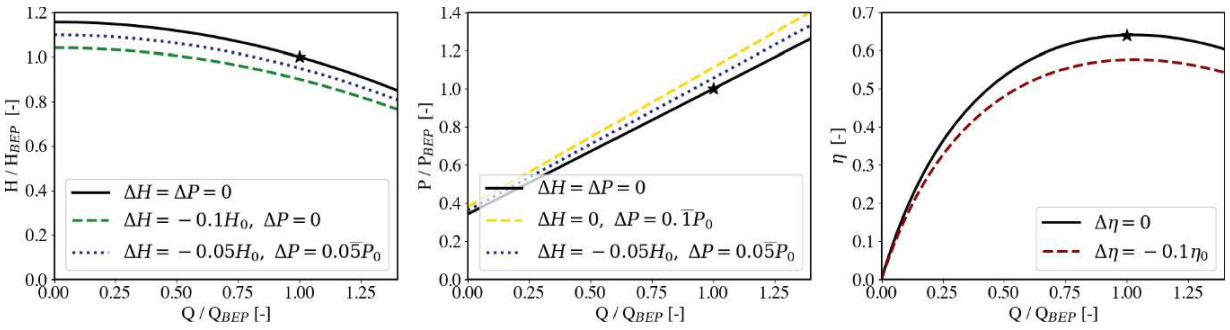


Fig. 10.3 Illustration of three degradation scenarios with identical efficiency loss ($\Delta\eta/\eta_0 = -0.1$), affecting head, power, or both

For illustration, Fig. 10.3 presents three degradation scenarios, each corresponding to a relative efficiency reduction of $\Delta\eta/\eta_0 = -10\%$. In the first scenario, degradation is purely hydraulic in nature, appearing exclusively as a drop in delivered head. In the second, the degradation is non-hydraulic, manifested only as an increase in power consumption while the hydraulic head remains unchanged. The third scenario reflects a hybrid condition in which both head decreases and power increases. The ability to distinguish between degradation scenarios depends on the available instrumentation, particularly whether head can be measured or inferred.

10.2.2 Reliability Estimation Based on Operating Range

Figure 10.4 illustrates the relationship between performance characteristics and reliability, referred to as the Barringer curve. In this diagram, the pump's hydraulic behavior is represented by the pump curve, which plots head over flow normalized by the Best Efficiency Point (BEP) to highlight deviations from optimal operating conditions. Reliability is shown alongside, expressed in terms of Mean Time Between Failures (MTBF) on the right axis. The **Best Efficiency Point** represents the design condition at which the pump operates with maximum efficiency and optimal reliability. Centered around this point is the bell-shaped **reliability curve**, indicating that MTBF reaches its peak when operating near the BEP. As flow deviates from this optimal point, either toward lower or higher flow rates, reliability declines sharply.

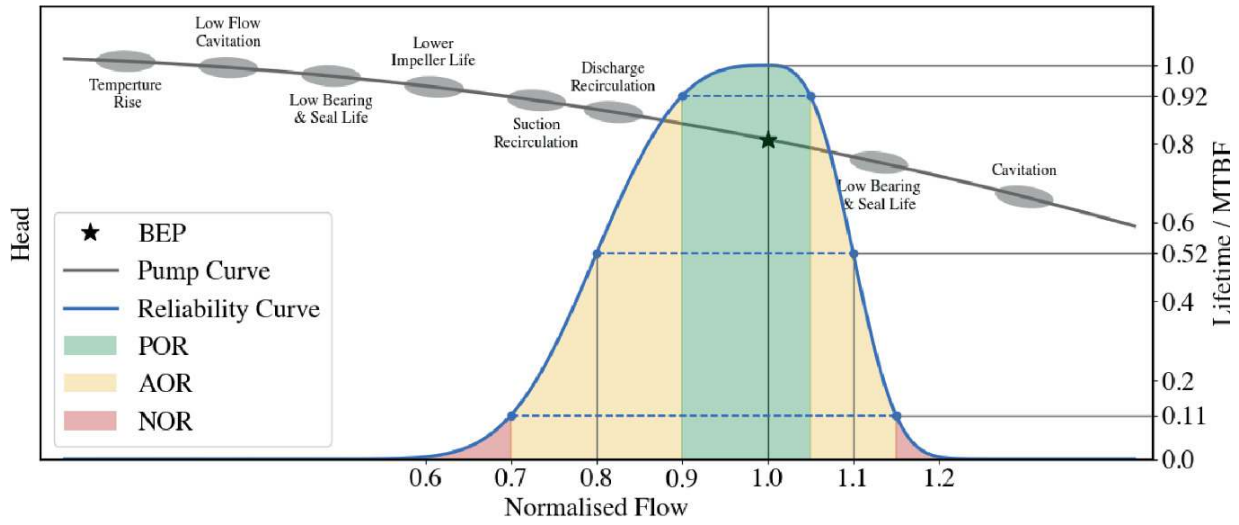


Fig. 10.4 Relationship between pump performance and reliability, highlighting Preferred (POR), Acceptable (AOR), and Not Allowed Operating Ranges (NOR)

While efficiency is an important factor, maintaining operation close to the BEP is even more critical from a reliability perspective. Operating away from BEP not only reduces efficiency, leading to increased energy consumption, but also accelerates mechanical wear and the risk of failure. Common adverse effects associated with off-design operation are annotated in Fig. 10.4. At very low flow rates, a significant

temperature rise can occur due to insufficient fluid movement to carry away the heat generated within the pump. Generally, when operating away from the BEP, the impeller design no longer matches the prevailing flow conditions. The flow detaches from the blade surfaces on the suction side at low flow rates, and on the pressure side during overload. The flow separation causes mechanical vibrations and cavitation that accelerate wear on critical components such as bearings, seals, and shaft.

Hodgson and Walters (2002) provide indicative values for the characteristic degradation of MTBF as operation deviates from the BEP. When operating within 90% to 105% of BEP, reliability remains high, maintaining approximately 92% of the maximum MTBF. However, operating in the range of 80%–110% results in a noticeable decline, with MTBF dropping to around 53%. Operating between 70% and 115% of BEP leads to a drastic reduction in reliability, with MTBF decreasing to approximately 11%. Notably, while the operating regimes are asymmetrical, they exhibit a form of scaled symmetry, extending twice the distance toward lower flow rates compared to higher flow rates.

The reliability curve in Fig. 10.4 is functionally approximated by a continuous distribution, designed to capture both the peak at the BEP and the asymmetric decline in reliability as the operating point deviates from it. This function is constructed in a manner similar to a normal distribution, where the mode defines the point of maximum reliability and the shape parameter *s* controls the dispersion of the curve. However, instead of the quadratic argument in a normal distribution, the reliability function employs a cubic power to better reflect the sharper decay in reliability

$$R(x) = \exp\left(-\frac{|x-\text{mode}|^3}{\left(\frac{3-\text{sign}(x-\text{mode})}{2}\, s\right)^3}\right). \tag{10.7}$$

Here, *x* represents the normalized flow rate. The asymmetry of the curve is introduced through the scaling term in the denominator, which

modifies the spread depending on whether the operating point lies to the left or right of the mode. Specifically, the term

$$\frac{3-\text{sign}(x-\text{mode})}{2} = \begin{cases} 1 & \text{if } x > \text{mode} \\ 2 & \text{if } x < \text{mode} \end{cases} \tag{10.8}$$

ensures that the dispersion is twice as wide for flow rates below the BEP compared to those above it. To align this functional approximation with the indicative MTBF degradation values provided by Hodgson and Walters (2002), the mode is set to align with the BEP, thus $\text{mode} = 1$. The shape parameter is fitted to $s = 0.1154$, which allows the curve to closely match the characteristic reliability values across the defined operating regimes, with deviations remaining within approximately 1%.

For practical operation, the pump's performance is divided into three distinct regimes. The **Preferred Operating Range** (POR) is defined between 90% and 105% of the BEP. Within this range, the pump operates under optimal conditions, ensuring both high reliability and maximum efficiency. Beyond this, but still within tolerable limits, lies the **Acceptable Operating Range** (AOR), which extends from 70% to 115% of the BEP. While continuous operation in this range is feasible, it comes with a noticeable increase in risk due to the declining reliability as the pump moves further away from its design point. Operation outside of this window, beyond 70% and 115% of the BEP, falls into the **Not Allowed Operating Range** (NOR). In this regime, reliability drops sharply, and the likelihood of failure becomes critical. Prolonged operation in the NOR should be avoided, as it significantly accelerates wear and increases the probability of severe mechanical issues. These operating regimes are not fixed limits but are defined according to the specific balance between performance and risk in a given context.

10.2.3 Dataset for Pump Operation

The dataset discussed here covers two centrifugal pumps operated at constant speed, assuming a constant working fluid density. Available sensor signals include flow rate, required motor power, and delivered head, recorded over the years 2020 and 2021 at a 10 min sampling frequency. In addition, pump characteristics including the Best Efficiency Point (BEP) are provided and used for reference.

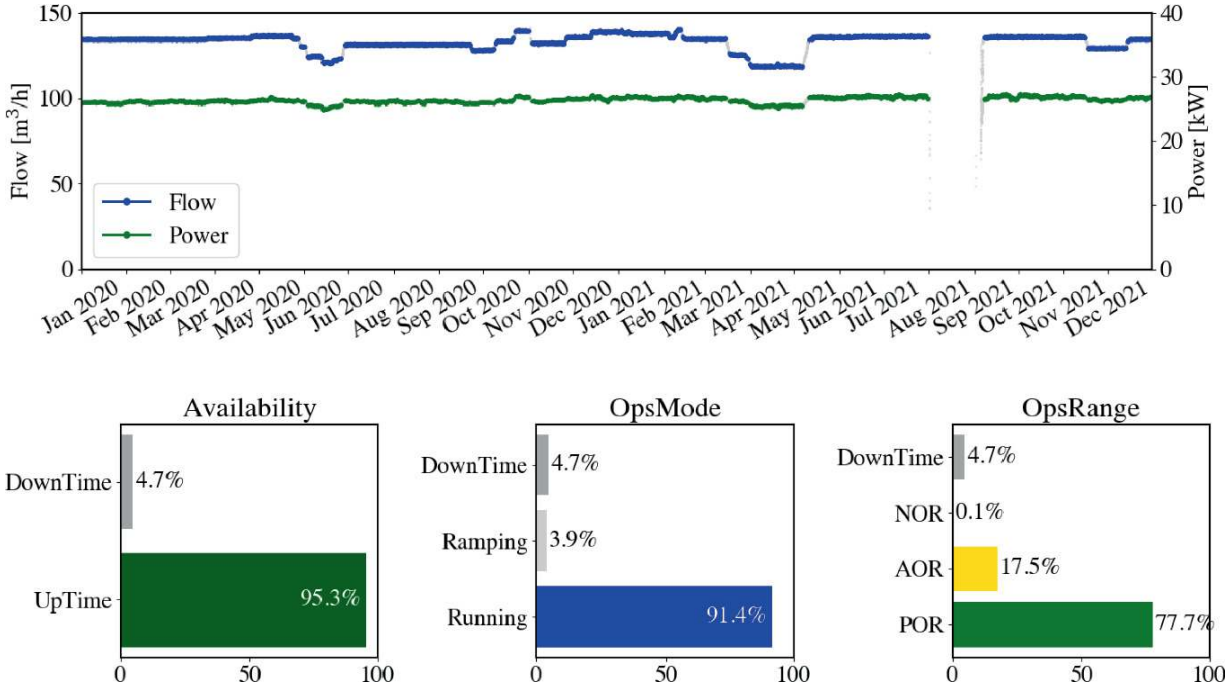


Fig. 10.5 Pump 1 showing time series of control variables together with aggregated operating regime labels over two years

While the operational profiles reflect real industrial operation, the actual sensor values are synthetically generated using pump maps with modeled degradation. Unlike laboratory datasets that are designed to span the full operational envelope, this dataset reflects realistic field operation, where the pumps fulfill their intended operating function and thus do not cover the entire possible operating condition spectrum in a balanced manner. Over the regarded two-year time span, Pump 1 is subject to a relative efficiency degradation of $\eta = 4\%$, primarily due to mechanical losses, while Pump 2 experiences a more significant efficiency loss of $\eta = 10\%$, mainly resulting from reduced hydraulic energy conversion.

To enhance the interpretability of the data, time series are labeled with operational context, as described in Sect. 10.1.4. The power sensor was used to determine availability, distinguishing between up and down time. The flow sensor served as the control variable for identifying dynamic operating modes, such as ramping versus steady-state running. The operating regions, POR, AOR, and NOR are derived based on flow sensor data using threshold definitions provided in the previous Sect. 10.2.2. Figure 10.5 and 10.6 show the time series of the control variables for Pump 1 and Pump 2, respectively, along with aggregated label sets that summarize the corresponding operating regimes.

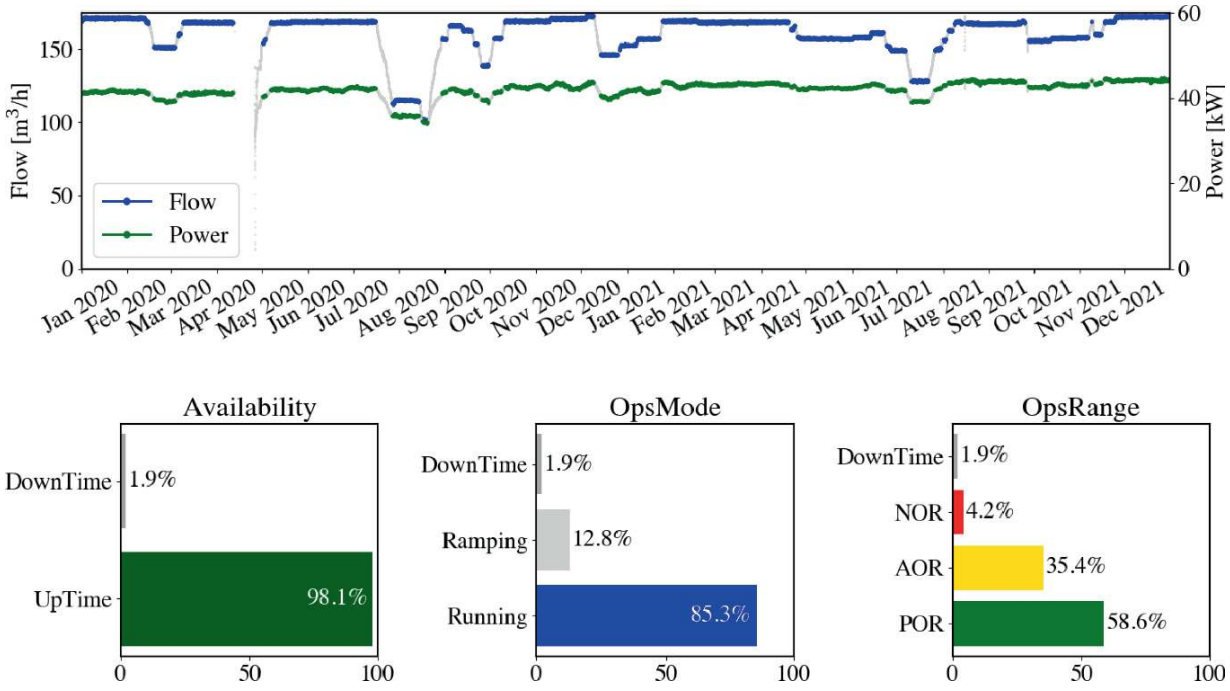


Fig. 10.6 Pump 2 showing time series of control variables together with aggregated operating regime labels over two years

Both pumps are operated in relatively stable flow plateaus over time intervals spanning days to weeks. Pump 1 shows one significant downtime in Q3 2021, yielding an overall utilization of approximately 95%, with steady-state running accounting for around 91.4%. Ramping behavior is limited. The pump operates in the Preferred Operating Region during 77.7% of total time, with 17.5% in the AOR, and a small

fraction of 0.1% in the NOR, mostly attributable to brief transients during start-up and shutdown.

Pump 2 shows a higher overall utilization of approximately 98% but exhibits considerably more frequent ramping and greater variation in flow levels. It spends only 58.6% of total time in the POR, with a substantial 35.4% in the AOR. Notably, in Q3 2020, Pump 2 operates for several consecutive weeks below the acceptable flow range, contributing to the 4.2% of operation classified as NOR.

MTBF Degradation Based on Operating History The MTBF degradation provides a quantitative measure of how pump operation, relative to design conditions, affects long-term reliability. It maps the recorded flow rates over time against the statistically reasoned reliability curve introduced in Eq. (10.7). While this measure does not incorporate direct indicators of the machine's physical state, it serves as a useful proxy to assess operational impact on expected reliability. It can support maintenance decision-making by identifying when adjusted intervals may be appropriate based on accumulated operational stress.

To compute the time-integrated MTBF penalty factor, the inverse of the reliability function from Eq. (10.7) is applied. To prevent unrealistically large penalties caused by brief passages through NOR, particularly during ramp-up phases, the reliability values are clipped at a lower bound, which corresponds to an upper limit on the applied penalty. The resulting MTBF is always expressed relative to continuous operation at BEP, which defines a baseline value of 100%. During downtime, the MTBF value is held constant, as the pump is not in operation. It is important to note that the resulting MTBF curve is not necessarily monotonic. Periods of off-design operation can be offset by subsequent operation closer to the BEP, leading to partial recovery in the penalty factor. The applied degradation model here is intentionally simplified. It does not account for the number of start-stop cycles, the impact of transients, or degradation that may accumulate during calendar time when the machine is offline.

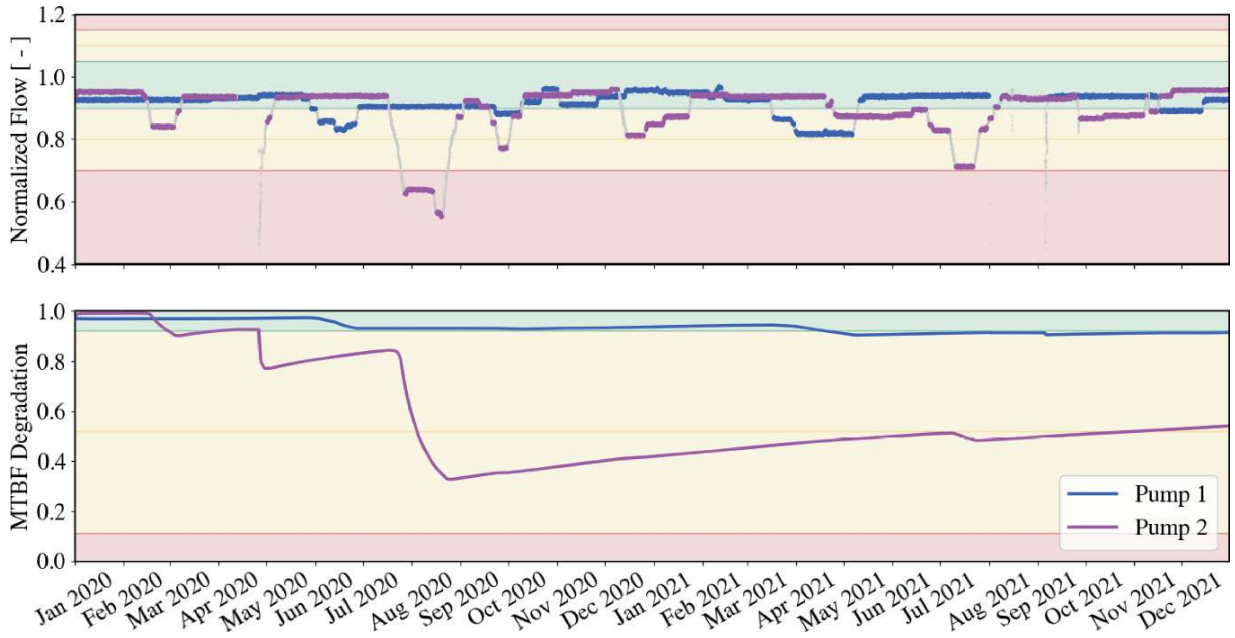


Fig. 10.7 MTBF degradation based on operating history for Pump 1 and Pump 2, with background shading indicating operating regimes and corresponding relative penalty factors

Figure 10.7 shows the flow rate normalized by BEP for Pump 1 and Pump 2, overlaid on a background indicating the corresponding operating regimes (POR, AOR, NOR). Below, the resulting MTBF degradation curves are plotted for both pumps, highlighting the cumulative penalty factors and their correspondence to the different operating ranges. In line with the operational profiles presented earlier, Pump 1 operates predominantly within POR, resulting in an MTBF degradation that remains close to 90%. In contrast, Pump 2 shows more extensive off-design operation, especially in Q2 and Q3 of 2020, where prolonged operation in the NOR region leads to a degradation as low as 40%. Due to improved operating conditions in 2021, the penalty factor gradually recovers to around 50%.

As introduced at the beginning, the MTBF degradation metric can serve as decision support for adapting maintenance intervals. For instance, assume that under ideal POR operation, expected lifetimes are approximately 2 years for seals, 5 years for bearings, and 10 years for casing and impeller (Hodgson and Walters 2002). By tracking the operational profile and resulting MTBF degradation over time, these

intervals can be adjusted systematically, improving the alignment between maintenance planning and operational exposure.

Parameter Estimation from Operational Data To estimate the characteristic parameters of the pumps, we focus exclusively on time segments corresponding to steady-state running. This selection filters out transients and dynamic states where machine behavior is not yet settled, ensuring that the extracted performance characteristics reflect stable operating conditions. The analysis uses the theoretically derived ansatz functions for head and power, as defined in Eqs. (10.3) and (10.4). Since both pumps operate at constant speed, rotational speed Ω can be treated as fixed, leading to reduced forms of the ansatz functions. In this simplified setting, head and power are modeled as second- and third-order polynomials in flow rate Q, respectively. Assuming constant fluid density, efficiency η is calculated as the ratio of these two polynomials, forming a rational function.

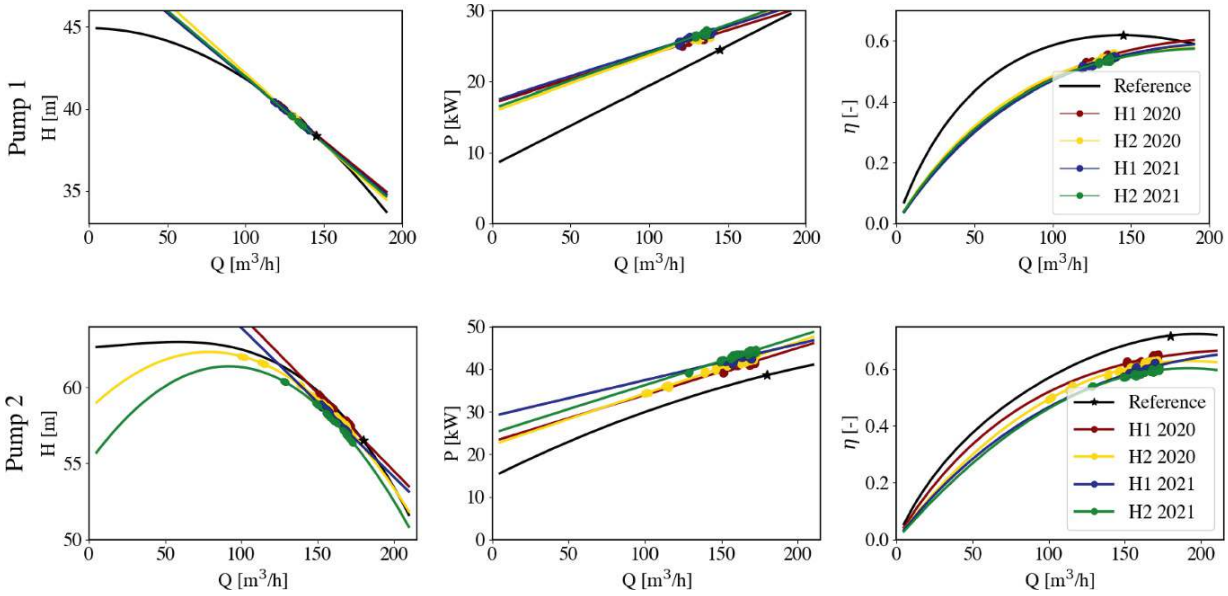


Fig. 10.8 Operational data and fitted characteristic curves for head, power, and efficiency across two pumps and time segments

To explore degradation trends over time, the dataset is divided into half-year intervals, allowing the evolution of model fits to be examined across successive operating periods. Figure 10.8 shows both the raw data and the fitted characteristic curves for Pumps 1 and 2. Pump 1

operates within a narrow flow range, slightly below the BEP, leading to a tightly clustered data distribution. Head values align closely with the reference curve, while power consistently exceeds it, largely due to contributions from coupling and auxiliary systems not captured in the reference curve. This results in observed efficiency values that are systematically lower. The data points are tightly clustered, and no clear degradation trend is immediately visible. In contrast, Pump 2 operates over a broader flow range, particularly for H2 2020 and H2 2021. This broader distribution allows for better resolution of performance changes over time. A downward trend in head, relative to the reference curve, becomes visible, accompanied by an increase in power demand and a corresponding decrease in efficiency. This pattern is consistent with the imposed predominantly hydraulic degradation.

The generally narrow operational ranges limit the model complexity that can be supported. Applying higher-order polynomials leads to overfitting, especially in head modeling. For Pump 1 a first-order polynomial proves most appropriate, as the available data does not sufficiently span the operational envelope to justify more complex fits. As a result, performance degradation cannot be reliably inferred. Pump 2 benefits from its broader operational variability. For H1 2020 and H1 2021, flow ranges are similarly constrained, making only a first-order polynomial a justifiable choice for head modeling. For H2 2020 and H2 2021, the operating envelope widens, requiring the use of second-order polynomials to capture changes in machine behavior. For power modeling a first-order polynomial is applied and the resulting rational function for the efficiency generally captures the degradation trend over time for Pump 2. While no regularization was applied here to keep the analysis focused, regularization becomes valuable when scaling this approach and model complexity must be systematically controlled.

The key takeaway is that while theoretically derived hypothesis functions are essential for informed model structure, their practical application requires adequate and well balanced data variability. Without sufficient range in the operating data, even well-reasoned functional forms may become difficult to effectively leverage. The

complexity of the proposed model needs to be adequately reflected by the dataset.

10.3 System-Level Modeling of a Two-Stage Centrifugal Compressor

In the previous section, the focus was placed on reliability modeling of an individual component within a system. We now shift toward a holistic, system-level perspective by examining a compressor setup instrumented with both process and condition-related sensors. The emphasis here is on sensor mapping, contextualization, and the interpretation of signal relationships, and incorporating the notion of coupling as discussed in Sect. 10.1.4. Since the dataset is synthetic, aspects such as metadata integrity and time series data quality, as discussed in Sect. 1.5.3, are not addressed here. However, it should be emphasized that these aspects are essential for real operational data. For time series data specifically, typical preprocessing steps would include labeling intervals where time series data is available or missing, detecting duplicated timestamps, identifying missing timestamps or missing values, filtering out unphysical value ranges, and detecting frozen sensors.

10.3.1 Two-Stage Centrifugal Compressor Dataset

To illustrate these concepts, we consider an example of a two-stage centrifugal compressor system designed for high-throughput gas compression. This configuration is representative of setups commonly used in natural gas services, such as pipeline booster stations. The example is intended to reflect a realistic and practically typical configuration, with characteristics and gas properties drawn from natural gas service applications, including molecular weight and compressibility factor values based on the study by Almeida et al. (2014). The stage specifications are summarized in Table 10.4. The considered system operates at a substantial mass flow rate of approximately 285 kg/s, with the pressure increasing from an inlet of

60 bar to a discharge pressure of 95 bar. Compression is achieved in two stages, with intercooling applied between them to reduce the inlet temperature of the second stage.

Table 10.4 Specifications for Compressor Stage 1 and Stage 2

The **polytropic head** quantifies the mass-specific energy added to the gas during compression and corresponds to the enthalpy increase discussed in Sect. 5.1.4. The effects of the real and irreversible compression process, such as pressure losses, internal friction, and heat transfer, are reflected through the use of a polytropic exponent that differs from the ideal isentropic value. The exponent *n* captures the deviation from ideal gas behavior and describes the actual thermodynamic path, following the relation $p^{n-1}T^n = \text{const}$. Accounting for real gas behavior via the compressibility factor *Z*, the polytropic head is given by

$$\Delta h_p = \frac{n}{n-1}\frac{ZRT_{in}}{M}\left[\left(\frac{p_{out}}{p_{in}}\right)^{\frac{n-1}{n}} - 1\right] . \tag{10.9}$$

From this, the **shaft power**, which is the actual power required to drive the compressor, is computed. It depends on the realized mass flow rate and the polytropic efficiency η_p, which accounts for mechanical and transmission losses with

$$W_{\text{shaft}} = \frac{1}{\eta_p}\dot{m}\Delta h_p \ . \tag{10.10}$$

The use of intercooling between the two compression stages reduces the inlet temperature of the second stage, thereby lowering the required polytropic head. In this example, the resulting cooling effect yields a power reduction of approximately 10% in the second stage.

Instrumentation The compressor system is instrumented with a comprehensive set of 39 sensors to support system control, monitor process conditions, assess equipment health, and track the auxiliary

subsystems. Control-related sensors include setpoints for pressure and rotor speed indicators. Speed indicators SI2100A and SI2100B represent redundant or at least directly comparable measurements, both capturing the same physical quantity. As discussed in Sect. 10.1.5, such redundant configurations are characteristic of tightly coupled systems. They enable sensor validation and reliability checks based on expected signal similarity, and support the mapping of operating states and the detection of dynamic transitions over time.

The process sensors capture the thermodynamic state of the working fluid. These include pressure and temperature measurements at the suction and discharge of each compression stage, as well as flow rate measurements at the system inlet. These signals describe the compressor's operating behavior and enable continuous evaluation of stage performance. Their readings are physically coupled through thermodynamic and fluid dynamic relations, which allows for inference of operating regimes and energy efficiency. Note that in the current configuration, no dedicated sensor is available for measuring the pressure at the inlet of Stage 2. For modeling purposes, the outlet pressure of Stage 1 is used as the closest available approximation. However, due to the pressure drop introduced by the interstage cooler, the actual Stage 2 inlet pressure will be slightly lower.

Condition sensors are mounted on the rotor and bearing components to monitor vibration, axial displacement, and temperature at multiple locations. Measurements are available for both A/B tags and at both the drive end (DE) and non-drive end (NDE). For example, vibration sensors VI2113A and VI2113B are installed in orthogonal directions to capture mechanical oscillations along distinct axes. A mirrored configuration is applied at the NDE side using VI2114A/B. These vibration signals are expected to be highly correlated, though with axis-specific and phase-dependent characteristics, as discussed in Sect. 10.1.5. Bearing temperature measurements follow a similar pattern, providing perspectives on thermal loading and frictional

behavior. These signals are critical for detecting early signs of misalignment, wear, or lubrication issues.

Support system sensors monitor parameters within the lubrication and seal oil subsystems. These include supply pressure, oil level, and differential pressures that help assess subsystem functionality. The dynamics of support systems are typically only indirectly coupled to the compressor's core operation, often visible only at the system state level. These may signal deviations such as increased bearing temperatures following lubrication degradation.

The resulting structured sensor map, enriched with relevant attributes and shown in Table 10.5, enables consistent interpretation of sensor data in modeling and diagnostics. It is aligned with the system boundary and hierarchy introduced in Sect. 10.1.3, enabling monitoring of the operational, performance, and condition behavior of the compressor and its auxiliary systems.

Table 10.5 Overview of sensor tags by associated system, element type, measured physical quantity and unit, and location attributes

10.3.2 Operating Profile

Figure 10.9 illustrates the operating profile of the compressor, showing speed and flow signals normalized by their respective design values from Table 10.4. In the time series plots, transient periods are shown in light gray to visually deemphasize them relative to the colored segments that represent steady-state operation. The accompanying box plot summarizes only the data recorded during those steady-state intervals.

The machine operates continuously over a period of approximately six months, with a single start-up at the beginning and a shutdown at the end of the regarded period. Throughout this time, the rotational speed remains consistently within ±2 % of the design value. As shown in the plot, the speed setpoint and both speed indicators are closely aligned, with no observable discrepancies. The normalized compressor flow rate spans a broader range, approximately 83–103% of the design

condition. The flow rate sensor FI2100 reports volumetric flow in Nm^3/h, meaning the values are referenced to normal conditions (1.01325 bar, 0 °C). Because the working fluid is highly compressed, the absolute volume flows at the Stage 1 and Stage 2 inlets are substantially lower than the value reported by FI2100. In Fig. 10.9, these inlet flows are shown as normalized quantities, scaled relative to their respective design values listed in Table 10.4, enabling a direct comparison with the normalized FI2100 signal.

For most of the operating period, the normalized Stage 1 inlet volume flow corresponds closely to the normalized value reported by FI2100. In contrast, the Stage 2 inlet volume flow reflects not only the system operating mode but also inherits any performance deviations of upstream Stage 1. It therefore captures the cumulative effects of Stage 1 compression, as seen in the associated pressure and temperature signals in Fig. 10.9. A visible reduction in both volume flow and speed occurs after approximately three months, lasting for around ten days. This interval appears in the box plot as an extension of the lower quantiles and whiskers.

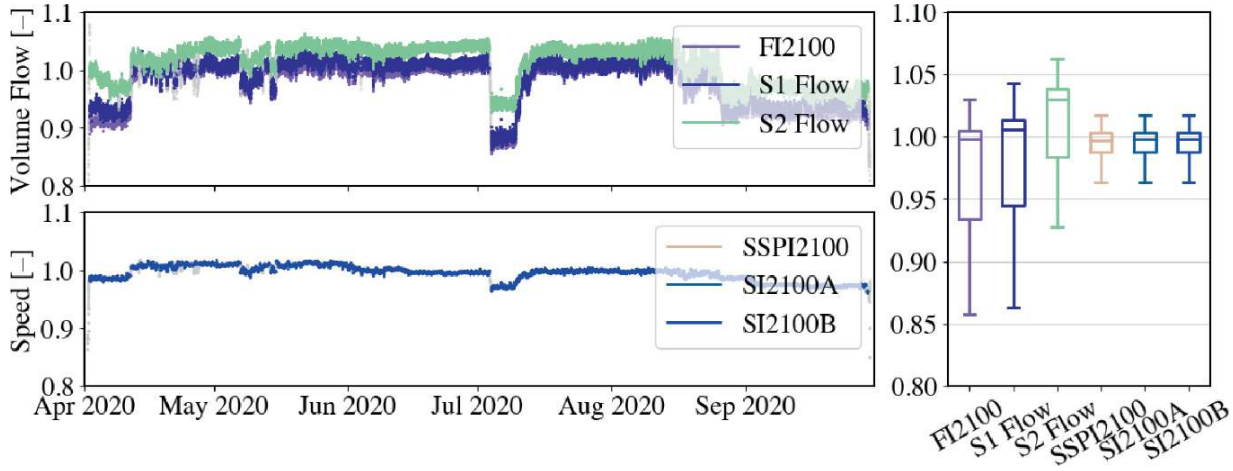


Fig. 10.9 Normalized compressor flow and speed signals over time, with boxplot summarizing values during steady-state operation

To provide operational context, the time series are labeled with respect to availability and operating modes, following the categorization introduced in Fig. 10.3. Availability is determined using

speed and flow signals, indicating near-full utilization over the six-month period. Within this uptime, the operation is further distinguished between regular running, which accounts for approximately 93%, and ramping phases, which cover around 6.4%. Identifying the intervals when the system operates under steady-state conditions is essential, as performance KPIs are only meaningful during such periods. The third histogram in Fig. 10.10 shows the origin of transient behavior, categorized by whether it is attributed to control, process, or condition-related tags. Transient detection is based on thresholding and configurable time intervals used to evaluate changes.

Only those periods in which all tags within a given category exhibit transient behavior are labeled accordingly. This ensures that detected transitions reflect actual system dynamics rather than single sensor faults or spurious signal fluctuations. Note that the breakdown of transient periods by category is not additive, since certain intervals may simultaneously involve transients across multiple categories. As in the previous time series plots, transient intervals are consistently displayed in light gray to visually deemphasize them relative to steady-state segments.

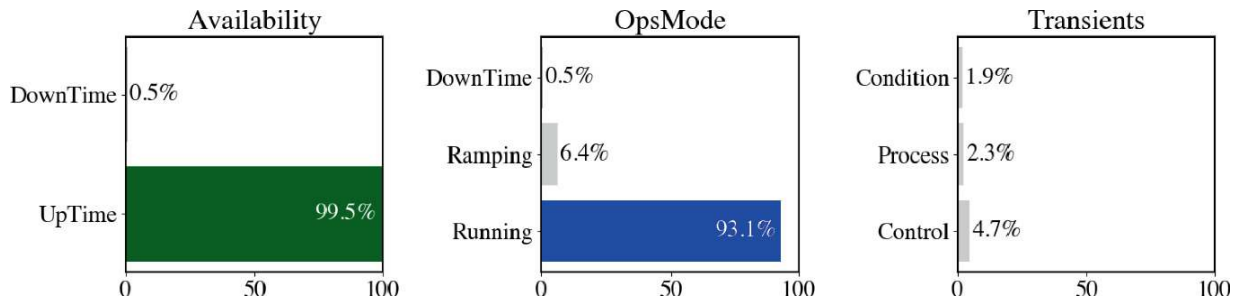


Fig. 10.10 Distribution of operating modes and origin of transient behavior based on control, process, and condition signals

10.3.3 Performance Profile

A structured tag map is essential for calculating typical engineering performance indicators, such as pressure and temperature ratios or the polytropic coefficient. These derived quantities provide insight into the compressor's thermodynamic behavior and energy conversion efficiency. To interpret performance in the context of varying speed and

flow conditions, the analysis must also incorporate equipment performance curves. As emphasized before, such evaluations are meaningful only during steady-state operation.

To illustrate the underlying compression behavior, Fig. 10.11 shows pressure and temperature signals at the suction and discharge sides of both compression stages. According to the coupling discussion in Sect. 10.1.5, pressure and temperature sensors located at the same point in the system are strongly coupled through the thermodynamic state of the working fluid. Across the stages, pressure and temperature evolution is coupled through the compression process itself.

For Stage 1, the pressure setpoint PSPI2101 and the measured value PI2101 are nearly identical throughout the operating period. The inlet pressure remains relatively stable around 60 bar, while the inlet temperature varies between about 13 °C and 21 °C. Since no dedicated pressure sensor is installed at the inlet of Stage 2, the discharge pressure from Stage 1 is used as proxy. The actual inlet pressure of Stage 2 is slightly lower due to pressure loss across the interstage cooler. The corresponding inlet temperature of Stage 2 is also reduced by intercooling to the range of 13 °C to 19 °C, which, as expected is lower than the Stage 1 discharge temperature. Variations in discharge pressure and temperature reflect changes in operating conditions. These are particularly noticeable around July 2020, when a shift in the operating regime becomes visible for both stages.

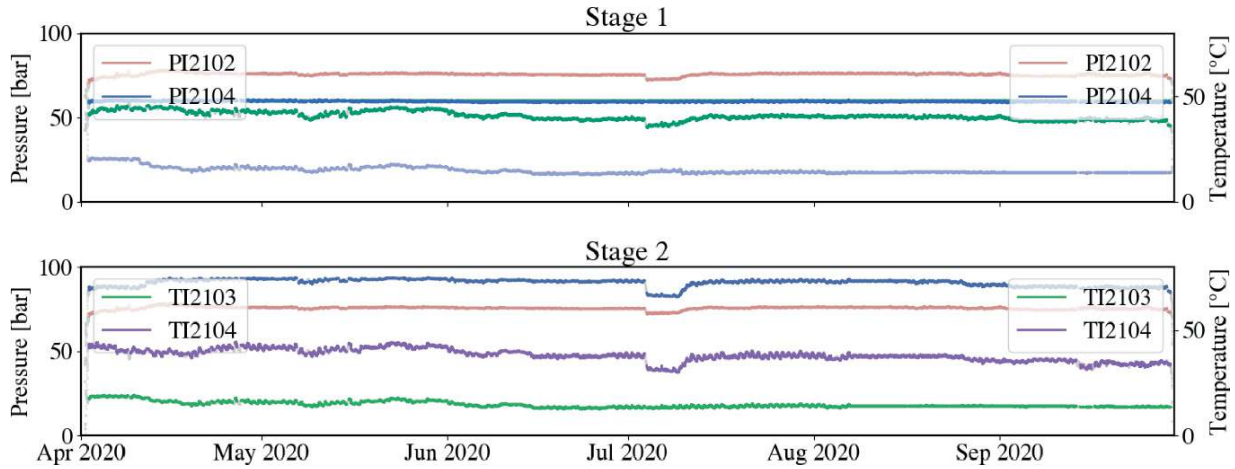


Fig. 10.11 Stage wise process variables over time. Shown are suction and discharge pressures and temperatures for both compression stages

To characterize the compression process more directly, Fig. 10.12 presents two sets of plots. On the left, pressure and temperature ratios for both stages are shown as time series. On the right, the upper plot shows temperature ratio versus pressure ratio, while the lower plot displays the polytropic coefficient as a function of pressure ratio. In both right-hand plots, gray data points indicate intervals where the system is not in steady-state operation and correspondingly exhibit larger deviations in value range. The design-point values from Table 10.4 are included for reference. In general, the observed pressure and temperature ratios lie below the design expectations. The computed polytropic coefficient tends to be higher than the design value, indicating a less efficient compression process. This is consistent with physical expectations, as increasing polytropic exponent corresponds to greater deviation from ideal isentropic compression.

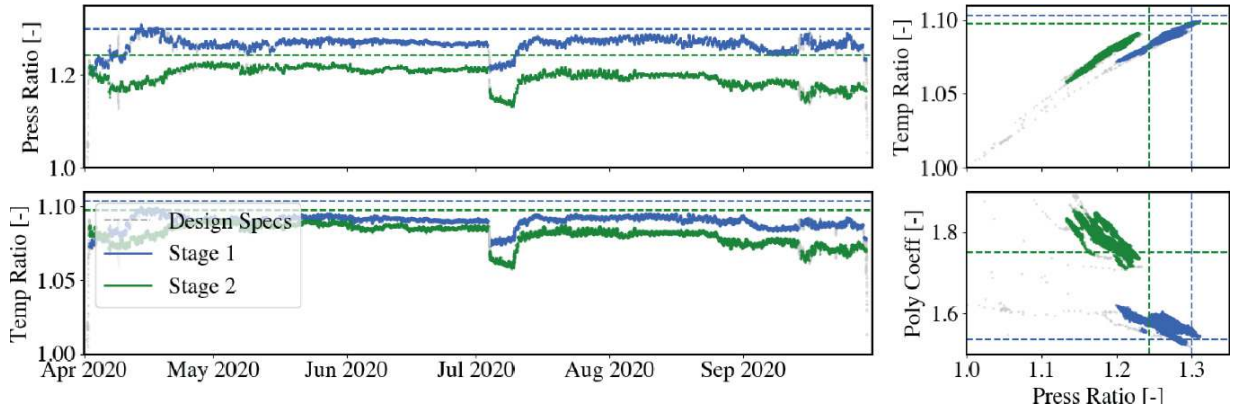


Fig. 10.12 Evolution of pressure and temperature ratios over time for both stages (left). Stage wise temperature ratio and polytropic coefficient as a function of pressure ratio (right). Design values from Table 10.4 are shown for comparison

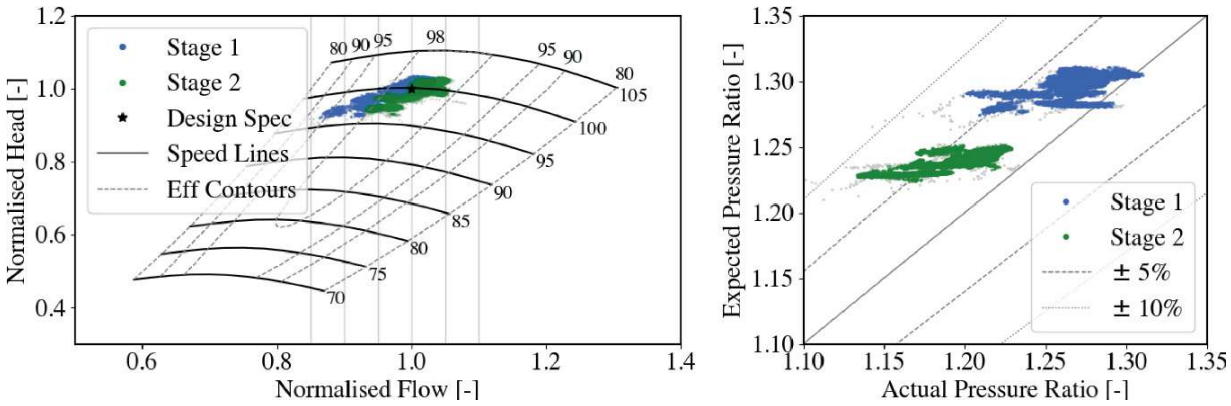


Fig. 10.13 Compressor operating points shown on the performance map (left) and compared to expected pressure ratios derived from map interpolation (right)

While the design specifications offer a useful point of reference, they represent only a single nominal operating condition and do not capture the full range of behavior across varying flow and speed regimes. A more dynamic representation is provided by the compressor map, discussed in greater detail in Sect. 4.4. In Fig. 10.13, the measured operating states for each stage are contextualized within the compressor map. The left plot shows the polytropic head as a function of normalized flow, overlaid with speed lines and efficiency contours. This map provides a comprehensive representation of the compressor's performance characteristics and helps identify where the current operating regime lies relative to the design envelope. The measured flow and speed conditions are superimposed on the map to indicate the distribution of operating points.

Based on interpolation of the polytropic head and efficiency values at each operating point, expected pressure ratios are calculated and compared to actual measurements in the right plot. This comparison allows for the identification of deviations from expected behavior and supports performance assessment under varying load conditions.

Across most of the operating range, the measured pressure ratios lie within a 5% margin below the expected values, indicating reasonable performance consistency. The same methodology can be extended to compare other derived quantities as well, such as the polytropic head

or shaft power, allowing for targeted performance monitoring under variable load conditions.

10.3.4 Condition Profile

The structured tag mapping and sensor contextualization introduced earlier also support condition monitoring during steady-state operation. As an example, we examine the temperature signals from thrust and radial bearing sensors, shown in Figs. 10.14 and 10.15. These sensors are grouped to A/B pairs at both the drive end (DE) and non-drive end (NDE), as listed in Table 10.5. As discussed in Sect. 10.1.5, such A/B sensor pairs are tightly coupled, and analyzing them together helps reveal underlying patterns and anomalies.

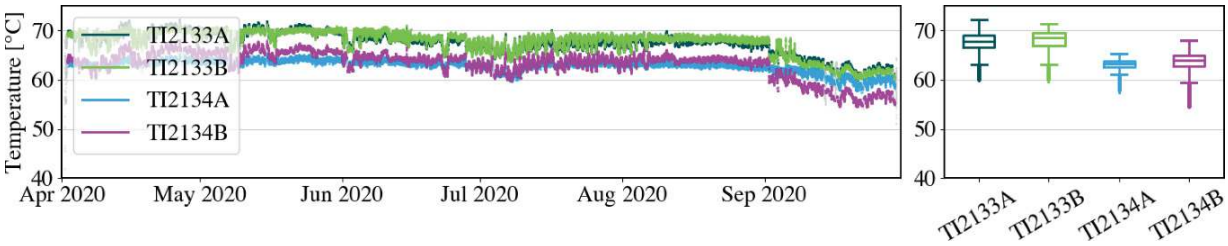


Fig. 10.14 Thrust bearing temperature indicators at the drive end (TI2133A/B) and non-drive end (TI2134A/B), with corresponding boxplots during steady-state operation

Figure 10.14 shows the temperature indicators from the thrust bearings. The signals exhibit consistent behavior within each A/B pair and across ends, with a systematic temperature offset of a few degrees between the DE and NDE. In contrast, the radial bearing temperatures in Fig. 10.15 show a more pronounced deviation. While three of the sensor signals remain closely aligned, the measurement from TI2124A begins to diverge significantly, particularly from mid-June onward. This deviation may indicate an instrumentation fault. Such deviations become apparent through comparison across sensor groups and would be difficult to detect without the structured mapping of sensor function, location, and coupling relationships.

By analyzing sensor groups with shared function and physical proximity, one can identify patterns such as level shifts, variance changes, signal drift, or emerging seasonal trends. While the plots

shown here rely on visual inspection, reliable anomaly detection in practice requires dedicated time series analysis techniques. These may include trend detection, outlier identification, or statistical feature extraction. For further details on time series methodologies, including feature selection and detection frameworks, the reader is referred to Nielsen (2019) and specialized software libraries (Christ et al. 2018).

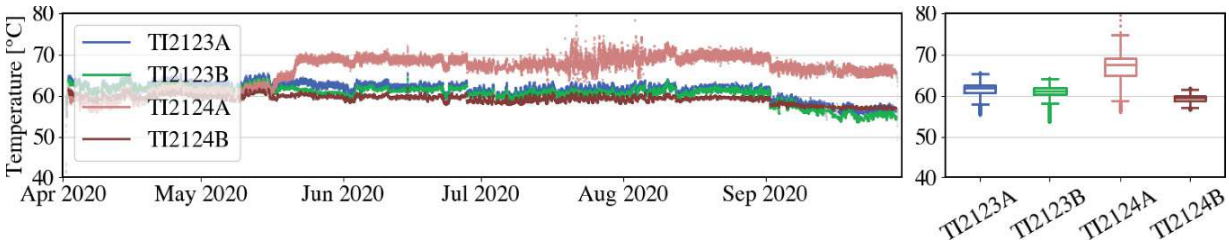


Fig. 10.15 Radial bearing temperature indicators at the drive end (TI2123A/B) and non-drive end (TI2124A/B), with corresponding boxplots during steady-state operation

10.4 Data Centric Analysis of Turbofan Engine Degradation

In contrast to the previous examples that focused on physical modeling at the component or system level, this section presents an example where insight is developed from sensor data without relying on predefined physical relationships. The goal is not to build a predictive model directly, but to showcase enriching the data context in a data-driven way, supporting subsequent modeling efforts.

The dataset used in this case is provided by NASA's Prognostics Center of Excellence and was originally developed for the Prognostics and Health Management data challenge (Saxena et al. 2008). It is based on simulations from the Commercial Modular Aero-Propulsion System Simulation (C-MAPSS) and describes the behavior of turbofan engines under a variety of operating conditions and fault modes. The data have been widely adopted for the development and benchmarking of prognostic models.

Unlike the previous case studies that begin from system knowledge and structured variables, this example takes a data-first perspective.

The process is guided by the evolution of signal patterns and observed variability in the data, rather than by governing equations. Within the modeling framework introduced in Sect. 1.1.2, this corresponds to a data-driven or dark-gray-box setting. Only limited domain knowledge is applied, and the emphasis is on learning structure and context from the data itself.

The detailed modeling of Remaining Useful Life (RUL) is omitted here. Instead, we focus on augmenting the dataset with contextual labels that classify operational regimes and distinguish between failure modes. This step-wise enrichment supports the effective application of machine learning models by making the structure in the data more accessible and interpretable.

10.4.1 Turbofan Dataset Description

The dataset represents a fleet of identical turbofan engines, each operating under different conditions and subject to different degradation paths. All simulations were conducted at high fidelity, designed to reflect realistic sensor behavior, including measurement noise and non-stationary signal trends. Each engine starts in a nominal operational state and is simulated until failure, allowing for the modeling of Remaining Useful Life (RUL). Figure 10.16 shows a schematic of the simulated engine components as well as a flowchart outlining the structure of the modeled subsystems. Sensor readings include temperature, pressure, flow rates, and rotational speed.

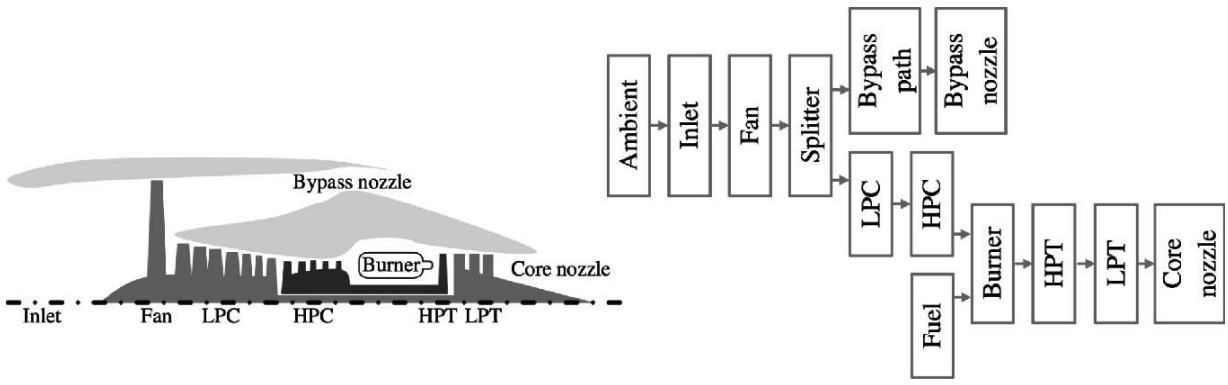


Fig. 10.16 Engine diagram with basic fragments of a C-MAPSS engine simulation (left). Flow chart with assembly of different simulated subsystems (right). Adopted from Saxena et al. (2008)

Table 10.6 Overview of the four turbofan datasets with their trajectories, operating conditions, and failure modes

Four separate datasets are provided, denoted as FD001 through FD004. Each case reflects a different level of complexity in terms of operating conditions and failure modes. FD001 represents the simplest scenario, with a single operating condition at sea level and one failure mode involving degradation of the high-pressure compressor (HPC). FD002 introduces variability in operating conditions across six different regimes while still retaining a single failure mode. FD003 returns to constant sea level operation but includes two distinct failure modes, involving either the HPC or the fan. FD004 combines both operational variability and multiple failure modes, making it the most complex of the four cases. A summary is provided in Table 10.6.

Each dataset contains 26 columns. The first column gives the engine unit, the second provides the cycle count that serves as a time index, and columns three to five record the operational settings, which vary depending on the simulation scenario. The remaining 21 columns capture sensor measurements from different engine subsystems, as detailed in Table 10.7. These operational settings strongly influence engine behavior and must be considered when interpreting sensor trends. As summarized in Table 10.6, the data are split into training and test sets. In the training sets, each engine starts from an unknown initial condition that reflects variability in wear or manufacturing and is operated until failure, with the final cycle marking its end of life.

Table 10.7 Mapping of dataset columns to corresponding sensor signals and units

In order to model the remaining useful life, it is helpful to augment the dataset with additional contextual labels. These include the RUL target variable, urgency classes indicating time to failure, and labels for operating modes and failure modes. These derived variables allow the dataset to accommodate the increasing complexity across cases FD001

to FD004 and support more targeted modeling approaches, as shown in the following.

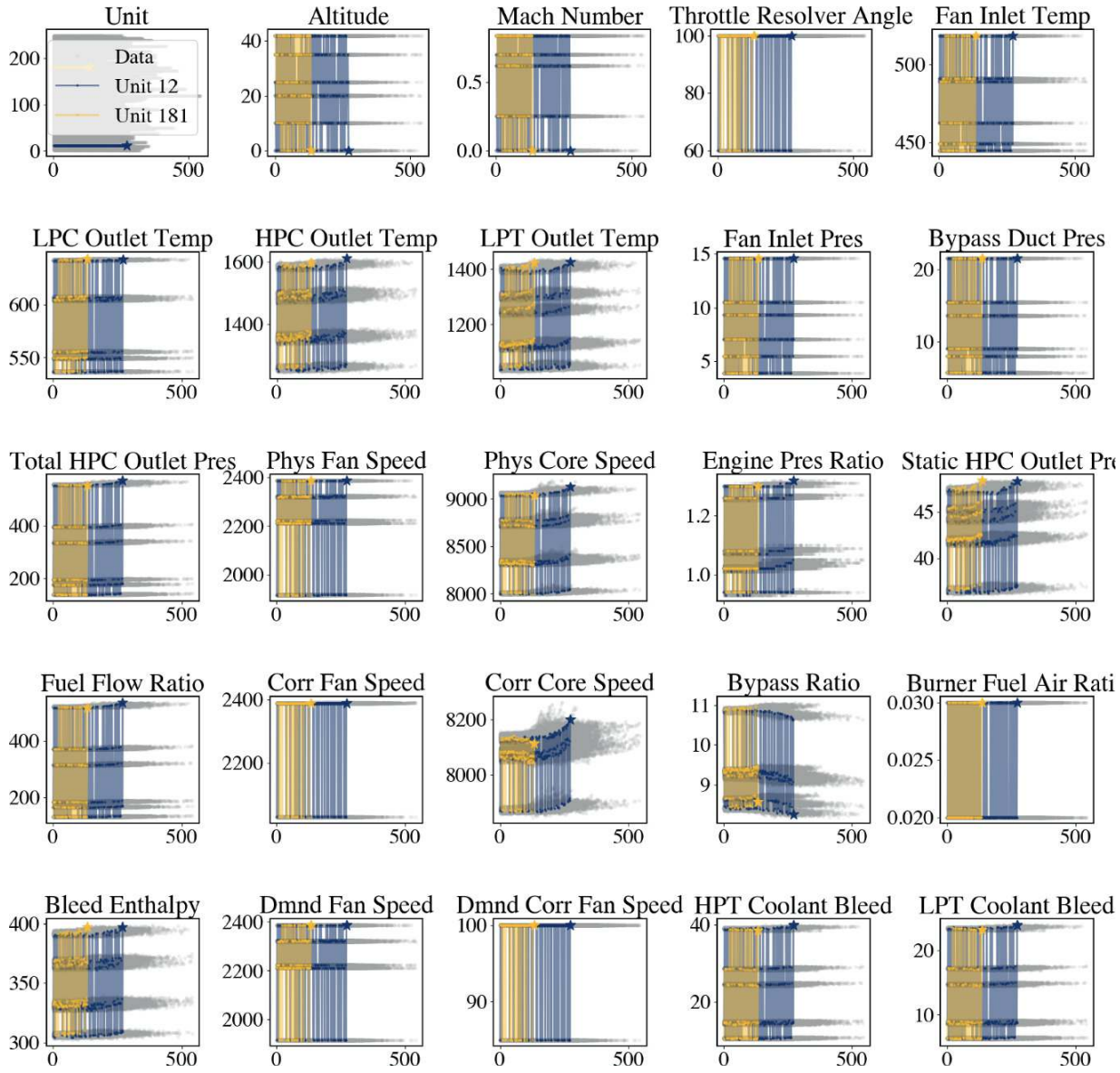


Fig. 10.17 Sensor signals over time for engines in FD004, showing signal trajectories for two engine units

10.4.2 Operational Settings

Datasets FD001 and FD003 operate under a single condition at sea level. As a result, the operational settings remain constant across all engine units, aside from minor variations due to noise. In contrast, datasets FD002 and FD004 include variation across six operating

conditions. These reflect different simulation regimes defined by combinations of three operational settings, namely altitude, Mach number, and throttle setting. Figure 10.17 shows the signal trajectories across the full FD004 training set, with selected trajectories highlighted for two engines. In the top row, the three operational settings display clear discrete levels. The operational settings vary over time for each individual engine unit, and this variability propagates through the system, producing corresponding changes in the measured sensor signals.

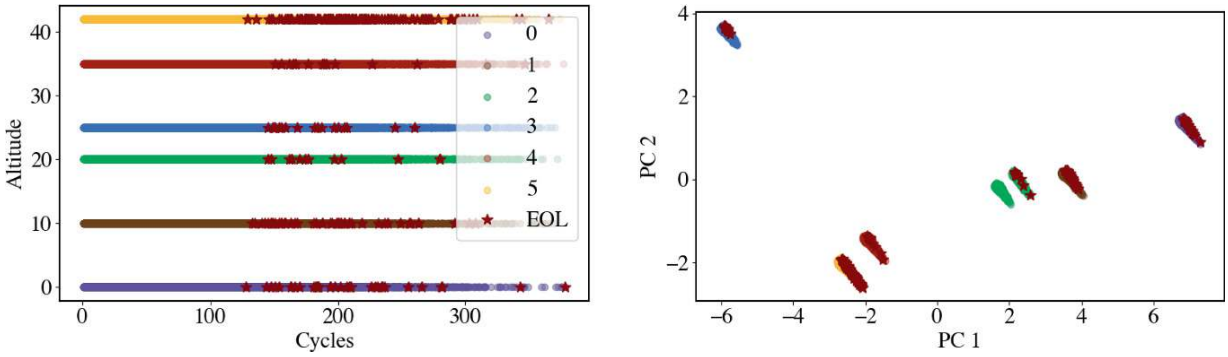


Fig. 10.18 Labeled operating regimes by altitude (left) and in reduced-dimensionality space (right) for case FD002

For the altitude variable, six distinct levels can be observed. The Mach number takes on five distinct values, and the throttle resolver angle switches between two. Based on this, the operational settings can be grouped into six discrete regimes, which are labeled in the following. The sensor measurements, such as LPTOutletTemp, TotalHPCOutletPres, or BypassRatio, form clusters whose value ranges depend on the operational regime. This introduces an important source of variability, since changes in sensor values may reflect either a shift in operating conditions or the onset of degradation. Therefore, classifying and labeling the operational regimes is an important step.

Figure 10.18 shows the labeled operating regimes for dataset FD002. On the left, the labels are shown based on altitude. On the right, the same labels are used to color the data projected onto the first two

principal components, showing that the operating regime has a significant signature onto the overall data structure.

Figure 10.19 shows two selected sensor signals of FD002, again colored by operating regime. The clear separation in value ranges confirms the strong influence of operational mode on signal behavior. Incorporating the context of the respective operational regime is helpful to modeling the degradation trajectories and serves as an effective form of feature engineering for a reliable Remaining Useful Life estimation. By accounting for changes in operational conditions, it becomes possible to separate normal operating variability from true degradation effects. This context allows degradation patterns to be identified within consistent operating regimes, where signal trends are more comparable and less affected by confounding shifts.

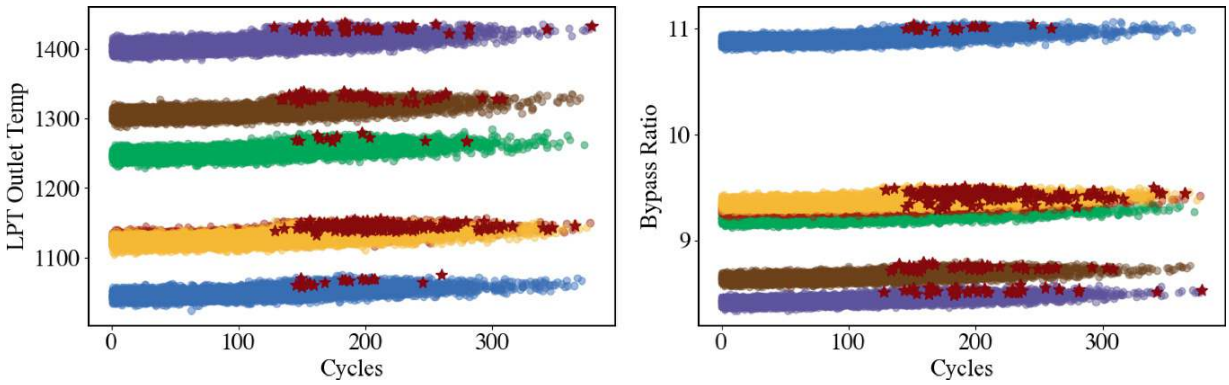


Fig. 10.19 Labeled operating modes for case FD002 for selected sensor measurements

10.4.3 Degradation Trends and Fault Modes

The remaining useful life (RUL) represents the target variable and is defined for all four datasets. It is a numerical variable that measures the number of cycles remaining until failure, making it suitable for regression-based modeling approaches. RUL reaches zero at the end of life (EOL). To aid interpretation and exploratory analysis, the RUL values can also be categorized into urgency classes as follows

- **Long** $\geq$ 201 cycles
- **Medium** 126–200 cycles
- **Short** 51–125 cycles

- **Urgent** 0–50 cycles

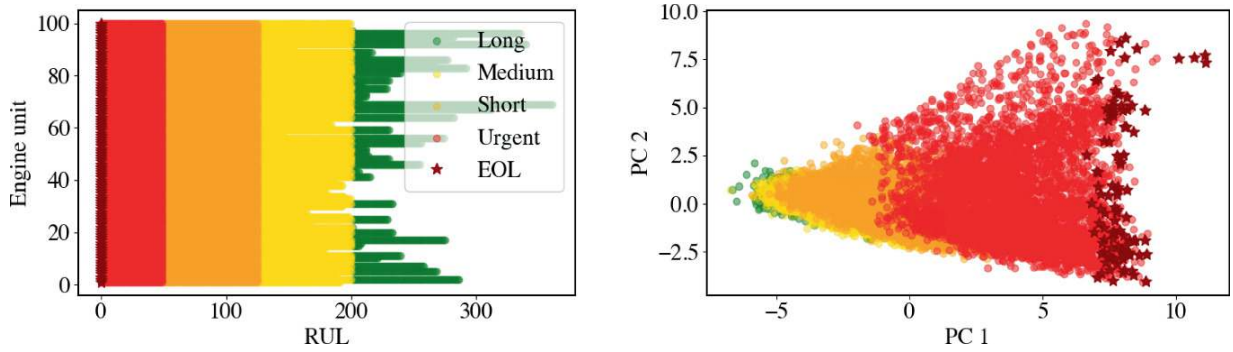


Fig. 10.20 Remaining useful life for the different engine units for case FD001 (left). First two principal components of sensor readings for case FD001 colored by the urgency indicator (right)

These class boundaries are arbitrarily chosen and can be adjusted. The classification is particularly useful when visually analyzing degradation behavior. It helps to identify signal patterns that become more pronounced as failure approaches. In cases where RUL modeling is framed as a classification task instead of a regression task, the urgency label can also serve directly as a target variable. Both the RUL and the categorical urgency labels are illustrated in Fig. 10.20 for dataset FD001. The left panel shows the RUL progression across different engine units. On the right, sensor signals are projected into a reduced-dimensionality space using the first two principal components, and colored according to urgency class. A clear trend emerges along the first principal component, with EOL occurring at values around PC1 > 6.

In datasets FD001 and FD002, the only failure mode is the progressive degradation of the high-pressure compressor. This failure behavior is reflected in the dimensionality reduced signal space, where the degradation trend aligns with one dominant direction. In contrast, datasets FD003 and FD004 include two different fault modes. Each engine can degrade either through high-pressure compressor failure or through fan degradation. These two modes follow distinct physical mechanisms and develop with different signal characteristics and progression rates. Identifying and labeling the respective fault modes is therefore an important preparatory step for modeling.

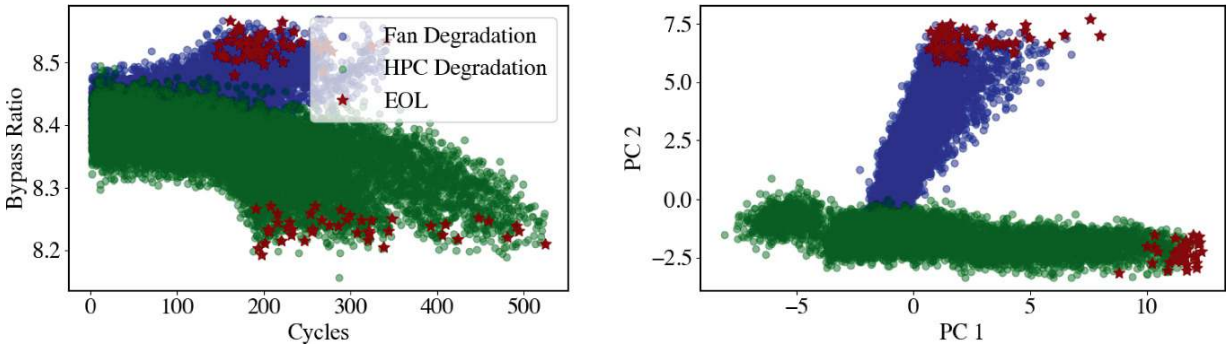


Fig. 10.21 Labeled fault modes illustrated for the BypassRatio of case FD003 (left). First two principal components of sensor readings for case FD003 colored by the fault modes (right)

In Fig. 10.21 this labeling is shown for dataset FD003. The left panel highlights differences in the bypass ratio for the two fault types. The right panel shows the same data projected into the first two principal components. It is important to note that the PCA transformation is applied independently for each dataset, so the interpretation of principal components differs between cases. Insights into the contributing signals for the respective principal components can be obtained from Fig. 8.17 in Sect. 8.4. As illustrated in Fig. 10.21, each failure mode imprints a distinct trend into the sensor data. For high-pressure compressor degradation, the BypassRatio signal tends to gradually decrease. In contrast, fan degradation shows a slight upward trend in the same signal. While BypassRatio serves as a useful example, many other signals contribute to the evolving system behavior. In the reduced space, these combined effects are captured through principal components, which summarize dominant patterns across all sensors. HPC degradation is mostly associated with increasing values of PC1, whereas fan degradation tends to manifest more clearly along PC2. These differing trends reflect the underlying physics of the fault mechanisms and provide valuable input when designing condition indicators or predictive models.

References

Almeida J, Velásquez J, Barbieri R (2014) A methodology for calculating the natural gas compressibility factor for a distribution network. Pet Sci Technol 32(21):2616–2624

Christ M, Braun N, Neuffer J, Kempa-Liehr AW (2018) Time series feature extraction on basis of scalable hypothesis tests (tsfresh – a python package). Neurocomputing 307:72–77 [https://doi.org/10.1016/j.neucom.2018.03.067]

DEXPI e.V. (2025) Data exchange in the process industry, 2025. URL www.dexpi.org. Accessed: July 2025

Gülich JF (2010) Centrifugal pumps. Springer, Berlin

Hodgson JE, Walters TW (2002) Optimizing pumping systems to minimize first or life-cycle cost. In: Proceedings of the 19th international pump users symposium

International Organization for Standardization (2016) ISO 14224:2016 – petroleum, petrochemical and natural gas industries – collection and exchange of reliability and maintenance data for equipment, 2016. ISO Standard

Isermann R (2011) Fault-diagnosis applications: model-based condition monitoring: actuators, drives, machinery, plants, sensors, and fault-tolerant systems. Springer, Berlin [https://doi.org/10.1007/978-3-642-12767-0]

Nielsen A (2019) Practical time series analysis: prediction with statistics and machine learning. O'Reilly

OPC Foundation (2025) OPCUA Reference, 2025. www.opcfoundation.org. Accessed: July 2025

Saxena A, Goebel K, Simon D, Eklund N (2008) Damage propagation modeling for aircraft engine run-to-failure simulation. In: Proceedings of the 1st international conference on prognostics and health management (PHM08), Denver CO

SINTEF Technology, Society, Norges teknisk-naturvitenskapelige universitet, and DNV GL (2015) OREDA: offshore and onshore reliability data handbook. Topside equipment. Number v. 1 in OREDA: offshore and onshore reliability data handbook. OREDA participants

© The Author(s), under exclusive license to Springer Fachmedien Wiesbaden GmbH, part of Springer Nature 2026
H. Gomaa, *Modeling with Knowledge and Data*, Mathematical Engineering
https://doi.org/10.1007/978-3-658-50679-7_11

11. Conclusion

Hassan Gomaa[1] ✉
(1) Strategic Projects Co-Innovation, Cognite, Oslo, Norway

In this book we have explored modeling approaches that combine physical knowledge with data, with emphasis on thermo-fluid systems such as fluid mechanics, multiphase flows, heat transfer, and turbomachinery. These domains have strong physical foundations, yet their complexity often calls for the complementary use of data to achieve models that are both accurate and applicable. We have presented hybrid modeling as a spectrum, ranging from models based primarily on first principles to those shaped predominantly by data. The appropriate position on this spectrum depends on the system, the available knowledge and data, and the goals of the modeling task.

Modeling Foundations The introductory Chap. 1 presented the central concepts of modeling, beginning with physical systems and extending toward aspects of knowledge and data. The discussion highlighted the importance of being explicit about the purpose of a model, its objective, and the strategy adopted in its construction. A clear articulation of these elements supports a systematic and deliberate modeling practice.

We also introduced a scale of hybrid models ranging from purely knowledge-based approaches to those relying predominantly on data. Pure knowledge-based models, termed white-box models, are grounded in first principles. These models are typically derived from fundamental conservation laws expressed as differential equations.

Their structure provides transparency and causal interpretability. However, in order to achieve solvability, such models usually rely on simplifying assumptions that can reduce their fidelity with respect to reality. Between white-box and fully data-driven models lie the family of gray-box approaches. These combine elements of physical theory with data-based inference. In light-gray-box models, the governing structure is retained but parameters or closure terms are estimated from data. In dark-gray-box models, even the functional structure of the model is shaped by data, while physical reasoning remains a guiding element for the selection of relevant quantities, nondimensional groups, or plausible functional forms.

Physical Systems Knowledge and Behavior Part I developed the first-principles foundation. It began with dimensional analysis in Chap. 2 to expose the structure of variables and equations, with the Π-theorem introduced as a central tool for identifying intrinsic relations through dimensionless numbers. Such abstractions provide invariance across scales and geometries, and they offer a powerful means for model generalization. Chapter 3 then introduced the primary variables and governing equations of thermo-fluid systems. The conservation of mass, momentum, energy, and entropy was established as the backbone of first-principle models, with typical boundary conditions presented alongside these laws.

In Chap. 4 we examined how the general governing equations can be simplified to capture the dominant behavior in specific regimes. This involved identifying which terms may be neglected, choosing appropriate fluid models, and analyzing scales relevant to compressible flows, viscous flows, turbulence, and other regimes. Similarity principles were introduced to enable the transfer of results across different operating conditions, with particular attention to turbomachinery. Chapter 5 provided canonical flow problems that serve both as benchmarks and as didactic cases capturing the foundational flow phenomenology. These included one-dimensional nozzle flows, shock waves, boundary layers, and internal flows in ducts and pipes. Each case illustrates how governing equations and their

simplifications are applied, and together they form the basis for more complex system models.

Uncertainty, Data, and Learning Part II addressed the role of uncertainty and data in modeling. Probability theory was introduced in Chap. 6, followed by statistical analysis and inference methods in Chap. 7. The transition to machine learning methods in Chap. 8 provided tools for model training, pattern recognition, and handling uncertainty. Together these chapters laid the groundwork for the data-oriented components of hybrid models.

Engineering Applications Modeling Part III integrated knowledge and data threads in application-oriented engineering contexts.

In Chap. 9, the discussion centered on relatively isolated processes, typically studied in laboratory experiments or high-fidelity simulations. In such settings the influencing variables can be controlled and boundary conditions precisely specified, which makes it possible to establish clear links between physical assumptions and model structure. A recurring theme in these examples is that generalization across regimes is enabled by nondimensional groups, which capture the balance of governing effects and provide a foundation for validity and transferability across different flow conditions and configurations. This principle underlies classical correlations in heat transfer and fluid mechanics and remains central to the construction of hybrid models where both physics and data play a role.

The examples in this chapter ranged from the damped pendulum, governed entirely by first principles, to turbulence modeling where data influences both the choice of parameters and aspects of the model form. The intermediate cases, such as heat transfer in boundary layers or droplet impact on wetted surfaces, demonstrated how nondimensional analysis guides the model structure, while empirical calibration extends fidelity where theoretical knowledge is incomplete. These cases illustrate how data complements physics in the development of hybrid models, while nondimensional reasoning anchors the results in physically meaningful and generalizable forms.

Chapter 10 turned to complex industrial systems, particularly turbomachinery. Unlike isolated processes, these systems are embedded in larger operational and environmental contexts. Their boundaries are shaped not only by design but also by operational demands. Influencing factors cannot be fully controlled, and data often reflect operational priorities rather than modeling requirements. This leads to challenges such as uneven coverage of operating regimes, limited representation of transients, and imbalanced datasets.

In this industrial context the modeling process begins not with isolated equations but with system-level understanding of boundaries, operational conditions, and data availability. Hybrid approaches are particularly valuable here, as they integrate physical reasoning with data-driven inference to support tasks such as monitoring, reliability estimation, and maintenance planning. The examples included component-level pump models, system-level compressor models, and data-driven analyses of turbofan engine degradation. These cases highlighted the need for contextualization of data and domain knowledge as prerequisites for meaningful modeling.

A challenge is that even when the structure of a model can, in principle, be derived from first principles, the available data may be too imbalanced, sparse, or noisy to utilize the full richness of such formulations. What enables meaningful modeling in this setting is the incorporation of context at multiple levels. At the system hierarchy level, context defines how subsystems interact and exchange mass, work, and heat. At the sensor level, context provides information about placement, reliability, and relevance of measurements. At the operational level, context captures typical profiles, off-design behavior, and patterns of system use. At the diagnostic level, context is linked to degradation trends, failure modes, and reliability considerations. Each of these layers contributes to interpreting data in a way that connects it back to the governing physics.

In this sense, hybrid modeling of industrial systems is less about deriving a closed set of equations and more about integrating partial physical descriptions with operational data, guided by contextual

knowledge. This perspective recognizes the limitations of both purely first-principle and purely data-driven strategies, and frames hybrid models as a means to remain applicable to practical settings while retaining a foundation in domain understanding.

Appendix A

A Curvilinear Coordinates

Many engineering problems involve geometries that are more naturally described using non-Cartesian coordinates. Although Cartesian coordinates are intuitive and mathematically convenient, they can become cumbersome for domains with curved boundaries or complex geometric alignment. In such cases, curvilinear coordinates provide a better fit to the underlying geometry. They offer analytical simplifications in symmetric problems and enable geometry-conforming discretizations in numerical simulations. The formulation presented here follows the treatments in Back (1968) and Spurk (1996).

We describe the physical domain by $\Omega(\mathbf{x}) \subset \mathbb{R}^3$, where $\mathbf{x} = (x, y, z)$ are the standard Cartesian coordinates. To better align with geometric features of the domain, we introduce the **curvilinear coordinate system** $\mathbf{q} = (q_1, q_2, q_3)$, related to Cartesian coordinates through a smooth, invertible mapping $\mathbf{x} = \mathbf{x}(\mathbf{q})$ with inverse $\mathbf{q} = \mathbf{q}(\mathbf{x})$. We restrict our attention to **orthogonal curvilinear coordinates**, in which coordinate lines intersect at right angles. At each point, the tangent vectors to the coordinate curves define the orthonormal basis

$$\mathbf{e}_1 = \frac{1}{h_1}\frac{\partial \mathbf{x}}{\partial q_1} \ , \quad \mathbf{e}_2 = \frac{1}{h_2}\frac{\partial \mathbf{x}}{\partial q_2} \ , \quad \mathbf{e}_3 = \frac{1}{h_3}\frac{\partial \mathbf{x}}{\partial q_3} \ , \tag{A.1}$$

where h_1, h_2, and h_3 are the **metric scale factors**, given by

$$h_1 = \left|\frac{\partial \mathbf{x}}{\partial q_1}\right| \ , \quad h_2 = \left|\frac{\partial \mathbf{x}}{\partial q_2}\right| \ , \quad h_3 = \left|\frac{\partial \mathbf{x}}{\partial q_3}\right| \ . \tag{A.2}$$

These scale factors describe local stretching or compression of the coordinate system and are essential for expressing physical quantities such as distances, areas, and volumes. The orthogonality simplifies the structure of differential operators by eliminating mixed derivatives and off-diagonal terms in the metric tensor. The metric tensor $\mathbf{J}^\top \mathbf{J}$, with $\mathbf{J} = \partial \mathbf{x} / \partial \mathbf{q}$ the Jacobian of the transformation, becomes diagonal with

entries h_1^2, h_2^2, and h_3^2. This structure not only simplifies the derivation of governing equations but also allows inverse transformations to be computed directly from the Jacobian transpose, greatly simplifying coordinate changes in practice.

In the following, we develop the mathematical tools needed to work in orthogonal curvilinear coordinates. Figure A.1 shows a schematic of a volume element, where the local basis vectors and scale factors define the differential geometry of the coordinate system. We begin by representing infinitesimal line, surface, and volume elements in the new basis. We then proceed to derive the expressions for the gradient, divergence, curl, and Laplacian operators to express the governing equations in general geometries.

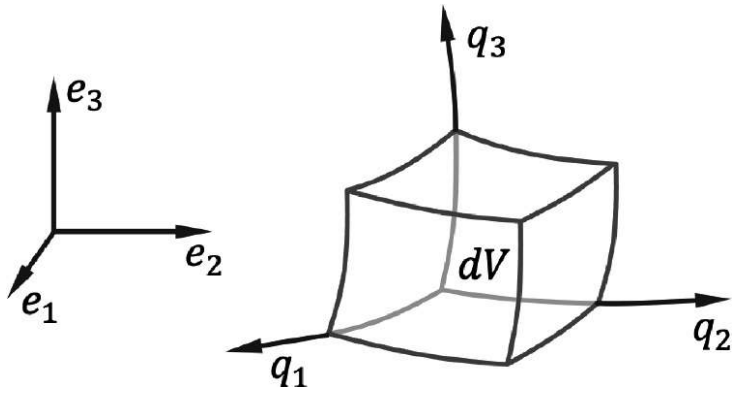


Fig. 1 Volume element in orthogonal curvilinear coordinates (Spurk 1996)

Infinitesimal Increments To express differential operators in curvilinear coordinates, we first examine how infinitesimal increments in space relate to the transformed coordinate system. These differential elements define how lengths, areas, and volumes are measured locally. A natural starting point is the total differential of the position vector $\mathbf{x} = \mathbf{x}(\mathbf{q})$, which expresses an infinitesimal displacement in physical space in terms of differentials in the curvilinear coordinates

$$d\mathbf{x} = \frac{\partial \mathbf{x}}{\partial q_1} dq_1 + \frac{\partial \mathbf{x}}{\partial q_2} dq_2 + \frac{\partial \mathbf{x}}{\partial q_3} dq_3 = h_1 dq_1 \mathbf{e}_1 + h_2 dq_2 \mathbf{e}_2 + h_3 dq_3 \mathbf{e}_3 \quad . \text{(A.3)}$$

The result is a decomposition of the infinitesimal displacement into orthogonal contributions along each coordinate direction.

The differential **arc length** of a line element ds is then obtained by computing the Euclidean norm of $d\mathbf{x}$

$$ds = \sqrt{d\mathbf{x} \cdot d\mathbf{x}} = \sqrt{h_1^2 (dq_1)^2 + h_2^2 (dq_2)^2 + h_3^2 (dq_3)^2} \ . \tag{A.4}$$

The infinitesimal **surface elements** are oriented perpendicular to each coordinate direction and can be computed as the magnitude of the cross product of the two tangent vectors spanning the surface. For surfaces normal to q_1, q_2, and q_3, respectively, we obtain

$$\begin{aligned} dS_1 &= |h_2 dq_2 \mathbf{e}_2 \times h_3 dq_3 \mathbf{e}_3| = h_2 h_3 \, dq_2 dq_3 \ , \\ dS_2 &= h_1 h_3 \, dq_1 dq_3 \ , \quad dS_3 = h_1 h_2 \, dq_1 dq_2 \ . \end{aligned} \tag{A.5}$$

The infinitesimal **volume element** dV is obtained from the scalar triple product of the differential vectors along the three coordinate directions, resulting in

$$dV = [(\mathbf{e}_1 \cdot d\mathbf{x})\mathbf{e}_1 \times (\mathbf{e}_2 \cdot d\mathbf{x})\mathbf{e}_2] \cdot (\mathbf{e}_3 \cdot d\mathbf{x})\mathbf{e}_3 = h_1 h_2 h_3 \, dq_1 dq_2 dq_3 \ . \tag{A.6}$$

These expressions provide the geometric foundation for constructing differential operators in curvilinear coordinates and will be used in the following derivation of governing equations.

Differential Operators To express the governing equations in curvilinear form, general expressions for the differential operators must be derived. The **gradient** of a scalar field f in curvilinear coordinates is given by

$$\nabla f = \tfrac{1}{h_1} \tfrac{\partial f}{\partial q_1} \mathbf{e}_1 + \tfrac{1}{h_2} \tfrac{\partial f}{\partial q_2} \mathbf{e}_2 + \tfrac{1}{h_3} \tfrac{\partial f}{\partial q_3} \mathbf{e}_3 \ . \tag{A.7}$$

The **divergence** of a vector field $\mathbf{u} = (u, v, w)$ is defined as the limit of the net flux of $\mathbf{u}$ through a closed surface S enclosing a vanishingly small volume V, that is,

$$\nabla \cdot \mathbf{u} = \lim_{V \to 0} \ \tfrac{1}{V} \oint_S \mathbf{u} \cdot \mathbf{n} \ dS \ , \tag{A.8}$$

where $\mathbf{n}$ is the outward-pointing unit normal to the surface S. To evaluate this, we project $\mathbf{u}$ onto the $\mathbf{q}$-basis and multiply each component by the corresponding differential surface area element. For instance, the q_1-component contributes $\oint_{S_1} \mathbf{u}\cdot\mathbf{n}\, dS = \frac{\partial}{\partial q_1}(h_2 h_3 u)\, dq_1 dq_2 dq_3$, and similar expressions hold for q_2 and q_3. Summing all contributions and dividing by the differential volume, we obtain the general expression

$$\nabla\cdot\mathbf{u} = \frac{1}{h_1 h_2 h_3}\left[\frac{\partial}{\partial q_1}(h_2 h_3 u) + \frac{\partial}{\partial q_2}(h_1 h_3 v) + \frac{\partial}{\partial q_3}(h_1 h_2 w)\right] . \tag{A.9}$$

The divergence of a second-order tensor field, such as the stress tensor $\boldsymbol{\tau}$, follows from a similar procedure but includes additional terms due to the variation of the basis vectors. The components of the divergence $\nabla\cdot\boldsymbol{\tau}$ are given by

$$\begin{aligned}
(\nabla\cdot\boldsymbol{\tau})_1 = &\ \frac{1}{h_1 h_2 h_3}\left[\frac{\partial}{\partial q_1}(h_2 h_3 \tau_{11}) + \frac{\partial}{\partial q_2}(h_1 h_3 \tau_{21}) + \frac{\partial}{\partial q_3}(h_1 h_2 \tau_{31})\right] \\
&+ \frac{\tau_{21}}{h_1 h_2}\frac{\partial h_1}{\partial q_2} + \frac{\tau_{31}}{h_1 h_3}\frac{\partial h_1}{\partial q_3} - \frac{\tau_{22}}{h_1 h_2}\frac{\partial h_2}{\partial q_1} - \frac{\tau_{33}}{h_1 h_3}\frac{\partial h_3}{\partial q_1} , \\
(\nabla\cdot\boldsymbol{\tau})_2 = &\ \frac{1}{h_1 h_2 h_3}\left[\frac{\partial}{\partial q_1}(h_2 h_3 \tau_{12}) + \frac{\partial}{\partial q_2}(h_1 h_3 \tau_{22}) + \frac{\partial}{\partial q_3}(h_1 h_2 \tau_{32})\right] \\
&+ \frac{\tau_{12}}{h_1 h_2}\frac{\partial h_2}{\partial q_1} + \frac{\tau_{32}}{h_2 h_3}\frac{\partial h_2}{\partial q_3} - \frac{\tau_{11}}{h_1 h_2}\frac{\partial h_1}{\partial q_2} - \frac{\tau_{33}}{h_2 h_3}\frac{\partial h_3}{\partial q_2} , \\
(\nabla\cdot\boldsymbol{\tau})_3 = &\ \frac{1}{h_1 h_2 h_3}\left[\frac{\partial}{\partial q_1}(h_2 h_3 \tau_{13}) + \frac{\partial}{\partial q_2}(h_1 h_3 \tau_{23}) + \frac{\partial}{\partial q_3}(h_1 h_2 \tau_{33})\right] \\
&+ \frac{\tau_{23}}{h_2 h_3}\frac{\partial h_3}{\partial q_2} + \frac{\tau_{13}}{h_1 h_3}\frac{\partial h_3}{\partial q_1} - \frac{\tau_{22}}{h_2 h_3}\frac{\partial h_2}{\partial q_3} - \frac{\tau_{11}}{h_1 h_3}\frac{\partial h_1}{\partial q_3} .
\end{aligned} \tag{A.10}$$

In this notation, the first index of τ_{ij} indicates the direction of the surface normal, and the second index the direction of the stress component. For example, τ_{12} refers to the component acting in the q_2 direction on a surface normal to q_1.

The **curl** or rotation of a vector field $\mathbf{u}$ is defined by the line integral around an infinitesimal surface S oriented normal to a given vector direction $\mathbf{n}$

$$\nabla\times\mathbf{u}\big|_{\mathbf{n}} = \lim_{S\to 0}\ \frac{1}{S}\oint_{\partial S}\mathbf{u}\cdot d\mathbf{r} , \tag{A.11}$$

where ∂S is the closed boundary curve encircling the infinitesimal area S. Using Taylor expansions and collecting the component-wise circulation terms, the curl in curvilinear coordinates becomes

$$\begin{aligned}\nabla \times \mathbf{u} = \quad & \frac{1}{h_2 h_3}\left[\frac{\partial}{\partial q_2}(h_3 w) - \frac{\partial}{\partial q_3}(h_2 v)\right]\mathbf{e}_1 \\ + \quad & \frac{1}{h_1 h_3}\left[\frac{\partial}{\partial q_3}(h_1 u) - \frac{\partial}{\partial q_1}(h_3 w)\right]\mathbf{e}_2 \\ + \quad & \frac{1}{h_1 h_2}\left[\frac{\partial}{\partial q_1}(h_2 v) - \frac{\partial}{\partial q_2}(h_1 u)\right]\mathbf{e}_3 \ .\end{aligned} \tag{A.12}$$

Conservation Equations With the previously defined operators, the symbolic form of the conservation laws from Sect. 3.2 can now be expanded into their representations in orthogonal curvilinear coordinates. The continuity equation from Eq. (3.49) becomes

$$\frac{\partial \rho}{\partial t} + \frac{1}{h_1 h_2 h_3}\left[\frac{\partial}{\partial q_1}(h_2 h_3 \rho u) + \frac{\partial}{\partial q_2}(h_1 h_3 \rho v) + \frac{\partial}{\partial q_3}(h_1 h_2 \rho w)\right] = 0 \ . \tag{A.13}$$

Applying the vector identity $(\mathbf{u}\cdot\nabla)\cdot\mathbf{u} \equiv \nabla\mathbf{u}^2/2 - \mathbf{u}\times(\nabla\times\mathbf{u})$ to restructure the convective terms, the momentum equation from Eq. (3.53) is written in curvilinear components as

$$\begin{aligned}
q_1: \quad & \rho\Big[\frac{\partial u}{\partial t} + \frac{u}{h_1}\frac{\partial u}{\partial q_1} + \frac{v}{h_2}\frac{\partial u}{\partial q_2} + \frac{w}{h_3}\frac{\partial u}{\partial q_3} + \frac{uv}{h_1 h_2}\frac{\partial h_1}{\partial q_2} + \frac{uw}{h_1 h_3}\frac{\partial h_1}{\partial q_3} \\
& \qquad - \frac{v^2}{h_1 h_2}\frac{\partial h_2}{\partial q_1} - \frac{w^2}{h_1 h_3}\frac{\partial h_3}{\partial q_1}\Big] = -\frac{1}{h_1}\frac{\partial p}{\partial q_1} + (\nabla\cdot\boldsymbol{\tau})_1 + f_1 \ , \\
q_2: \quad & \rho\Big[\frac{\partial v}{\partial t} + \frac{u}{h_1}\frac{\partial v}{\partial q_1} + \frac{v}{h_2}\frac{\partial v}{\partial q_2} + \frac{w}{h_3}\frac{\partial v}{\partial q_3} + \frac{uv}{h_1 h_2}\frac{\partial h_2}{\partial q_1} + \frac{vw}{h_2 h_3}\frac{\partial h_2}{\partial q_3} \\
& \qquad - \frac{u^2}{h_1 h_2}\frac{\partial h_1}{\partial q_2} - \frac{w^2}{h_2 h_3}\frac{\partial h_3}{\partial q_2}\Big] = -\frac{1}{h_2}\frac{\partial p}{\partial q_2} + (\nabla\cdot\boldsymbol{\tau})_2 + f_2 \ , \\
q_3: \quad & \rho\Big[\frac{\partial w}{\partial t} + \frac{u}{h_1}\frac{\partial w}{\partial q_1} + \frac{v}{h_2}\frac{\partial w}{\partial q_2} + \frac{w}{h_3}\frac{\partial w}{\partial q_3} + \frac{uw}{h_1 h_3}\frac{\partial h_3}{\partial q_1} + \frac{vw}{h_2 h_3}\frac{\partial h_3}{\partial q_2} \\
& \qquad - \frac{u^2}{h_1 h_3}\frac{\partial h_1}{\partial q_3} - \frac{v^2}{h_2 h_3}\frac{\partial h_2}{\partial q_3}\Big] = -\frac{1}{h_3}\frac{\partial p}{\partial q_3} + (\nabla\cdot\boldsymbol{\tau})_3 + f_3 \ .
\end{aligned} \tag{A.14}$$

As detailed in Sect. 3.1.2, for Newtonian fluids the viscous stress tensor $\boldsymbol{\tau}$ is defined by Eq. (3.29) as $\boldsymbol{\tau} = 2\mu\mathbf{S} + \lambda_b(\nabla\cdot\mathbf{u})\mathbf{I}$, where the components of the strain rate tensor $\mathbf{S}$ in curvilinear coordinates are

$$
\begin{aligned}
S_{11} &= \frac{1}{h_1}\frac{\partial u}{\partial q_1} + \frac{v}{h_1 h_2}\frac{\partial h_1}{\partial q_2} + \frac{w}{h_1 h_3}\frac{\partial h_1}{\partial q_3} \ , \\
S_{22} &= \frac{1}{h_2}\frac{\partial v}{\partial q_2} + \frac{u}{h_1 h_2}\frac{\partial h_2}{\partial q_1} + \frac{w}{h_2 h_3}\frac{\partial h_2}{\partial q_3} \ , \\
S_{33} &= \frac{1}{h_3}\frac{\partial w}{\partial q_3} + \frac{u}{h_1 h_3}\frac{\partial h_3}{\partial q_1} + \frac{v}{h_2 h_3}\frac{\partial h_3}{\partial q_2} \ , \\
S_{21} = S_{12} &= \frac{1}{2}\left[\frac{h_2}{h_1}\frac{\partial (v/h_2)}{\partial q_1} + \frac{h_1}{h_2}\frac{\partial (u/h_1)}{\partial q_2}\right] \ , \\
S_{31} = S_{13} &= \frac{1}{2}\left[\frac{h_1}{h_3}\frac{\partial (u/h_1)}{\partial q_3} + \frac{h_3}{h_1}\frac{\partial (w/h_3)}{\partial q_1}\right] \ , \\
S_{23} = S_{32} &= \frac{1}{2}\left[\frac{h_3}{h_2}\frac{\partial (w/h_2)}{\partial q_2} + \frac{h_2}{h_3}\frac{\partial (v/h_2)}{\partial q_3}\right] \ .
\end{aligned}
\tag{A.15}
$$

In Sect. 3.2.5, the energy equation was introduced in various forms for internal energy, enthalpy, and total enthalpy. Here, the contributing terms are expanded individually. For any scalar field f, such as e, h, h_t, or p, the convective term becomes

$$
(\mathbf{u}\cdot\nabla) f = \frac{u}{h_1}\frac{\partial f}{\partial q_1} + \frac{v}{h_2}\frac{\partial f}{\partial q_3} + \frac{w}{h_3}\frac{\partial f}{\partial q_3} \ .
\tag{A.16}
$$

The heat conduction term $\nabla\cdot\mathbf{q}$, using Fourier's law $\mathbf{q} = -k\nabla T$, is written as

$$
\begin{aligned}
\nabla\cdot\mathbf{q} = -\frac{1}{h_1 h_2 h_3} \quad & \left[\frac{\partial}{\partial q_1}\left(k\frac{h_2 h_3}{h_1}\frac{\partial T}{\partial q_1}\right) + \frac{\partial}{\partial q_2}\left(k\frac{h_1 h_3}{h_2}\frac{\partial T}{\partial q_2}\right)\right. \\
& \left. + \frac{\partial}{\partial q_3}\left(k\frac{h_1 h_2}{h_3}\frac{\partial T}{\partial q_3}\right)\right] \ .
\end{aligned}
\tag{A.17}
$$

The rate of work by body forces $\mathbf{f}\cdot\mathbf{u}$ is

$$
\mathbf{f}\cdot\mathbf{u} = f_1 u + f_2 v + f_3 w \ .
\tag{A.18}
$$

The viscous work term in the total enthalpy equation is

(A.19)

$$\begin{aligned}\nabla \cdot (\boldsymbol{\tau} \cdot \mathbf{u}) = \tfrac{1}{h_1 h_2 h_3} \quad & \Big(\tfrac{\partial}{\partial q_1} [h_2 h_3 (\tau_{11} u + \tau_{21} v + \tau_{31} w)] \\ & + \tfrac{\partial}{\partial q_2} [h_1 h_3 (\tau_{12} u + \tau_{22} v + \tau_{32} w)] \\ & + \tfrac{\partial}{\partial q_3} [h_1 h_2 (\tau_{13} u + \tau_{23} v + \tau_{33} w)] \Big) \ .\end{aligned}$$

Since the viscous stress tensor $\boldsymbol{\tau}$ is symmetric for Newtonian fluids, the dissipation function $\Phi = \boldsymbol{\tau} : \nabla \mathbf{u}$ can be expressed using the symmetric part of the velocity gradient, i.e., the strain rate tensor. Thus, the dissipation function evaluates to

$$\begin{aligned}\Phi = \boldsymbol{\tau} : (\nabla \mathbf{u}) \quad & = \tau_{11} \left(\tfrac{1}{h_1} \tfrac{\partial u}{\partial q_1} + \tfrac{v}{h_1 h_2} \tfrac{\partial h_1}{\partial q_2} + \tfrac{w}{h_1 h_3} \tfrac{\partial h_1}{\partial q_3} \right) \\ & + \tau_{22} \left(\tfrac{1}{h_2} \tfrac{\partial v}{\partial q_2} + \tfrac{u}{h_1 h_2} \tfrac{\partial h_2}{\partial q_1} + \tfrac{w}{h_2 h_3} \tfrac{\partial h_2}{\partial q_3} \right) \\ & + \tau_{33} \left(\tfrac{1}{h_3} \tfrac{\partial w}{\partial q_3} + \tfrac{u}{h_1 h_3} \tfrac{\partial h_3}{\partial q_1} + \tfrac{v}{h_2 h_3} \tfrac{\partial h_3}{\partial q_2} \right) \\ & + \tau_{12} \left(\tfrac{1}{h_2} \tfrac{\partial u}{\partial q_2} + \tfrac{1}{h_1} \tfrac{\partial v}{\partial q_1} - \tfrac{v}{h_1 h_2} \tfrac{\partial h_2}{\partial q_1} - \tfrac{u}{h_1 h_2} \tfrac{\partial h_1}{\partial q_2} \right) \\ & + \tau_{13} \left(\tfrac{1}{h_3} \tfrac{\partial u}{\partial q_3} + \tfrac{1}{h_1} \tfrac{\partial w}{\partial q_1} - \tfrac{w}{h_1 h_3} \tfrac{\partial h_3}{\partial q_1} - \tfrac{u}{h_1 h_3} \tfrac{\partial h_1}{\partial q_3} \right) \\ & + \tau_{23} \left(\tfrac{1}{h_3} \tfrac{\partial v}{\partial q_3} + \tfrac{1}{h_2} \tfrac{\partial w}{\partial q_2} - \tfrac{w}{h_2 h_3} \tfrac{\partial h_3}{\partial q_2} - \tfrac{v}{h_2 h_3} \tfrac{\partial h_2}{\partial q_3} \right) \ .\end{aligned} \tag{A.20}$$

Coordinate Systems Table A.1 lists the Cartesian representations and scale factors for cylindrical and spherical coordinate systems, along with two substrate-aligned local coordinate systems designed to conform to the surface geometry.

The first case corresponds to a body-aligned system where (ξ, y) span the substrate surface, and *z* points orthogonally outward from it. This configuration captures curvature in a single direction κ_ξ along ξ, while remaining Cartesian in the transverse *y*- and *z*-directions. The second case generalizes this to surfaces with curvature in two directions. Here, the surface is parameterized by (ξ, η), which follow the orthogonal lines of curvature on the substrate, and *n* points outward, normal to the surface. The coordinate system (ξ, η, n) is orthogonal and conjugate, such that the

principal curvatures κ_ξ and κ_η appear directly in the scale factors. It shall be noted that the negative sign in the scale factors results from defining the unit normal to point outward, while the principal normal vector points toward the center of curvature (Gomaa 2014). These values are directly used to evaluate metric terms and apply the general curvilinear formulations developed earlier. In particular, the scale factors determine how distances and differential operators transform in each system.

Table 1 Coordinate systems and scale factors (Back 1968; Gomaa 2014)

Orthogonal system and coordinates	**Rectangular coordinates**			**Scale factors**		
	x	***y***	***z***	h_1	h_2	h_3
Cylindrical (r, θ, z)	$r\cos\theta$	$r\sin\theta$	x	1	r	1
Spherical (r, ϕ, θ)	$r\cos\theta\sin\phi$	$r\sin\theta\sin\phi$	$r\cos\phi$	1	r	$r\sin\phi$
Surface with curvature κ_ξ **in** ξ	ξ	y	z	$1-\kappa_\xi z$	1	1
Surface with curvatures κ_ξ, κ_η	ξ	η	n	$1-\kappa_\xi n$	$1-\kappa_\eta n$	1

Appendix B

Selected Analytical Solutions

B.1 Harmonic Oscillator

A central theme in modeling mechanical systems is the description of oscillatory motion. In many cases, the dynamics can be approximated by a linear system with a single degree of freedom. This leads to the classical second-order linear differential equation with corresponding initial conditions

$$m\ddot{x} + d\dot{x} + kx = F \ , \quad x(t=0) = x_0 \ , \quad \dot{x}(t=0) = \dot{x}_0 \ . \tag{B.1}$$

Here, *m* denotes the mass or moment of inertia, *d* the translational or rotational damping coefficient, and *k* the stiffness of the system. The variable *x* represents the displacement, deflection, or angular position of the body, and *F* is the external force or torque. The parameters *m*, *d*, and *k* are assumed constant in time. For analytical convenience, the equation is transformed to its standard form

$$\ddot{x} + 2\delta\omega_0\dot{x} + \omega_0^2 x = \tfrac{\omega_0^2}{k} F \ , \quad \text{where} \quad \omega_0^2 = \tfrac{k}{m} \ , \quad \delta = \tfrac{d}{2\sqrt{mk}} \ , \tag{B.2}$$

which introduces the two key dimensionless system parameters ω_0 and δ. The quantity ω_0 is the natural angular frequency of the undamped system, while δ is the damping ratio.

Because the equation is linear, its general solution can be constructed through superposition. We begin with the homogeneous case. Introducing the ansatz $x(t) = c\,e^{\lambda t}$ leads to the characteristic equation $\lambda^2 + 2\delta\omega_0\lambda + \omega_0^2 = 0$, with roots $\lambda_{1,2} = -\delta\omega_0 \pm \omega_0\sqrt{\delta^2 - 1}$. The general solution is a linear combination of the two exponential terms with coefficients c_1 and c_2 determined by the initial conditions. The exact form of the solution depends on whether the characteristic

equation has real or complex roots, which is determined by the sign of $\delta^2 - 1$.

Classification by Damping Ratio The nature of the solution is governed by the damping ratio δ. In the case $\delta < 1$, known as the **underdamped** regime, the characteristic roots are complex conjugates with negative real parts $\lambda_{1,2} = -\delta\omega_0 \pm i\omega$ with the damped angular frequency $\omega = \omega_0\sqrt{1-\delta^2}$. For small damping ratios, ω remains close to the undamped natural frequency ω_0. The general solution takes the form

$$x(t) = e^{-\delta\omega_0 t}\left(c_1 e^{i\omega t} + c_2 e^{-i\omega t}\right) \ , \tag{B.3}$$

with constants c_1 and c_2 determined by the initial conditions.

In the **overdamped** case, where $\delta > 1$, the characteristic roots $\lambda_{1,2} = -\delta\omega_0 \pm \alpha$ are real and distinct with $\alpha = \omega_0\sqrt{\delta^2 - 1}$. The general solution becomes

$$x(t) = e^{-\delta\omega_0 t}\left(c_1 e^{\alpha t} + c_2 e^{-\alpha t}\right) \ . \tag{B.4}$$

For the special case of **critical damping**, $\delta = 1$, the two roots coincide and the general solution reduces to

$$x(t) = e^{-\omega_0 t}(c_1 + c_2 t) \ . \tag{B.5}$$

To determine the coefficients c_1 and c_2, we apply the initial conditions $x(0) = x_0$ and $\dot{x}(0) = \dot{x}_0$. Substituting the general solution and its derivative at $t = 0$ leads to the conditions

$$\begin{aligned} x(0) &= c_1 + c_2 = x_0 \ , \\ \dot{x}(0) &= c_1\lambda_1 + c_2\lambda_2 = x_0 \ . \end{aligned} \tag{B.6}$$

The conditions can be formulated as a linear system that can be solved by matrix inversion

(B.7)

$$
\begin{aligned}
\begin{pmatrix} 1 & 1 \\ \lambda_1 & \lambda_2 \end{pmatrix} \begin{pmatrix} c_1 \\ c_2 \end{pmatrix} &= \begin{pmatrix} x_0 \\ \dot{x}_0 \end{pmatrix} , \\
\begin{pmatrix} c_1 \\ c_2 \end{pmatrix} &= \tfrac{1}{\lambda_2 - \lambda_1} \begin{pmatrix} \lambda_2 & -1 \\ -\lambda_1 & 1 \end{pmatrix} \begin{pmatrix} x_0 \\ \dot{x}_0 \end{pmatrix} \\
&= \tfrac{1}{\lambda_2 - \lambda_1} \begin{pmatrix} \lambda_2 x_0 - \dot{x}_0 \\ -\lambda_1 x_0 - \dot{x}_0 \end{pmatrix} .
\end{aligned}
$$

Special and Closed-Form Solutions For each case, the general exponential solution can be refined by incorporating the initial conditions, yielding a complete description of the system's response.

For the underdamped case $\delta < 1$, substituting the coefficients into Eq. (B.3) and applying Euler's identity yields the solution in terms of sine and cosine functions

$$
\begin{aligned}
x(t) &= e^{-\delta\omega_0 t} \left(x_0 \cos(\omega t) + \tfrac{x_0 \delta\omega_0 + \dot{x}_0}{\omega} \sin(\omega t) \right) , \\
\dot{x}(t) &= e^{-\delta\omega_0 t} \left(\dot{x}_0 \cos(\omega t) - \tfrac{x_0 \omega_0^2 + \dot{x}_0 \delta\omega_0}{\omega} \sin(\omega t) \right) .
\end{aligned}
\tag{B.8}
$$

As a special case, when $\delta = 0$, the system becomes undamped, and the solution simplifies to

$$
\begin{aligned}
x(t) &= x_0 \cos(\omega_0 t) + \tfrac{\dot{x}_0}{\omega_0} \sin(\omega_0 t) , \\
\dot{x}(t) &= \dot{x}_0 \cos(\omega_0 t) - x_0 \omega_0 \sin(\omega_0 t) ,
\end{aligned}
\tag{B.9}
$$

where $\omega = \omega_0$ corresponds to the natural frequency.

For the overdamped case $\delta > 1$, substituting the coefficients into Eq. (B.4) leads to a solution expressed using hyperbolic functions

$$
\begin{aligned}
x(t) &= e^{-\delta\omega_0 t} \left(x_0 \cosh(\alpha t) + \tfrac{x_0 \delta\omega_0 + \dot{x}_0}{\alpha} \sinh(\alpha t) \right) , \\
\dot{x}(t) &= e^{-\delta\omega_0 t} \left(\dot{x}_0 \cosh(\alpha t) - \tfrac{x_0 \omega_0^2 - \dot{x}_0 \delta\omega_0}{\alpha} \sinh(\alpha t) \right) .
\end{aligned}
\tag{B.10}
$$

In the critically damped case $\delta = 1$, the solution from Eq. (B.5) becomes

$$
\begin{aligned}
x(t) &= e^{-\omega_0 t}(x_0 + (\omega_0 \varphi_0 + \dot{x}_0)t) \ , \\
\dot{x}(t) &= e^{-\omega_0 t}(\dot{x}_0 + \omega_0(\omega_0 \varphi_0 + \dot{x}_0)t) \ .
\end{aligned} \tag{B.11}
$$

B.2 Stokes Flow Past a Sphere

The steady, incompressible flow past a rigid sphere at low Reynolds numbers represents a key result in hydrodynamics and is often referred to as the classical Stokes solution (Acheson and Acheson 1990; Lamb 1932). Stokes (Stokes 1851) originally investigated the motion of a sphere through a viscous fluid to develop what are now known as the Stokes equations, which describe creeping flows where inertial effects are negligible. In such a regime, he determined the drag force acting on a sphere to follow the well-known linear relationship. As outlined in Sect. 4.3.4, the governing equations for creeping flow are obtained by neglecting inertial terms in the Navier-Stokes equations. The resulting system consists of the incompressible continuity equation

$$
\nabla \cdot \mathbf{u} = 0 \ , \tag{B.12}
$$

and the simplified momentum equation

$$
0 = -\tfrac{1}{\rho}\nabla p + \nu \nabla^2 \mathbf{u} \ , \tag{B.13}
$$

which describes the balance between pressure forces and viscous diffusion in the absence of inertia. Physically, this form of the momentum equation implies that the fluid motion is maintained purely by a pressure gradient overcoming the viscous resistance. We consider a sphere of radius R that is immersed in an otherwise uniform flow of velocity U_∞, that is aligned with the z-axis in Cartesian coordinates (x, y, z).

Simplification in Spherical Coordinates Due to the spherical geometry and axial symmetry of the problem, it is convenient to switch to spherical coordinates (r, θ, ϕ), discussed in Sect. A. Here, r denotes the radial distance from the origin, θ is the polar angle measured from

the z-axis, and ϕ is the azimuthal angle. The flow is assumed axisymmetric to the z-axis, and the boundary conditions become

$$\begin{aligned} r = R \;\; &: && u_r = 0, \quad u_\theta = 0 \;, \\ r \to \infty \;\; &: \;\; u_r = U_\infty \cos\theta, && u_\theta = -U_\infty \sin\theta \;. \end{aligned} \tag{B.14}$$

These express the no-slip condition at the surface of the sphere and the requirement that the velocity field tends to a uniform stream infinitely far away. Axisymmetry implies that the flow is independent of the azimuthal angle ϕ, and that the velocity field has no ϕ-component. Therefore, the velocity field may be written as

$$\tfrac{\partial}{\partial\phi} = 0 \;, \quad \mathbf{u} = (u_r(r,\theta), u_\theta(r,\theta), 0)^\top \;. \tag{B.15}$$

Substituting into the continuity equation and expressing it in spherical coordinates leads to

$$\tfrac{1}{r^2}\tfrac{\partial}{\partial r}(r^2 u_r) + \tfrac{1}{r\sin\theta}\tfrac{\partial}{\partial\theta}(u_\theta \sin\theta) = 0 \;. \tag{B.16}$$

To automatically satisfy the continuity equation, we introduce the scalar stream function $\psi(r,\theta)$ such that

$$u_r = \tfrac{1}{r^2\sin\theta}\tfrac{\partial\psi}{\partial\theta} \;, \quad u_\theta = -\tfrac{1}{r\sin\theta}\tfrac{\partial\psi}{\partial r} \;. \tag{B.17}$$

These definitions ensure that the velocity field is divergence free by design. With this, the velocity vector can also be expressed in a compact vector form

$$\begin{aligned} \mathbf{u} = \;& \tfrac{1}{r^2\sin\theta}\tfrac{\partial\psi}{\partial\theta}\mathbf{e}_r - \tfrac{1}{r\sin\theta}\tfrac{\partial\psi}{\partial r}\mathbf{e}_\theta \\ = \;& \nabla \times \left(\tfrac{\psi}{r\sin\theta}\mathbf{e}_\phi \right) \;. \end{aligned} \tag{B.18}$$

This representation identifies the velocity field as the curl of a vector potential in the ϕ-direction, which is a common approach for axisymmetric, incompressible flows. To now express the momentum

equation in terms of the stream function ψ, we begin by considering the vector identity $\nabla \times (\nabla \times \mathbf{u}) = \nabla(\nabla \cdot \mathbf{u}) - \nabla^2 \mathbf{u}$. Since the velocity field is incompressible, as stated in Eq. (B.12), the first term on the right-hand side vanishes, and the identity simplifies to

$$\nabla \times (\nabla \times \mathbf{u}) = -\nabla^2 \mathbf{u} \ . \tag{B.19}$$

To eliminate the pressure term in the momentum equation, we take the curl of Eq. (B.13). Applying the identity above leads to the vector equation

$$\nabla \times (\nabla \times (\nabla \times \mathbf{u})) = 0 \ . \tag{B.20}$$

Substituting the compact form of the velocity field from Eq. (B.18), we obtain

$$\nabla \times \nabla \times \left[\nabla \times \left(\nabla \times \tfrac{\psi}{r \sin\theta} \mathbf{e}_\phi \right) \right] = 0 \ . \tag{B.21}$$

This triple curl expression is cumbersome to evaluate directly, but it simplifies significantly due to the structure of the vector potential. The result of this operation, after simplification, is a scalar fourth-order partial differential equation for ψ

$$\left(\tfrac{\partial^2}{\partial r^2} + \tfrac{\sin\theta}{r^2} \tfrac{\partial}{\partial \theta} \left(\tfrac{1}{\sin\theta} \tfrac{\partial}{\partial \theta} \right) \right)^2 \psi = 0 \ . \tag{B.22}$$

This is the **biharmonic equation** for the stream function in spherical coordinates, and it governs the creeping flow of a viscous fluid around a sphere under the assumptions of axisymmetry and incompressibility (White 1991).

Solving the Equations To solve the governing equation (B.22) for the stream function $\psi(r, \theta)$, we begin by applying the far field boundary conditions given in Eq. (B.14). In the limit as $r \to \infty$, the flow must approach a uniform velocity field with components

(B.23)

$$
\begin{aligned}
u_r &= \quad U_\infty \cos\theta = \tfrac{1}{r^2 \sin\theta} \tfrac{\partial \psi}{\partial \theta} \quad , \\
u_\theta &= -U_\infty \sin\theta = -\tfrac{1}{r \sin\theta} \tfrac{\partial \psi}{\partial r} \quad ,
\end{aligned}
$$

The expressions relate the velocity components to the stream function in spherical coordinates. We now integrate the expressions in the far field limit to determine the asymptotic form of ψ as $r \to \infty$. Integrating the second equation with respect to *r* yields

$$
r \to \infty : \psi = \tfrac{U_\infty r^2}{2} \sin^2\theta \ . \tag{B.24}
$$

This expression serves as a boundary condition for the general solution. Motivated by its form, we assume that the full solution for ψ can be separated into radial and angular components, and propose an ansatz of the form

$$
\psi(r,\theta) = f(r) \sin^2\theta \ . \tag{B.25}
$$

This choice not only satisfies the far field structure but also simplifies the PDE (B.22), as all angular dependence is now contained in the $\sin^2\theta$ term. Substituting the ansatz into the governing PDE and factoring out the angular part leads to an ordinary differential equation for the radial function *f*(*r*)

$$
\left(\tfrac{d^2}{dr^2} - \tfrac{2}{r^2} \right)^2 f = 0 \ . \tag{B.26}
$$

This is a fourth-order linear differential equation with variable coefficients. A common solution approach is to assume a power-law of the form $f(r) \sim r^n$. Substituting into the differential equation yields a characteristic equation with possible powers $n \in \{-1, 1, 2, 4\}$. Thus, the solution ansatz for *f*(*r*) can be written as a linear combination of these power laws, thus $f(r) = Ar^{-1} + Br + Cr^2 + Dr^4$. The ansatz for the general stream function thus becomes

$$
\psi = \left(\tfrac{A}{r} + Br + Cr^2 + Dr^4 \right) \sin^2\theta \ . \tag{B.27}
$$

To determine the constants *A*, *B*, *C*, and *D*, we now apply the boundary conditions. From the far field behavior (B.24), we identify $C = U_\infty/2$ and must set $D = 0$ to prevent the solution from diverging as $r \to \infty$. The remaining constants *A* and *B* are fixed by the no-slip boundary conditions at the sphere's surface (Eq. (B.14)), which require the velocity components to vanish at $r = R$. Using the expressions for u_r and u_θ in terms of ψ from Eq. (B.23), we evaluate at $r = R$

$$\begin{aligned} u_r &= \quad 0 = \tfrac{U_\infty}{2}\,\cos\theta + \tfrac{A}{R^3}\,\cos\theta + \tfrac{B}{R}\,\cos\theta \ , \\ u_\theta &= \quad 0 = -U_\infty\,\sin\theta + \tfrac{3A}{2R^3}\,\sin\theta - \tfrac{B}{2R}\,\sin\theta \ . \end{aligned} \tag{B.28}$$

These simplify to a linear system for *A* and *B*

$$\begin{aligned} \tfrac{U_\infty}{2} + \tfrac{A}{R^3} + \tfrac{B}{R} &= \quad 0 \ , \\ -U_\infty + \tfrac{3A}{2R^3} - \tfrac{B}{2R} &= \quad 0 \ , \end{aligned} \tag{B.29}$$

with the solution

$$A = \tfrac{U_\infty R^3}{4}, \qquad B = -\tfrac{3UR}{4} \ . \tag{B.30}$$

Substituting the values of *A*, *B*, and *C* into the expression for ψ yields the final stream function

$$\psi = \tfrac{U_\infty}{2}\left(r^2 + \tfrac{R^3}{2r} - \tfrac{3Rr}{2}\right)\sin^2\theta \ . \tag{B.31}$$

Physical Deductions The final expressions for the **velocity components** follow from the stream function in the previous section. The radial and tangential velocity components in spherical coordinates as functions of position read

(B.32)

$$
\begin{aligned}
u_r &= \; U_\infty \cos\theta \left(1 - \tfrac{3R}{2r} + \tfrac{R^3}{2r^3}\right) \,, \\
u_\theta &= -U_\infty \sin\theta \left(1 - \tfrac{3R}{4r} - \tfrac{R^3}{4r^3}\right) \,.
\end{aligned}
$$

The expressions describe the velocity field of the steady, axisymmetric Stokes flow around a rigid sphere. As expected, the flow tends toward the uniform background velocity U_∞ far from the sphere, while the terms involving inverse powers of r represent the disturbance induced by the presence of the sphere. Both velocity components vanish at $r = R$, satisfying the no-slip boundary condition at the surface of the sphere.

We now compute the **pressure distribution** around the sphere. This can be obtained directly from the momentum equation. In particular, we focus on the r-component of Eq. (B.13), written here in the form

$$
\frac{\partial p}{\partial r} = -\rho\nu(\nabla \times (\nabla \times \mathbf{u}))_r \,. \tag{B.33}
$$

Substituting the expression for the velocity field derived from the stream function and evaluating the radial component of the double curl (see e.g., Lamb (1932)), we find

$$
\frac{\partial p}{\partial r} = \frac{3\mu U_\infty R}{2r^3} \cos\theta \,. \tag{B.34}
$$

This expression indicates that the pressure decreases with distance from the sphere along the flow direction. To find the pressure distribution, we integrate the expression in the radial direction to infinity. Assuming the pressure decays to the ambient value p_∞ at large distances, we obtain

$$
p(r,\theta) = p_\infty - \tfrac{3}{2}\frac{\mu U_\infty R}{r^2} \cos\theta \,. \tag{B.35}
$$

This pressure field reflects the symmetry of the problem, as it is axisymmetric and varies with $\cos\theta$, as expected for flow aligned with

the z-axis. The pressure is highest at the front stagnation point ($\theta = 0$) and lowest at the rear stagnation point ($\theta = \pi$).

We now compute the viscous **stress components** acting on the surface of the sphere. The relevant components in spherical coordinates are the normal stress T_{rr} and the shear stress $\tau_{r\theta}$. These are expressed in terms of the pressure and the rate of strain tensor as

$$T_{rr} = -p + 2\mu S_{rr} \ , \qquad \tau_{r\theta} = 2\mu S_{r\theta} \ . \tag{B.36}$$

First, we compute the radial strain rate

$$S_{rr} = \tfrac{\partial u_r}{\partial r} = U_\infty \cos\theta \Big(\tfrac{3R}{2r^2} - \tfrac{3R^3}{2r^4} \Big) \ . \tag{B.37}$$

Evaluating this expression on the surface of the sphere ($r = R$), we find $S_{rr} = 0$, and accordingly $\tau_{rr} = 0$, so that the radial normal stress on the surface reduces to

$$T_{rr} = -p + \tau_{rr} = -p_\infty + \tfrac{3}{2} \tfrac{\mu U_\infty}{R} \cos\theta \ . \tag{B.38}$$

Next, we evaluate the tangential strain rate $S_{r\theta}$. This component involves derivatives of both u_r and u_θ with

$$S_{r\theta} = \tfrac{1}{2} \Big(r \tfrac{\partial}{\partial r} \big(\tfrac{u_\theta}{r} \big) + \tfrac{1}{r} \tfrac{\partial u_r}{\partial \theta} \Big) \ . \tag{B.39}$$

Carrying out the differentiation, and substituting the expressions for the velocity components, we obtain

$$S_{r\theta} = -\tfrac{3}{4} \tfrac{U_\infty R^3}{r^4} \sin\theta \ . \tag{B.40}$$

Evaluating this on the surface at $r = R$ gives

$$T_{r\theta} = \tau_{r\theta} = 2\mu S_{r\theta} = -\tfrac{3}{2} \tfrac{\mu U_\infty}{R} \sin\theta \ . \tag{B.41}$$

The **total force** on the sphere is obtained by integrating the surface stress components in flow direction, i.e., along the z-axis. The relevant

projection of the stress vector in this direction is

$$\Sigma_z = T_{rr}\,\cos\theta - T_{r\theta}\,\sin\theta\ . \tag{B.42}$$

Substituting the expressions derived above

$$\Sigma_z = \left(-p_\infty + \tfrac{3}{2}\,\tfrac{\mu U_\infty}{R}\,\cos\theta\right)\cos\theta + \tfrac{3}{2}\,\tfrac{\mu U_\infty}{R}\,\sin^2\theta\ , \tag{B.43}$$

and with the identity $\cos^2\theta + \sin^2\theta = 1$, we simplify

$$\Sigma_z = -p_\infty\,\cos\theta + \tfrac{3}{2}\,\tfrac{\mu U_\infty}{R}\ . \tag{B.44}$$

The term involving p_∞ integrates to zero over the surface of the sphere due to its symmetry relative to $\theta = \pi/2$. Hence, the net drag force in the z-direction is

$$F_D = \int_0^{2\pi} R d\phi \int_0^{\pi} d\theta\ \sin\theta \cdot R^2 \quad \Sigma_z = \tfrac{3}{2}\,\tfrac{\mu U_\infty}{R} 4\pi R^2 = 6\pi\mu U_\infty R\ . \tag{B.45}$$

This is the classical result known as **Stokes' law**, which states that the drag force on a sphere at low Reynolds number is directly proportional to its radius and velocity, and to the dynamic viscosity of the fluid. For convenience, we can express this in terms of the sphere diameter $D = 2R$, giving $F_D = 3\pi\mu U_\infty D$. The corresponding nondimensional drag coefficient is defined as

$$C_D = \frac{F_D}{\frac{1}{2}\rho U_\infty^2 \pi R^2} = \frac{24}{\mathrm{Re}_D}\ , \tag{B.46}$$

where $\mathrm{Re}_D = \frac{\rho U_\infty D}{\mu}$ is the diameter based Reynolds number. This inverse relationship between C_D and Re_D characterizes creeping flow and is referred to as the **Stokes formula**.

Appendix C

Mathematical Background

C.1 The Normal Equation

In hybrid modeling, we frequently encounter overdetermined systems of equations arising from parameter estimation, model calibration, or the regression of empirical closure terms against experimental or simulated data. In many such problems, the model can be assumed to be **linear in the unknown parameters**, even if it may be nonlinear in the physical input variables, as discussed in Sect. 8.1. Under this assumption, the estimation task can be formulated as a linear system of the form

$$\mathbf{A}\mathbf{x} = \mathbf{b} \ , \tag{C.1}$$

with $\mathbf{A} \in \mathbb{R}^{m \times n}$ denoting the **feature matrix**, constructed from input variables, $\mathbf{x} \in \mathbb{R}^n$ the vector of unknown parameters, and $\mathbf{b} \in \mathbb{R}^m$ the vector of observed outputs. In typical data-driven settings, the number of observations satisfies $m \gg n$, resulting in an overdetermined system that is generally inconsistent, meaning that no exact solution $\mathbf{x}$ exists such that $\mathbf{A}\mathbf{x} = \mathbf{b}$ holds entry-wise. In such cases, we aim to find an approximate solution $\hat{\mathbf{x}}$ that minimizes the squared L_2-norm of the residual vector $\mathbf{r} := \mathbf{A}\mathbf{x} - \mathbf{b}$, that is

$$\|\mathbf{A}\mathbf{x} - \mathbf{b}\|_2^2 = \min_{\mathbf{x} \in \mathbb{R}^n} \ \|\mathbf{A}\mathbf{x} - \mathbf{b}\|_2^2 \ . \tag{C.2}$$

Defining the objective function $f : \mathbb{R}^n \to \mathbb{R}$ as

$$f(\mathbf{x}) := \|\mathbf{A}\mathbf{x} - \mathbf{b}\|_2^2 = (\mathbf{A}\mathbf{x} - \mathbf{b})^\top (\mathbf{A}\mathbf{x} - \mathbf{b}) \ , \tag{C.3}$$

the gradient is obtained by expanding the scalar product

(C.4)

$$
\begin{aligned}
f(\mathbf{x}) &= (\mathbf{A}\mathbf{x} - \mathbf{b})^\top (\mathbf{A}\mathbf{x} - \mathbf{b}) \\
&= \mathbf{x}^\top \mathbf{A}^\top \mathbf{A}\mathbf{x} - \mathbf{b}^\top \mathbf{A}\mathbf{x} - \mathbf{x}^\top \mathbf{A}^\top \mathbf{b} + \mathbf{b}^\top \mathbf{b} \\
&= \mathbf{x}^\top \mathbf{A}^\top \mathbf{A}\mathbf{x} - 2\mathbf{x}^\top \mathbf{A}^\top \mathbf{b} + \mathbf{b}^\top \mathbf{b} \ .
\end{aligned}
$$

The least squares problem necessarily satisfies $\nabla f(\mathbf{x}) = 0$.
Differentiating the objective function with respect to $\mathbf{x}$ yields

$$
\mathbf{A}^\top \mathbf{A}\mathbf{x} = \mathbf{A}^\top \mathbf{b} \ . \tag{C.5}
$$

This relation is referred to as the **normal equation**, and provides the optimality condition for the least squares solution. It follows that the residual vector $\mathbf{r} = \mathbf{A}\mathbf{x} - \mathbf{b}$ is orthogonal to the column space of $\mathbf{A}$,

$$
\mathbf{A}^\top (\mathbf{A}\mathbf{x} - \mathbf{b}) = 0 \quad \Leftrightarrow \quad \mathbf{A}^\top \mathbf{r} = 0 \ . \tag{C.6}
$$

To confirm convexity, we compute the Hessian of $f(\mathbf{x})$ as the matrix of second derivatives

$$
H := \left(\frac{\partial^2 f}{\partial x_i \partial x_j} \right) = 2\mathbf{A}^\top \mathbf{A} \ . \tag{C.7}
$$

Since $\mathbf{A}^\top \mathbf{A}$ is symmetric and positive semi-definite, the objective function is convex. In particular, the condition for a local minimum requires the Hessian to be positive definite, that is second derivatives strictly greater than zero along all directions. If
$\text{rank}\ (\mathbf{A}) = n = \min\ (m, n)$, then $\mathbf{A}^\top \mathbf{A}$ is positive definite and invertible, and the minimizer is unique with

$$
\mathbf{x} = (\mathbf{A}^\top \mathbf{A})^{-1} \mathbf{A}^\top \mathbf{b} \ . \tag{C.8}
$$

If $\mathbf{A}$ does not have full column rank, then $\mathbf{A}^\top \mathbf{A}$ is singular and not invertible. This occurs, for instance, when redundant or linearly dependent features are present in the model. In such cases, computing the exact inverse becomes numerically unstable or undefined. To overcome this, numerical solvers rely on the *Moore-Penrose*

pseudoinverse, which always exists and yields the minimum-norm solution to Eq. (C.2), even in rank-deficient or underdetermined settings. The pseudoinverse is computed via the singular value decomposition (SVD). As discussed in detail in the following Sect. C.2, the SVD expresses any matrix $\mathbf{A} \in \mathbb{R}^{m \times n}$ as

$$\mathbf{A} = \mathbf{U}\mathbf{S}\mathbf{V}^\top \ , \tag{C.9}$$

where $\mathbf{U} \in \mathbb{R}^{m \times m}$ and $\mathbf{V} \in \mathbb{R}^{n \times n}$ are orthogonal, and $\mathbf{S} \in \mathbb{R}^{m \times n}$ is diagonal with non-negative singular values. Letting $r = \text{rank}\,(\mathbf{A})$, the decomposition is partitioned as

$$\mathbf{A} = \begin{bmatrix} \mathbf{U}_1 & \mathbf{U}_2 \end{bmatrix} \begin{bmatrix} \mathbf{S}_1 & 0 \\ 0 & 0 \end{bmatrix} \begin{bmatrix} \mathbf{V}_1 & \mathbf{V}_2 \end{bmatrix}^\top = \mathbf{U}_1 \mathbf{S}_1 \mathbf{V}_1^\top \ , \tag{C.10}$$

where the block structure separates the nonzero and zero singular values. The lower block with zeros corresponds to directions in which $\mathbf{A}$ has zero eigenvalues, which prevents the exact inverse from existing. The reduced factors $\mathbf{U}_1 \in \mathbb{R}^{m \times r}$, $\mathbf{S}_1 \in \mathbb{R}^{r \times r}$, and $\mathbf{V}_1 \in \mathbb{R}^{n \times r}$ contain only the nonzero singular values and associated singular vectors. The **pseudoinverse** of $\mathbf{A}$ is then given by

$$\mathbf{A}^+ = \mathbf{V}_1 \mathbf{S}_1^{-1} \mathbf{U}_1^\top \ . \tag{C.11}$$

This formulation is robust to noise and redundancy, and is well suited for coping with imperfect data that may lead to ill-conditioned feature matrices.

C.2 The Singular Value Decomposition

In many applications, it is useful to understand not only how a linear system can be solved, but also how a matrix itself acts as a transformation of space. The singular value decomposition (SVD) provides exactly that insight. For any matrix $\mathbf{A} \in \mathbb{R}^{m \times n}$, it can be expressed as a product of two orthogonal matrices and a diagonal scaling. In this way, the SVD captures the geometric characterization of

the action of $\mathbf{A}$ on vectors. To explore how $\mathbf{A}$ transforms vectors, consider the ratio

$$R(\mathbf{x}) = \frac{\|\mathbf{A}\mathbf{x}\|}{\|\mathbf{x}\|}, \qquad \mathbf{x} \neq \mathbf{0} \ . \tag{C.12}$$

This measures how much $\mathbf{A}$ stretches or shrinks a given vector $\mathbf{x}$. Since scaling $\mathbf{x}$, that is $\alpha\mathbf{x}$ with $\alpha \in \mathbb{R}$, does not change the ratio, we can restrict attention to unit vectors $\|\mathbf{x}\| = 1$. Squaring gives

$$R(\mathbf{x})^2 = \|\mathbf{A}\mathbf{x}\|^2 = \mathbf{x}^\top \mathbf{A}^\top \mathbf{A}\mathbf{x} \ . \tag{C.13}$$

The stationary points of this quadratic form are eigenvectors $\mathbf{v}_i$ of $\mathbf{A}^\top\mathbf{A} \in \mathbb{R}^{n\times n}$, with eigenvalues $\lambda_i \geq 0$. Because $\mathbf{A}^\top\mathbf{A}$ is symmetric and positive semi-definite, these eigenvectors can always be chosen mutually perpendicular and of unit length. This means they form an **orthonormal basis** of $\mathbb{R}^n$, so that the vectors are orthogonal to each other, $\mathbf{v}_i^\top \mathbf{v}_j = 0$ for $i \neq j$, each has norm one with $\|\mathbf{v}_i\| = 1$, and together they span the entire space $\mathbb{R}^n$. For each eigenvector $\mathbf{v}_i$ of $\mathbf{A}^\top\mathbf{A}$, we define a new vector $\mathbf{u}_i := \mathbf{A}\mathbf{v}_i$. Substituting this relation gives

$$\mathbf{A}^\top\mathbf{A}\mathbf{v}_i = \lambda_i \mathbf{v}_i \quad \Rightarrow \quad \mathbf{A}\mathbf{A}^\top(\mathbf{A}\mathbf{v}_i) = \lambda_i(\mathbf{A}\mathbf{v}_i) \ , \tag{C.14}$$

that is equivalent to $\mathbf{A}\mathbf{A}^\top\mathbf{u}_i = \lambda_i\mathbf{u}_i$. Thus, $\mathbf{u}_i$ is either the zero vector (when $\lambda_i = 0$) or an eigenvector of $\mathbf{A}\mathbf{A}^\top \in \mathbb{R}^{m\times m}$ with the same eigenvalue. This shows that the nonzero eigenvalues of $\mathbf{A}^\top\mathbf{A}$ and $\mathbf{A}\mathbf{A}^\top$ coincide, and that their eigenvectors are linked through the mapping $\mathbf{u}_i = \mathbf{A}\mathbf{v}_i$. Normalizing $\mathbf{u}_i$ and $\mathbf{v}_i$ to unit length, we assemble them into the matrices

$$\mathbf{U}_1 = \begin{bmatrix} \mathbf{u}_1 & \cdots & \mathbf{u}_r \end{bmatrix} \in \mathbb{R}^{m\times r}, \qquad \mathbf{V}_1 = \begin{bmatrix} \mathbf{v}_1 & \cdots & \mathbf{v}_r \end{bmatrix} \in \mathbb{R}^{n\times r}, \tag{C.15}$$

where $r = \text{rank}\,(\mathbf{A})$. The corresponding positive square roots $\sigma_i = \sqrt{\lambda_i}$ are called the **singular values** of $\mathbf{A}$. With $\mathbf{S}_1 = \text{diag}\,(\sigma_1, \ldots, \sigma_r)$ we then have

$$\mathbf{U}_1^\top \mathbf{A} \mathbf{V}_1 = \mathbf{S}_1 \ . \tag{C.16}$$

To obtain a full factorization, we extend $\mathbf{U}_1$ and $\mathbf{V}_1$ to complete orthogonal bases $\mathbf{U} \in \mathbb{R}^{m \times m}$ and $\mathbf{V} \in \mathbb{R}^{n \times n}$ by adding vectors corresponding to zero eigenvalues. In this way, the decomposition takes the form

$$\mathbf{A} = \begin{bmatrix} \mathbf{U}_1 & \mathbf{U}_2 \end{bmatrix} \begin{bmatrix} \mathbf{S}_1 & 0 \\ 0 & 0 \end{bmatrix} \begin{bmatrix} \mathbf{V}_1 & \mathbf{V}_2 \end{bmatrix}^\top = \mathbf{U} \mathbf{S} \mathbf{V}^\top \ , \tag{C.17}$$

with $\mathbf{S} \in \mathbb{R}^{m \times n}$ a rectangular diagonal matrix containing the singular values $\sigma_1 \geq \sigma_2 \geq \cdots \geq 0$ on its main diagonal. A schematic overview of the decomposition is shown in Fig. C.1, illustrating the shapes of the factors and the orthogonality relations $\mathbf{U}^\top \mathbf{U} = \mathbf{I}_m$ and $\mathbf{V}^\top \mathbf{V} = \mathbf{I}_n$.

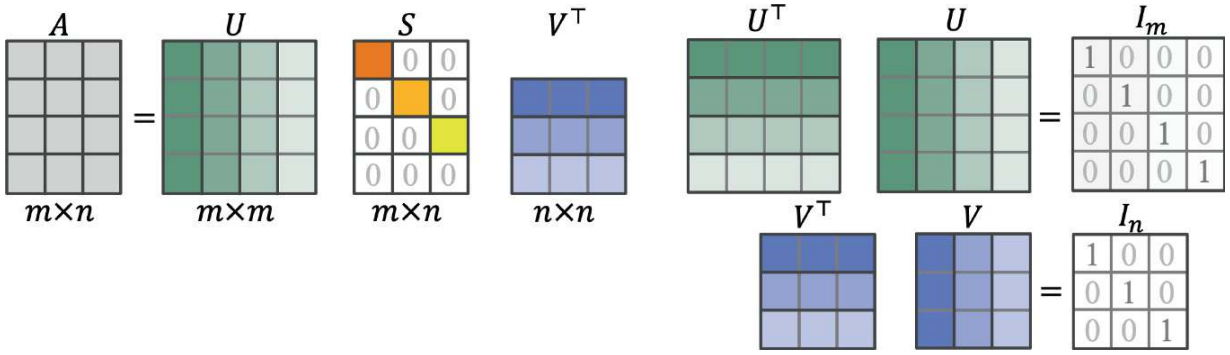


Fig. 2 Singular value decomposition of $\mathbf{A} \in \mathbb{R}^{m \times n}$, showing matrix dimensions and orthogonality relations. Adapted from Wikipedia (2018)

When $\mathbf{A}$ has rank $r < \min(m, n)$, many of its singular values are zero. In this case, it is often convenient to discard the corresponding vectors and write the **reduced SVD** as

$$\mathbf{A} = \mathbf{U}_1 \mathbf{S}_1 \mathbf{V}_1^\top \ , \tag{C.18}$$

where $\mathbf{U}_1 \in \mathbb{R}^{m \times r}$, $\mathbf{S}_1 \in \mathbb{R}^{r \times r}$, and $\mathbf{V}_1 \in \mathbb{R}^{n \times r}$ contain only the singular vectors and singular values associated with the nonzero part of the spectrum. This compact representation highlights the effective

degrees of freedom of $\mathbf{A}$ and is central to applications such as the pseudoinverse and low-rank approximation, discussed in Sect. C.1.

In the geometric characterization of the action of $\mathbf{A}$, the decomposition shows that any matrix $\mathbf{A}$ can be understood as the composition of three simple transformations. The right singular vectors in $\mathbf{V}$ specify a rotation or reflection of $\mathbb{R}^n$, the diagonal matrix $\mathbf{S}$ scales the resulting coordinates along orthogonal directions by the singular values σ_i, and finally the left singular vectors in $\mathbf{U}$ apply another rotation or reflection in $\mathbb{R}^m$. Geometrically, this means that $\mathbf{A}$ maps the unit sphere in $\mathbb{R}^n$ to an ellipsoid in $\mathbb{R}^m$, whose principal axes have lengths given by the singular values and directions determined by the left singular vectors $\mathbf{u}_i$.

An important property of the SVD is that transposition simply swaps the roles of $\mathbf{U}$ and $\mathbf{V}$. If $\mathbf{A} = \mathbf{U}\mathbf{S}\mathbf{V}^\top$, then

$$\mathbf{A}^\top = \mathbf{V}\mathbf{S}\mathbf{U}^\top, \tag{C.19}$$

since $\mathbf{S}$ is diagonal. Thus $\mathbf{A}$ and $\mathbf{A}^\top$ share the same singular values, and in particular $\|\mathbf{A}\|_2 = \|\mathbf{A}^\top\|_2$, meaning the induced L_2-norm is invariant under transposition. This also highlights the close link between singular values and eigenvalues. While the eigenvalue decomposition applies only to square matrices, the SVD extends the idea to all rectangular matrices, with the singular values acting as generalized eigenvalues that capture the stretching effect of $\mathbf{A}$. We recall that $\mathbf{U}$ and $\mathbf{V}$ are orthogonal matrices, meaning that their columns form orthonormal bases of $\mathscr{R}^m$ and $\mathscr{R}^n$, respectively. In matrix terms this is expressed as $\mathbf{U}^\top\mathbf{U} = \mathbf{I}_m$ and $\mathbf{V}^\top\mathbf{V} = \mathbf{I}_n$, as also illustrated in Fig. C.1. In the reduced SVD, the factors $\mathbf{U}_1$ and $\mathbf{V}_1$ have fewer columns, but their columns remain orthonormal, so that $\mathbf{U}_1^\top\mathbf{U}_1 = \mathbf{I}_r$ and $\mathbf{V}_1^\top\mathbf{V}_1 = \mathbf{I}_r$ on the corresponding subspaces. Using these properties, we find that

$$\begin{aligned} \mathbf{A}^\top\mathbf{A} &= \mathbf{V}\mathbf{S}^\top\mathbf{U}^\top\mathbf{U}\mathbf{S}\mathbf{V}^\top = \mathbf{V}\mathbf{S}^2\mathbf{V}^\top, \\ \mathbf{A}\mathbf{A}^\top &= \mathbf{U}\mathbf{S}\mathbf{V}^\top\mathbf{V}\mathbf{S}^\top\mathbf{U}^\top = \mathbf{U}\mathbf{S}^2\mathbf{U}^\top. \end{aligned} \tag{C.20}$$

Hence, the squared singular values $\sigma_1^2, \ldots, \sigma_r^2$ are exactly the nonzero eigenvalues of both $\mathbf{A}^\top \mathbf{A}$ and $\mathbf{A}\mathbf{A}^\top$, with $\mathbf{v}_i$ as eigenvectors of $\mathbf{A}^\top \mathbf{A}$ and $\mathbf{u}_i$ as eigenvectors of $\mathbf{A}\mathbf{A}^\top$.

References

Acheson DJ, Acheson FDJ (1990) Elementary fluid dynamics. Clarendon Press

Back LH (1968) Conservation equations of a viscous, heat-conducting fluid in curvilinear orthogonal coordinates. Technical report 32-1332, NASA-JPL, 1968

Gomaa H (2014) Modeling of liquid dynamics in spray laden compressor flows. Verlag Dr. Hut

Lamb H (1932) Hydrodynamics. The University Press

Spurk J (1996) Strömungslehre: Einführung in die Theorie der Strömungen. Springer

Stokes GG (1851) On the effect of the internal friction of fluids on the motion of pendulums. Camb Philos Trans 9:8–106

White FM (1991) Viscous fluid flow, 2nd edn. McGraw-Hill

Wikipedia (2018) Singular value decomposition. Accessed: 2025-09-24

Index

A

Acceleration 69
Adiabatic 12, 152
  index 65
  reversible 64, 80, 150, 151
Anomaly detection 272, 303–308
Anscombe's quartet 276
Asymptotic regime 100, 325, 327

B

Base quantity 46
Bayes' theorems 222
Bernoulli equation 150
Best efficiency point 371
Boundary conditions 87–91
  fluid interface 89, 90
  free surface 89, 90
  solid interface 88, 89
Boundary layer 104–106, 173, 322
  Blasius equation 174
  equations 123
  momentum 104, 173
  pressure gradient 175
  thermal 105, 176, 322
Boxplot 254
Buckingham Π-theorem 48–56, 99, 128
Bulk modulus 66

C

Capacity 156
Causality 6
Central limit theorem 244

Characteristic scale 99
capillary length 122
convective timescale 100
diffusive timescale 100
turbulent mixing length 115
Chebyshev inequality 241
Choked flow 156
Classification 271, 284–295, 391
F_1-score 290
accuracy 289
binary 284
confusion matrix 289
multiclass 293
multinomial 294
one versus all 293
performance measures 289
precision 290
recall 290
regularization 288
ROC curve 289, 292
sigmoid function 285
Clustering 271, 295–298, 388, 391
Compressible fluid 97, 101
Compressor 152, 377
axial 164
centrifugal 167
choking 136
map 136
operating line 136
surge line 136
Confidence intervals 258
Conservation laws 3, 57, 77, 402
angular momentum 163
energy 79, 84, 85, 147, 315, 404

mass 78, 79, 83, 147, 402
momentum 78, 79, 84, 147, 403
Control volumes 82
Convective derivative 82
Cordier diagram 138
Correlation 6, 230
Cost function 274, 287
convexity 275
Couette flow 116
Coupling degree 16, 364
Covariance 231, 300
Creeping flow 127, 320, 410
Critical point 60
Curvilinear coordinates 399, 410

D

Data 31–41
information 31
label 31
metadata 31
Data measurement scale 32–33
interval 33
nominal 32
ordinal 33
ratio 33
Data quality, 41
Data source, 39
analytical 312, 317
numerical 333, 338, 339, 342
operational 366, 377, 386
Data types, 33
categorical 31
continuous 32
discrete 32
numerical 31, 32

Data quality 39
Data source 33
  analytical 34
  experimental 36
  numerical 35
  operational 38
Data types 31
Degradation 369, 391
Density 62
Dimension matrix 49
Dimensionality 16
Dimensionality Reduction 298–303
Dimensionality reduction 272, 388
Dimensionless product 48, 55
  Bond number 121
  Darcy friction factor 170
  drag coefficient 171, 181, 317
  Eckert number 107
  Fanning friction factor 170
  flow coefficient 131, 140, 367
  Froude number 121
  Grashof number 106
  loss coefficient 170, 202
  Mach number 101, 154
  Nusselt number 107, 171, 322
  Ohnesorge number 122, 330
  Peclet number 105
  power coefficient 131, 367
  Prandtl number 105, 322
  pressure coefficient 131, 367
  Reynolds number 103, 330, 337, 338
  skin friction coefficient 169, 190
  stage loading coefficient 140, 141
  stage reaction 142

Stanton number 107
Strouhal number 100
turbulent Prandtl number 112
Weber number 122, 330
Dissipation 404
Distribution 232, 256, 305
F-distribution 258, 268
χ^2-distribution 257, 264, 268, 308
t-distribution 256
binomial 234
lognormal 237
normal 236
Poisson 235
uniform 232, 234
Weibull 238
Drop wall impact 329–337, 338
deposition 331
impact factor 332
splashing 331
splashing threshold 330, 334
Dynamic viscosity 70, 71

E

Efficiency 161, 369, 382
Energy dissipation 63, 79, 80, 85, 86, 106, 189, 315, 404
Enthalpy 63, 86, 378, 403
fusion 59
relative total 164
total 148, 404
vaporization 59
Entropy 63, 86, 87
production 63, 64, 79, 80, 87, 88, 149, 152, 157
transfer 63
Euler equations 103, 124

Euler work equation 163
Eulerian description 81
Expected value 224–226
External flow 172–186

F

Failure mechanism 357, 366
Failure mode 366, 387, 391
Feature 272
  matrix 272, 417
  vector 272
Flow regime 99
  compressible 101, 134, 153, 154
  creeping flow 127, 180, 320, 410
  hypersonic 102
  incompressible 101, 129, 153
  inviscid 103
  laminar 108
  potential flow 126
  subsonic 102
  supersonic 102, 153
  transonic 102
  turbulent 108–121, 337, 338
  viscous 103
Fourier's law 73, 403

G

Gibbs equation 65, 86, 87

H

Harmonic oscillator 407
Head 150, 369
Heat 62
Heat capacity 64
Heat transfer coefficient 90, 91, 171, 322

Hugoniot equation 157
Hydraulic diameter 170, 171, 196, 197
Hypothesis testing 260–268
  p-value 262
  dispersion test 261, 268
  distribution test 261, 264
  error 262
  hypothesis 261
  location test 261, 266
  multigroup test 261
  null hypothesis 261
  one-sample test 261, 264, 266
  significance level 262
  two-sample test 261, 264, 267, 268

I

Ideal gas 60, 67
  calorically perfect 68, 97, 151
  thermally perfect 97
Incompressible fluid 68, 83, 95, 149
Internal energy 62, 86, 403
Internal flow 186–208
Irreversible 63, 65, 80, 85–87, 149, 151, 157
Irrotational field 69
Isentropic 64, 150, 151, 154
Isentropic compressibility 67
Isentropic exponent 65
Isobaric thermal expansivity 66
Isochoric pressure coefficient 66
Isothermal compressibility 66

K

Kinematic viscosity 71
Knowledge 2, 24, 27–31, 313, 318, 324
  algebraic equations 29, 48, 76

definition 27
differential equations 29, 123
formalization 28
industrial domain 355, 356
industry standards 357
invariances 29, 48, 69
knowledge graphs 30
logic rules 29
representation 29, 54
stochastic relations 30
Kolmogorov hypotheses 114
Kurtosis 227

L

Lagrangian description 81
Laval nozzle 155
Law of large numbers 240
Law of the wall 117
buffer zone 118, 200
outer layer 118, 119, 201
pressure gradient 120
viscous sublayer 118
Liquid saturation curve 59
Local derivative 82

M

Mahalanobis distance 307
Markov inequality 240
Mass diffusivity 70
Material derivatives 81
Model 1, 3, 17
black-box 4
grey-box 5, 323
hybrid model 3
linear 18, 273, 279, 417

parameters 4, 273
requirements 22–24
scope 4, 19
structure 3, 17, 272, 273, 279
subscale 169
variables 3, 272
white-box 4, 312, 317
Modeling 1, 8, 11, 20–27
hypothesis 9, 26
modeling flow 8
modeling flow 25
objective 20, 22–24, 311, 312, 317, 324, 329
purpose 20–21, 311, 312, 317, 323, 329
strategy 20, 24–27, 311, 312, 317, 324, 329

N

Near wall shear flow 116–121
Newtonian fluids 71, 403
Normal equation 277, 417
Normalization 253

O

Operational profile 357, 372–374, 376, 380–382, 388
Overfitting 281, 288

P

Pendulum 312
Perfect gas 95, 97, 125, 134, 151, 154, 158, 165, 166
Phase 58
vapor quality 60
Physical variables 46–48
base quantity 46
solitary 54
base quantity system 47
base units 47

derived quantities 47
equations 48
nondimensional 48
unit 47
Pipe flow 187
Borda-Carnot equation 205
constant wall heat flux 192
constant wall temperature 194
contraction 205
entrance 206
entrance length 197, 206
expansion 203, 205
fully developed 187
fully developed thermal 192
Hagen-Poiseuille flow 187
inlet 207
loss coefficient 202
noncircular duct 195
rough wall 200
rough walls 198
smooth walls 198
temperature profile 191
turbulent 197, 337, 338
Potential flow 126
Pressure 62
mechanical 73
thermodynamic 73
total 148, 149
Principal component analysis 299, 388, 391
retained variance 301
Principal strain rates 69
Probability 214–232
distribution 219, 223, 224
elementary event 217

event 216
event space 218
independence 223, 229, 265
map 221
random variable 219
sample space 216
space 216
uncorrelatedness 230
Probability distribution 223
Pseudoinverse 277, 418
Pump 167, 366–377
Pure substance 58

Q

Quartiles 252

R

Random experiment 215
Rate of strain tensor 69, 72, 110, 403, 414
Real gas 99
Regression 7, 271–283, 327, 334, 345, 346, 376, 382, 391
regularization 282, 283, 345, 346
Reliability 370
curve 371
mean time between failures 371, 374
remaining useful life 386, 391
Reynolds analogy 179
Reynolds stress tensor 109
Reynolds transport theorem 82
Reynolds-averaged Navier-Stokes equations 109, 337, 338
Rotation rate tensor 70
Rothalpy 163

S

Scientific method 36

deduction 8
induction 8
Scientific method 8
Second Law of Thermodynamics 79, 80, 86, 87, 315
Sensor 361–364, 379, 386
auxiliary 362, 379
condition 361, 379, 385
control 130, 361, 379
process 361, 379, 380, 382
Shock wave 102, 156, 157
Similarity 128
complete 129
partial 129
turbomachine 128–142, 366
Singular value decomposition 300, 419
Skewness 227
Speed of sound 56, 65, 67, 68, 101, 153, 155, 158
Sphere flow 179–186, 317–322, 409–415
drag correlations 184, 317, 321
drag crisis 184
high Re regime 182
Stokes' law 181, 409, 415
Stagnation state
State equation 61, 65–68
caloric 61
thermal 61
Statistics 247
descriptive 247, 248
inferential 247
interquartile range 252, 254
mean 250
median 251
mode 250
parameters 248

population 248
quartiles 252
sample 248
variance 251
Stokes flow
Stokes hypothesis 73
Strain rate 70, 338, 339
Stream function 83, 84
Stress tensor
rate of strain 69
Reynolds 109, 337, 338
total 73
viscous 72, 413
Substantial derivative 81, 82
Supercritical state 60
Surface roughness 200
Surface tension 71, 74, 89, 90, 121, 329
Sutherland formula 77
System 12, 358
adiabatic
boundary 12, 358, 359
closed 12, 78, 148
component 13, 358, 360, 366
control volumes 82
equipment 13, 356, 360, 377, 386
hierarchy 358
isolated 12
model 12
open 12, 78
part 13, 360, 366

T

T-score 256, 266, 267
Temperature 62
bulk 191

total 151
Thermal conductivity 70, 73
Thermodynamic state 61
Total state 148
enthalpy 86, 87, 148, 403, 404
pressure 148, 149
temperature 151, 154
Triple line 60
Turbine 152, 166
Turbomachine 128–142, 160–169, 172, 366–392
characteristics 129–140, 367, 382
compressible 134–137, 162
incompressible 129–134, 161
local flow parameters 140–142
multistage 139
Turbulence closure 110, 337, 338
Turbulent diffusivity 112
Turbulent energy cascade 113, 114, 340, 341
Turbulent kinetic energy 110, 340
dissipation rate 114, 340, 341
Turbulent viscosity 110, 338, 339

V

Validation 40
Vapor saturation curve 59
Variable 14–15
extensive 61
intensive 61
kinematic variables 14, 68
nondimensional 48
physical variables 46, 57
process 62
random 219
target 15, 272
thermodynamic state 61

thermodynamic variables 14, 58
transport variables 14, 70
Variance 227, 231, 240–243, 245, 251
Velocity 69
Verification 40
Viscosity 71
dynamic 71
kinematic 71
viscous stress tensor 72
Viscous stress tensor 72, 404
Vorticity 69

W

Water anomaly 59
Work 62

Z

Z-score 253, 266

Table 10.4 Specifications for Compressor Stage 1 and Stage 2

Property			**Stage 1**	**Stage 2**
Molecular weight	M	[kg/kmol]	18.37	
Mass flow rate	$\dot{m}$	[kg/s]	284.6	
Inlet pressure	p_{in}	[bar]	60.0	76.4
Inlet temperature	T_{in}	[°C]	15.0	14.8
Inlet gas density	ρ_{in}	[kg/m^3]	51.2	66.8
Inlet volume flow	Q	[m^3/h]	20000	15330
Compressibility factor	Z	[–]	0.88	0.86
Outlet pressure	p_{out}	[bar]	78.0	95.0
Outlet temperature	T_{out}	[°C]	44.8	42.9
Polytropic head	H_p	[kJ/kg]	36.7	30.3
Polytropic efficiency	η_p	[–]	0.76	0.73
Shaft power	W_{shaft}	[MW]	13.7	11.8
Rotational speed	n	[rpm]	5800.0	

Table 10.5 Overview of sensor tags by associated system, element type, measured physical quantity and unit, and location attributes

	Tag name	Quantity and type	Unit	Component	Attributes
Control	SSPI2100	Speed set point	rpm	Compressor	
Control	PSPI2101	Pressure set point	bar	Stage 1	Suction
Process	FI2100	Flow rate indicator	Nm^3/h	Compressor	
Process	SI2100A	Speed indicator	rpm	Compressor	
Process	SI2100B	Speed indicator	rpm	Compressor	
Process	PI2101	Pressure indicator	bar	Stage 1	Suction
Process	TI2101	Temperature indicator	°C	Stage 1	Suction
Process	PI2102	Pressure indicator	bar	Stage 1	Discharge
Process	TI2102	Temperature indicator	°C	Stage 1	Discharge
Process	TI2103	Temperature indicator	°C	Stage 2	Suction
Process	PI2104	Pressure indicator	bar	Stage 2	Discharge
Process	TI2104	Temperature indicator	°C	Stage 2	Discharge
Condition	VI2113A	Vibration indicator	mils	Rotor	DE
Condition	VI2113B	Vibration indicator	mils	Rotor	DE
Condition	VI2114A	Vibration indicator	mils	Rotor	NDE
Condition	VI2114B	Vibration indicator	mils	Rotor	NDE
Condition	TI2123A	Temperature indicator	°C	Radial Bearing	DE
Condition	TI2123B	Temperature Indicator	°C	Radial Bearing	DE
Condition	TI2124A	Temperature Indicator	°C	Radial Bearing	NDE
Condition	TI2124B	Temperature Indicator	°C	Radial Bearing	NDE
Condition	TI2133A	Temperature Indicator	°C	Thrust Bearing	DE
Condition	TI2133B	Temperature Indicator	°C	Thrust Bearing	DE
Condition	TI2134A	Temperature Indicator	°C	Thrust Bearing	NDE
Condition	TI2134B	Temperature Indicator	°C	Thrust Bearing	NDE
Condition	ADI2143	Axial Displacement Indicator	mils	Rotor	
Condition	ADI2144	Axial Displacement Indicator	mils	Rotor	
Support	PDI2161	Pressure Difference Indicator	bar	Lube Oil	
Support	PI2162	Pressure Indicator	bar	Lube Oil	

	Tag name	Quantity and type	Unit	Component	Attributes
Support	PI2163	Pressure Indicator	bar	Lube Oil	Supply
Support	PI2164A	Pressure Indicator	bar	Lube Oil	Supply
Support	PI2164B	Pressure Indicator	bar	Lube Oil	Supply
Support	PI2153	Pressure Indicator	bar	Seal Oil	Supply
Support	LIC2181	Level Indicator Controller	%	Oil Tank	
Support	LIC2182	Level Indicator Controller	%	Oil Tank	
Support	LI2183	Level Indicator	%	Oil Tank	

	F_D	u	ν	D
$\boldsymbol{L}$	1	1	2	1
$\boldsymbol{M}$	1	0	0	0
$\boldsymbol{T}$	-2	-1	-1	0

Table 9.2 DNS configurations used for model training and evaluation. All geometries are given in units of channel half-height $H/2$

Re_τ	$\mathrm{Re}_{\mathrm{bulk}}$	**Domain size** $(L_x, L_y, L_z)/(H/2)$	**Mesh resolution** $(N_x \times N_y \times N_z)$
180	5673 .	$6.4 \times 2 \times 3.2$	$2048 \times 480 \times 512$
395	14 124 .	$6.4 \times 2 \times 3.2$	$2048 \times 480 \times 512$
640	24 428 .	$12.8 \times 2 \times 6.4$	$1024 \times 256 \times 1024$
1020	41 441 .	$12.8 \times 2 \times 6.4$	$2048 \times 448 \times 1536$

	F_D	u	μ	ρ	D
	k_1	k_2	k_3	k_4	k_5
$\boldsymbol{L}$	1	1	-1	-3	1
$\boldsymbol{M}$	1	0	1	1	0
$\boldsymbol{T}$	-2	-1	-1	0	0

Table 5.1 Fully developed laminar flow parameters for various duct geometries (Kays et al. 2005; Shah and London 1978)

Geometry	Nu_H	Nu_T	$f_F\ \mathrm{Re}$	L^+
Parallel plates ($b/a = \infty$)	8.235	7.541	24.00	0.0056
Rectangular $b/a = 8$	6.49	5.60	20.59	0.0094
Rectangular $b/a = 4$	5.33	4.44	18.23	0.0147
Circle	4.36	3.66	16.00	0.038
Rectangular $b/a = 2$	4.12	3.39	15.55	0.0255
Square $b/a = 1$	3.61	2.98	14.23	0.0324
Equilateral triangle	3.11	2.49	13.33	0.0398

	E	ε	κ
$\boldsymbol{L}$	3	2	-1
$\boldsymbol{T}$	-2	-3	0

Table 10.2 Components of subunits within the compressor *Equipment Class* according to ISO 14224 (International Organization for Standardization 2016)

Subunit	Maintainable items
Power transmission	Gearbox/ variable drive, Bearings, Belt/ sheave, Coupling to driver, Coupling to driven unit, Lubrication, Seals, Sensors[a]
Compressor	Casing, Rotor with impellers, Balance piston, Interstage seals, Radial bearing, Thrust bearing, Shaft seals, Internal piping, Valves, Antisurge system[b], Piston, Cylinder liner, Packing, Sensors[a]
Control and monitoring	Actuating device, Control unit, Cables and junction boxes, Internal power supply, Monitoring, Sensors[a], Valves, Wiring, Piping, Seals
Lubrication system	Oil tank with heating system, Pump, Motor, Check valves, Coolers, Filters, Piping, Valves, Lube oil, Sensors[a]
Shaft seal system	Oil tank with heating, Reservoir, Pump, Motor, Gear, Filters, Valve, Seal oil, Dry gas seal, Mechanical seal, Scrubber, Sensors[a]
Miscellaneous	Base frame, Piping, pipe support and bellows, Control valves, Isolation valves, Check valves, Coolers, Silencers, Purge air, Magnetic-bearing control system, Flange joints

[a]In deviation from ISO 14224, where all sensors are assigned to the control and monitoring subunit, sensors are here allocated to their respective functional subunits to better reflect their operational context with finer granularity

[b]Including recycle valves and controllers

Table 10.6 Overview of the four turbofan datasets with their trajectories, operating conditions, and failure modes

Data set	**FD001**	**FD002**	**FD003**	**FD004**
Train trajectories	100	260	100	248
Test trajectories	100	259	100	249
Condition	Sea level	6	Sea Level	6
Failure modes	HPC	HPC	HPC, Fan	HPC, Fan

	a	p	ρ
$\boldsymbol{L}$	1	-1	-3
$\boldsymbol{M}$	0	1	1
$\boldsymbol{T}$	-1	-2	0

Table 9.1 Raw input features λ_i used for eddy viscosity model inference

Raw feature name	**Expression λ_i**
Ratio of turbulent to mean strain time scale	$\tau\|S\|$
Ratio of turbulent to mean rotation time scale	$\tau\|\Omega\|$
Ratio of mean strain to mean rotation time scale	$\|S\|/\|\Omega\|$
Ratio of wall distance and channel height	y/H
Wall-distance-based Reynolds number	$\sqrt{k}y/\nu$
Ratio of wall coordinate and turbulence time scale	y^+/τ
Ratio of production and dissipation of turbulent kinetic energy	P_k/ε
Ratio of turbulent length scale to TKE gradient decay length	$\tau\|\nabla k\|/\sqrt{k}$
Ratio of TKE convection and production	$\nabla k \cdot u/P_k$
Elliptic blending model parameter	φ
Turbulent intensity	$\sqrt{2k/(3\|u\|^2)}$
Ratio of turbulent length scale and wall distance	$2\sqrt{k}/(0.09\omega y)$
SST model variable 2	$500\nu/(\omega y^2)$

Table 3.3 Correlation coefficients for power law Eq. (3.35) and Sutherland formula Eq. (3.36) for viscosity and thermal conductivity White (1991)

Gas	T_0 [K]	μ_0 [μPa s]	k_0 [W/(m K)]	***n*** [−]	**Validity range** [K] **and error**	***S*** [K]	**Validity range** [K] **and error**
Steam	350	11.2		1.15	280–1500 ±3%	1064	360–1500 ±2%
Dry air	273	17.16		0.666	210–1900 ±3%	111	170–1900 ±2%
Steam	350		0.0181	1.35	300–900 ±2%	2200	160–2000 ±2%
Dry air	273		0.0241	0.81	210–2000 ±3%	194	300–700 ±2%

	τ	ℓ	m	g
$\boldsymbol{L}$	0	1	0	1
$\boldsymbol{M}$	0	0	1	0
$\boldsymbol{T}$	1	0	0	-2

Table 3.1 Caloric and critical data of selected substances according to Verein Deutscher Ingenieure (2013). The boiling point and vaporization enthalpy are provided at 1.013 bar

Substance	**Melting Temperature** [°C]	**Fusion Enthalpy** [kJ/kg]	**Boiling Point** [°C]	**Vaporization Enthalpy** [kJ/kg]	**Critical Temperature** [K]	**Critical Pressure** [bar]	**Critical Density** [kg/m³]
Hydrogen	259.3	58.1	252.8	459.2	33.19	13.15	30
Air	210.1	25.7	194.2	191.9	132.53	37.86	343
R143a	111.4	73.7	47.2	226.7	345.86	37.62	431
Water	0.0	333.1	100.0	2256.6	647.10	220.64	322

Table 10.7 Mapping of dataset columns to corresponding sensor signals and units

Column	Sensor	Unit	Column	Sensor	Unit
1	Engine unit number	–	14	Phys Core Speed	rpm
2	Cycle count	–	15	Engine Pres Ratio	–
3	Altitude	ft	16	Static HPC Outlet Pres	psia
4	Mach number	–	17	Fuel Flow Ratio	pps/psia
5	Throttle resolver angle	–	18	Corr Fan Speed	rpm
6	Fan inlet temp	°R	19	Corr Core Speed	rpm
7	LPC outlet temp	°R	20	Bypass Ratio	–
8	HPC outlet temp	°R	21	Burner Fuel Air Ratio	–
9	LPT outlet temp	°R	22	Bleed Enthalpy	–
10	Fan inlet pres	psia	23	Demand Fan Speed	rpm
11	Bypass duct pres	psia	24	Demand Corr Fan Speed	rpm
12	Total HPC outlet pres	psia	25	HPT Coolant Bleed	lb/s
13	Phys fan speed	rpm	26	LPT Coolant Bleed	lb/s

Table 10.1 Hierarchical classification of industrial systems based on ISO 14224 (International Organization for Standardization 2016). The taxonomy organizes systems from broad industrial context to individual parts, supporting scalable modeling and data analysis

Main category	Level	Taxonomy hierarchy	Definition	Examples
Industrial context	1	Industry	Type of main industry	Petroleum, natural gas, petrochemical
	2	Business	Type of business or processing stream	Exploration, Production, Transportation, Refining, Petrochemical Processing
	3	Installation	Type of facility	LNG plant, refinery, offshore platform,
	4	Plant category	Type of plant	Ethylene cracker, methanol plant
	5	Section	Main section of plant	Compression, liquefaction, distillation section
Equipment subdivision	6	Equipment class	Class of similar equipment units	Compressors, pumps, gas turbines, heat exchangers
	7	Subunit	Subsystem necessary for equipment unit to function	Cooling subunit, lubrication unit, control module
	8	Component	Group of parts or subsystems	Motor, gearbox, lube oil pump, pressure sensor
	9	Part	A single piece of equipment	Gasket, seal, impeller, bearing, bolt

	η	ε	ν
$\boldsymbol{L}$	1	2	2
$\boldsymbol{T}$	0	-3	-1

Table 3.2 Material properties covering density ρ, heat capacity c_p, thermal conductivity k, dynamic viscosity μ and kinematic viscosity ν for selected materials at specified temperature and atmospheric pressure. Data from Kays et al. (2005) and Verein Deutscher Ingenieure (2013)

Substance	ρ $[\mathrm{kg/m^3}]$	c_p $[\mathrm{J/(kg\ K)}]$	$\boldsymbol{k}$ $[\mathrm{W/(m\ K)}]$	μ [mPa s]	ν $[\mu\mathrm{m^2/s}]$
Steam (200 °C**)**	0.46	1979	0.334	0.0162	35.2
Dry air (20 °C**)**	1.19	1006	25.87	0.018	15.32
JP-4 fuel (15 °C**)**	776	1995	0.138	0.868	0.112
Hydraulic fluid (15 °C**)**	858	1845	0.124	19.2	22.4
Engine Oil (15 °C**)**	889	1845	0.145	1060	120
Water (20 °C**)**	998	4185	0.60	1.002	1.003
Pinewood	500	1600	0.13		
Ice (0 °C**)**	900	2000	2.2		
Plastic PP (20 °C**)**	910	1710	0.22		
Glass	2500	750	1.0		
Aluminum (0 °C**)**	2700	837	236		
Steel (0 °C**)**	7870	435	84		
Copper (0 °C**)**	8960	381	401		

Table 10.3 Hierarchical breakdown of total time for representation of availability states, operating ranges, and load conditions. Timeline definitions are adapted from ISO 14224 (International Organization for Standardization 2016)

